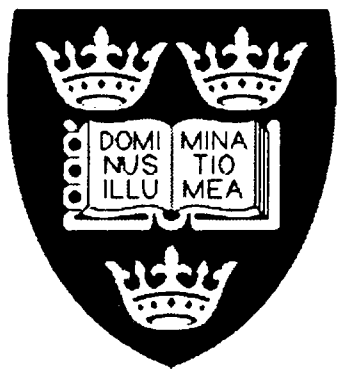
A Study of Moderately Under-Expanded Single and Twinjet Rocket Exhaust Plumes in Quiescent and in a Mach 7 Hypersonic Freestream

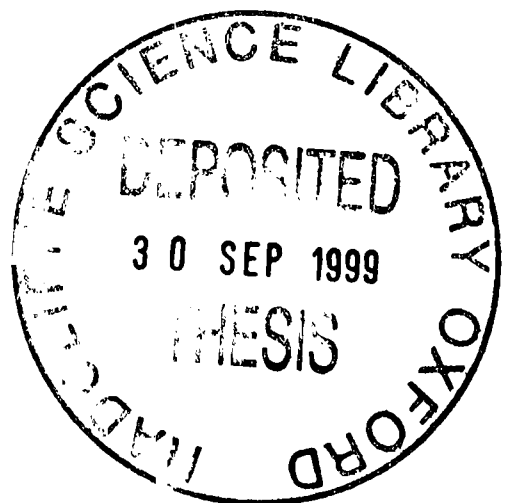
H H-W S Shek



Keble College
University of Oxford

A thesis submitted in partial fulfilment of the requirement of the degree of Doctor of Philosophy at the University of Oxford, Hilary Term, 1997

Department of Engineering Science
Parks Road, Oxford



Abstract

Rocket plume flowfields have an importance due to their influence on the signature of the rocket and also on the distribution of the plume gases around the vehicle. Little information on the co-flowing situation exists other than a previous study at Oxford. This thesis thus represents a significant database for co-flowing rocket plumes of this form. The work presented deals with two new aspects of co-flowing rocket plumes in that detailed flowfield measurements have been made and plumes from twin nozzle have been investigated for the first time in this thesis. This study on twinjet rocket plumes was carried out using the University of Oxford Gun Tunnel. Twinjet rockets with nozzle exit Mach numbers of 3 and 5 were tested in quiescent and in co-flow at Mach 7 using nitrogen and hydrogen injections. A major feature of the twinjet case was the so-called *impingement shock* between the flows from the two nozzles. It was discovered that this shock was insensitive to the freestream and scaling parameters are suggested for its geometry. Comparisons with single equivalent thrust nozzles are made at downstream locations and similar Pitot pressure profiles were observed for nitrogen injection in a nitrogen freestream after approximately 3 nozzle diameters downstream. Shear layers were studied and fluctuations in this region were measured by fast-response Pitot pressure and heat transfer probes sampled at 1.1 MHz. The extent of the shear layer was deduced using a new Oxford Total Temperature Probe. With the freestream stagnation temperature at approximately 650 K and injected gas at 350 K, a linear variation for the deduced total temperature across the shear layer was obtained. This was consistent with the Pitot pressure variations across this region. Convective heat transfer coefficient fluctuations and flow total temperature fluctuations across rocket flowfields were obtained using three thin-film heat transfer probes and found to be closely correlated. Experimental results for the twinjet and the single jet were compared with CFD simulations and good overall agreements were achieved. Instrumentation for the hypersonic experiments was investigated and a fast-response (~ 20 kHz) Pitot probe suited for flows heavily contaminated with particulate was developed and tested.

Acknowledgements

I would like to thank Professor Terry Jones for taking me on and going through this thesis. I wish to acknowledge the support from Dr David Buttsworth. I am indebted to him for his patient guidance, for the frequent brainstorming sessions and for introducing me to the art of experimental research. Also, I would like to thank the DRA team: Dr Martin Gilmore, Dr Martin Collyer, Dr Ian Wrisdale and Dr Terry Cain for their support and guidance. Especially Martin and Ian for their CFD work on the twinjet. Furthermore, I would like to express my sincere gratitude to friends at Osney Laboratory for the enjoyable three years at Oxford. Last but not least, I would like to thank Samantha and everyone at Withy Brook for looking after me over the years.

This work has been carried out with the support of the Defence Research Agency.

Nomenclature	
σ	constant in radial conduction term
θ	angle of trajectory of gas particles
θ_e	initial nozzle exit flow angle
Λ	constant in Knudsen number expression
γ	ratio of specific heats
μ	Newtonian or molecular viscosity
ω	angular frequency
ρ	static density
δ	boundary or shear layer thickness
Θ	continuity constant
α	conical flow angle
Φ	shock angle on ψ-ξ plane
β	shock angle on x-z plane
ρ_∞	freestream static density
θ_∞	jet expansion angle at exit
γ_∞	freestream ratio of specific heats
$\nu(M)$	Prandtl-Mayer function
γ_0	stagnation ratio of specific heats
ρ_0	stagnation density
ν_b	Prandtl-Meyer angle based on background conditions
γ_e	exit ratio of specific heats
ν_e	Prandtl-Meyer angle based on nozzle exit conditions
θ_{el}	lower flow turning angle at nozzle exit on x-z plane
θ_{eu}	upper flow turning angle at nozzle exit on x-z plane
ρ_f	density of thin-film deposit
θ_f	temperature difference (instantaneous - initial) for thin-film
L_y	co-flow plume scaling parameter
L_z	co-flow plume scaling parameter
ω_n	angular resonance frequency
θ_N	nozzle exit metal angle
σ_N	normalised standard deviation $\sqrt{\sum_i \overline{p_{ti} - \overline{p_{ti}}} \Big/ \overline{p_{ti}}}$
ξ_p	co-ordinate of impingement point on ψ-ξ plane
Y_{pt}	relative Pitot pressure turbulence intensity
α_R	first order temperature coefficient of heat transfer probe
β_R	second order temperature coefficient of heat transfer probe
ρ_s	heat transfer probe substrate bulk density
a	sonic speed
A	area
a^*	critical speed $\sqrt{\gamma R T^*}$
A^*	nozzle throat area
C	constant in lateral conduction term
C_{cr}	Chapman-Rubinsen number $\frac{\rho^* \mu^*}{\rho_e \mu_e}$
C_D	drag coefficient

c_f	specific heat of thin-film deposit
C_F	thrust coefficient
C_f	skin friction coefficient
C_{Fmax}	maximum thrust coefficient
c_p	specific heat
c_s	specific heat of heat transfer probe substrate
D	drag
D^*	nozzle throat diameter
D_e	nozzle exit diameter
f_0	resonance frequency
g_c	constant in Kendall Pitot probe model expression
h	convective heat transfer coefficient
$J_n(\alpha)$	Bessel function $\sum_{m=0}^{\infty} \frac{(-1)^m (\alpha/2)^{2m+n}}{m!(m+n)!}$
Kn	Knudsen number
Kn_0	Knudsen number based on plenum chamber conditions
Kn_p	penetration Knudsen number based on l_{m12}/L_c
k_s	thermal conductivity of heat transfer probe substrate
L	quiescent plume scaling parameter $\sqrt{N}D^*$
L_c	characteristic length
l_f	thin-film thickness
l_m	length scale
l_{m12}	mean free path for impinging twinjet
M	Mach number
M_∞	freestream Mach number
M_c	convective Mach number $\frac{U-U_c}{a}$
M_e	nozzle exit Mach number
M_R	reflected shock Mach number
M_s	incident shock Mach number
M_z	Mach number along z-axis
M_{zc}	local Mach number where leading characteristics intercepts z-axis
N	pressure ratio P_{0c}/P_b
Nu	Nussult number hD/k_e
p	static pressure
P_∞	freestream static pressure
P_0	stagnation pressure
$P_{0\infty}$	freestream stagnation pressure
P_{0c}	rocket plenum chamber pressure or injection pressure
P_{0s}	total pressure in shear layer
P_b	background static pressure
P_e	nozzle exit static pressure
Pr	Prandtl number
p_t	Pitot pressure
p_{ti}	Pitot pressure for different nozzle configurations
q	convective heat flux
q_∞	freestream dynamic head $\rho_\infty U_\infty^2/2$

q_c	convective heat flux of *cold* heat transfer probe
q_h	convective heat flux of *hot* heat transfer probe
q_w	convective heat flux of *warm* heat transfer probe
R	resistance
r	radius
R	gas constant
R^*	nozzle throat radius
r_c	effective conical nozzle radius from cone vertex
R_e	nozzle exit radius
Re	Reynolds number
Re_x	Reynolds number based on freestream conditions and length of the rocket body
Re_0^*	Reynolds number based on nozzle throat $\rho_{0c} u^* R^* / \mu^*$
Re_L^*	plume Reynolds number $\mathrm{Re}^* / \sqrt{N}$
Re_N	Reynolds number based on nose radius
Re_s	Reynolds number based on twinjet nozzle spacing $\rho u S / \mu$
Re_t	Pitot probe Reynolds number
Re_z	Reynolds number based on downstream displacement
R_N	heat flux probe nose radius
R_{ref}	reference resistance at reference temperature
S	twinjet nozzle spacing
s	entropy
T	static temperature
T_x	freestream static pressure
T^*	critical static temperature at nozzle throat
T_0	stagnation temperature
T_{0c}	rocket plenum chamber temperature or injection total temperature
T_e	static temperature at nozzle exit
T_F	rocket vacuum thrust
T_m	static temperature at centre of shear layer
T_s	heat transfer probe substrate temperature at stagnation point
T_{sc}	heat transfer probe substrate temperature, *cold* heat transfer probe
T_{sh}	heat transfer probe substrate temperature, *hot* heat transfer probe
T_{sw}	heat transfer probe substrate temperature, *warm* heat transfer probe
T_t	flow total temperature
u	velocity in downstream direction
U_∞	freestream velocity
U_c	convective velocity $\dfrac{a_2 U_1 + a_1 U_2}{a_1 + a_2}$
U_e	velocity at edge of the stagnation region boundary layer
u_e	nozzle exit velocity
U_{lim}	limiting velocity $\sqrt{2 c_p T_0}$
u_p	shock induced gas velocity behind incident shock
v	velocity in y direction
V_{out}	voltage output from the analogue circuit
W	velocity in z direction
W_x	freestream velocity in z direction
W_e	nozzle exit velocity in z direction

x	radial displacement in z direction
x_v	x-coordinate of jet source
y	radial displacement in y direction
z	downstream displacement
z_m	location of Mach disk or regular reflection
z_p	impingement point on x-z plane
z_v	z-coordinate of jet source

TABLE OF CONTENTS

1 INTRODUCTION TO ROCKET EXHAUST PLUMES 1-1

1.1 BACKGROUND 1-1

1.1.1 Aim of This Thesis 1-2

1.2 SUPERSONIC EXHAUST JET PLUME 1-2

1.2.1 Over-expanded Plume 1-3

1.2.2 Under-expanded Plume 1-3

1.3 HYPERSONIC ROCKET EXHAUST PLUMES 1-4

1.4 AN OVERVIEW OF THE COMPLETE ROCKET AND EXHAUST PLUME FLOWFIELD 1-5

1.5 STRUCTURE OF THIS THESIS 1-6

2 HYPERSONIC EXPERIMENTAL FACILITIES UTILISED 2-1

2.1 HYPERSONIC TESTING TUNNELS 2-1

2.1.1 Shock Tube 2-1

2.1.2 Gun Tunnels 2-3

2.2 THE OXFORD GUN TUNNEL 2-5

2.2.1 Ludwieg Tube and Plume Gas Supply System 2-6

2.2.2 Operation Procedures 2-8

2.2.3 Real Gas and Condensation Effects 2-9

2.3 THE TRAVERSE MECHANISM 2-13

2.4 ROCKET MODELS 2-14

2.4.1 Nozzle Design and Manufacture 2-16

2.4.2 Rocket Model Sting Effects 2-17

2.5 DATA ACQUISITION AND PROCESSING 2-17

2.5.1 Data Sampling Units 2-17

2.5.2 Data Format and Processing 2-18

3 INSTRUMENTATION 3-4

3.1 PRACTICAL ASPECTS OF HYPERSONIC INSTRUMENTATION 3-4

3.1.1 Influence of Probe Traverse Speed and Angle of Attack on Measurement 3-4

3.1.2 Requirements on Spatial and Frequency Resolution 3-4

3.2 PRESSURE MEASUREMENTS 3-5

3.2.1 Pressure Probes 3-5

3.2.1.1 PIT Pitot Probe 3-5

3.2.1.2 BPT Pitot Probe 3-6

3.2.1.3 FPT Pitot Probe 3-6

3.2.1.4 RPT Pitot Probe 3-8

3.2.2 Shock Tube Tests 3-8

3.2.3 Experimental Arrangement 3-9

3.3 TEMPERATURE MEASUREMENTS 3-9

3.3.1 Introduction 3-9

3.3.2 Thin-Film Heat Transfer Probes 3-10

3.3.2.1 Stagnation Point Heat Transfer Analysis 3-11

3.3.2.2 Probe Construction & Calibration 3-16

3.3.2.3 Operation of the Heat Transfer Probes 3-17

3.3.2.4 Lateral Conduction and Nose Curvature Effects 3-20

3.3.2.5 Variable Substrate Thermal Properties of Thin-film Probe 3-23

3.3.2.6 Application of Heat Transfer Probes in Gun Tunnels 3-24

3.3.3 Total Temperature from Heat Transfer Probes 3-24

3.3.3.1 Deduced Total Temperature Error in an Unsteady Flow 3-25

3.3.4 Turbulence Measurements using Thin-Film Heat Transfer Probes 3-27

3.4 FLOW VISUALIZATION 3-28

3.4.1 Schlieren Photography 3-28

3.4.2 Experimental Setup 3-28

3.5 A NOTE ON THE INSTRUMENTATION USED IN THIS THESIS 3-29

4 SINGLE NOZZLE ROCKET FLOWFIELD 4-5

4.1 INTRODUCTION 4-5

4.2 TYPICAL FLOW OVER A SINGLE NOZZLE ROCKET 4-6

4.2.1 Rocket Nose Conical Shock 4-6

4.2.2 Rocket Body Flowfield 4-7

4.2.3 Rocket Nozzle Throat Flowfield 4-7

4.2.4 Boundary Layer in Nozzle 4-8

4.2.5 Rocket Exhaust Plume Flowfield 4-8

4.2.6 Initial Expansion at Nozzle Exit 4-8

4.3 UNDEREXPANDED ROCKET PLUME IN HYPERSONIC FREESTREAM 4-9

4.3.1 Nozzle Exit Flowfield 4-9

4.3.2 Shock Structure of Under-expanded Rocket Plumes 4-10

4.3.3 Rocket Plume Core Flow 4-12

4.3.4 Shear Layer and Shock Layers 4-12

4.3.5 Rocket Plume Scale 4-13

4.4 EXPERIMENTAL RESULTS 4-15

4.4.1 Quiescent Experiments 4-16

4.4.1.1 Background Pressure Level and Apparent Plume Distortion 4-16

4.4.1.2 Quiescent Schlieren Analysis 4-16

4.4.1.3 Quiescent Plume Scale 4-18

4.4.1.4 Quiescent Pitot Pressure 4-18

4.4.1.5 Quiescent Heat Transfer 4-19

4.4.1.6 Quiescent Total Temperature 4-20

4.4.2 Co-flow Runs 4-21

4.4.2.1 Co-flow Schlieren Analysis 4-21

4.4.2.2 Co-flow Plume Scale 4-22

4.4.2.3 Co-flow Pitot Pressure Measurements 4-22

4.4.2.4 Co-flow Heat Transfer and Total Temperature Analysis 4-23

4.5 SHEAR LAYER ANALYSIS 4-24

4.5.1 Introduction 4-24

4.5.2 Previous Work 4-25

4.5.3 Shear Layer Turbulence 4-26

4.5.4 Rocket Plume into Quiescent Medium 4-28

4.5.5 Rocket Plume in Hypersonic Freestream 4-29

4.6 PARABOLISED NAVIER STOKES CODE - SHARC 4-31

5 TWIN NOZZLE ROCKET FLOWFIELD 5-4

5.1 INTRODUCTION 5-4

5.2 ROCKET MODELS 5-8

5.3 EXPERIMENTAL STRATEGY 5-8

5.3.1 Visualization 5-8

5.3.2 Quiescent Medium Tests 5-8

5.3.3 Co-flow Tests 5-9

5.4 SCHLIEREN PHOTOGRAPH VISUALISATION 5-9

5.4.1 Quiescent Injection Schlieren Photography 5-9

5.4.2 Co-flow Schlieren Photography 5-10

5.4.3 Plume Structure from Schlieren Visualization 5-10

5.5 QUIESCENT RUNS 5-12

5.5.1 Plume Scale Analysis 5-12

5.5.2 Base Flow Between Primary Jets 5-13

5.5.3 Backflow Prior to Impingement 5-14

5.5.4 Quiescent Pitot Pressure Measurements 5-15

5.5.5 Quiescent Heat Transfer Measurements 5-16

5.5.6 Quiescent Total Temperature *5-17*

5.5.7 Quiescent Shear Layer *5-18*

5.6 CO-FLOW INJECTION IN A MACH 7 FREESTREAM 5-19

5.6.1 Co-flow Pitot Pressure Measurements *5-19*

5.6.2 Co-flow Heat Transfer Measurements *5-21*

5.6.3 Co-flow Total Temperature *5-22*

5.6.4 Co-flow Shear Layer *5-23*

5.7 COMPARISON WITH SINGLE EQUIVALENT NOZZLE 5-24

5.7.1 Rocket Injecting in Quiescent *5-24*

5.7.2 Rocket Injecting in Mach 7 Freestream *5-24*

5.8 IMPINGEMENT SHOCK AND SECONDARY JET 5-25

5.8.1 Influence of Impingement Region on Plume Structure *5-25*

5.8.2 Inviscid Impingement Shock Locus *5-26*

5.8.3 Impingement Shock Surface Scaling Parameters *5-27*

5.8.4 Secondary Jet Analysis *5-27*

5.9 COMPARISON OF CFD WITH EXPERIMENTAL RESULTS 5-28

5.9.1 Introduction *5-28*

5.9.2 CFD Results *5-30*

5.9.2.1 Mach Number Distribution 5-30

5.9.2.2 Static Pressure Distribution 5-31

5.9.2.3 Density Distribution 5-32

5.9.3 Pitot Pressure Profile Comparison *5-32*

5.9.4 Significance of Rocket Base Region in Plume Modeling *5-33*

6 SUMMARY AND CONCLUSIONS 6-40

6.1 CONCLUSIONS 6-40

6.2 SUMMARY 6-40

6.2.1 Summary of Chapter 1 ..... *6-40*

6.2.2 Summary of Chapter 2 ..... *6-40*

6.2.3 Summary of Chapter 3 ..... *6-40*

6.2.4 Summary of Chapter 4 ..... *6-40*

6.2.5 Summary of Chapter 5 ..... *6-40*

6.3 RECOMMENDATIONS 6-40

6.3.1 Thin-film heat transfer probes *6-40*

6.3.2 Pitot pressure probes *6-40*

6.3.3 Nozzle Design *6-40*

A REFERENCES A-1

B GUN TUNNEL OPERATION AND TROUBLESHOOTING B-1

C RUN CONDITIONS C-1

1 Introduction to Rocket Exhaust Plumes

1.1 BACKGROUND

Although the first rocket was launched some 50 years ago, the exhaust flowfield of this type of flight vehicle is still under extensive research. A better understanding of rocket exhaust characteristics is important for new vehicle design and its plume signature. A signature can be defined as those properties such as microwave, infrared, visible and ultraviolet radiation emitted or reflected from the complex exhaust flowfield. Different missile or rocket designs have their unique signatures, which depend mainly on body and nozzle geometry, operating conditions and altitude. Knowledge of these different signatures plays an important role in remote vehicle recognition with obvious application in defence against incoming missile threats. The exhaust characteristics also play a significant role in rocket guidance and tracking applications as signals undergo losses and distortion on passing the exhaust plume, depending on the local conditions encountered along the path through the plume.

Three-dimensional rocket exhaust structures are aerodynamically and thermochemically complex and the prediction of plume properties such as temperature, velocity, pressure, chemical species concentrations and turbulence properties is a formidable task as there are no definitive models for viscous and chemical effects. With the advances in super-computers, full Navier-Stokes equations could be solved with reasonable accuracy. It is the turbulent nature of the rocket plume flow which is challenging even the state of the art Computational Fluid Dynamics (CFD) codes. Various turbulence models have been implemented, and seem to give reasonable results. Only through validation of computer codes using experimental data, can CFD models be developed to the point where they can be confidently used as design and predictive tools.

1.1.1 Aim of This Thesis

Detailed knowledge of jet and rocket engine exhaust flowfields is sought in a wide variety of military and civilian programmes. Limited published data exist for under-expanded single nozzle plumes exhausting into quiescent media. However, data for moderately under-expanded single and twin nozzle rocket exhaust plumes in a continuum hypersonic co-flow are almost non-existent. Such data are much needed to check the ability of current CFD codes to correctly model viscous effects caused by the presence of a hypersonic freestream flow in addition to the plume flow. These viscous effects include interaction between boundary layers on the rocket body with the hypersonic freestream (including possible separation of the boundary layer induced by the near normal plume shock at the nozzle exit), and turbulent mixing between the plume gas and the freestream gas in the shear layer.

Significant effort has been devoted to twinjet nozzle plumes in this thesis. The complex plume structure was investigated using an array of instrumentation to obtain measurements of Pitot pressure, heat transfer, total temperature and density distributions.

Significant work presented in this thesis was also devoted to facility development and improvement, including model design and manufacture, probe development and calibration. The emphasis of this thesis is on the interpretation of experimental data with the help of CFD simulation.

This study was carried out in collaboration with the Defence Research Agency (DRA), where most of the CFD simulations were carried out.

1.2 SUPERSONIC EXHAUST JET PLUME

Rockets, missiles and spacecrafts are usually equipped with thrusters for thrust or altitude control. The exhaust jets of these thrusters expand into high velocity freestreams. The flowfield of this expansion outside the thruster nozzle is called a plume.

The first research work on supersonic jets were by Mach and Salcher (1889). In rocket exhaust plumes, expansion and compression waves accompanied by shock waves appear. Under

certain conditions these waves repeat themselves many times as the jet proceeds out from the nozzle exit which forms the most prominent feature of a rocket plume. Emden (1899) was the first to make a systematic study of supersonic plumes and deduced an empirical formula for the wavelength of the periodic structure of supersonic jet in quiescent. Prandtl (1904, 1907), Von Karman (1907) and Rayleigh (1916) all made substantial contributions in developing a theory to predict the periodic structure of supersonic plumes in a quiescent medium. Sauer (1947) calculated the flow pattern of quiescent plumes by the method of characteristics. Schaefer (1949) used a similar method to study the flow of a jet under the influence of an external flow.

1.2.1 Over-expanded Plume

For a two-dimensional, supersonic, nearly parallel jet issuing from a nozzle into a quiescent medium, if the background pressure of the medium P_b is larger than that at the exit of the nozzle P_e, oblique shock waves first form at the edge of the nozzle. These oblique shocks will be reflected as wedge-shaped expansion waves on the boundary of the jet. Figure 1-1 shows a schematic illustration of such a jet. If the pressure difference between P_b and P_e is small, periodic structures will exist in the jet. The wave length of these periodic structures increases with the exit Mach number.

1.2.2 Under-expanded Plume

If the background pressure P_b is less than that at the exit of the nozzle P_e, a series of Prandtl-Meyer expansion waves occur at the lip of the nozzle. These waves cross one another and are reflected from the opposite boundaries of the jet as waves of compression. The compression waves again cross one another and are reflected from the boundary of the jet as expansion waves. Figure 1-2 shows a schematic illustration of such a jet.

If the jet at the exit of the nozzle is not parallel as in a diverging nozzle, the wave pattern is much more complicated. Consider a diverging nozzle operating in under-expanded mode, even though waves of expansion start from the edge of the nozzle first, there may exist an intercepted shock (or barrel shock in the case of an axisymmetric nozzle) wave

immediately behind the waves of expansion. The reason being that as the jet leaves the nozzle, its pressure drops due to the divergence of the exit streamlines which lead to expansion of the injected gas. As a result, its static pressure after passing through the expansion waves may become lower than the background pressure P_b. The jet is then turned back by this static pressure gradient. A series of compression waves are formed originating at the boundary of the inward turning streamlines and they coalese to form the intercepted/barrel shock. This effect is more pronounced for an axisymmetric divergent nozzle. Here the expansion is three-dimensional and the static pressure gradient along the leading expansion wave is greater than the two-dimensional planar case (see Figure 4-4 of Chapter 4).

1.3 HYPERSONIC ROCKET EXHAUST PLUMES

There are many different fluid dynamic phenomena associated with the exhaust plume aerodynamics of a rocket travelling at high speeds. The supersonic exhaust plume from the rocket is imperfectly expanded at typical flight conditions. It is generally thought to equilibrate to ambient pressure levels via a decaying sequence of expansion and shock waves, which can be strong in the plume nearfield (close to the nozzle exit). The rocket plume is additionally characterised by the after-burning of the un-burnt exhaust products with the entrained freestream gas. For solid propellant rocket exhausts, a multi-phase flow must be dealt with where the influence of gas/particle interactions on the plume structure may be quite pronounced at high particle loadings (Dash, 1993).

Complete analysis of rocket exhaust plumes must therefore encompass a wide treatment of flow regimes from subsonic and transonic flows right through to supersonic and hypersonic flows. Some parts of the plume flowfield can be considered to be rotational while others are irrotational, some parts viscous while others inviscid. In the combustion chamber and nozzle of the rocket, as well as in the exhaust plume, non-equilibrium reactions of chemical species may be occurring. The detailed analysis of a rocket exhaust plume can entail the integration of over 100 partial differential equations (Dash, 1993) which describe the complex

interplay of wave/turbulent/chemical/particle processes occurring in the plume. Analysis of such a flowfield, therefore, poses a formidable challenge to the experimental and computational aerothermodynamicists.

The work presented in this thesis is mainly concerned with exhaust plumes that would be typical of a rocket travelling at hypersonic speeds at an altitude of between 25 and 35 km. At these altitudes, the pressure at the exit of the rocket nozzle P_e is in the order of 11 times larger than that of the freestream static pressure P_∞ and the plumes belong to the class of jet known as moderately under-expanded.

There is a high degree of uncertainty as to which current computer codes can be relied upon to give accurate predictions. A common practice today is code verification, where one computer code is compared with another code or analytical model without ever having been validated with reliable experiments. Significant effort in this thesis is placed on gaining well-defined experimental data, which could be used for code validation.

1.4 AN OVERVIEW OF THE COMPLETE ROCKET AND EXHAUST PLUME FLOWFIELD

The axisymmetric rocket and exhaust plume flowfield associated with a conventional single engine with rear/centred propulsive nozzle can be subdivided into four regions as suggested by Dash (1993) as shown in Figure 1-3. These are:

(1) The flowfield over the rocket body including boundary layers.

(2) The predominantly inviscid plume nearfield, where wave strengths are strong and turbulent mixing processes are generally confined to thin shear layers.

(3) A transitional region, where the mixing layers engulf the entire plume and wave strengths diminish due to turbulent dissipation.

(4) The fully viscous plume farfield, where wave processes have totally diminished and a constant pressure turbulent mixing environment prevails.

In this study, only region (1) to (3) are investigated in detail. This is mainly due to the limitation of the testing facilities. As will be seen from experimental results presented later, however, it seems to be the case that wave processes die out completely after the first two shock cells. This leaves a cylindrical core of plume gas separated from the freestream by shear layers, presumably all at constant pressure. This observation is quite different from the representation of the *transition* region as proposed by Dash, which showed an ever-decaying series of shock cells.

Although attention is generally focused on the farfield (region 4) for applications keyed to missile detection, guidance, etc., it is the nearfield solution that is used to provide starting conditions for a farfield constant pressure mixing/after-burning calculation. Validation of nearfield computational methods with experimental data is therefore important.

1.5 STRUCTURE OF THIS THESIS

This thesis is divided into 6 chapters. This is intended firstly to give the reader a general understanding of under-expanded rocket plumes and then to explore issues such as the instrumentation used in this thesis and detailed analyses of single and twin nozzle rocket exhaust plume flowfields.

A brief introduction to all the chapters in this thesis is given below.

Chapter 1: Introduction to supersonic jets and hypersonic rocket flows are presented which set the scene for this thesis.

Chapter 2: It gives a brief introduction to the Oxford Gun Tunnel. The experimental arrangement used throughout this thesis is explained, together with an investigation into the effects of model support stings and their influence on the downstream flowfield.

Chapter 3: This explains the instrumentation used in this thesis. The application of Pitot pressure probes in a short duration hypersonic rocket flowfield is investigated. The new FPT Pitot pressure and the Oxford Total Temperature probe are analysed and the background theories presented.

Chapter 4: This is devoted entirely to single nozzle rocket exhaust plumes. Various plume models are explained and their validity tested with experimental results. Pitot pressure, heat flux and total temperature profiles are obtained through traverses across the rocket plumes. A section on plume shear layer is included which investigates the three-dimensional shear layer of under-expanded rocket plumes using fast response Pitot pressure and heat transfer probes.

Chapter 5: Twinjets are investigated in detail in this chapter. Various instruments are used in plume traverses, which include three kinds of Pitot pressure probes, three heat transfer probes and extensive use of Schlieren photography. Scaling parameters and an empirical formula for the impingement shock surface and locus are suggested. Shear layer of the twinjet is sampled at high frequency using a fast response miniature pressure transducer. Finally, twinjets are compared with single equivalent nozzles of the same thrust and geometry to test the validity of simulating a twinjet with such an equivalent nozzle at downstream locations. Experimental results are then compared with CFD simulation to test the capability of the underlying code to predict this complex flowfield.

Chapter 6: Conclusions of this thesis are given, and achievements are highlighted. Summaries of the main chapters are also given together with recommendations for future research work in this area.

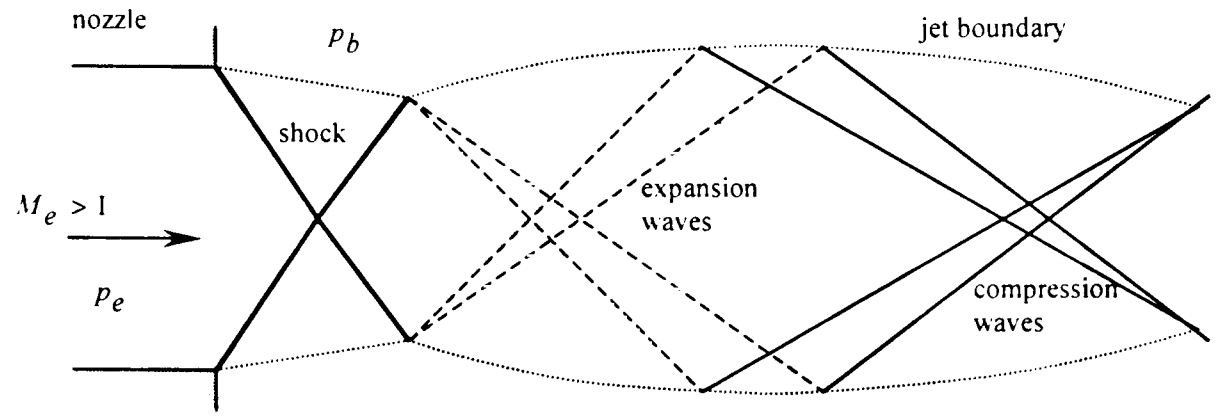


Figure 1-1 Schematic illustration of a two-dimensional over-expanded plume

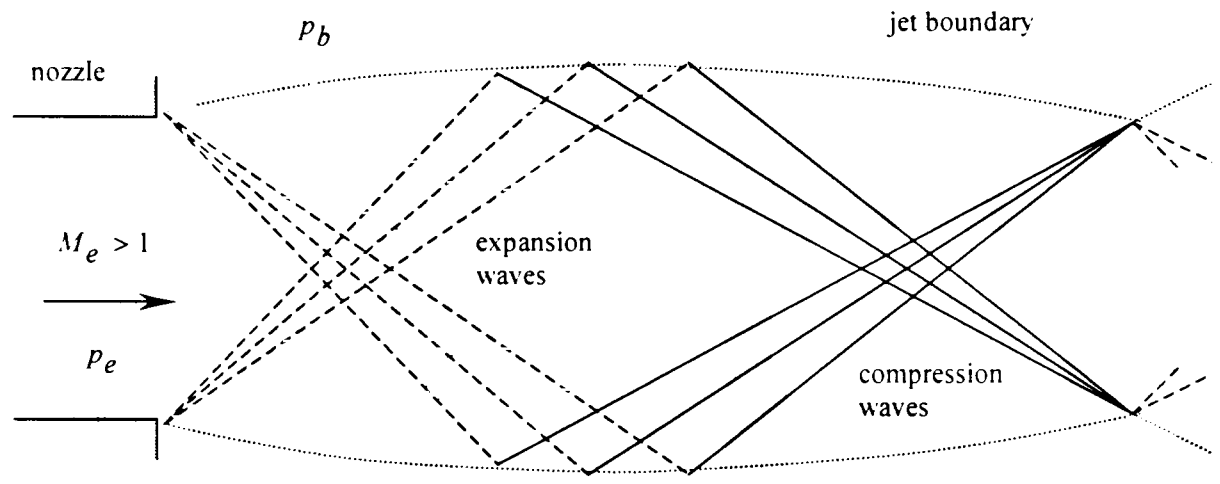


Figure 1-2 Schematic illustration of a two-dimensional under-expanded plume

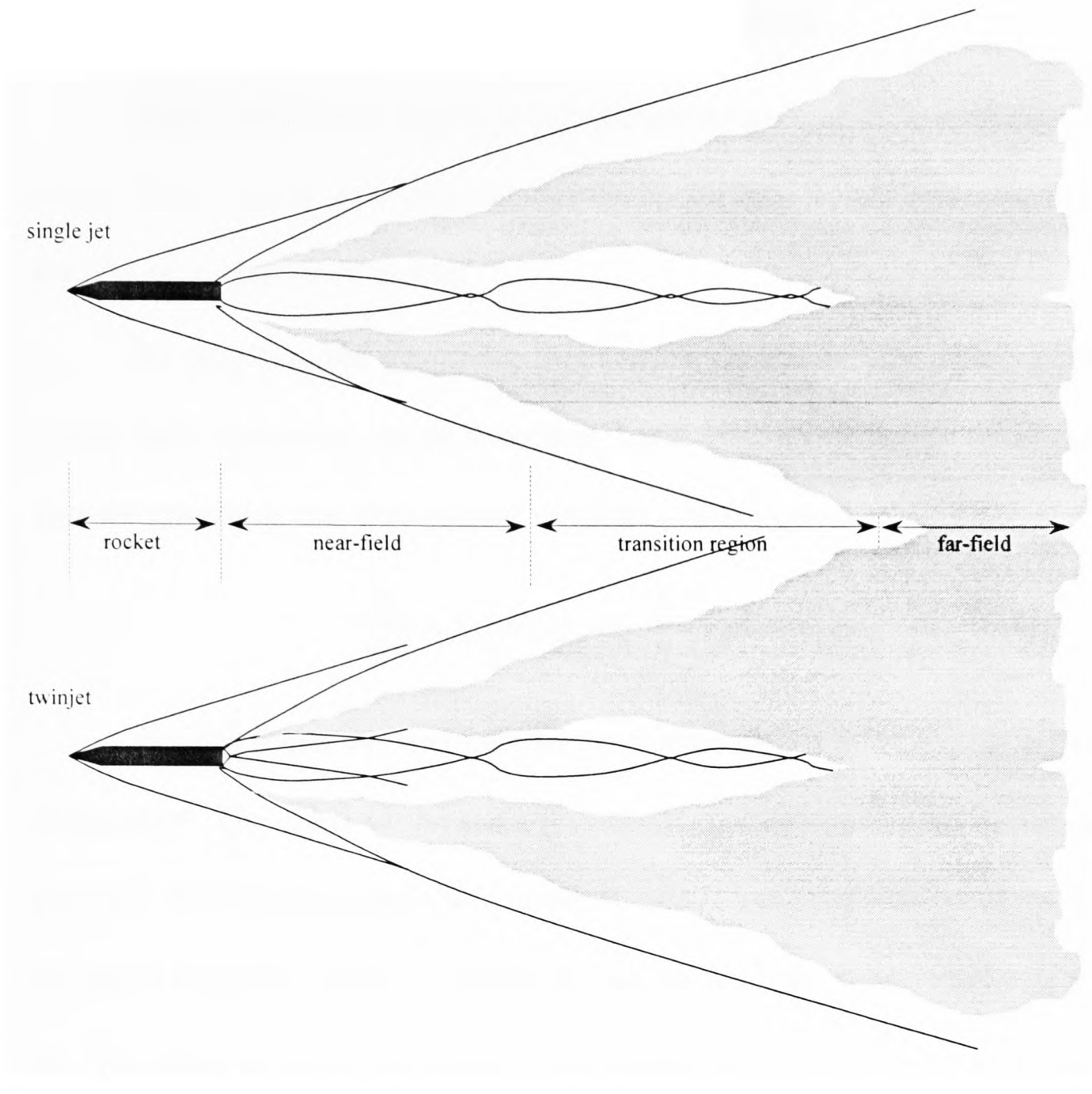


Figure 1-3 Overview of complete rocket and plume flowfield

2. Hypersonic Experimental Facilities Utilised

This chapter gives a general introduction to some of the testing facilities used for this thesis. Note that the wave diagrams given in this chapter are representative of the general features of the particular facility.

By adjusting the governing thermodynamic and aerodynamic variables, a range of rocket flight conditions can be simulated. Let L_c be a characteristic dimension of the plume, then the governing non-dimensional variables can be expressed,

$$\frac{L_c}{D^*} = f_n\left\{M_e, \gamma_e, \theta_N, \frac{P_e}{P_\infty}, \mathrm{Re}^*, M_\infty, \mathrm{Re}_\infty, \frac{T_e}{T_\infty}, \frac{u_e}{U_\infty}, \gamma_\infty\right\}$$

For this thesis, N_2 was used as the freestream gas at Mach 7 at a fixed pressure and temperature. The effect of the static pressure ratio was investigated by varying the injection pressure. Two diatomic gases were used (N_2 and H_2) to test the effect of the velocity ratio and the throat Reynolds number. The monatomic He was also used, which has a different γ_e and M_e. The effect of metal exit angle θ_N was studied using two single nozzles with different angles.

2.1 HYPERSONIC TESTING TUNNELS

2.1.1 Shock Tube

Schematic illustration of a shock tube is shown in Figure 2-1. It consists of two chambers of equal and constant cross-sectional area, which contain gases at different pressures and is divided initially into two compartments by a diaphragm. The part of the tube to the right of the diaphragm is filled with a test gas at a low pressure or at atmospheric, and the part to the left of the diaphragm by a driving gas at high pressure. The diaphragm bursts as a result of the pressure gradient across the diaphragm. Expansion of the driving gas causes a shock wave to propagate along the tube, and as the test gas passes through the shock it is compressed, heated and set in motion in the shock direction.

If the shock velocity is constant along the tube, a region of uniform high temperature flow then follows the shock. This can be used for experimental purposes if a model is held in the tube. This uniform flow is terminated by the so-called *contact surface*, behind which the driving gas is at relatively low static temperature. The duration of uniform flow is frequently less than a millisecond, but in this time very high enthalpies and densities may be achieved. However, allowing for real gas effects, the Mach number of the gas flow behind the shock is limited to about 3 (Holder, 1959).

The bursting of the diaphragm causes the driver gas on the left to expand into the low-pressure region and to compress the driven gas on the right. The resulting basic gas dynamic cycle is shown in the form of a wave diagram in Figure 2-2. The cycle comprises unsteady, isentropic expansion of the driver gas and normal shock compression and acceleration of the driven gas. For given initial conditions of the driver and driven gas pressure and temperature ratios, unique flow results as a consequence of pressure and velocity matching at the contact surface. If the shock tube consists of the same driver and driven gas initially at pressure ratio p_4/p_1, then the ratio of the incident shock aerodynamic parameters p_2/p_1, T_2/T_1 can be written as,

$$\frac{p_4}{p_1} = \frac{p_2}{p_1}\left\{1 - \frac{(\gamma-1)(p_2/p_1 - 1)}{\sqrt{2\gamma\left[2\gamma + (\gamma+1)(p_2/p_1 - 1)\right]}}\right\}^{-2\gamma/(\gamma-1)}$$

$$\frac{T_2}{T_1} = \frac{p_2}{p_1}\left(\frac{\frac{\gamma+1}{\gamma-1} + \frac{p_2}{p_1}}{1 + \frac{\gamma+1}{\gamma-1}\frac{p_2}{p_1}}\right)$$

Where subscripts (1) and (2) correspond to the conditions in front of and behind the moving shock respectively. The Mach number of the incident shock M_s and the induced velocity of the gas behind this shock u_p can be written as,

$$M_S = \sqrt{\frac{\gamma+1}{2\gamma}\left(\frac{p_2}{p_1} - 1\right) + 1}$$

$$u_p = \frac{a_1}{\gamma}\left(\frac{p_2}{p_1} - 1\right)\left(\frac{\frac{2\gamma}{\gamma+1}}{\frac{p_2}{p_1} + \frac{\gamma-1}{\gamma+1}}\right)^{1/2}$$

Gas particles on the high-pressure side of the interface are accelerated by a series of expansion waves, while gas particles on the low-pressure side of the interface are accelerated by compressive shock waves. As a result, gas on the left of the interface has a higher momentum than the ones on the right due to the fact that it is now at a relatively low static temperature. The reflected shock from the end wall is strong enough to bring the gas on the right of the interface to rest. When this shock wave meets the gas particles coming from the left at a higher momentum, a reflected shock travelling back towards the end and a transmitted shock travelling to the left are formed. This is known as an *over-tailored* condition.

The Mach number of the reflected shock from the end wall, M_R can be expressed in terms of the incident shock Mach number as,

$$\frac{M_R}{M_R^2 - 1} = \frac{M_s}{M_s^2 - 1}\sqrt{1 + \frac{2(\gamma-1)}{\gamma+1}\left(M_s^2 - 1\right)\left(\gamma + \frac{1}{M_s^2}\right)}$$

Flow parameters across subsequent shock waves can then be deduced using the above set of equations. The slug of gas between the incident shock and the contact surface represents a region of relatively uniform shock heated and shock compressed flow, which is of interest for experiments.

The basic shock tube cycle described above has not taken into account effects of viscosity, heat losses, finite diaphragm bursting time, mixing at the contact surface and flow non-uniformities. As the reflected shock meets the non-ideal contact surface, part of it is transmitted into the driver gas and the rest is reflected as a series of Mach waves. Hence a more gentle increase in pressure is observed after the steady period. The drop in pressure that follows is due to the arrival of the reflected expansion waves.

2.1.2 Gun Tunnels

In this device, a piston is propelled down a barrel by the pressure of a driver gas contained in a vessel of large volume, and does work on a comparatively small volume of test gas trapped ahead of the piston in the barrel section. When the primary diaphragms rupture, the piston is driven down the barrel by the gas from the high-pressure driver gas.

The primary shock formed in front of the piston increases in strength as it is accelerated by the pressure difference across it. This shock compresses the gas in the barrel. The primary shock then reflects off the nozzle entrance at the barrel end, and travels towards the driver bringing the test gas to rest. When the reflected shock encounters the piston, it reflects again and applies an impulse sufficient to impart the piston velocity to the now stagnant gas. This process continues until the piston is brought to rest and the reflections gradually decrease to acoustic waves (see Figure 2-3). During the initial compression stages, a secondary diaphragm at the barrel end will rupture and release the compressed test gas through the test section.

Apart from being one of the most economical means of generating hypersonic test flows of acceptable quality and being mechanically simple, the use of the piston makes the gun tunnel advantageous over other facilities for two main reasons:

(i) the driven gas would undergo compression through many shock waves (due to reflections from the barrel end and the piston face), and thus would be subjected to a large temperature and entropy rise, and

(ii) the piston would prevent mixing between the driver and driven gases, so that the tunnel run time would be increased and this also means a different, more economical gas or less hazardous gas can be used as the driver gas.

Theses are based on the assumption that the piston is sufficiently light to attain the contact surface velocity corresponding to the initial driver/driven gas conditions. Original estimates based on the above model indicated the possibility of attaining very high stagnation

temperatures in excess of 10 000 K and relatively long run times in the region of 100 ms (Cox, 1957). However, in reality, the performance of the gun tunnel is limited by the structural inability of the light piston to withstand high peak pressure shock loading and by the high rate of stagnation temperature decay due to boundary layer cooling (Edney, 1967 and Hartunian, 1960).

2.2 THE OXFORD GUN TUNNEL

The Oxford Gun Tunnel (Figure 2-4 and Figure 2-5) is a hypersonic testing facility which is located in the Osney Laboratory of the Department of Engineering Science. It employs a large high-pressure air reservoir to drive an 80 g piston to approximately Mach 2.4 in N_2, down a 10 m barrel of 96 mm bore. For a typical run, the barrel is initially filled to 2.5 bar with N_2 and the driver to 1100 psi with air and the test section is pumped down to approximately 0.0127 bar.

The test section is a 0.9 m* 0.6 m* 0.6 m enclosure that is connected to a 28 m^3 dump tank by a 8 m long 0.4 m diameter channel.

Under typical conditions, the gun tunnel is configured with the Mach 7 nozzle that has a throat diameter of 19.1 mm and an entry to the nozzle restricted to 74.5 mm. The test gas is exhausted after approximately 60 ms and the available steady test time is in the region of 30 ms. The steady period occurs after a noisy 40 ms of tunnel starting processes during the period when the piston is gradually brought to rest. The nozzle exhausting into the test section creates an ejector action which results in an intense noise field which was found to be uniform within the confines of the test section at frequencies below 500 Hz (Cain et al, 1992).

Although the stagnation pressure of the Mach 7 freestream may be relatively steady during the test period, the total temperature is not and its mean level varies with time. The primary shock increases in strength as the piston accelerates, so the test gas close to the piston is compressed isentropically while that at the nozzle end is not. The entropy gradient in the slug of gas implies a non-uniform temperature distribution at the end of the compression pro-

cess when the pressure is uniform throughout the slug. Cain carried out a detailed analysis of this effect and found that there would be a 12 per cent drop in temperature. However, most of this drop occurred in the last 10 per cent of the test slug. In addition, boundary cooling in the barrel could result in an almost linear fall in the freestream total temperature as measured by a set of thin-film heat transfer probes (Buttsworth, 1996).

Given the short duration available for tests to be carried out, the challenge was to inject the test gas at a steady pressure to the rockets at the same time that the gun tunnel pressure itself was steady, then traverse the plume using various probes, as well as taking Schlieren photographs. All these constraints meant that timing of the mechanical operations of gun tunnel, various valves and traverses had to be accurate to within 5 ms, otherwise data would be lost or taken at unsteady conditions. Therefore significant effort was spent in the development of apparatus before experiments became reliable and repeatable.

2.2.1 Ludwieg Tube and Plume Gas Supply System

Ludwieg tube is simply a reservoir of chosen length, which contains the test gas. For this thesis a 25 mm diameter, 25 m length Ludwieg tube was filled with room temperature N_2 or He, which supplied the test gas to the conical nozzle at the rear of the rocket.

The gas in the Ludwieg tube was separated from the model by a fast-acting valve. A 139 g aluminium cylinder was used as the shut-off piston in the fast-acting valve. This was activated directly by exposing it to the high pressure in the Ludwieg tube for quiescent runs or by the high pressure behind the primary shock in the barrel of the gun tunnel for co-flow runs with the Mach 7 freestream.

A closing valve was also installed at the end of the Ludwieg tube, which was activated electronically from the stagnation or injection pressure signal after a delay of 45 ms. This was to save the injection gas and minimise the release of potentially explosive gases into the dump tank.

For H_2 injections, only round the last 8 per cent of the Ludwieg tube between the fast-acting valve and the ball valve was filled with this potentially explosive gas for safety reasons. The rest of the tube was filled with N_2 at the same pressure which acted as the driving gas. The presence of two significantly different gases complicated the wave processes in the Ludwieg tube. Therefore, the following analysis was based on the assumption that a single gas was present in the tube.

When the fast-acting valve opens, compression waves are formed at the throat of the valve and travel towards the throat of the rocket model. These compression waves rapidly coalesce to form an unsteady shock wave. At the same time, gas behind the contact surface in the tube is processed by a series of unsteady expansion waves, which travel back through the Ludwieg tube and set the gas in motion towards the throat of the rocket nozzle. Note that the time it takes for the leading expansion wave front to make its way back to the rocket model after the flow has started is proportional to the length of the tube for any given gas molecular weight and gas temperature.

A pressure transducer was mounted inside the rocket model plenum chamber which monitored the injection flow stagnation pressure. A typical trace is shown in Figure 2-6. Tests were carried out within the first plateau. The pressure steps are due to the reflected expansion waves. The corresponding stagnation temperature in the plenum chamber was measured by a fine (0.0005" diameter) thermocouple and shown in Figure 2-7. Initially, gas was at the room temperature of 292 K. As the shock moved towards the nozzle throat, gas between the fast-acting valve and the throat was compressed and its temperature raised. This is shown as the initial rise in the measured temperature. Due to viscous effects, there would be a loss in stagnation temperature in the injected gas (Shek, 1994). Therefore the measured gas temperature levelled off to a lower temperature than expected. The temperature measured by another thermocouple on the rocket body near the lip of the nozzle is also shown in the figure. The initial fall in temperature measured is believed to be due to the ejector action of the rocket plume.

Factory quoted response for the thermocouple is roughly 20 Hz in still air and 250 Hz in a flow stream. To protect the sensing bead of the thermocouple, the thermocouple used to measure the chamber temperature was mounted in a recess in the shoulder joint connected to the plenum. This raises the question of the adequacy of its application in the short duration test where the temperature variation was relatively large within a short period of time.

A much quicker response can be achieved by thin-film heat transfer probes (refer to Chapter 3). Two such heat transfer probes were placed at the exit of the single Mach 5 nozzle (SM5M), with one pre-heated prior to injection. The total temperature of the injected gas could then be deduced from the substrate temperature history and the corresponding heat flux. Figure 2-8 shows the deduced exit flow total temperature and the corresponding plenum chamber pressure and the background static pressure.

A majority of the experiments in this thesis were carried out within the period when the mean level of the injection pressure and the corresponding total temperature of the test gas were relatively steady. However, due to timing constrains, some of the measurements were taken during the period when the injection gas total temperature had not reached its steady level. One way to alleviate this problem is to use a nozzle with a higher flow rate, so that the gas that has been subjected to the initial unsteady compression process would be vented before measurements are taken. This can be seen in Figure 2-9 when the Mach 5 (M5) nozzle was used which had four times the flow rate of the SM5M nozzle. The main reason for using a nozzle with a smaller flow rate was to maintain compatibility with the existing arrangement so that the same rocket body could be used. This restricted the dimensions of the twinjet nozzles, which in turn restricted the single equivalent nozzles.

2.2.2 Operation Procedures

Prior to firing, the barrel was cleaned by firing a cleaning piston to flush out any aluminium debris from the previous run. This was done in order to avoid damaging the delicate instruments in the test section when the tunnel was fired again. Once the barrel had been

cleaned, a piston was inserted into the upstream end of the barrel. Behind the piston was a pair of scored aluminium sheets (with a bursting pressure of 34.5 bar) at the two ends of the breach section, which separated the driver section from the piston and barrel. At the other end of the barrel was the nominal Mach 7 contoured nozzle, which was separated from the test section by a Mylar diaphragm just upstream of the throat. This diaphragm had a bursting pressure of approximately 3.8 bar and was used to separate the pressurised barrel (initially at 2.5 bar) from the low-pressure test section prior to firing. The Mach 7 nozzle provided a parallel flow into the test section, which was attached to a dump tank. The test section was separated from the dump tank by means of a large 20" diameter isolation valve. A hard-wired interlock was installed so that the gun tunnel could not be accidentally fired if the large valve was closed, thus preventing the possibility of over-pressuring the test section.

Once all the instruments were ready, the test section and the dump tank were pumped down to about 0.0127 bar with the isolation valve open. The fast-acting valve was then set to close. The Ludwieg tube was filled up with an appropriate gas to the desired pressure with the closing valve set to the open position. The barrel section was subsequently pumped down to vacuum and filled to 2.5 bar with N_2. The final stage consisted of filling the driver section with air to 1100 psi while maintaining the breach section at half of the driver pressure. Venting the breach thus exposing the first aluminium diaphragm to a pressure high enough to break this and the second diaphragm across the breach. A flow chart on operating the Oxford Gun Tunnel can be found in Appendix B.

2.2.3 Real Gas and Condensation Effects

Gases used as injection gas for this thesis were expanded within the nozzle and in the plume core to thermodynamic states under which most gases would normally exist as a mixture of solid and gaseous phases. Calculations of the quantitative states of these gases are outside the scope of this thesis. However, it can be deduced from experimental results whether condensation should be taken into account when carrying out detailed analyses. In addition,

real gas characteristics can also have a significant effect on the thermodynamic states of the flow stream. This is shown by the measured nozzle exit total temperature of the injection gas.

Figure 2-10 shows a plot of the experimental estimation of the onset of condensation for air and nitrogen (Lukasiewicz, 1973). When a gas cools to its saturation temperature during an expansion, small droplets of condensed gas particles may appear. The production of the initial particles is known as *nucleation*, which can prevent appreciable condensation until the vapour is much colder than the saturation temperature. In this case, the vapour has reached a metastable *super-saturated* state. The subsequent transition from the metastable state to the equilibrium state is generally irreversible as the sudden release of latent heat and the subsequent rise in static pressure can generate a shock wave in the vapour.

During quiescent runs when the nozzle exit was within the line of sight, condensation could be visually detected as the jet turns slightly opaque. This was initially believed to be entirely due to the plume gas condensing. However, in quiescent runs the background pressure drops considerably due to entrainment of the background gas by the injection gas (see Figure 2-8 and Figure 2-9). A simple isentropic calculation shows that a corresponding drop in the test section static temperature of approximately 13 per cent could occur for a typical 100 bar gauge injection. This drop could cause the background temperature to decrease below the triple point of any residual water vapour in the test section and lead to considerable condensation. This condensed vapour could then be entrained into the shear layer which affects measurements downstream. This explains the asymmetrical nature of the measured heat flux signal and the deduced total temperature as formation of the condensed water vapour increases with decreasing test section static pressure over the period of an experiment (see Chapter 3, Figure 3-32 and Figure 3-35).

The presence of condensates in the flow could affect the heat flux to the thin-film probes. Firstly by considering the heat transfer mechanism close to the stagnation point of the probe, under normal running conditions, heat is transmitted by molecular diffusion across the stagnation point boundary layer. However, when there is condensation, the solid condensates

can penetrate the boundary layer and come into direct contact with the thin-film. This tends to increase the magnitude of the measured heat flux and affects the deduced total temperature. Secondly, when gas molecules condense, latent heat is given out as a result. This raises the flow temperature to a value higher than the expected isentropic value. When these molecules are brought to rest at the stagnation point, heat is needed from the flow to vaporise the condensates to vaporous gas. However, as the flow is brought to rest by a strong shock within a short period of time, the liquefied-gas particles are unlikely to be totally vaporised before reaching the stagnation region of the heat transfer probe. This effect on the measured heat flux depends on the driving temperature gradient across the stagnation point boundary layer. Finally, as mentioned previously, the transition from the metastable state to the equilibrium state is generally irreversible. The unsteady shock wave generated can further affect the measured heat flux.

Condensation effects in the plume core are believed to be small. The measured total temperature variation, as shown in the following paragraph, is believed to be due mainly to the combined effects of real gas characteristics and unsteady expansion process in the Ludwieg tube. Regions most likely to be affected to a significant degree are believed to be near the nozzle exit and in the shear layer. Near the nozzle exit, static temperature is in the region of 40 K and static pressure at approximately 0.0127 bar. The static temperature, density and pressure decrease further downstream. This combined with a rapid expansion reduces the probability of random collisions between gas molecules which could lead to the formation of stable nuclei.

Figure 2-11 shows a series of runs with the Mach 5 single nozzle (M5) in quiescent. A pressure transducer in the model plenum chamber recorded the injection pressures. Two heat transfer probes were placed at 11 mm downstream of the nozzle exit, above and below the axis of symmetry. The total temperatures were obtained by a regression process using the measured probe substrate temperatures and heat flux signals (see Chapter 3). Analysis of various features of the signals can be found in Chapter 2.

It can be seen that the asymptotic value of the injection gas total temperature is a function of the injection pressure. This temperature is dependent on the real gas expansion process, viscose losses in the Ludwieg tube and to a lesser degree, condensation of the injection gas.

Change in enthalpy for a gas can be expressed as,

$$dh = \left.\frac{\partial h}{\partial T}\right|_p dT + \left.\frac{\partial h}{\partial p}\right|_T dp = c_p dT + \left.\frac{\partial h}{\partial p}\right|_T dp$$

This can be written in the form,

$$dh = c_p dT + \frac{1}{\rho}(1 - \beta_v T)dp$$

where β_v is the coefficient of volumetric expansion,

$$\beta_v = \rho \left.\frac{\partial(1/\rho)}{\partial T}\right|_p$$

For an isentropic process,

$$dT = \frac{1}{c_p \rho}(\beta_v T - 1)dp$$

Consider a streamline from the stagnation chamber to the stagnation point of the heat transfer probe, if the injection gas was assumed ideal, then $\beta_v T = 1$ and there would be no change in total temperature. However, for a real gas which has undergone an adiabatic expansion there would be an increase or decrease in the measured gas total temperature depending on the value of $\beta_v T$. For N_2, the term $\beta_v T > 1$ and the magnitude of the expected decrease in total temperature,

$$\Delta T_0 = \frac{T_{0measured} - T_{0c}}{T_{0c}}$$

can be estimated by using a suitable thermodynamic table (i.e. Reynolds, 1979).

P_{0c}, bar	ΔT_0, %
75	-5
40	-2
7.5	-0.1

Table 2-1 Change in injection gas total temperature with injection pressure for N_2, based on initial total temperature T_{0c} = 300 K.

Figure 2-12 shows the measured total temperature when the injection gas was He. In this case, the term $\beta_i T < 1$. Therefore, we would expect an increase in the measured total temperature. However, in this particular experiment, the expected increase was balanced by the decrease in total temperature as a result of the viscous losses in the Ludwieg tube. The combined effect can be seen to bring the measured value back to the initial value in the region of 300 K (note that the dip at around 140 ms was due to expansion waves, travelling at nearly 3 times the speed as in N_2, being reflected back from the end of the Ludwieg tube).

2.3 THE TRAVERSE MECHANISM

Heat transfer and Pitot probes were mounted on a moveable horizontal bar, which was supported by two precision linear bearings located at either end (see Figure 2-14 and Figure 2-15). These linear bearings were located sufficiently far apart to keep them from interfering with the flowfield. Prior to a run the traverse bar was raised by hand, thus tensioning the elastics. The traverse was held in its initial position by a lever with a large level arm. The force of the elastics trying to pull the traverse down was counteracted by an upward force supplied by a very thin nylon thread slung between the long end of the lever and the base of the traverse. This thread was wound again around the lever arm and over to a point on the other linear bearing so that it crossed the section where tests were carried out. When the gun tunnel was fired, the nylon thread melts from the high stagnation temperature in the flow and the traverse would start its travel across the plume flow field. A reflective optical sensor was used to read positions of 4 mm equi-spaced black lines on one of the traverse bearing supports. The triggering arrangement was adjusted until the traverse was capable of traversing about 100 mm of

the flow field in 30 ms at the appropriate time when conditions were relatively steady. A cubic spline was used to interpolate between the peaks caused by the passage of the sensor past each mark, giving displacement.

Timings of various operations are shown in Figure 2-13, which indicates that the Mylar diaphragm bursts at about 1.5 ms after the aluminium diaphragms, and the traverse is released 10 ms afterwards.

2.4 ROCKET MODELS

Various rocket models were used in this study. They can be classified into two main categories: single nozzle and twin nozzle. Single nozzles are given the prefix M or SM (i.e. SM5, M3), and twin nozzles are given the prefix TM (i.e. TM5) (see Figure 2-16). Table 2-2 gives a brief summary of the rocket models used. Detailed drawings of the nozzle can be found in Figure 2-17 to Figure 2-21.

Exit Mach numbers quoted are nominal values assuming no viscous effects. Boundary layer growth in hypersonic nozzles can be significant, and the knowledge of the boundary layer thickness can be used to compensate the inviscid theoretical nozzle profile for the effects of wall boundary layer. The correction usually takes the form of addition of the estimated wall boundary layer displacement thickness to the inviscid flow profile, on the assumption that on this basis the actual nozzle flow can be sufficiently well represented. Satisfactory procedures of boundary layer compensation for axisymmetric nozzle profiles have resulted from extensive experimental and thoretical studies. Depending on the Reynolds number and Mach number ranges, different methods have been developed, (Potter et al 1968, Whitfield 1970 and Edenfield 1968). One method given by Lukasiewicz (1973), although initially verified for $10^6 < \mathrm{Re}_z < 10^8$ and $7 < \mathrm{M} < 22$, is in good agreement with the Mach 5 nozzle results. It can be expressed as,

$$\frac{\delta}{z} = 0.195 M_e^{0.375} \mathrm{Re}_z^{-0.166}$$

Model	Throat Diameter, mm	Exit Diame-ter, mm	Divergence Angle, degree	Nominal Exit Mach Number	Corrected Exit Mach Number	Displacement Thickness, mm
M5	6.00	31.50	10.2	5	4.90	0.5644
M3	3.40	7.00	33.0	3	-	-
SM5	15.2	31.50	10.0	5	4.89	0.3245
SM5M	15.2	31.50	7.0	5	4.84	0.3264
SM3	3.04	6.26	5.0	3	-	-
TM5	2.15	10.75	7.0	5	4.83	0.4361
TM3	2.15	4.42	5.0	3	-	-

Table 2-2 Rocket models used in this thesis

The corrected exit Mach number and the corresponding displacement thickness is given in Table 2-2. The calculated values are based on a typical 100 bar gauge injection at room temperature. (Boundary layer calculation was not applied to the Mach 3 nozzles, because of the uncertainties in the empirical formula at this Mach number.)

2.4.1 Nozzle Design and Manufacture

A total of five nozzles comprising two twin nozzles and three single equivalent nozzles with the same vacuum thrust were used for this thesis. Two additional single nozzles (M5) and (M3) from existing stocks were also used. The twin nozzles were designed so that they shared a common receptacle (see Figure 2-22). This meant that the nozzle attachments are able to rotate to give two orthogonal orientations. This allowed measurements and Schlieren photographs to be taken along the two major axes without the need to re-arrange the traverse mechanism.

Precision lathes were used to manufacture nozzles that have large enough bores for detailed work. For small-bore nozzles, a spark erosion process was used to give a precise and smooth finish. However, due to the limitation of the manufacturing process, nozzles could take up to two weeks to erode.

2.4.2 Rocket Model Sting Effects

All nozzles shared a common base and rocket body, except the M3 nozzle with its integrated body. The rocket body was connected to the plenum chamber via a single sting (or in the case of the M3 nozzle, to the frame tubing via two stings. See Figure 2-23 and Figure 2-24.

The model sting should have negligible effect on the plume flowfield in quiescent runs. However, in the co-flow case, disturbances from the stings could be relatively significant. Early studies on rocket plumes ignored its effects on the downstream flowfield. A symmetrical plume was assumed and data within the sting region was obtained by mirroring the undisturbed side.

A detailed study was carried out by Shek (1995) and showed that stings could have a significant effect on the downstream rocket plume flowfield. The extent of their influence was measured with Pitot pressure probes by traversing along different paths across the plume crossflow plane. Figure 2-25 and Figure 2-26 show the schematic illustrations of the measured barrel shock positions and the assumed values. The estimated plume shapes are shown based on the measured data points.

If measurements need to be taken along the vertical centreline, influences from the sting could be minimised by installing it horizontally as in the case of the M3 rocket nozzle model. Unfortunately, this adds complication to Schlieren photography as the shock produced by the horizontal sting can cause saturation to the Schlieren images. Enlarging the light source can compensate this. However, problems arising due to aberration meant that a graded filter must be used, resulting in trade off in overall sensitivity.

2.5 DATA ACQUISITION AND PROCESSING

2.5.1 Data Sampling Units

For acquiring low frequency data, a Hewlett Packard 6944A Series 200 Multiprogrammer was used. This served as a multiplexer linked to a Hewlett Packard 9836 minicom-

puter: Signals from the transducers were multiplexed into the 6944A and stored in a 64K memory. The multiplexer switches every 11 μs and up to 12 channels can be recorded depending on the particular experiment, equivalent to a sampling rate of 7.5 kHz for 12 channels. Data were then transferred to the 9836 for storage in binary format on 92190A flexible disks, and subsequently converted into ASCII format using a proprietary conversion programme. Sampling rates were at worst 0.8 ms when the maximum number of channels was used on the HP. This meant one measurement every 2.8 mm across the flowfield. For discontinuities in pressure and heat transfer measurements such as those found across shocks, sudden changes could therefore be smeared slightly depending on probe velocity and geometry.

For high frequency data, an Adtek AD402 analogue to digital sampling unit was used in conjunction with a mini-computer. The AD402 A/D converter board has four single ended 12-bit channels and can sample each channel at a rate up to 2.0 MHz per channel. At this rate the amount of digital information generated by the board is 16-MB per second. One unique feature of this board is its allocation of an A/D converter to each active channel. This then eliminates noise and cross-talk problems that can be associated with the combination of a multiplexer and an ultra high-speed converter, thus resulting in a better digital representation of an analogue signal.

2.5.2 Data Format and Processing

Matlab was used extensively as the main processing engine. Additional add-on toolboxes (Image Processing, Signal Processing, Control System and System Identification Toolboxe) were also used in conjunction with the main program to enhance its overall capability.

Schlieren images were scanned at a high resolution and processed in the Image Processing Toolbox. This enabled detailed analyses on the flowfield features with the freedom to zoom in on areas of interest, and provided an accurate way of obtaining plume dimensions.

Raw data were saved in ASCII, Matlab and binary formats depending on the instrumentation used for the run. A general format was adopted where runs were saved with the

prefix LT for quiescent runs and GT for co-flow runs in the presence of the Mach 7 freestream. High frequency data captured by the ADTEK were saved with the prefix FLT and FGT for quiescent and co-flow runs respectively. For example, a quiescent run number 156 will have two sets of files, LT156 for the HP and FLT156 for the ADTEK.

The vectors for each run were prefixed according to what the signal represented. A list of vectors is shown below in Table 2-3.

Prefix	Measurement
tim	time in milliseconds from the beginning of the run
dsp	displacement vector deduced from the optic sensor signal
stg	gun tunnel stagnation pressure measured at the end of the barrel
txp	test section pressure measured on the floor of the section
inj	rocket injection pressure measured in the plenum chamber of the model
opt	optical sensor output for a traverse
spk	spark signal of the Schlieren camera
pit	PIT Pitot pressure probe
fpt	FPT Pitot pressure probe
rpt	RPT Pitot pressure probe
bpt	BPT Pitot pressure probe
tht	substrate temperature of the *hot* heat transfer probe
twm	substrate temperature of the *warm* heat transfer probe
tcd	substrate temperature of the *cold* heat transfer probe
qht	heat flux signal from the analogue circuit for the *hot* probe
qwm	heat flux signal from the analogue circuit for the *warm* probe
qcd	heat flux signal from the analogue circuit for the *cold* probe

Table 2-3 Nomenclature of the data format adopted for this thesis

Data were processed to convert voltage levels from raw signals to meaningful measurements. The conversion process was carried out in Matlab using a program written for this purpose. A sample screen dump of the program is shown in Figure 2-27. This program could be configured to take into account adjustments to measured signals based on various correc-

tion algorithms. Additional programs were also written to apply corrections to the data from the heat transfer probes and to facilitate the subsequent analyses.

Successful runs were tabulated for ease of reference (see Appendix C). *Run number* indicates the name of the run. The downstream positions given indicate the station where the measurements were taken and are accurate to within 3 mm. Precise location of the probe can be measured on the Schlieren images when necessary. *Fast data* gives the file names of the data recorded by the ADTEK AD402. *Probes* shows the instrumentation used for that particular run with abbreviations corresponding to: (H)-heat transfer measurements, (S)-Schlieren photography, (P)-Pitot pressure measurements, (T)-Total temperature calculation, (CBC) laser cross-beam correlation.

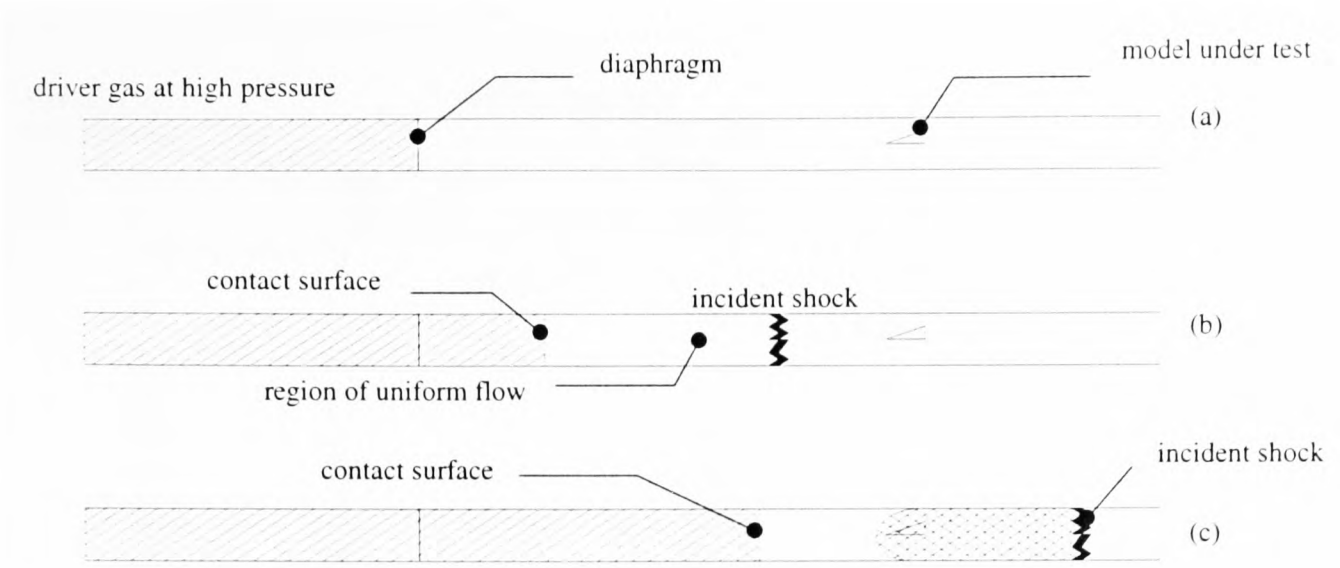


Figure 2-1 Sketches illustrating the operation of a shock tube. (a) Initial conditions, (b) after diaphragm bursts and (c) after establishment of flow in the working section.

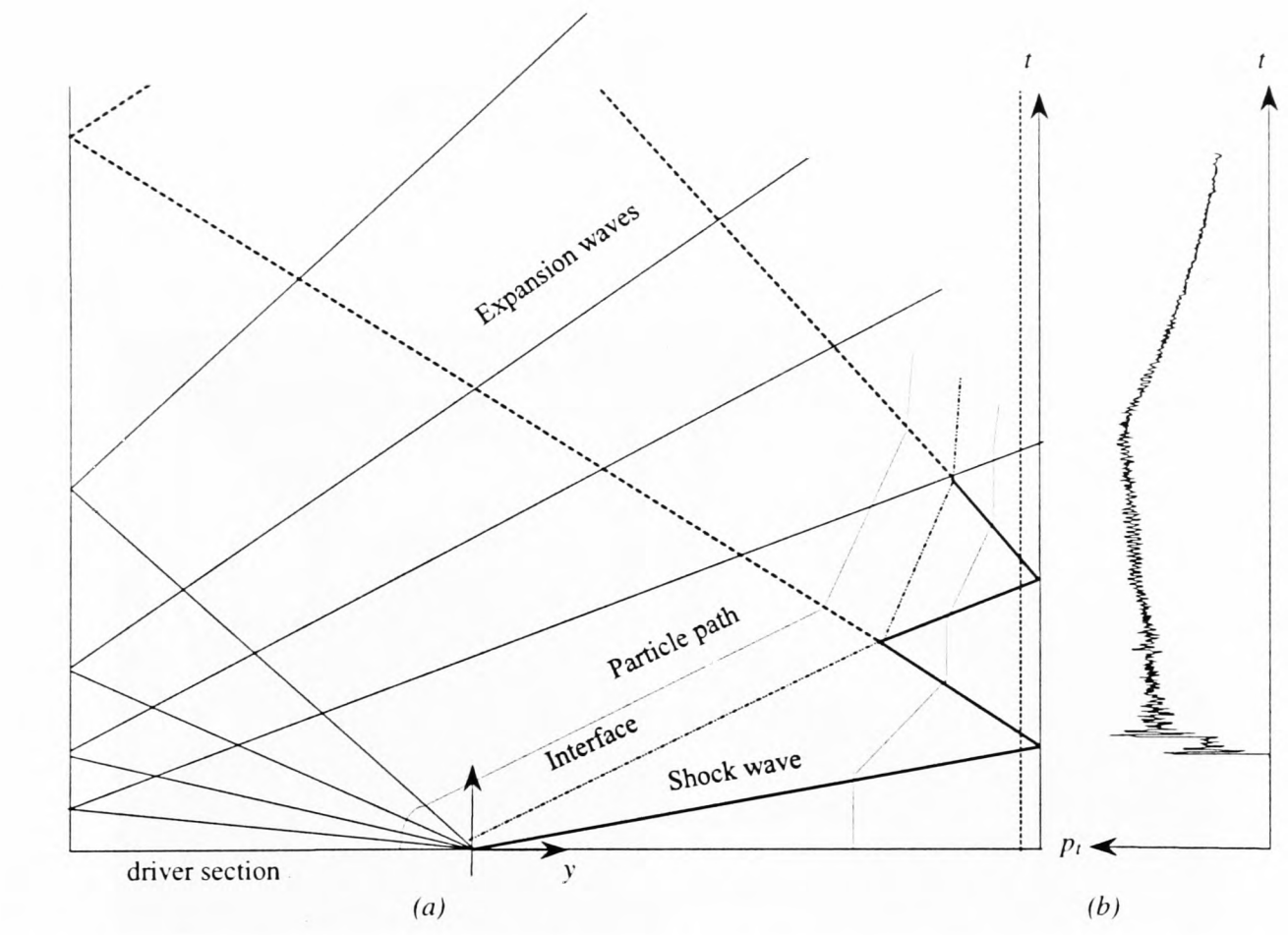


Figure 2-2 (a) Wave diagram for an *over-tailored* shock tube, (b) Pitot pressure profile measured from the end wall

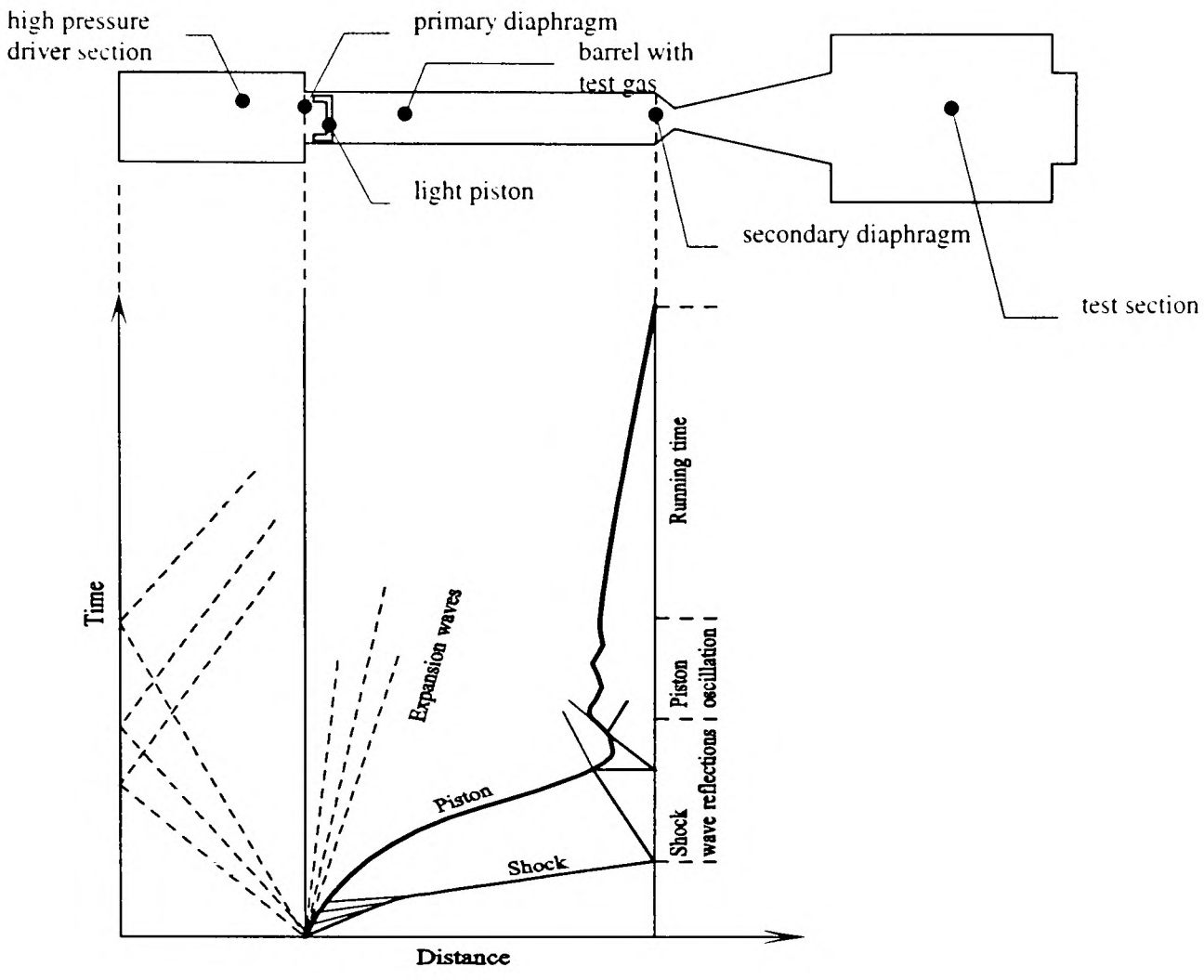


Figure 2-3 General layouts of gun tunnels and the corresponding wave diagram

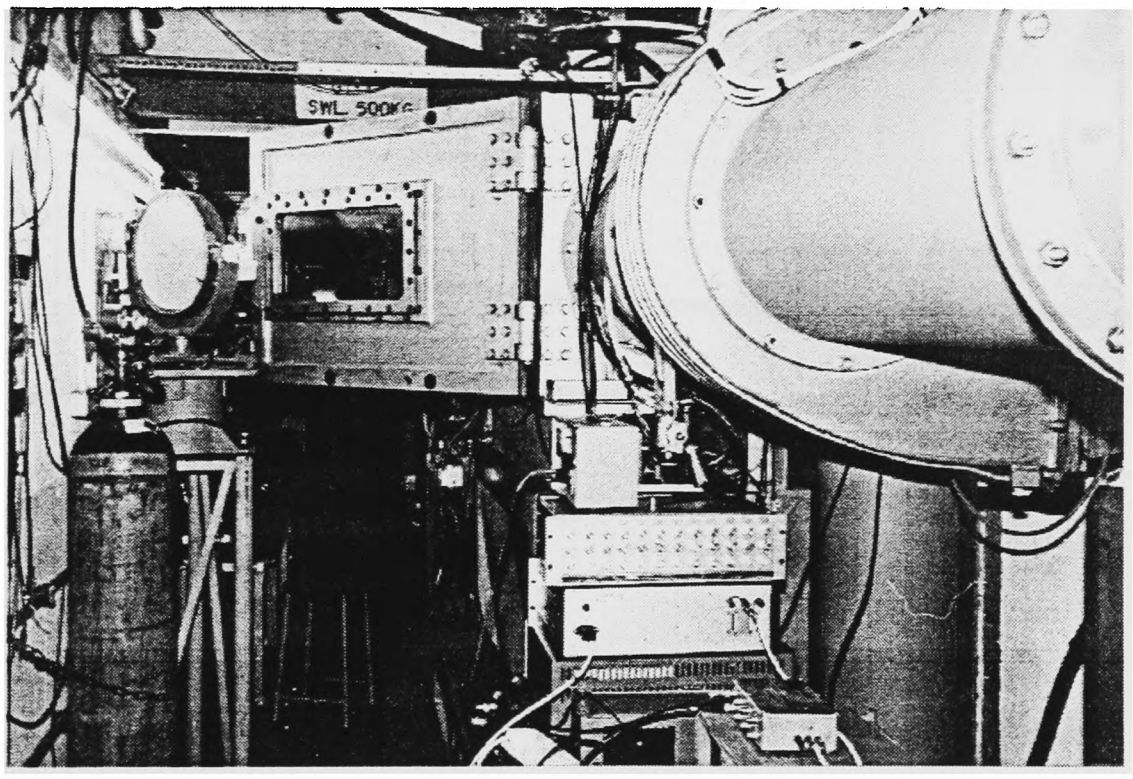


Figure 2-4 Photograph of the Oxford Gun Tunnel

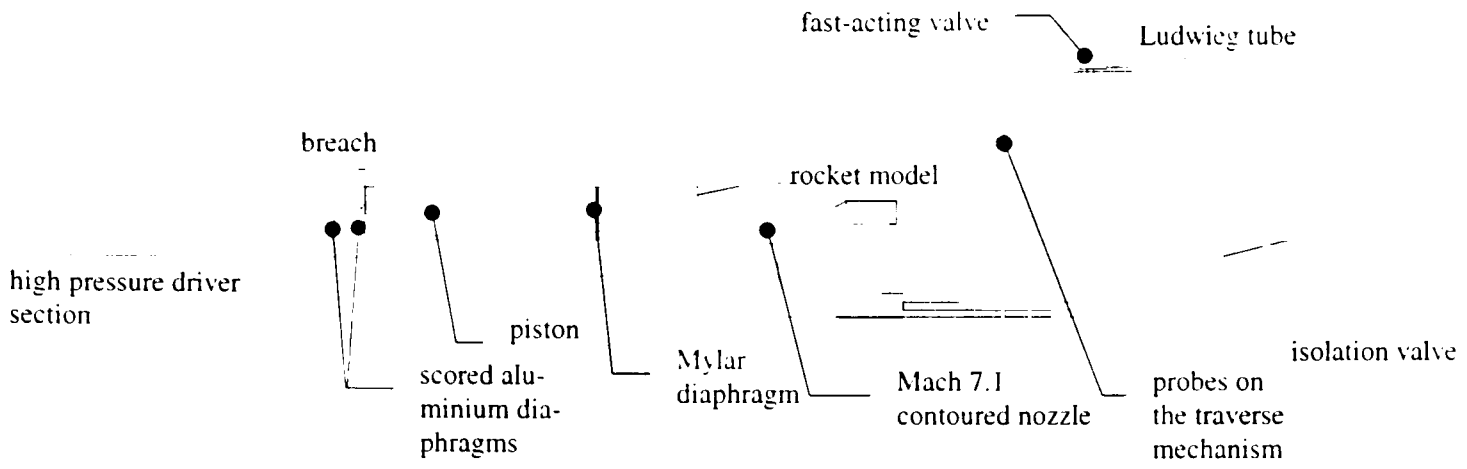


Figure 2-5 Schematic illustration of the Oxford Gun Tunnel

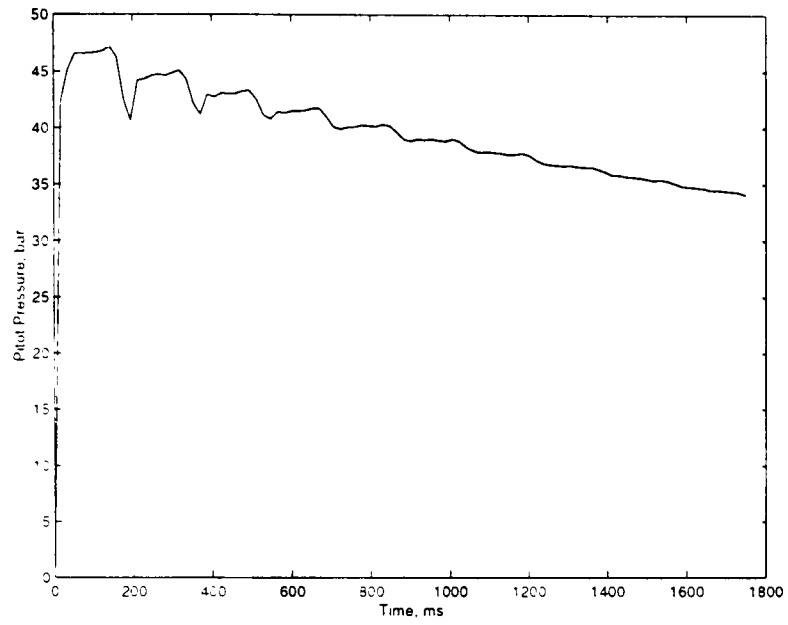


Figure 2-6 Plenum chamber pressure with 50 bar gauge injection of N_2 in quiescent *(LT166)*

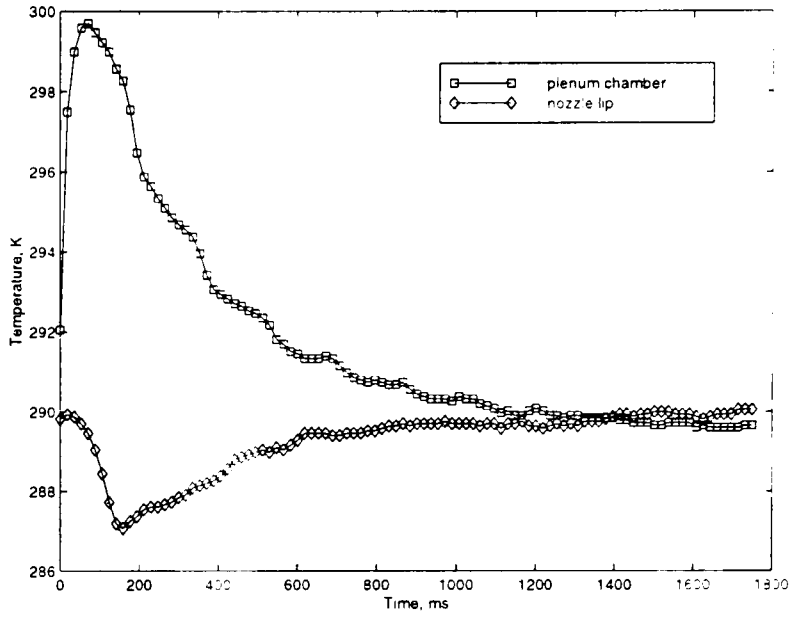


Figure 2-7 Plenum and nozzle lip temperature with 50 bar gauge injection of N_2 in quiescent *(LT166)*

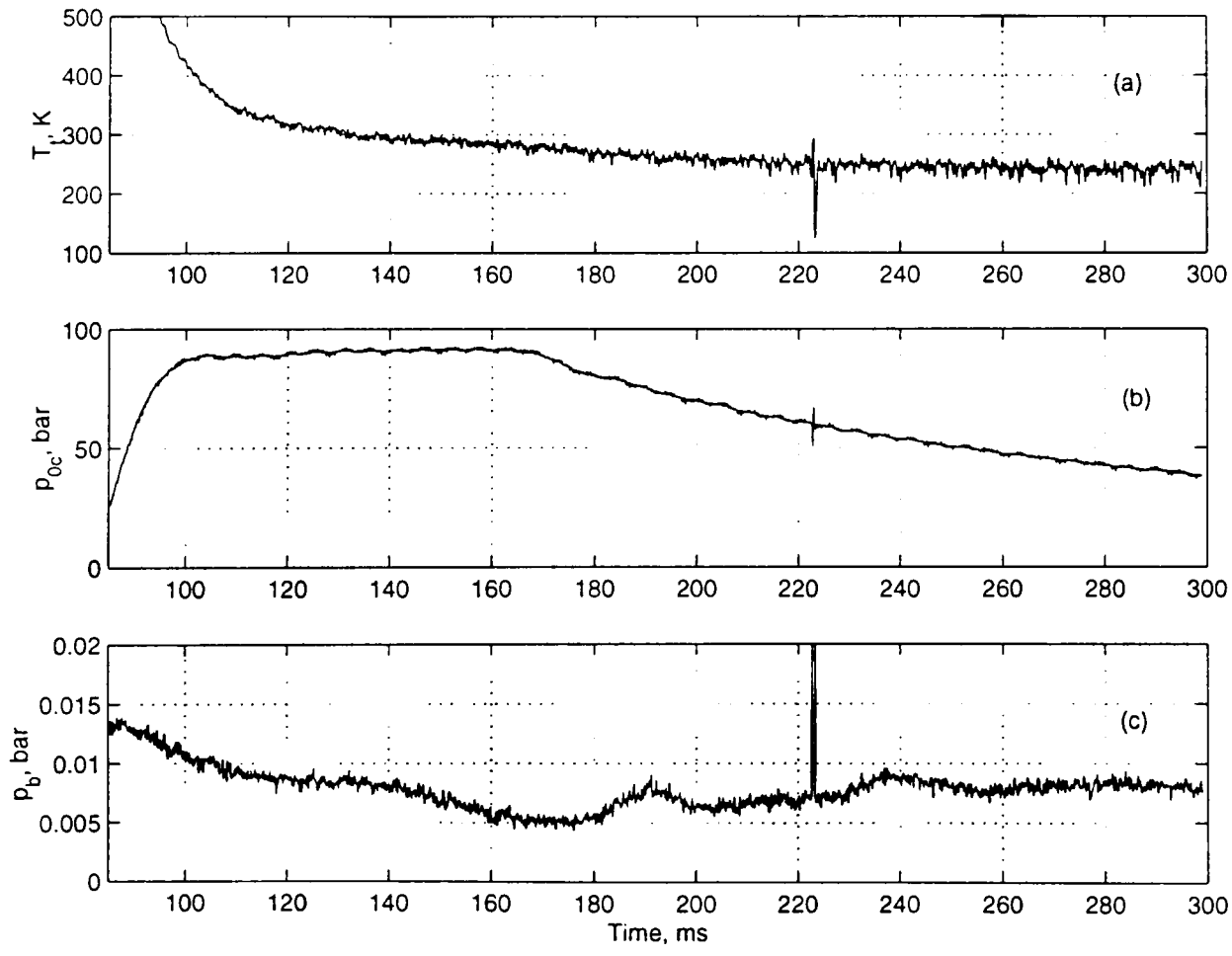


Figure 2-8 (a) injection total temperature, (b) injection pressure, (c) test section pressure with N_2 injection *(SM5M, LT201)*

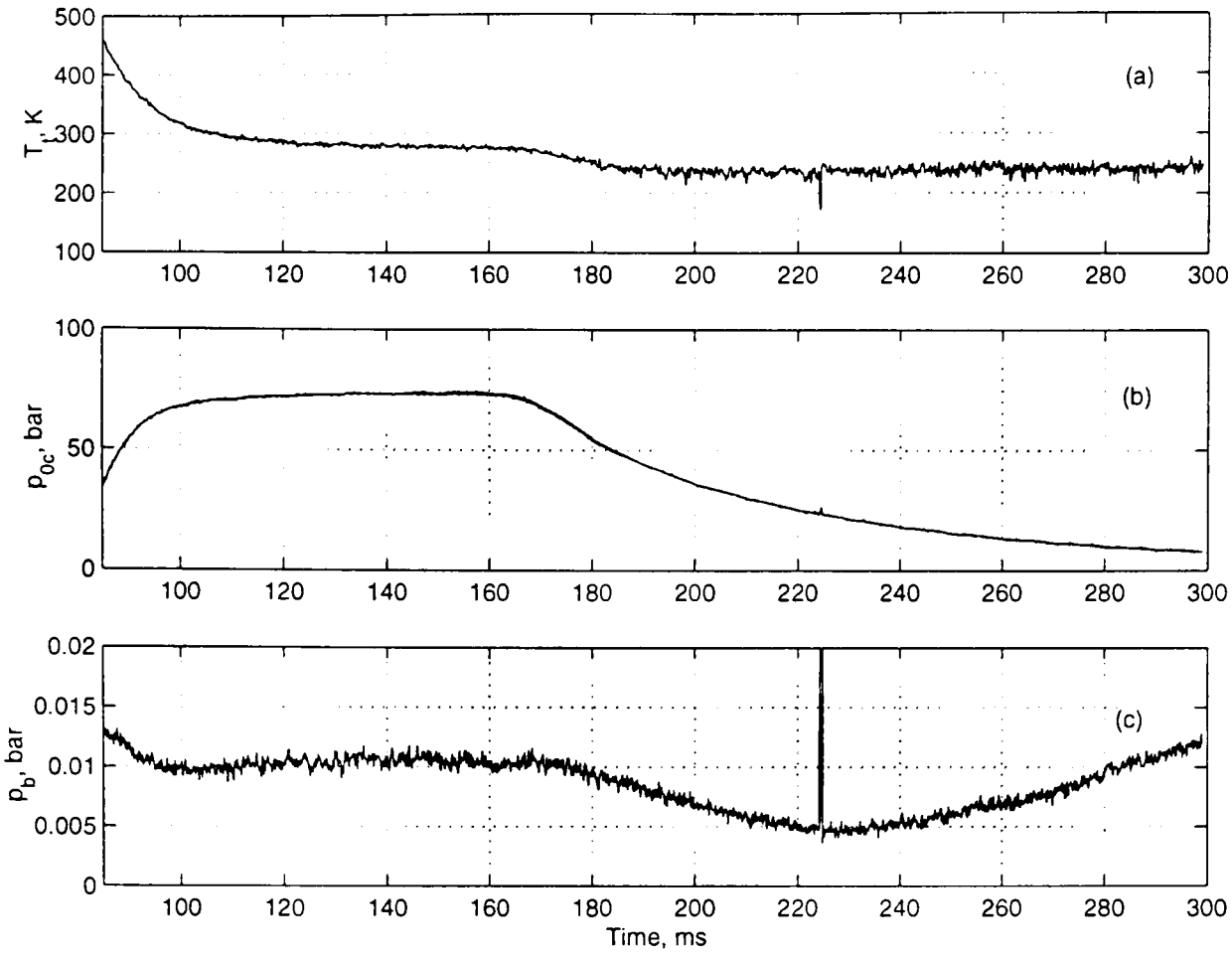


Figure 2-9 (a) injection total temperature, (b) injection pressure, (c) test section pressure with N_2 injection *(M5, LT187)*

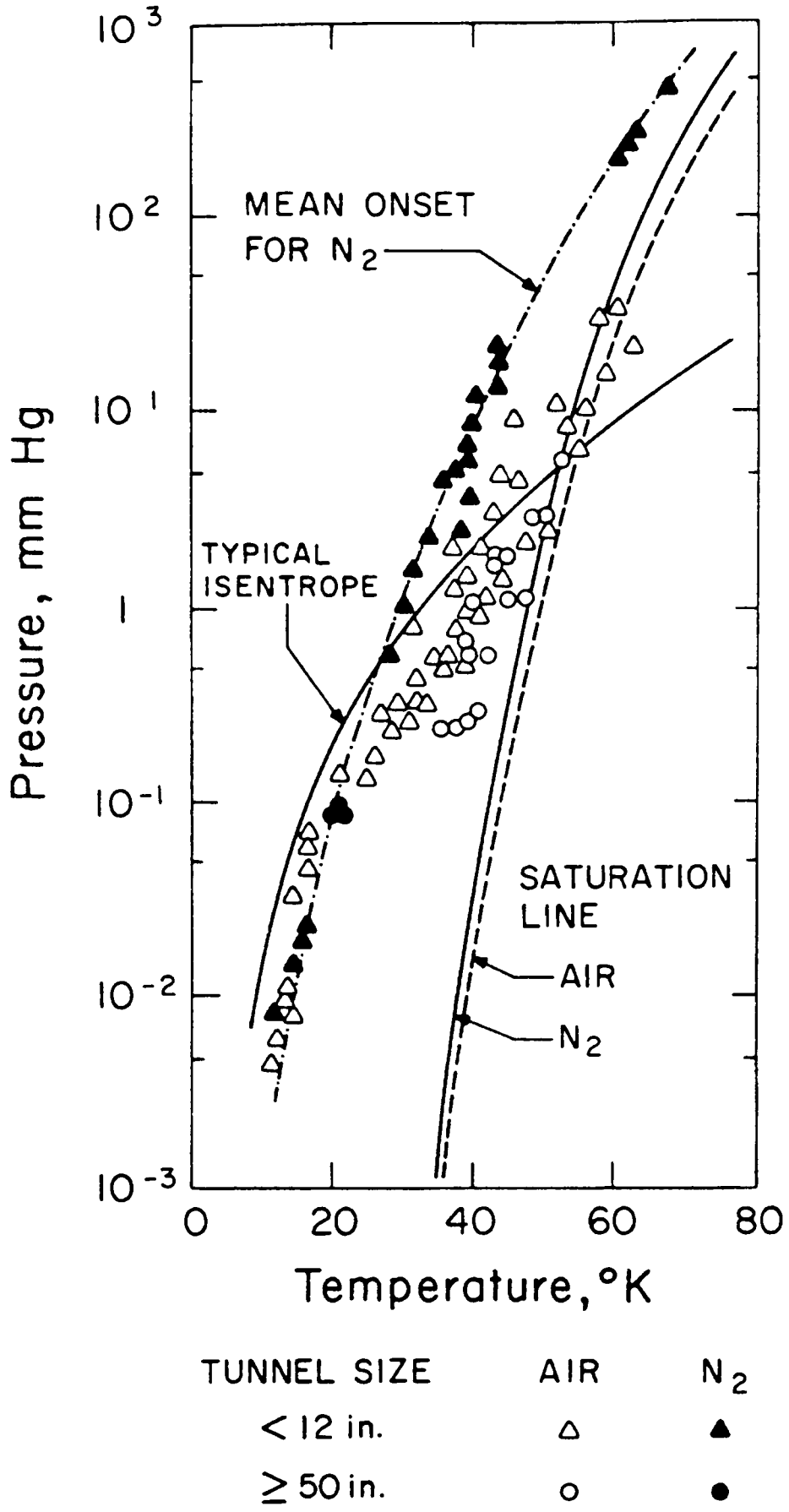


Figure 2-10 Experimental estimation of the onset of condensation *(Lukasiewicz, 1973)*

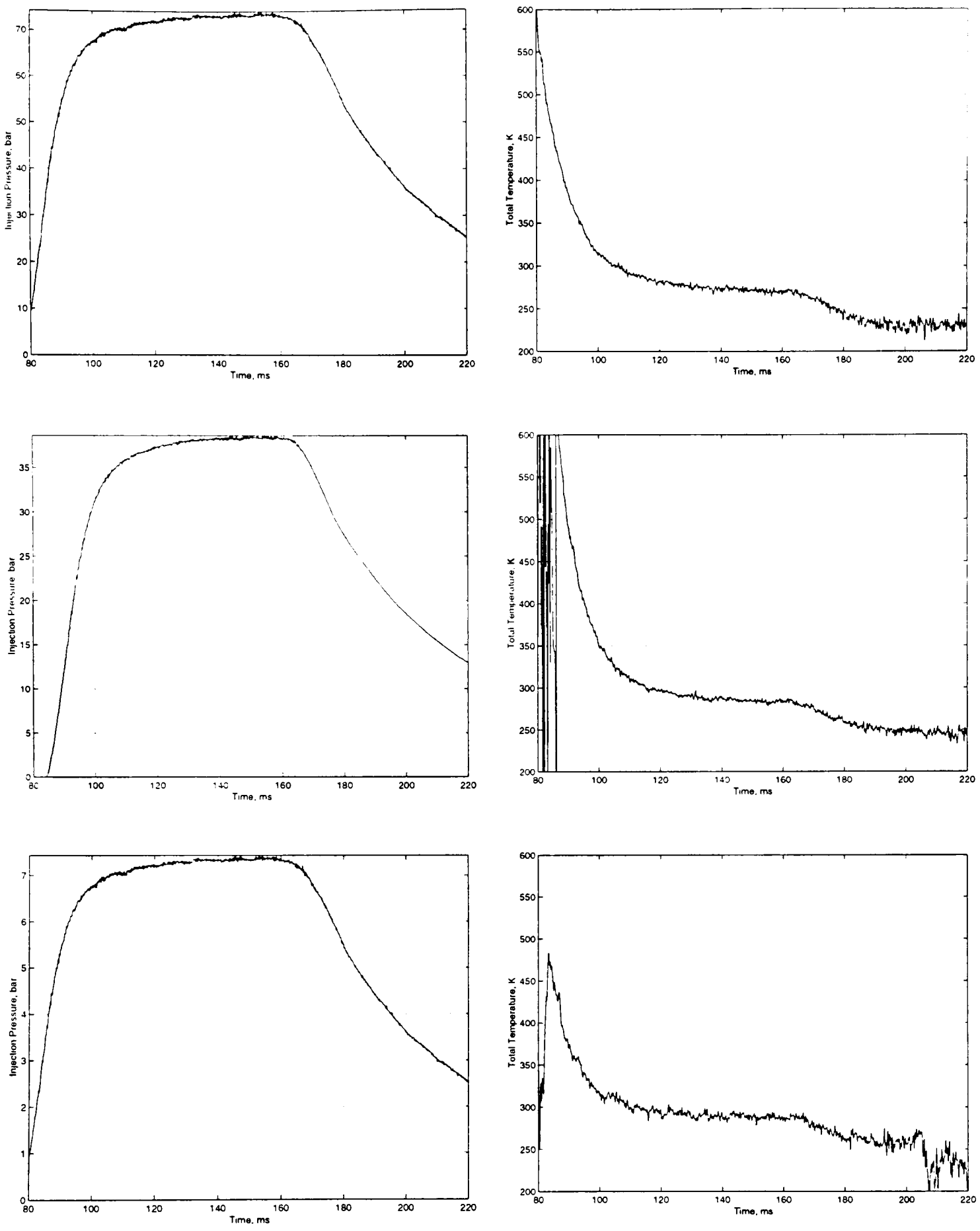


Figure 2-11 Injection pressures and corresponding total temperatures for Mach 5 (M5) single nozzle jet at 11 mm downstream with N_2 injection *(left: injection pressure in plenum chamber by pressure transducer, right: total temperature at exit from heat transfer probes)*

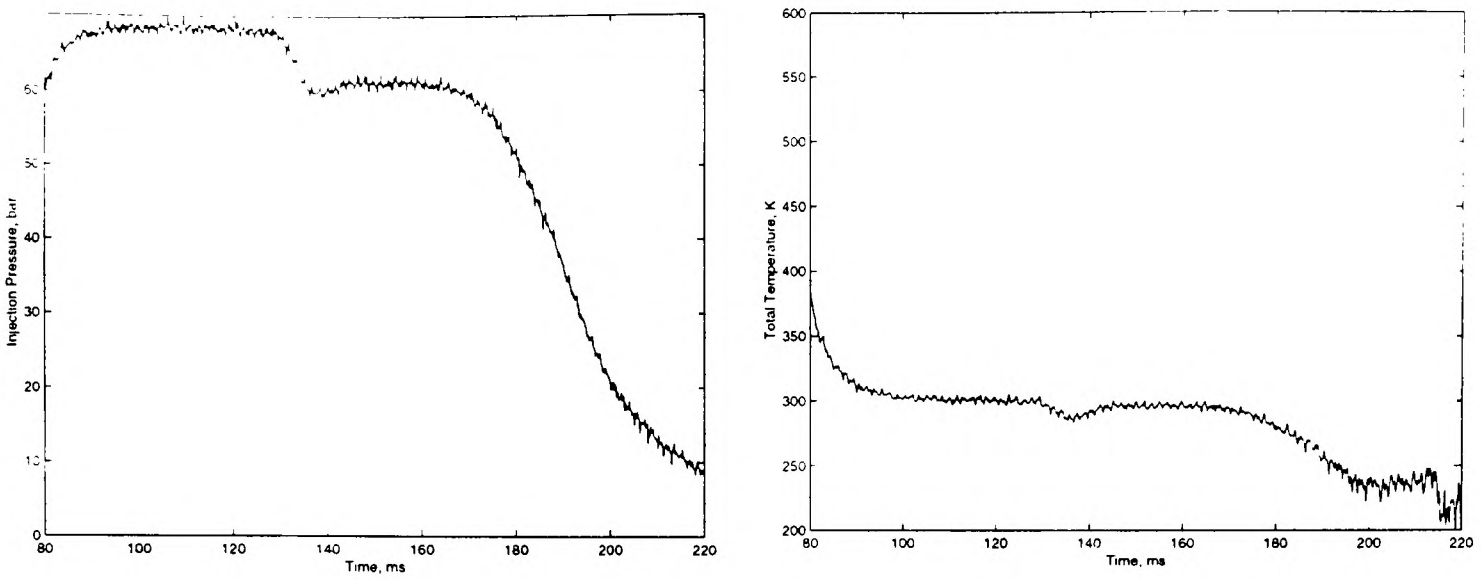


Figure 2-12 Injection pressure and corresponding total temperature for Mach 5 (M5) single nozzle jet at 11 mm downstream with He injection *(left: injection pressure in plenum chamber by pressure transducer, right: total temperature at exit from heat transfer probes)*

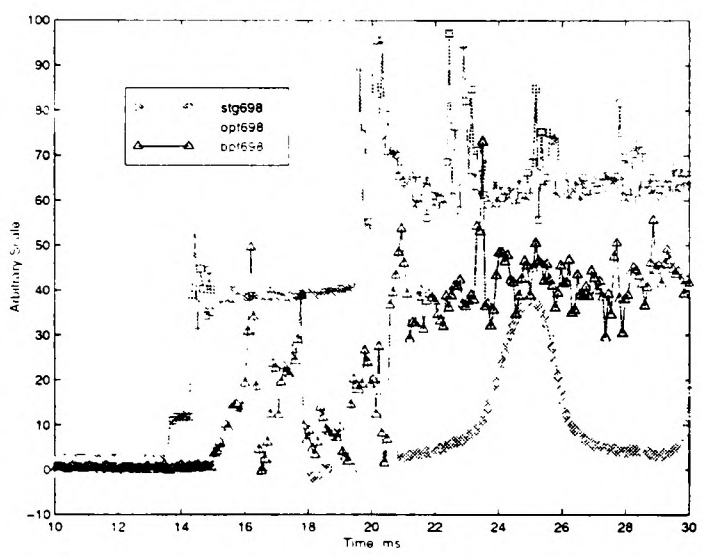


Figure 2-13 Timing for a typical gun tunnel run with 100 bar gauge injection in Mach 7 freestream *(GT698)*

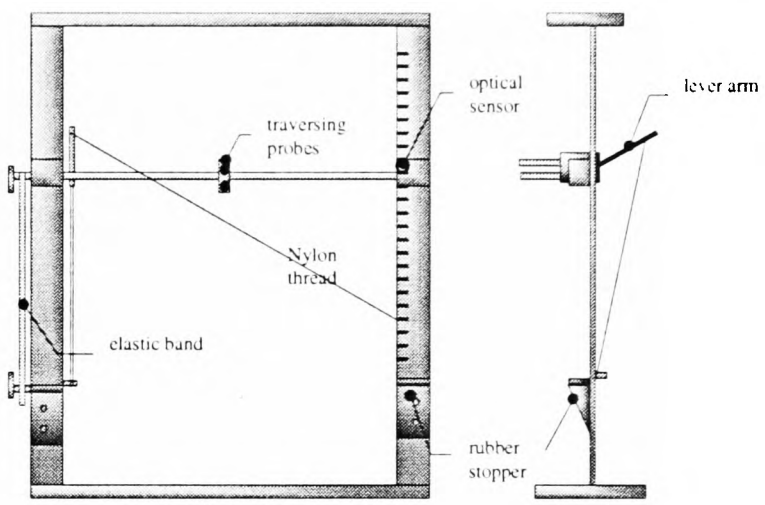


Figure 2-14 Schematic illustration of the traverse mechanism

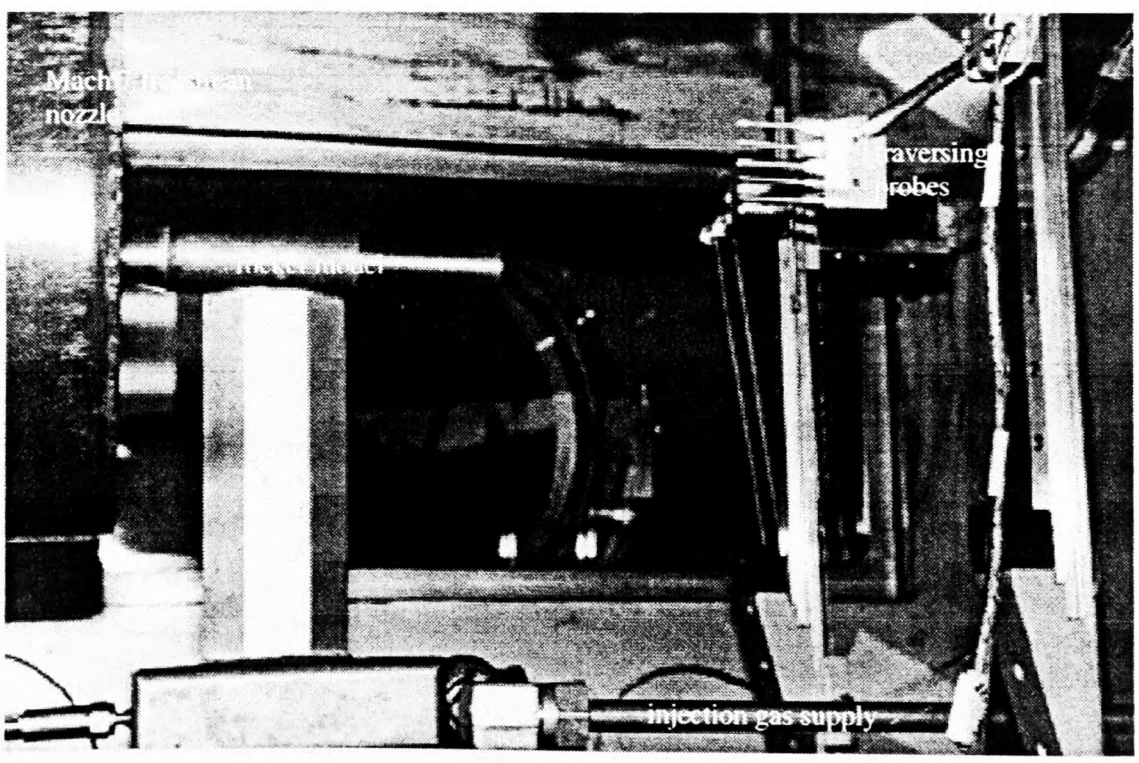


Figure 2-15 Typical arrangement in the test section

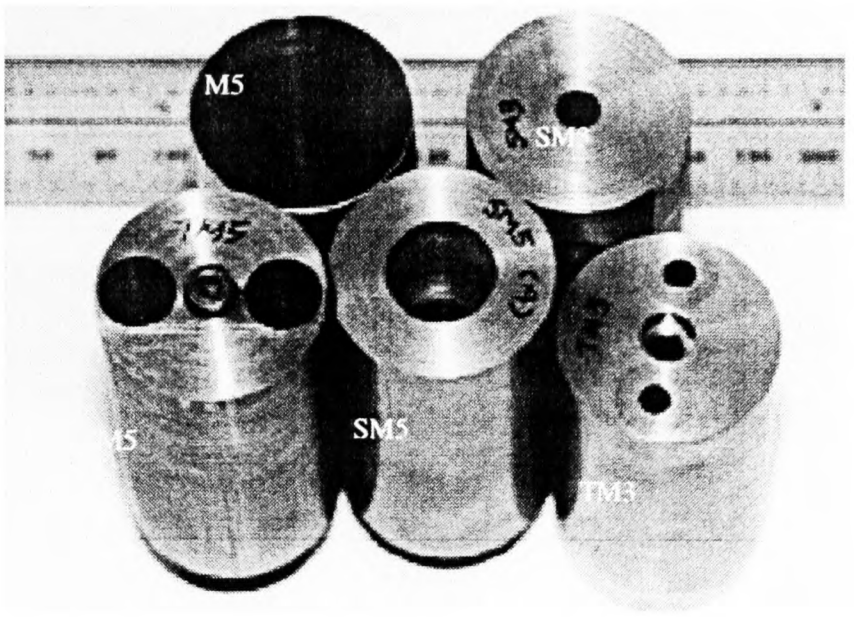


Figure 2-16 Photograph of rocket nozzles used in this thesis

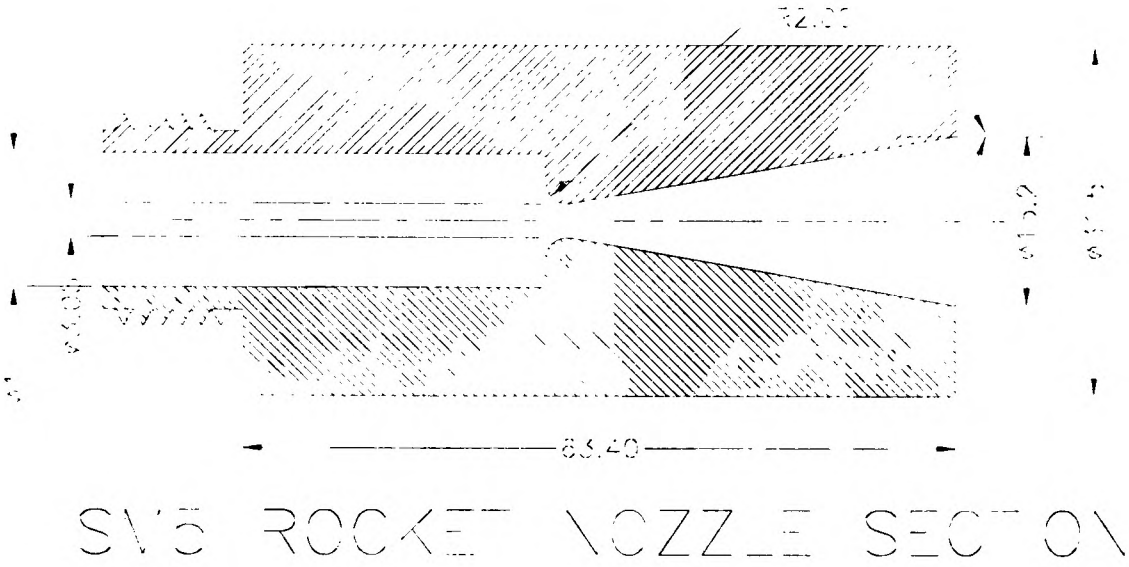


Figure 2-17 Mach 5 (SM5) single nozzle sectional view

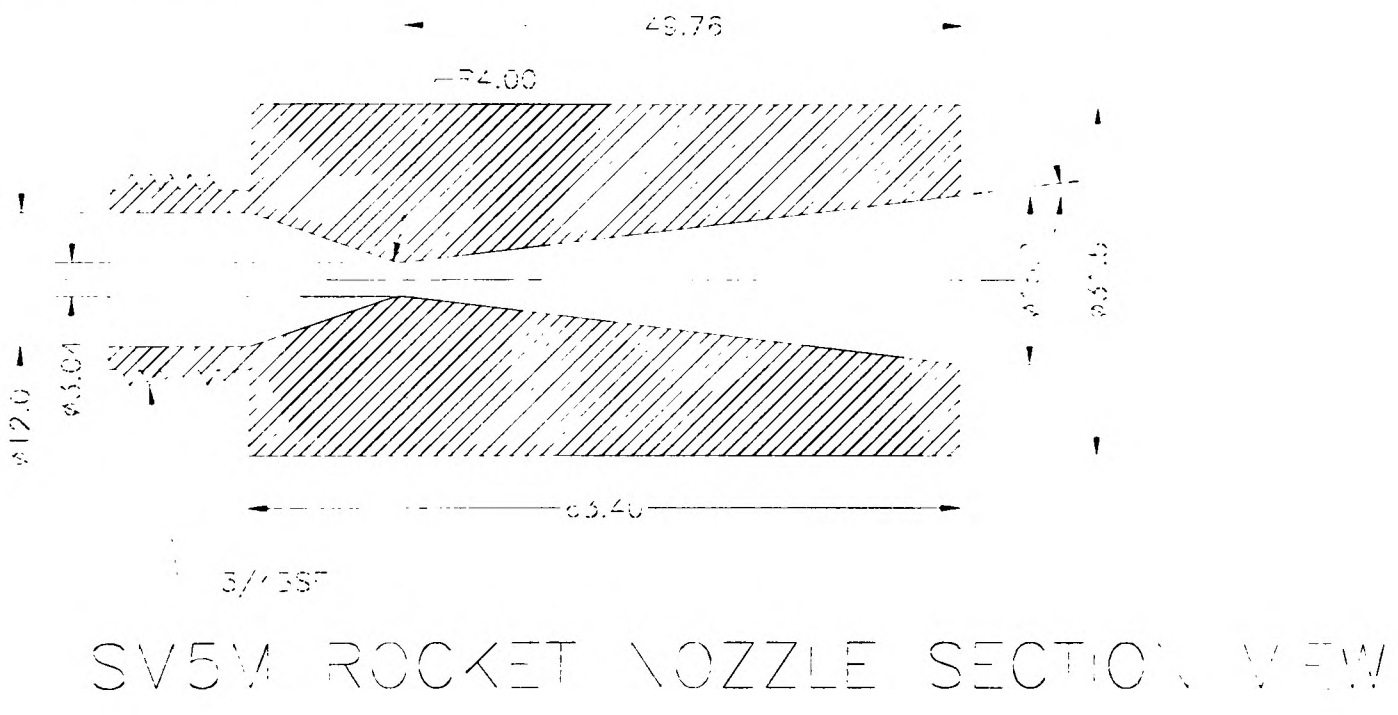


Figure 2-18 Mach 5 (SM5M) single nozzle sectional view

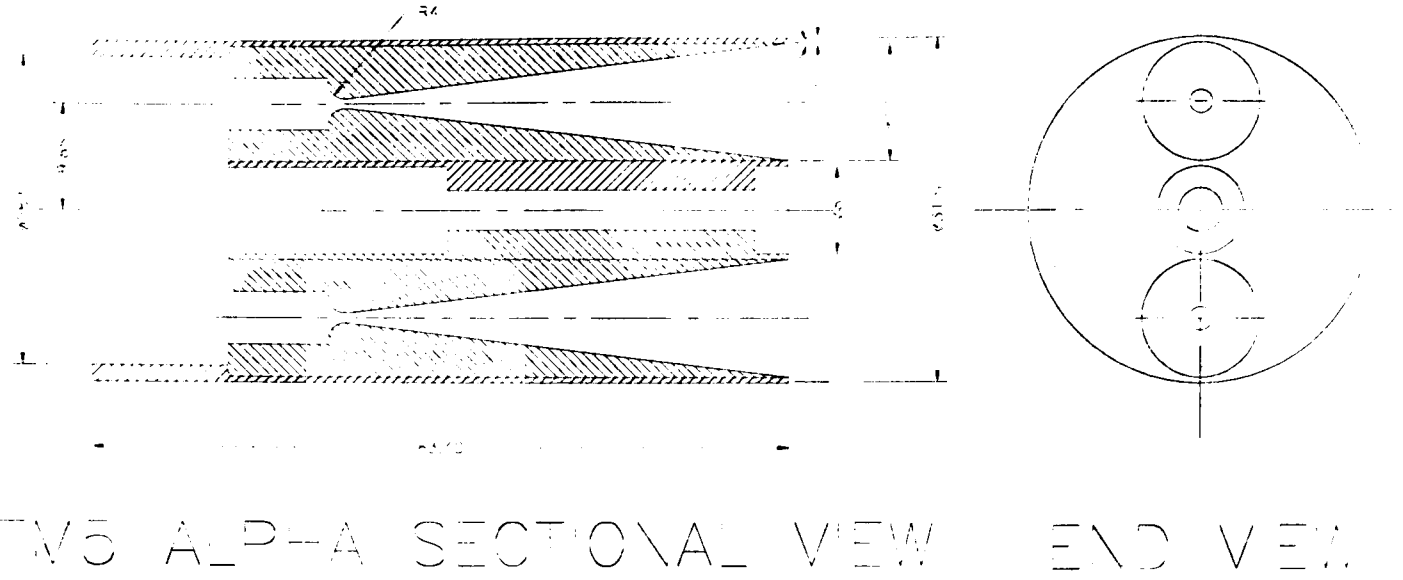


Figure 2-19 Mach 5 (TM5) twinjet nozzle sectional view

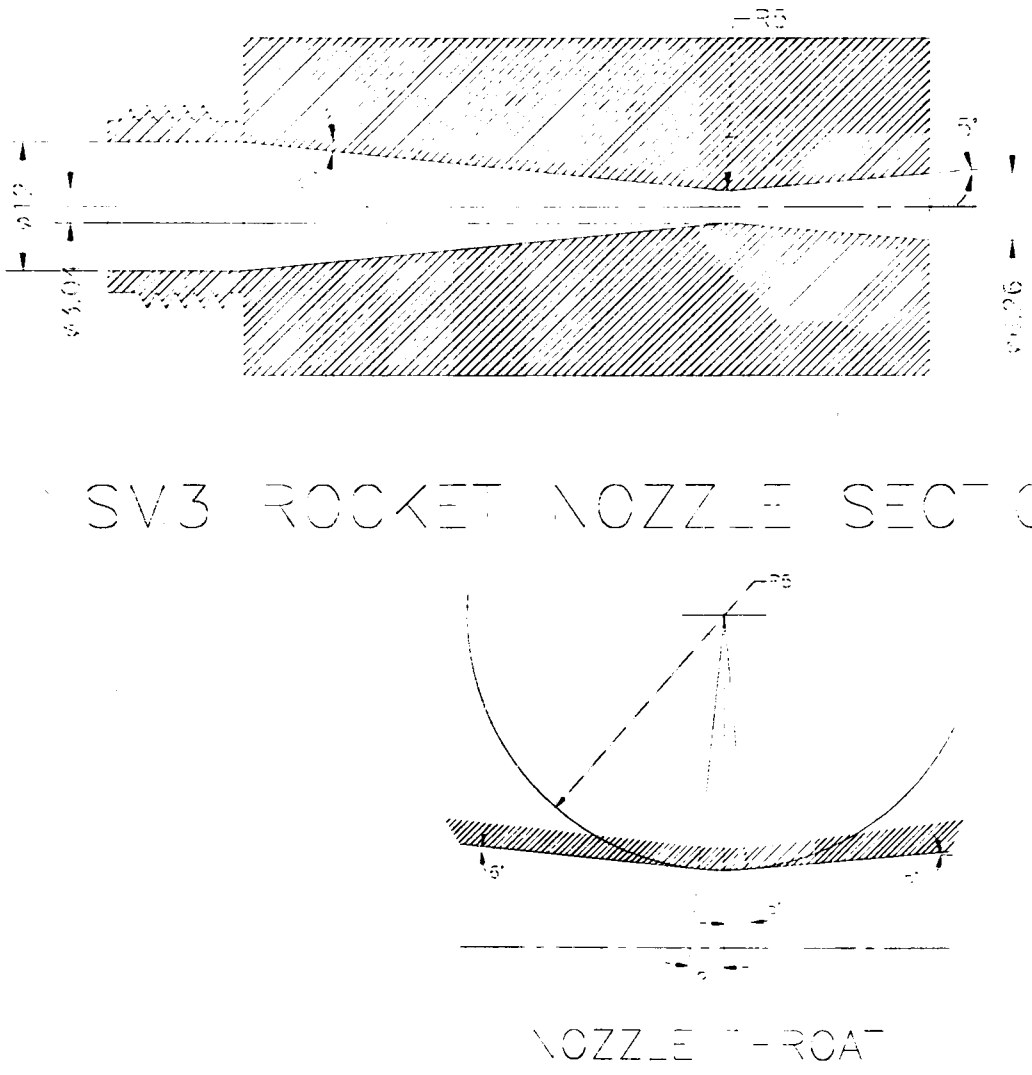


Figure 2-20 Mach 3 (SM3) single nozzle sectional view

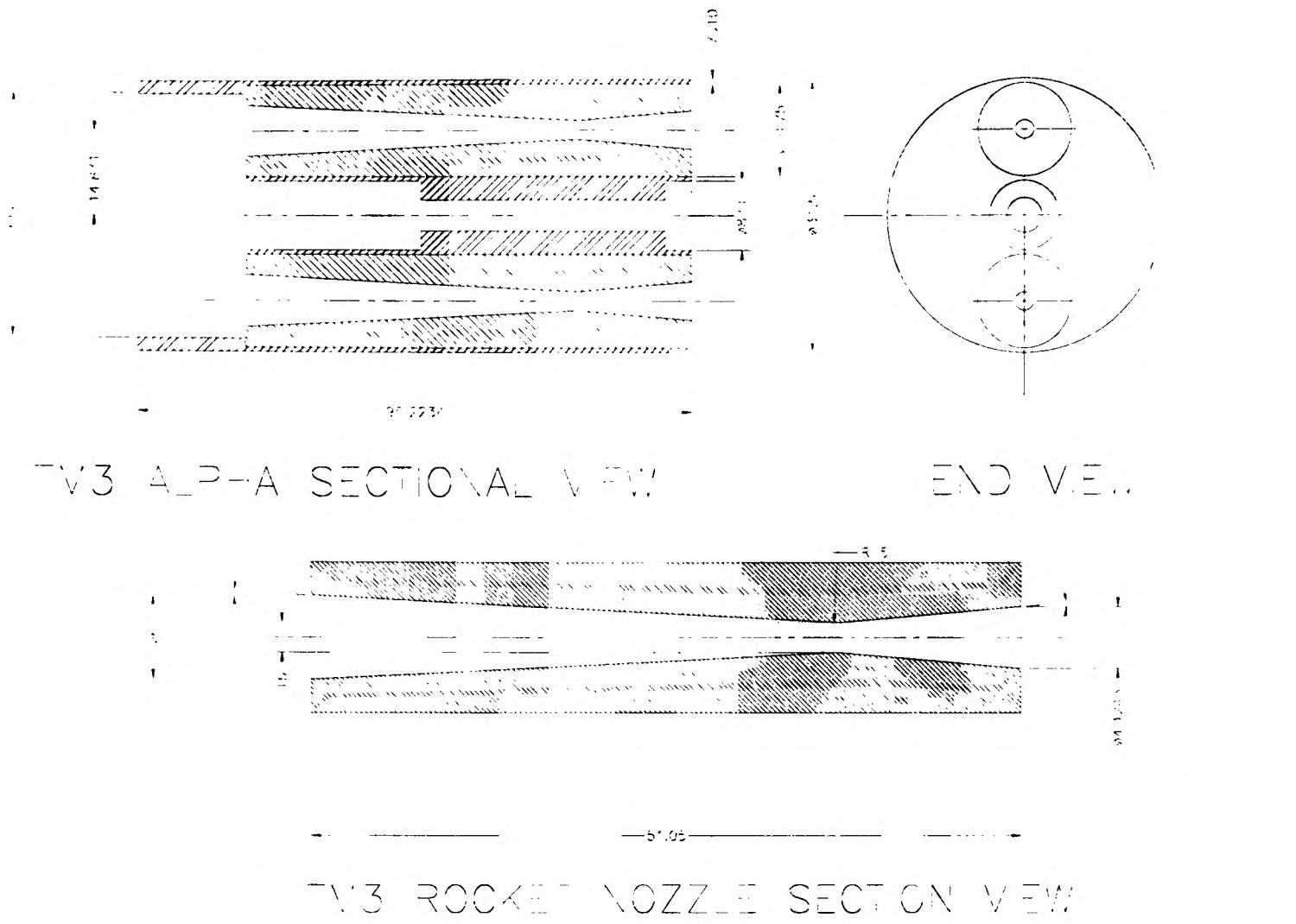


Figure 2-21 Mach 3 (TM3) twinjet nozzle sectional view

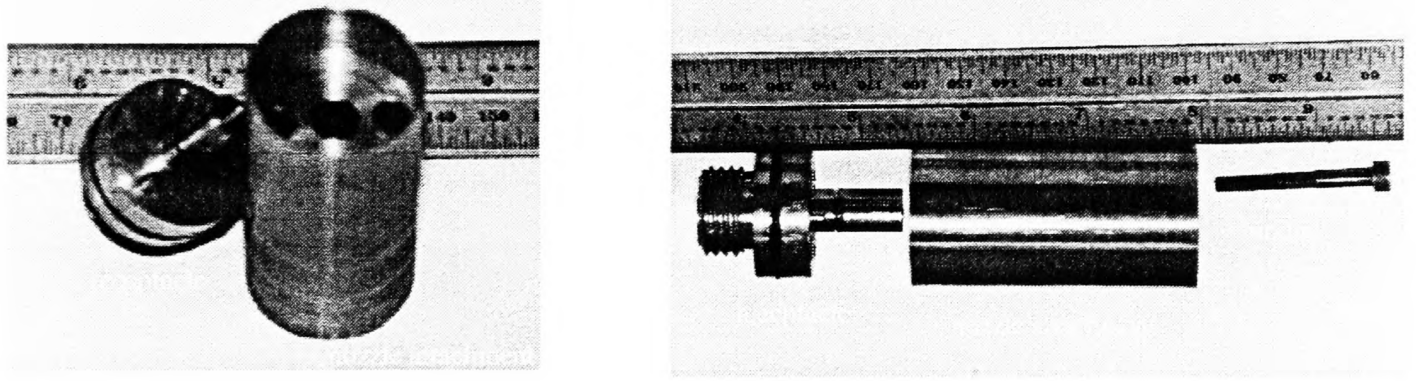


Figure 2-22 Photographs showing the Mach 5 (TM5) twinjet nozzle attachment and the common receptacle

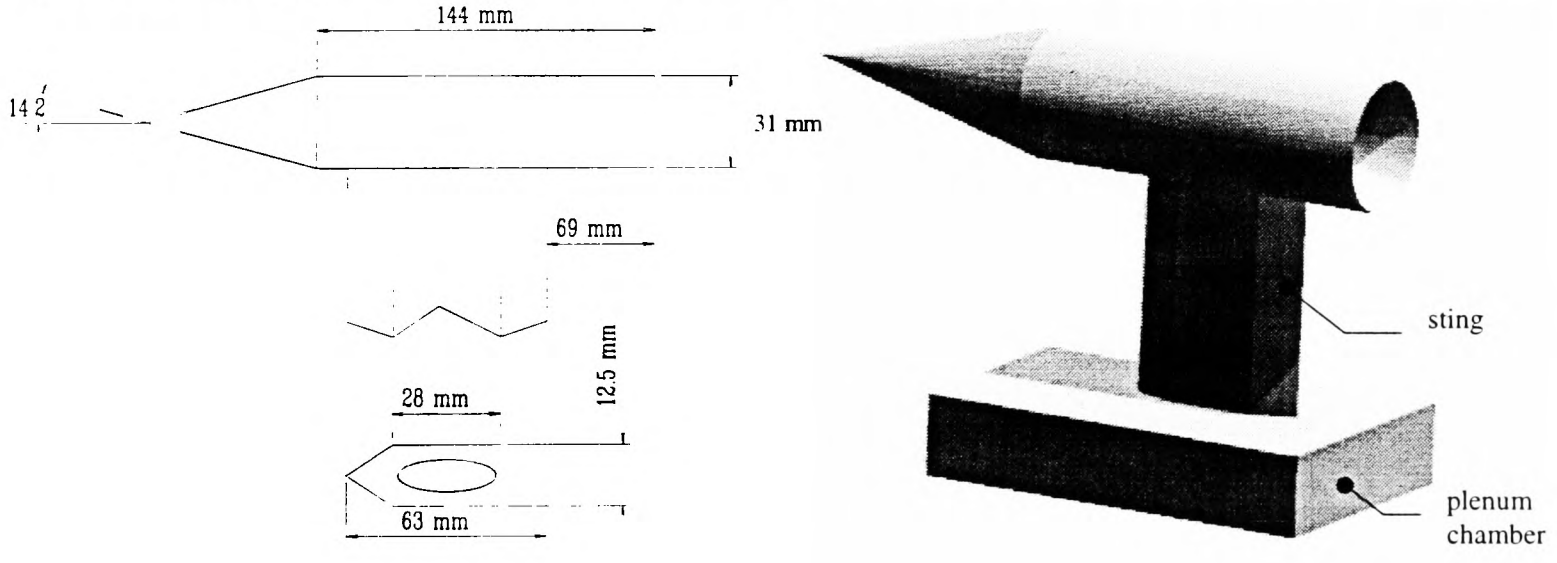


Figure 2-23 Mach 5 (M5) single nozzle and rocket body

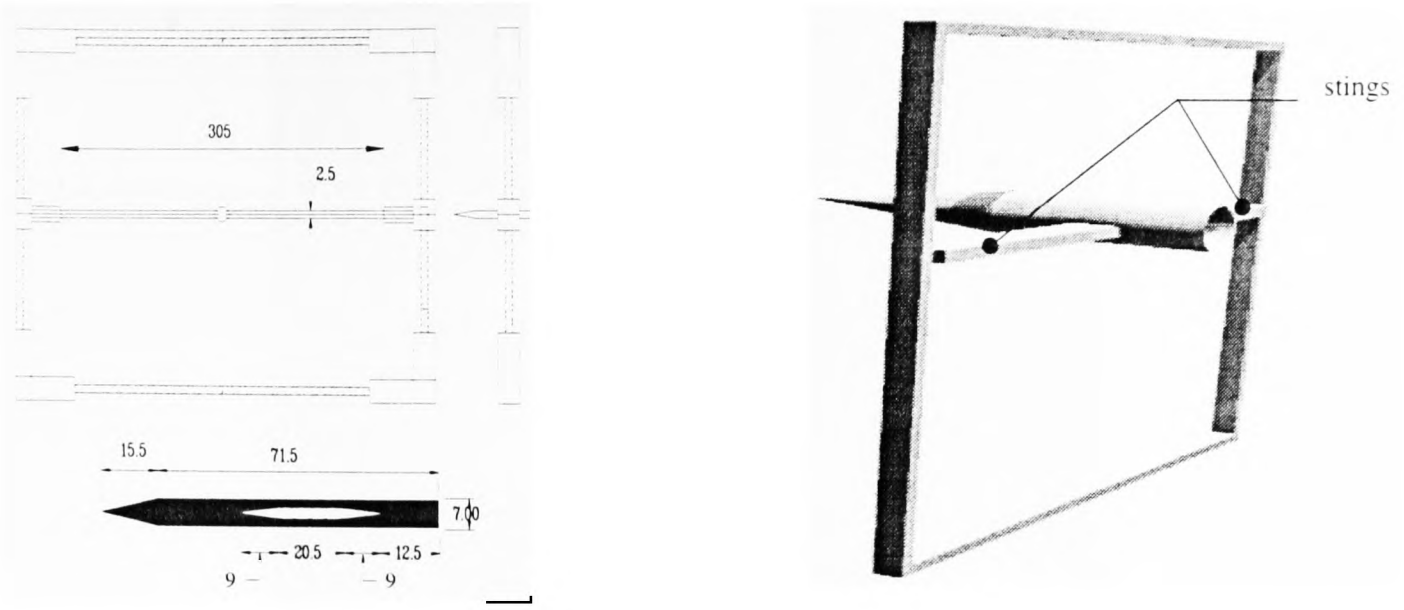


Figure 2-24 Mach 3 (M3) single nozzle and rocket body

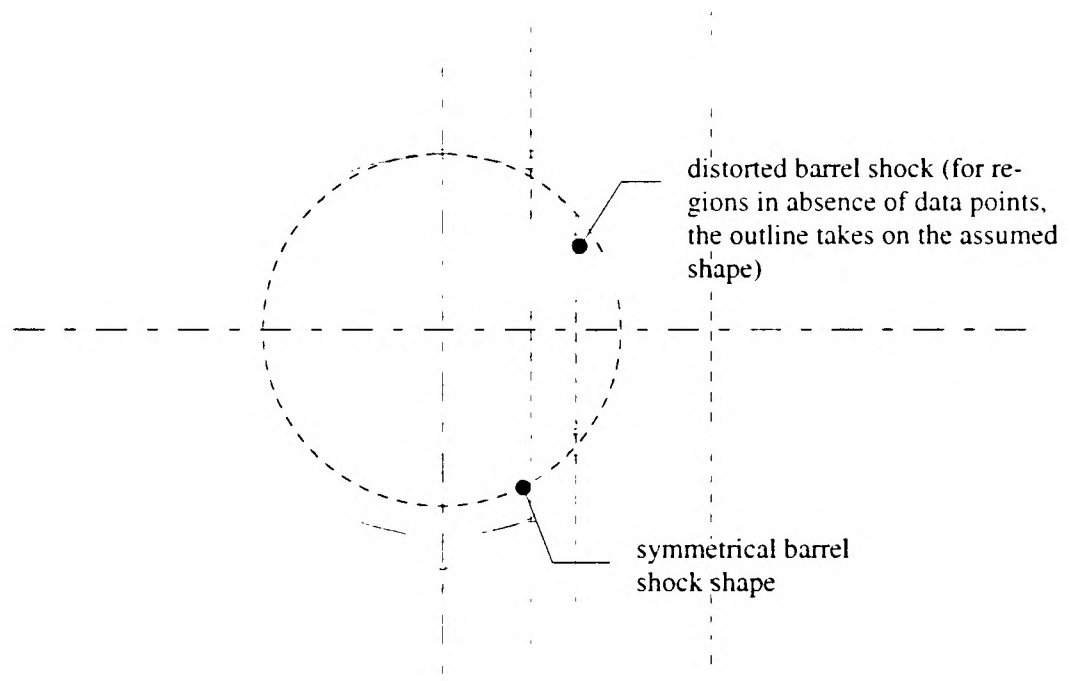


Figure 2-25 Mach 5 (M5) rocket plume on crossflow plane in Mach 7 freestream showing an assumed barrel shock due to the presence of the sting

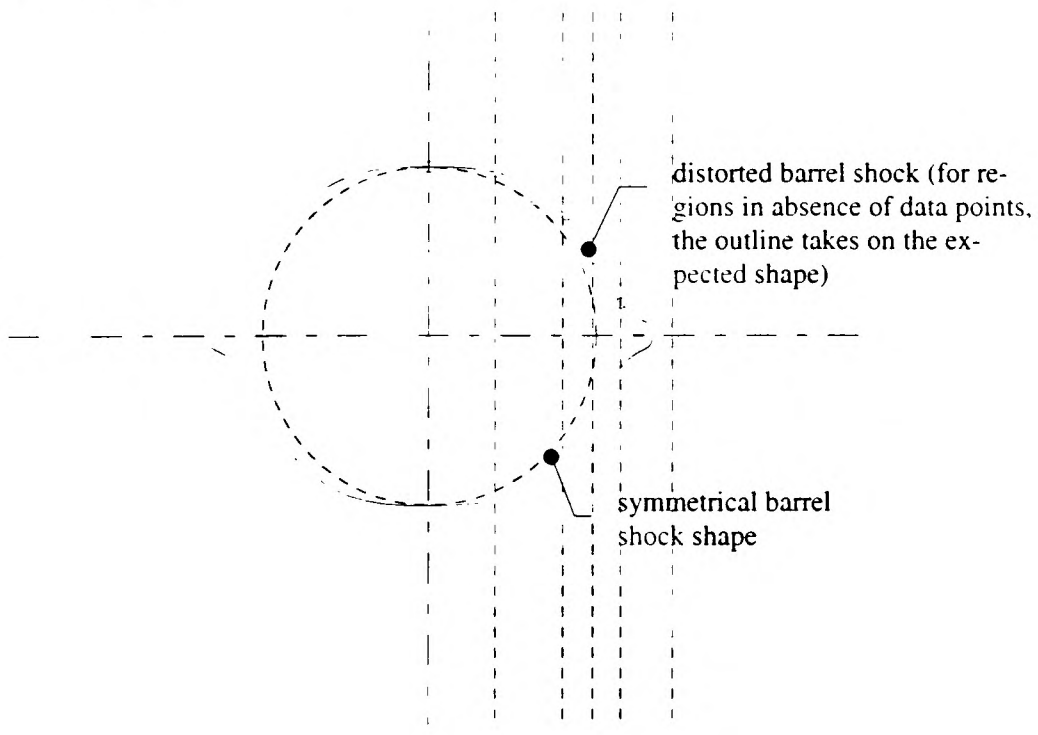
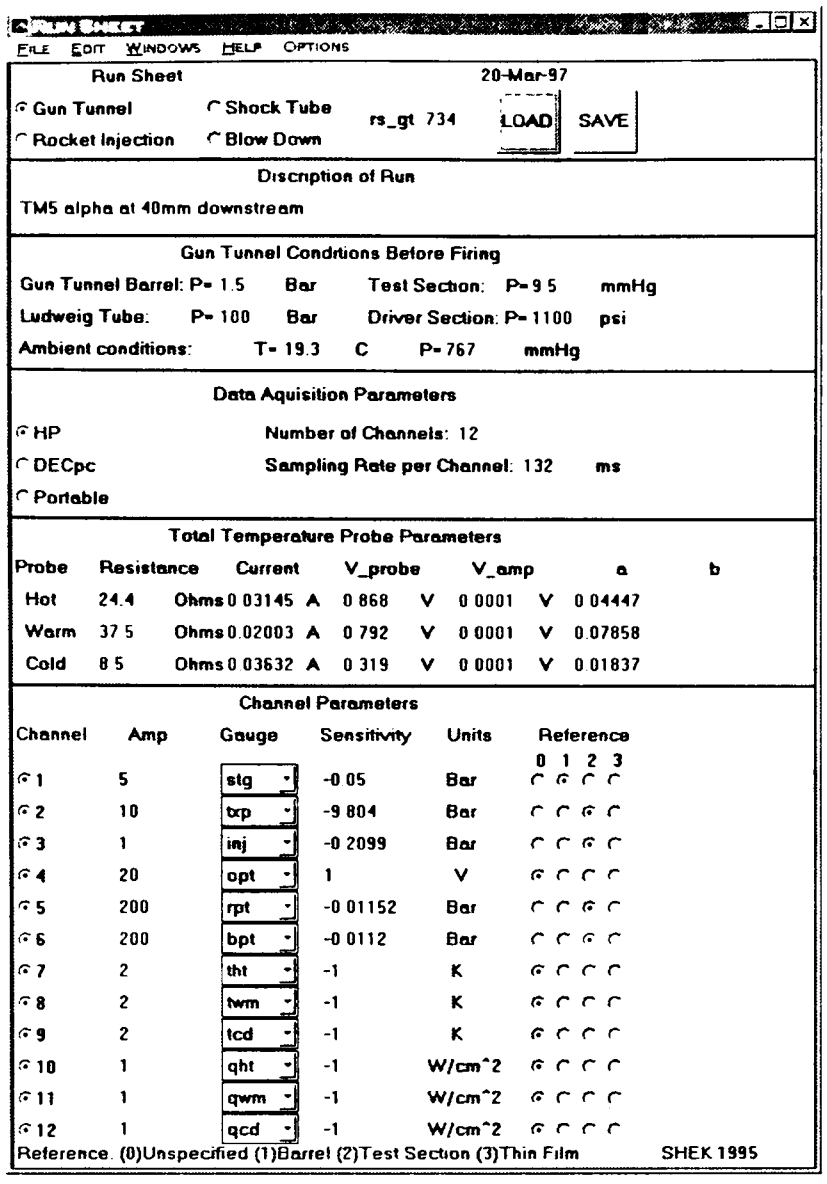


Figure 2-26 Mach 3 (M3) rocket plume on crossflow plane in Mach 7 freestream showing an assumed barrel shock due to the presence of the stings



FILE EDIT WINDOWS HELP OPTIONS

Run Sheet 20-Mar-97

(•) Gun Tunnel ( ) Shock Tube rs_gt 734 LOAD SAVE

( ) Rocket Injection ( ) Blow Down

Discription of Run

TM5 alpha at 40mm downstream

Gun Tunnel Condrtions Before Firing

Gun Tunnel Barrel: P= 1.5 Bar Test Section: P= 9 5 mmHg

Ludweig Tube: P= 100 Bar Driver Section: P= 1100 psi

Ambient conditions: T= 19.3 C P= 767 mmHg

Data Aquisition Parameters

(•) HP Number of Channels: 12

( ) DECpc Sampling Rate per Channel: 132 ms

( ) Portable

Total Temperature Probe Parameters

Probe	Resistance	Current	V_probe	V_amp	a	b
Hot	24.4 Ohms	0 03145 A	0 868 V	0 0001 V	0 04447	
Warm	37 5 Ohms	0.02003 A	0 792 V	0 0001 V	0.07858	
Cold	8 5 Ohms	0 03632 A	0 319 V	0 0001 V	0 01837	

Channel Parameters

Channel	Amp	Gauge	Sensitivity	Units	Reference 0	1	2	3
(•) 1	5	stg	-0 05	Bar	( )	(•)	( )	( )
(•) 2	10	txp	-9 804	Bar	( )	( )	(•)	( )
(•) 3	1	inj	-0 2099	Bar	( )	( )	(•)	( )
(•) 4	20	opt	1	V	(•)	( )	( )	( )
(•) 5	200	rpt	-0 01152	Bar	( )	( )	(•)	( )
(•) 6	200	bpt	-0 0112	Bar	( )	( )	(•)	( )
(•) 7	2	tht	-1	K	(•)	( )	( )	( )
(•) 8	2	twm	-1	K	(•)	( )	( )	( )
(•) 9	2	tcd	-1	K	(•)	( )	( )	( )
(•) 10	1	qht	-1	W/cm^2	(•)	( )	( )	( )
(•) 11	1	qwm	-1	W/cm^2	(•)	( )	( )	( )
(•) 12	1	qcd	-1	W/cm^2	(•)	( )	( )	( )

Reference: (0)Unspecified (1)Barrel (2)Test Section (3)Thin Film SHEK 1995

Figure 2-27 RUNSHEET data conversion programme

3. Instrumentation

3.1 PRACTICAL ASPECTS OF HYPERSONIC INSTRUMENTATION

3.1.1 Influence of Probe Traverse Speed and Angle of Attack on Measurement

Probes were mounted on the traverse mechanism and made to travel across the plume at about 3.5 m/s. Compare this traverse speed with gas velocities in the region of 800 m/s and 1300 m/s, the probe speed was at worst around 0.4 per cent of the gas velocity. Induced Pitot pressure variations due to the probe velocity were therefore negligible. However, for quiescent runs, gas could be moving at a speed comparable to the probe traverse speed near the outer edge of the shock layer. Therefore care must be taken in interpreting the Pitot pressure measurements around this region.

Cain (1992) showed that the angle of attack of the Pitot probe used (which had the same geometry as the PIT used in this thesis) had little effect on Pitot pressure readings up to about 10 degrees. Subsequently in this thesis, this is assumed to be applicable to the other probes utilised. As the half angles of the rocket models used are less than 10 degrees, except for the M3 nozzle which has an exit metal angle of 33 degrees; the angle of the flow to the probe is assumed to have negligible effect on measurement within the plume core.

3.1.2 Requirements on Spatial and Frequency Resolution

The short testing duration typical of rocket exhaust experiments demands high frequency response from the instrumentation used, especially if any turbulent fluctuation is to be measured with a reasonable degree of confidence. To measure turbulence accurately, spatial and frequency resolutions of the measuring instrument are crucial.

An estimate of the required frequency response could be obtained if the mean eddy convection velocity and scale are known. For a typical shear layer in this study, the shear layer width is in the region of 10 mm. Assume that the largest eddy spans the whole shear layer and moves with a velocity equal to the mean velocity across the shear layer, which is in the region of 900 m/s, then a probe with a frequency response better than 90 kHz is needed to

completely resolve this turbulent eddy. Only the RPT probe used in this thesis was free from any resonance characteristic near this region. This means that the fluctuating components measured by the Pitot probes were not due to individual turbulent eddies but an integral effect of the probe and turbulent eddy frequency characteristics.

Spatial resolution depends mainly on the geometry of the probes. For conventional Pitot probe designs, smaller inlet tubing generally corresponds to better spatial resolution. However, there is a minimum tube diameter for such a Pitot probe. Beyond this point, improvement in spatial resolution will be at the expense of the frequency response of the probe as viscose effects become dominant. Note that across shock waves conditions change discontinuously. Depending on the probe geometry, a shock could appear thicker than it really is as a result of smearing.

3.2 PRESSURE MEASUREMENTS

3.2.1 Pressure Probes

3.2.1.1 PIT Pitot Probe

This probe consisted of a Kulite XCQ-062-100A pressure transducer (Figure 3-1) mounted inside an aluminium housing with the sensing surface of the transducer perpendicular to the incoming flow (see Figure 3-2). The Kulite sensing diaphragm was protected by an M-type screen, which consisted of a 0.005" thick fine metallic mesh with 0.006" diameter holes (see Figure 3-3). The screen was mounted in a screen holder, which was installed on the transducer housing in front of the diaphragm. Distance between the diaphragm and the screen was about 0.01". The relatively long hypodermic tube extends out into the incoming flow, and a detached shock forms a small distance in front of the mouth. Information travels down this tube and is transmitted onto the transducer. The exposed surface of the Kulite transducer was protected from particle impact by three design features: a relatively long hypodermic tube helped to slow down any incoming particle, a wire mesh screen and a silastomer layer protected the delicate silicon diaphragm.

A simplified organ-pipe type calculation based on the probe dimensions and the flow conditions could be used to obtain a rough estimate of the resonance frequency of the cavity between the diaphragm and the protective screen. For this particular probe configuration, an estimated resonance frequency was calculated in the region of 7.84 kHz.

3.2.1.2 BPT Pitot Probe

This was essentially an off-the-shelf Kulite pressure traducer with a protective B-screen and mounted directly in the flow. The B-screen consisted of a 0.005" thick plate with 0.006" diameter holes positioned around the outer perimeter of the plate (see Figure 3-3). The diameter of the protected area was greater than the active diameter of the diaphragm. This arrangement eliminated any possibility of gas particles penetrating the holes and hitting the exposed part of the diaphragm. The minimum distance between the diaphragm and the screen is 0.155 mm. Other distances of 0.15 mm to 0.325 mm are used in standard Kulite probes. This gives a range of fundamental resonance frequencies between 301.5 kHz to 653.25 kHz. However, due to viscous effects and the presence of an RTV layer, the actual resonance frequency of the BPT was expected to be lower. In addition, the particular design of the B-screen, including orifice diameter and screen thickness and material could cause the measured resonance frequency to differ further from the calculated value.

3.2.1.3 FPT Pitot Probe

This unique Pitot probe developed for this thesis incorporated a fast response miniature pressure transducer mounted closed to the flow. By mounting the transducer diaphragm parallel to the incoming flow, it significantly improved the robustness of the probe without any significant trade off in terms of spatial or frequency response.

The Kulite XCQ-061-100A pressure transducer used had an RTV protection layer but no protective screen. The design of this probe differed from the conventional PIT probe in three main areas:

- The inlet tube was taken into the probe head to reduce the pneumatic cavity. This reduced filling time and increased resonance frequency.
- The Kulite pressure transducer was mounted sideways with the sensing diaphragm parallel to the flow. This eliminated the need for a protective screen and enabled the sensing diaphragm to be placed close to the flow without the risk of particle impact.
- The probe head was shaped so that the detached shock formed in front of the probe was symmetrical and normal to the entry duct.

A reasonable estimate of the resonance frequency of this particular design could be obtained from the dimensions of the pneumatic cavity. Consider a Pitot probe configuration with circular entry duct of diameter D and length L. The pneumatic cavity in front of the transducer is V. This system can be modelled as a spring-mass oscillator, with the gas included in the volume V regarded as a spring moving the mass in the entry duct. Thus, the eigen-frequency of the oscillation system could be described by the Helmholtz equation for resonators (Ruck et al, 1990). This simplified approach allows a rough estimation of the resonance frequency given by the equation,

$$f_0 = \frac{a}{4} \cdot \sqrt{\frac{D^2}{V \cdot L \cdot \pi}}$$

The FPT Pitot probe differs from this model in that the cross-section of the entry duct was not circular but rectangular. Therefore an equivalent diameter was obtained to give the same cross-sectional area. Subsequent calculation gave an estimated resonate frequency in the region of 25.11 kHz.

3.2.1.4 RPT Pitot Probe

This was essentially a Kulite pressure transducer with only an RTV silastomer layer. By omitting the protective screen, it eliminated the problem of cavity resonance. However, the lack of a protective shield meant its application was restricted to flows that were free of high velocity debris. Its main application in this thesis was to study the turbulent shear layer

of quiescent rocket plumes, where its high frequency response and small probe diameter were clearly advantageous over the other designs.

3.2.2 Shock Tube Tests

The Pitot pressure probes, with the exception of the RPT probe were tested in a shock tube in order to obtain the resonance frequencies. Here the driver section was pressurised to approximately 50 psi when a Mylar diaphragm burst and caused a shock wave to propagate down to the end of the tube where the probes were mounted. The first incident and reflected shock wave pair was utilised when the influence of the reflected expansion waves had not yet reached the end of tube. The pressure levels for these two shocks could be calculated based on the initial pressure ratio of the high-pressure and low-pressure sections and the temperature of the tube (Shek, 1994). The predicted Pitot pressure values for the incident and reflected shock were 2.30 bar 3.30 bar respectively. The corresponding total temperatures were 359.8 K and 423.4 K.

Plots showing the first two steps in pressure as measured by various pressure probes are shown in Figure 3-4, Figure 3-5 and Figure 3-6 for the BPT, FPT and PIT Pitot probes respectively. Mean levels of the measured Pitot pressures are in good agreement with the theoretical values. It can be seen that the transient responses of different probes differ significantly.

The BPT probe has the highest resonance frequency because of its configuration, where the pneumatic cavity was minimised by mounting the silicon sensing-chip close to the mouth of the probe. Its resonance frequency is comparable to that of the silicon chip, which is quoted at 500 kHz by Kulite. The initial apparent overshoot was due to the shock wave being reflected back from the diaphragm raising the internal pressure between the screen and the sensing surface to that of the pressure behind the reflected shock. A low frequency oscillation of 2 kHz can clearly be seen in the region from 7.5 ms to 9 ms. This is believed to be caused by the mechanical vibration of the shock tube during the run. The PIT probe clearly has the poorest frequency response with a low effective damping as shown by large pressure

oscillations. Its usefulness in obtaining fluctuating signals at high frequencies is clearly in doubt.

3.2.3 Experimental Arrangement

The Pitot pressure probes were mounted in a holder (see Figure 3-8) and fastened onto the traverse mechanism. The probe holder was designed to facilitate the process of swapping different probes when necessary according to the nature of the flowfield to be measured. This was important as the thin-film heat transfer probes had a limited life span of around 10 runs, so frequently new probes were needed to replace defective ones.

Before each run, the probes were checked to ensure they were pointing with the mouth facing the incoming flow and the traverse was along the centreline of the nozzle exit. The amount of tension of the traverse driving mechanism was also adjusted to ensure that traverses were carried out during the relatively steady period of the run, which was typically less than 30 ms.

3.3 TEMPERATURE MEASUREMENTS

3.3.1 Introduction

Temperature measurement in supersonic flows has been traditionally conducted with hot-wire anemometers. The important issue in applying this technique in a hypersonic gun tunnel experiment is the structural endurance of the hot-wire in the high temperature, high dynamic pressure flow, which is often laden with destructive projectiles in the form of aluminium or Mylar particles travelling at supersonic speeds. Under such an environment, the endurance problem should be eased for thin-film anemometers or heat transfer probes, which replaces the fragile wire by a thin metallic film deposited on a rigid substrate.

3.3.2 Thin-Film Heat Transfer Probes

The technique of thin-film resistance thermometry has been used quite extensively to make heat transfer measurements in shock tubes and shock tunnels. In essence, the probe measures the surface temperature history of the material upon which the thin-film is

deposited. The use of one-dimensional heat conduction theory and basic calibration of the probe convert this measured temperature history into heat flux.

The flow of heat into a semi-infinite material is analogous to the flow into a medium containing distributed capacitance and resistance. The assumption of constant substrate properties is appropriate when the substrate temperature variation is small or where substrate thermal properties are nearly independent of temperature. This is the case for the quiescent runs of this thesis, where substrate temperature variation was at most 26 per cent of the initial value. However, for co-flow runs in presence of the Mach 7 freestream, temperature variation could be as large as 60 per cent. Here, the use of variable substrate properties is appropriate.

The accuracy in measuring temperature fluctuations is limited by the frequency response of the probe. The time constant of the probe depends on the flow conditions (type of fluid and velocity) and the probe's thermal capacitance (thin-film thickness and properties). Because the flow conditions are generally fixed, the sensor characteristics must be chosen such that the minimum time scale (highest frequency) of interest is measured (Thole, 1994).

Response of thin-film heat transfer probes to velocity is more than 100 times greater than that of the Pitot probe since the velocity perturbations are large compared to the pressure defect (Ng et al, 1983). They have a good frequency response, which is ideal in measuring turbulent fluctuations. However, the diameter of the probes used in this thesis was approximately 3 mm. Although the thin-film sensor was narrow (~ 1 mm), the spatial resolution could be coarser than the Pitot probes used, especially at upstream stations where gradients in heat transfer measurements were large across the width of the nose of the probes.

The application of thin-film probes to measure steady and unsteady heat transfer rates to the surface of turbine blades, re-entry bodies and other test models immersed in aerodynamic flows is well established (e.g. Oldfield, Burd and Doe, 1982). The advantages of such devices are their non-intrusiveness, relatively wide bandwidths limited by manufacturing process and their high sensitivity. However, such measurements need to be taken on the surface to achieve a meaningful heat flux. Although the materials needed for

such gauges are relatively inexpensive, they are brittle and difficult to manufacture, and the electronics needed are expensive. Note that the thickness and width of the thin-film deposit limit the bandwidth and rise time of the probe respectively. The length of the thin-film is critical to the spatial resolution of a heat transfer probe: it must be shorter than the smallest structure to be resolved.

There are two main modes of operation for thin-film devices. In the constant temperature mode of operation, as constant-temperature hot-wire anemometers, the thin-film forms one arm of a Wheatstone bridge and feedback is used to keep the gauge resistance and hence the temperature constant. The output voltage is used to measure the electrical heating power to the gauge. The other mode is the constant current mode, which was used for the transient heat transfer probes in this thesis.

3.3.2.1 Stagnation Point Heat Transfer Analysis

The stagnation point heat transfer rate assuming a recovery factor of unity is given by,

$$q = h(T_t - T_s)$$

The convective heat transfer coefficient h is a property of the stagnation point boundary layer and is thus a function of the probe geometry and the upstream flow conditions. For a laminar flow it can be expressed as (White, 1991),

$$Nu = G(\mathrm{Pr})\,\mathrm{Re}^{0.5}\,C_{cr}^{\;0.1}\sqrt{\frac{2KR_N}{U_\infty}}$$

where,

$$Nu = \frac{hR_N}{k_e},\ \mathrm{Pr} = \frac{c_p\mu_e}{k_e},\ \mathrm{Re} = \frac{\rho_e U_\infty R_N}{\mu_e},\ K = \frac{du_e}{dx},\ C_{cr} = \frac{\rho_s\mu_s}{\rho_e\mu_e}$$

$$G(\mathrm{Pr}) \approx 0.57\,\mathrm{Pr}^{0.4} \text{ for planar flow}$$

$$G(\mathrm{Pr}) \approx 0.762\,\mathrm{Pr}^{0.4} \text{ for axisymmetric flow}$$

C_{cr} is known as the Chapman-Rubesin parameter, which could be evaluated at a suitable reference temperature T^* to give (White, 1974),

$$C_{cr}^{*} = \frac{\rho^{*}\mu^{*}}{\rho_e \mu_e} \approx \left(\frac{T^{*}}{T_e}\right)^{-1/3}$$

The temperature ratio can be approximated by (Eckert, 1956),

$$\frac{T^{*}}{T_e} = 1 + 0.032M_e^2 + 0.58\left(\frac{T_s}{T_e} - 1\right)$$

Figure 3-9 shows a schematic illustration of the stagnation point region of a thin-film heat transfer probe. The theoretical heat flux for the heat transfer probes could be written as (Anderson, 1989),

$$q = 0.763\,\mathrm{Pr}^{-0.6} C_{cr}^{0.1} (\rho_e \mu_e)^{1/2} \sqrt{\frac{du_e}{dx}} (h_e - h_s)$$

Where the velocity gradient can be modelled by the straight Newtonian pressure distribution,

$$p_e - p_\infty = \rho_\infty U_\infty^2 \cos^2 \phi$$

to give the velocity gradient at the stagnation point,

$$\frac{du_e}{dx} = \frac{1}{R_N}\sqrt{\frac{2(p_e - p_\infty)}{\rho_e}}$$

The above equations define the heat flux and velocity gradient at the stagnation region. q_s, h_s and h_e are the heat flux and enthalpy on the surface of the substrate, and the enthalpy at the edge of the boundary layer respectively.

M_e could be obtained by integrating the velocity gradient along the edge of the boundary layer to give $M_e \approx \frac{2}{R_N\sqrt{\gamma}}x$. This enables us to deduce the influence of the Chapman-Rubesin parameter on the convective heat transfer coefficient. Figure 3-10 shows that the dependence of C_{cr} on T_s/T_e and M_e is weak under typical running conditions in this thesis. Values chosen for M_e are representative of the values at the stagnation point and at the end of the platinum thin-film element 0.5 mm away from the stagnation point.

Assuming that ideal gas relations together with an irrotational and quasi-steady flowfield are applicable around the nose region, then the above equation could be simplified to,

$$\frac{du_e}{dx} = \frac{1}{R_N}\sqrt{\frac{2p_e}{\rho_e}}$$

$$q_s = 0.763\,\mathrm{Pr}^{-0.6}\,C_{cr}^{0.1}\left(\frac{\rho_e\mu_e}{R_N}\right)^{\frac{1}{2}}\left(\frac{2p_e}{\rho_e}\right)^{\frac{1}{4}}c_p(T_e - T_s)$$

q is a function of the probe substrate temperature at the surface T_s, the pressure and temperature at the edge of the boundary layer p_e and T_e. At the stagnation point, the gas temperature at the edge of the boundary layer T_e is simply the flow total temperature T_t, and p_e can be approximated by the Pitot pressure. Therefore applying the usual hypersonic approximations, the above equation could be further reduced to,

$$q_s = 0.763\,\mathrm{Pr}^{-0.6}\,C_{cr}^{0.1}\sqrt{\mu_e}R^{-\frac{1}{4}}c_pT_t^{-\frac{1}{4}}\sqrt{\frac{2p_t}{R_N}}(T - T_s)$$

This gives an estimate for the heat transfer coefficient,

$$h = 0.763\,\mathrm{Pr}^{-0.6}\,C_{cr}^{0.1}\sqrt{\mu_e}R^{-\frac{1}{4}}c_pT_t^{-\frac{1}{4}}\sqrt{\frac{2p_t}{R_N}}$$

The parameters in the above equation could be deduced by using the appropriate approximations and models given below.

$$c_p = \frac{1}{m}\left[a_1 - a_2\left(\frac{T_t}{100}\right)^{-\frac{1}{5}} + a_3\left(\frac{T_t}{100}\right)^{-2} - a_4\left(\frac{T_t}{100}\right)^{-3}\right]$$

$$\mu_e = \mu_{ref}\left(\frac{T_t}{T_{ref}}\right)^{1.5}\left(\frac{T_{ref} + S_\mu}{T_s + S_\mu}\right)$$

$$k_e = k_{ref}\left(\frac{T_t}{T_{ref}}\right)^{1.5}\left(\frac{T_{ref} + S_k}{T_s + S_k}\right) \text{ and } \mathrm{Pr} = \frac{c_p\mu_e}{k_e}$$

Parameters	N_2	H_2
a_1	39.06×10^3	56.505×10^3
a_2	512.79×10^3	702.74×10^3
a_3	1072.7×10^3	1165×10^3
a_4	820.4×10^3	560.7×10^3
$\mu_e\ \left(Nsm^{-2}\right)$	1.663×10^{-5}	0.8411×10^{-5}
S_μ	107	97
k_{ref}	0.0242	0.168
S_k	150	120
m	28.013	2.016
$R\ \left(Jkg^{-1}K^{-1}\right)$	297	4121

Table 3-1 Parameters at reference temperature T_{ref} = 273 K

The variation of $h/\sqrt{p_t/R_N}$ with total temperature is shown in Figure 3-11. It changes by 15.79 per cent as the total temperature increases from 300 K to 800 K. This variation is small in comparison to the other parameters, therefore it could be regarded as constant for quick estimation and analysis purposes.

This is an elegant analysis, which relates the heat flux to the Pitot pressure measurements for a hypersonic flow. However, in deriving the above equations, multidimensional effects such as vorticity in the shear layer are ignored. Therefore validity of the equations in this region is in some doubt. However, Buttsworth (1996) performed heat transfer traverses across a Mach 4 single quiescent plume under matched pressure conditions. The measured fluctuation in heat flux within the mixing region was compared to the fluctuation in the measured Pitot pressure, and the agreement was shown to be good.

Figure 3-12 shows the convective heat transfer coefficient plotted against the square root of the measured Pitot pressure in the core region of the rocket plume. The variation is essentially linear and a first-order curve fit could be made to give,

$$h = 0.916\,\mathrm{Pr}^{-0.6}\,C_{cr}^{0.1}\sqrt{\mu_e}R^{-\frac{1}{4}}C_p T_t^{-\frac{1}{4}}\sqrt{\frac{2p_t}{R_N}}$$

This is 20 per cent higher than the modelled value. The cause for this discrepancy is investigated in the following sections.

3.3.2.2 Probe Construction & Calibration

The thin-film heat transfer probes used in this thesis were calibrated in an oven to a temperature of approximately 700K. The temperature-resistance calibration can be expressed in the form

$$\frac{R}{R_{ref}} = 1 + \alpha_R\left(T - T_{ref}\right) + \beta_R\left(T - T_{ref}\right)^2$$

Calibrations of different probes showed that the non-linear coefficient β_R is a small negative number. The error in neglecting this term is at worst 3 per cent at 700 K and smaller at lower temperatures (Buttsworth, 1996). Consequently, the effect of this coefficient on the measured substrate temperature is assumed negligible for this thesis. It is perhaps not immediately obvious to see the reason for a decrease in the rate of increase of probe resistance with increasing substrate temperature. It is believed to be due to semi-conducting effects of the substrate. Although the resistivity of platinum increases with temperature and with the subsequent thermal expansion of the substrate, at high temperatures the substrate itself becomes semi-conductive, hence the overall resistance of the probe is lowered.

It was encouraging that calibrations performed by Buttsworth (1994) before and after every run yielded roughly the same coefficients, even though there was a slight increase in ambient resistance R_{ref} accumulated throughout the series of runs due to small gas-borne particles that caused abrasive wear of the thin-films. However, it has been shown that film wearing does not significantly degrade the accuracy of the results because the change in resistance during any one experiment was typically less than 0.1 per cent.

Attempts have been made to calibrate the probes on-site, by inserting a thermocouple in the heater in close proximity of the heat transfer probe and recording both the substrate and the thermocouple temperature. Temperature of the heater was varied from 300 K to 500 K

over a period of two minutes. Although this technique gave an accurate value for α_R, it indicated a β_R which was orders of magnitude larger than the oven calibrated result. This large discrepency is most likely due to different temperature gradients along the probe and the thermocouple shaft. However, for less strigent measurement criteria, this provides a quick and convenient way to calibrate the probes without having to take the whole mechanism off-line.

The heat transfer probes took the form of quartz cylinders, which acted as the low conductive substrate with hemispherical ends. A schematic illustration of such a probe is shown in Figure 3-13. Small platinum thin-film gauges were painted on the ends of the hemispheres approximately 3 mm in diameter (this point corresponded to the stagnation point on a probe when the cylinder was aligned with the direction of the flow) and baked at 650 $^{\circ}C$. The platinum films had an estimated thickness of less than 1 μm, and a resistance in the region of 10 Ω to 40 Ω at room temperature. Since high temperatures were induced at the sensor end of the probes, leads formed by a silver paste (baked at 650 $^{\circ}C$) ran to the cool end of the probes. This permitted the sustained integrity of the solder that joins the electrical leads to the probes. The probes were then mounted in a Macor collar, which provided electrical and thermal insulation.

3.3.2.3 Operation of the Heat Transfer Probes

For a typical run, three heat transfer probes were made to traverse across the rocket plume. To generate the necessary difference in substrate temperatures, a pre-heating unit shown schematically in Figure 3-14 was utilised to heat one of the probes (the *hot* probe) to a temperature in the region of 600K. Power was supplied to the unit through an aluchrom heating coil, which had a resistance of approximately 2 Ω, with a typical excitation of around 7 V. An oxide ceramic material provided thermal insulation for the heating coil. In pre-heating of the *hot* probe, temperatures of the other two probes also increased slightly due to

radiation. Immediately before a run, the heating unit was swung clear of the probes and thus allowed the measuring device to be driven into position or to traverse the flow as required.

The probes operated with constant sensing current of around 20 mA, passed through the thin-film gauge in order to generate a change of voltage proportional to the change of film resistance with substrate temperature. There was a measurable temperature rise in the region of 15 K as a result of Ohmic heating.

Sensitivity of the thin-film probes can be written,

$$\frac{V}{V_i} = 1 + \alpha_R (T_s - T_i) + \beta_R (T_s - T_i)^2$$

Where V_i is the initial voltage of the probe when the substrate temperature T_s is at T_i. Voltage output from the thin-film probes was processed in real time using analogue circuits on the premise that semi-infinite flat plate conditions applied.

The flat plate heat flux including the thin-film calorimeter term is given in the time domain by (Buttsworth and Jones, 1997),

$$q = \sqrt{\frac{\rho_s c_s k_s}{\pi}} \int_0^t \frac{d(T_s - T_i)}{d\tau} \frac{1}{\sqrt{t-\tau}} d\tau + \rho_f c_f l \frac{d\theta_f}{dt}$$

and in the frequency domain by,

$$T_s(j\omega) = \frac{q(j\omega)}{\sqrt{j\omega}\sqrt{\rho_s c_s k_s} + j\omega \rho_f c_f l_f}$$

By assuming that the sensing thin-film remains at a temperature that is equal to the substrate surface temperature and combing this with the sensitivity of the thin-film to give,

$$q = \sqrt{\frac{\rho_s c_s k_s}{\pi}} \int_0^t \left[\frac{dV_s}{d\tau} \frac{1}{V_i \sqrt{\alpha_R^2 - 4\beta_R^2 \left(1 - \frac{V_s}{V_i}\right)}} \right] \frac{1}{\sqrt{t-\tau}} d\tau + \rho_f c_f l_f \frac{d\theta_f}{dt}$$

Neglecting the effect of the second order coefficient β_R and assuming a negligible thin-film thickness, the relationship between the heat flux signal and the output from the analogue circuit is obtained by (Schultz and Jones, 1973),

$$q = C\sqrt{\frac{\rho_s c_s k_s}{\pi}}\frac{V_{out}}{\alpha_R V_i}$$

Where $V_{out} = \int_0^t \frac{dV_s}{d\tau}\frac{1}{\sqrt{t-\tau}}d\tau$, and C is a constant depending on the analogue circuit. Typical error in neglecting the calorimeter term is in the region of 14 per cent over the bandwidth of the current analogue circuit (Buttsworth, 1997).

One of the main applications of thin-film probes is to study unsteady turbulent flows where we are interested in looking at as wide a bandwidth as possible. Therefore, it is pertinent to study the frequency response of the thin-film probes. It can be seen in the frequency domain that the measured heat flux is frequency dependent. This would cause digitisation problems if the substrate temperature signal were recorded directly. This was the reason for electrically processing the continuous thin-film signal before digitisation took place. The electronics used consisted of a constant current source, which supplied current to the thin-film, an analogue resistor-capacitor network to give the desired magnitude response approximating to a $\sqrt{j\omega}$ frequency characteristic, and a current to voltage converter that was used to convert the current in the RC analogue to the corresponding voltage. Finally the voltage signal was passed through a low-pass filter before being digitised. The current source and the current to voltage converter of the analogue device used for this thesis were optimised for low noise over the bandwidth of 0.023 Hz to 85 kHz. The result was a relatively flat response within this bandwidth.

Note that when converting voltage output from the analogue circuit to the corresponding heat flux, a suitable constant $\sqrt{\rho_s c_s k_s}$ should be used, as the internal circuitry does not take variable substrate properties into the convolution. To improve the accuracy of the measured heat flux signal, especially if it is to be used to deduce the total temperature of the flowfield where a small error would be amplified in the regression calculations, a modified finite-difference routine was used (Buttsworth, 1994). This routine takes the recorded substrate temperature as input, performs radiation and convection correction on the

temperature signal, then calculates the resultant heat flux by taking into account variable substrate properties, curvature and lateral conduction effects.

Once the heater is removed, there will be a small temperature loss due to radiation and conduction along the quartz probes (free convective heat transfer to the probes is considered insignificant due to the low-pressure quiescent environment at around 0.0127 bar in the test section). The fall in substrate temperature before the start of a traverse was originally believed to be largely due to this. However, on closer examination and by comparing the injection and substrate temperature profiles as shown in Figure 3-15, entrainment of the background gas into the exhaust plume seems to be the main cause of this initial drop in probe temperature. This is shown by the fact that the substrate temperature begins to drop as soon as the flow comes on as shown by an increasing injection pressure measured.

3.3.2.4 Lateral Conduction and Nose Curvature Effects

The magnitude of the resulting error in assuming a flat plate heat transfer behaviour for the probes depends on the penetrative depth of heat relative to the radius of curvature of the nose and on the amount of lateral conduction in the region. Lateral variation of heat flux near the stagnation region gives rise to lateral temperature gradients, which drives the lateral conduction process. This increases the heat flux if the stagnation temperature of the flow is lower than the substrate temperature near the stagnation region and vice versa. To study the radial and lateral conduction effects, one can start with the basic energy equation and the Fourier heat-conduction law at the wall of the substrate near the stagnation point. Assuming constant thermal properties,

$$\rho_s c_s \frac{\partial T_s}{\partial t} = k_s \nabla^2 T_s$$

$$q = -k_s \nabla T_s$$

With suitable substitutions, the above equations can be expanded in spherical co-ordinates,

$$\frac{\rho_s c_s}{k_s}\frac{\partial T_s}{\partial t} = \frac{1}{r}\frac{\partial}{\partial r}\left(r^2 \frac{\partial T_s}{\partial r}\right) + \frac{1}{r^2 \sin\theta}\frac{\partial}{\partial \theta}\left(\sin\theta \frac{\partial T_s}{\partial \theta}\right) + \frac{1}{r^2 \sin^2\theta}\frac{\partial^2 T_s}{\partial \psi^2}$$

Due to the geometry at the stagnation region of the thin-film probe, temperature distribution is symmetrical about the azimuthal angle ψ. This together with the assumption that the thin-film thickness is negligible compared to the radius of the probe, the above equation can then be simplified to give,

$$\frac{\partial^2 T_s}{\partial r^2} + \frac{2}{r}\frac{\partial T_s}{\partial r} + \frac{2}{r}\frac{\partial^2 T_s}{\partial \theta^2} = \frac{\rho_s c_s}{k_s}\frac{\partial T_s}{\partial t}$$

If we assume that heat penetrates only a relatively small distance into the substrate and a parabolic heat flux distribution on the surface of the probe in the stagnation region (Schultz & Jones, 1973) holds, this equation can be broken down into two heat flux components due to conduction normal to the surface q_n, and in the lateral direction q_l (Buttsworth, 1997).

Heat flux normal to the substrate surface could be written as,

$$q_n = \sqrt{\frac{\rho_s c_s k_s}{\pi}} \int_0^t \frac{dT_s}{d\tau}\frac{1}{\sqrt{t-\tau}}d\tau - \frac{k\sigma}{2R_s}(T_s - T_t).$$

The first term in the normal heat flux equation corresponds to the flat plate result (i.e. $\sigma = 0$ or equivalently $R_s \to \infty$). The second term in the equation is the correction needed for curvature effects. The combined heat flux at the stagnation point can then be written as,

$$q = q_n - C\frac{4k_s}{R_s \rho_s c_s}\int_0^t q_n d\tau$$

The second term on the right hand side is the lateral conduction heat flux correction term,

$$q_l = 4C\frac{k_s}{R_s \rho_s c_s}\int_0^t q_n d\tau$$

The constant C depends on the gradient of the convective heat flux around the stagnation point, which takes a value in the region of unity. Although the above derivation is based on the initial assumption that heat penetration depth is small compared to the probe radius. Buttsworth (1997) had shown that it is reliable within 1 per cent for the heat transfer probe

geometry almost up to the point at where heat had penetrated to a depth comparable to the radius.

To illustrate the validity of the above correction terms, measurement taken by the *hot* heat flux probe for a quiescent injection (LT157) is shown in Figure 3-16 together with the required curvature correction term (lateral conduction effects were negligible for this particular run). Note that on the corrected plot, once the probe is out of the plume, heat flux is again brought back to zero as expected. For typical co-flow runs, both lateral and radial corrections were needed and the constants σ and C were adjusted to give the desired zero heat flux at the end of the run.

For most of the quiescent runs, the *hot* heat flux probe was heated to a temperature around 600 K. The *warm* probe was heated by radiation due to its close proximity to the *hot* probe to around 400 K. The *cold* heat flux probe was left at roughly room temperature. Ignoring viscous effects, the maximum stagnation temperature for a typical quiescent run was around room temperature. Therefore the maximum temperature gradient for such a run was about 300 K. However, for a typical co-flow traverse with the Mach 7 freestream, the *cold* probe will experience a temperature gradient at its stagnation point in excess of 500 K in the freestream gas. Therefore, significant lateral conduction could take place, and the correction term should be used to account for this.

Since run times were relatively short, conduction along the quartz rod substrate was negligible. For most quiescent runs, radial curvature correction alone would suffice to bring the heat flux to its correct level. However, a combination of curvature and lateral conduction corrections was needed for co-flow runs.

3.3.2.5 Variable Substrate Thermal Properties of Thin-film Probe

The analogue circuit used to convert substrate temperature to the corresponding heat flux did not take into account the variation of substrate properties with temperature. A mean value was used based on the mean temperature of the substrate over the duration of the run. This is valid as long as the temperature variation was small. Figure 3-17 shows the magnitude

of the combined variation of density, specific heat and thermal conductivity for quartz based on the experimental results complied by Toulokian (1970). This large variation over the flow total temperature could have a significant effect on the heat flux signal for co-flow runs, where the substrate temperature variation was typically over 100 K compared to around 40 K for quiescent runs.

Figure 3-18 shows the effect of a variable thermal property using a typical heat flux signal from a co-flow run. Here the output of the analogue circuit was converted to heat flux using thermal property based on the mean temperature of the substrate over the run. Curvature corrections were applied as before. To calculate the heat flux based on variable thermal properties, the finite difference routine was used which also included curvature effects. It can be seen from the figure that a variable substrate thermal property can have a significant effect on the converted heat flux. This is particularly important if total temperature is to be deduced from the probes, as small errors could be amplified in the process of the regression calculation.

For a typical quiescent run, the change in substrate temperature over the run was relatively small, therefore the conversion of output from the analogue circuit assuming constant substrate thermal properties was justified and shown to be in good agreement with the corrected value from the finite difference routine.

3.3.2.6 Application of Heat Transfer Probes in Gun Tunnels

Thin-film heat transfer probes were used in co-flow plumes because of their relative robustness compared to hot-wire anemometers. However, they can still be contaminated by the debris-laden freestream. Considerable amount of effort was spent cleaning the barrel before each run to flush out aluminium and Mylar debris. A typical aluminium particle of 1 mm radius travelling at 1132 m/s can generate an impulsive loading on the thin-film equivalent to a particle of 5 mm in radius travelling at 10 m/s. This could have a significant effect on the integrity of the thin-film deposit and cause the film resistance to increase suddenly on impact, and show up as discontinuities superimposed onto the measured

substrate temperature signal. However, subsequent work hardening of the platinum film helps to reduce this effect to some extent.

This means that corrections were needed to recover the actual substrate temperature. Experience and general knowledge of the plume flowfield were pertinent in separating real effects from the noise due to particle impact. This was particularly difficult if the impacts occurred during the initial unsteady freestream flow, as these noises would be hidden in the high amplitude fluctuations in the freestream temperature.

3.3.3 Total Temperature from Heat Transfer Probes

Convective heat transfer to or from a body is proportional to the difference between the surface temperature of the body and the total temperature of the fluid or the recovery temperature of the flow, in cases where viscous dissipation is significant. Therefore, if the convective heat transfer is measured at two or more known surface temperatures, the total or recovery temperature may be deduced. This is the fundamental principle of the current total temperature probe.

The total temperature of the flow and the corresponding convective heat transfer coefficient of the probes could be deduced using two different probes with the same construction and dimensions but different substrate temperatures T_s and different heat flux q as follows,

$$h = (q_1 - q_2)/(T_{s2} - T_{s1})$$

$$T_t = \frac{q_1 T_{s2} - q_2 T_{s1}}{q_1 - q_2}$$

The above method provides the means to measure the flow total temperature which is independent of other flow parameters such as the Mach number, Reynolds number, pressure and the flow composition. The assumption that steady, low-turbulence flow conditions prevail is not made with the present method. This is a significant advantage of the present method because it means that accurate total temperature measurements can now be obtained in unsteady compressible turbulent flow environments in which the steady compressible

assumptions are inappropriate. A further advantage of the present device is that it can be used to determine total temperatures in flows of arbitrary composition.

Figure 3-19 shows the deduced total temperature within the plume core of a single jet in quiescent. This calculation was based on both the heat flux signals from the analogue circuit and the finite difference equation routine, and showed a good agreement between the two. However, it has been found that applying the same regression technique to obtain the total temperature in the shear layer could be prone to potentially large errors, as large fluctuations in the flow total temperature in this region coupled with a relatively large probe separation distance between the probes resulting in uncertainties in the regression calculation process.

3.3.3.1 Deduced Total Temperature Error in an Unsteady Flow

Operation of the total temperature probe is based on the assumption that the mean flow conditions are quasi-steady with respect to the separation distance between the heat transfer probes in the time domain. In other words, all three heat transfer probes are required to be exposed to the same mean flow conditions at a particular point along the traverse. This would be the case if the probes were closely mounted together and kept stationary in the flow. However, in the present configuration the probes were approximately 15 mm apart, and were made to traverse across a flowfield where mean levels of both the injected flow and the freestream varied to some degree.

In the freestream, the change in mean total temperature was due to a combination of the entropy gradient in the piston compression process and boundary layer cooling of the freestream gas in the barrel. As a result, a steady drop of around 7 per cent was measured (Buttsworth, 1996).

For the injected gas, although a considerable amount of effort was spent in timing the traverse so that the steady period of the injection coincides with that of the freestream, a number of runs were affected by the initial unsteady compression process in the Ludwieg tube.

The effects of the above on the deduced total temperature could be explained with the help of Figure 3-20, which shows a typical temperature-heat flux plot for a co-flow plume where the flow temperature is lower than the substrate temperature. Remember that the *cold* probe travels 19.5 mm in front of the *hot* probe. For a typical traverse speed of 5 m/s, this means the *cold* probe is leading the *hot* probe by about 3.9 ms. At a particular instance during a traverse, the *cold* probe is at a substrate temperature T_{sc} with a corresponding heat flux q_c. If the flow is quasi-steady, then the *hot* probe will see the same mean flow total temperature when its substrate temperature is at T_{sh}, to give a corresponding heat flux q_h. These two sets of measurements will together give the desired flow total temperature T_t. However, if the mean level of the flow decreases with time, then the *hot* probe will experience a flow total temperature lower than the *cold* probe at the same location. Hence it will be subjected to a higher driving temperature gradient. As a result, the magnitude of the corresponding heat flux will be higher than expected as shown. The deduced flow total temperature from the two probes will then be higher than predicted. This error could be minimised if the probe spacing is minimised and the traverse speed is increased to reduce its separation distance in the time domain.

3.3.4 Turbulence Measurements using Thin-Film Heat Transfer Probes

For turbulence measurements, the heat flux equation can be separated into its mean and fluctuating components. Assuming that $\overline{h'T_t'} << \overline{hT_t}$, $\left|T_s'\right| << \left|T_t'\right|$, and that second order terms such as $h'T_t'$ can be neglected relative to terms such as $h'\overline{T_t}$ and $\overline{h}T_t'$, then by taking time-average to arrive at the following expression (Buttsworth, 1996),

$$\overline{q'^2} = \overline{T_t'^2}\,\overline{h}^2 + \overline{h'T_t'}\,\overline{q} + \frac{\overline{h'^2}\,\overline{q}^2}{\overline{h}^2}$$

Buttsworth (1996) proposed that when the mean heat flux is low (i.e. $\overline{q} \to 0$), the total temperature fluctuations could be approximated by $\overline{T_t'^2} = \overline{q'^2} / \overline{h}^2$. This provides a quick approximation for the total temperature fluctuation using just one heat transfer probe where

the mean convective heat flux coefficient can be deduced with the help of the measured Pitot pressure signal. However, if the mean heat flux level is high, at least two probes are needed to solve for the fluctuating total temperature. To solve for all three fluctuating components $\overline{T_t'^2}$, $\overline{h'T_t'}$ and $\overline{h'^2}$, three heat transfer probes operating at different temperatures are needed.

Due to limitations in computing power and time, the fluctuating heat flux equation was solved for a selected number of experiments. The single equivalent nozzle SM5M at 40 mm downstream (LT182) was solved and presented here to give the reader a feel for the magnitude of the various fluctuating components. A time averaging window was used to obtain $\overline{q'^2}$ and $\bar{q}$, and a combination of time window and ensemble averaging was used to yield $\bar{h}^2$ from the three probes. The time average window spans 100 data points at a sampling rate of 1132.8 kHz. This is equivalent to a spatial window of 2.45 mm, which is comparable to the heat transfer probe diameter of 3.0 mm. It can be seen in Figure 3-21 that the term $\overline{h'T_t'}$ is a few degrees of magnitude smaller than the rest, which suggests that the total temperature and the convective heat transfer fluctuations are not perfectly correlated. This is another way of saying that the underlying mechanism, which causes the fluctuations for these two parameters, is dissimilar. This justifies neglecting the second term of the heat flux fluctuation equation.

It can be seen in the figure that in the core region, very little fluctuation in the root-mean-square value of the flow total temperature was measured. However, once into the shear layer, where the flowfield was dominated by a complex mixture of shocklets and expansion waves; this led to relatively large fluctuations in the measured total temperature in this region.

3.4 FLOW VISUALIZATION

3.4.1 Schlieren Photography

The Schlieren method is a commonly applied optical method since it combines a simple optical arrangement with a high resolution.

The local change in intensity on a Schlieren image is proportional to the integrated density gradients across the flowfield perpendicular to the orientation of the Toppler knife-edge. For a horizontal knife-edge, the Schlieren image is sensitive to vertical changes. A horizontal knife-edge is therefore effective for detecting horizontally aligned shocks, while the opposite is true for a vertical knife-edge. This system is most sensitive to the area of a shock that has a normal vector, which is orthogonal to both the incident light and the knife-edge. Graded filters are used to avoid saturation in intensity where there are shocks that extend across the entire flowfield. In this case, details of all the shocks in the flow are revealed, although the overall sensitivity is reduced.

3.4.2 Experimental Setup

The gun tunnel Schlieren system uses either a Toppler knife-edge or graded filter and 8" spherical mirrors with 6" focal lengths. An argon spark light source was used for taking instantaneous photographs with a spark time in the order of 1 μs.

In order for the Schlieren system to be sensitive to density variations along both major axes, a double knife-edge technique was used for this thesis. The two knife-edges were arranged so that they were perpendicular to each other. This was shown to be effective in enhancing all the shock structures regardless of their orientation (see Figure 3-22).

3.5 A NOTE ON THE INSTRUMENTATION USED IN THIS THESIS

Significant effort was spent developing and testing various instruments. However, due to the shear volume of data acquired, most of the theory mentioned in this chapter was restricted to a selected number of runs to illustrate their effectiveness.

The FPT Pitot pressure probe developed for this thesis was unique in its design. It could be further improved via miniaturisation in order to increase its frequency and spatial resolution. Instead, the less robust BPT probe was used for most of the experiments in this thesis because of limited time and resources that could be devoted to the development of instrumentation. The pertinent task for this thesis is, in the end, to study rocket plumes. However, most of the groundwork has been done and future improvements could be made

based on this. It must be emphasised that the advantage of the FPT Pitot pressure probe is its robustness. The BPT was fortunate to have survived for many runs, but the superiority of the FPT probe would really show when the flow is significantly contaminated with debris and high velocity particles, which can severely threaten the integrity of a standard protective screen.

Analytical models for Pitot probes have been shown to be an effective tool for correcting slow responding probes when their use is inevitable. Again, due to a vast amount of data each the size of over 10-megabyte, correcting these signals using the models was considered uneconomical on a large scale. Therefore the analysed frequency bandwidth was limited to 40 kHz. Within this range, the response of the probes used (RPT, BPT) could be assumed to be relatively flat.

Buttsworth (1994, 1996 and 1997) has done some solid groundwork on the total temperature probes. Their application in the gun tunnel (1996) and in high-pressure turbine work (1996) has been shown to be satisfactory. However, complications arose when they were made to traverse the rocket plume, which might at one time have a combination of condensation and unsteady effects. Further work is needed to improve their application in this area.

Flow visualisation was used extensively for this thesis. Schlieren photographs were taken for most of the runs. This led to a considerable amount of time spent developing the negatives. Bypassing the need to project the negatives onto photographic papers by scanning them directly using a high-resolution scanner shortened this process. The use of digital cameras in the future can bring further savings in time and labour.

Time has also been spent investigating crossbeam correlation methods using low power lasers. It was met with difficulties due to vibrational interference from the gun tunnel. However, reasonable success with a low noise, low-pressure quiescent injection meant that this could still be a useful way to measure flow properties in the gun tunnel environment if proper support for the instruments could be implemented.

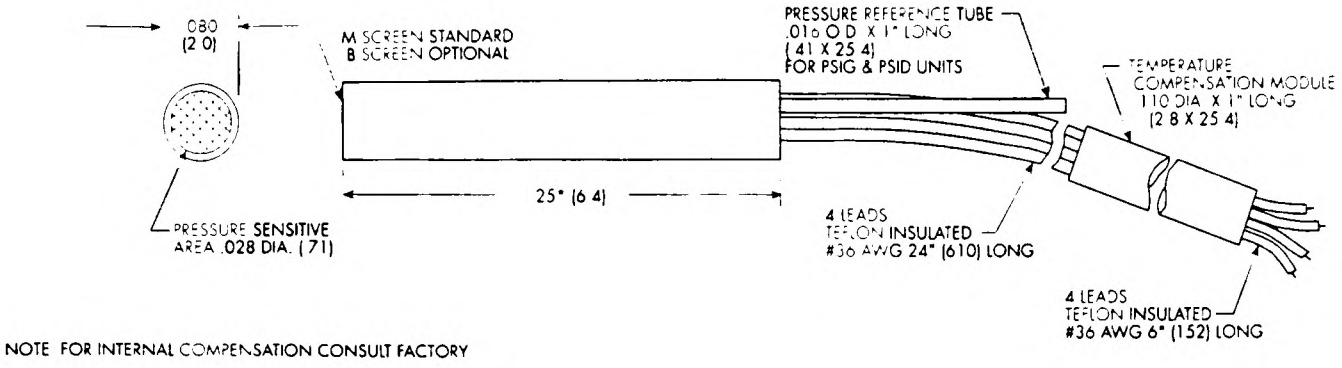


Figure 3-1 Kulite XCQ-093 miniature pressure transducer used in the BPT Pitot probe *(Kulite Bulletin KS-1000F)*

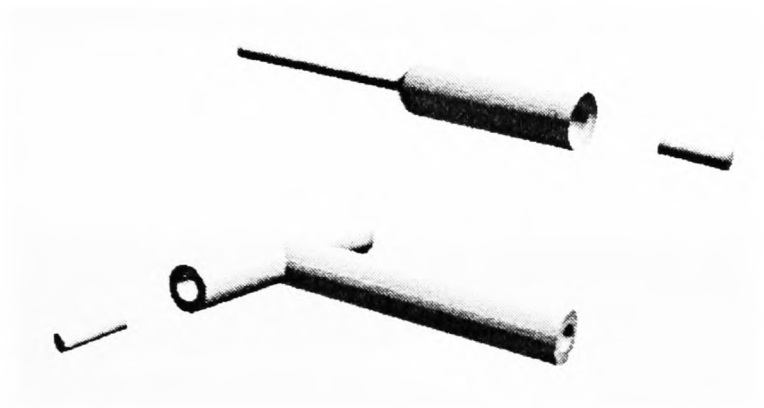


Figure 3-2 Three-dimensional illustration of the PIT and FPT Pitot pressure probes

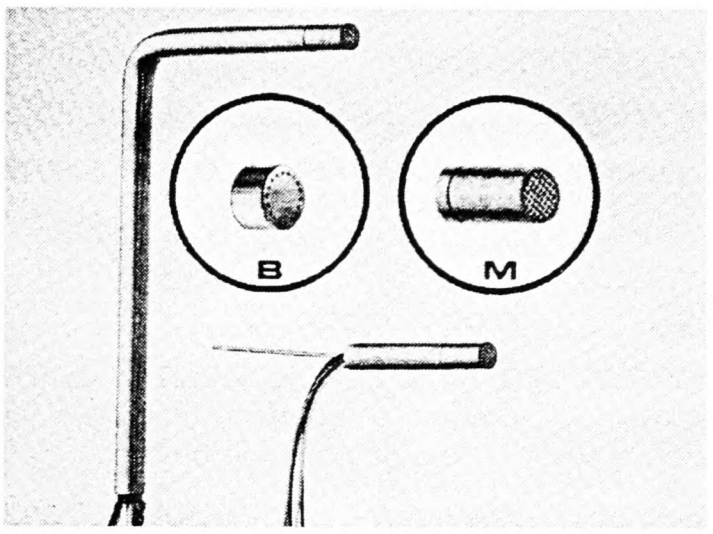


Figure 3-3 Kulite pressure transducers with different protective screens *(Kulite Bulletin KS-1000F)*

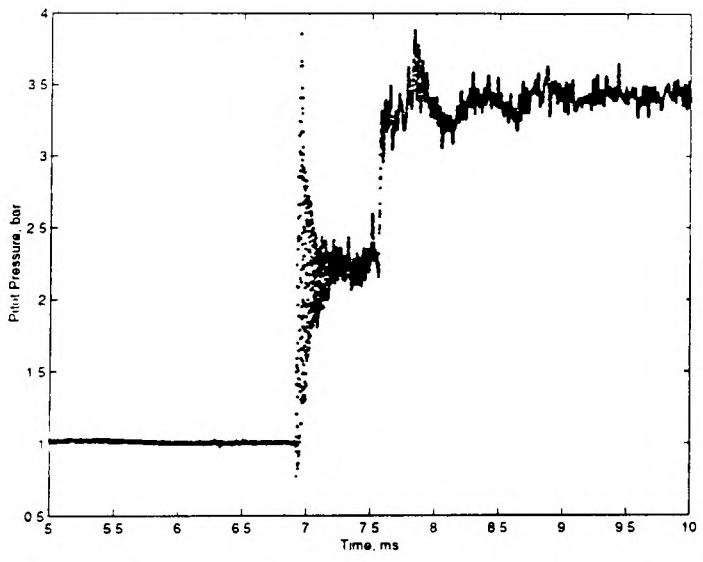


Figure 3-4 BPT Pitot pressure probe shock tube signal

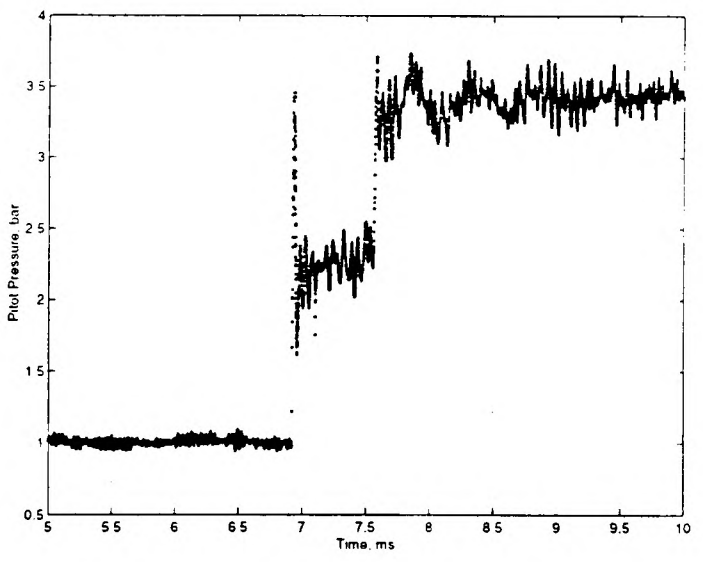


Figure 3-5 FPT Pitot pressure probe shock tube signal

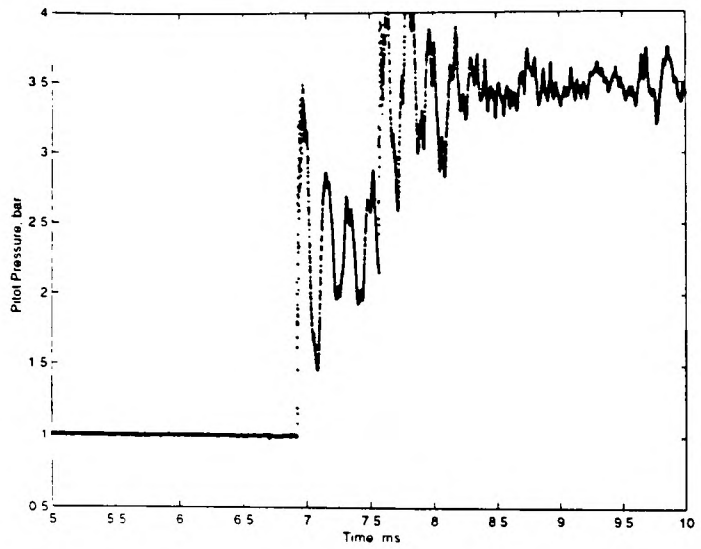


Figure 3-6 PIT Pitot pressure probe shock tube signal

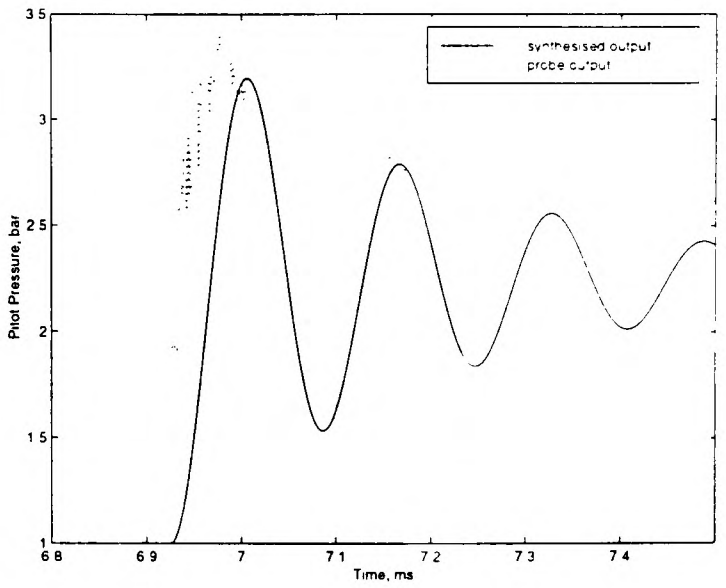


Figure 3-7 PIT Pitot pressure probe second order model synthesised output compared with measured output

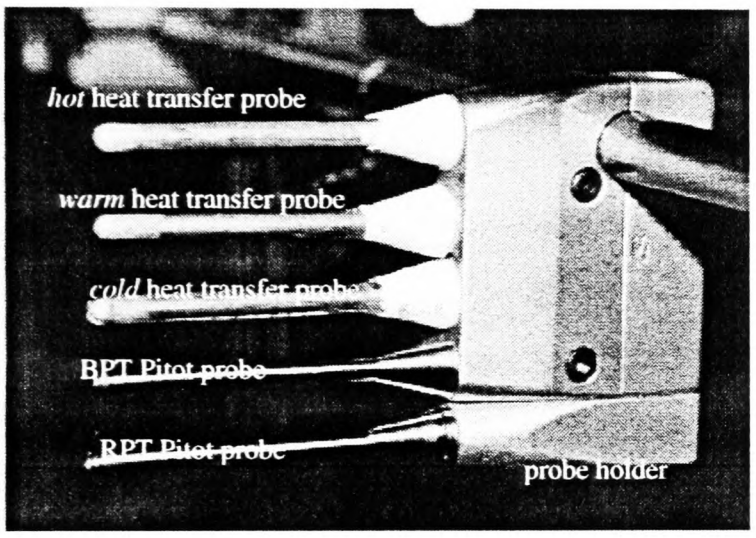


Figure 3-8 Photograph showing the heat transfer and Pitot pressures probes mounted on the traverse

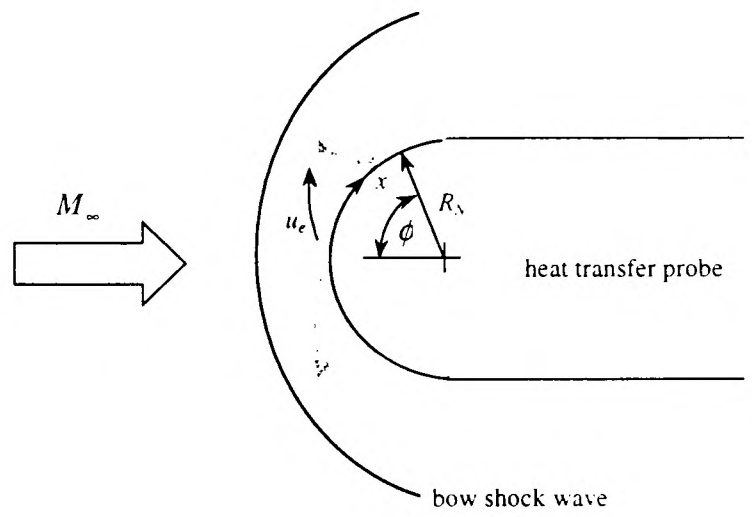


Figure 3-9 Schematic illustration of the stagnation region of the heat flux probe in a hypersonic freestream

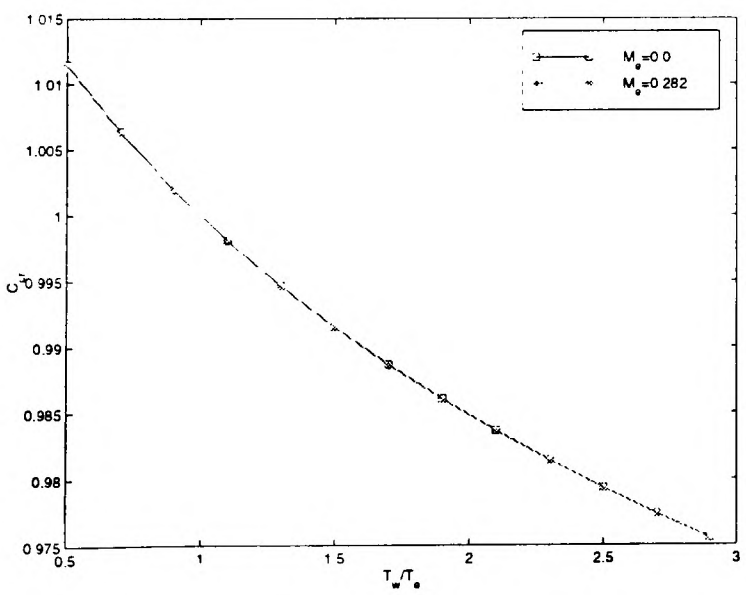


Figure 3-10 Variation of Chapman-Rubesin parameter against substrate wall to stagnation boundary edge temperature ratio

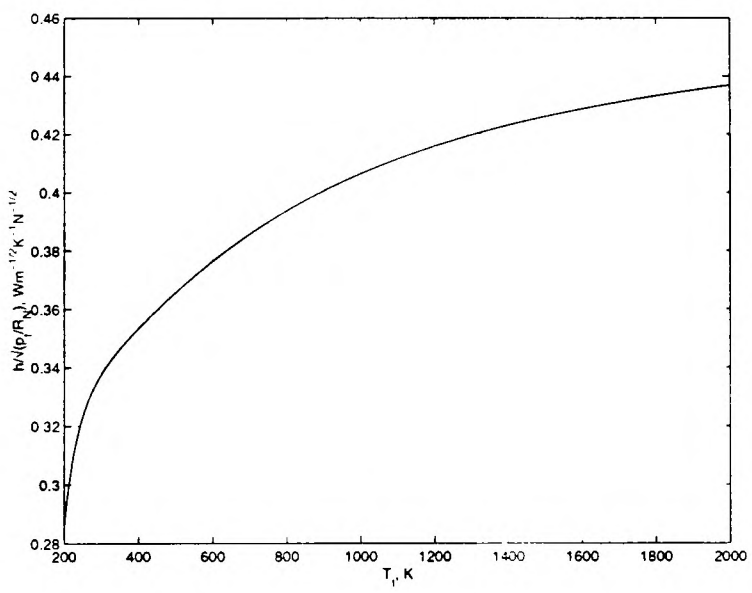


Figure 3-11 Convective heat transfer coefficient scaled with Pitot pressure and plotted against flow total temperature

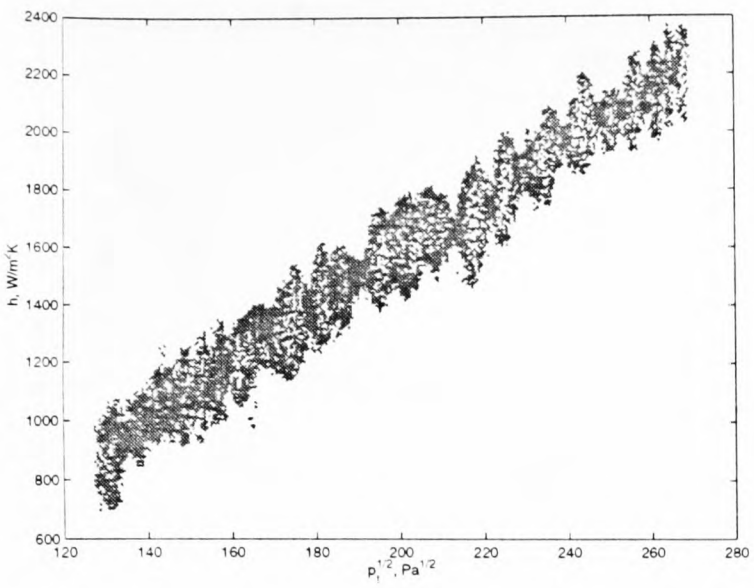


Figure 3-12 Variation of convective heat transfer coefficient in the isentropic plume core region *(LT157)*

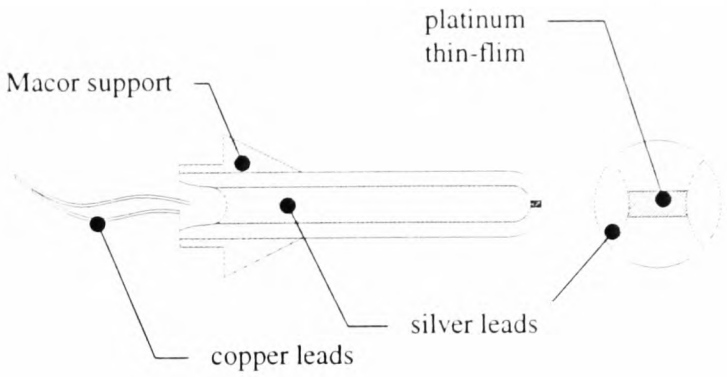


Figure 3-13 Schematic illustration of the heat transfer probe

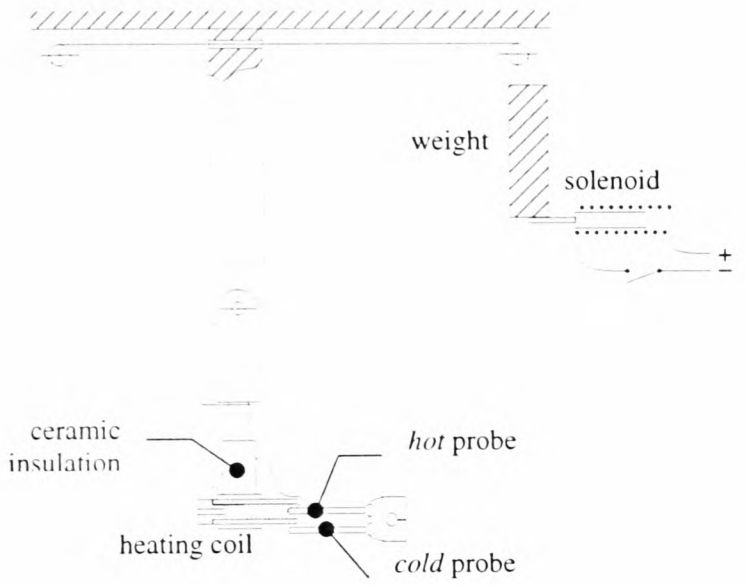


Figure 3-14 Schematic illustrations of the total temperature probe and the heating mechanism *(Buttsworth, 1996)*

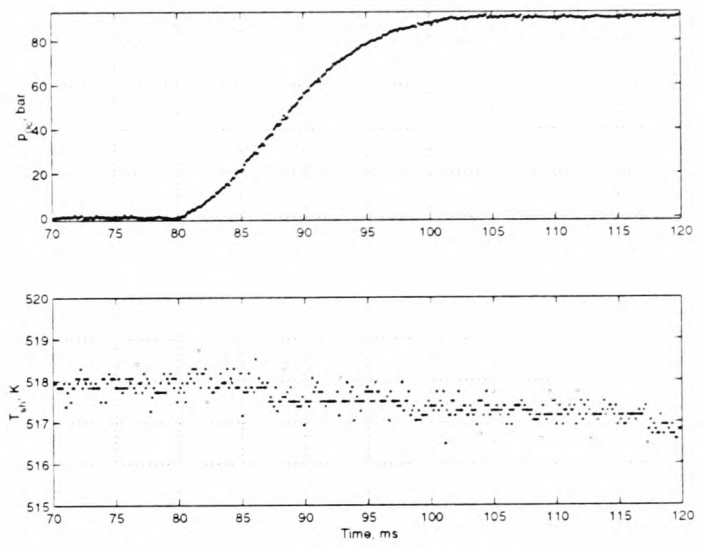


Figure 3-15 Substrate temperature variation due to entrainment before traverse commences *(LT183)*

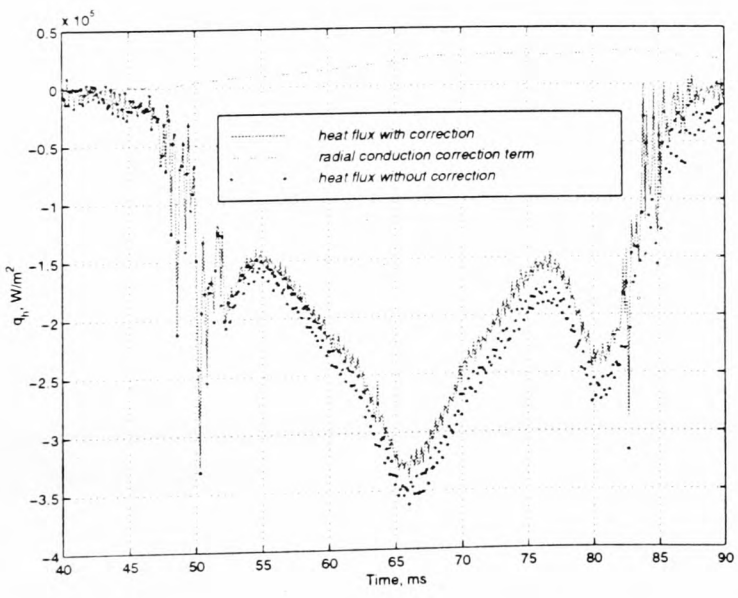


Figure 3-16 Curvature correction applied to heat flux data *(LT157)*

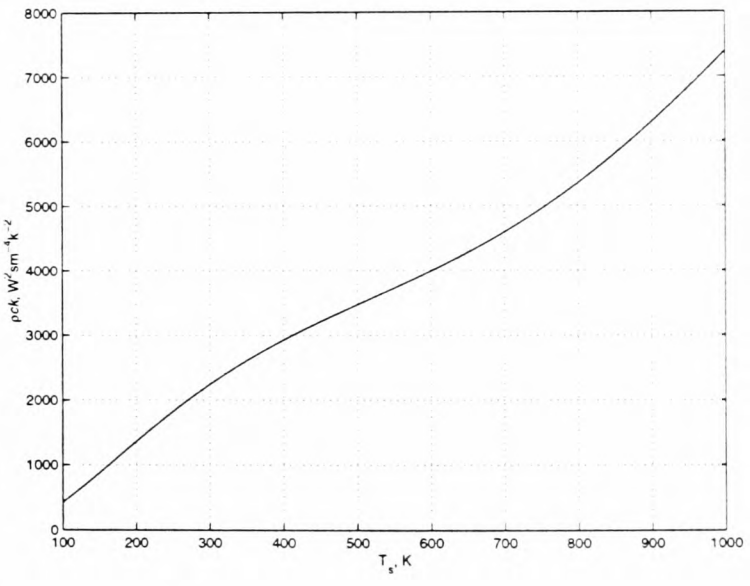


Figure 3-17 Variation of heat transfer probe substrate properties with substrate temperature

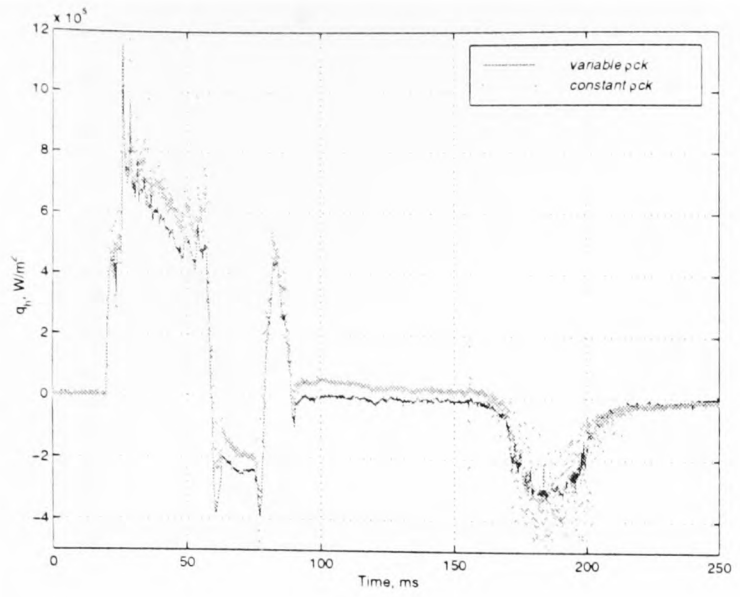


Figure 3-18 Heat flux from substrate temperature with and without variable substrate properties, both include radial conduction correction *(GT747, hot probe)*

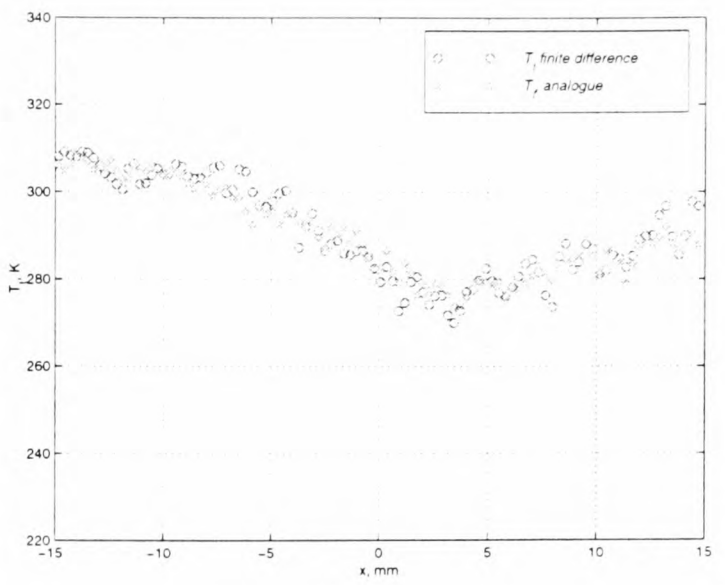


Figure 3-19 Total Temperature for single nozzle jet (SM5M) in quiescent with 100 bar gauge injection of He *(LT191)*

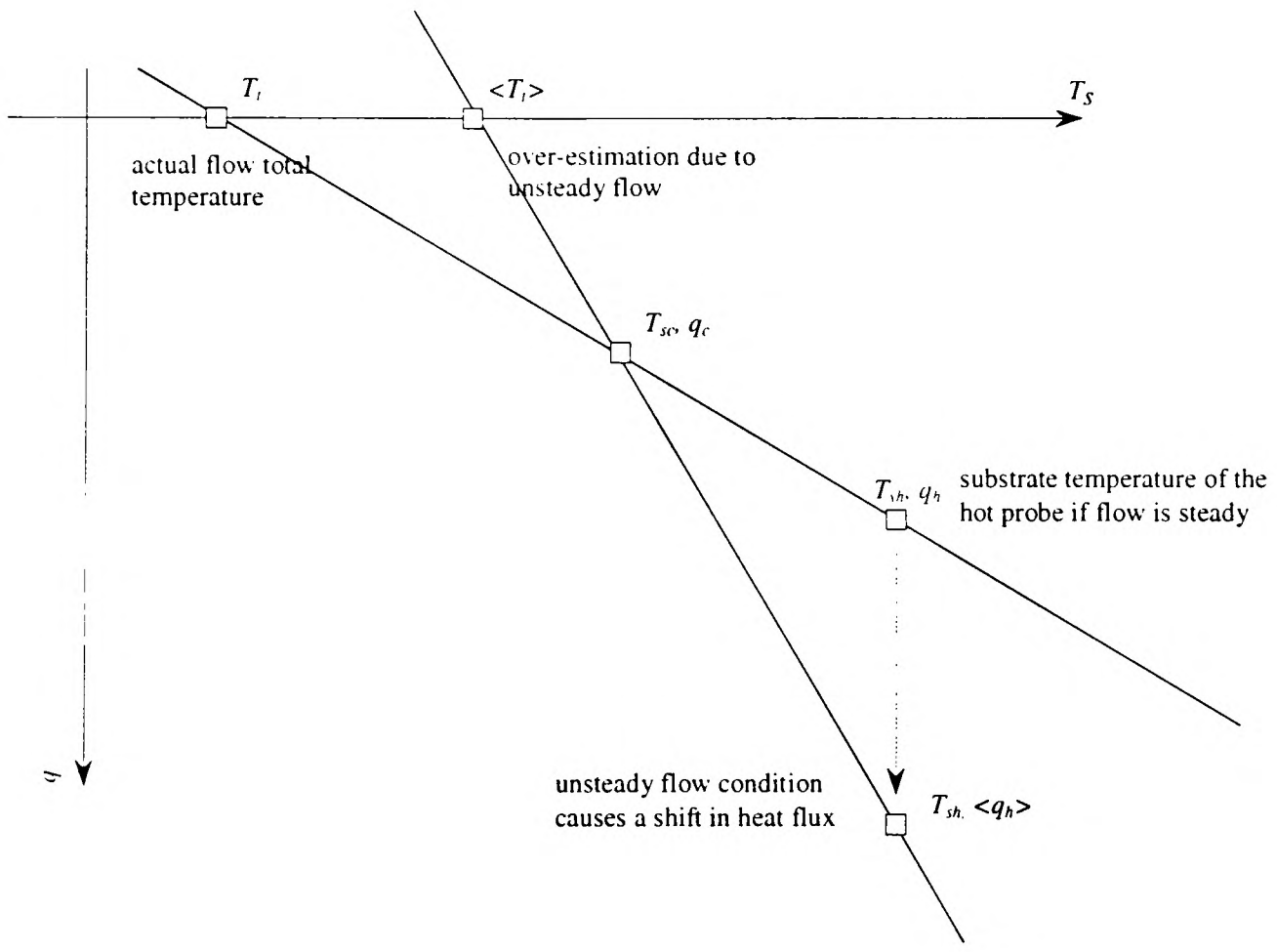
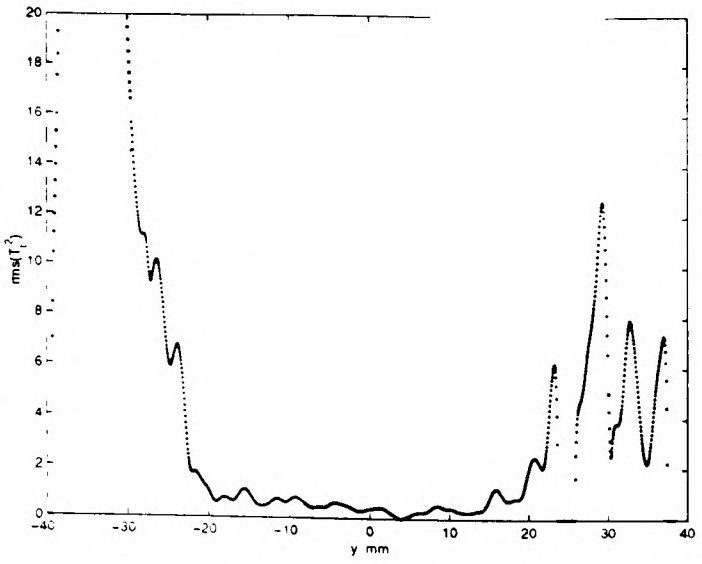
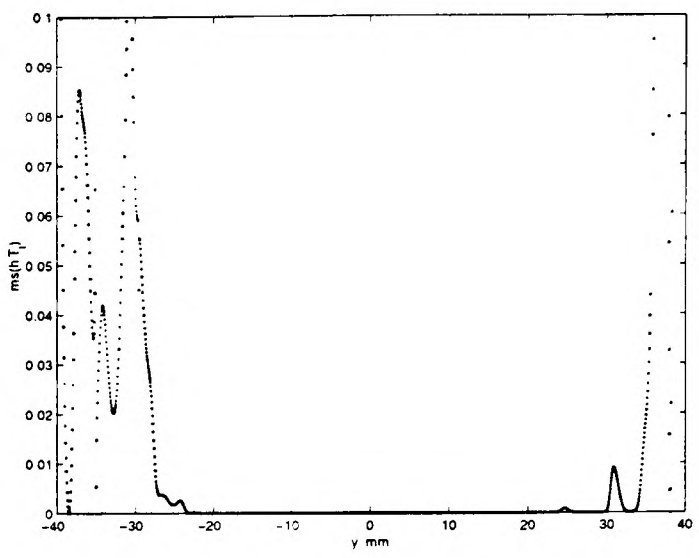


Figure 3-20 Total temperature variations when the probe spacing in the time domain is comparable to changes in mean flow conditions





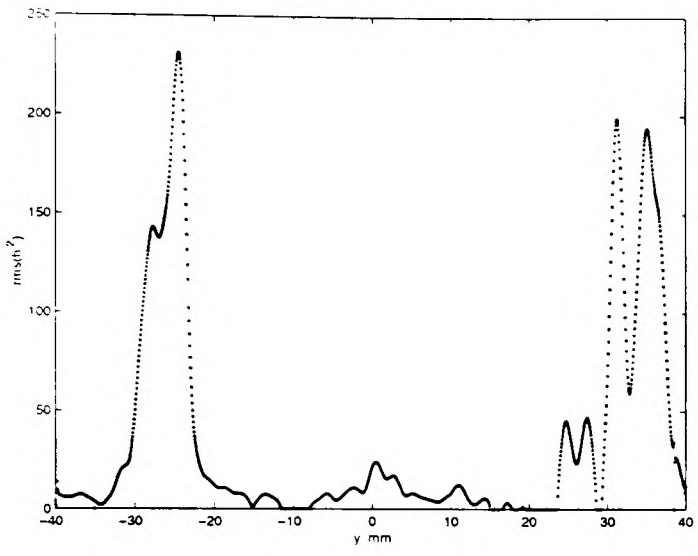


Figure 3-21 $\sqrt{\overline{T_t'^2}}$, $\overline{h'T_t'^2}$ and $\sqrt{\overline{h'^2}}$ variations for Mach 5 single jet nozzle (SM5M) at 40 mm downstream *(LT182)*

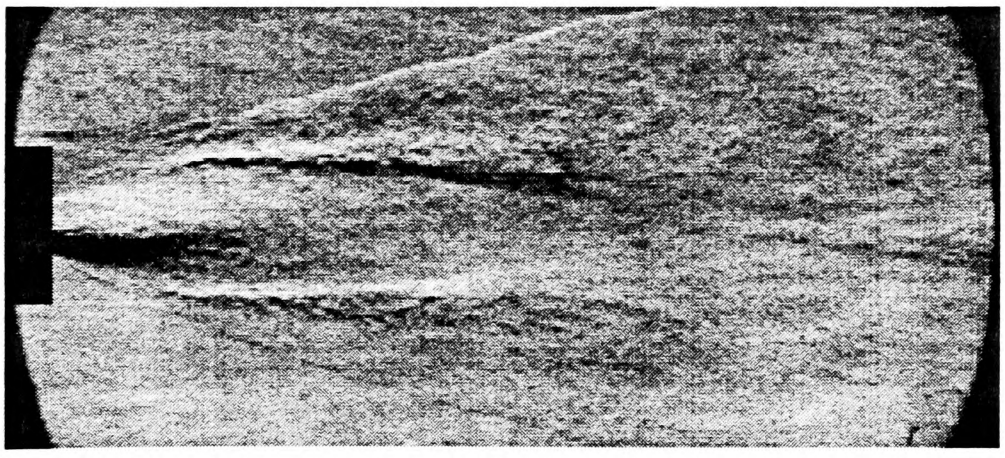


Figure 3-22 Schlieren image of the Mach 5 twinjet in a Mach 7 hypersonic freestream on *y*-*z* plane *(Shek, 1997)*

4. Single Nozzle Rocket Flowfield

4.1 INTRODUCTION

Single nozzle thrusters can be found in a majority of rocket and missile designs. A great deal of effort has been spent in understanding the characteristics of such a flowfield. Much of the attention has been on the exhaust plume of such a vehicle. Many analytical calculations and empirical models have been proposed with relative success.

Previous theoretical studies have been carried out on single jet flowfields at high altitudes (e.g. Hill et al, 1963; Adamson et al, 1963). These were primarily concerned with the prediction of the plume size and shape. Some of these were semi-empirical (Jarvinen et al, 1966; Alden et al, 1964) in that simplified solutions for the plume boundary were obtained by fitting equations for the density variations to solutions obtained by the method of characteristics. Some experimental data have been obtained from plumes exhausting from rockets into a quiescent medium. There is almost a complete absence of experimental results on the interaction of a plume and a hypersonic freestream.

Morris, Cain and Jones have carried out a considerable amount of work over the past few years at Oxford University. Cain (1993) carried out angular and axial Pitot surveys of heated, high pressure N_2 injection from a Mach 3 conical nozzle into a quiescent low-pressure tank. Results indicated that there was strong turbulent mixing throughout the flowfield downstream of the first Mach disk in addition to a repetitive shock cell structure.

Cain et al (1992) also studied under-expanded single Mach 5 jet in a Mach 7 freestream. The pressure ratios N were of the order 10^3 and plume Reynolds number were greater than 10^4. The shear layer of the jet was found to be turbulent and supersonic. They detected condensation in the N_2 plume at 60 bar injection, which lowered the measured Pitot pressure from the analytical value.

Morris et al (1995) carried out extensive experiments on single under-expanded jets in a Mach 7 hypersonic freestream. They found that the plume scale L was a particularly effec-

tive scaling parameter for regular reflections for various rocket geometry and injection gases. They also observed condensation for some of the N_2 runs and that no more than one shock cell was formed over a wide range of pressure ratios. The shock cell always terminated in a regular reflection rather than a Mach reflection (or known as a Mach disk). The experimental result was compared to a parabolised Navier-Stokes simulation. Best agreement was obtaind when a compressible k-ε_{cc} turbulence model was implemented in the computer code.

Norman et al (1970) carried out experimental and theoretical studies to determine density variation of the exhaust and the ambient gases across the plume, as well as the size and shape of the freestream and plume interaction region. Effect of parameters such as freestream Mach number, density, exhaust gas properties and rocket nozzle geometry on plume characteristics were also investigated. Scaling parameters for rocket plumes were determined on the basis of a simplified inviscid theory. These parameters were then used to determine test conditions for the simulation of the flight of a typical rocket through the atmosphere at an altitude of 80 km at Mach numbers of 10 and 18.

Rocket plume flow at hypersonic speed in space contains a large number of gas dynamic phenomena: continuum and free molecular expansion flow, isentropic flow and viscous effects.

Crist et al (1966) carried out experimental studies of highly under-expanded single jet plumes in quiescent using a modified hotshot wind tunnel. Stagnation pressures were varied up to 1034 bar with ambient pressures down to 0.0013 bar. Mach disk location was found to be insensitive to ratio of specific heats, condensation, nozzle lip geometry, and absolute pressure level. For overall pressure ratio N up to about 300000, the Mach disk location was found to vary as the square root of the static pressure ratios. Diameters of Mach disk, jet boundary, and barrel shock were found to increase with condensation and γ, and decreased at high stagnation density where intermolecular forces became important. At high values of static pressure ratio, the ratio of Mach disk diameter to its downstream location appeared to be a constant for a given gas. It was also found that properties along the jet axis could be ap-

proximated by properties of the flow through a hypothetical conical nozzle whose half-angle was given as a function of specific heat ratio. They noted that condensation was observed with naked eye when Ar was used as the injected gas.

Numerical computation based on a Lagrangian finite-difference technique carried out by Boynton (1967) came to the conclusion that there was relatively small difference in boundary location for quite different undisturbed flow representations of the shock layer. This suggested that the common practice of comparing calculated and photographically observed jet boundaries and shock structures did not necessarily lead to firm conclusions about the calculation's description of the local flow properties.

The Computational Fluid Dynamics (CFD) modelling of low altitude (< 70 km) moderately under-expanded rocket exhaust plume flowfields has direct application to the prediction of infrared signatures and missile aerodynamics (Dash, 1980). Although a reasonable amount of work has been done on single nozzle under-expanded jets, experimental data are still very much in demand to further verify and fine-tune the turbulence prediction methods for these hypersonic, aerodynamically complex flows. The recent advances in CFD capability mean that a new tool could be used for predicting conditions of the behaviour of various rockets. The single nozzle rocket plume is particularly suited to CFD because of its axisymmetrical structure, which is less demanding in terms of computing power. However, under-expanded jets contain shocks, shear layers and both supersonic and subsonic regions make numerical modelling difficult and the task of code verification of plume flowfield models used in CFD requires well-defined data. Such data are needed to check the ability of current codes to correctly model viscous effects caused by the presence of a freestream flow in conjunction with the plume flow. These viscous effects include interaction between boundary layers on the rocket body with the plume (including possible separation of the boundary layer), and turbulent mixing between the plume gas and the freestream gas.

4.2 TYPICAL FLOW OVER A SINGLE NOZZLE ROCKET

4.2.1 Rocket Nose Conical Shock

When the rocket nose angle and the freestream Mach number fall within certain limits, a shock wave is formed which is attached to the vertex of the conical fore-body of the rocket as illustrated in Figure 4-1. The subsequent flowfield can be modelled by the well-known Taylor-Maccoll flow where flow properties depend only on the spherical angle α and not on the radius r_c. Consequently, it is assumed that the flow properties are constant along any ray emanating from the vertex of the cone. Since the nose shock is conical, it has the same inclination to the freestream everywhere. The strength of the shock therefore is constant and the flow properties immediately behind the shock wave are uniform and irrotational. Therefore there is no entropy gradient within the conical shock flowfield.

4.2.2 Rocket Body Flowfield

From the point where the straight body contour of the conical nose meets the curved body contour of the start of the rocket body, expansion waves emanate and finally intersect with the conical shock (see Figure 4-2). It is downstream from this point on the conical shock that the rocket body shock wave, on meeting the expansion wave, becomes curved to accommodate the new body contour. Local shock angles become smaller downstream implying less entropy increases across the shock wave. Flow downstream of the shock wave is assumed to be inviscid and adiabatic and so entropy along the streamlines is constant. However, the curved shock condition means that there will be gradients in entropy and stagnation properties normal to the streamlines. This condition implies vorticity in the flowfields and so the flow downstream of the initial expansion wave on the rocket body is rotational.

4.2.3 Rocket Nozzle Throat Flowfield

For short thrust-nozzles such as those typically found on rockets, the radius of curvature of the throat can be of the same order as the throat radius. This geometric condition introduces significant velocity gradient in the plane of the throat and so flow in the throat re-

gion is two-dimensional with the sonic line distended along the nozzle axis towards the exit plane. Figure 4-3 shows schematically the general features of the throat and nozzle exit regions of a converging-diverging nozzle. The parabolic sonic surface is the locus of all the points in the flowfield where the local Mach number equals one. The sonic line starts from the wall at a point slightly upstream from the throat, the minimum flow area, proceeds downstream, and crosses the centreline of the nozzle at a point past the throat.

When the nozzle throat curvature is an order of magnitude larger than the throat radius, then flow in the throat region can be considered to be planar. Conditions at the exit can still be assumed to be conical, i.e. properties are constant on a spherical surface dictated in length from a point originating at the imaginary vertex of the cone formed by the walls of the nozzle to the lip of the nozzle exit.

4.2.4 Boundary Layer in Nozzle

Nozzle boundary layers can have a significant effect on the effective area ratio of the nozzle, particularly for long thrust-nozzles where boundary layer thickness can be a significant percentage of the exit diameter. They must therefore be considered when calculating such a nozzle flowfield.

Bird (1974) has suggested that the sonic line in the nozzle boundary layer intersects the nozzle lip and thus effectively insulates the nozzle boundary layer from external influences unless condensation occurs. Therefore, in most rocket plumes, the initial expansion of the exhaust gas is the same at low altitude as it is in vacuum.

However, for significant reductions in background pressure below the exit plane centreline value, the nozzle centreline flow properties are affected. Bailey (1987) had shown that the nozzle boundary layer thickness (and hence nozzle centreline flowfield properties) was affected by changes in the centreline to background static pressure ratio. For a range of ratios up to 100, the change was not significant. However, when the ratio was increased to 1000, a decrease of 1 per cent in Mach number was observed. Static pressure ratios used in this thesis ranged from 1.5 to 15, therefore it is reasonable to assume that this effect was negligible.

4.2.5 Rocket Exhaust Plume Flowfield

A schematic illustration for a typical single nozzle under-expanded rocket plume in a hypersonic freestream is show in Figure 4-4. Which shows some of the most commonly observed features. Note that regular reflections instead of Mach disks were observed for all experiments in this thesis.

4.2.6 Initial Expansion at Nozzle Exit

The initial angle of expansion of the flow is dependent on the static pressure ratio, the nozzle exit geometry and thermodynamic conditions and viscous effects such as the nozzle boundary layer. Figure 4-5 shows the effect of external factors on the initial flow angle of the injected gas at the nozzle exit. The theoretical values are based on the assumption that the jet expands by the Prandtl-Meyer expansion waves at the lip to the background static pressure. The measured values were obtained from quiescent experiments using the Mach 5 (SM5) single nozzle. Schlieren images taken for the runs were scanned into a computer and digitised. There is a certain degree of uncertainty as to the locations of the jet boundary, which is hindered by the presence of a turbulent shear layer. This uncertainty is indicated by means of error bars.

Despite the difficulty of obtaining the exit angles accurately, measured values exhibit a significant discrepancy from the analytical values. This could only be accounted for by considering the viscous nature of the flowfield. Within the boundary layer, Mach number varies from zero at the wall to the mainstream value outside of the layer. The slow moving low-density gas inside the boundary layer expands further into the freestream than the core injection. Also, entrainment of the background gas in quiescent injections and freestream gas in co-flow cases into the shear layer helps to lower the background pressure even further. These combined with the displacement effect of the boundary layer contribute to the increase in discrepancy between the theoretical and experimental values with increasing pressure ratio N.

4.3 UNDEREXPANDED ROCKET PLUME IN HYPERSONIC FREESTREAM

4.3.1 Nozzle Exit Flowfield

Assuming an isentropic expansion within the nozzle, then the Mach number at the exit of an inviscid supersonic nozzle is a function of the nozzle area ratio and γ only.

$$\left(\frac{A}{A^*}\right)^2 = \frac{1}{M^2}\left[\frac{2}{\gamma+1}\left(1+\frac{\gamma-1}{2}M^2\right)\right]^{\gamma+1/\gamma-1}$$

The static pressure is a function of area ratio and the stagnation pressure. Under-expanded jet is a class of jets, which the exit static pressure P_e is higher than the ambient static pressure P_b. This means that the exhaust jet is still capable of expansion through a series of expansion waves originating from the nozzle lip on the edge of the nozzle boundary layer. When P_e is greater than $2P_b$, the pressure gradient at the nozzle lip is sufficient to accelerate the subsonic boundary layer flow to Mach 1 (Morris, 1994).

Local two-dimensional Prandle-Meyer expansion waves expand the streamlines close to the nozzle wall to the background pressure P_b. Along all other streamlines, right-running characteristics travelling at the local Mach angle dictate the degree of expansion. Eventually, radial momentum of the jet causes the exhaust plume to over-expand and subsequently to be turned back by the centrifugal force provided by the pressure gradient across the shock layer. Compression waves are emanated as a result, which are reflected back towards the core at the free jet boundary.

4.3.2 Shock Structure of Under-expanded Rocket Plumes

The coalescence of the compression waves emanating from the inward turning injected gas forms what is know as the barrel shock, which increases in strength as more compression waves collapse together downstream. The flow within the barrel shock is not influenced by the external flow and it assumes the source-like nature similar to which it would take on in vacuum. The radial component of velocity which the exhaust acquires in the expansion process results in the barrel shock being initially swept away from the nozzle axis. This is subsequently driven back towards the centreline by the difference in static pressure

between the expanded injection gas and the ambient freestream. The barrel shock can reflect on the centreline either as a Mach disk or a regular reflection depending on the pressure ratio N, nozzle exit angle and boundary layer thickness, ambient density and shear layer characteristics. Barrel shocks of the plumes in this study were all reflected by a regular reflection even though high values of pressure ratio N were used under which Mach disks have been observed in other low density testing facilities.

Shock cells are defined as the region of the plume bounded by the barrel shock and the regular reflection. If the jet boundary is quiescent or a slow moving freestream, the underexpanded jet takes the form of a series of shock cells, with wave strengths diminishing downstream due to turbulent dissipation, interaction with expansion waves and the irreversible nature of shock waves. It can be seen in Section 4.3.5 that for the co-flow case the location of the barrel shock is not only dependent on the static pressure in the freestream but also on its Mach number.

When the rocket plume flowfield is immersed in a hypersonic freestream, the jet boundary is no longer a boundary of constant pressure because the jet expands and the freestream changes direction to accommodate such a change. The rocket plume will be seen by the freestream as a solid blunt body, which leads to the formation of a shock wave known as the plume shock. This significantly reduces the expansion of the plume compared to its quiescent counterpart. When the jet boundary turns back towards the centreline, the background pressure seen by the plume drops as the freestream expands. This in turn tends to reduce the contraction of the jet. Both processes help to adjust the jet pressure to that of the freestream value and tend to dampen the formation of downstream shock cells as observed by Hsu (1991). For co-flow plumes, the barrel shocks are more likely to reflect in a regular reflection rather that a Mach disc, this is believed to be due to the axial momentum gained by the jet from the high-speed freestream. This decreases the inward turning angle of the barrel shocks downstream.

Influence of the nozzle metal turning angle on the downstream flowfield was investigated using the two Mach 5 single nozzles SM5 (θ_N = 10°) and SM5M (θ_N = 7°). Figure 4-6 shows the Pitot pressure signals across the plume at 100 mm downstream. In the core region, measurements for both cases were the same as expected. It can be seen that the barrel shock for the SM5 nozzle turns inwards tighter than the SM5M nozzle with a smaller metal turning angle. Immediately after the nozzle exit, the plume gas in the SM5 nozzle was given a greater radial momentum due to a larger metal turning angle. This resulted in the static pressure decreasing rapidly downstream and led to a corresponding increase in the pressure gradient across the shock layer. Therefore the shock compressed injection gas was turned back at a tighter angle by the centrifugal force. Hence, the barrel shock downstream of the SM5 nozzle was swept inwards towards the centreline at a steeper angle than that of the SM5M nozzle. Note that the difference in the plume shock locations for the two nozzles is somewhat exaggerated in the figure. The traverse mechanism was released slightly early in run GT740, leading to the BPT probe passing through the plume shock when the injection pressure was still on its approach to the final steady value. The corresponding injection pressure at this instant is approximately 78.9 per cent of the steady level. Since the shock locations are dependent on the square root of the injection pressure (see Section 4.3.5), this corresponds to an 11 per cent variation in the plume shock location.

4.3.3 Rocket Plume Core Flow

The core of a typical rocket plume is defined as the region enclosed by the barrel shock and the regular (or Mach) reflection. The first right running characteristic or Mach line of the expansion waves defines the conical expansion region of the plume. Within this boundary, the jet behaves as if in a conical nozzle and the equations for such a flow applies. For a conical flow, the condition along the characteristic can be obtained by noting that $\Delta\theta = \pm\Delta\upsilon/2$. The isentropic nature of the core enables the use of Method of Characteristic (MOC) calculations to predict properties of the flowfield at downstream locations with a good degree of accuracy.

4.3.4 Shear Layer and Shock Layers

For an inviscid co-flow plume there exists an inviscid jet boundary, which separates the freestream gas and the plume gas. The layer between the barrel shock and the jet boundary is termed the inner shock layer and the layer between the jet boundary and the plume shock is the outer shock layer. Cain (1993) showed that near the maximum diameter of the plume, 60 per cent of the gas flow is within the inner shock layer. Therefore correct prediction of flow characteristics in this region is of pertinent importance to the overall understanding of the rocket exhaust plume flowfield.

4.3.5 Rocket Plume Scale

There are various methods that can be used to calculate hypersonic plume scales, depending on the assumptions made in each respective analysis. The plume scale L in the axial direction can be thought of as the distance to the Mach disc or regular reflection of the first shock cell. One common quiescent plume scale used is,

$$L = \sqrt{N} D^* \text{ Where } N = \frac{P_0}{P_b}$$

It is based on the assumption that near the end of the first shock cell, the gas within the barrel shock has expanded to its limiting velocity $U_{\lim} = \sqrt{2c_p T_0}$, together with the assumption that the pressure in the subsonic flow immediately behind the Mach disks is the background pressure P_b.

This correlation agrees well with experimental data obtained by Emden (1899). He found that the wavelength of the almost periodic structure of axially symmetrical supersonic jet in a medium at rest was given by the following empirical formula,

$$z_M = 0.89\sqrt{N} D^*$$

Lewis and Carlson (1964) correlated Mach disc (found to be favourable at higher N) and regular reflection (found to be the favourable mode at lower N) positions z_M. They measured Schlieren photographs of turbulent jets into quiescent air over a range of γ from 1.22 to

1.67, a range of M_e from 1 to 3 and a range of P_e/P_b from 1 to 550 and obtained the expression,

$$\frac{z_M}{D_e} = 0.69 M_e \left(\frac{\gamma P_e}{P_b} \right)^{\frac{1}{2}}$$

This equation can be written in the form $z_M = 0.69 f(M, \gamma) L$

where

$$f(M, \gamma) = \left(\frac{2}{\gamma + 1} \right)^{\frac{\gamma+1}{2(\gamma-1)}} M_e \left(1 + \frac{\gamma - 1}{2} M_e^2 \right)^{\frac{3\gamma+1}{2(\gamma-1)}}$$

Buckley (1975) demonstrated that this also correlated the Mach disc position determined from Schlieren photographs of jets in low Mach number co-flowing air-streams taken by Love et al (1985) and Rousso and Baugham (1975). However, from the measurements by Morris (1994) and Norman (1970) of shock shell lengths of plumes in Mach 7 and Mach 18 freestreams, the Mach disc/regular reflections were about 68 per cent and 25 per cent of the distance that were predicted by the equation. The validity of this empirical expression for predicting regular reflection positions for a co-flow hypersonic jet is therefore questionable.

For hypersonic co-flow plumes, Jarvinen and Hill's Universal Plume Model can be written as,

$$\overline{L_z} = \sqrt{\left(\frac{T_F}{q_\infty} \right)} = \left(\frac{C_F A^* P_0}{q_\infty} \right)^{\frac{1}{2}} = \frac{L}{M_\infty} \sqrt{\frac{\gamma_e}{\gamma_\infty}} \left(\frac{\pi}{2\gamma_\infty} \right)^{\frac{1}{2}} \left(\frac{2}{2 + (\gamma_e - 1)} \right)^{\frac{1}{4}} \left(\frac{2}{\gamma_e + 1} \right)^{\frac{\gamma_e+1}{2(\gamma_e-1)}}$$

$$\overline{L_y} = \overline{L_z} \left(\frac{D}{T_F} \right)^{-1/4} = \overline{L_z} \left[\left(\frac{C_{F\max}}{C_F} \right) - 1 \right]^{-1/4}$$

where $C_F = \sqrt{\frac{\gamma^2}{\gamma - 1} \left(\frac{2}{\gamma + 1} \right)^{\frac{\gamma+1}{\gamma-1}} \left(1 - \left(\frac{P_e}{P_{0c}} \right)^{\frac{\gamma-1}{\gamma}} \right)} + \frac{A}{A^*} \frac{P_e}{P_{0c}}$ and $C_{F\max} = \sqrt{\frac{2\gamma^2}{\gamma - 1} \left(\frac{2}{\gamma + 1} \right)^{\frac{\gamma+1}{\gamma-1}}}$

This model is intended for high altitude plumes larger than the rocket body and with near normal plume shock near the nozzle exit. It also assumes an inviscid contact surface along the jet boundary rather than a shear layer.

For moderately under-expanded jets, the terms $(P_e/P_{0c})^{-(\gamma-1)/\gamma}$ and $(A/A^*)(P_e/P_{0c})$ are small compared with the other terms. Note that the axial scaling parameter $\overline{L_z}$ is independent of the exit Mach number and is only a function of γ and the quiescent plume scale L normalised by the freestream Mach number. The radial and axial scaling parameter in this case, can be simplified to,

$$\overline{L_y} = \overline{L_z} = L/M$$

Morris (1994) showed that this scaling parameter gave satisfactory results for plumes at moderate under-expansion and altitude, as well as highly rarefied plumes at high altitude.

4.4 EXPERIMENTAL RESULTS

Significant time was spent studying quiescent single jets. The experimental arrangement was relatively straightforward and less demanding on the instrumentation used. The average turn-a-round time for a run was about one hour. Quiescent shear layer was studied using fast responding Pitot pressure and heat transfer probes.

Co-flow runs with the Mach 7 freestream were mechanically more complex and labour intensive. The average turn-a-round time for a run was in the region of five hours. It put great stress on the instrumentation and it was important to get the correct timing so that the steady period of the gun tunnel, Ludwieg tube injection and traverse release were all within a 30 ms time window, which meant an overall accuracy within 5 ms.

Typical freestream conditions are shown in Table 4-1, which could be reproduced with reasonable accuracy.

M_e	$P_{0\infty}$, bar	$T_{0\infty}$, K	γ_0	γ_e	P_∞, kPa	T_∞, K
7.1	72	885	1.36	1.40	1.58	79.8

Table 4-1 Gun tunnel Mach 7 freestream conditions

Both N_2 and H_2 were used as the injection gas for co-flow runs. Exit conditions of the two gases are given in Table 4-2 for a typical experiment with 100 bar gauge injection.

Gas	M_e	P_{0c}, bar	T_{0c}, K	P_e, bar	T_e, K	ρ_e, kg/m^3	u_e, m/s	N
N_2	5	92	300	0.173	50	1.165	720.94	5823
H_2	5	86	300	0.163	50	0.079	2694.72	5443

Table 4-2 Nominal exit conditions for SM5M and SM5 with N_2 and H_2 injection

4.4.1 Quiescent Experiments

4.4.1.1 Background Pressure Level and Apparent Plume Distortion

It has been shown that the rocket plume dimensions are a strong function of the pressure ratio N. Experiments in this thesis were checked to ensure that traverses were carried out when the injection pressure, as measured by a pressure transducer in the rocket plenum chamber showed a steady level. However, N was almost certainly changing to a certain degree due to a decreasing background pressure as a result of the ejector action of the plume gas.

Figure 4-7 shows this change in the test section static pressure against the injection pressure. Values for the test section pressure were taken at mid-traverse (roughly 50 ms after the injection gas came on). The obvious trend indicates an increasing effect on the test section pressure by the injection pressure. The higher the injection pressure, the more static gas in the test section was entrained into the shear layer, which in turn lowered the background static pressure. This effect also showed a significant degree of dependence on the type of gas used as shown in Figure 4-8. It can be seen that the ejector effect is relatively lower for the He injection as result of a lower jet momentum.

4.4.1.2 Quiescent Schlieren Analysis

Schlieren photographs were taken for a majority of the runs. This served the purpose of locating various features of the plume structures and to give accurate positions of the probes within the flowfield. These photographs were scanned using a high-resolution scanner

and then digitally enhanced to adjust brightness and contrast, and to correct any alignment error of the negatives.

Figure 4-9 shows three quiescent spark Schlieren photographs at increasing injection pressures. Referring to run LT35, across the shear layer the static temperature gradient was greater than the static pressure gradient. This meant there would be a positive density gradient across the layer up to the edge of the inviscid jet boundary. This can be seen on the upper half of the plume on the Schlieren image as the intensity of the image increases into the shear layer and decreases after the inviscid jet boundary. A sharp decrease in intensity that follows indicates a discontinuous drop in density caused by the barrel shock. The barrel shock can be seen to converge on the centreline to form a regular reflection. Along the inviscid jet boundary, mixing between the injected gas and the background gas took place. Gas molecules in the shock layer followed a curved path outside the barrel shock due to a positive static pressure gradient across the width of the shock layer, which provided the centrifugal turning force. When the reflected barrel shock met the inviscid jet boundary, it was reflected back towards the centreline as expansion waves. This expansion region can be seen at the middle of the second shock cell. These expansion waves caused the jet to expand again below the background static pressure, and subsequently be turned back by the pressure gradient across the shock layer. Compression waves from the inward turning jet coalesced to form another set of barrel shocks in the second shock cell.

When the injection pressure was increased further as shown in run LT6, the regular reflection was forced downstream and the plume expanded further outwards into the quiescent medium. At an even higher injection pressure as shown in LT8, the regular reflection was moved further downstream out of the range of the Schlieren mirrors.

Distinguishable convective structures as shown in Figure 4-53 for planar shear layers were not clearly visible in the Schlieren images taken for this thesis. This is investigated further using fast response Pitot pressure probes in Section 4.5.

4.4.1.3 Quiescent Plume Scale

The empirical quiescent scaling equation proposed by Lewis and Carlson predicts the regular reflection positions to lie near the region,

$$z_M = 0.92L$$

Since the test section static pressure P_b decreases due to entrainment of the injection gas into the shear layer, consequently L varies over the run. This will almost certainly have an effect on the position of the regular reflection point. Figure 4-10 shows the experimental result measured on Schlieren images and the empirical Lewis and Carlson regular reflection predictions at different injection pressures. If L was calculated based on the initial background pressure, the empirical model appears to under-estimate the regular reflection positions. To obtain better estimates of the actual background pressure, spark signals from the Schlieren camera were compared with the signals from the test section static pressure transducer. An improved estimate of the background pressure was obtained by taking the mean value of the measured background pressure during the run. This was used to correct the Lewis and Carlson correlation parameters for the regular reflections and shown in the same figure.

The digitised barrel shock positions of the Mach 5 (SM5) single jet with increasing injection pressures are shown in Figure 4-11. To test the quiescent plume scaling parameter given in Section 4.3.5, the barrel shock positions were scaled with L and shown in Figure 4-12.

4.4.1.4 Quiescent Pitot Pressure

Pitot probe traverses were carried out at downstream locations for two injection pressures. This was to capture detailed Pitot pressure variations at representative downstream locations of the flowfield and to obtain high frequency data for shear layer analyses.

A brief description of a typical quiescent plume can be deduced by referring to Figure 4-13. This is a run with 80 bar gauge injection at 120 mm downstream. The RPT Pitot probe

was initially in the upper shear layer of the plume. As it was traversed across the plume, the probe first met the barrel shock at –38 mm. This is indicated by a sharp fall in Pitot pressure due to a large negative density gradient across the shock surface. The strength of this barrel shock itself depends on the downstream location. The RPT probe then entered the isentropic plume core, which at this downstream location was dominated by the expansion waves originating at the nozzle lip. This is indicated by a gentle rise in Pitot pressure up to the local maximum at the centreline. This is then followed by a gentle fall as the RPT probe was traversed past the plane of symmetry. At 48 mm, the sharp increase in Pitot pressure indicates the lower barrel shock. Pitot pressure increases after this shock due to a positive density gradient across the inner shock layer, and decreases again once into the shear layer.

Figure 4-15 to Figure 4-20 shows the measured Pitot pressure variation across the plume with 80 bar and 100 bar gauge injections. For both injection pressures, the asymmetric nature of the plume increases downstream. Changes in background pressure discussed in the previous section are believed to be the main causes of this discrepancy.

4.4.1.5 Quiescent Heat Transfer

Figure 4-14 shows a typical N_2 quiescent injection heat flux signal as measured by the *warm* heat transfer probe. Away from the plume, there was virtually no heat flow into or out of the probe. Once the probe entered the shear layer at –47 mm, a significant increase in heat flux is shown as a result of the turbulence assisted cooling of the quartz substrate of the probe and the positive density gradient across the shear layer. The measured heat flux drops after the barrel shock as the density decreases across this shock. The relative straight region in the plume core indicates the region of the flow bounded by the leading characteristic of the expansion waves. Unsteady effects in the injection gas resulted in a gentle fall in the measured heat flux. Ejector action of the plume caused the pressure ratio N to increase and consequently the plume size increased. This is reflected in the thicker shear layer in the lower plume region.

Heat transfer data was obtained at downstream locations with 100 bar gauge injection. It was difficult to locate the centres of the heat flux signal, therefore the centres of the RPT Pitot probe were used and displacements of the heat flux probes were referred to this position. Substrate temperature signal was first smoothed to eliminate noise. Then a finite difference routine was applied to calculate the corresponding heat flux (see Chapter 3).

Figure 4-21 to Figure 4-26 show a typical set of heat flux probe signals taken at 40 mm downstream. Heat flux is shown next to the corresponding substrate temperature for the three heat transfer probes (*hot*, *warm* and *cold*) used. Heat flux signals increased in the plume core as expected because the density of the flow increased further into the core as measured by the Pitot probe. Figure 4-27 to Figure 4-32 show the heat transfer signals at 60 mm downstream. Here, effects of the shear layer can clearly be seen as regions of large negative heat flux either side of the plume core. This increase in heat flux was mainly due to a relatively high gas density in the inviscid injected flow just outside the barrel shock. The turbulent nature of the flow in the shear layer could also have an effect on the measured heat flux by increasing the convective heat flux coefficient in this region.

4.4.1.6 Quiescent Total Temperature

Total temperatures of the plume were obtained from the heat transfer probes using a regression method. Figure 4-33 shows the deduced total temperature of a 100 bar gauge injection of He into quiescent obtained from a traverse across the plume. Note that only the region around the plume core is shown. This is because away from the core, the heat flux measured by the probes decreases, which could lead to significant error in the regression process in obtaining the total temperature. The agreement between the total temperatures calculated by using the *hot-cold* probe and the *hot-warm* probe is good. Also, the mean total temperature level is in reasonable agreement with the value measured by stationary heat transfer probes at the nozzle exit (see Chapter 3). Note that the total temperature drop in the plume core was due to reflected unsteady expansion waves in the Ludwieg tube.

4.4.2 Co-flow Runs

4.4.2.1 Co-flow Schlieren Analysis

Schlieren photographs were taken for most of the co-flow runs in order to deduce various features of the flowfield. A complete shock cell could be obtained by digitally merging two images taken at two downstream locations. This is shown in Figure 4-34 for an N_2 injection in the N_2 Mach 7 freestream and Figure 4-35 for an H_2 injection in the N_2 Mach 7 freestream.

In addition to the usual flowfield features for a typical quiescent run, rocket plumes in a hypersonic freestream show additional shock structures, namely the plume shock and the rocket nose shock, which can be seen on the Schlieren images.

On closer examination, a weak shock wave can be seen adjacent to the plume shock approaching it at an angle. This shock is believed to be due to viscous interaction between the freestream and the rocket body boundary layer. The thick boundary layer could exert a major displacement effect on the inviscid flow outside the boundary layer, causing the rocket body shape to appear thicker than it really was. This could cause a significant change in the outer inviscid flow, which is in turn fed back to affect the growth of the boundary layer. When the outer inviscid flow was deflected away from the rocket body, weak Mach waves were generated and swept downstream. These Mach waves eventually coalesced to form the observed weak body shock.

The interaction between the rocket plume and the hypersonic freestream can be seen in Figure 4-34 for injection in the Mach 7 freestream and in Figure 4-9 (run LT8) with the same injection pressure but in a quiescent medium. The co-flow plume has a significantly smaller plume diameter than the quiescent case despite the fact that the static pressure ratio was about 25 per cent lower for the co-flow case.

The H_2 injection plume shown in Figure 4-35 shows a significant reduction in plume size. Note that the regular reflection point in this case is further upstream than the N_2 plume.

This was also observed by Morris (1995) and was believed to be due to the difference in plume velocities which gave rise to different degrees of viscous mixing..

4.4.2.2 Co-flow Plume Scale

Shock locations were digitised from Schlieren images and shown in Figure 4-36 and Figure 4-37. The relatively smaller plume size of the H_2 jet can be clearly seen. Shock positions were scaled with the modified universal plume scale in 4.3.5 and shown in Figure 4-38. The scaled regular reflection is in the region of 5.5 *L/M*. This is comparable with previous studies by Morris (1994) and Norman (1971) on high Mach number co-flow plumes.

4.4.2.3 Co-flow Pitot Pressure Measurements

Pitot pressure probes were made to traverse across the exit plume flowfield at various downstream locations. Detailed knowledge about the flowfield could be deduced from Pitot pressure plots at these locations. Figure 4-39 shows the Pitot pressure profile for the Mach 5 single jet with N_2 injection at 100 mm downstream of the nozzle exit. The plume shock can be seen at –35 mm, which is followed by the inviscid shock-compressed freestream. At about –28 mm the BPT Pitot probe enters a region where turbulent mixing between the freestream gas and the injected gas took place. The dip in Pitot pressure corresponds to the region in which the freestream gas is slowed by the slower plume gas. The higher Pitot pressure in the plume gas is a result of the higher density of the cold N_2 freestream. The low-density gas from the rocket body boundary layer could also have a significant influence on the flowfield near the exit. The local maximum at –19 mm corresponds to the edge of the inviscid injected gas boundary. The measured Pitot pressure falls after this peak as the probe traverses further into the inner shock layer with a decreasing static density. This is terminated by the barrel shock at –16 mm. Passage through the barrel itself is indicated by a sharp drop in Pitot pressure. In the plume core, the Pitot pressure rises as the probe traverses across a series of right running expansion waves with increasing static density across them.

Pitot surveys for N_2 and H_2 injections at representative downstream locations are shown in Figure 4-40 to Figure 4-42. It can be seen that the near field features are quiet different for the two gases. However, there is a fair degree of similarity achieved at about 250 mm in the shock layer.

4.4.2.4 Co-flow Heat Transfer and Total Temperature Analysis

Heat transfer probes were used at three downstream locations for the Mach 5 (SM5M) single jet with 100 bar gauge injection in the Mach 7 freestream. Complications as a result of timing and the maximum capable speed of the traverse mechanism meant that for most of the runs only signals from the upper half of the plume were analysed.

Figure 4-43 to Figure 4-48 show typical sets of heat transfer signals from the probes. Large positive heat transfer was observed when the probes were in the freestream. The freestream total temperature, which was in the region 800 K, was considerably higher than the probe substrate temperature before the run. Hence a large driving temperature resulted in a large heat flux into the probes. In the core region, however, the injected gas total temperature was roughly the room temperature. This could be considerably lower than the probe temperature, which had just been heated by the freestream gas to a higher value. This generated a negative driving temperature gradient at the stagnation point hence a negative heat flux.

Total temperatures for the Mach 5 single jet at two downstream locations, corresponding to the first and the second shock cells, were calculated from the heat transfer signals with N_2 injections and shown in Figure 4-49 and Figure 4-50. At 100 mm downstream, the total temperature signal indicates a freestream total temperature in the region of 620 K. The slope of the total temperature drop in the freestream as result of boundary cooling is comparable to the experimental result obtained by Buttsworth (1996) using a pair of thin-film heat transfer probes near the exit of the Mach 7 contoured nozzle. The location of the plume shock is captured at around –37 mm. Note that the peak in total temperature is artificial as flow

across this shock is expected to be adiabatic. It is accountable by the slightly varying injection pressure at the beginning of the traverse.

Behind the plume shock, the total temperature indicates the shock compressed freestream value until the shear layer is reached (~ -30 mm). In this region, mixing between the freestream and injected gas brings the total temperature from the freestream value to the level of the injected gas. This shear layer ends at the edge of the inviscid injected gas boundary (~ -22 mm) just outside the barrel shock. Thickness of this inner shock layer could be obtained by identifying the barrel shock location (~ -14 mm) from the corresponding Schlieren image. This gives an estimated inner shock layer thickness in the region of 7 mm. The higher than expected injection total temperature is comparable with measurements taken downstream of the nozzle with stationary heat transfer probes (see Chapter 3).

4.5 SHEAR LAYER ANALYSIS

4.5.1 Introduction

From a practical viewpoint, it would be of enormous benefit to the aerodynamicist to be able to predict the behaviour of shear layers. As most of the plume gas is concentrated in the shock layer, shear layers play an important part in the structural characteristics of visible plumes. A thorough understanding of this mixing layer would enable the engineer to be more confident in predicting infrared signature of hypersonic rocket or missile plumes. There are doubts as to the degree of influence that shear layers have on the overall shock structure of the downstream flowfield and the mode of reflection of the barrel shocks. Published experimental data concerning shear layers of supersonic and hypersonic three-dimensional plumes in co-flow freestreams are virtually non-existent.

4.5.2 Previous Work

It is only until recently that there has been a relatively intensive effort to understand the stability of, and mixing process in, supersonic planar shear layers. This has been brought about by the development of the hypersonic aeroplane concept, which relies on the rapid mixing of fuel and air and supersonic combustion for its propulsion.

Experimental studies of planar supersonic turbulent mixing layers have been abundant in recent years, concentrating on the interaction between two constant pressure, but different Mach number, high velocity streams. A variety of computational models are now available which are able to reasonably predict growth rates of such planar shear layers under certain conditions (Brescianini, 1992; Kim, 1990). The suitability of such models to the analysis of rocket plumes where there could be significant pressure and Mach number gradients both axially and in the radial direction, is unknown. Experimental data is needed to gauge the usefulness of existing turbulence models for the case of modelling three-dimensional rocket plumes.

Philips and White (1974) defined a plume Reynolds number, which could be expressed as,

$$\mathrm{Re}_L = \frac{\mathrm{Re}^*}{\sqrt{N}}$$

Novopashin et al (1989) characterised the shear layer of the first shock cell of a rocket plume in quiescent medium as shown in Table 4-1,

Plume Reynolds Number	Shear Layer Behaviour
$\mathrm{Re}_L > 10^4$	turbulent
$10^3 < \mathrm{Re}_L < 10^4$	laminar to turbulent transition
$10^2 < \mathrm{Re}_L < 10^3$	laminar
$\mathrm{Re}_L < 10^2$	the effects of rarefaction influence the gas dynamic structure

Table 4-3 Influence of Plume Reynolds Number on the shear layer in the first shock cell

Figure 4-51 shows the variation of this plume Reynolds number with the rocket plenum chamber pressure representative of a typical range of injection conditions in this thesis. It can clearly be seen that shear layers in this thesis are expected to be turbulent.

The Schlieren image taken by Papamoschou et al (1988) shown in Figure 4-53 indicates that the planar shear layer is comprised of large scale eddies with a convective speed near the average of the two streams of gas. Their experiments typically looked at mixing of

planer streams with Mach numbers of between 3.3 and 0.3. Similar structures can be spotted near the nozzle exit (see Figure 4-9 and Figure 4-34).

Besides the possible presence of convective large structures, shear layers are regions of turbulent activities. Hence fluctuating turbulence intensities could be seen as another characteristic of the shear layer. The BPT Pitot probes used in this thesis had a relatively flat response up to 66 kHz before reaching its cavity resonance. It has the advantage of a protective screen, which means it could be used for gun-tunnel co-flow runs. The faster responding RPT Pitot probe could be used in flows which are free of foreign particles as in quiescent injections. It has a smooth frequency response up to 100 kHz (Moss, 1992).

Morris (1994) had carried out a series of experiments on under-expanded single jets using heat transfer and Pitot pressure probes. However, due to the relatively poor frequency responses of the instrumentation used, results were limited to give only a low bandwidth (< 5 kHz) picture of the plume. Therefore this thesis aims to extend the limits using fast response Pitot pressure and thin-film heat transfer probes sampled at up to 2 MHz.

4.5.3 Shear Layer Turbulence

In this section, one of the major characteristics of shear layers, namely turbulent mixing, is analysed using fast response pressure transducers and heat transfer probes. The difference in intensity at various downstream locations is analysed and discussed. Note that the sensitivity to fluctuating quantities is different for pressure transducers and heat transfer probes. This enables a broader picture of the various fluctuating components in the flowfield to be obtained.

Due to uncertainties in the frequency response of the Pitot probes over the sampled bandwidth, a low-pass filter was used. The design of such a filter is crucial, as one needs to take into considerations of both the time and frequency responses so that little distortion is introduced in the desired bandwidth: too steep a cut-off would result in oscillations in the time domain and, conversely, a shallow cut-off would mean that a substantial amount of energy above the cut-off frequency would leak into the required domain.

Based on the sampling rate and the amount of data points, an order 28 FIR filter with a cut-off frequency of 40 kHz was deemed most suitable. A bode plot of such a filter is shown in Figure 4-52. The filter was tested with a step input to check if there was any oscillation in the time domain, the result showed the filter introduced no such disturbance.

The Pitot pressure turbulence intensity $Y_{p_t'}$ is defined here as the root-mean-square fluctuation of the measured Pitot pressure normalised by the mean value, which can be expressed as,

$$Y_{p_t'} = \sqrt{\overline{\left(\frac{p_t'}{\overline{p_t}}\right)^2}}$$

Where the fluctuations in Pitot pressure is given by $p_t' = p_t - \overline{p_t}$. The normalisation means that turbulence levels at different parts of the plume flowfield can be compared. The mean Pitot pressure levels were obtained by using a 2 kHz low-pass filter.

Note that at high Mach numbers, turbulent viscous dissipation within the shear layer may result in losses comparable to losses suffered through a shock. This is reflected in the Pitot pressure variation across this layer under typical conditions in this thesis. The minimum Pitot pressure level in the shear layer could also be affected by the presence of a low-density boundary layer from the rocket body.

4.5.4 Rocket Plume into Quiescent Medium

A series of experiments was carried out by injecting N_2 in a quiescent medium. These results were then compared to the shear layer generated by the same injection pressure but in the presence of the Mach 7 hypersonic freestream.

The Mach 5 (SM5M) and Mach 3 (SM3) nozzles were used for this purpose. Injection was maintained at three steady gauge pressures (50 bar, 80 bar and 100 bar) with the test section pumped down to 0.0125 bar before each run. Both the BPT probe and the RPT were used. The convective Mach number was around 1.8 for such a configuration, which is high in comparison to earlier research efforts.

Figure 4-54 to Figure 4-56 show the Pitot pressure signals at three downstream locations for the quiescent 100 bar gauge injection into 0.0127 bar quiescent background. The extent of the shear layer can clearly be seen outside the boundaries of the core region. Figure 4-57 shows the corresponding relative Pitot pressure turbulence intensity. The low intensity in the core region is expected, however, once into the shear layer the intensity increases due to turbulent mixing. The first peak out of the core region corresponds to the barrel shock, this is immediately followed by a dip in intensity when the probe is in the region immediately behind the barrel shock. Intensity again increases as the probe moves further out of the shock layer as the amount of mixing between the injected gas stream and the entrained gas increases. At the outer edge of the shear layer, the Pitot pressure is low in the region of 0.0127 bar. Fluctuations in this region result in high relative intensities. Figure 4-58 to Figure 4-60 show the effect of a lower rocket injection pressure at 80 bar gauge injection at the same downstream locations. The corresponding plot of the Pitot pressure turbulence intensity is shown in Figure 4-61 and similar behaviour in the shear layer is observed.

Figure 4-62 to Figure 4-64 show the fluctuating Pitot pressure signals for the Mach 3 (SM3) single jet with 50 bar gauge injection in quiescent and the corresponding turbulence intensity is shown in Figure 4-65. The smaller exit Mach number means that the injected gas had not been expanded as much as it would have been at the exit of the Mach 5 nozzle. Therefore the exit static pressure and the pressure ratio were large in this case (note that the effect of a lower injection pressure was small compared to the lower exit Mach number for the Mach 3 single nozzle). This resulted in the plume expanding further outwards with a corresponding increase in the width of the shear layer. Entrainment of the background gas was higher in this case as reflected in large Pitot pressure fluctuations in this region.

Frequency content within the shear layer was investigated by means of power spectrum analysis. Fluctuating Pitot pressure signal across the width of the shear layer was isolated and fed into a spectrum analyser using a Welch method 1024-point FFT with a 512-point Hanning window. Figure 4-66 shows the output for three downstream locations at 100

bar gauge injection (note that the anti-aliasing filter used attenuated the RPT signal with a cut-off frequency at 69 kHz). The spectrum outputs show a high concentration of broadband energy under 40 kHz. There is a noticeable shift to higher frequencies downstream. With an estimated shear layer width of 12 mm obtained from the Pitot pressure signals, the peak around 60 kHz at 100 mm downstream corresponds to a convective velocity in the region of 800 m/s. This is comparable to the freestream velocity of around 1200 m/s and injected gas speed around 700 m/s and is believed to be caused by large structures travelling at speeds comparable to that of the shock compressed injected gas.

4.5.5 Rocket Plume in Hypersonic Freestream

The fluctuating Pitot pressure measurements for the Mach 5 (SM5M) nozzle with N_2 injection in a Mach 7 freestream are shown in Figure 4-67 and Figure 4-68. These readings were taken at 100 mm and 250 mm downstream of the nozzle exit respectively, corresponding to the first and the second shock cells . The Pitot pressure relative turbulence intensity plot is shown in Figure 4-69. At 100 mm downstream, the peak at approximately -37 mm corresponds to the plume shock. This is followed by the inviscid shock-compressed freestream. A rise in intensity at -30 mm indicates the beginning of the shear layer region where mixing between the freestream and plume gas takes place. As the probe enters the inviscid jet boundary, the corresponding intensity again drops as it is now submerged in the inviscid shock-compressed injection gas. The peak at -16 mm corresponds to the barrel shock. In the core region, low turbulence intensities were measured as expected. At 250 mm downstream, the traverse passes through the reflected barrel shock from the centreline at –8 mm. The peak in intensity near the axis of symmetry is believed to be due to mixing between the subsonic gas after the regular reflection and the supersonic plume gas along a slip line.

Figure 4-70 and Figure 4-71 shows the fluctuating Pitot pressure measurement and the corresponding turbulence intensity under similar conditions as above but with H_2 injection. Similar features were observed.

Figure 4-73 shows a series of runs at various locations along the Mach 5 single jet (SM5M) plume flowfield at 100 mm downstream. Heat transfer probes were used to investigate the frequency contents of the flowfield. Noise spectrum for the heat transfer probes is shown in Figure 4-72. Signal strength for a typical run was in the order of 100 times that of the noise level; therefore it was reasonable to assume that the frequency response of the probes was flat up to 100 kHz.

Fluctuating heat flux signals at stations 1 and 2 were obtained by keeping two heat transfer probes (*hot* and *warm*) stationary in the flow. A total of 20000 points were obtained from the heat transfer probe. A Fast Fourier Transform was applied using a 2048-point Hanning window to obtain the relative power spectrum $G(f)/G(f)_{\max}$. Station 1 was located slightly above the rocket body nose shock. Streaks could be seen on the Schlieren images in this region with spacing at around 10 mm to 30 mm. These are believed to be shocklets formed in front of supersonic structures in the shear layer from the Mach 7 nozzle. This translates to a frequency range of 10 kHz to 80 kHz. A distinctive peak can clearly be seen in the region of 40 kHz as shown in Figure 4-74.

Power spectrums within the shock layer were obtained by traversing the *hot* thin-film probe across the plume. Over 20000 data points were recorded within the layer. Note that the spatial resolution of the heat probe was about 3 mm, which was equivalent to about 1000 data points. Therefore, data were divided into groups of 1000 points and a 1024-point FFT was used with a 512-point Hanning window to obtain the power spectrums shown. In the inviscid freestream closely behind the plume shock at station 3, a peak in the region of 52 kHz can be seen.

In the shear layer, the frequency content was more broadband which suggests that the large-scale structures at these stations are not highly organised. A distinctive peak at around 64 kHz can be seen at station 6 within the injected gas just outside the barrel shock.

Origins of the fluctuation causing the peaks at station 3 and station 6 is not clear. It is believed to be due to mechanical vibration of the testing structure.

4.6 PARABOLISED NAVIER STOKES CODE - SHARC

The CFD code SHARC written by Brescianini (1993) was used to compare single nozzle CFD modelling with experimental data. The code itself was originally written to model the flow within a scramjet combustor. It solves the Parabolised Navier-Stokes (PNS) equations and is applicable to two-dimensional, steady and parabolic flows which may be planar or axisymmetric, reacting or non-reacting, laminar or turbulent, confined or unconfined. The algorithm for solving the equations is based on a finite difference method developed by Pantankar and Spalding (1970).

For simplicity, SHARC was run assuming a uniform freestream at undisturbed conditions, i.e. effect of the rocket body on the inviscid flowfield was ignored. A turbulent 1/7 power law velocity profile was assumed and a spatial temperature distribution was calculated for inclusion of the rocket body boundary layer in the initial conditions. The effect of the boundary layer in the nozzle was assumed to be negligible.

The initial start-line at the nozzle exit plane consisted of 99 equi-spaced nodes. Axial and radial velocities, temperature, pressure and specie concentrations were specified at each node. Figure 4-75 shows a typical spatial distribution of output nodes for a run. As the solution marches downstream, it can be seen that the grid spacing expands or contracts in accordance to whether the flow is expanded or compressed. Morris (1994) investigated the effect of different turbulence models. The compressible k-ε_{cc} turbulence model was found to give the best agreement between experimental Pitot pressure profiles and the CFD results. SHARC was configured to simulate the co-flow Mach 5 (SM5) single jet in a Mach 7 freestream. Due to limitations of the code, the base region of the rocket exit plane was not modelled. This essentially modelled a *flying* plume with the added effect of a rocket body boundary layer whose thickness was obtained visually from Schlieren images. The net effect was to alter the shock positions of the simulated plume as shown in Figure 4-76. This is believed mainly due to a higher expansion at the nozzle exit in the presence of a base region. Since the freestream gas

sees the plume as a blunt nosed body, the higher expansion at the exit means a larger effective nose radius. This causes the plume shock to move further away from the axis of symmetry.

Figure 4-77 shows the CFD predicted contours of the first shock cell. The plume shock and barrel shock positions are clearly visible on the Pitot pressure contours, together with the rocket body boundary layer near the exit. It can be seen in the figure that across the plume and barrel shocks, the total temperatures stay constant as expected. Across the shock layer, total temperature drops and approaches the value of the injected gas. This agrees with the experimentally deduced total temperature profile. In the core of the plume, the Mach number increases as the plume expands downstream causing a corresponding decrease in static pressure as shown on the static pressure contours. It can be seen on the Mach number contours that high Mach numbers can be reached near the end of the first shock cell on the centreline. The relatively low Mach number flow near the exit of the nozzle off the rocket body is due to the rocket body boundary layer. This layer gives rise to a flow with a relatively high static temperature as shown on the static temperature contours. Velocity variation in the plume core is small and approximately equal to its limiting value of $\sqrt{2c_pT}$, which with a 300 K injection of N_2 is approximately 790 m/s.

For complete simulation of the shock structures, the inviscid flowfield over the rocket body should be considered.

The SHARC CFD simulation was intended for reference purposes in this thesis where experimental results were frequently checked against the code and general flowfield order-of-magnitude estimations were deduced.

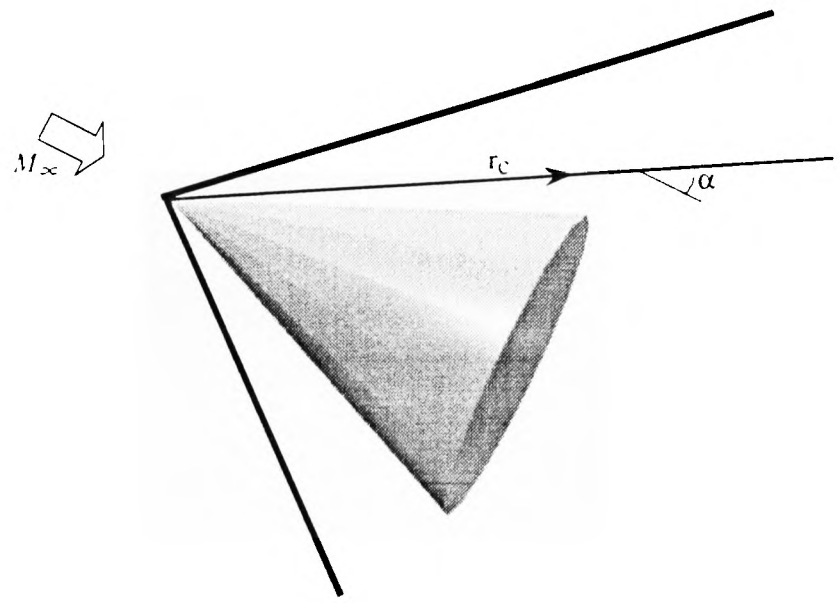


Figure 4-1 Shock wave on the nose of a rocket travelling at supersonic speed

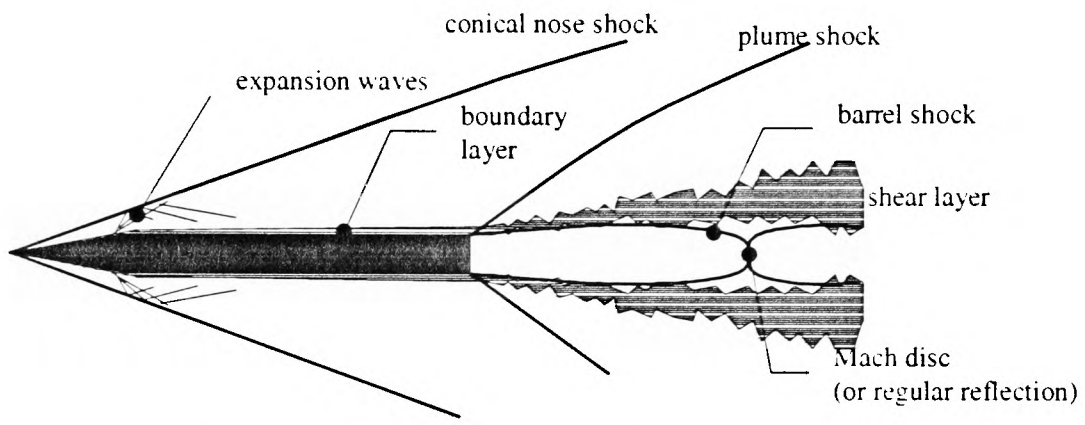


Figure 4-2 Schematic illustration of a typical rocket body flowfield

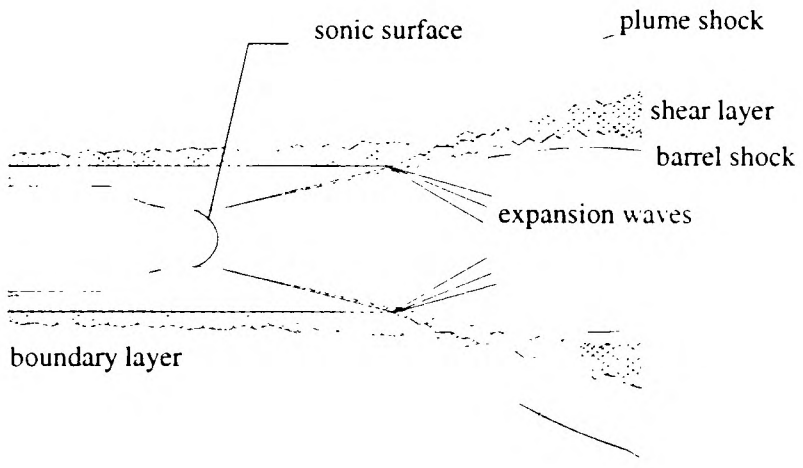


Figure 4-3 Schematic illustration of rocket exhaust plume near-field features

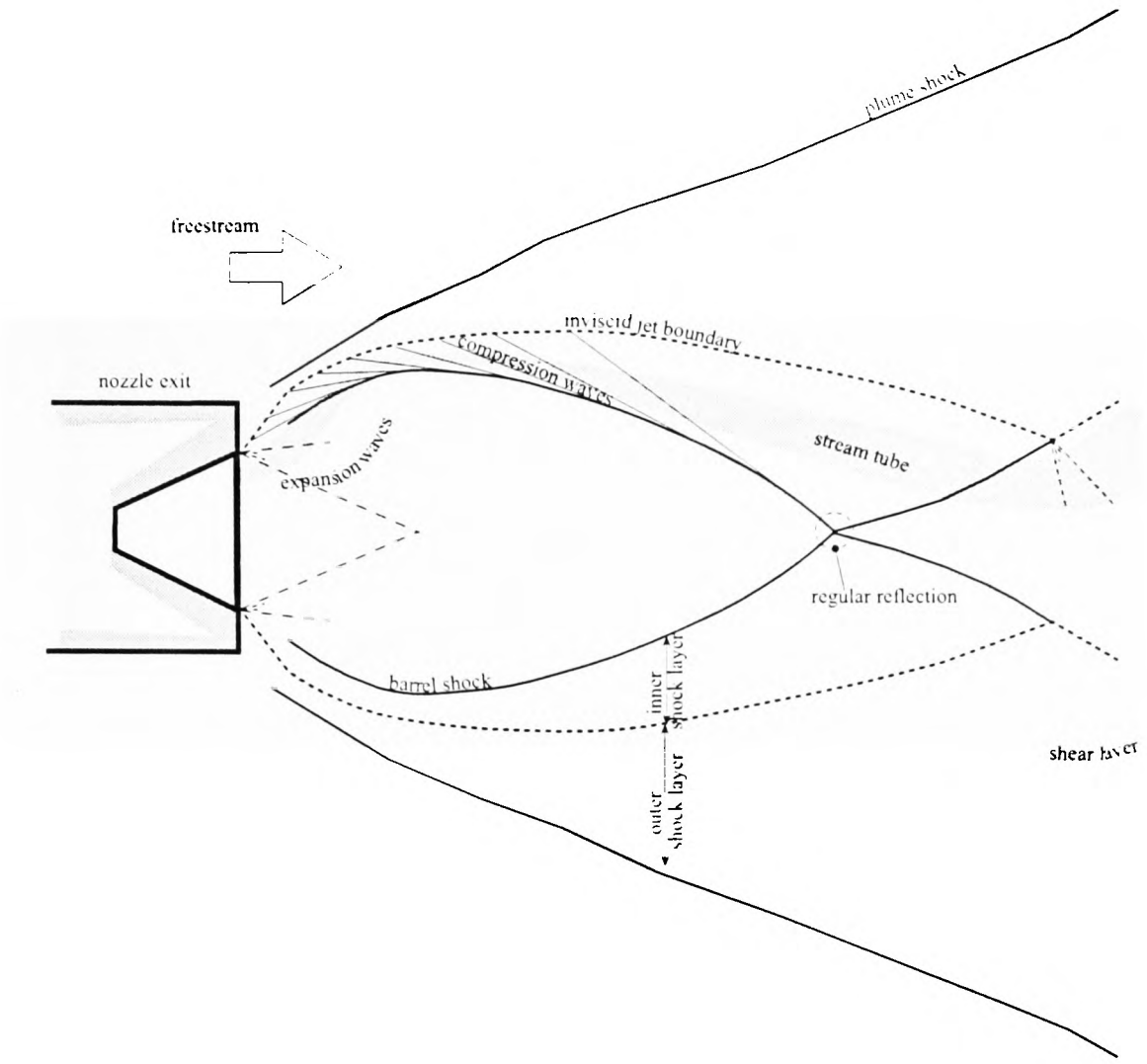


Figure 4-4 Schematic illustration of an under-expanded rocket plume in a supersonic freestream

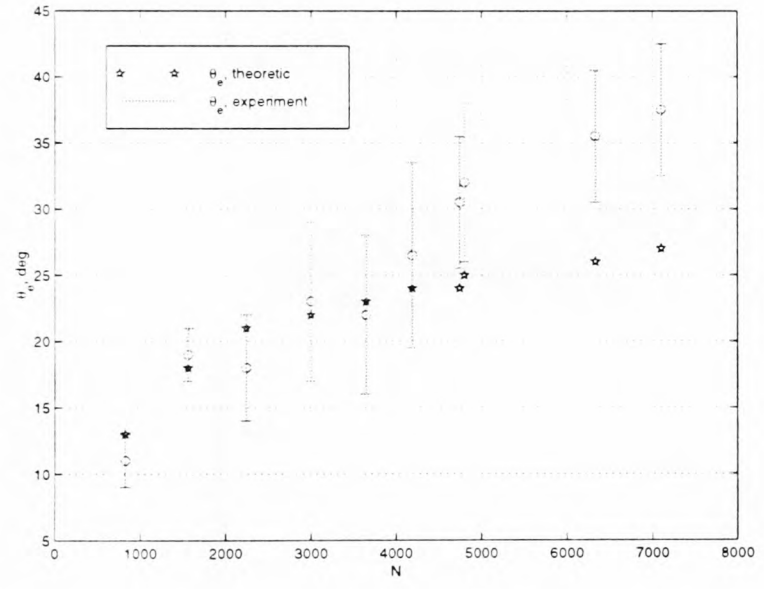


Figure 4-5 Initial nozzle exit flow angle against pressure ratio *N*

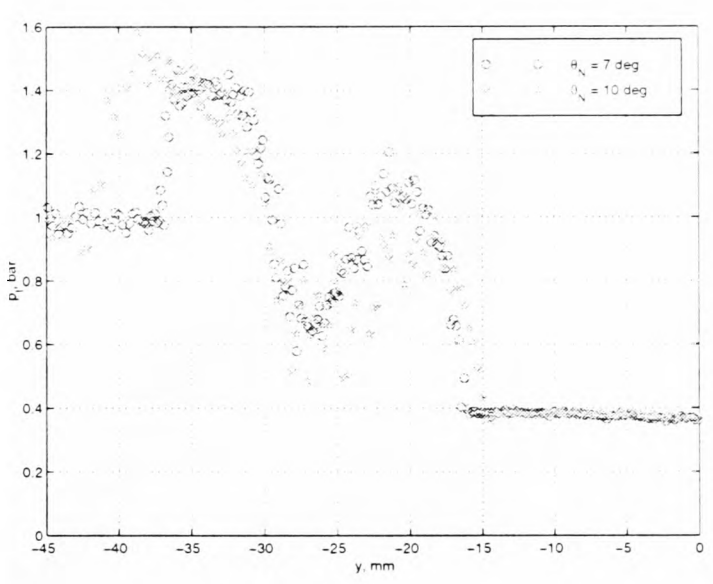


Figure 4-6 BPT Pitot pressure at 100 mm downstream for Mach 5 single nozzles SM5 *(θ_N = 10°, GT717)* and SM5M *(θ_N = 7°, GT740)*

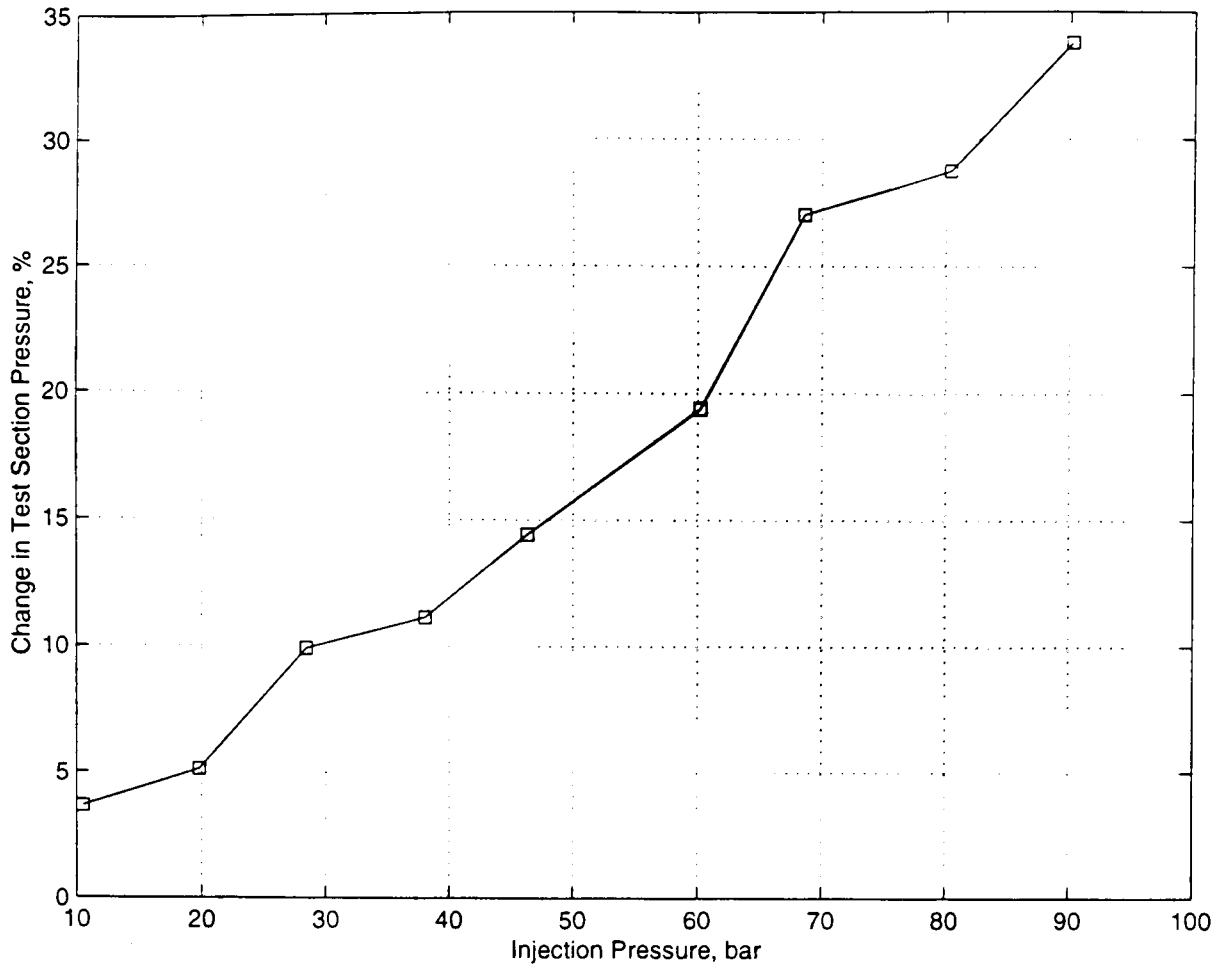


Figure 4-7 Test section static pressure against injection pressure

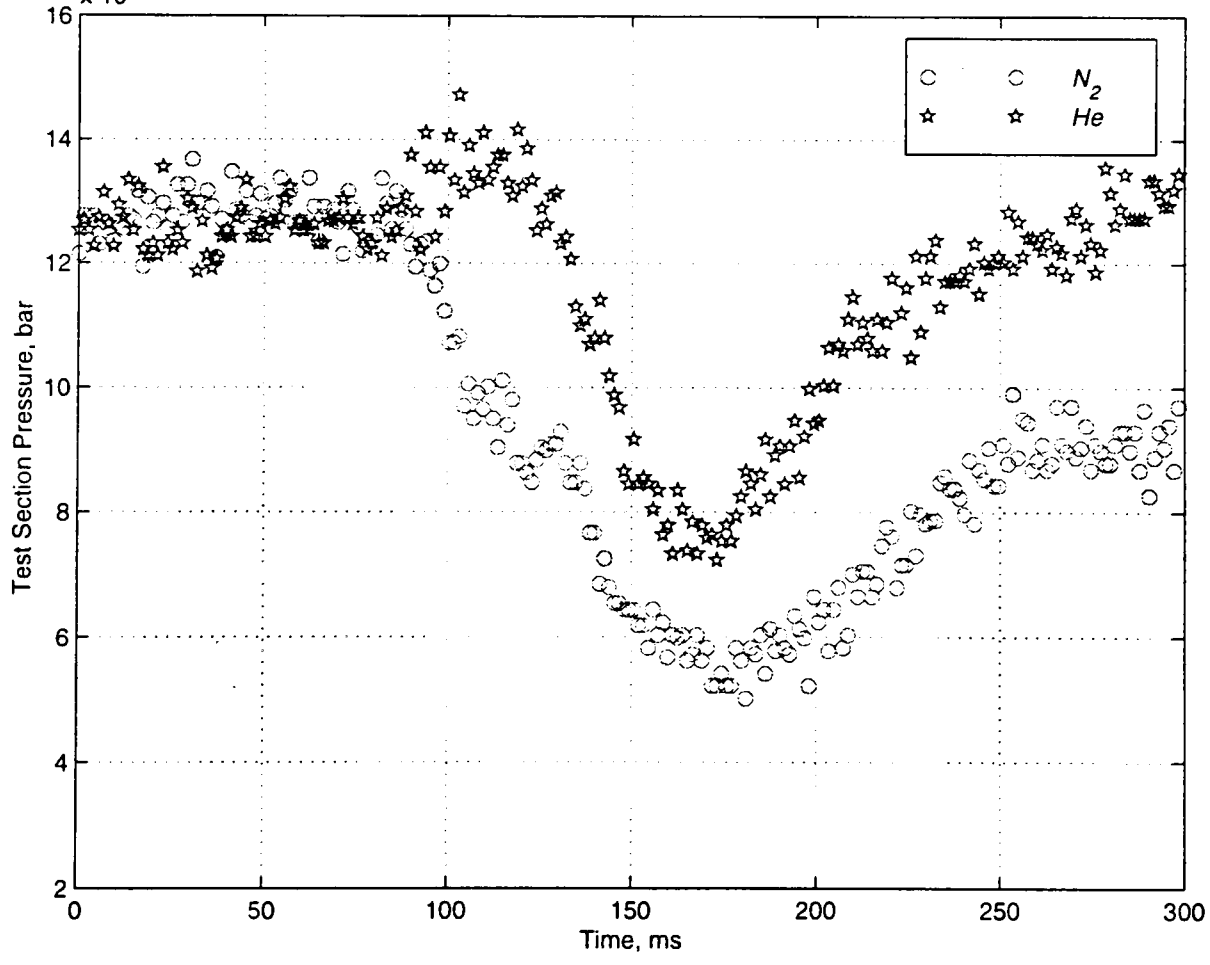


Figure 4-8 Test section pressures with He and N_2 injections in quiescent. Injection started at around 100 ms and ended at around 170 ms. *(LT193, LT194)*

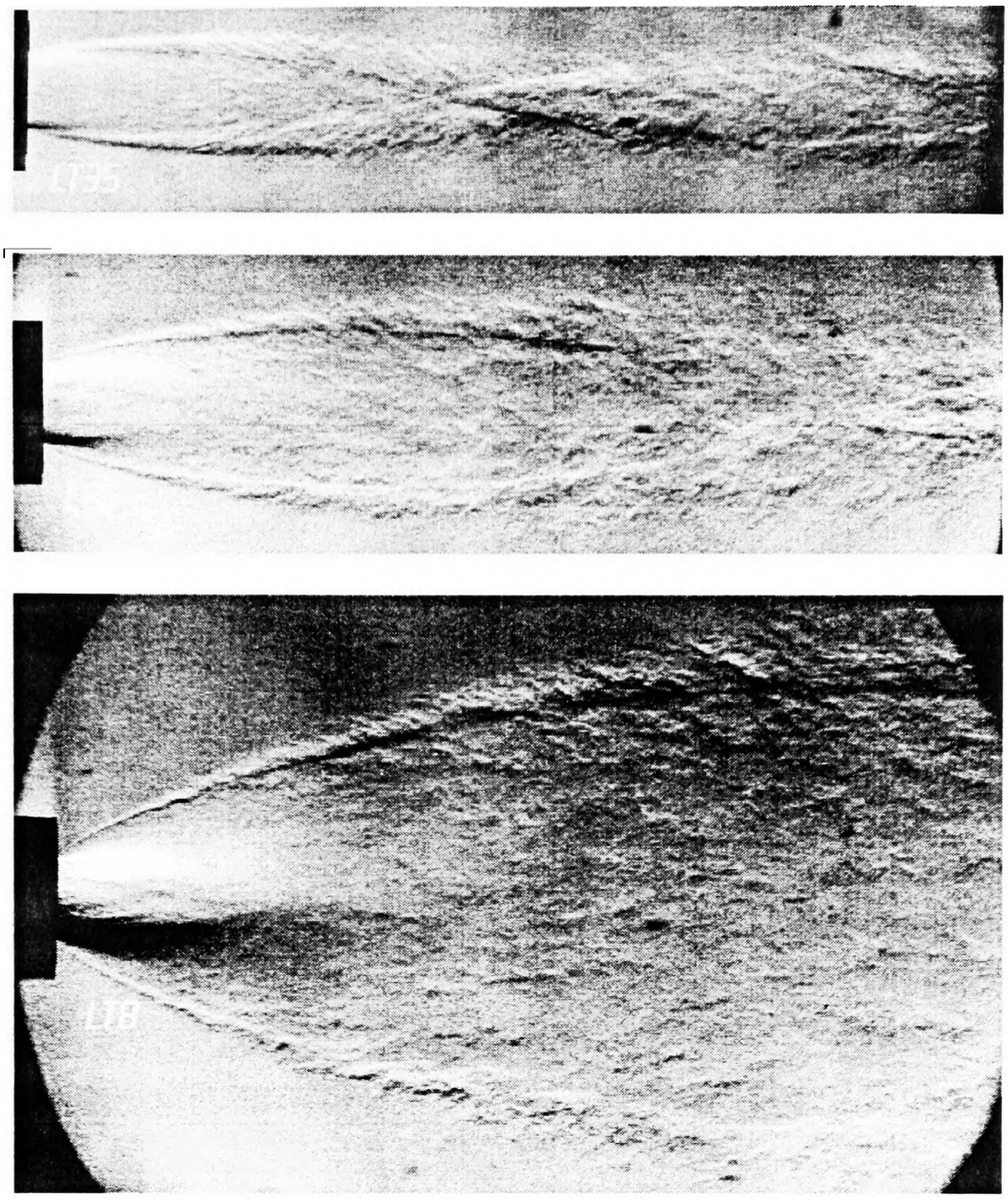


Figure 4-9 Spark Schlieren photographs of Mach 5 single jet (SM5) in quiescent medium *(LT35: N=787. LT6: N=4724, LT8: N=7087)*

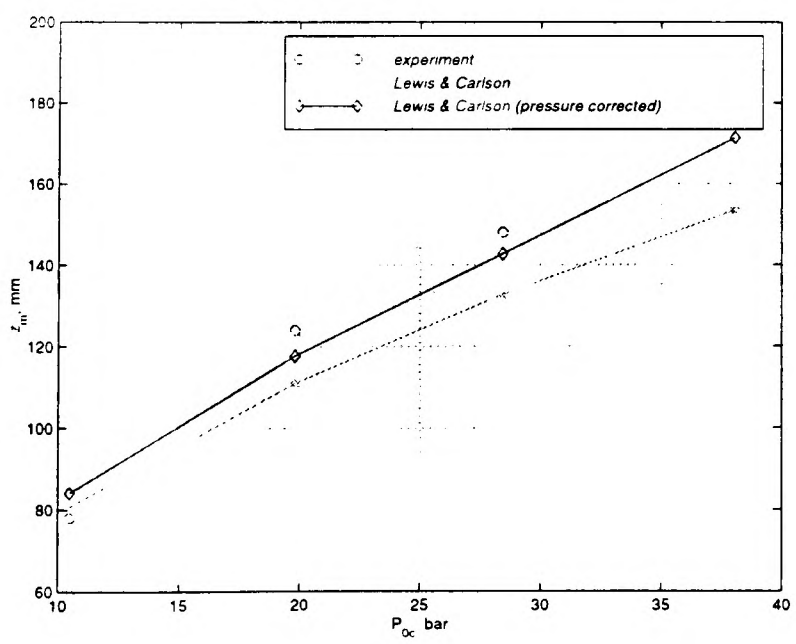


Figure 4-10 Measured and predicted regular reflection locations for Mach 5 (SM5) signal nozzle in quiescent

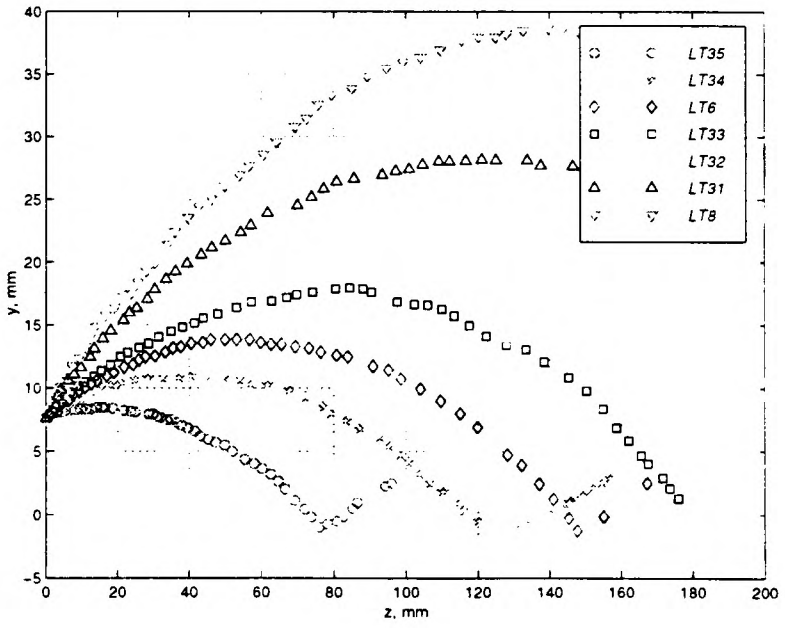


Figure 4-11 Digitised barrel shock positions for the Mach 5 (SM5) single jet in quiescent

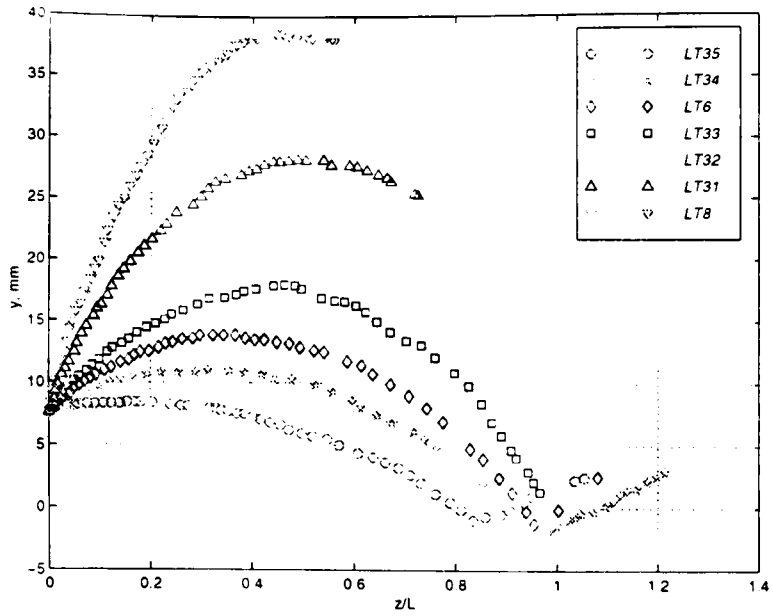


Figure 4-12 Scaled quiescent barrel shock positions for the Mach 5 (SM5) single jet in quiescent

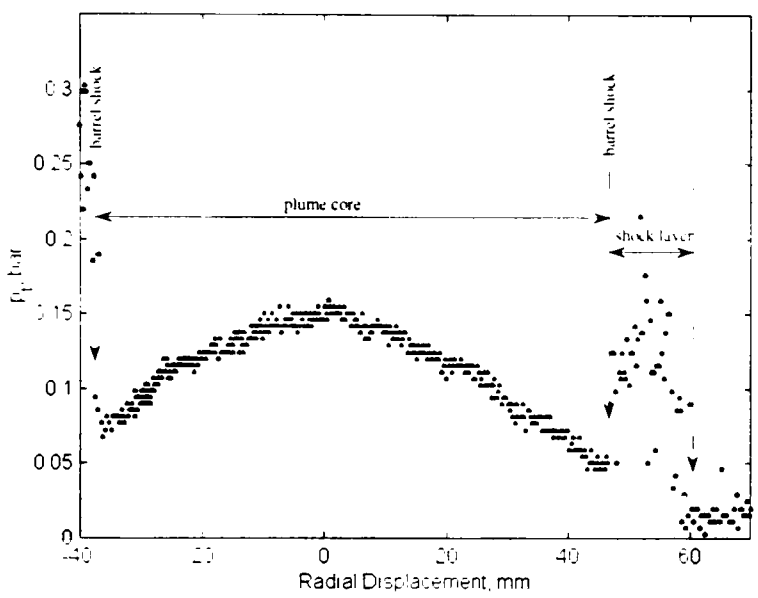


Figure 4-13 Pitot pressure signal for Mach 5 (SM5M) single nozzle with 80 bar gauge injection in quiescent at 120 mm downstream *(LT139)*

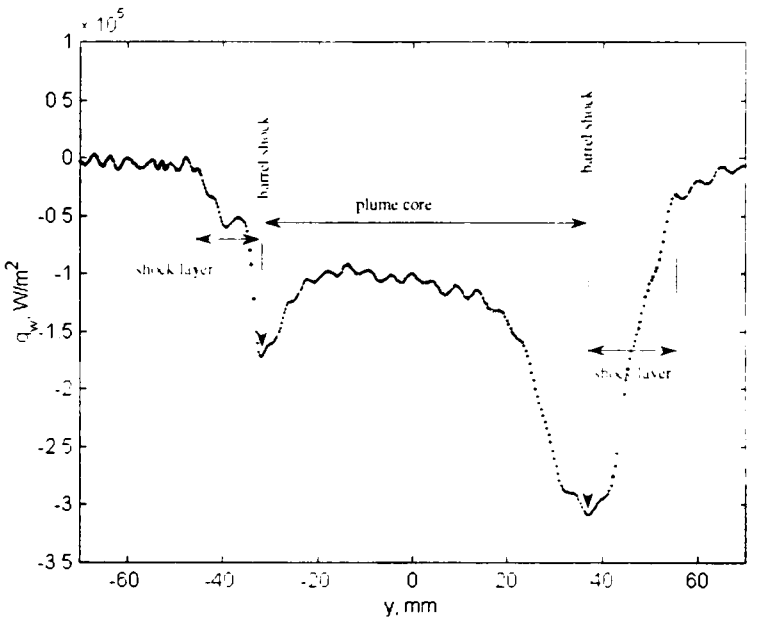


Figure 4-14 Heat flux signal for Mach 5 (SM5M) single jet at 100 mm downstream in quiescent *(warm probe, LT196)*

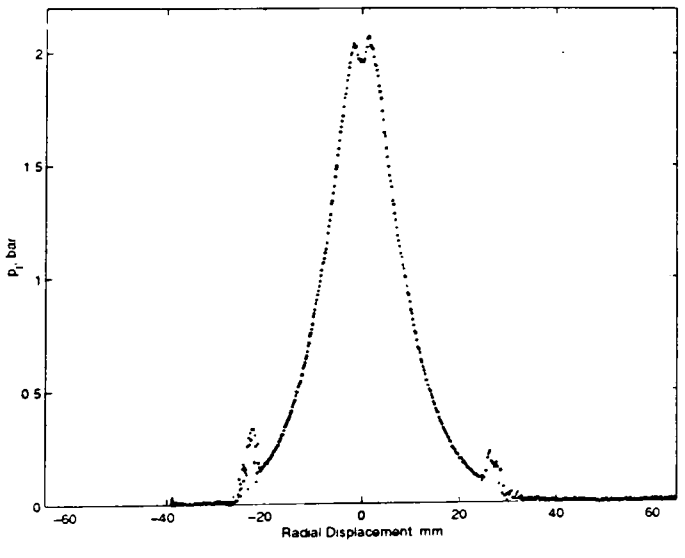


Figure 4-15 Mach 5 (SM5M) quiescent 80 bar gauge injection 40 mm downstream *(LT132)*

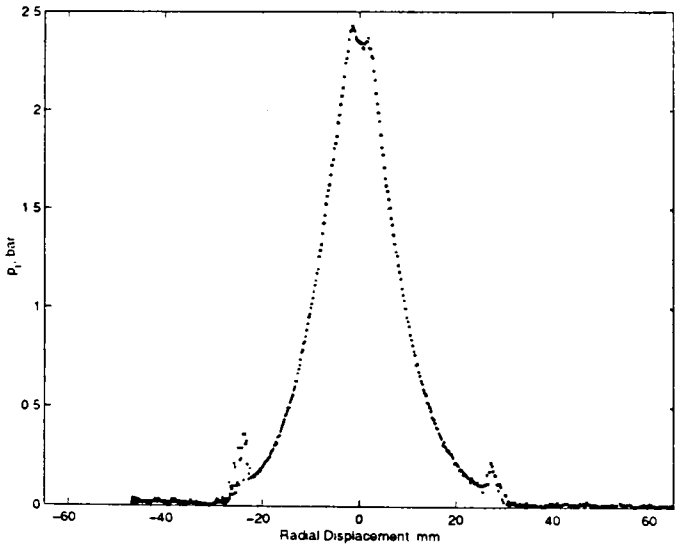


Figure 4-16 Mach 5 (SM5M) quiescent 100 bar gauge injection 40 mm downstream *(LT182)*

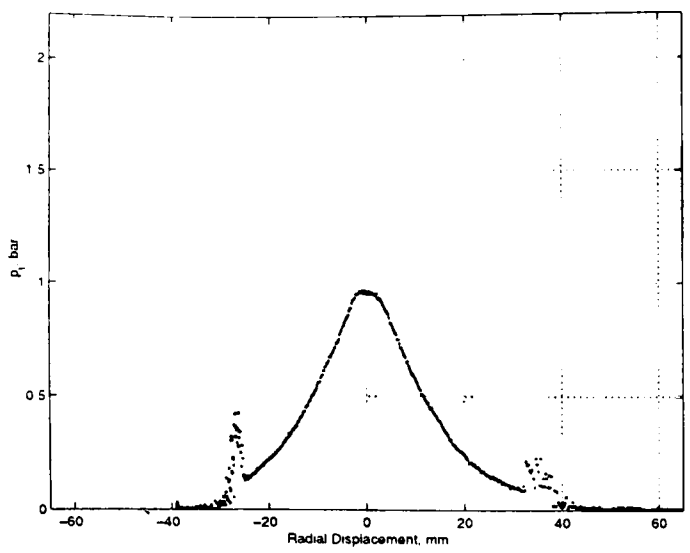


Figure 4-17 Mach 5 (SM5M) quiescent 80 bar gauge injection 60 mm downstream *(LT130)*

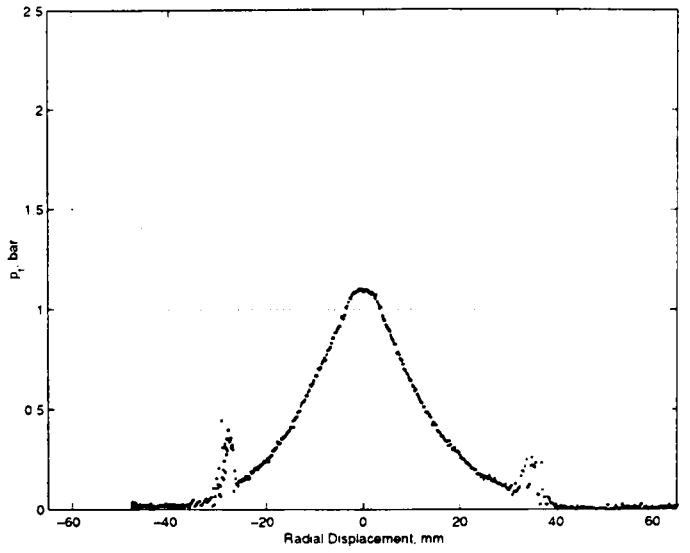


Figure 4-18 Mach 5 (SM5M) quiescent 100 bar gauge injection 60 mm downstream *(LT181)*

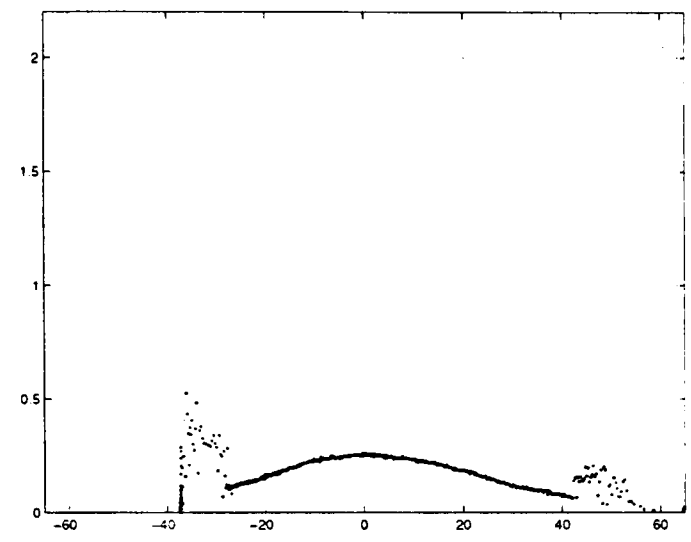


Figure 4-19 Mach 5 (SM5M) quiescent 80 bar gauge injection 100 mm downstream *(LT129)*

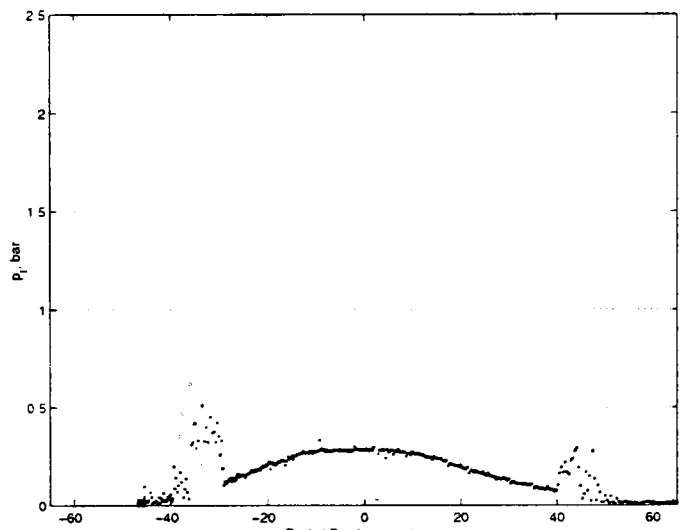


Figure 4-20 Mach 5 (SM5M) quiescent 100 bar gauge injection 100 mm downstream *(LT196)*

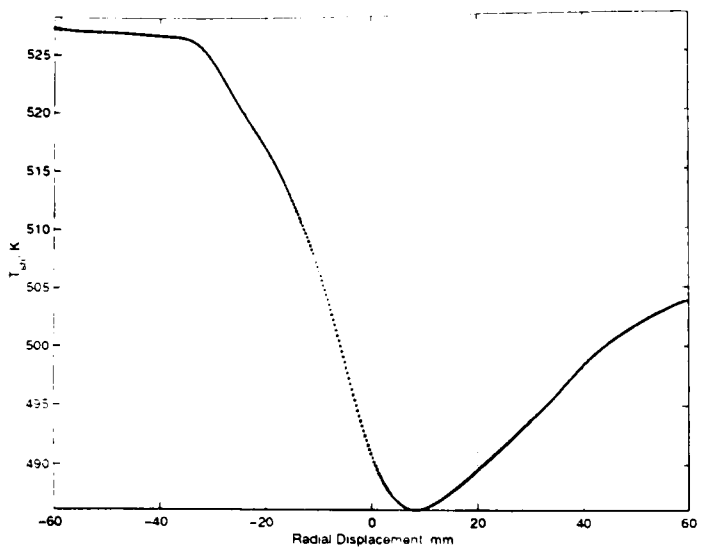


Figure 4-21 Substrate temperature signal, *hot* probe at 40 mm downstream with 100 bar gauge injection *(LT182)*

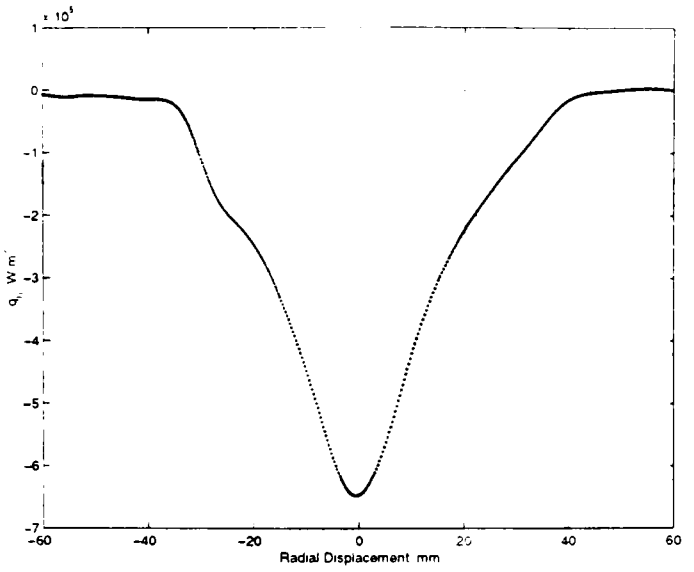


Figure 4-22 Heat flux signal, *hot* probe at 40 mm downstream with 100 bar gauge injection *(LT182)*

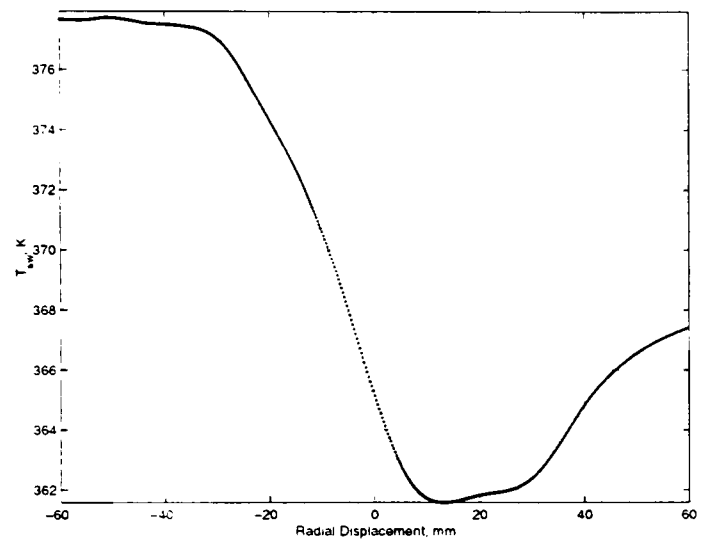


Figure 4-23 Substrate temperature signal, *warm* probe at 40 mm downstream with 100 bar gauge injection *(LT182)*

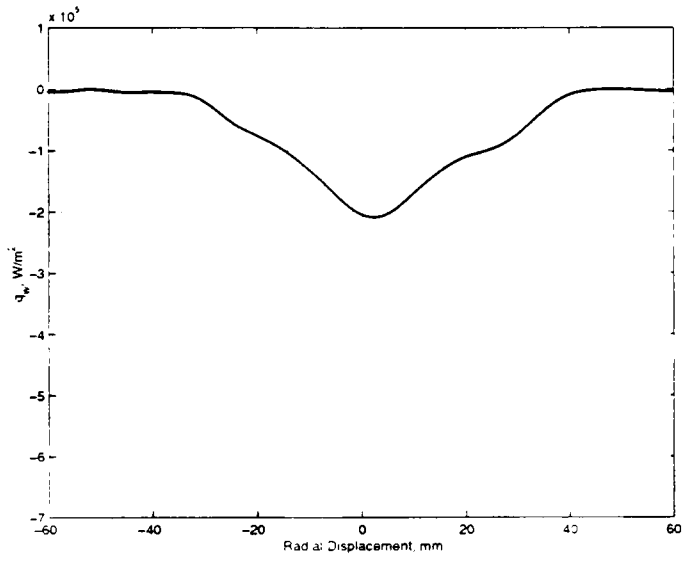


Figure 4-24 Heat flux signal, *warm* probe at 40 mm downstream with 100 bar gauge injection *(LT182)*

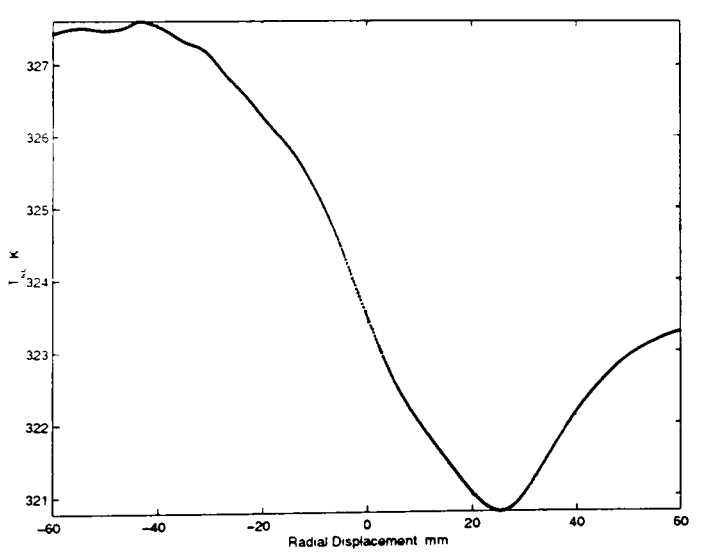


Figure 4-25 Substrate temperature signal, *cold* probe at 40 mm downstream with 100 bar gauge injection *(LT182)*

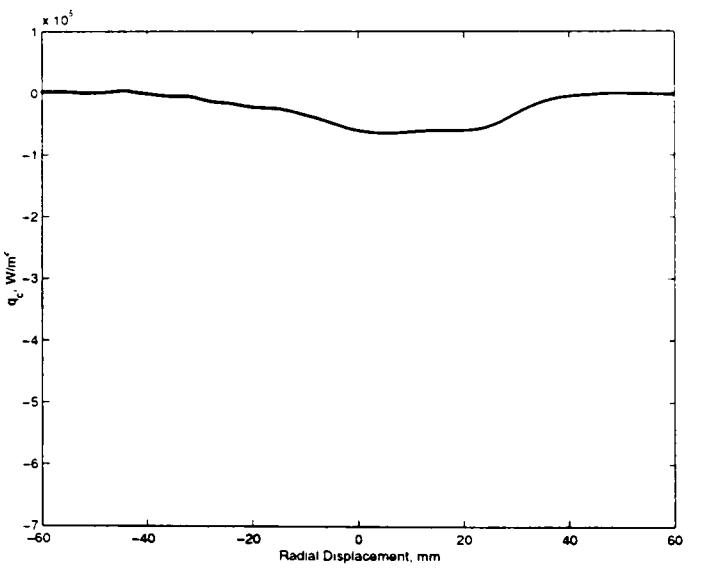


Figure 4-26 Heat flux signal, *cold* probe at 40 mm downstream with 100 bar gauge injection *(LT182)*

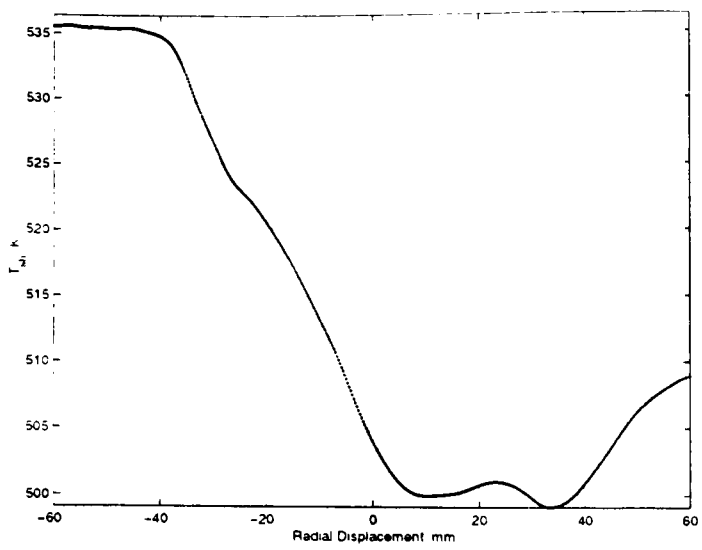


Figure 4-27 Substrate temperature signal, *hot* probe at 60 mm downstream with 100 bar gauge injection *(LT181)*

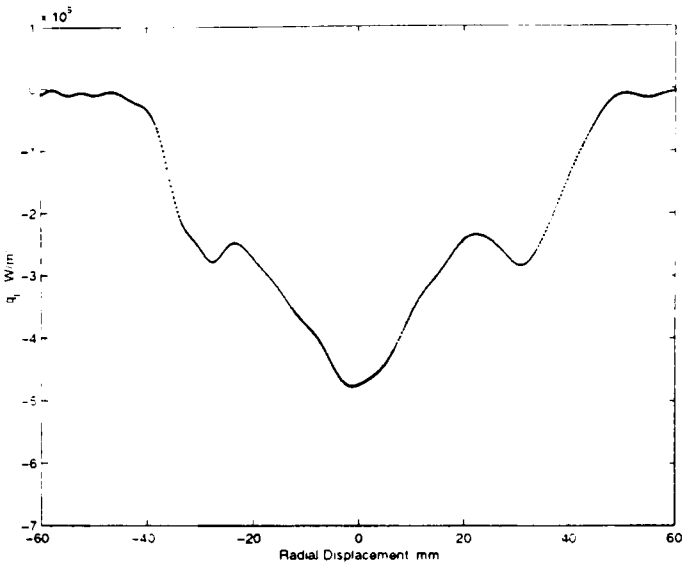


Figure 4-28 Heat flux signal, *hot* probe at 60 mm downstream with 100 bar gauge injection *(LT181)*

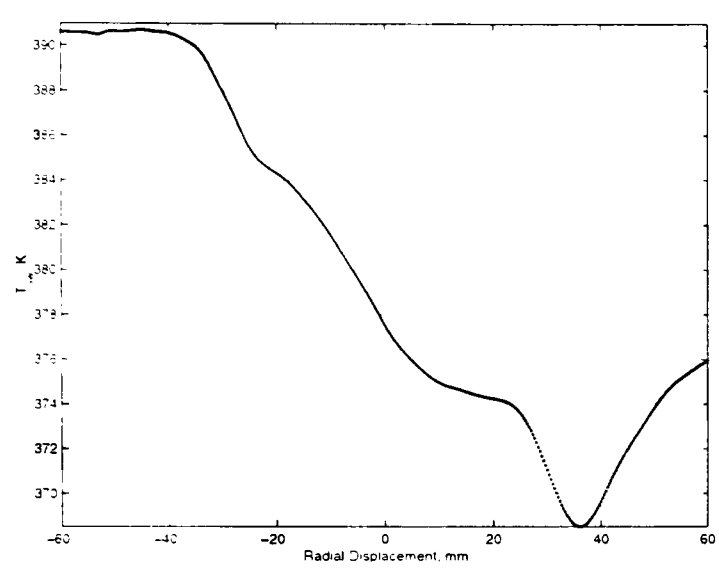


Figure 4-29 Substrate temperature signal, *warm* probe at 60 mm downstream with 100 bar gauge injection *(LT181)*

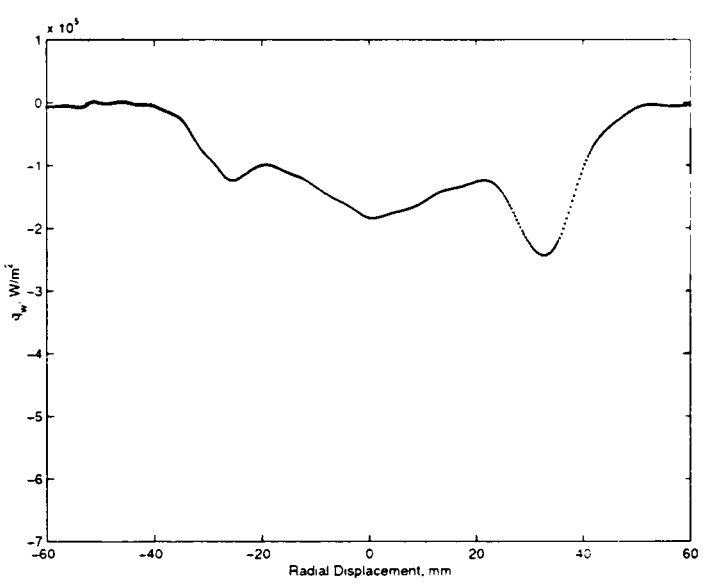


Figure 4-30 Heat flux signal, *warm* probe at 60 mm downstream with 100 bar gauge injection *(LT181)*

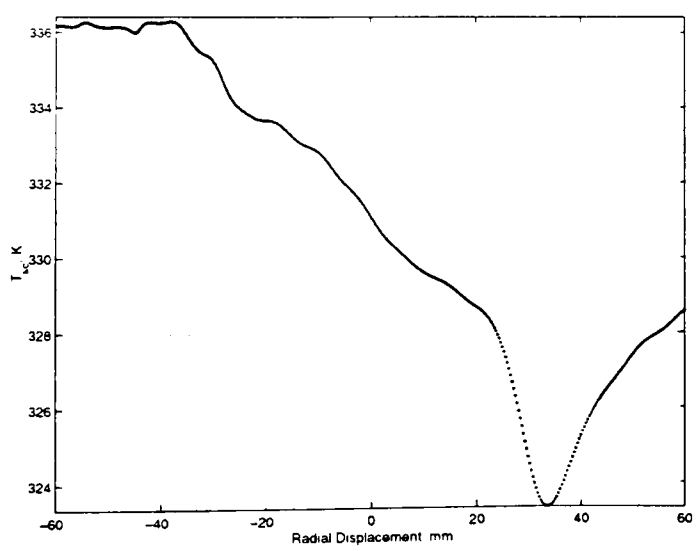


Figure 4-31 Substrate temperature signal, *cold* probe at 60 mm downstream with 100 bar gauge injection *(LT181)*

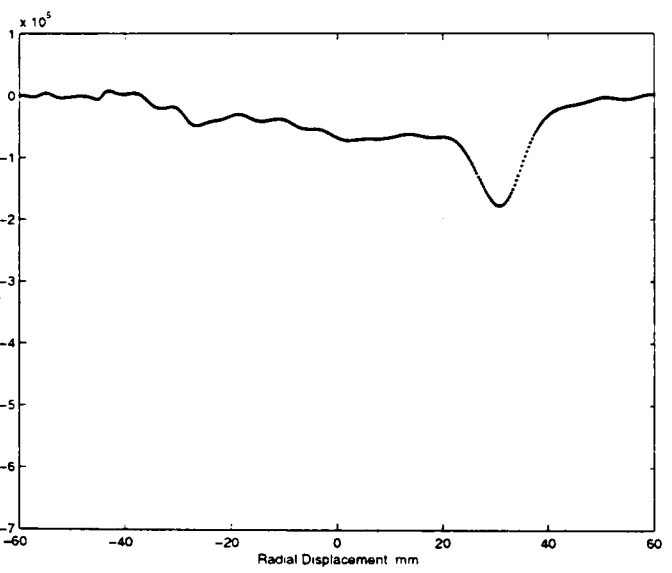


Figure 4-32 Heat flux signal, *cold* probe at 60 mm downstream with 100 bar gauge injection *(LT181)*

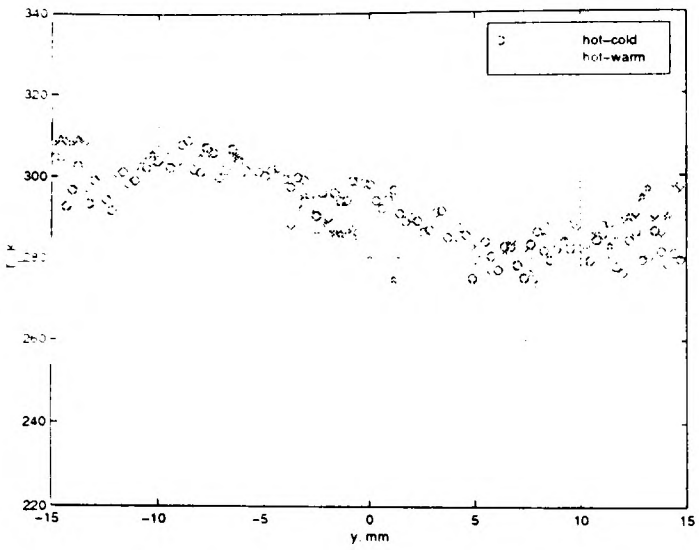


Figure 4-33 Total temperature signal with He injection in quiescent at 100 mm downstream *(LT191)*

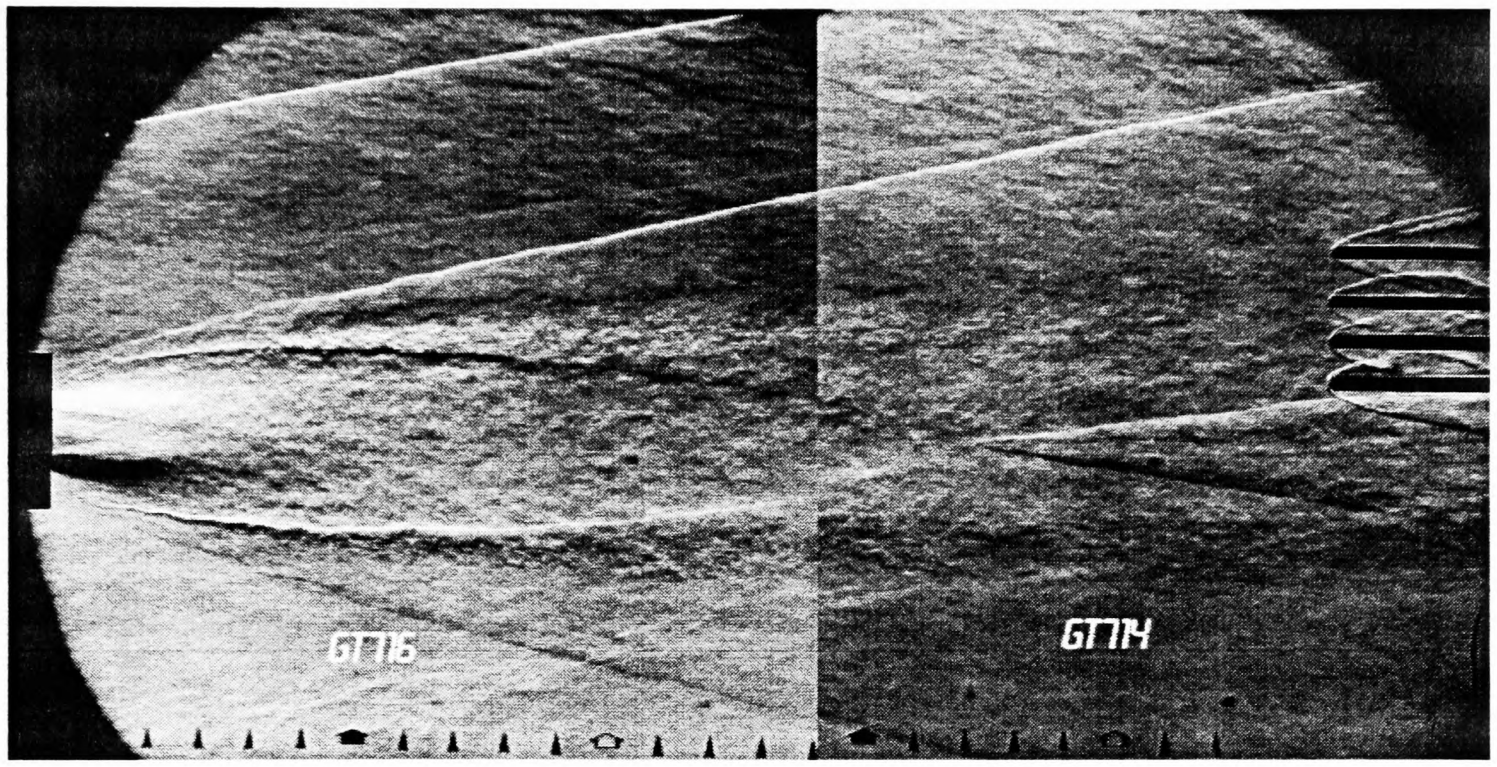


Figure 4-34 Schlieren photograph for Mach 5 (SM5) single nozzle with N_2 injection in Mach 7 freestream

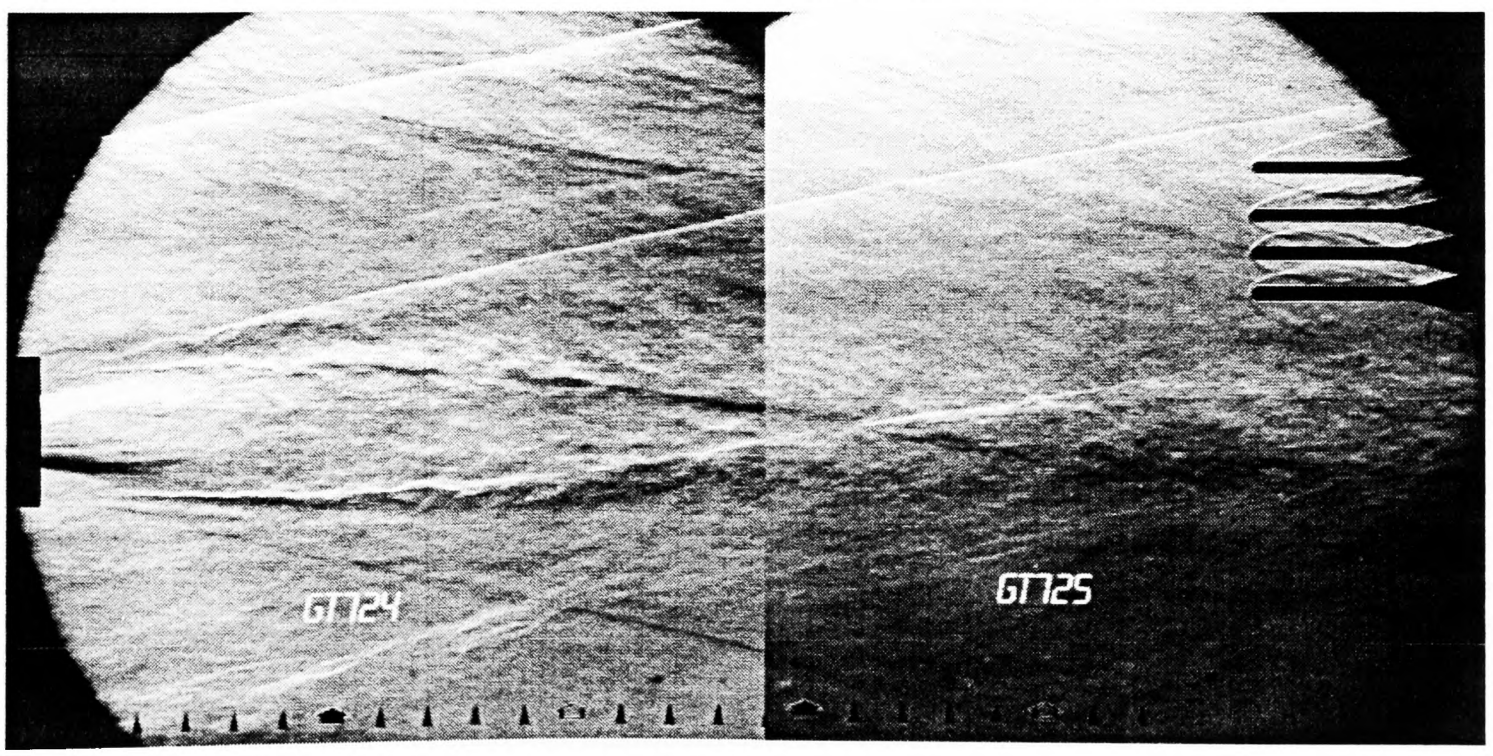


Figure 4-35 Schlieren photograph for Mach 5 (SM5) single nozzle rocket with H_2 injection in Mach 7 freestream

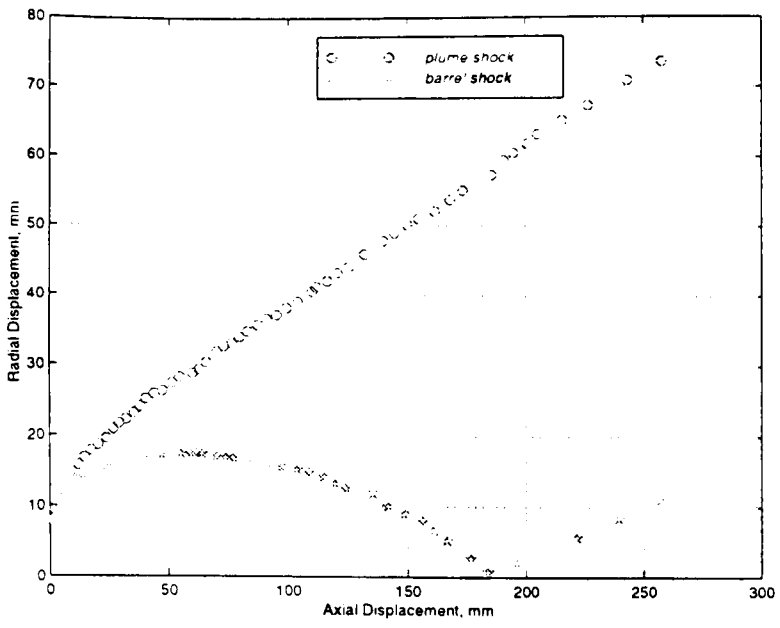


Figure 4-36 Shock positions for Mach 5 (SM5) single nozzle with N_2 injection in Mach 7 freestream *(from Schlieren photograph)*

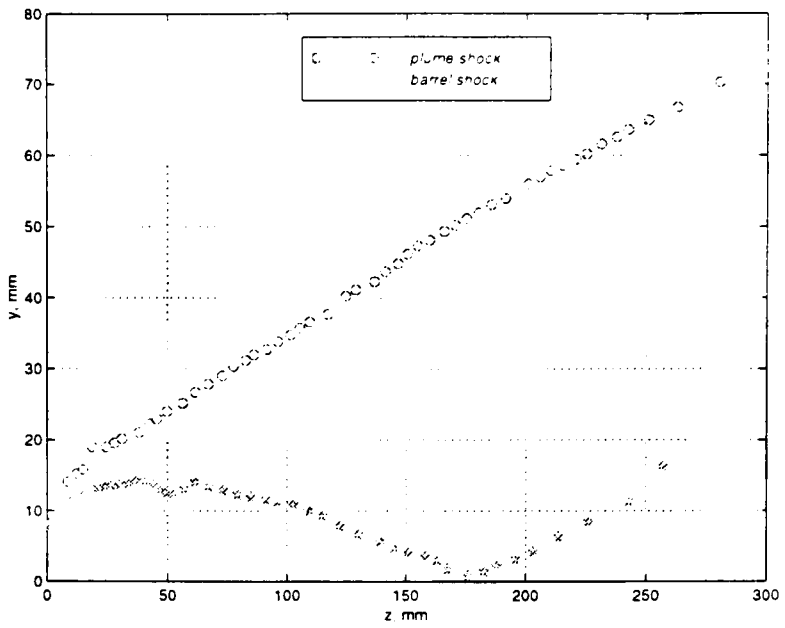


Figure 4-37 Shock positions for Mach 5 (SM5) single nozzle with H_2 injection in Mach 7 freestream *(from Schlieren photograph)*

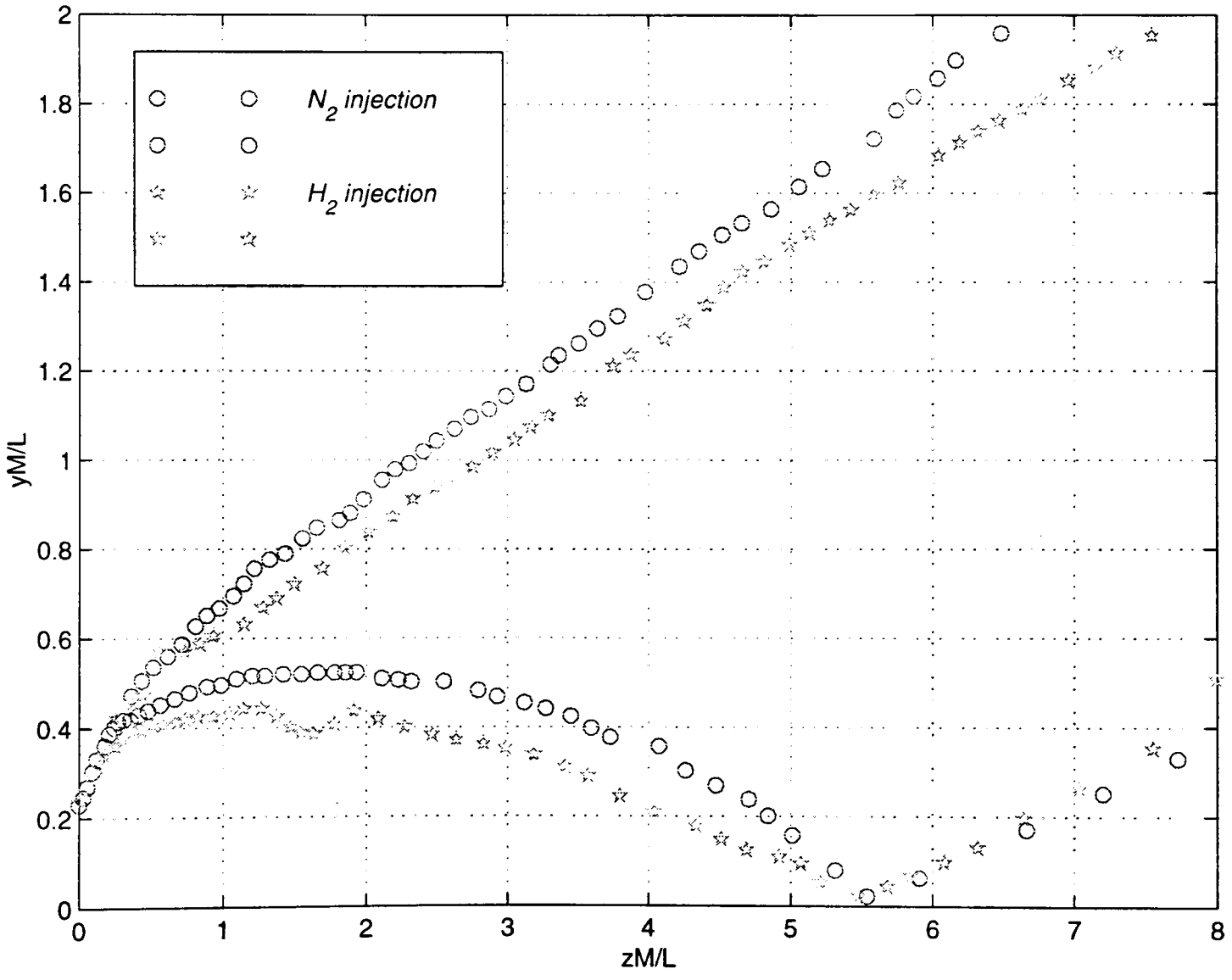


Figure 4-38 Scaled shock positions for Mach 5 (SM5) single nozzle injection in Mach 7 freestream

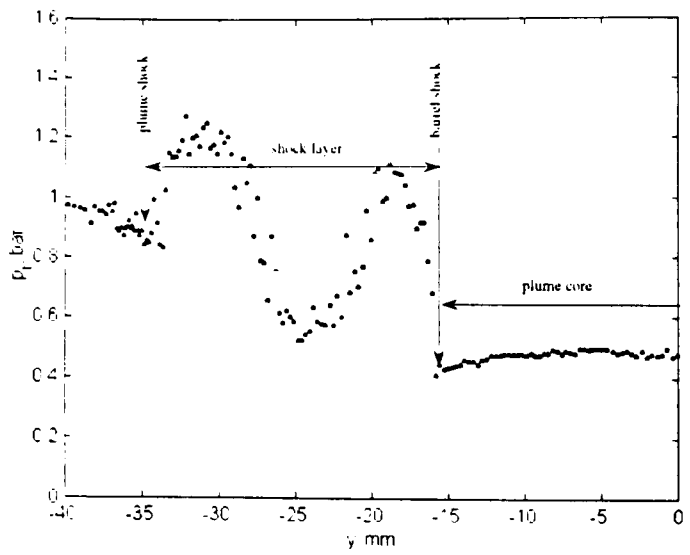


Figure 4-39 Pitot pressure for Mach 5 single jet with N_2 injection in Mach 7 freestream at 100 mm downstream *(GT747)*

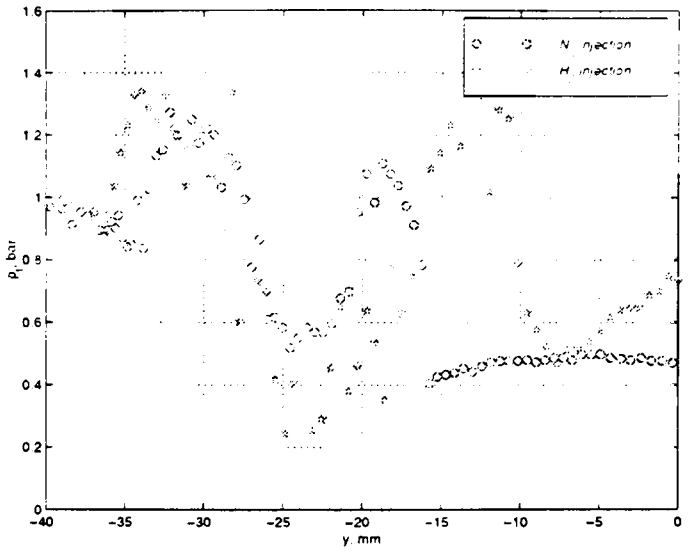


Figure 4-40 Pitot pressure for Mach 5 single nozzle in Mach 7 freestream at 100 mm downstream *(N_2: GT747, H_2: GT719)*

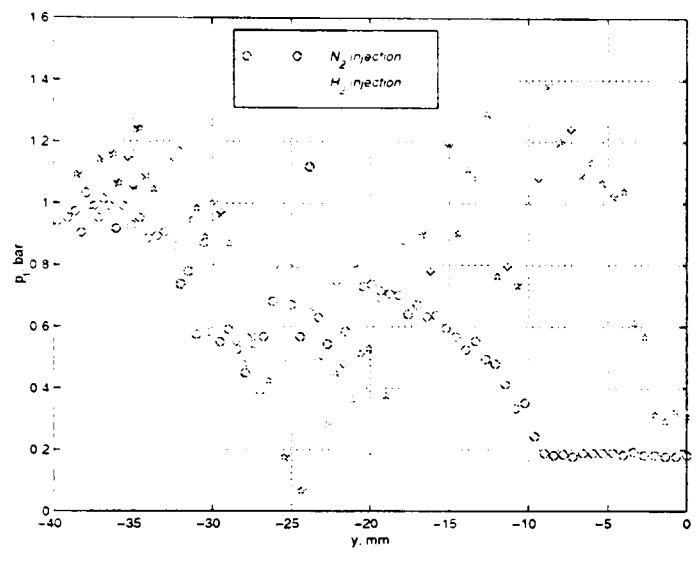


Figure 4-41 Pitot pressure signal for Mach 5 single nozzle in Mach 7 freestream at 150 mm downstream *(N_2: GT716, H_2: GT724)*

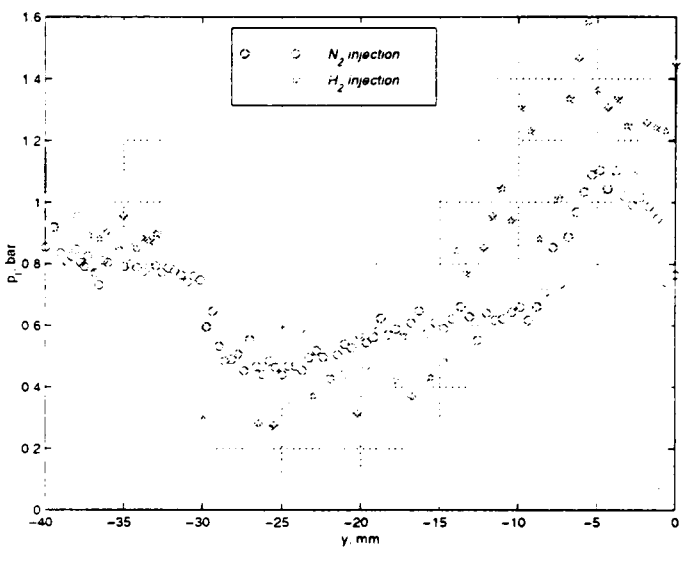


Figure 4-42 Pitot pressure signal for Mach 5 single nozzle in Mach 7 freestream at 250 mm downstream *(N_2: GT748, H_2: GT725)*

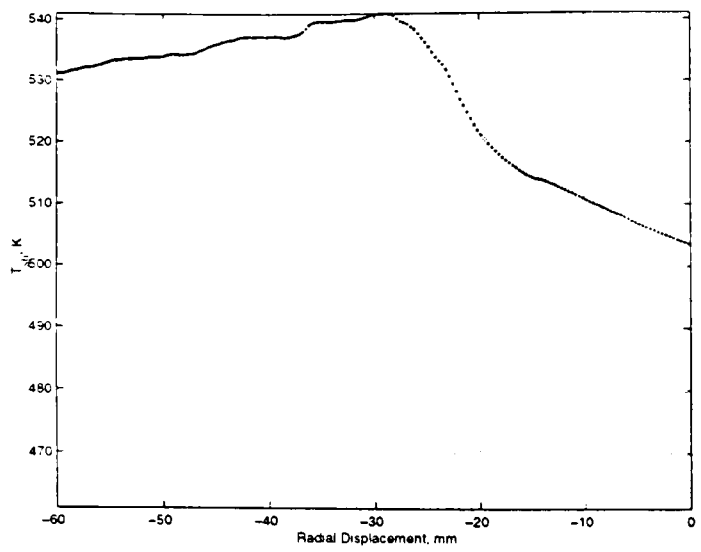


Figure 4-43 Substrate temperature signal for Mach 5 injection in Mach 7 freestream *(hot probe, GT747)*

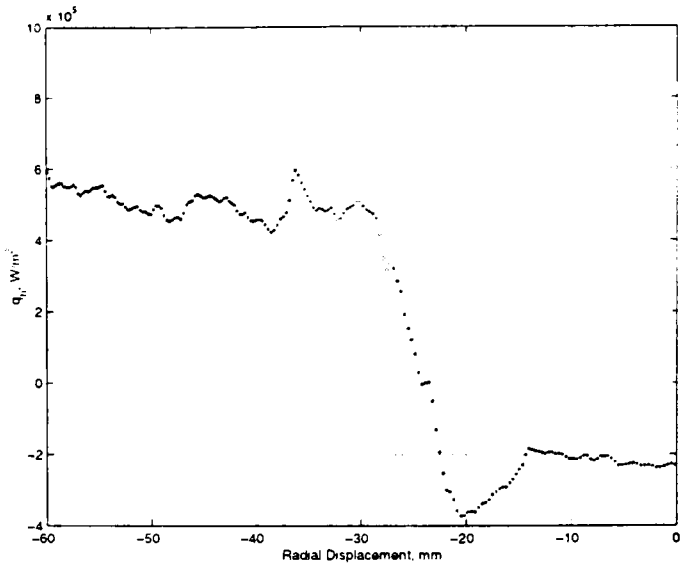


Figure 4-44 Heat flux signal for Mach 5 injection in Mach 7 freestream *(hot probe, GT747)*

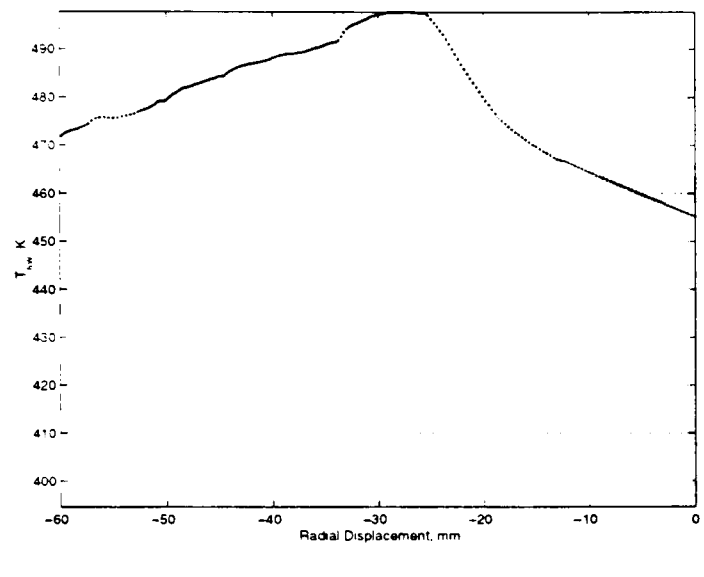


Figure 4-45 Substrate temperature signal for Mach 5 injection in Mach 7 freestream *(warm probe, GT747)*

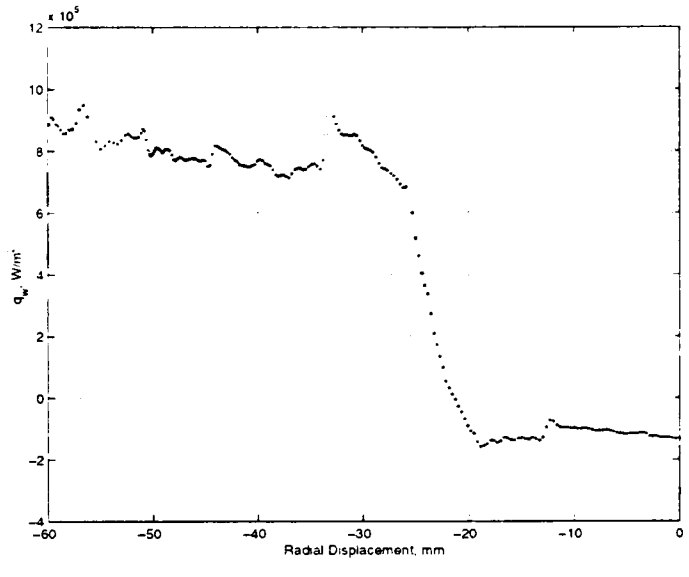


Figure 4-46 Heat flux signal for Mach 5 injection in Mach 7 freestream *(warm probe, GT747)*

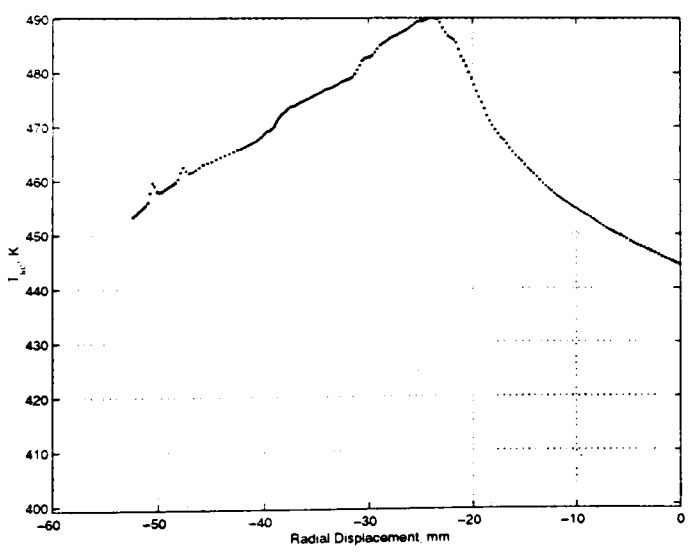


Figure 4-47 Substrate temperature signal for Mach 5 injection in Mach 7 freestream *(cold probe, GT747)*

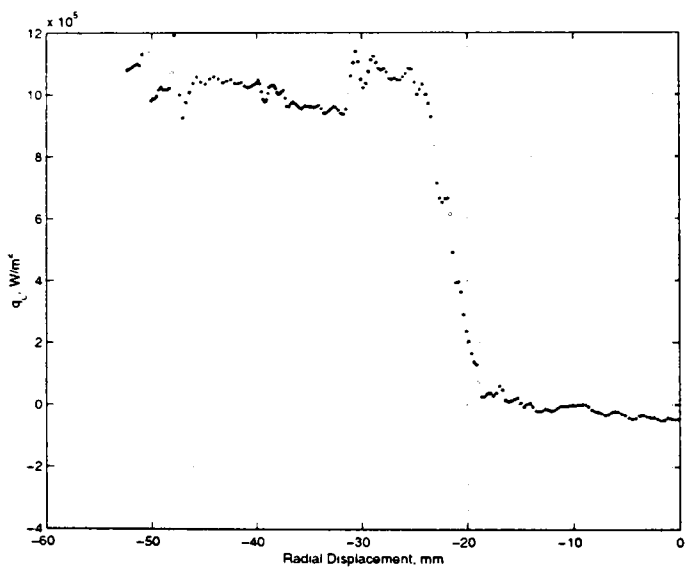


Figure 4-48 Heat flux signal for Mach 5 injection in Mach 7 freestream *(cold probe, GT747)*

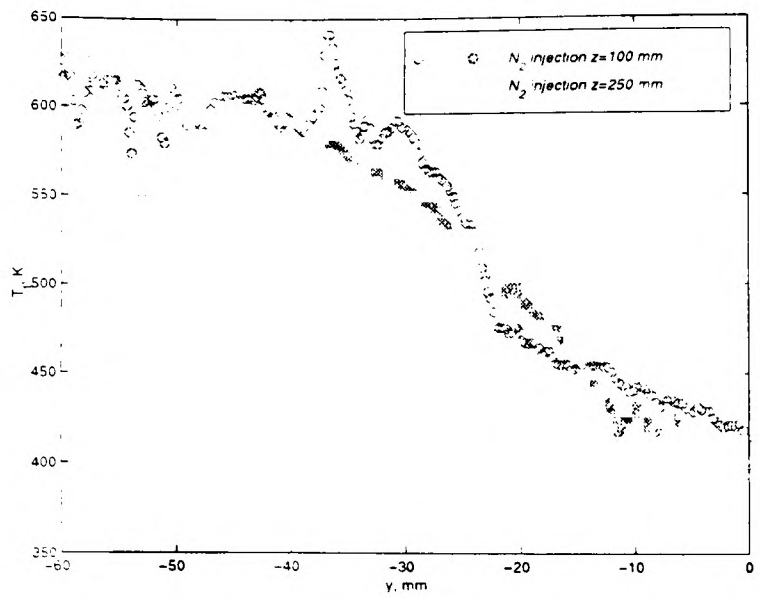


Figure 4-49 Total temperature for Mach 5 N_2 injection in Mach 7 freestream at 100 mm downstream *(GT747 and GT748)*

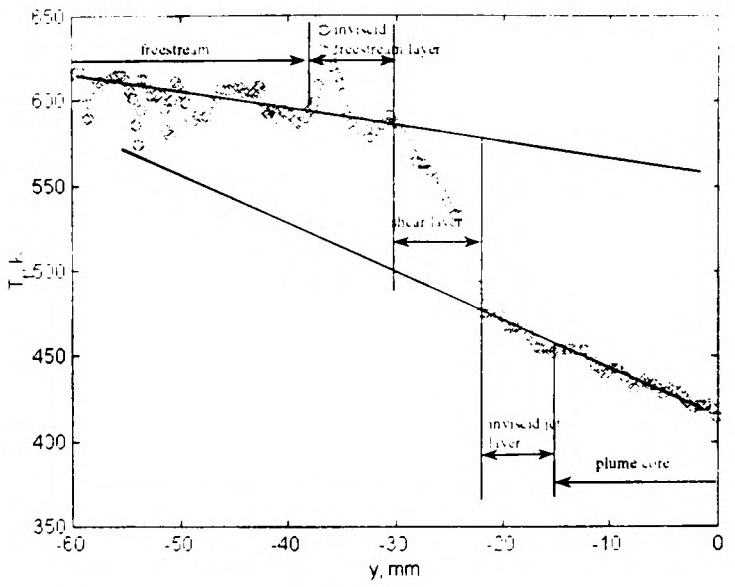


Figure 4-50 Total temperature showing locations of the shear layer for Mach 5 single jet in Mach 7 freestream at 100 mm downstream *(GT747)*

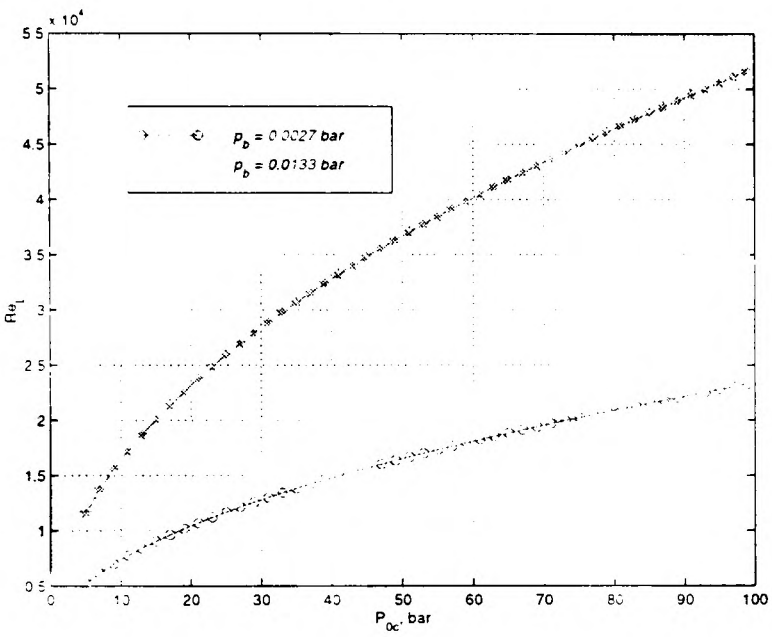


Figure 4-51 Plume Reynolds number against rocket plenum chamber pressure for single jet (SM5M) with N_2 injection at two background pressures

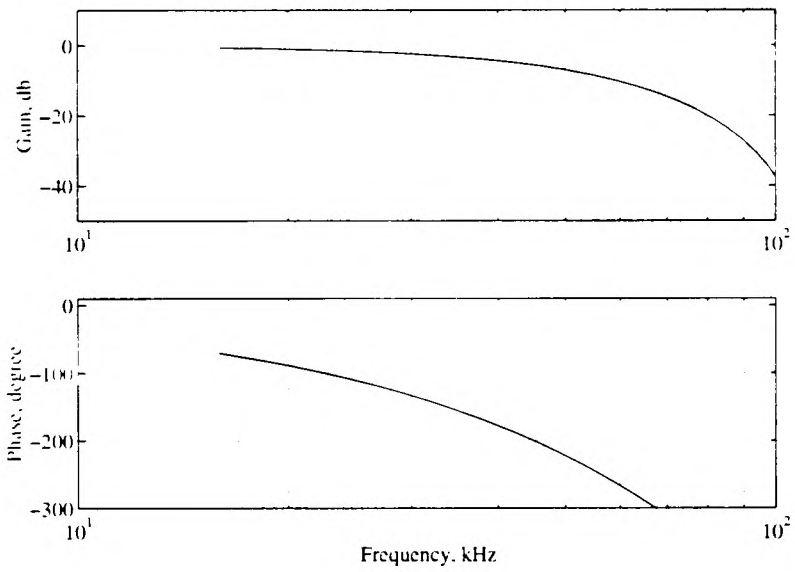


Figure 4-52 Frequency response of a 28-order FIR filter *(Matlab command: b40=fir1(28,2/28))*

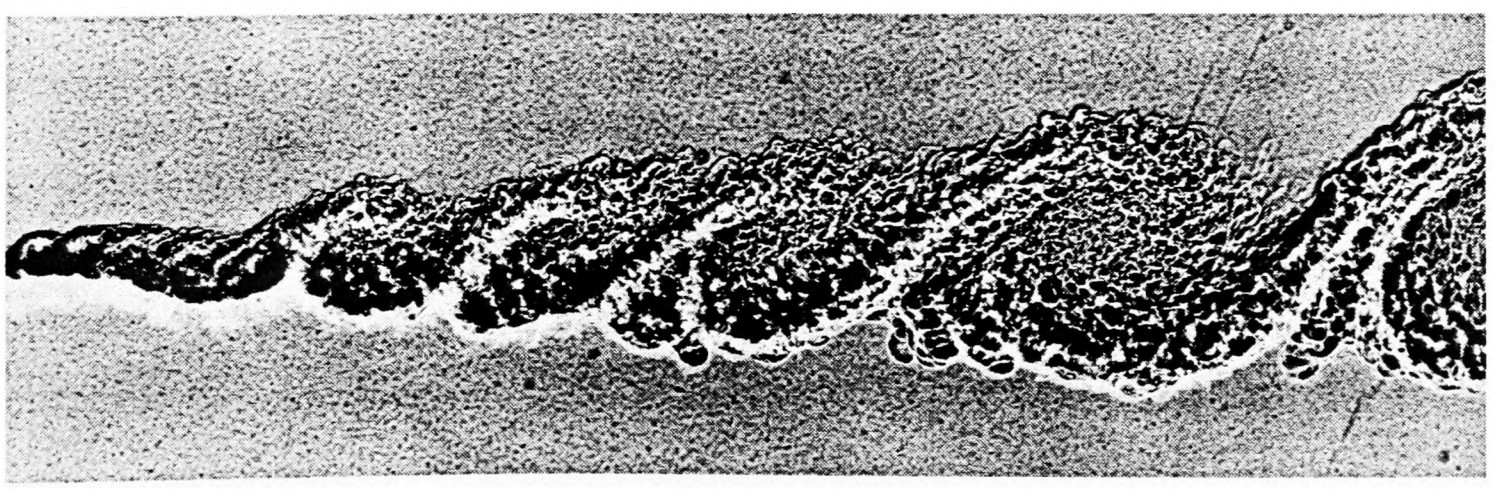


Figure 4-53 Coherent structure at higher Reynolds number (*M. R. Rebollo, Ph.D. thesis, CIT, 1976; Brown & Roshko 1974)*

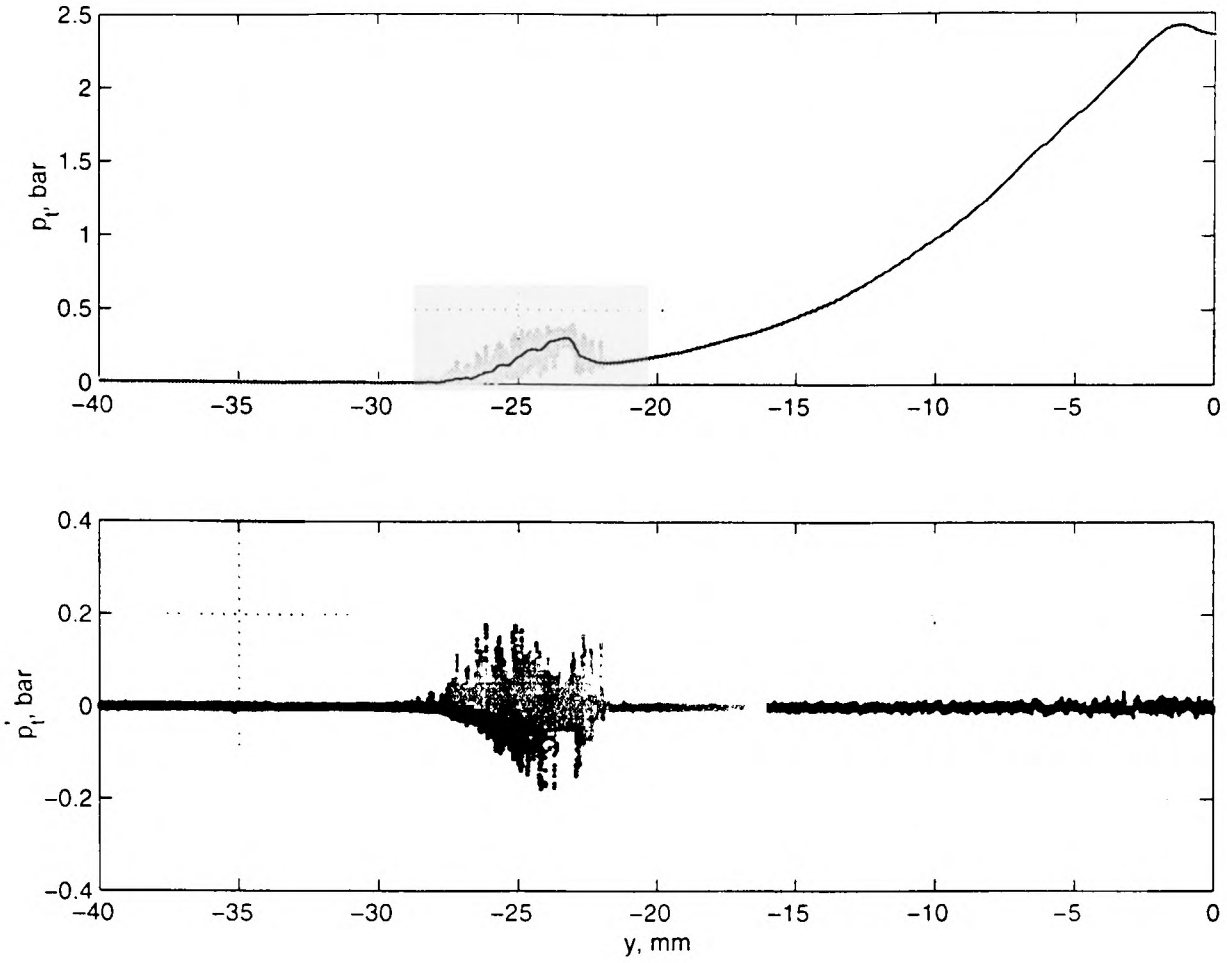


Figure 4-54 Fluctuating RPT Pitot pressure for Mach 5 (SM5M) single jet in quiescent with 100 bar gauge injection at 40 mm downstream *(LT182)*

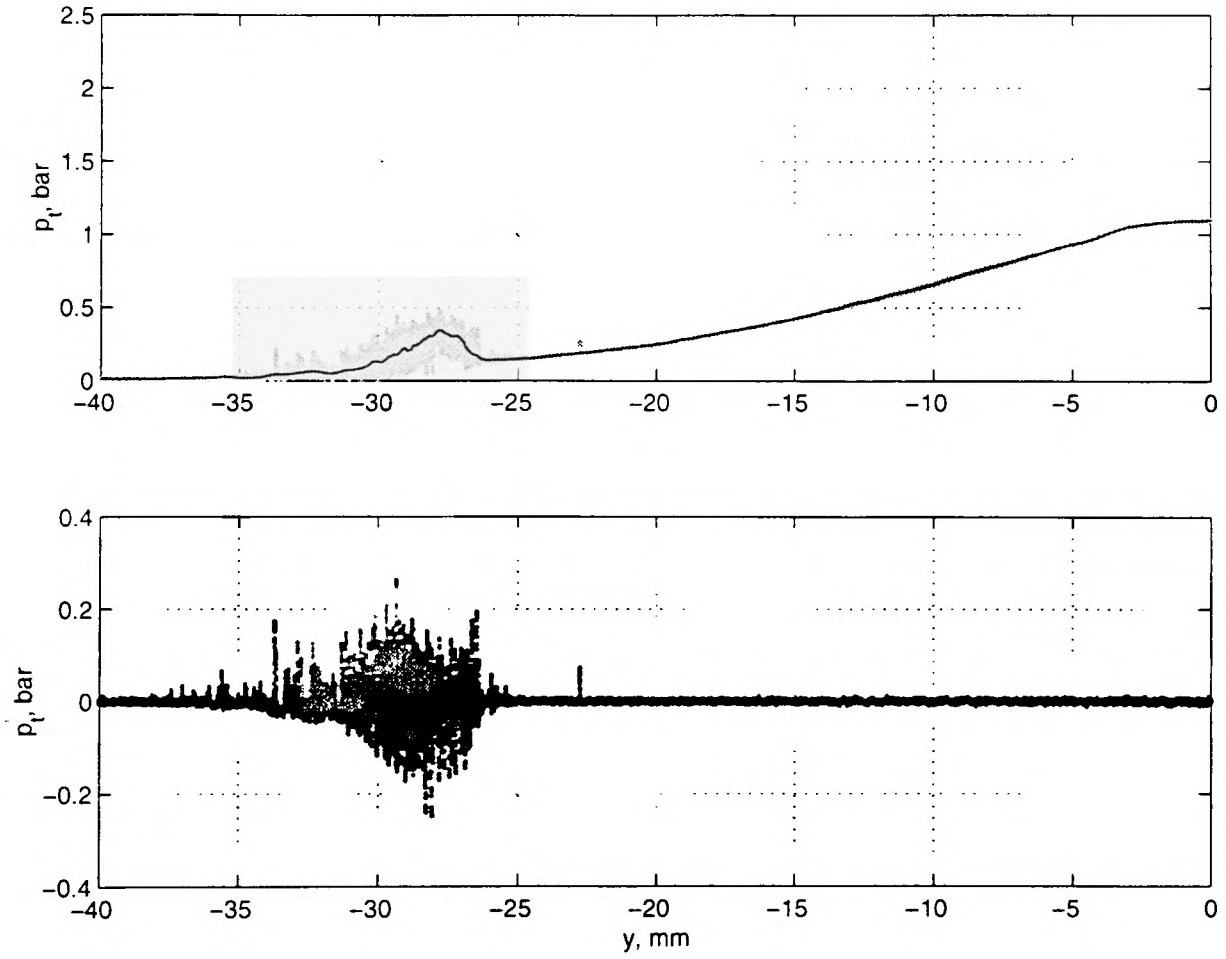


Figure 4-55 Fluctuating RPT Pitot pressure for Mach 5 (SM5M) single jet in quiescent 100 bar gauge injection at 60 mm downstream *(LT181)*

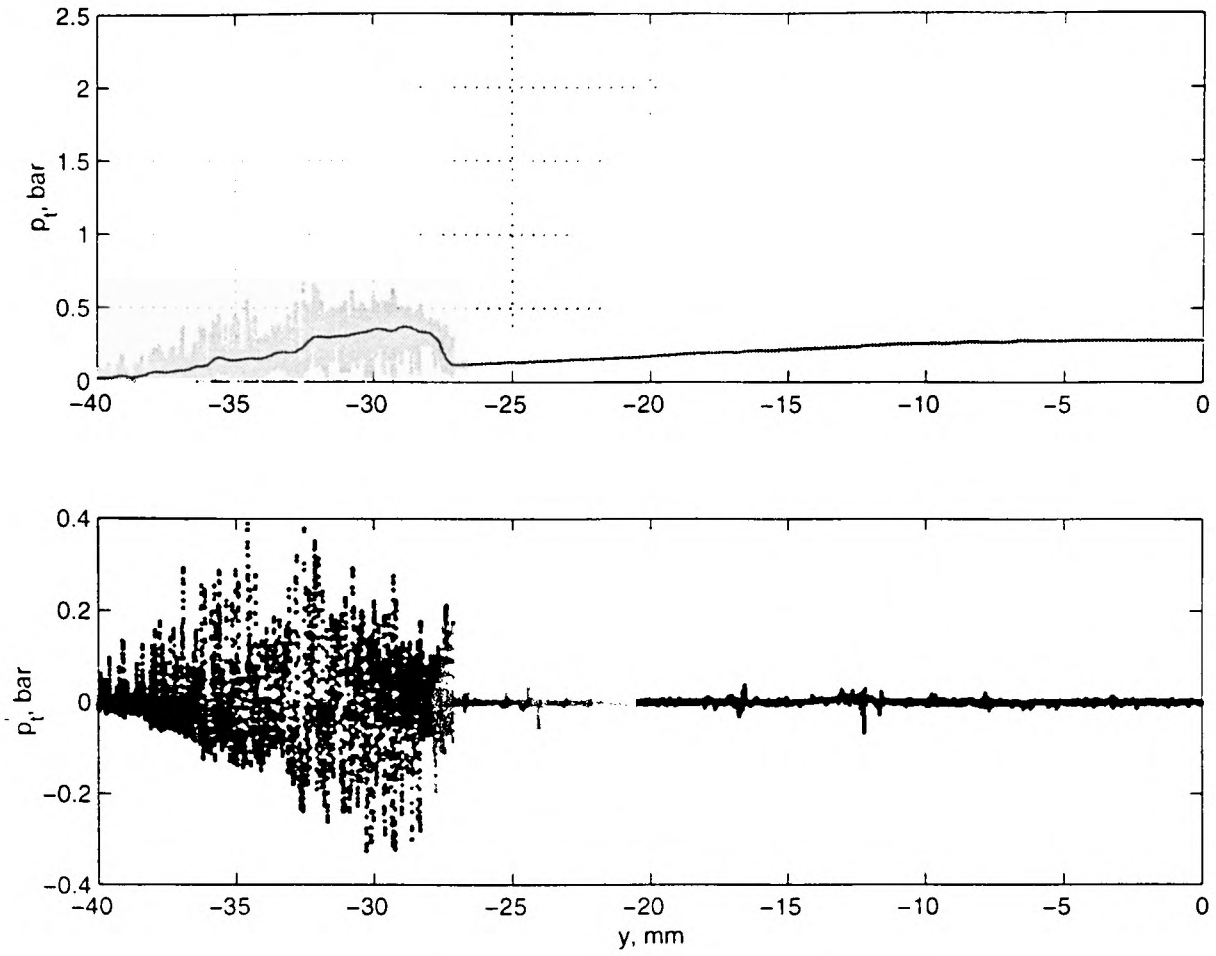


Figure 4-56 Fluctuating RPT Pitot pressure for Mach 5 (SM5M) single jet in quiescent 100 bar gauge injection at 100 mm downstream *(LT196)*

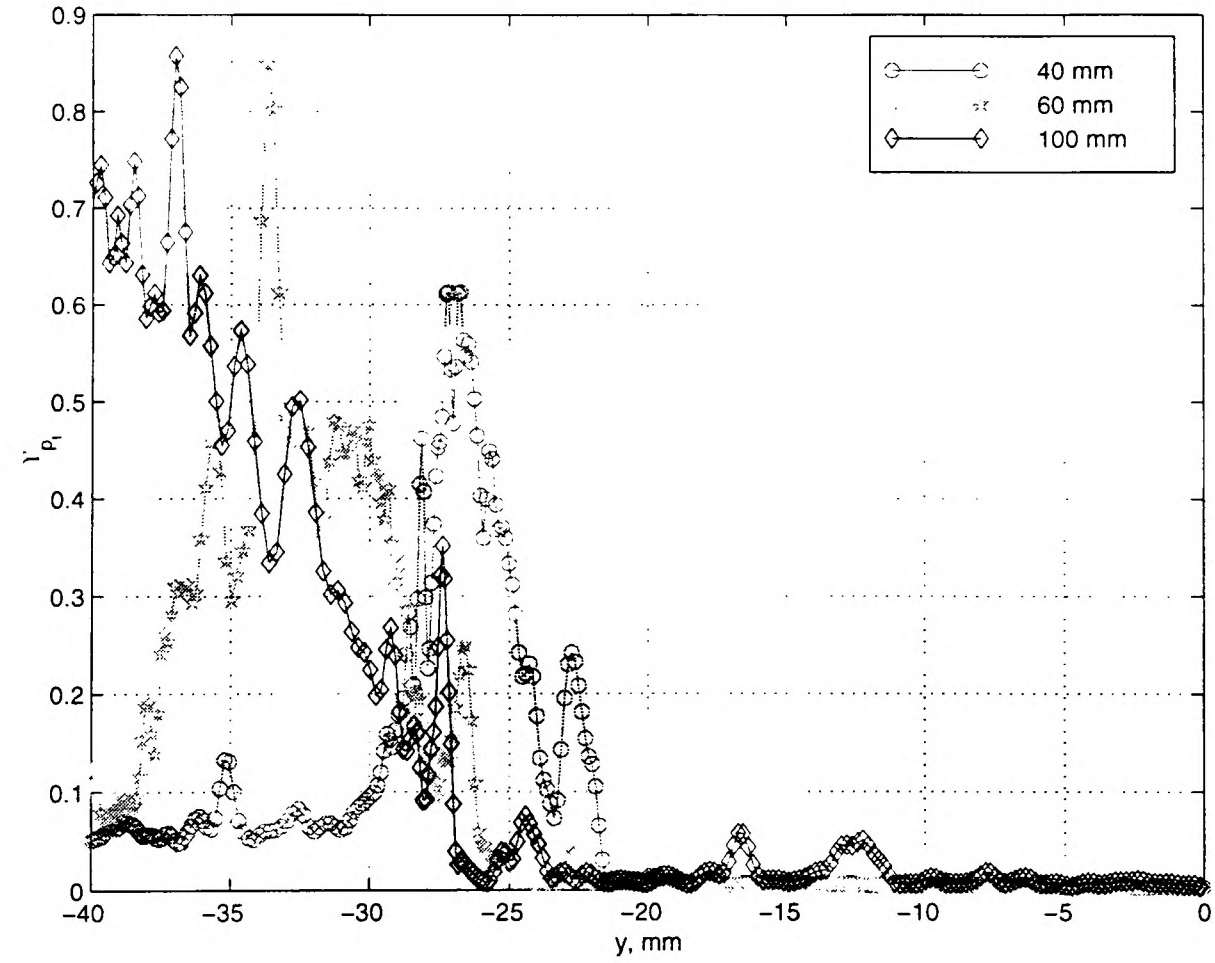


Figure 4-57 Shear layer relative Pitot pressure turbulence intensity for Mach 5 (SM5M) nozzle with 100 bar gauge injection in quiescent

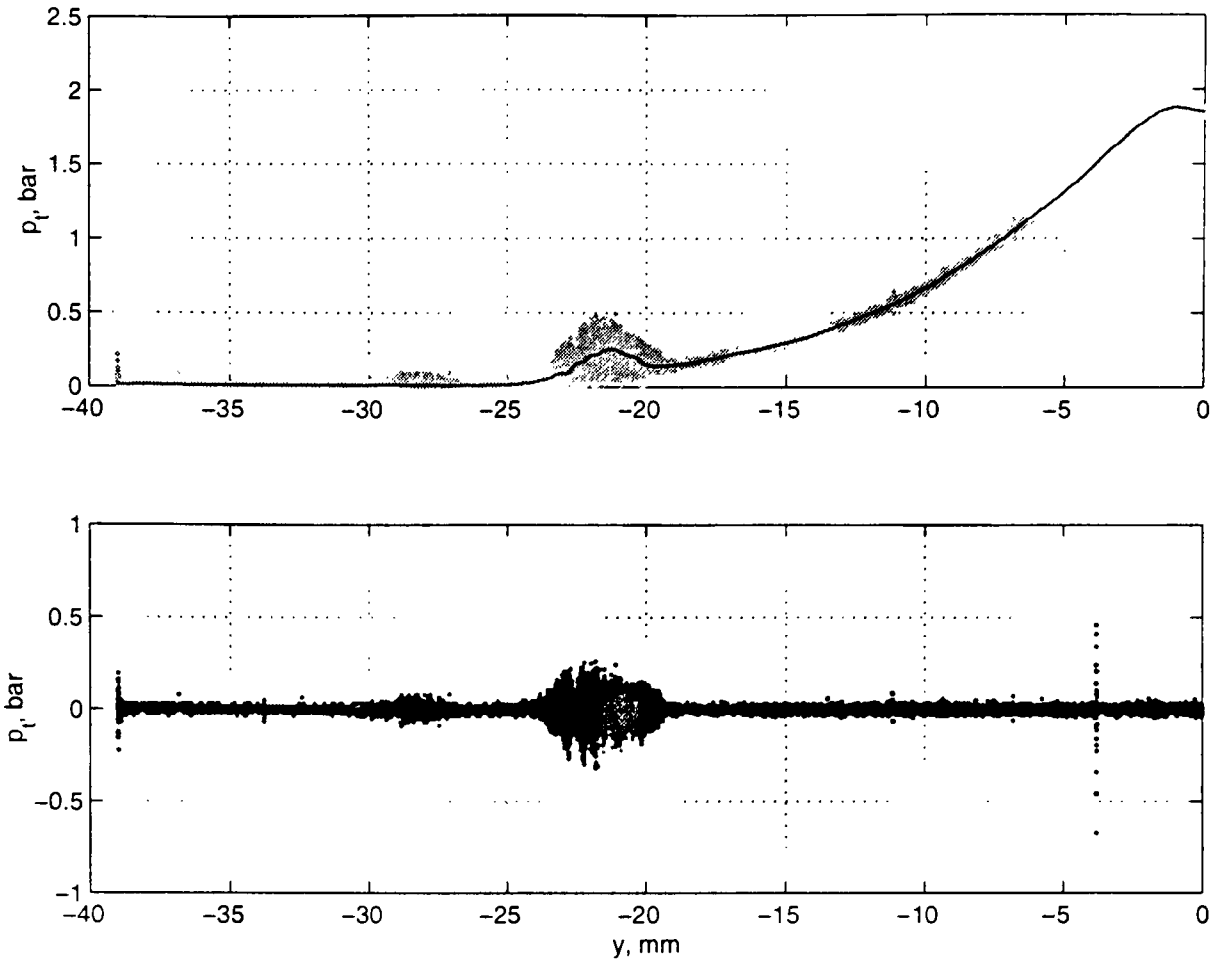


Figure 4-58 Fluctuating RPT Pitot pressure for Mach 5 (SM5M) single jet in quiescent with 80 bar gauge injection at 40 mm downstream *(LT132)*

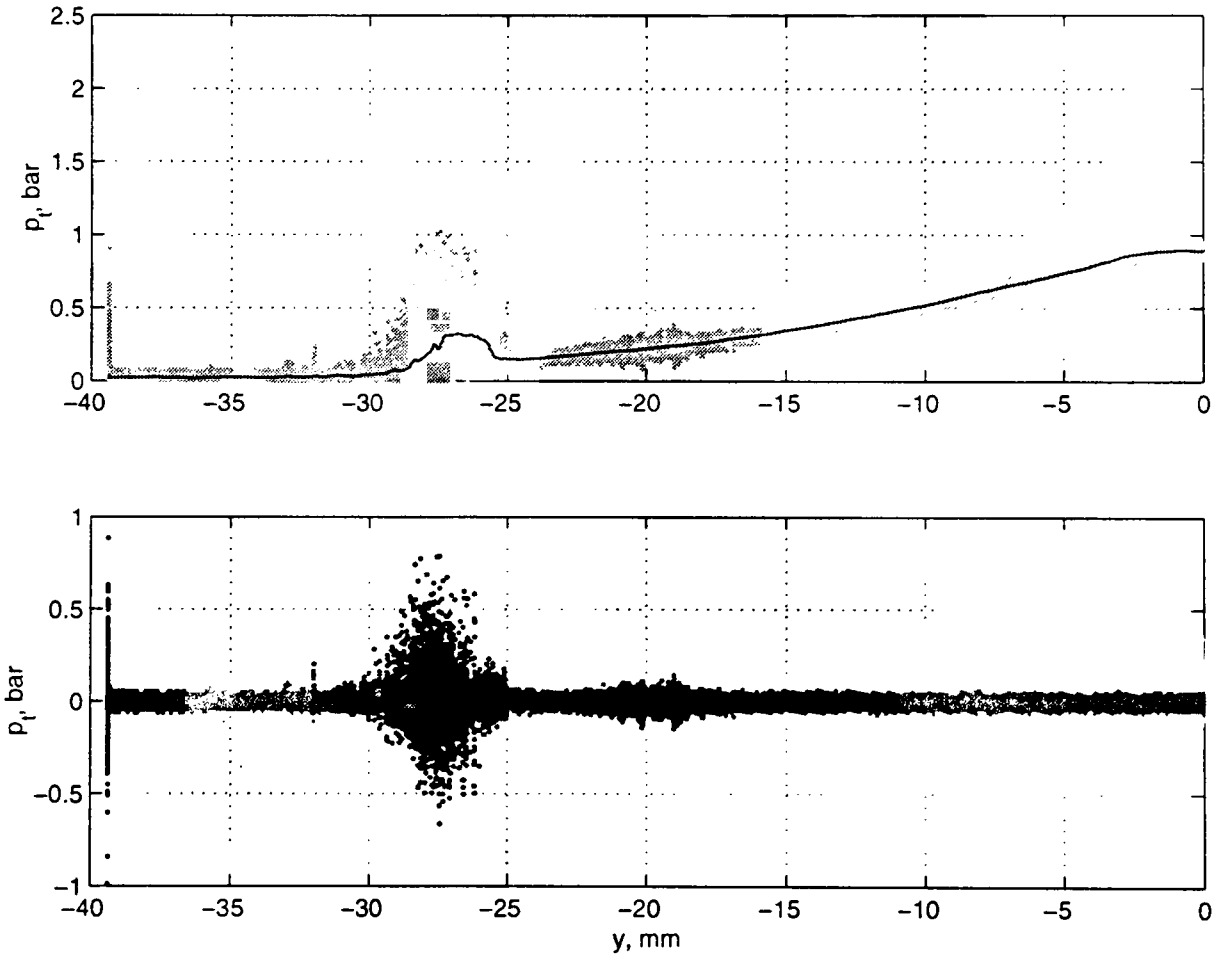


Figure 4-59 Fluctuating RPT Pitot pressure for Mach 5 (SM5M) single jet in quiescent 80 bar gauge injection at 60 mm downstream *(LT130)*

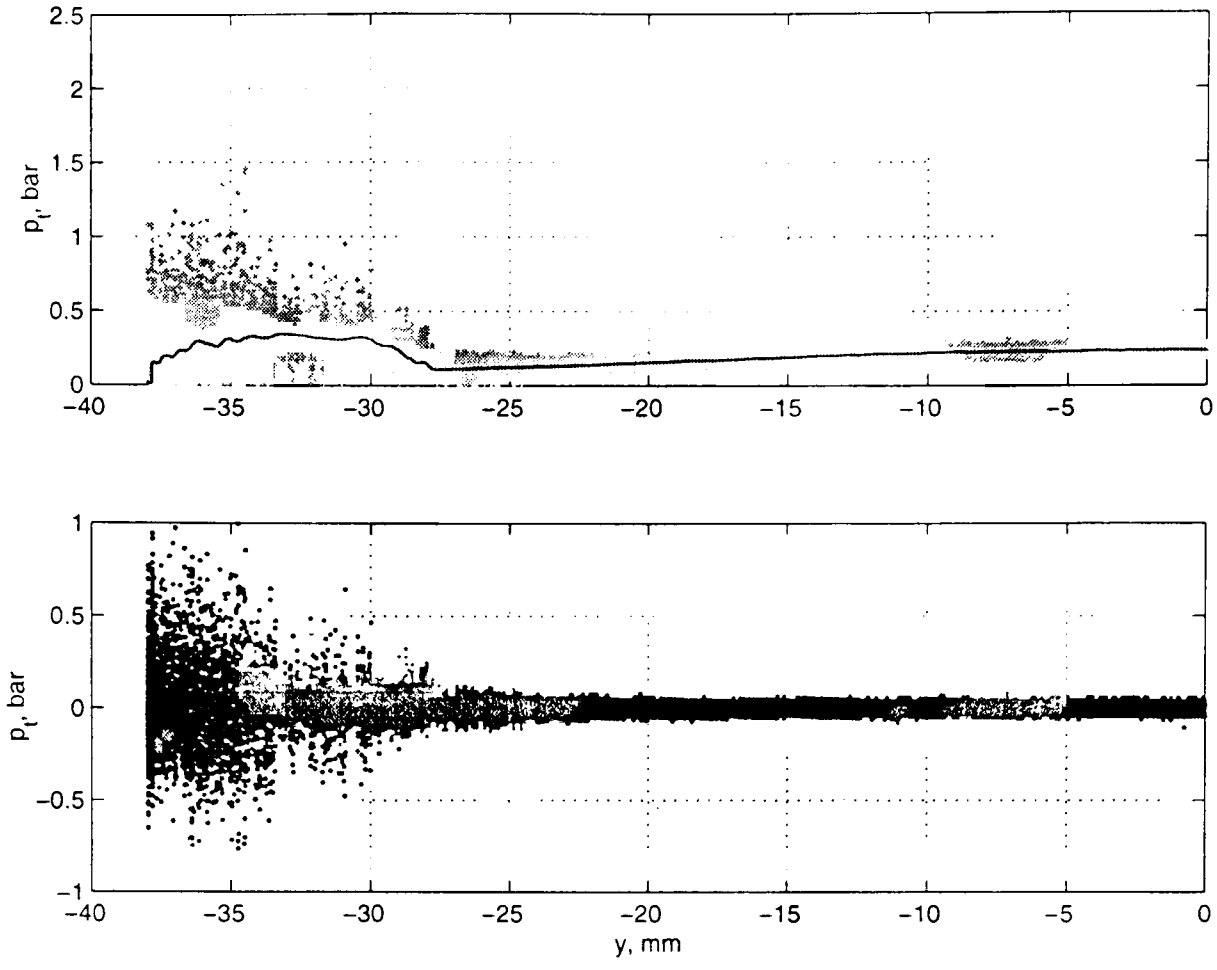


Figure 4-60 Fluctuating RPT Pitot pressure for Mach 5 (SM5M) single jet in quiescent 80 bar gauge injection at 100 mm downstream *(LT129)*

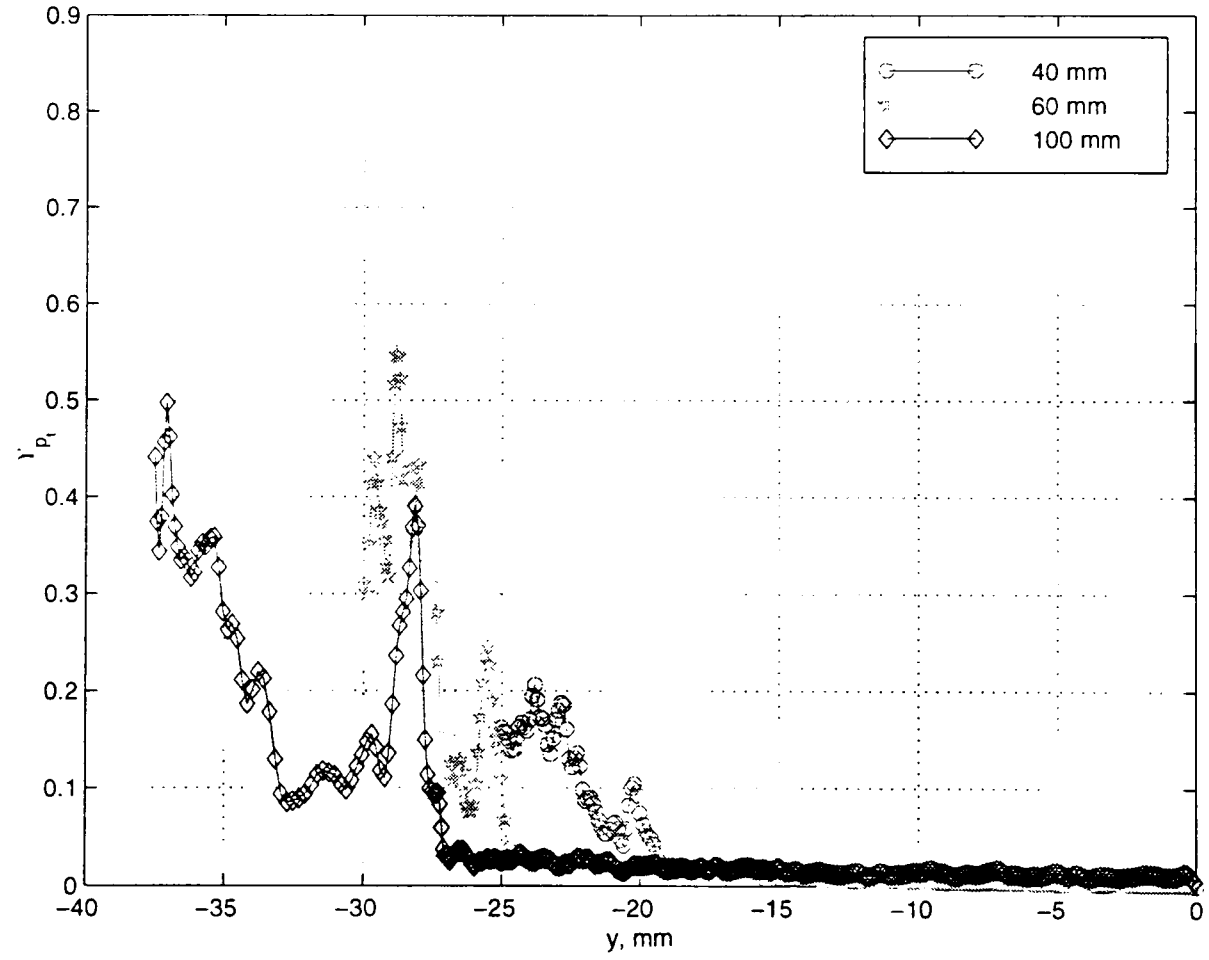


Figure 4-61 Shear layer relative Pitot pressure turbulence intensity for Mach 5 (SM5M) single jet with 80 bar gauge injection into quiescent

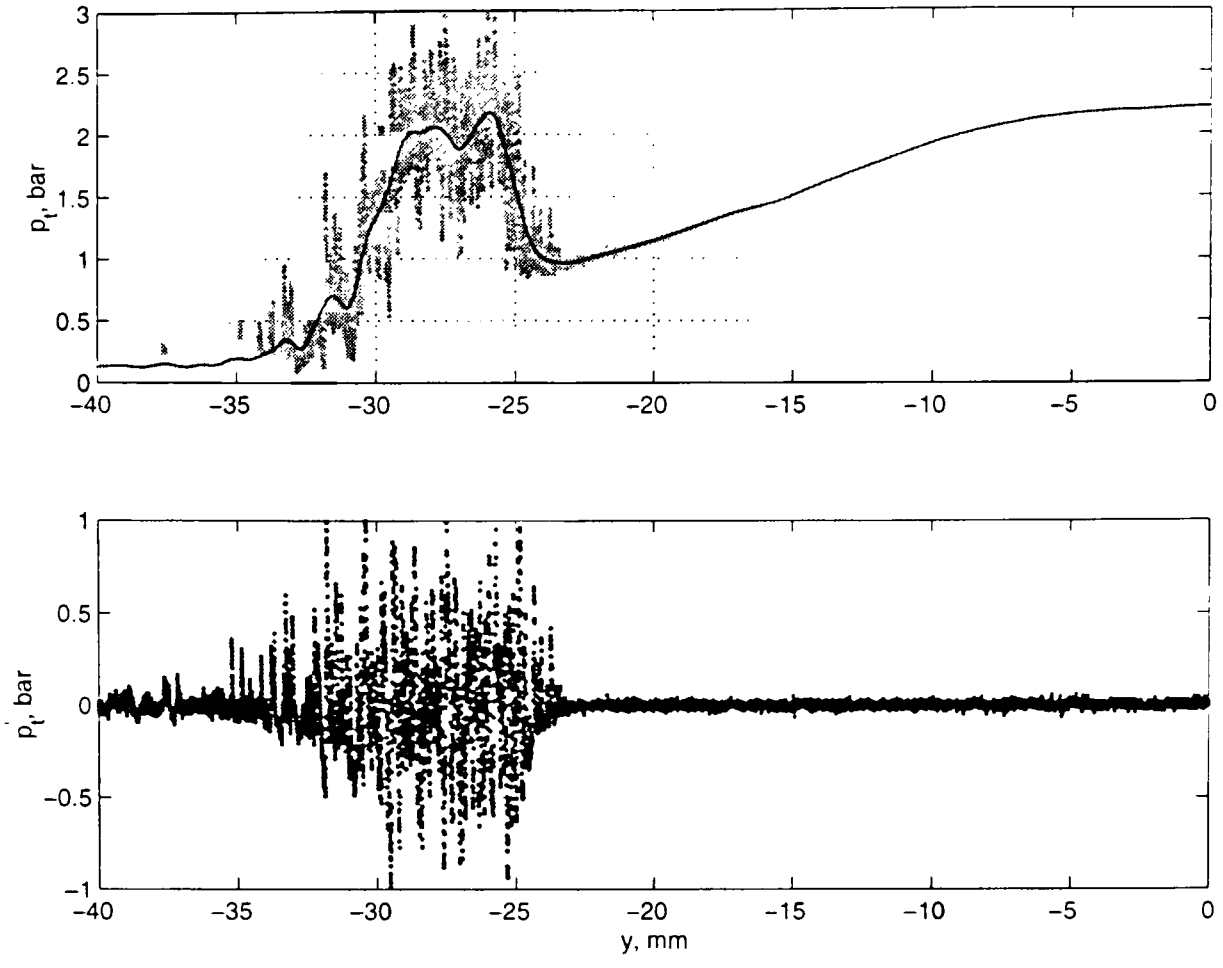


Figure 4-62 Fluctuating BPT Pitot pressure for Mach 3 (SM3) single jetin quiescent with 50 bar gauge injection at 53 mm downstream *(LT124)*

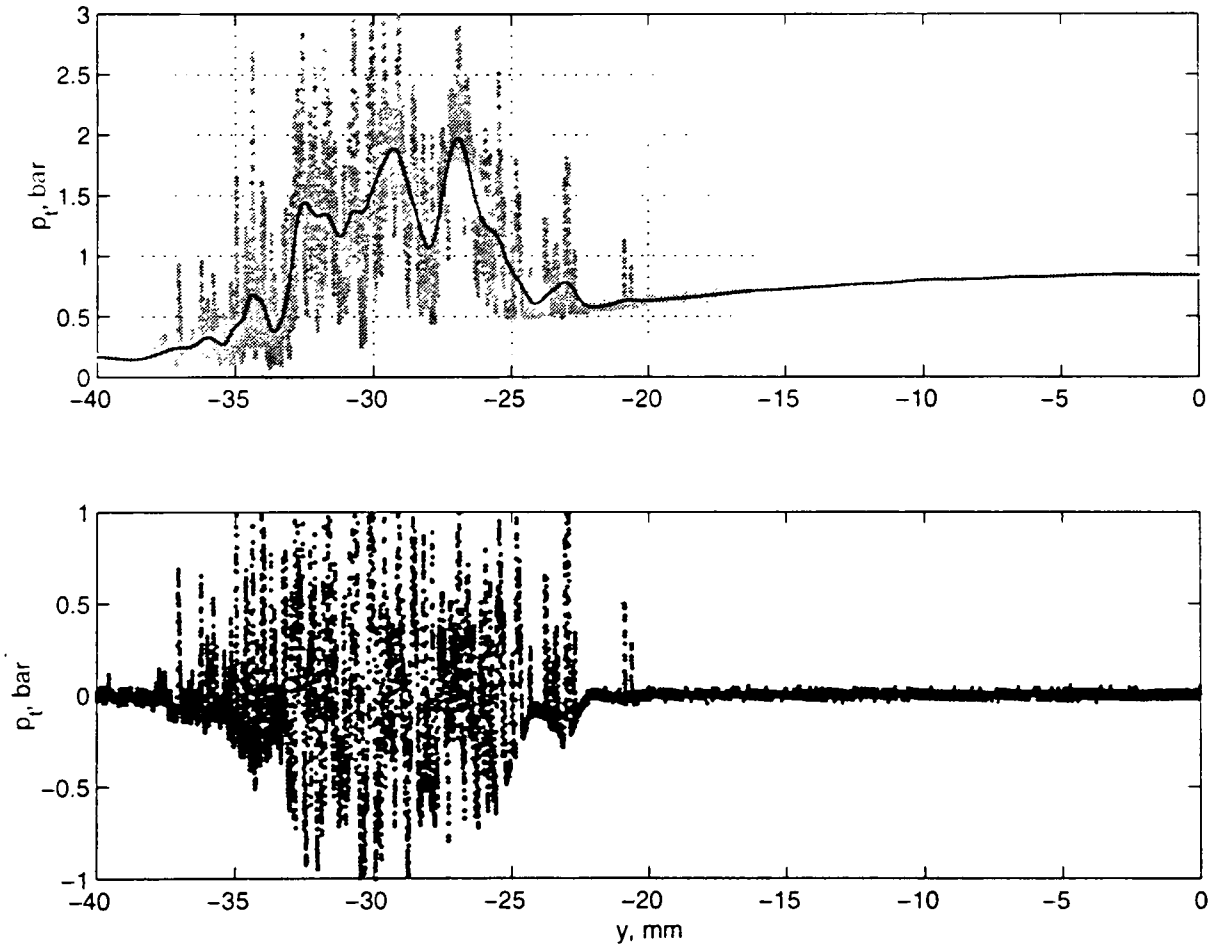


Figure 4-63 Fluctuating BPT Pitot pressure for Mach 3 (SM3) single jet in quiescent with 50 bar gauge injection at 80 mm downstream *(LT125)*

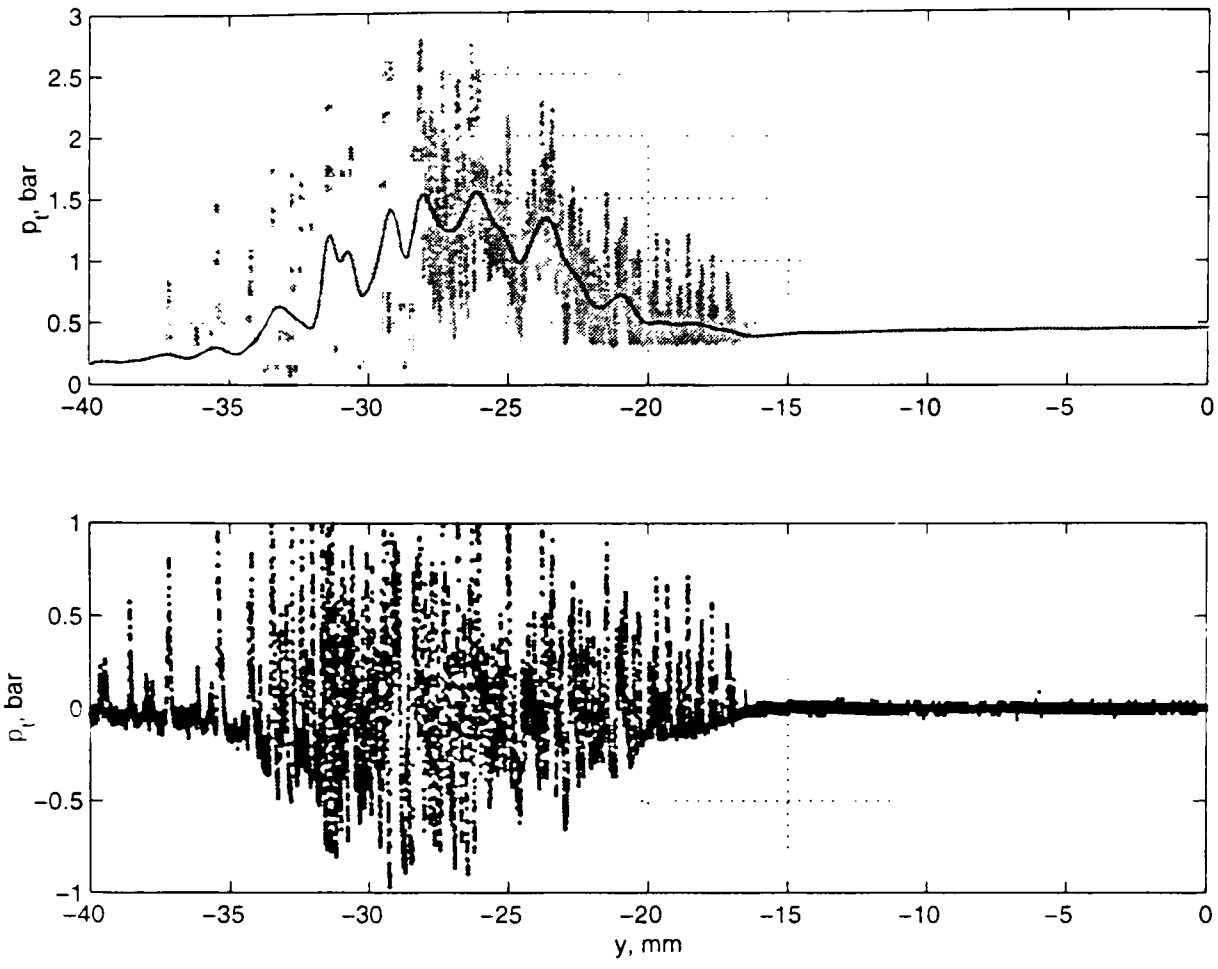


Figure 4-64 Fluctuating BPT Pitot pressure for Mach 3 (SM3) single jet in quiescent with 50 bar gauge injection at 103 mm downstream *(LT126)*

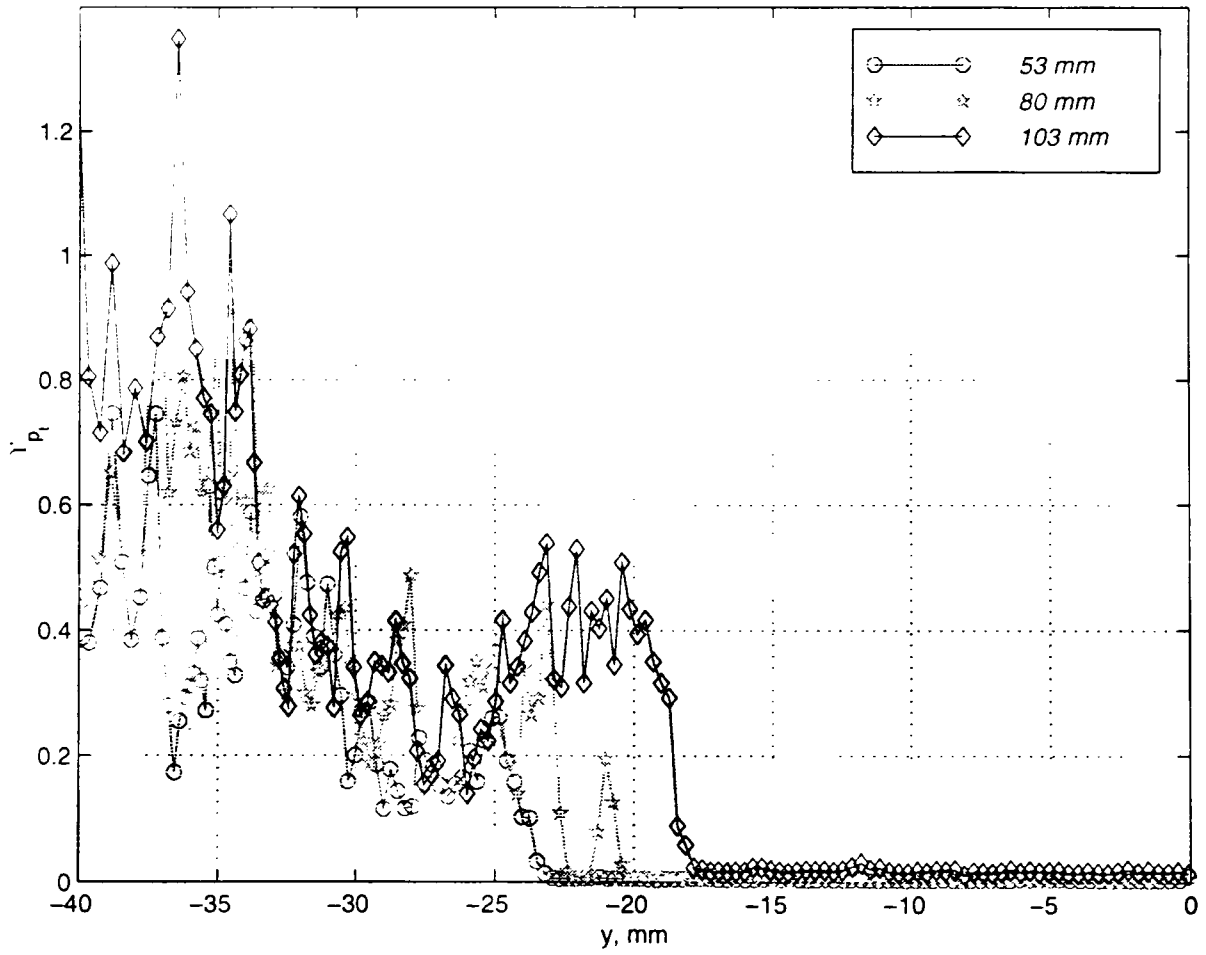


Figure 4-65 Shear layer relative Pitot pressure turbulence intensity for Mach 3 (SM3) single jet with 50 bar gauge injection into quiescent

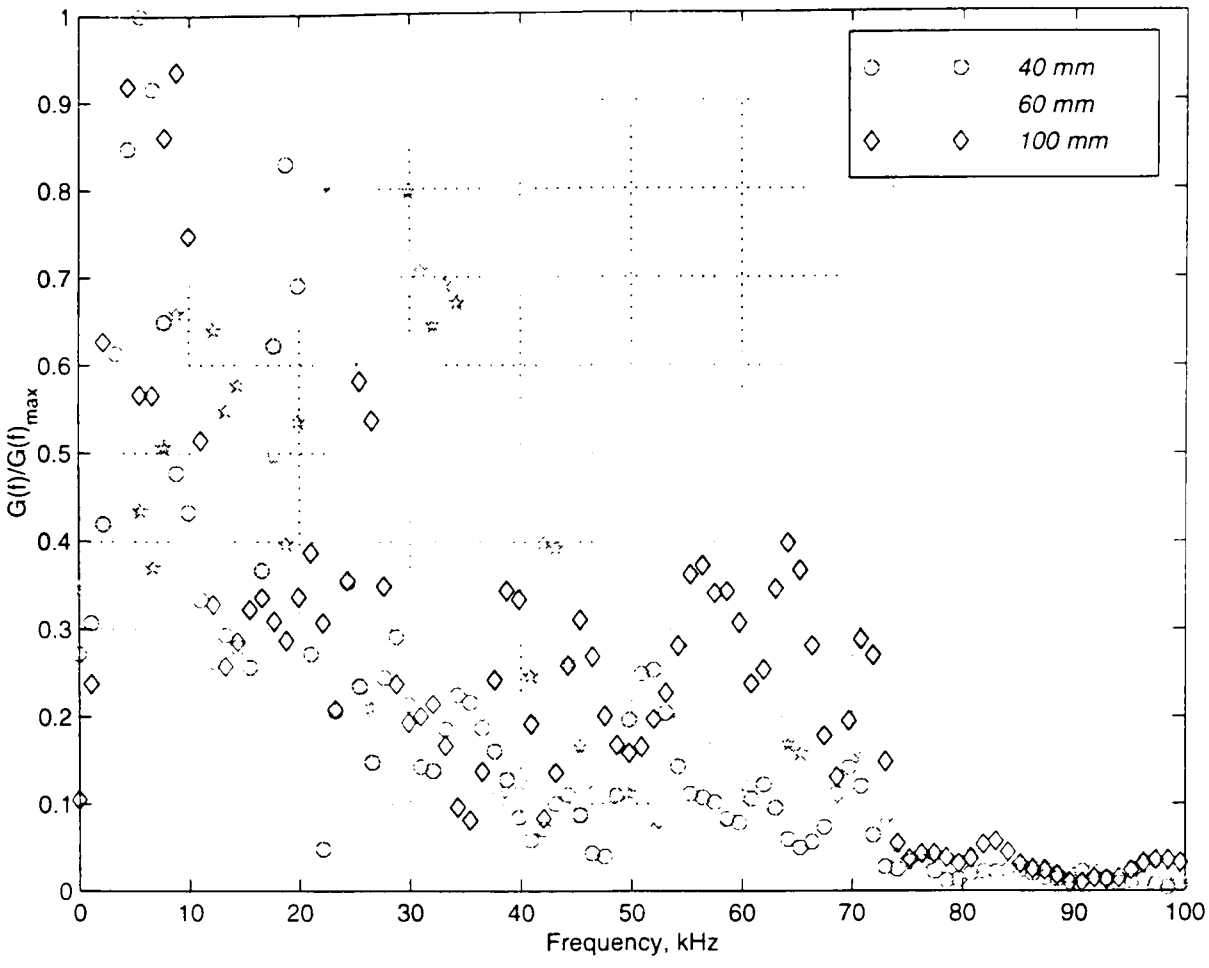


Figure 4-66 Power spectrum for Pitot pressure signals at selected downstream locations *(40 mm: LT182, 60 mm: LT182, 100 mm: LT196)*

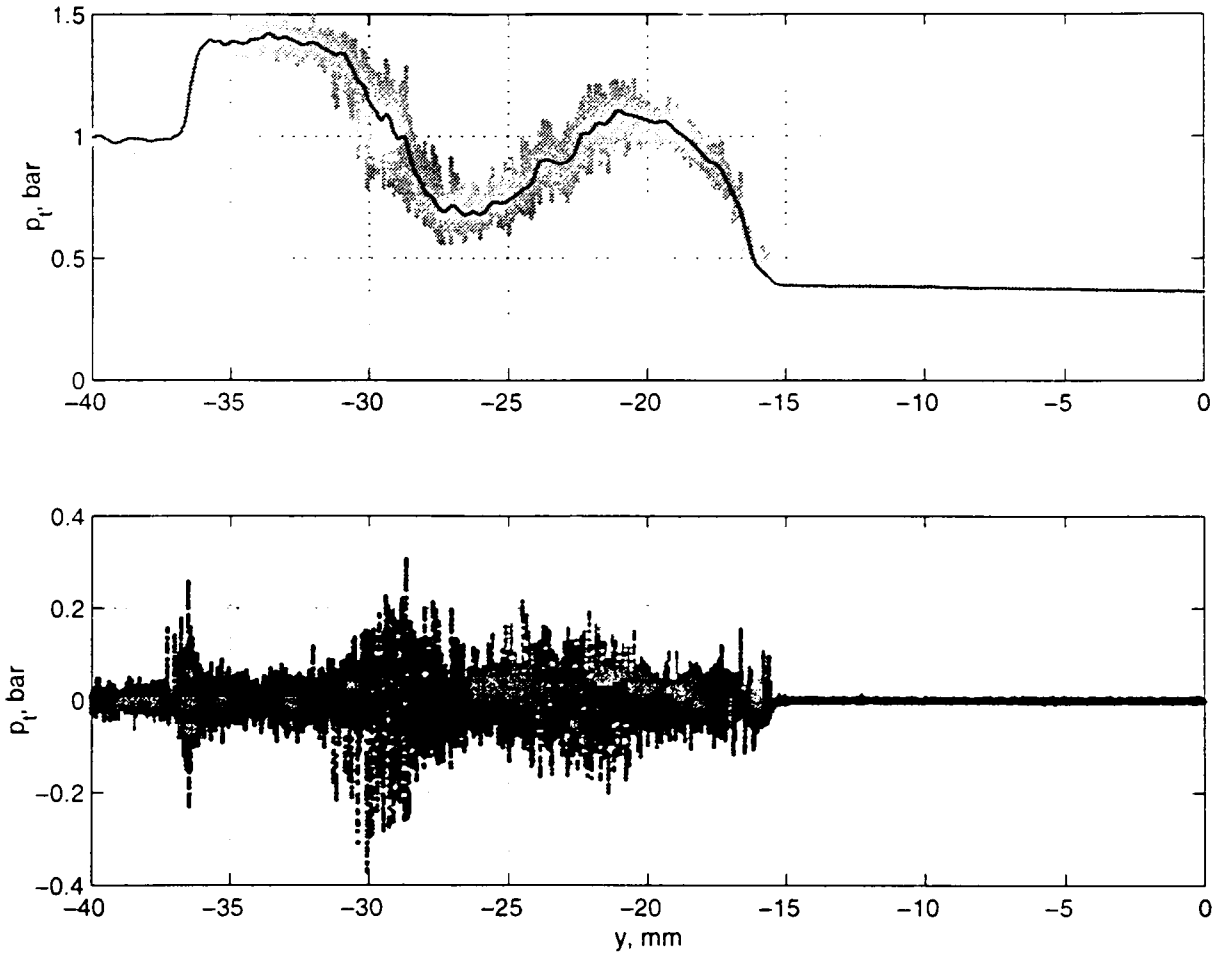


Figure 4-67 BPT Pitot pressure for Mach 5 (SM5M) single jet with N_2 injection in Mach 7 freestream at 100 mm downstream *(GT740)*

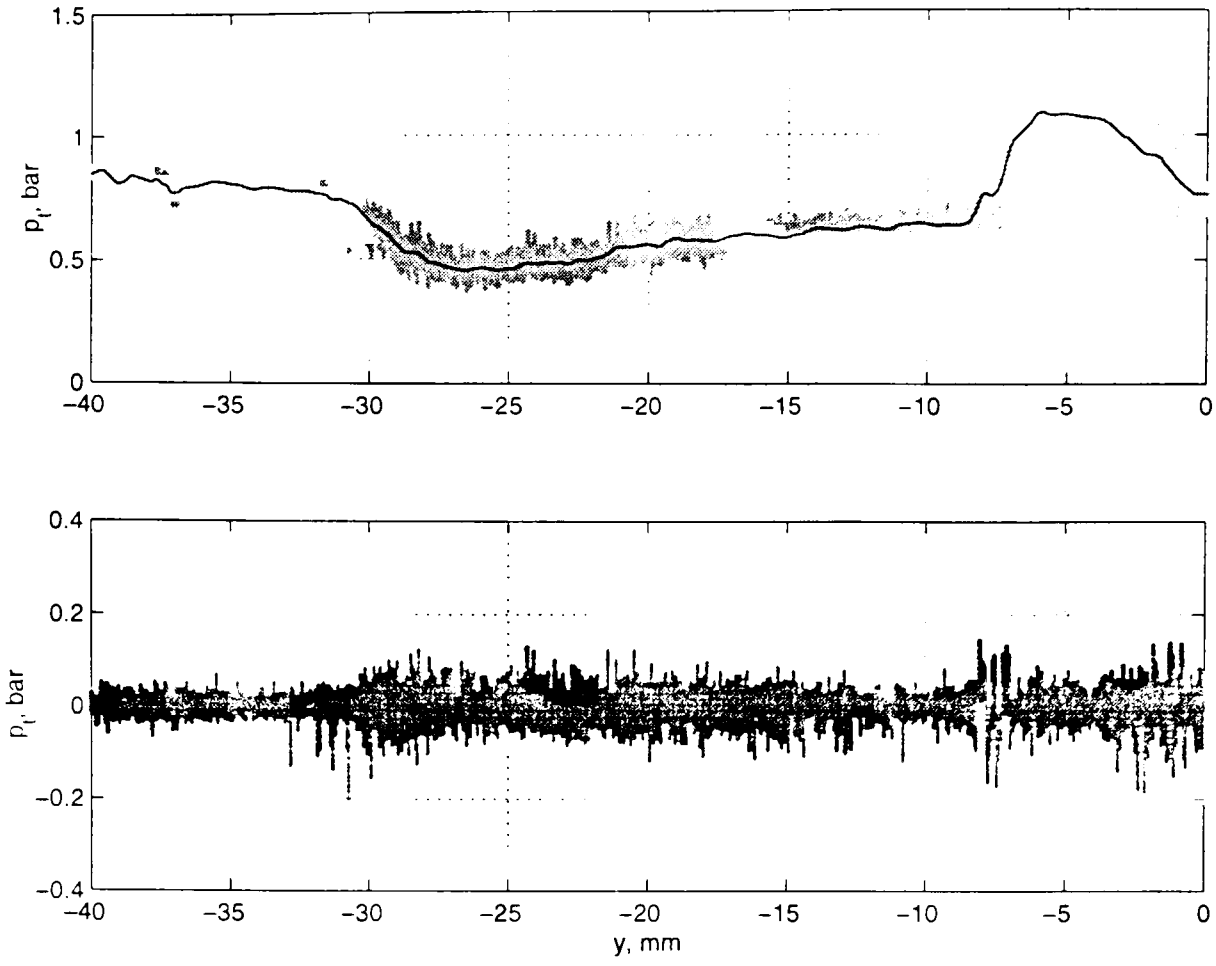


Figure 4-68 BPT Pitot pressure for Mach 5 (SM5M) single jet with N_2 injection in Mach 7 freestream at 250 mm downstream *(GT748)*

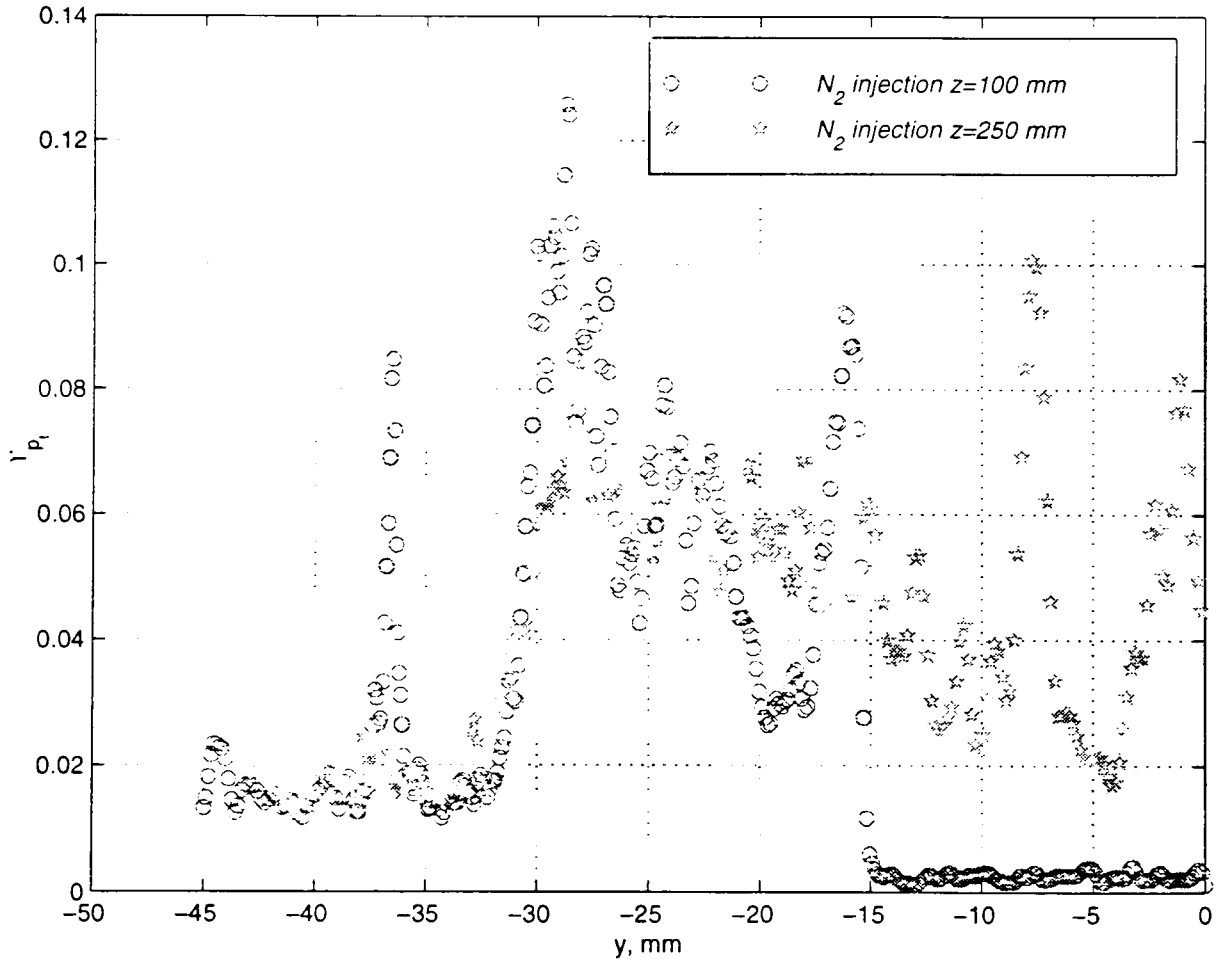


Figure 4-69 Relative Pitot pressure turbulence intensity for Mach 5 (SM5M) single jet with N_2 injection in Mach 7 freestream *(100 mm: GT740, 250 mm: GT748)*

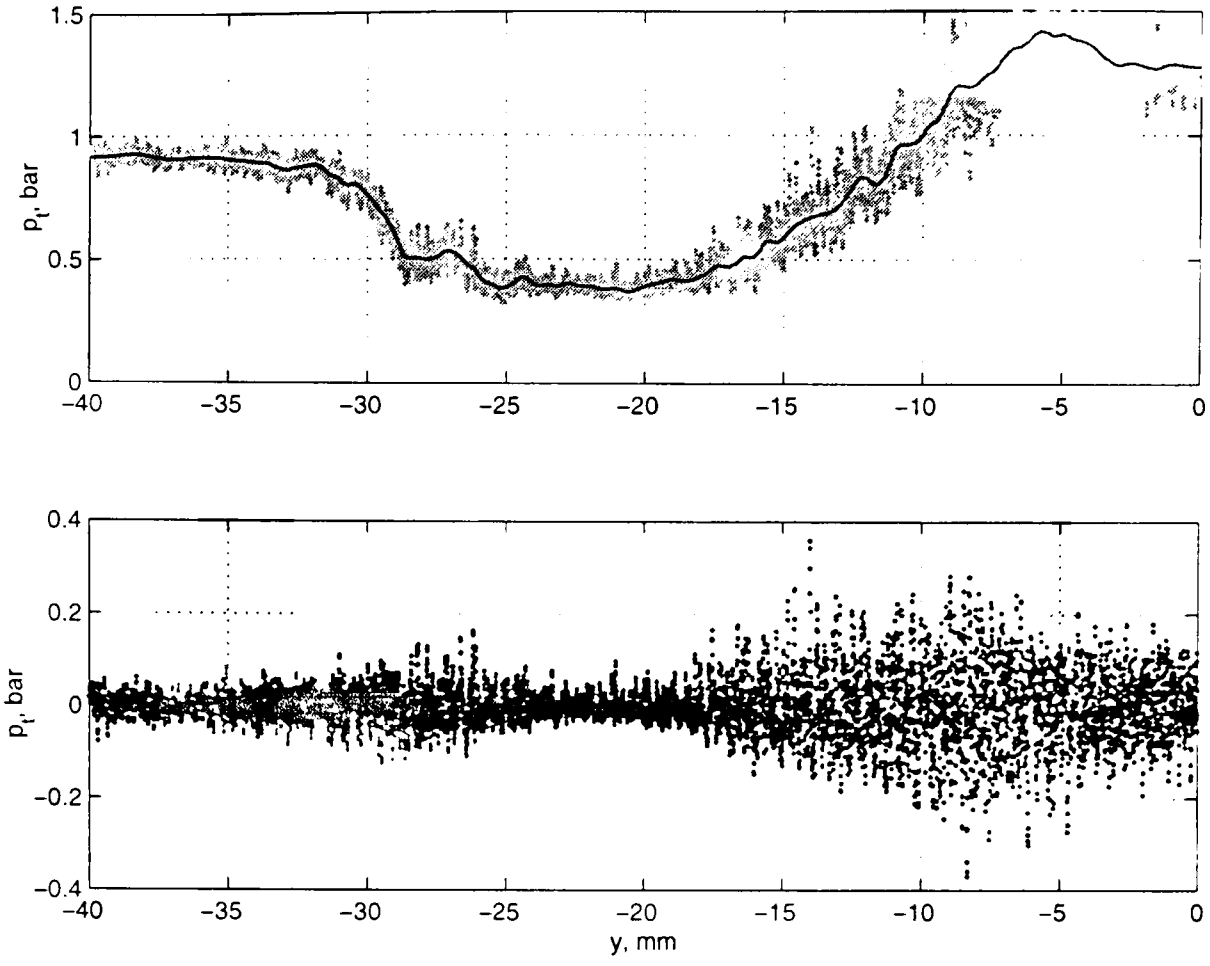


Figure 4-70 BPT Pitot pressure for Mach 5 (SM5M) single jet with H_2 injection in Mach 7 freestream at 250 mm downstream *(GT725)*

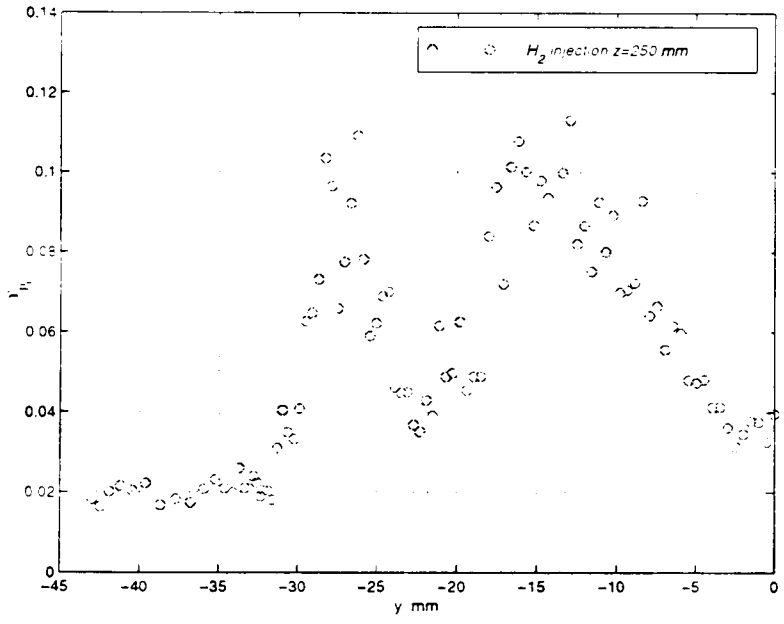


Figure 4-71 Relative Pitot pressure turbulence intensity for Mach 5 (SM5) single jet with H_2 injection in Mach 7 freestream *(250 mm: GT725)*

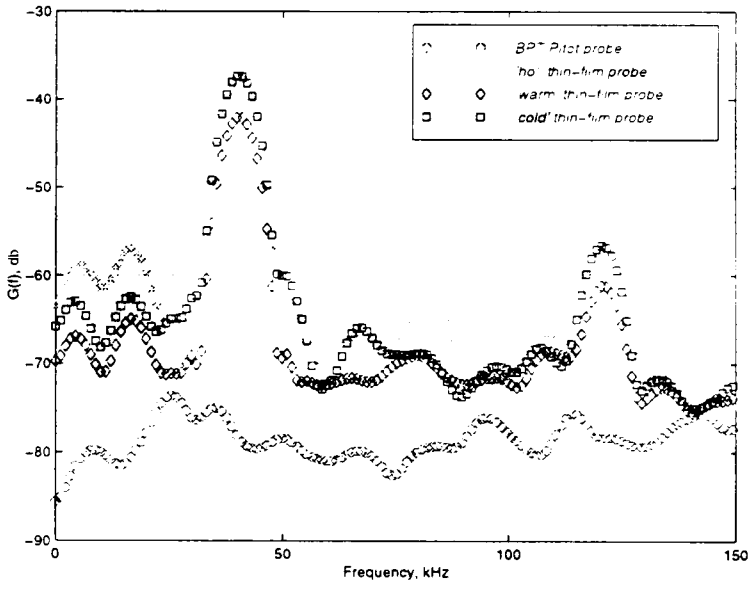


Figure 4-72 Noise spectrum of BPT Pitot probe and thin-film heat transfer probes in quiescent medium

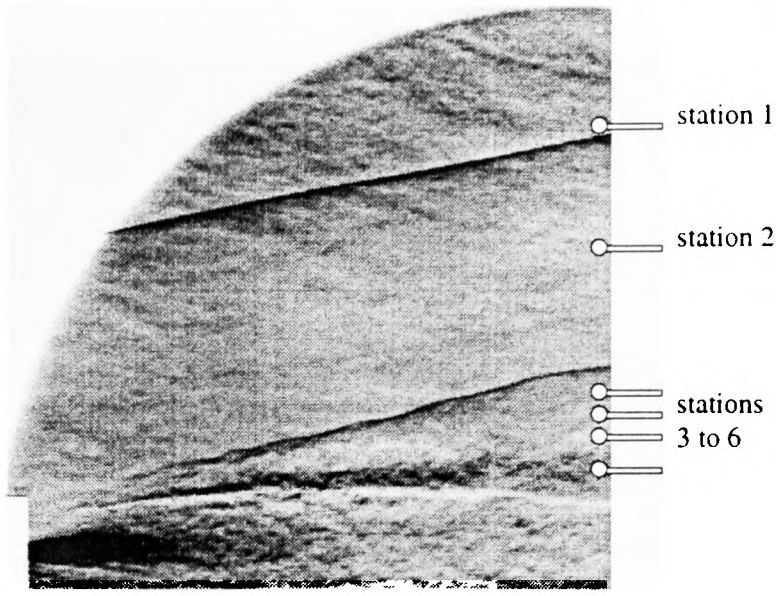


Figure 4-73 Power spectrum traverse stations for Mach 5 (SM5M) single jet in Mach 7 freestream

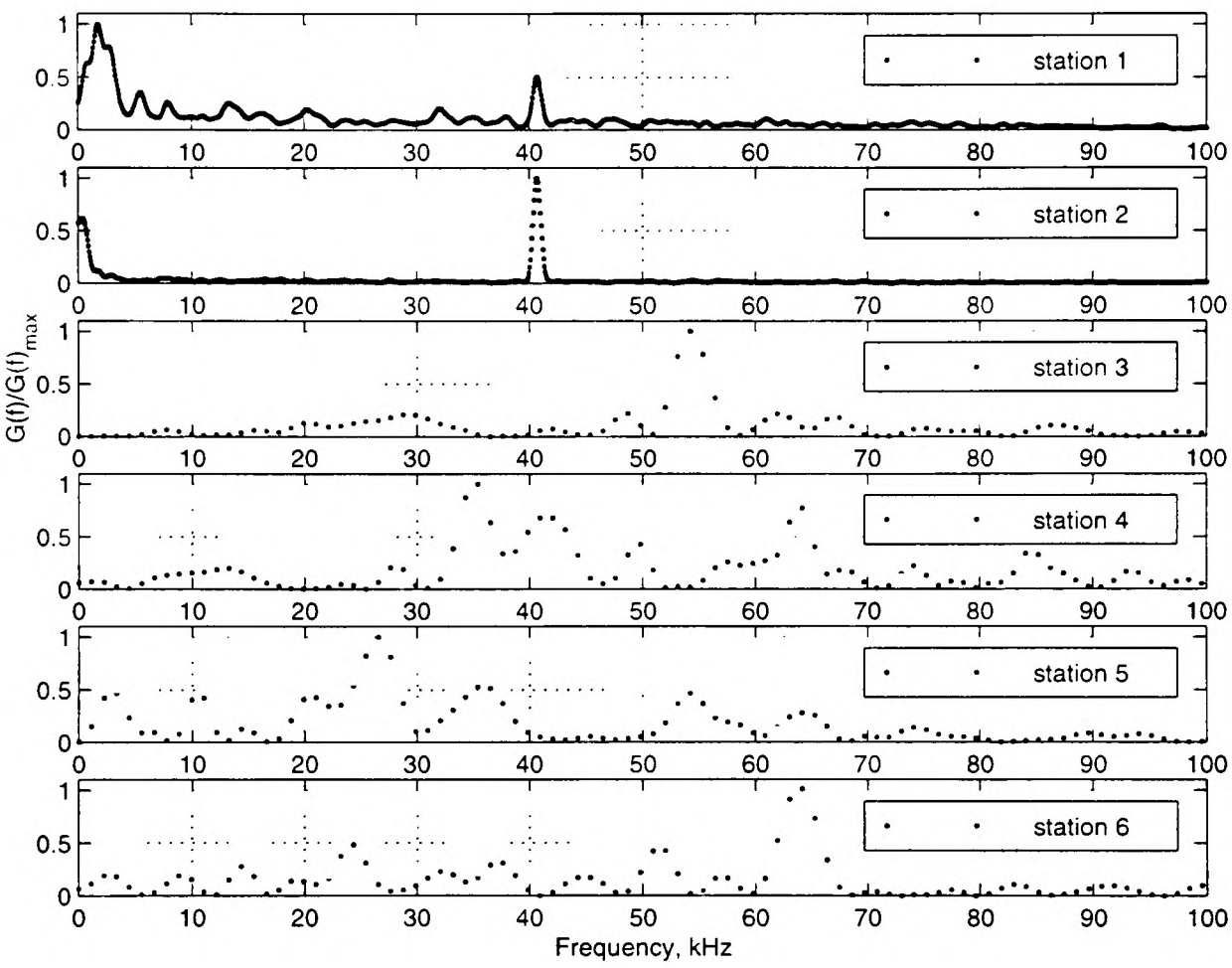


Figure 4-74 Power spectrum of Mach 5 (SM5M) single jet with 100 bar gauge injection in Mach 7 freestream at 100 mm downstream *(GT738, GT739)*

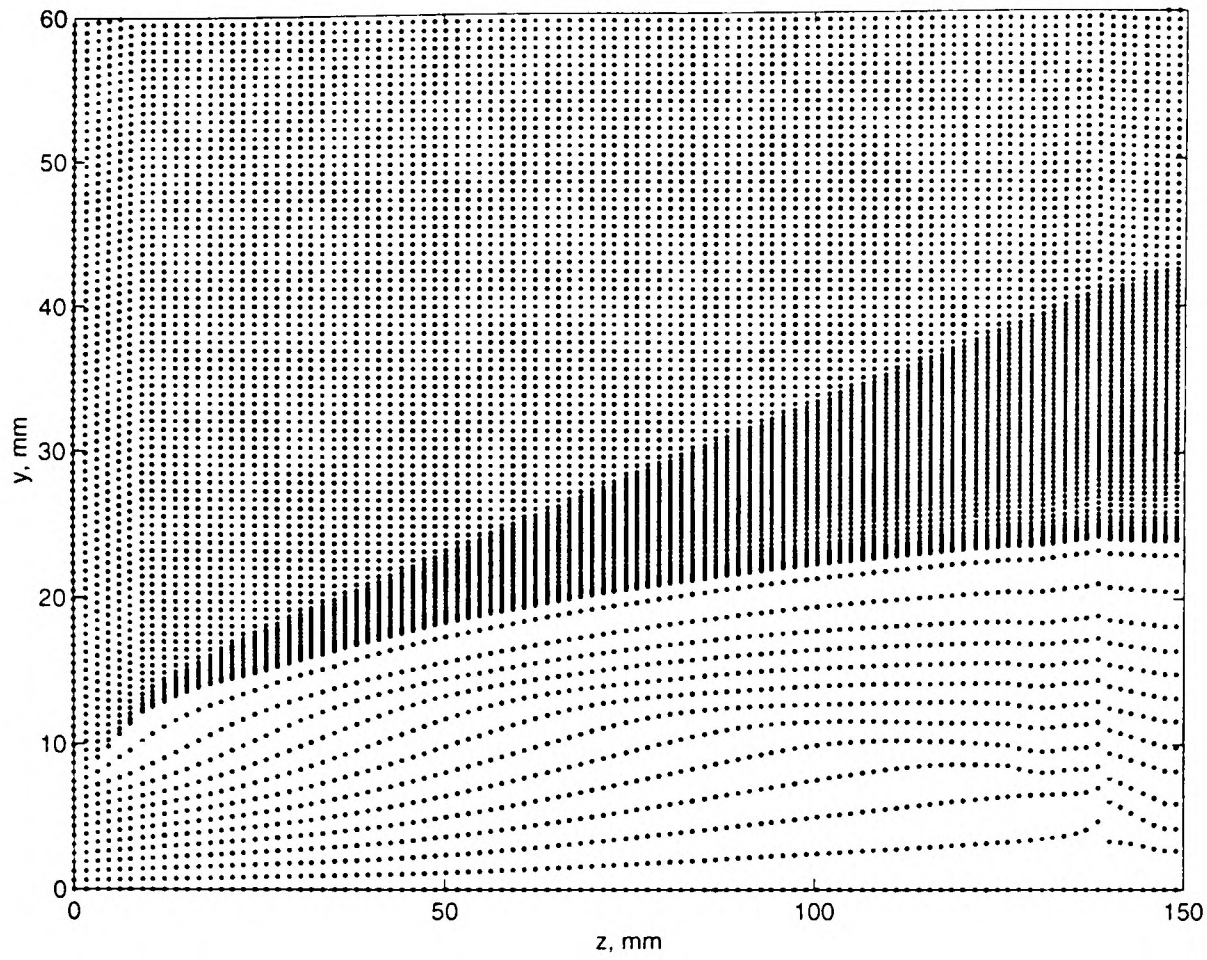


Figure 4-75 SHARC CFD computation mesh-grids for Mach 5 single jet with 92.96 bar N_2 injection in Mach 7 freestream

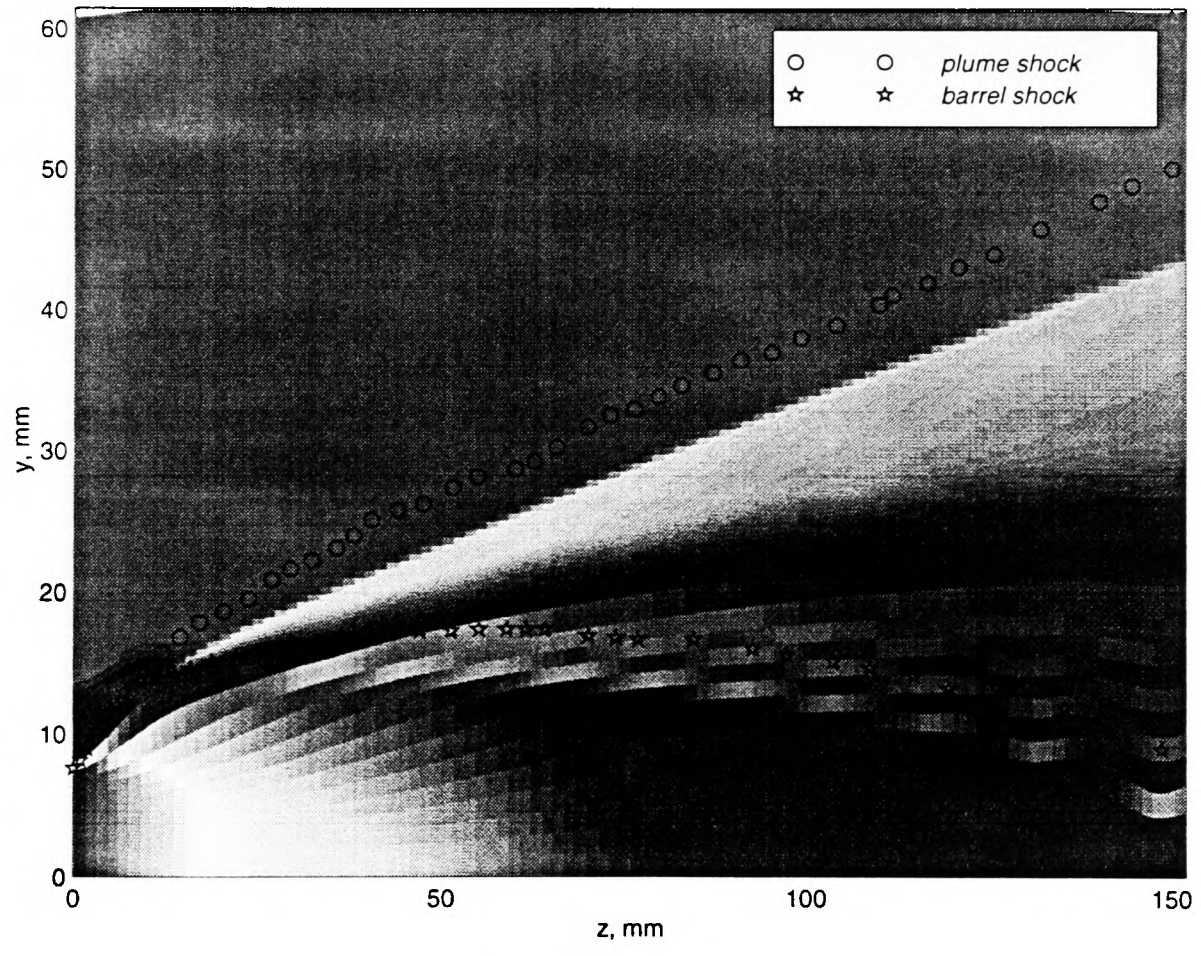


Figure 4-76 SHARC output compared to experimental shock structures

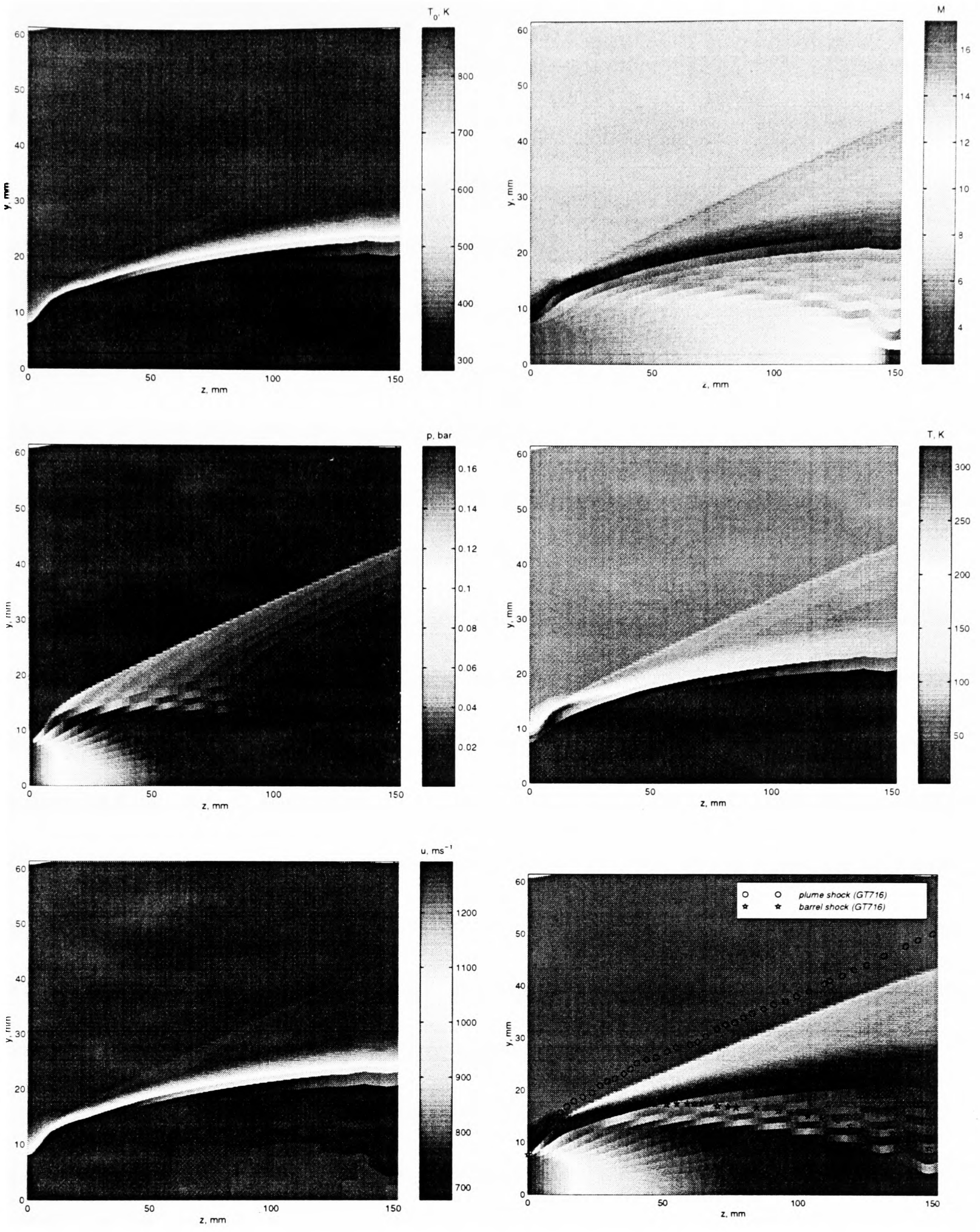


Figure 4-77 SHARC simulations for Mach 5 single jet with 93 bar N_2 injection in Mach 7 freestream

5. Twin Nozzle Rocket Flowfield

5.1 INTRODUCTION

Twinjets have been used in many engineering applications. Their application can be found in high-performance aircraft (e.g. F-15 which adopts a twin nozzle configuration at supersonic speeds), rockets (e.g. the Titan ICBM family which operates under hypersonic conditions, see Figure 5-1 and Figure 5-2) and thrusters (see Figure 5-3). High altitude rocket plumes are of great interest to the spacecraft designer and the use of multiple jets to attenuate the jet noise of propulsion systems is well known. Multiple jets, rectangular and circular, in an array with and without ejector shrouds have been a subject of recent investigations (Bocher 1976, Krothapalli 1979), the objective of which was to achieve better mixing, to control noise, and to develop efficient thrust. Most of the earlier investigations on multi-jets had been concerned with the structure and turbulence characteristics of the flowfield for incompressible jet flows and the screech phenomenon for high-speed jet flows (Wlezien 1989, Seiner 1988). Wlezien (1989) investigated coupled interaction of supersonic twinjets as a function of nozzle spacing and found that, for closely spaced nozzles, coupling occurred at low Mach numbers and was suppressed at high Mach numbers. Experimental and numerical studies on over- and under-expanded multiple free jets were also carried out by Gamal (1992).

When two jets with parallel axes issue from nearby nozzles into still surroundings, their centre of symmetry deviate from straight lines because of mutual entrainment of the surrounding fluid, as a result of turbulent momentum transfer from the individual jets to the central region. This mechanism is believed to be the same as that which causes jets to attach to nearby walls. Marsters (1977) carried out analysis of incompressible planar jets. The mean flow quantities for the mixing of two planar, parallel, ventilated incompressible jets had been examined experimentally and compared with predictions based on a crude integral model of the flow and the agreement was shown to be relatively good.

Miller et al (1989) also did a similar experiment and theoretical analysis of mildly compressible twin planar jets. The jet spacing was 6 nozzle-diameter. Merging was observed at 12 nozzle-diameter where the flow variables resembled those in a single jet flow. On merging, the converging jets of the twinjet flow lose their individual identities and behave as a single jet. It was also observed that a region of sub-atmospheric static pressure between the converging jets accounts for their convergence and for the reversal of a considerable fraction of the total flow at the centre-plane against a strong downstream force of turbulence shear. Associated with the flow reversal was the appearance of a pair of symmetrical contra-rotary stable vortices and a free stagnation point on the centre-plane. Where the two jets merged, a super-atmospheric static pressure mound redirected their momentum into a single resultant jet symmetrical about the centre-plane. The flow structure of the combined jet exhibited all characteristics of a single jet flow.

Studies of two-dimensional supersonic jets of air issued from parallel free-standing nozzles (Elbanna et al 1983) suggested the characteristics of the flowfield were influenced by spacing between the two nozzles. The nozzle spacing used for their study was 12.5 slot-width. Entrained secondary flow between the two jets was clearly noticeable. When the result was compared to a single equivalent slit nozzle, the distribution of the three components of turbulent velocity fluctuations show different behaviour than that for the single jet and true similarity was not observed up to 120 slot-width. The width of the combined jets spread linearly downstream as a single jet, but with a lower spread rate than the single equivalent jet. This was attributed to the streaming effect (which lowers the static pressure in the region between the two jets, and could cause significant bending of the jet axis) of the entrainment fluid, and depended upon the geometrical parameters of the flowfield, the nozzle spacing and the dimensions of the bounding plates. Due to limitation of the scale of the test section, the furthermost measurements could be taken downstream was about 10 nozzle-diameter. The

twinjet was not fully merged and comparison of spread rate to the single equivalent nozzle was not qualitatively conclusive.

A five-circular-nozzle-cluster study (Raghunathan et al. 1981) showed that multiple nozzles improved mixing and showed a rapid decrease in peak velocities when compared with a single equivalent nozzle. The nozzle spacing was 1.4 nozzle-diameter. The growth rate of the cluster jet was again shown to be lower than the single equivalent nozzle. In this case, the merging point was at 14 nozzle-diameter downstream. The momentum of multiple jets was found to be generally lower than that for a single jet. This could be due to viscous losses. It appeared that a multiple-jet nozzle with five jets offers an advantage in terms of noise reduction without significant reduction in the momentum of the jet.

There have been very few studies of supersonic twinjets at high exit Mach numbers. Gamal (1995) carried out studies of supersonic twinjets with varying design Mach numbers up to 2.5 and varying stagnation pressure and nozzle spacing in a quiescent medium. It was found that the merging point was proportional to the nozzle spacing and initial flow conditions, and the two jets merged over the distance range $5 < z/S < 20$. This agreed well with other studies at subsonic and supersonic speeds. The maximum value of the total pressure of the merged jet changed with Mach number as well as nozzle spacing. The influence of nozzle spacing on the maximum total pressure was believed to be attributable to bending of the jet axes towards the axis of symmetry. The bending of the axes affected the shock-cell structure, which led to alteration of the shock strength and, in turn, the maximum total pressure. The axes bending increased as the nozzle spacing was increased. It was found that, based on the attenuation of the peak velocity just downstream of the merging point, the processes of merging and combining between the jets were faster with smaller nozzle spacing. The Mach number directly affected the strength and position of shock cells, whereas the nozzle spacing affected the bending of the jet axes.

Rudman (1977) attempted an interpretation of the complex multi-nozzle flowfield. He carried out experiments on twinjets with different degrees of interaction and a numerical procedure was used based on finite difference techniques, which allowed for many discontinuities in the flowfield (Moretti 1974).

Hypersonic multi-jets were investigated by Cain et al (1991) in the form of a cluster-of-four small scale nozzle, with a nozzle spacing of 1.08 nozzle-diameter. The measurements of Pitot pressure on the axis of symmetry of the plume from the cluster were predicted to within 12 per cent at large downstream stations by an equivalent single nozzle source flow model that employed Boynton's (1967) angular density distribution. It was found that the interaction shock shapes and the Pitot measurements within the core flow were not influenced by the background pressure and compared favourably with previous experiments by Hurdle (1983).

Although there are published analyses on single jets, theoretical analyses of twinjets are considerably more difficult. The asymmetric nature of the flowfield near the exit and the entrainment of the surrounding gas of the same or a different composition play an important role in the merged jet structure further downstream. Lack of apparent symmetry also posed a major obstacle to CFD simulation.

A better understanding of flowfields of under-expanded multi-nozzle configurations is greatly needed. Many aircraft and missile designs have multiple exhaust nozzles operating at under-expanded conditions and the individual plumes impinge giving rise to highly complex three-dimensional flowfield, containing a number of three-dimensional shock surfaces and shock wave-plume boundary interactions.

A majority of currently adopted multiple-nozzle plume models are based on a single nozzle flowfield. An equivalent engine is defined that has the combined thrust of all the individual engines to model such a twin/multi nozzle plume flowfield at far enough distance downstream where the merging process is near completion.

Despite the interest in the multi-nozzle flows, there exists only a small experimental database and very little effort has been made along analytical and theoretical lines. This thesis makes a significant step towards the understanding and prediction of under-expanded twinjets through experiments, quantitative and qualitative analyses.

A three-dimensional CFD code, developed for the DRA, was used to predict this highly complex three-dimensional flowfield. Outputs from the CFD code formed an invaluable tool in visualising flowfield structures. Experimental data were used to validate this code to improve overall accuracy.

5.2 ROCKET MODELS

The Mach 5 (TM5) and Mach 3 (TM3) twinjet nozzles were used to study the complex three-dimensional flowfield. Each was capable of rotation about the axis of symmetry to give the two orthogonal planes, x-z and y-z (see Figure 5-4). Where the z-axis points downstream, the x-axis links the two nozzle centrelines and the y-axis runs in between. Three single equivalent-thrust nozzles, the Mach 5 (SM5M) and (SM5), and the Mach 3 (SM3) nozzles were also used for this thesis.

5.3 EXPERIMENTAL STRATEGY

5.3.1 Visualization

There is an obvious lack of published Schlieren images on co-flowing twinjets despite their obvious application. A significant programme was therefore undertaken to take such photographs under a range of conditions and in different planes of views.

5.3.2 Quiescent Medium Tests

Quiescent runs using different nozzles were undertaken. This was to investigate the twinjet plume structure in absence of a freestream, especially the secondary flow region between the two primary jets and the accompanying impingement shock surface. Different in-

jection pressure and nozzle geometry were used to test the behaviour of this shock surface in relation to the pressure ratio, exit Mach number and nozzle geometry.

An array of instruments was used in these experiments. In addition to the Pitot probes used in co-flow runs, the RPT probe was also used to achieve improved spatial and frequency response. Data were sampled by the HP 9836 at 7.5 kHz and also at a higher sampling rate of up to 1132 kHz by the ADTEK 502, to resolve high frequency contents of the flowfield, especially in the shear layer. Heat transfer probes were deployed to obtain heat flux signature of the flowfield and attempts were made to deduce the flow total temperatures from these probes.

5.3.3 Co-flow Tests

The first experiments were with the Mach 5 (TM5) twinjet rocket with N_2 injecting into the N_2 hypersonic Mach 7 freestream. In addition, to test the effect of an injected gas with a different density and gas constant, H_2 injection was also used.

The single equivalent nozzles were subjected to the same run conditions as the twin nozzles. Comparisons were made downstream to gauge the validity of modelling a complex three-dimensional flowfield with an equivalent, axisymmetric nozzle of the same geometry and vacuum thrust.

Schlieren photographs were taken for most of the runs. Data were again sampled by the HP 9836 at 7.5 kHz and also at a higher sampling rate of up to 1132 kHz by the ADTEK 502.

5.4 SCHLIEREN PHOTOGRAPH VISUALISATION

5.4.1 Quiescent Injection Schlieren Photography

Figure 5-5 shows a series of Schlieren photographs taken at different injection pressures in a quiescent medium. The degree of interaction between the two jets with increasing injection pressure can be seen clearly. It was found that once the jets impinged, the angle of

the impingement shock surface formed did not seem to change as the injection pressure was further increased. This is investigated in detail in Section 5.8. It can be seen that the flow features on the two orthogonal planes are significantly different. Schlieren photographs taken at three different injection pressures were enlarged and shown in Figure 5-6 and Figure 5-7 for the x-z and y-z planes respectively. Figure 5-8 shows the Mach 3 (TM3) twinjet nozzle with increasing injection pressure. It can be seen that impingement has occurred at a lower injection pressure (or lower N) due to a greater degree of under-expansion than the corresponding Mach 5 twinjet as a result of a lower exit Mach number.

5.4.2 Co-flow Schlieren Photography

Co-flow Schlieren photographs of the twinjets taken on the two orthogonal planes are shown in Figure 5-9 to Figure 5-12, which show some familiar features of an under-expanded plume structure in a hypersonic freestream. In both photographs, the primary barrel shocks of the individual jets and the plume shocks are clearly visible. The main features of the resulting plume structure can be deduced with the help of these Schlieren photographs and some knowledge of the general structures of a single under-expanded plume. Schematic illustrations of a typical twin nozzle plume flowfield are shown in Figure 5-15.

Schlieren photographs for the Mach 5 single and twinjet plumes with N_2 and H_2 injections are shown in Figure 5-9 to Figure 5-12. The shock locations for the twinjets were digitised and shown in Figure 5-16 and Figure 5-17. The reader should refer to Chapter 4 for digitised Mach 5 single jets.

5.4.3 Plume Structure from Schlieren Visualization

Mutual plume impingement of multiple jets leads to highly complex three-dimensional flowfields. In addition to the barrel shock observed in single plumes (and in the case of co-flow twinjets where plume shocks are also present), a third major shock feature, namely the impingement shock, forms as a direct result of the plumes colliding on the plane

of symmetry. A fourth shock feature, termed here the secondary barrel shock, can also be seen on the Schlieren images. The formation of this shock on the y-z plane is analogous to that of the barrel shock system in the axisymmetric single nozzle case.

Figure 5-18 shows an enlarged image of the region near the impingement point on the x-z plane. Background gas is entrained into the region bounded by the impingement shock surfaces and mixes with the shock compressed injection gas. The gas enclosed by the impingement shocks is termed the secondary jet. This consists of the entrained gas expanding through an imaginary duct formed by the impingement shock surfaces, and the injected gas from the primary jets. Mixing between the individual primary jets and the entrained gas takes place in this region. This is shown in the figure integrated turbulent density gradient fluctuations across the region.

It can be seen that the barrel shocks of the primary jets are not axisymmetric before the two jets impinge. This is mainly due to two effects: firstly, in the co-flow case, due to the presence of a relatively large base area, the barrel shocks near the centreline are not affected by the freestream to such an extent if the nozzles extend to the corner of the base. Since the co-flow plume scale is a function of the freestream pressure, the diminished effect of the freestream on the flowfield near the centre produces a relieving effect on the barrel shocks. Secondly, from the central portion of the twinjet, fluid is entrained into the shear layers adjacent to the jets due to viscous momentum transfer from the jet to the background gas in the base region assisted by the ejector action giving rise to a driving static pressure gradient. However, the fluid entrained is unable to be replaced by the surrounding freestream gas due to the base. Therefore the static pressure in this region is generally lower than the background. Note that there is an adverse pressure gradient in the downstream direction along the z-axis in the base region near the impingement point. If this pressure gradient is large enough, back flow may result.

Turbulent mixing takes place in the secondary jet, which is reflected in the Pitot pressure traverses across this region. This will be discussed later with the aid of Pitot pressure relative turbulence intensity plots.

Flow structures near the impingement region are sketched in Figure 5-19. Due to the shape of the primary jets near the exit, the resulting impingement locus is approximately hyperbolic. On the x-z plane, this shock can be seen to extend into the core region of the plume and forms two roughly flat impingement shock surfaces between the jets. The strength of this impingement shock weakens with downstream distance as the static pressure in the core decreases. This is evident in the Schlieren images taken around this area. On closer examination near the impingement region as shown in Figure 5-18, a second shock could be seen above the impingement shock. This was observed by Vick et al (1964) and its formation was not clearly understood. The author believes it may be due to bending of the impingement shock surface, which causes a local maximum in density gradient across the flowfield.

5.5 QUIESCENT RUNS

5.5.1 Plume Scale Analysis

Figure 5-5 shows the evolution of the Mach 5 twinjet with increasing injection pressure when the background pressure was kept at a constant level of 0.0127 bar. It can be seen that when the injection pressure is low, there is little interaction between the two jets. They behave essentially as individual or undisturbed primary jets. As the injection pressure increases, the primary jets expand further near the exit and begin to interact on the plane of symmetry. With the injection pressure raised to 19 bar, significant interaction can be seen to have taken place between the primary jets. The strength of this interaction increases as the injection pressure is increased further, and eventually the impingement shock is formed between the two jets.

Schlieren photographs were digitised using a high-resolution scanner. The digitised images were then fed into the image processor in Matlab and the shock positions were traced.

The quiescent plume scaling parameter L (see Chapter 4) was applied to the three-dimensional twinjet. The scaled plots on the x-z plane are shown in Figure 5-20 and Figure 5-21 for the Mach 5 (TM5) and Mach 3 (TM3) nozzles respectively. As clearly shown on both plots, the twinjet flowfield scales well under this parameter. Two scaled regular reflections can be seen: one corresponds to the reflection of primary barrel shock and the impingement shock on the x-z plane above the plane of symmetry, the other corresponds to the secondary jet regular reflection on the plane of symmetry.

The locations of the regular reflection for the primary barrel shock and the impingement shock on the x-z plane are in the region of,

$$\text{TM5 \& TM3 primary regular reflection } (x\text{-}z \text{ plane}): z_M = 0.9\ L$$

The regular reflections formed by the secondary jets are in the region of,

$$\text{TM5 \& TM3 secondary regular reflection } (x\text{-}z \text{ plane}): z_M = 1.4\ L$$

For the Mach 5 (SM5) single equivalent nozzle shown in Figure 5-22. The scaled regular reflections of this single equivalent jet are in the region of,

$$\text{SM5 regular reflection: } z_M = 1.1\ L$$

Compare this with the regular reflection of the secondary jet: the larger than expected value for the secondary jet is believed to be due to the fact that the hypothetical source of this jet was located further downstream than the single equivalent nozzle.

5.5.2 Base Flow Between Primary Jets

Due to the complexity of the three-dimensional flowfield and the presence of the base region as part of the nozzle exit geometry, the primary jet flowfield of the twinjet is significantly asymmetric near the base region at the exit. For single jets, the structural dimensions of the plumes are a function of the pressure ratio N. In the case of a twinjet, the pressure distribution in the base region before impingement is a function of the azimuthal angle. This is due

to entrainment of gas near the nozzle base before the impingement that creates a low-pressure environment in this area. One would expect the base pressure in this region to decrease with increasing N until the entrained flow becomes choked, and that further decreases in injection pressure will then have no effect on the flow exit turning angle at exit. To test this hypothesis, the flow exit angles for the Mach 5 twinjet were digitised and compared.

Figure 5-23 shows a the flow exit angle plotted against the pressure ratio N. This angle was chosen because single jet experiments have shown that there is a strong correlation between the two. At low pressure ratios, there is no visible interaction between the two primary jets as seen on Schlieren photographs. However, noticeable differences in exit angles as shown in the figure indicate that interaction between the two primary jets seems to have started at low values of N. As the pressure ratio increases, the difference in exit angles between the upper jet surface and the lower remains. When the pressure ratio is increased further, the flow in the base region has to overcome a stronger adverse pressure gradient across the impingement region and eventually entrainment ceases. This can be seen as the upper and lower exit angles approach one another with increasing injection pressure. As N is further increased, θ_{eu} is expected to become greater than θ_{el}.

5.5.3 Backflow Prior to Impingement

There is the question of whether the adverse pressure gradient near the impingement region is high enough to cause significant backflow. Experiments were carried out where nylon bristles were attached to a small gauge metal wire and placed between the two nozzles adjacent to the base. They were initially pointing downstream before the runs. Schlieren photographs were taken at increasing injection pressures in quiescent. Typical run time for the experiment was in the region of one second, which was assumed adequate for the bristles to respond.

The Schlieren photographs taken showed no such backflow had occurred over a range of pressure ratios. It is believed that the entrained flow between the jets was given enough

momentum by the high-energy primary jet to overcome the pressure gradient across the impingement region.

5.5.4 Quiescent Pitot Pressure Measurements

Figure 5-24 shows a typical Pitot pressure signal obtained from a traverse across the *x*-*z* plane at 40 mm downstream of the nozzle exit. Before the probe experiences any flow it indicates the test section pressure at 0.0127 bar. The first feature of the plume indicated on the traverse is the shock layer in the region of –35 mm to –31 mm. At the outer edge of the shock layer, speed of the flow is low. Therefore the probe measures roughly the flow total pressure. The shock layer consists of an inviscid region adjacent to the barrel shock and a region known as the shear layer, where mixing takes place between the entrained background gas at high static pressure and temperature, and the over-expanded hypersonic injected gas at a relatively low static pressure and temperature. The speed of the mixture and its static density increases further into the shear layer, causing a corresponding increase in the measured Pitot pressure.

The peak in Pitot pressure at –32.5 mm corresponds to the inviscid jet boundary, which divides the shock layer into an outer layer characterised by turbulent mixing, and a inner shock layer dominated by the inviscid shock-compressed injection gas. Within this inner shock layer, there is a positive static pressure and density gradient normal to the flow. This density gradient causes the Pitot pressure to drop across this layer. Gas particles in this layer are turned inwards by the centrifugal force provided by the static pressure gradient across. As a result, a series of right running compression waves is emanated at the jet boundary. These compression waves coalesce downstream to form the primary barrel shock, which is indicated –31 mm. In the core region, Pitot pressure is approximately proportional to the static density of the flow, which increases as the probe travels further upstream of the expansion waves originating from the nozzle lip.

Up to this point, the twinjet flowfield exhibits similar features to a single under-expanded jet. However, at –6 mm a feature unique to multi-nozzle plume known as the impingement shock forms. This shock forms as a result of the interaction and collision of the two primary jets. Within this region, shock compressed injection gas and entrained gas from the test section mix to form the secondary jet. This is indicated by a sudden rise in the measured Pitot pressure in this region. The dip in the centre of the pressure signal is due to incomplete mixing between the entrained low-density gas and the surrounding injected gas with the momentum concentrated off-axis.

On the *y*-*z* plane, the secondary jet dominates the flowfield. Figure 5-25 shows the Pitot pressure signal on this plane at the same downstream location as Figure 5-24. It can be seen that the secondary jet is still expanding outwards into the background and there is no trace of shocks at this downstream location.

Figure 5-26 shows the Pitot pressure signal on the *x*-*z* plane under the same run conditions, but at 100 mm downstream. It can be seen that the primary barrel shock is well defined with a distinctive Pitot pressure variation across it. In addition, the secondary barrel shock has emerged on the *y*-*z* at this station as shown in Figure 5-27. Note that the width of the secondary jet has now surpassed the combined primary jets on the *x*-*z* plane.

5.5.5 Quiescent Heat Transfer Measurements

Heat flux profiles across the plume were measured using a set of three thin-film heat transfer probes. Note that heat flux to blunt bodies in a hypersonic flow is a function of both the Pitot pressure and the flow total temperature (see Chapter 3), therefore these probes are able to reveal features that Pitot pressure probes alone are not able to resolve. Figure 5-28 shows the heat flux signal measured by the *hot* heat transfer probe during a traverse across the *x*-*z* plane of the Mach 5 (TM5) twinjet with 100 bar gauge injection at 40 mm downstream. In the region –40 mm to –36 mm, the Pitot pressure measurement in Figure 5-24 shows an almost constant level. However, the measured heat flux is clearly varying. This is believed to

be mainly due to cooling of the probes by radiation and conduction along the quartz substrate (effect of forced convection by the background gas is believed to be negligible).

In the plume core, the heat flux essentially follows the square root of the Pitot pressure variation. Impingement shock is indicated by a discontinuous increase in heat flux at –6 mm. Gas on the secondary jet side of the impingement shock has a relatively higher density than on the primary jet side; this increase in density results in a corresponding increase in the measured heat flux as shown in the region from –6 mm to the centreline.

The heat flux fluctuation equation in Chapter 3 was solved at 40 mm downstream for the Mach 5 (TM5) twinjet. Figure 5-29 to Figure 5-34 show the resulting fluctuating components on the x-z and y-z planes. The total temperature fluctuation shown in Figure 5-29 is small in the primary jet and increases slightly in the secondary jet near the centreline. However, relatively large fluctuations in total temperature can be seen in the shear layer as a result of turbulent mixing. The fluctuations in the heat transfer coefficient shown in Figure 5-33 clearly show the difference in the level of turbulent activities between the secondary jet and the primary jet.

On the y-z plane, the fluctuating total temperature shown in Figure 5-30 captures the turbulent nature of the secondary jet. The fluctuation in the convective heat transfer coefficient shown in Figure 5-34 can be seen to increase as the probes travel further into the core of the secondary jet. This can be explained by noting that the total temperature in this region is expected to be constant, so the convective heat transfer coefficient essentially follows profile of the measured Pitot pressure.

5.5.6 Quiescent Total Temperature

Total temperatures of the Mach 5 (TM5) twinjet in quiescent were obtained from the measured substrate temperature and heat flux signals of the three thin-film heat transfer probes (see Chapter 3). Figure 5-35 shows the total temperature of a 100 bar gauge injection of N_2 in quiescent obtained from a traverse across the plume on the y-z plane at 100 mm

downstream. It is in good agreement with the measured core total temperature shown in Figure 2-9 in Chapter 2, using stationary heat transfer probes.

5.5.7 Quiescent Shear Layer

This study was the first of its kind on the behaviour of twinjet shear layers. For a twinjet, the three-dimensional shear layer is expected to be different to that of a single equivalent jet as a large proportion of the injected gas is in the secondary jet. On the *y-z* plane, the high static pressure in the secondary jet as a result of two impinging plumes can lead to a significantly higher spreading rate on this plane (see Figure 5-36). This increases the amount of background gas entrained in the shear layers and facilitates subsequent mixing with the injected gas.

To capture turbulent shear layers in quiescent, the RPT Pitot pressure probe was used in order to achieve the best spatial and frequency resolution. Data were sampled at 1132 kHz and an anti-aliasing filter with a 66 kHz cut-off was used to extract information within the confident, distortion-free bandwidth of the Kulite pressure transducer. Traverses were carried out at several downstream stations at a slightly lower speed than normal to maximise the amount of data captured within the shear layer. For a typical traverse, up to 15 000 data-points could be recorded by the RPT over a typical shear layer thickness in the order of 10 mm. Fluctuating Pitot pressures were normalised in the same manner as in Chapter 4 to give the corresponding relative Pitot pressure turbulence intensities.

Figure 5-37 to Figure 5-39 show the Pitot pressure signals obtained from the RPT probe at three representative downstream locations on the *x-z* plane (note that the fluctuation in the primary jet core around the region of –10 mm is believed to have been caused by disturbances originating from the nozzle wall). In order to compare the turbulence intensities at these downstream locations, the relative Pitot pressure turbulence intensities are shown on a single plot in Figure 5-43. Local peaks in the low intensity region from –27 mm to the centreline correspond to the impingement shock locations, which separate the secondary jets to

the right of the shocks and the primary jets to the left. Although turbulent mixing took place within the secondary jet, the mean Pitot pressure level within this region was relatively high, therefore the normalised relatively intensities shown are relatively low.

A noticeable increase in intensities within the shear layer could be seen in the region of –40 mm to –30 mm. In this region, the shock compressed primary jet mixes with the entrained background gas. This together with a relatively low mean Pitot pressure level gives a considerably large increase in turbulence intensities.

Figure 5-41 to Figure 5-43 show the Pitot pressure signals on the *y*-*z* plane with the corresponding turbulence intensities shown in Figure 5-44 at the same downstream stations. The relatively high intensities in the secondary jet can clearly be seen in the region around –30 mm and the centreline. The turbulence intensities for the Mach 5 (SM5M) single equivalent nozzle are shown in Figure 5-45. The fluctuations in Pitot pressure in the plume core of the single jet are low as expected. While in the shear layer, large fluctuations can be seen due to mixing. The intensities in the shear layer are relatively high compared to that of the twinjet; this is because for the twinjet, less gas is in the outer shear layer, as a large proportion of the injected gas is between the two primary jets.

5.6 CO-FLOW INJECTION IN A MACH 7 FREESTREAM

5.6.1 Co-flow Pitot Pressure Measurements

Co-flow Pitot pressure measurements at five downstream locations are shown in Figure 5-46 and Figure 5-47. The corresponding positions are marked on the Schlieren images taken under the same conditions to indicate the relative positions of the Pitot traverses. It can be seen from the plots that the Pitot pressure profiles on the *x*-*z* and *y*-*z* planes show a fair degree of similarity at about 100 mm downstream. Both then proceed to approach that of the single equivalent jet at 150 mm, approximately 5 nozzle diameters downstream.

Features such as plume shocks, barrel shocks and shear layers can be seen on the measured Pitot pressure profiles, which are also present in single nozzle plumes; whereas features such as the impingement shock and the secondary flow between the jets are unique to twin nozzle flowfields.

Figure 5-48 shows a typical Pitot pressure signal for the Mach 5 (TM5) twinjet in the Mach 7 freestream at 40 mm downstream. Within the freestream region between –40 mm and –30 mm, the Pitot pressure remains approximately constant. This indicates that the rocket nose shock introduced little entropy gradient downstream. Significant pressures rise at about -30 mm marks the plume shock where the freestream gas is shock-compressed to a higher density. A drop in Pitot pressure follows this as the probe enters the shear layer. Mixing between the freestream and injected gas, together with the low-density gas from the rocket body boundary layer, resulted in significant entropy variation in this region. This is shown by the dip in Pitot pressure in the shock layer. Once past the inviscid injected gas boundary at –22 mm, the measured Pitot pressure drops as the gas density decreases across this shock. Passage through the barrel shock (~ -20 mm) is shown by a sharp fall in the measured signal. Once into the jet core, the Pitot pressure rises again as the probe passes through a series of right-running characteristics of the expansion waves originating from the upper lip of the nozzle exit. The measured Pitot pressure peaks on the centreline then falls as the probe again goes through a series of left-running characteristics of the expansion waves originating this time at the lower nozzle lip. There is a sharp rise in Pitot pressure at about -4 mm when the probe traverses across the impingement shock surface. The turbulent secondary jet between the impingement shock surfaces follows this, where the shock-compressed injection gas at relatively high density mixes with the entrained gas at a lower density, and accelerates this gas to supersonic speed.

Further downstream, the secondary jet dominates the flowfield. Figure 5-50 shows the Pitot pressure signal measured at 100 mm downstream. The primary jet is just noticeable in

the region -16 mm < x < -14 mm. The extent of the secondary jet can be seen to dominate the central region up to -14 mm.

Figure 5-51 shows the Pitot pressure profile on the y-z plane at 100 mm. Here the plume shock is indicated at -38 mm. This is followed by a relatively thick shear layer, which terminates at the secondary barrel shock at approximately -11 mm.

5.6.2 Co-flow Heat Transfer Measurements

Figure 5-49 shows the heat flux signal at 40 mm downstream. Within the nose-shock compressed freestream region, heat flux falls gently due to a decreasing freestream total temperature as a result of boundary cooling in the gun tunnel barrel. A sudden increase in density behind the plume shock causes the heat flux to increase discontinuously across the shock at -29 mm.

The heat flux signal then follows a gentle fall within the region dominated by the plume shock compressed freestream gas in the region –29 mm to –26 mm.

The shear layer starts at around -26 mm where considerable cooling of the probes is assisted by turbulent mixing in this region. This mixing region terminates at the inviscid jet boundary in the region of –22 mm. The measured heat flux decreases across this region due to a decreasing density. The barrel shock is marked by a decrease in the measured heat flux as the corresponding convective heat transfer coefficient decreases across the shock. Within the core region, the total temperature remains roughly constant and the heat flux is therefore dominated by the convective heat transfer coefficient. The impingement shock is shown as an increase in heat flux. Across this shock surface, the convective heat-transfer coefficient increases as a function of the highly turbulent Pitot pressure variation in this region. Heat flux profiles further downstream at 100 mm are shown in Figure 5-52 and Figure 5-53 for the x-z and y-z planes respectively. Shear layer and secondary jet can be seen to dominate on both planes.

Figure 5-60 to Figure 5-71 show the measured substrate temperature and the corresponding heat flux of the heat transfer probes. When the heat flux is zero, the corresponding substrate temperature is then the flow total temperature at that particular location. This provides a means to obtain total temperatures at discreet locations. However, to obtain a continuous variation across the plume flowfield, at least two thin-film probes are needed (see Chapter 3).

5.6.3 Co-flow Total Temperature

Co-flow plume total temperatures were deduced from the heat transfer probes using a regression process detailed in Chapter 3. Remember that the mean levels for both the freestream and the injection total temperatures varied to a certain degree during a traverse, therefore the total temperature deduced from the heat transfer probes would be affected. However, since this variation was essentially the same from run to run, comparisons could still be made for the twinjet and single equivalent nozzles.

Figure 5-72 shows the deduced total temperature for the twinjet at 100 mm downstream. It can be seen that the variations on the x-z and y-z planes closely follow each other. The region between -60 mm and -38 mm is dominated by the rocket nose shock-compressed freestream gas. The measured level and gentle fall in total temperature is comparable to an earlier study by Buttsworth (1994). The deduced total temperature in the shear layer can be seen to vary linearly from the freestream value to that of the injected gas. Note that the total temperature of a flowfield is unaffected by shocks, expansions or compressions, and should have constant values when in flow originating from the freestream or nozzle. Thus changes could only be present when the two streams are mixing or in regions where viscous dissipation take place. In the shear layer, mixing between the barrel shock compressed injection gas and the plume shock compressed freestream takes place.

Figure 5-73 shows the deduced total temperatures at 250 mm downstream. Similar profiles for the three nozzle configurations can be seen.

The fact that the total temperature plots of the twinjet and the single equivalent jet are similar seems to support the hypothesis that the secondary jet was not significantly contaminated by the freestream. This explains the apparent independence of the impingement shock to freestream conditions and is analysed in detail in Section 5.8.3.

Note that the freestream flow ceased soon after the probes were out of the core of the primary jet, therefore signals past 20 mm should be justifiably ignored.

5.6.4 Co-flow Shear Layer

Pitot pressure relative turbulence intensities for N_2 and H_2 injections into the Mach 7 freestream were obtained by the BPT Pitot probe sampled at 1132 kHz. Intensity plots are shown in Figure 5-83 and Figure 5-84 for the N_2 injection at 100 mm and 250 mm downstream respectively. The corresponding Pitot pressure signal is shown in Figure 5-74 to Figure 5-76 and Figure 5-77 to Figure 5-79. Turbulence intensities at 250 mm downstream for the H_2 injection are shown in Figure 5-85, with the corresponding Pitot pressure measurements shown in Figure 5-80 to Figure 5-82.

Features of a typical intensity plot shown in Figure 5-83 on the x-z plane can be analysed as follows: the peak around -42 mm corresponds to the plume shock, which is followed by the inviscid freestream region behind this shock. The beginning of the shear layer (~ -30 mm) is marked by a significant increase in turbulence intensity. As the probe enters the inviscid jet boundary at approximately -22 mm the corresponding intensity decreases. This is followed by two successive peaks at around –15 mm and –12 mm, which correspond to the primary barrel shock surfaces. The BPT probe then enters the secondary jet region, which is dominated by turbulent mixing between the entrained background gas and the injected gas. The turbulent intensity increases near the centreline where most of the mixing takes place.

Note that the overall intensity is lower than quiescent injection for the same injection pressures. This is mainly due to high mean Pitot pressure level for the co-flow runs.

Compare the turbulence intensity levels of the N_2 and H_2 injections at 250 mm downstream shown in Figure 5-84 and Figure 5-85. It can be seen that by injecting H_2 in the N_2 freestream, the overall intensity level increases. This is expected, as mixing gases of significantly different velocity and density inevitably results in higher turbulence.

5.7 COMPARISON WITH SINGLE EQUIVALENT NOZZLE

5.7.1 Rocket Injecting in Quiescent

Figure 5-86 to Figure 5-88 show the Pitot pressure profiles for the twinjet and the single equivalent jet in quiescent at three downstream locations. At 40 mm, the Pitot pressure profile of the single jet is significantly different to those of the twinjets. Further downstream at 60 mm, the Pitot pressure levels of the single jet and the twinjet on the y-z plane can be seen to approach some degree of similarity. At 100 mm downstream, the agreement between the three measured Pitot pressure profiles in the secondary jet region is remarkable. It is interesting to see that the measured Pitot pressure of the twinjet on the y-z plane follows closely to that of the single jet at this location.

5.7.2 Rocket Injecting in Mach 7 Freestream

Pitot pressure profiles up to 50 mm downstream are shown in Figure 5-89 to Figure 5-91. Flowfield on the two planes can be seen to be significantly different. However, at locations further downstream (Figure 5-54, Figure 5-56 and Figure 5-58), the similarities improve with the single equivalent nozzle approaching the profile of that of the twinjet flowfields on both planes.

Pitot pressure traverses for H_2 injections at the same downstream locations are shown in Figure 5-55, Figure 5-57 and Figure 5-59. Similarities between the twinjet and the single equivalent nozzle are not observed over this range.

A normalised standard deviation factor σ_N was introduced to indicate the degree of correlation between the different Pitot pressure profiles at various downstream stations. This factor could be expressed as,

$$\sigma_N = \frac{1}{\overline{p_{ti}}} \sqrt{\overline{\sum \left(p_{ti} - \overline{p_{ti}}\right)^2}}$$

Where subscript i refers to: twinjet on x-z plane, twinjet on y-z plane, and single equivalent jet at a particular radial co-ordinate.

This normalised deviation factor was calculated for three downstream locations and shown in Figure 5-92 and Figure 5-93 for N_2 and H_2 injections respectively. It can be seen that the H_2/N_2 case in general has a higher deviation between the three Pitot pressure profiles than the N_2/N_2 case. This is believed to be due to the fact that in the secondary jet of the H_2 injected plume, a significant amount of the freestream N_2 gas was entrained into the region. This entrained flow played an important part in determining the structure of the flowfield downstream. As the entrained N_2 gas from the freestream was compressed and expanded downstream, it mixed with the H_2 injected gas. This mixing was absent in the single equivalent nozzle case, where the jet core flow consisted of only H_2 gas.

This shows that the single equivalent nozzle concept gives a less accurate representation of the twinjet when the injected gas is significantly different to the gas in the freestream.

5.8 IMPINGEMENT SHOCK AND SECONDARY JET

5.8.1 Influence of Impingement Region on Plume Structure

Effects due to the presence of a impingement shock surface on the primary jet shock layer were investigated by blocking the lower Mach 5 twinjet nozzle (the resulting jet from the upper nozzle only is termed here the *upper-jet*). The resulting barrel shock positions were digitised and compared to twinjet quiescent injections. Figure 5-94 shows the barrel shock positions for the upper-jet and the normal twinjet.

Barrel shock positions for the upper-jet were normalised by the quiescent plume scale L and is shown in Figure 5-95 to give,

$$\text{Mach 5 (TM5) upper-jet regular reflection: } z_M = 1.1\ L$$

This is the same as the Mach 5 (SM5) single equivalent jet as expected since nozzles were geometrically similar. In the case of the twinjet, the primary barrel shock reflections were due to the interception of the primary jet barrel shock and the impingement shock and were a function of the geometry and running condition of the twinjet and the spacing between the two nozzles.

5.8.2 Inviscid Impingement Shock Locus

On the impingement plane, maximum interaction between the two primary jets occurs along the impingement line, which represents the locus of intersection of the plumes. If geometry and flow conditions are such that an oblique shock can turn the flow into the plane of symmetry, then the inviscid plume impingement line represents the shock attachment line.

Near the impingement region, the primary jets expand approximately in a conical manner. As an first order approximation, the impingement locus could be modelled as a hyperbola between two intersecting cones, where the vertex angles equal the nozzle exit gas turning angle θ_e (see Figure 5-96). By geometry, the impingement locus can be expressed as,

$$\tan^2\theta_e\left(z+\frac{D_e}{\tan\theta_e}\right)^2 - y^2 = \left(\frac{S}{2}\right)^2$$

Assuming ideal gas relations and an isentropic expansion up to the impingement region, the plume exit angle can be related to the background pressure, nozzle exit Mach number and metal angle, and injection pressure as follows,

$$\theta_e = \nu_b - \nu_e + \theta_N$$

$$\nu_e = \sqrt{\frac{\gamma+1}{\gamma-1}}\tan^{-1}\sqrt{\frac{\gamma-1}{\gamma+1}\left[M_e^2-1\right]} - \tan^{-1}\sqrt{M_e^2-1}$$

$$\nu_h = \sqrt{\frac{\gamma+1}{\gamma-1}}\tan^{-1}\sqrt{\frac{\gamma-1}{\gamma+1}\left[\frac{2}{\gamma-1}\left(N^{\frac{\gamma}{1-\gamma}}-1\right)-1\right]}-\tan^{-1}\sqrt{\frac{2}{\gamma-1}\left(N^{\frac{\gamma}{1-\gamma}}-1\right)-1}$$

The calculated impingement locus is superimposed onto the CFD Mach number contour and shown in Figure 5-97. It can be seen that the agreement is good up to the point where the impingement line joints the freestream.

5.8.3 Impingement Shock Surface Scaling Parameters

The digitised impingement shock surfaces for the Mach 5 (TM5) and Mach 3 (TM3) twinjets are shown in Figure 5-100. Note that the surface angle of the impingement shock is little affected by the stagnation injection pressure to background pressure ratio. Vick et al (1964) studied highly under-expanded Mach 5 single jet impinging on a flat surface over a range of pressure ratio N from 250 000 down to 20 000. They also noticed that the impingement shock angle was not affected by the pressure ratio to any significant degree.

The appropriate scaling parameters for the two axes along and across the nozzles are found empirically which can be expressed as,

$$\textit{along the } x\text{-axis: } \frac{S}{D_e}M_e$$

$$\textit{along the } z\text{-axis: } \frac{S}{D_e}M_e^2$$

Figure 5-101 shows the scaled impingement shock for the Mach 5 (TM5) and the Mach 3 (TM3) twinjets with N_2 injections in quiescent and in the Mach 7 freestream.

5.8.4 Secondary Jet Analysis

The secondary jet downstream of the impingement region was dominated by turbulent mixing between the entrained gas and the impingement shock compressed injection gas. The shock structure and turbulent fluctuation of the flow in this region were captured by Pitot pressure probe traverses along the x-z plane.

Figure 5-36 shows a view on the crossflow plane of a Mach 5 rarefied twinjet in quiescent with $N = 250$ (Welsh, 1997). This electron-beam-fluorescence image was taken downstream of the primary barrel shock reflections and indicates a high concentration of gas around the secondary jet. The side branches were due to the secondary jet expanding into the quiescent medium, as a result of high static pressure in the central region induced by the impinging primary jets.

To investigate the frequency contents of the secondary jet, the RPT Pitot pressure probe was placed on the centreline behind the impingement region and a total of 50 000 datapoints were taken over the steady injection period. The spectral density of the filtered signal was calculated using a 9162-point FFT with a 4096-point Hanning Window. Figure 5-98 shows the power spectrum at 40 mm downstream. It can be seen that the spectrum is broadband in the frequency range up to 35 kHz and has a relatively distinction peak near 60 kHz. Further downstream at 60 mm, as shown in Figure 5-99, this peak seems to have shifted to a lower frequency at around 50 kHz. This is believed to be an indication of organised structures in the secondary jet region and agrees with observations made by Vick et al (1964) with an under-expanded jet impinging on a parallel surface. The shift in frequency is believed to be caused by the enlargement of turbulent eddies as the mixing region in the secondary jet expanded downstream.

5.9 COMPARISON OF CFD WITH EXPERIMENTAL RESULTS

5.9.1 Introduction

CFD study on the three-dimensional Mach 5 twinjet was carried out in collaboration with the DRA CFD team (Gilmore, 1997). The DERA three-dimensional Navier-Stokes solver code TINA (Thermochemical Implicit Non-equilibrium Algorithm) was used for this purpose. The code was based on the methodology of Gnoffo (1990) and was a 3D, multi shock, TVD, point implicit, second order accurate, time marching code. Inviscid terms of the

Navier-Stokes equations followed the approximate Riemann solver of Roe (1981). The second order formulation used symmetric flux limiters of the MinMod form to maintain the TVD nature of the code (Yee, 1987). The viscous terms were represented by a central difference formulation of the thin layer equations. Transport data for viscosity, thermal conductivity and diffusion coefficients were computed using a standard combination of Blottner curves fits and the semi-empirical formulae of Eucken, Wilke and Lee. Convergence was enhanced by applying relaxation factors to inviscid and viscous terms.

CFD mesh-grids were generated by TAGG (Topology and Algebraic Grid Generator). The crossflow plane was divided into 5 regions each of 3 000 cells; this, together with 8 streamwise planes, gave a total of 294 000 cells. A three-dimensional plot of the mesh grid is shown in Figure 5-102 and the cross-flow grid system is shown in Figure 5-103.

The calculations were carried out on a Silicon Graphics Power Challenge XL and took approximately five days per simulation depending on mesh density.

Perfect gas parameters were used for N_2. Rocket base region was specified as symmetry condition (i.e. no-slip condition was not specified on the base). A *top-hat* jet input profile was adopted and turbulence modelling was by means of the Baldwin-Lomax Algebraic model.

Freestream and rocket exit conditions are given in Table 1. The rocket body flowfield, including the conical rocket nose shock and the relatively thick rocket body boundary layer were ignored. The effect of this on the CFD prediction is discussed in subsequent sections.

Parameters	Freestream	Parameters	Jet
M_∞	7.1	M_e	5
$P_{0\infty}$	69.9 bar	P_{0c}	92.96 bar
P_∞	1.527 kPa	P_e	17.57 kPa
T_∞	79.8 K	T_e	50 K
W_∞	1293.1 m/s	W_e	720.82 m/s

Table 1 CFD freestream and rocket injection conditions

5.9.2 CFD Results

Post analyses were carried out on a PC in Matlab. Data was first divided into manageable sections due to computer memory limitations, then converted into ASCII format. They were subsequently processed in Matlab to generate multi-dimensional matrixes that could be used to obtain three-dimensional plots. CFD simulated profiles were compared with experimental data at downstream locations to validate the underlying code and assumptions.

On the x-z plane, the predicted result from CFD shows a primary barrel shock regular reflection at z = 120 mm on the x-z plane and a secondary barrel shock regular reflection at z = 165 mm. This compares favourably with experimental measurements at z = 110 mm and z = 170 mm respectively.

Results are presented in Figure 5-104 to Figure 5-107 on the x-z and y-z plane together with cross-sectional values at selected downstream locations. Figure 5-108 shows the computed contours of Mach number, relative static pressure and density distributions on the x-z and y-z planes respectively. Figure 5-109 to Figure 5-126 show the distributions on the x-z cross-sectional plane at six downstream locations.

5.9.2.1 Mach Number Distribution

Figure 5-104 shows the Mach number contours on the x-z plane. The expected structures of shocks and regular reflections deduced from experimental means are clearly visible on the CFD contours.

Prior to impingement, individual jets expand in a non-axisymmetric fashion. Figure 5-108 clearly shows this uneven distribution of Mach numbers on the x-z plane near the base region prior to the impingement region. This apparent distortion of the jet plume is due to a combination of the presence of a nozzle base region and the mutual interaction between the two primary jets. A low-pressure region between the primary jets near the nozzle base region can be seen on the relative static pressure contours. The primary jets would be expanded to a

higher Mach number in this region and this subsequently leads to a strong impingement shock after the impingement region. This can be seen on the relative static pressure plot as the significant increase in static pressure across the impingement locus.

The Mach number distribution on the y-z plane reveals some interesting features. Near the corner of the rocket base, the freestream gas expands around the corner region through a series of Prandtl-Meyer expansion waves and is accelerated to around Mach 9. This gas is then shock compressed by the impingement shock to about Mach 5.5. However, if the rocket body boundary layer were included, a relatively slow moving flow from the boundary layer at low static density but high static temperature would replace this high speed gas.

Figure 5-13 and Figure 5-14 show Schlieren photographs taken near the nozzle exit with the Pitot probes in close proximity. Characteristics of the flowfield in this region could be deduced by means of the interaction between the probes and the rocket plume flowfield structure. Boundary layer on the rocket body can be seen near the exit on the x-z plane in Figure 5-13. On reaching the nozzle exit plane, gas inside the boundary layer was re-accelerated by the injected flow to supersonic speeds. However, on the y-z plane the boundary layer gas remained subsonic for a considerable distance downstream of the exit due the presence of the nozzle base. Therefore, information was able to travel upstream in this subsonic region and resulted in the boundary layer readjusting when the downstream shock structure was altered by the presence of the probes. This caused the boundary layer to separate from the rocket body near the nozzle exit and a separation shock was formed as a result.

5.9.2.2 Static Pressure Distribution

Shock strengths could be deduced from static pressure contours shown in Figure 5-108. The strength of the impingement shock can be seen to be almost twice as strong as the corresponding primary barrel shock at the same downstream locations on the x-z plane.

On the y-z plane (Figure 5-108) there are two high-pressure regions just downstream of the impingement locus. The high-pressure region just after the impingement shock locus on the centreline is due to the shock compressed injection gas. The high-pressure region off-centre is believed to be due to the barrel shock which further compresses the gas at high pressure from the impingement region.

5.9.2.3 Density Distribution

Schlieren photography depends on the first derivative of the density gradients normal to the knife-edge. CFD density distributions could therefore be compared with Schlieren images and a visual validation could be carried out. It can be seen on the y-z plane in Figure 5-108 that although the secondary barrel shock is clearly visible on the Schlieren images (see Figure 5-9), the presence of such a shock structure is not obvious on CFD contours (see Figure 5-108).

5.9.3 Pitot Pressure Profile Comparison

Figure 5-127 shows a comparison of CFD predicted and experimentally measured Pitot pressure levels on the centreline. The agreement between the two is remarkably good. Figure 5-128 to Figure 5-139 show the Pitot pressure comparisons on the x-z and y-z planes at downstream locations. The agreements are reasonably good despite the rocket nose shock and body boundary layer were neglected in the CFD computation.

It is believed that the main cause of the discrepancies between the CFD and experimental results is induced by the lack of inclusion of the rocket body boundary layer. The displacement thickness of this boundary layer was about 6 mm near the exit plane, which amounts to about 20 per cent of the nozzle exit diameter and could cause considerable realignment of downstream flow structures.

5.9.4 Significance of Rocket Base Region in Plume Modeling

Correct modelling of the base region is essential to accurately predict the initial expansion of the jets, location of the impingement shocks and the radiation intensity in this region. Comparison of predicted profiles with and without this base region as part of the CFD model is shown in Figure 5-141. It can be seen that downstream profile alters significantly if the base region is modelled.

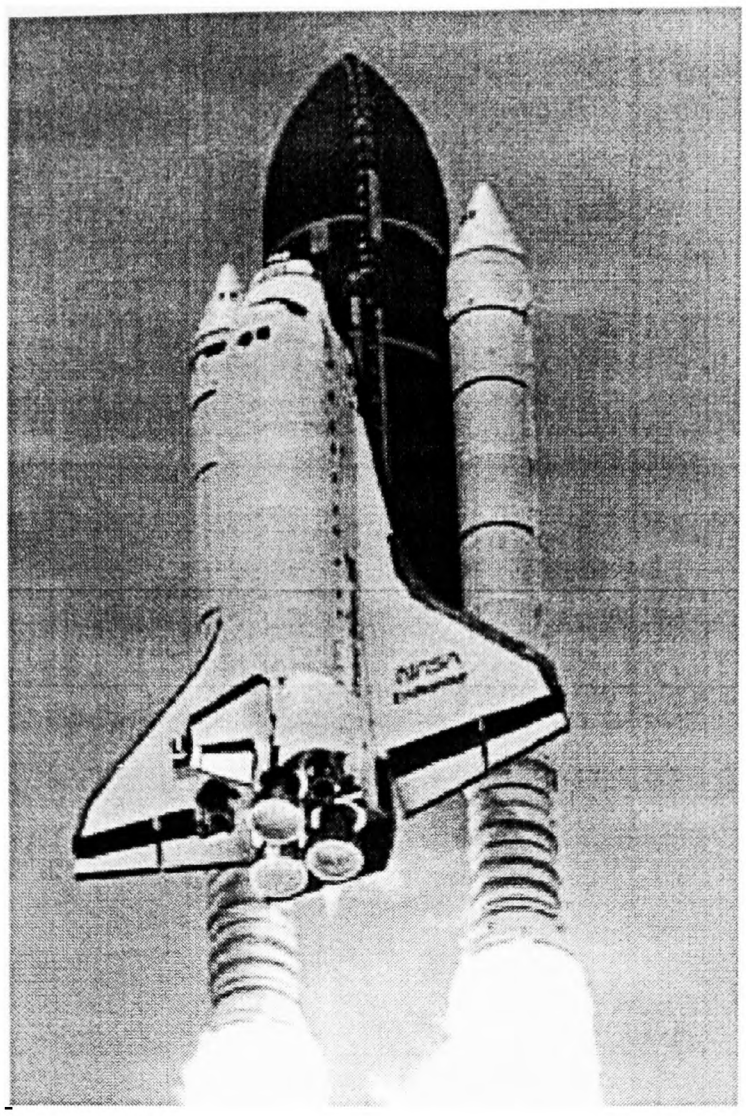


Figure 5-3 Twin booster rockets on Space Shuttle Endeavour at lift-off *(NASA Photographic Database)*

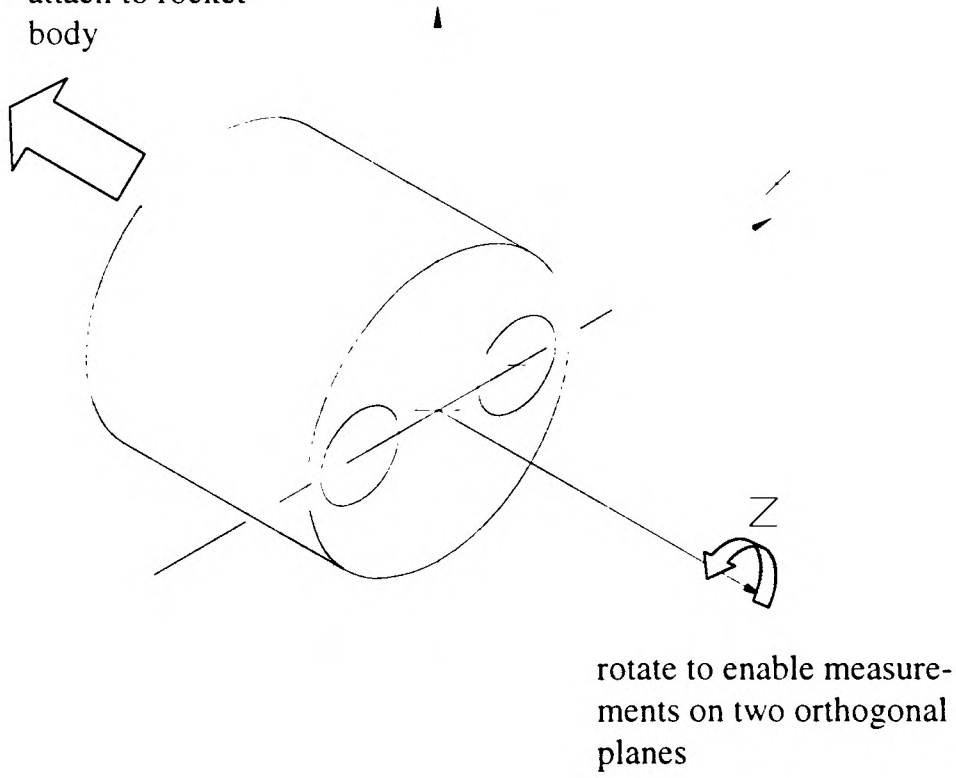
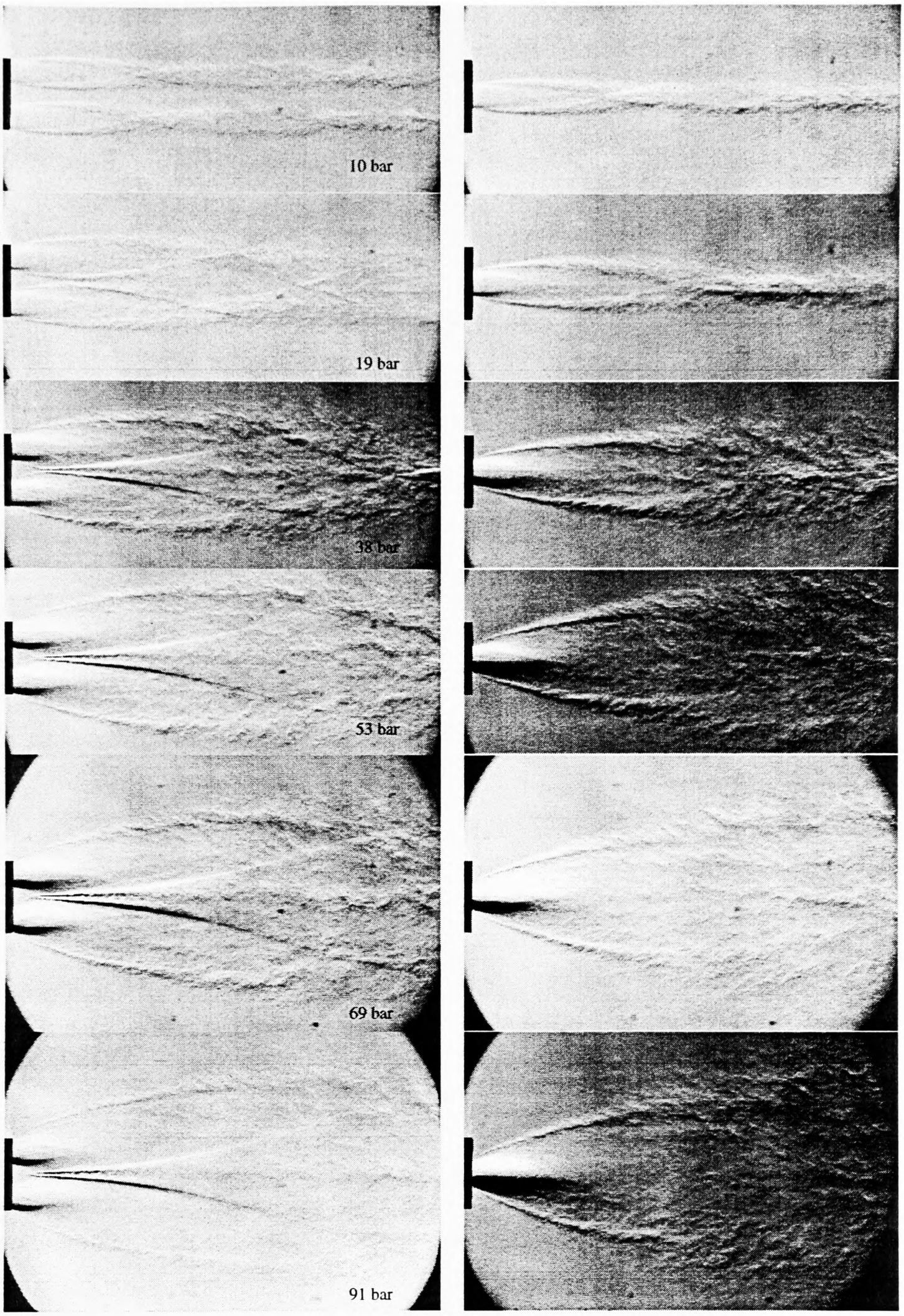


Figure 5-4 Mach 5 twinjet nozzle isometric illustration



x-z plane *y-z plane*

Figure 5-5 Schlieren photographs of Mach 5 (TM5) twinjet in quiescent on x-z and y-z planes: *from left to right, top to bottom (LT27,LT18), (LT26,LT19), (LT25,LT20), (LT24,LT21), (LT23,LT28), (LT9,LT17). Pressures shown are mean injection plenum chamber pressures.*

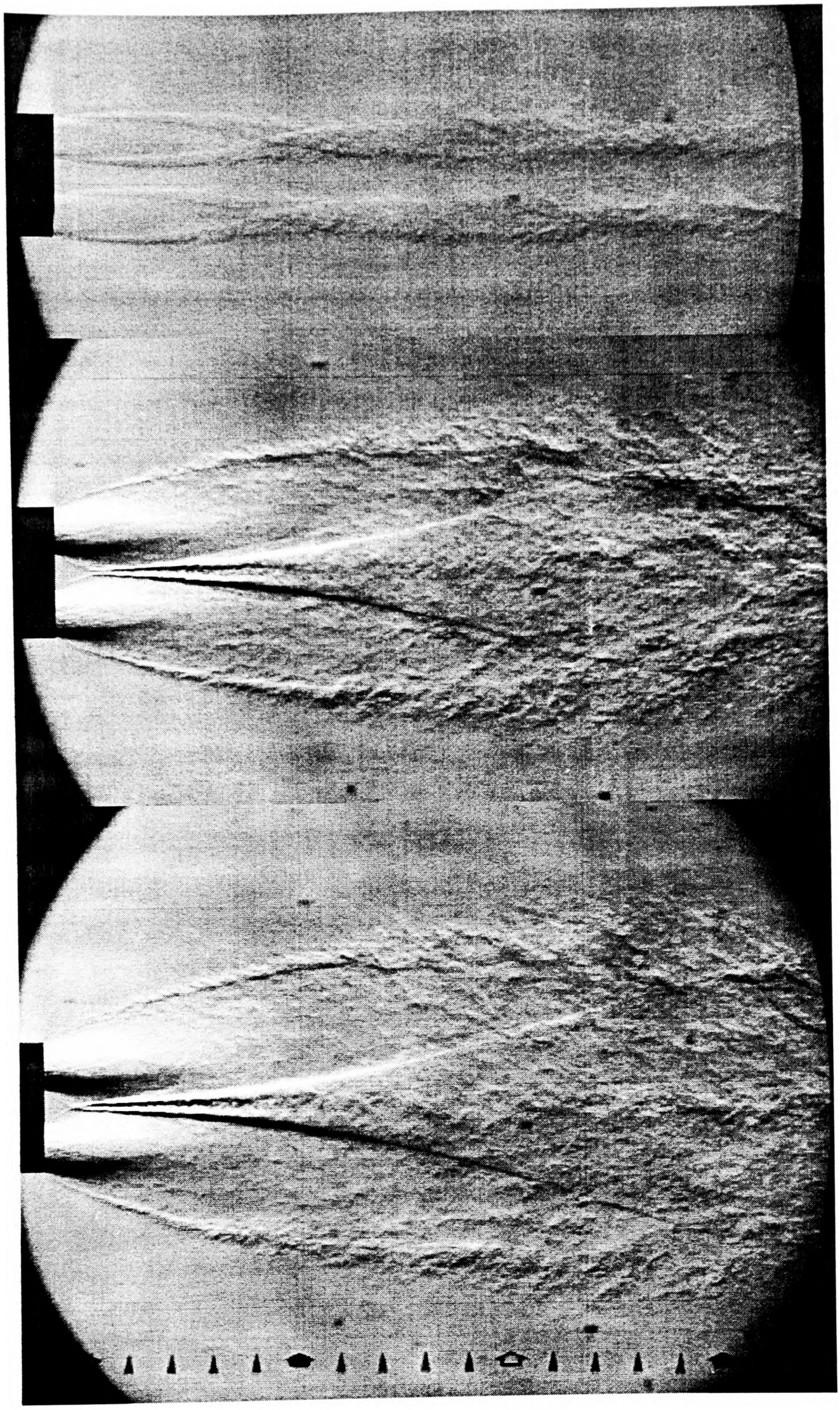


Figure 5-6 Schlieren photographs of Mach 5 (TM5) twinjet in quiescent on x-z plane *(from top to bottom: LT27, LT24 and LT22)*

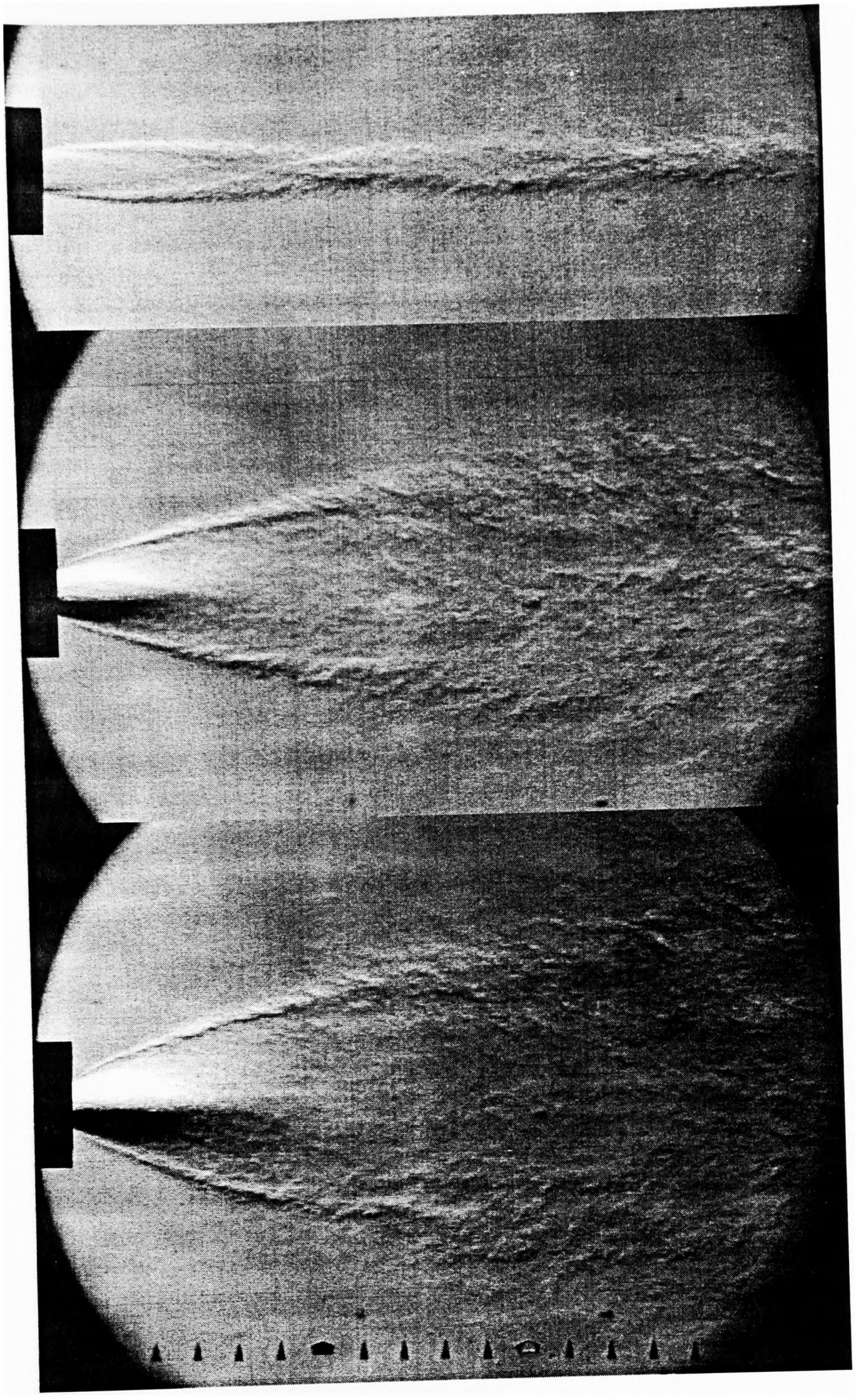


Figure 5-7 Schlieren photographs of Mach 5 (TM5) twinjet in quiescent on y-z plane *(from top to bottom: LT18, LT21 and LT17)*

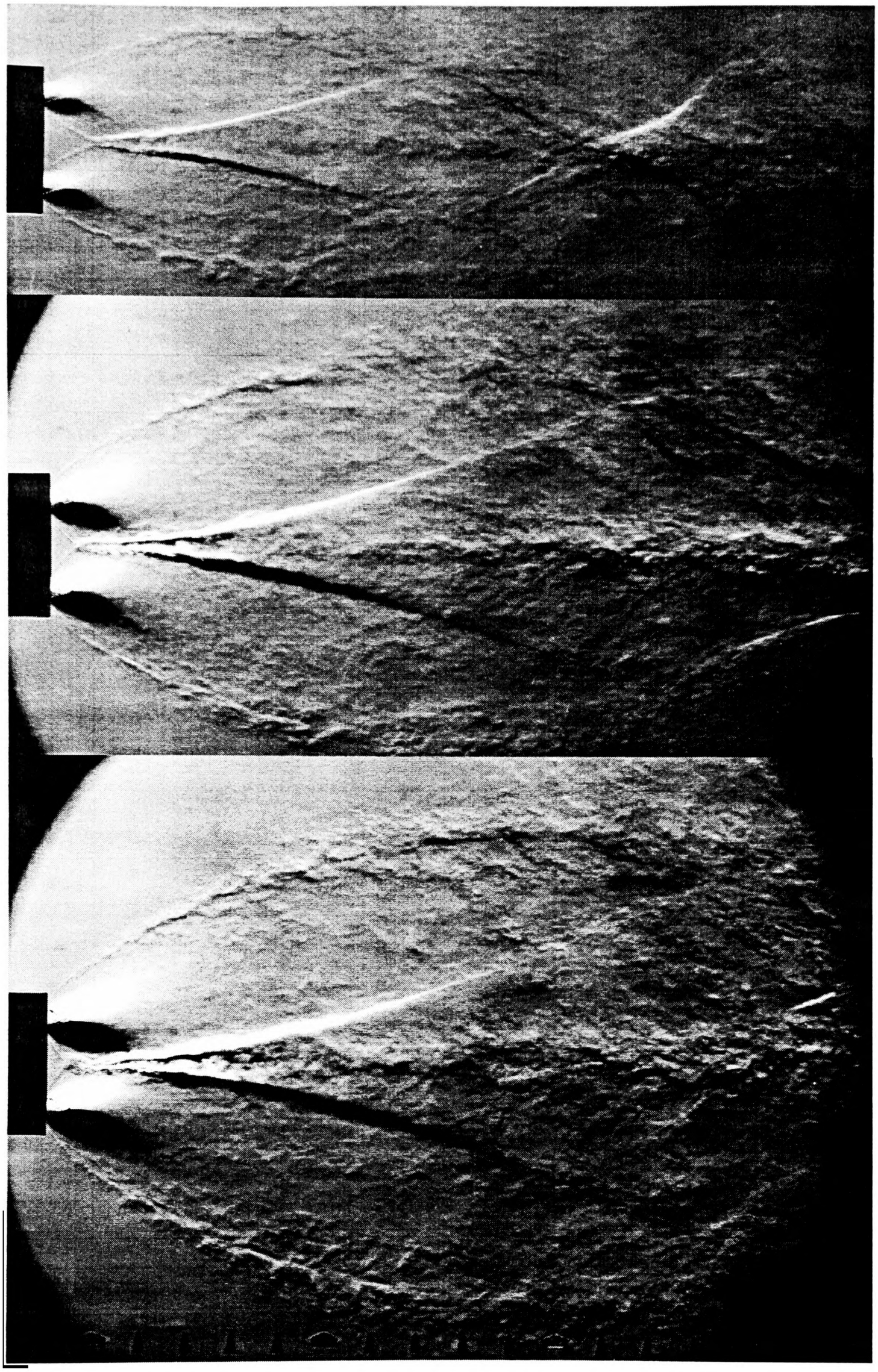


Figure 5-8 Schlieren photographs of Mach 3 (TM3) twinjet in quiescent on x-z plane *(from top to bottom: LT47, LT49 and LT51)*

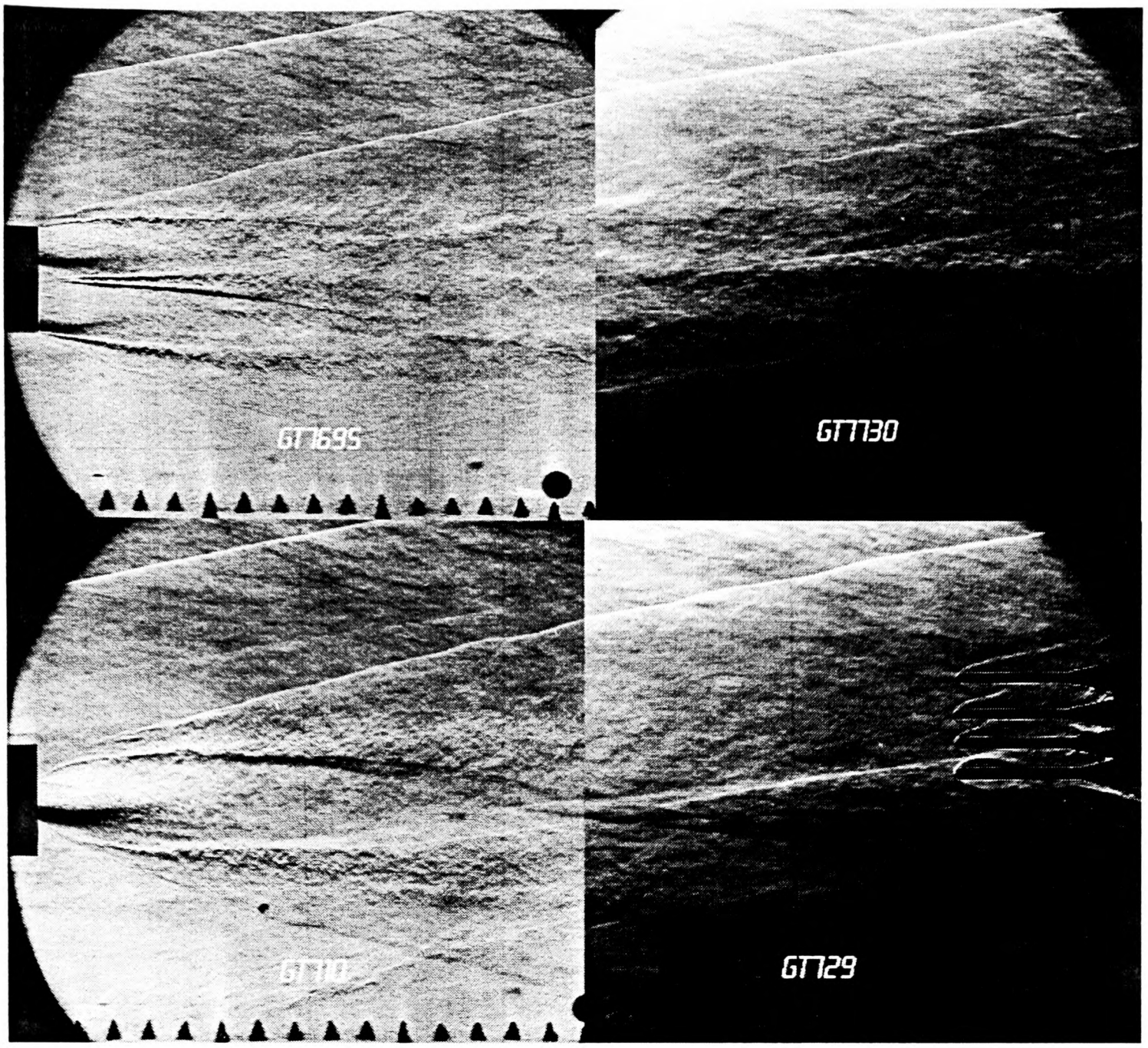


Figure 5-9 Schlieren photographs of Mach 5 (TM5) twinjet with N_2 injection in a N_2 Mach 7 freestream

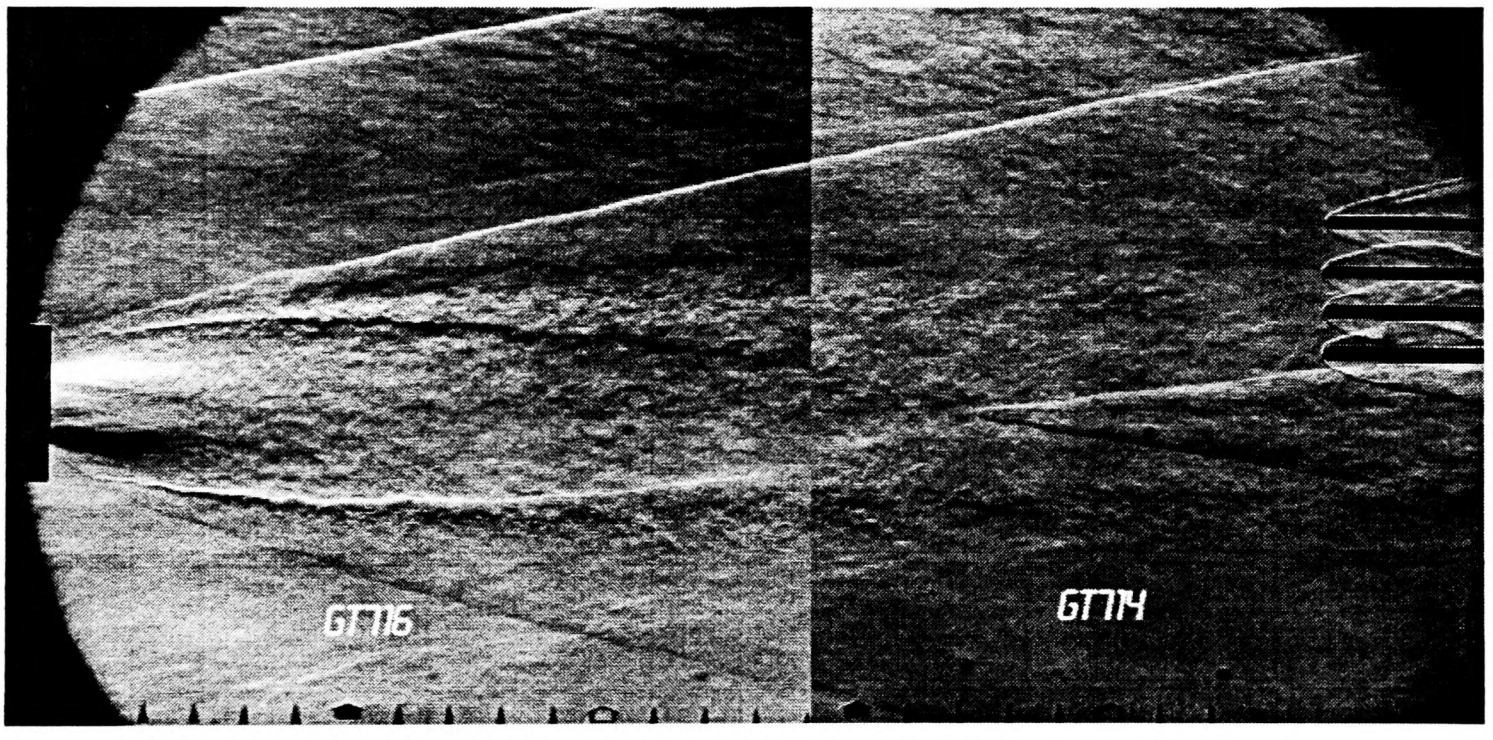


Figure 5-10 Schlieren photograph of Mach 5 (SM5) single jet with N_2 injection in a N_2 Mach 7 freestream

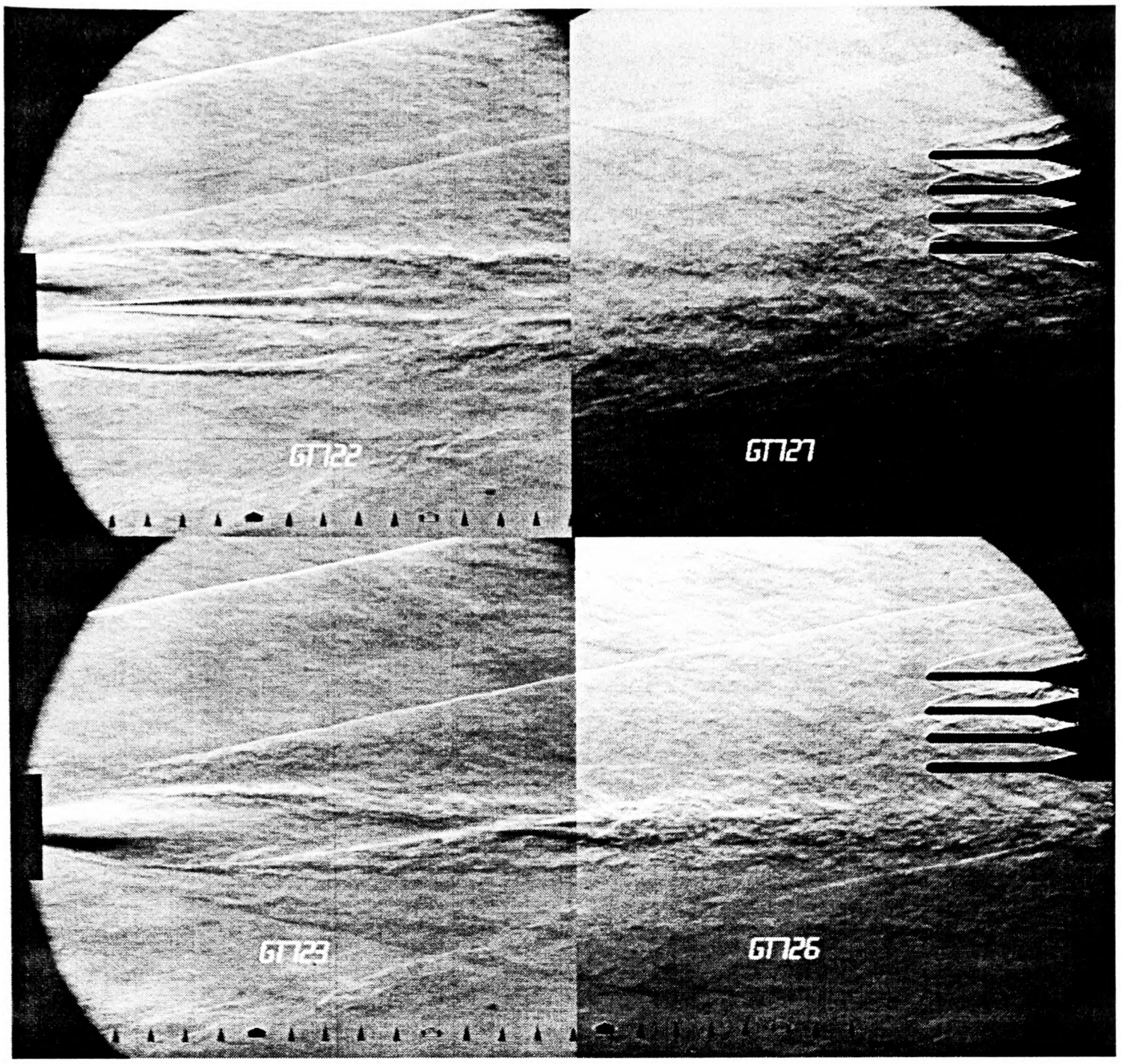


Figure 5-11 Schlieren photographs of Mach 5 (TM5) twinjet with H_2 injection in N_2 Mach 7 freestream

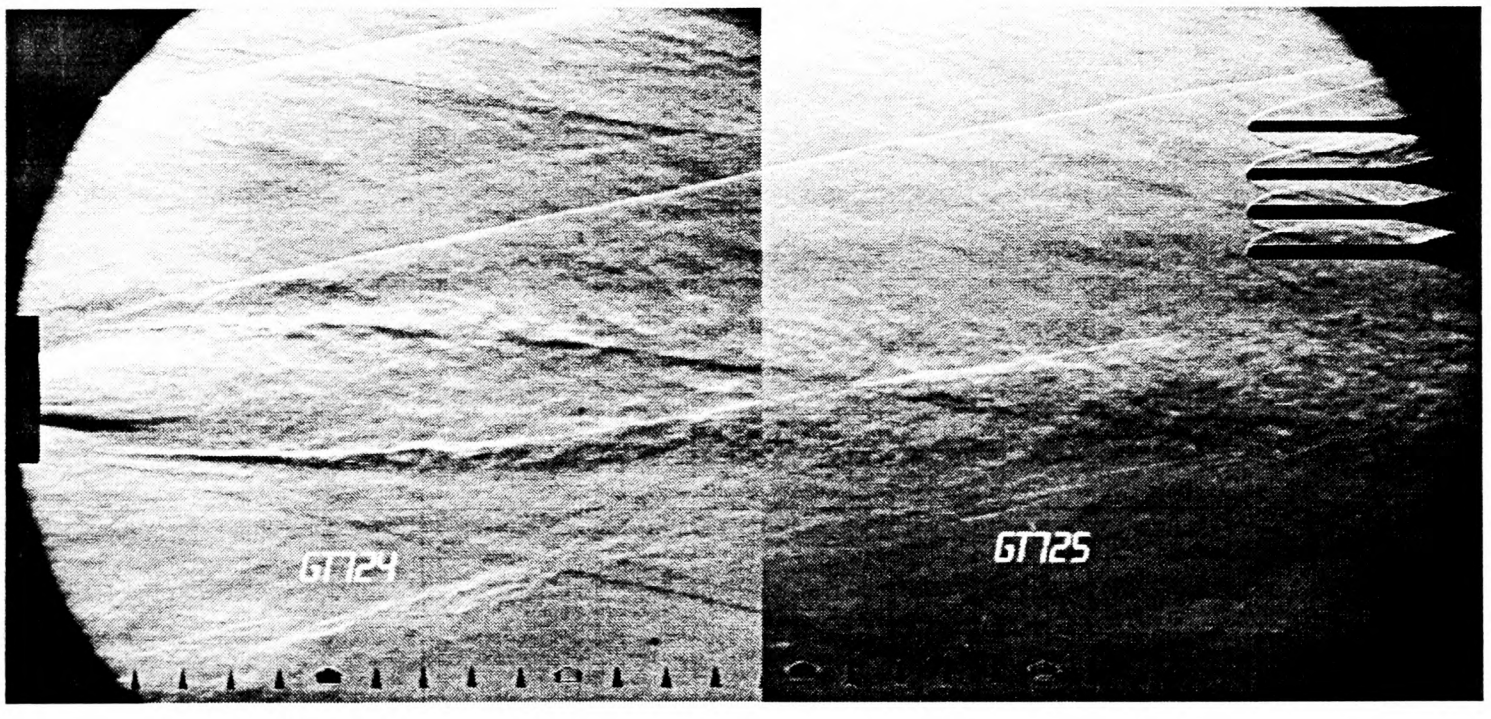


Figure 5-12 Schlieren photograph of Mach 5 (SM5) single jet with H_2 injection in N_2 Mach 7 freestream

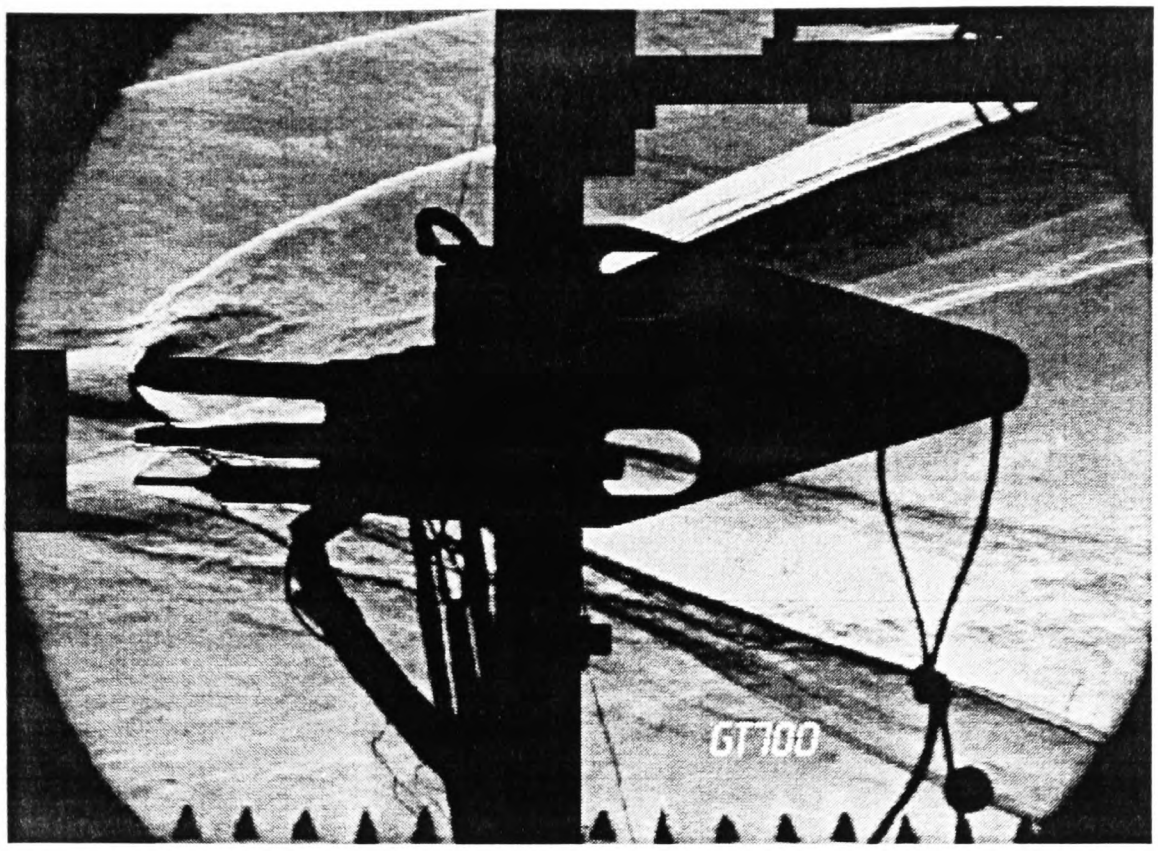


Figure 5-13 Schlieren photograph of Mach 5 (TM5) twinjet in Mach 7 freestream with Pitot probes near the nozzle exit on x-z plane *(GT700)*

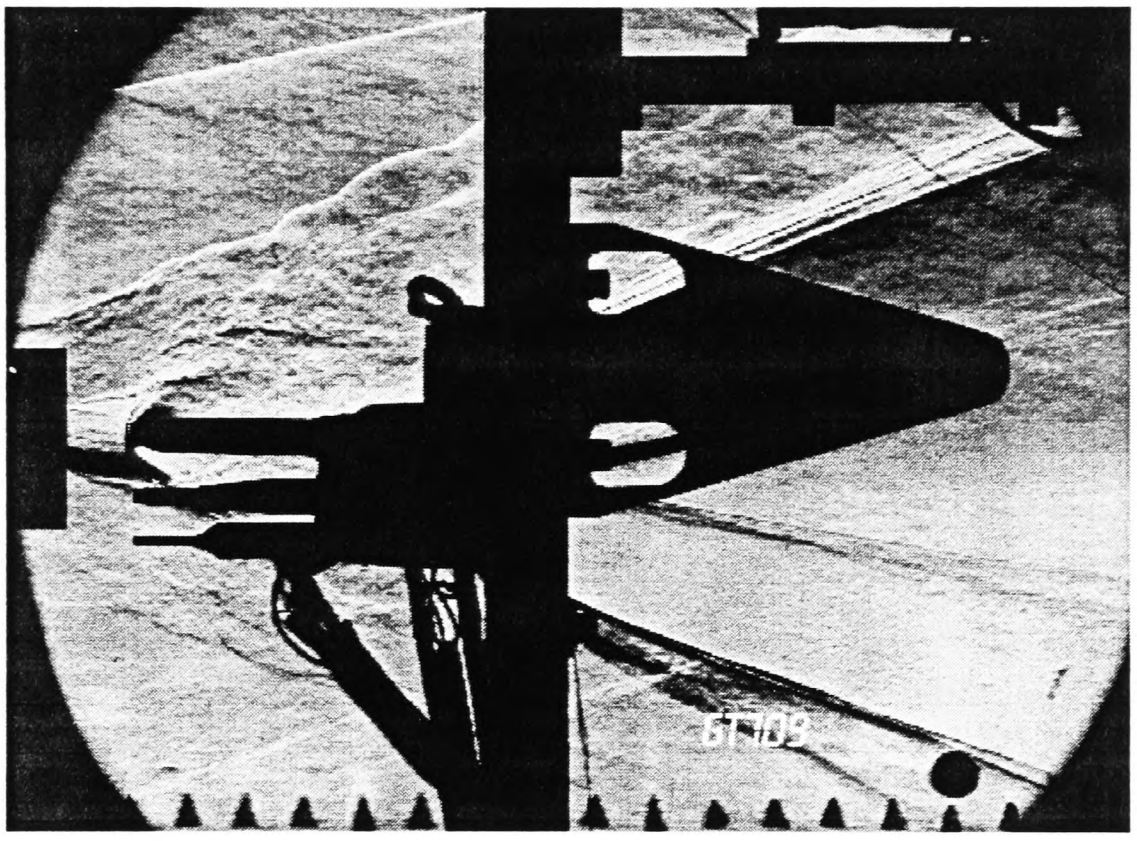
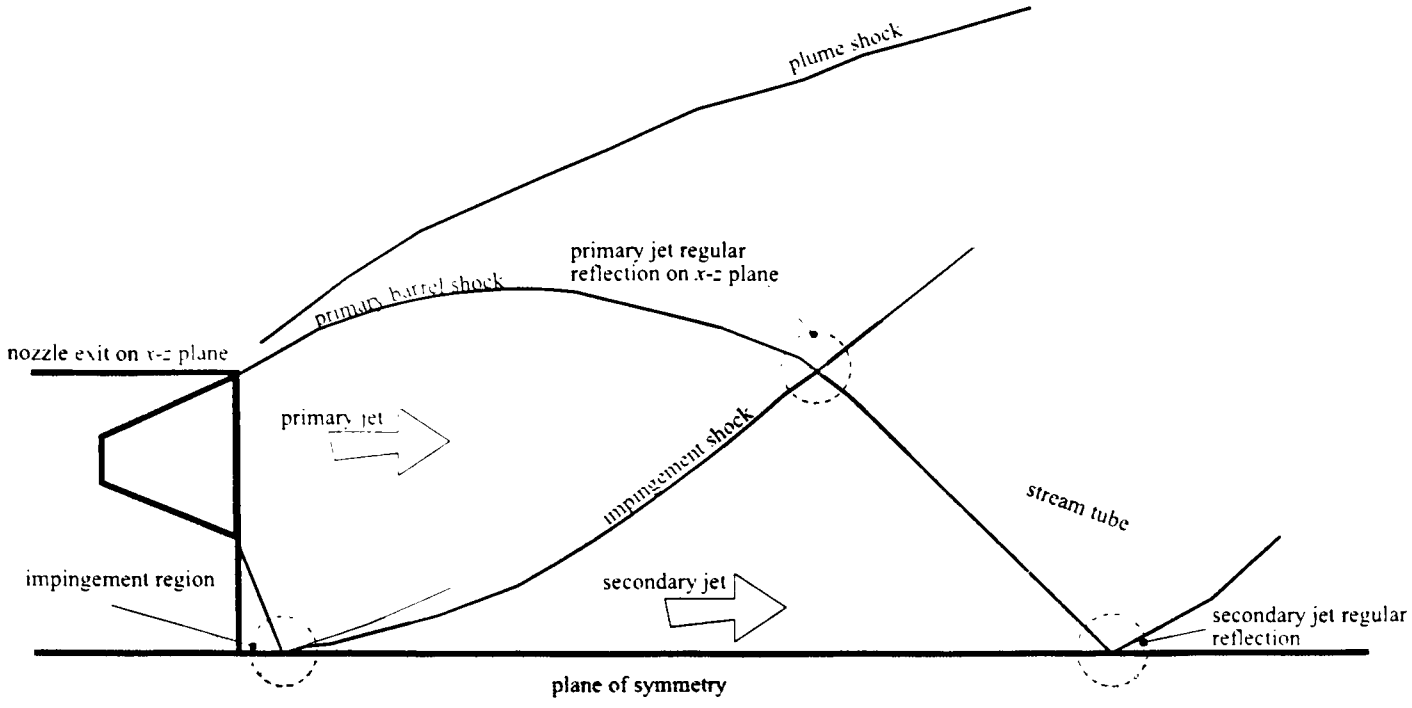


Figure 5-14 Schlieren photograph of Mach 5 (TM5) twinjet in Mach 7 freestream with Pitot probes near the nozzle exit on y-z plane *(GT709)*



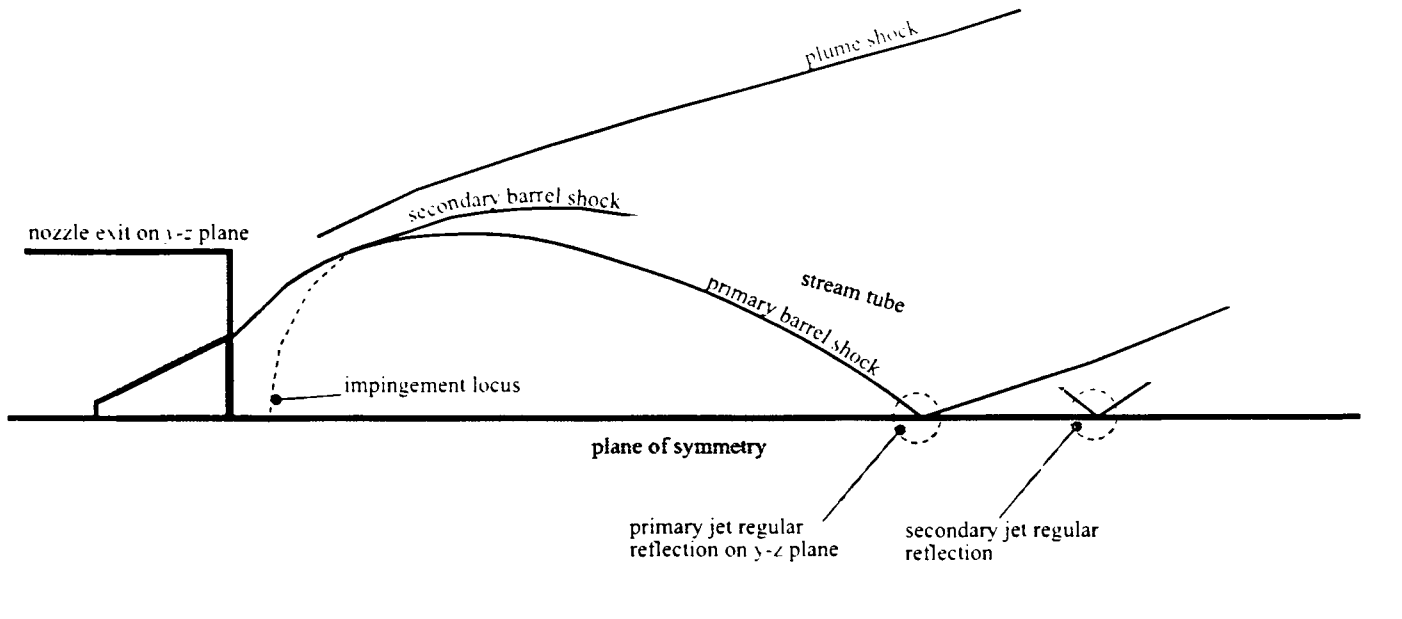


Figure 5-15 Schematic illustrations of a typical under-expanded co-flow hypersonic twinjet flowfield

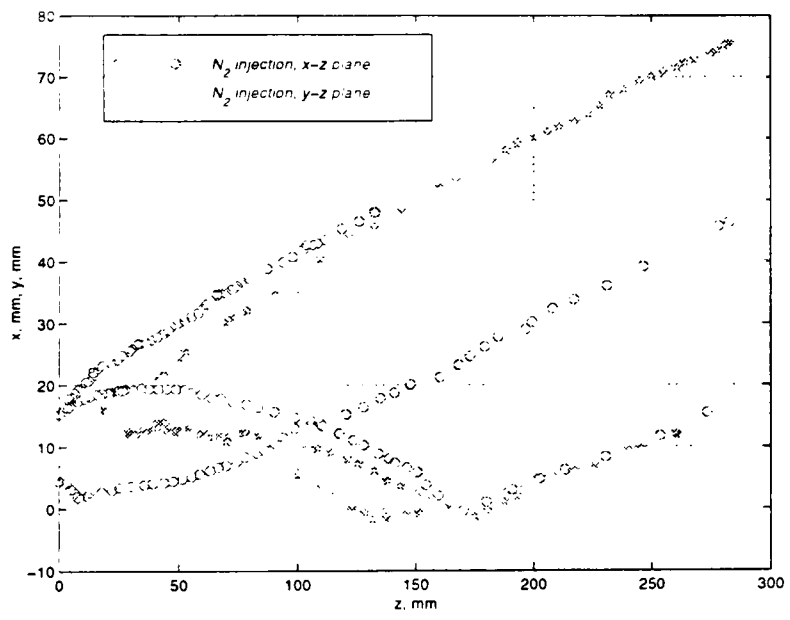


Figure 5-16 Twinjet Mach 5 (TM5) nozzle N_2 injection in Mach 7 freestream digitised shock position

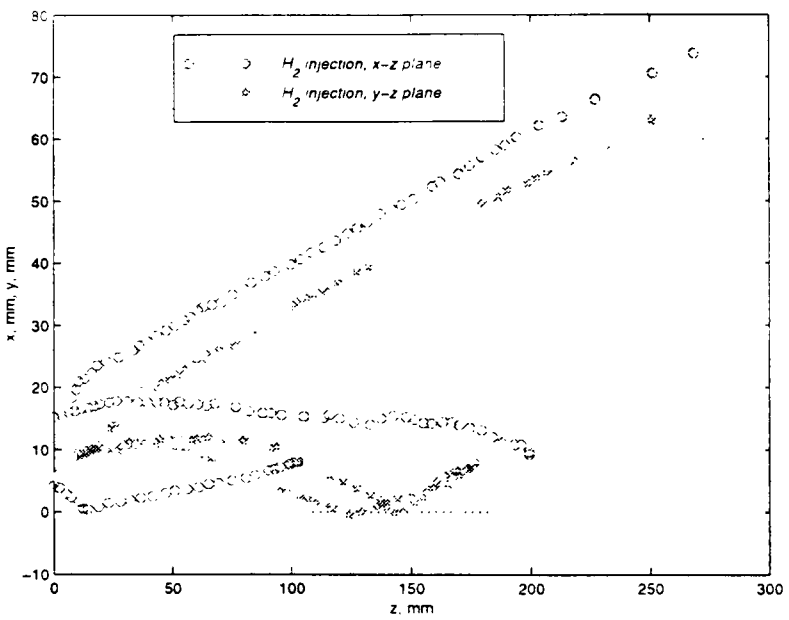


Figure 5-17 Twinjet Mach 5 (TM5) nozzle H_2 injection in Mach 7 freestream digitised shock position

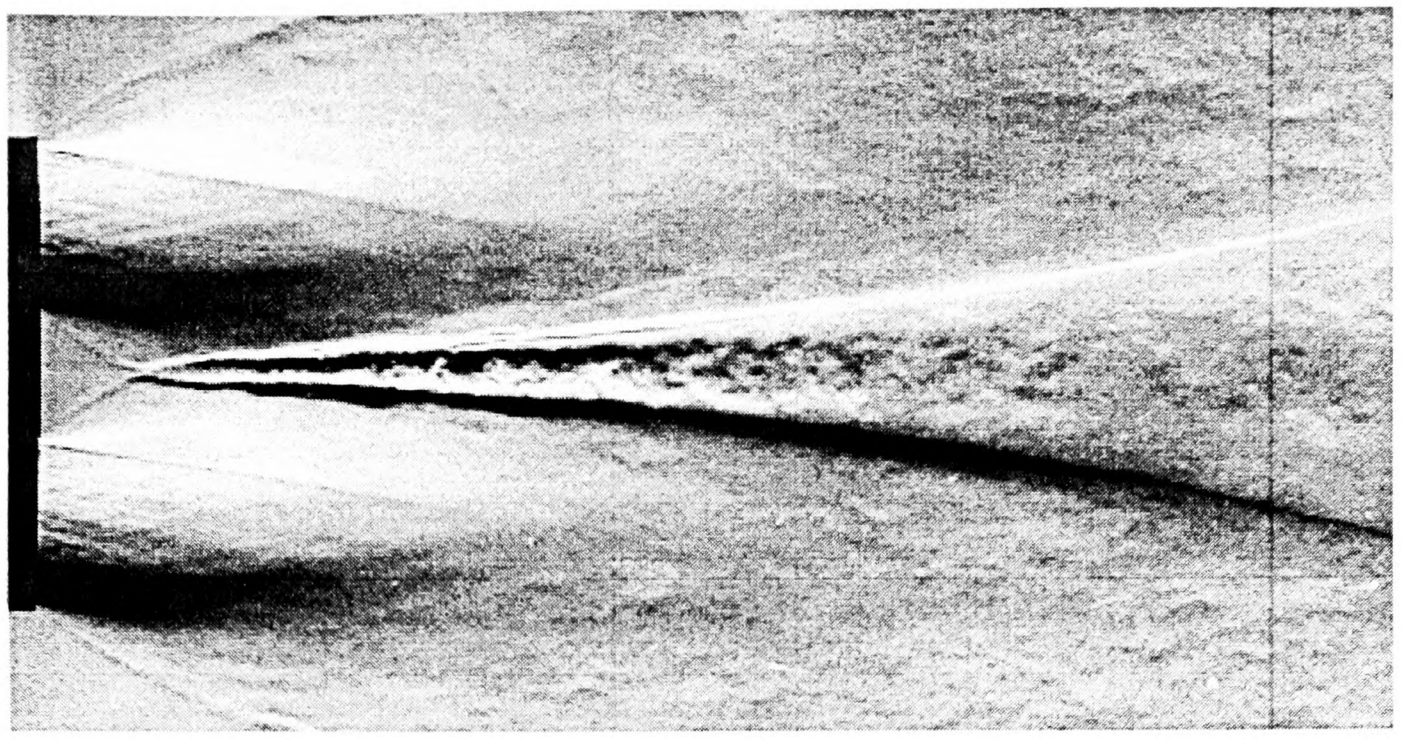


Figure 5-18 Secondary jet between the impingement shock surfaces for Mach 5 (TM5) twinjet in quiescent *(LT9)*

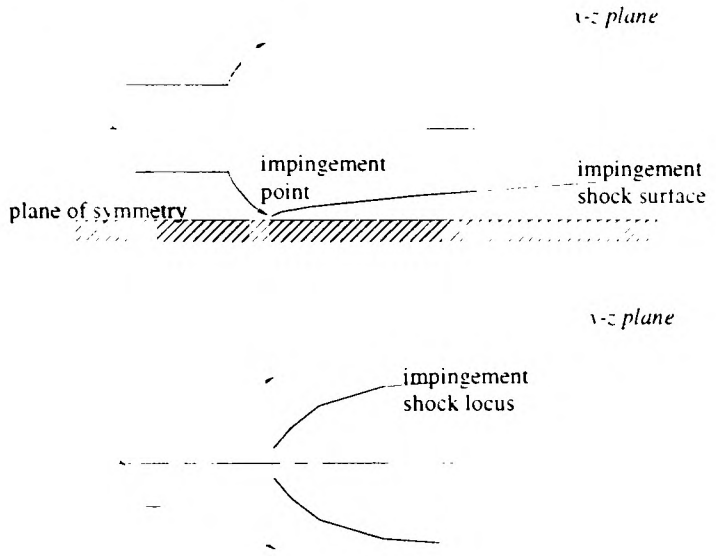


Figure 5-19 Schematic illustrations of the impingement shock locus and shock surface *(upper nozzle shown)*

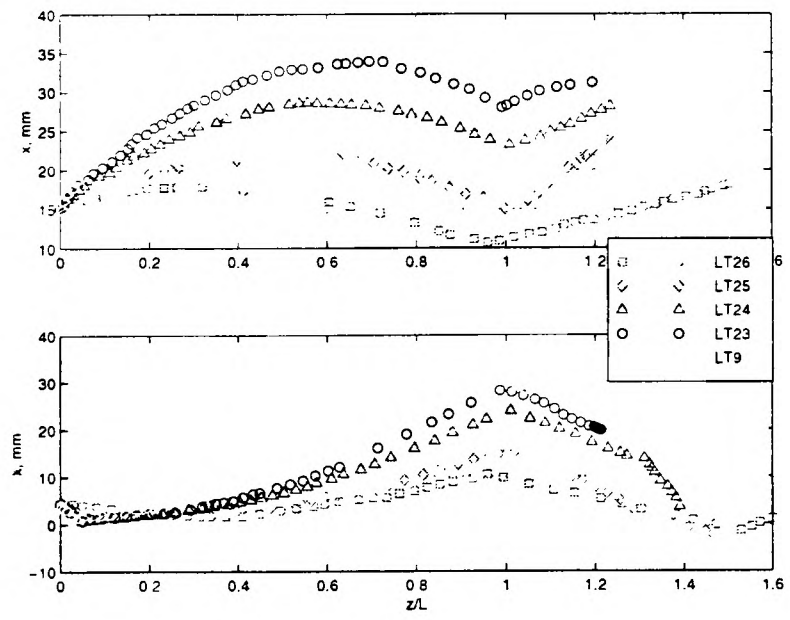


Figure 5-20 Mach 5 twinjet (TM5) shock positions scaled with quiescent plume scale parameter L

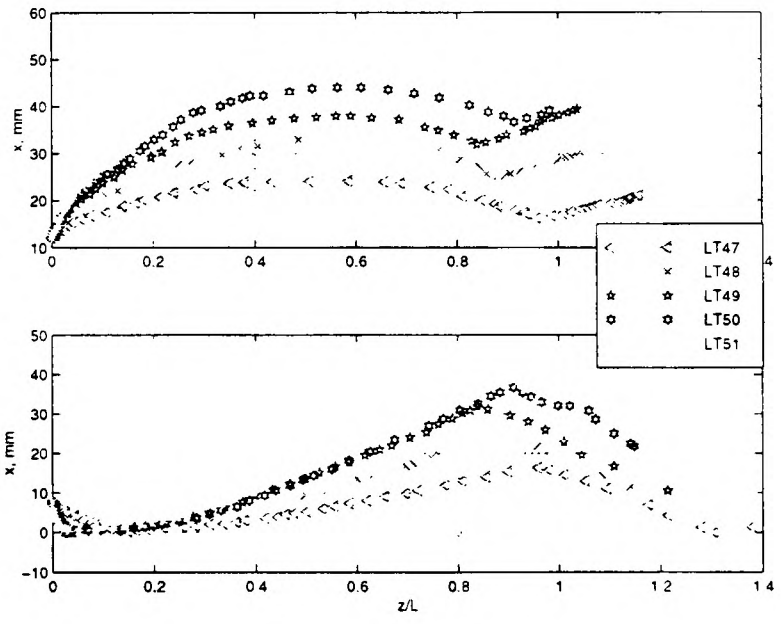


Figure 5-21 Mach 3 twinjet (TM3) shock positions scaled with quiescent plume scale parameter L

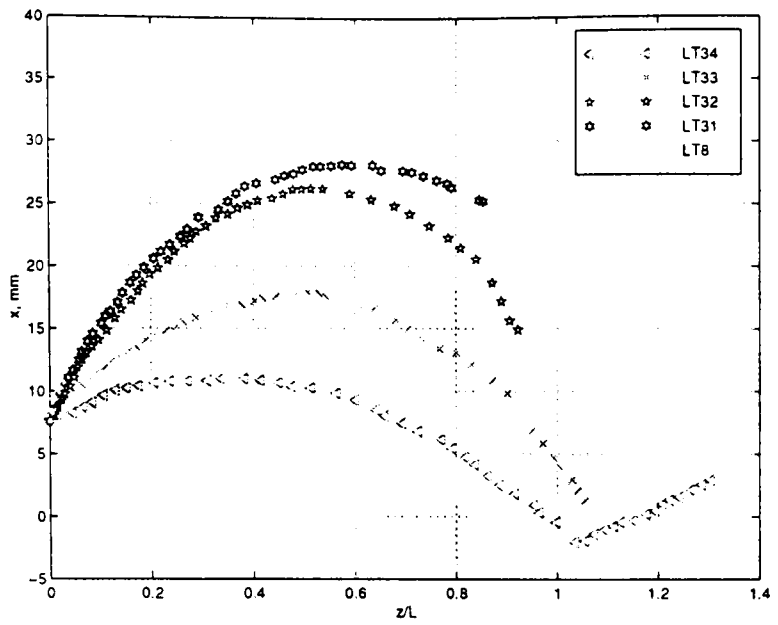


Figure 5-22 Mach 5 single jet (SM5M) shock positions scaled with quiescent plume scale parameter *L*

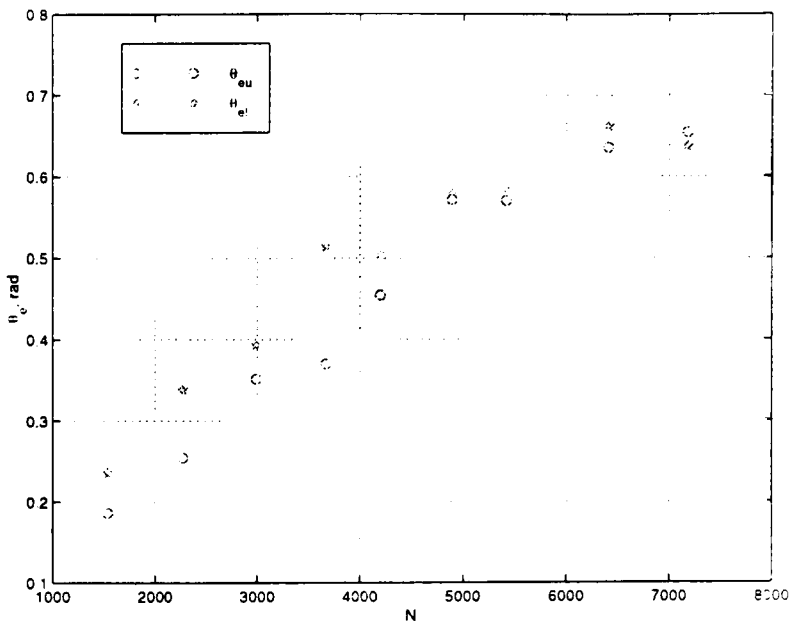


Figure 5-23 Mach 5 twinjet (TM5) nozzle exit angle in quiescent

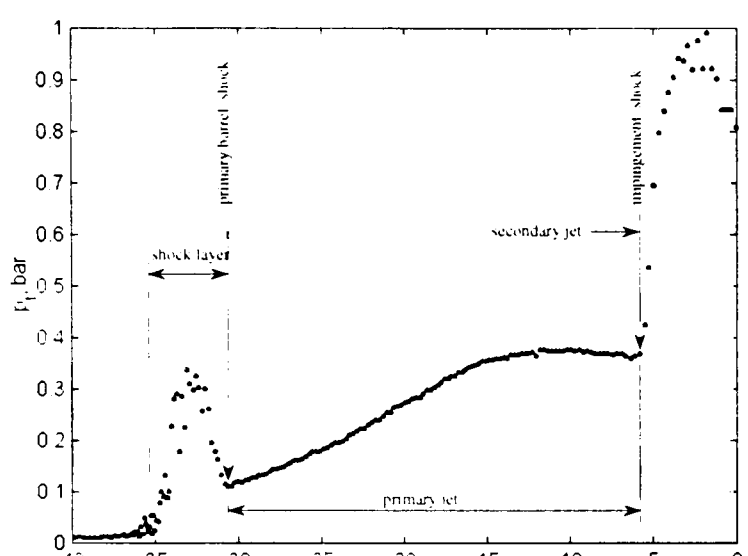


Figure 5-24 Pitot pressure for Mach 5 (TM5) twinjet on *x*-*z* plane with N_2 injection in quiescent at 40 mm downstream *(LT156, lower half)*

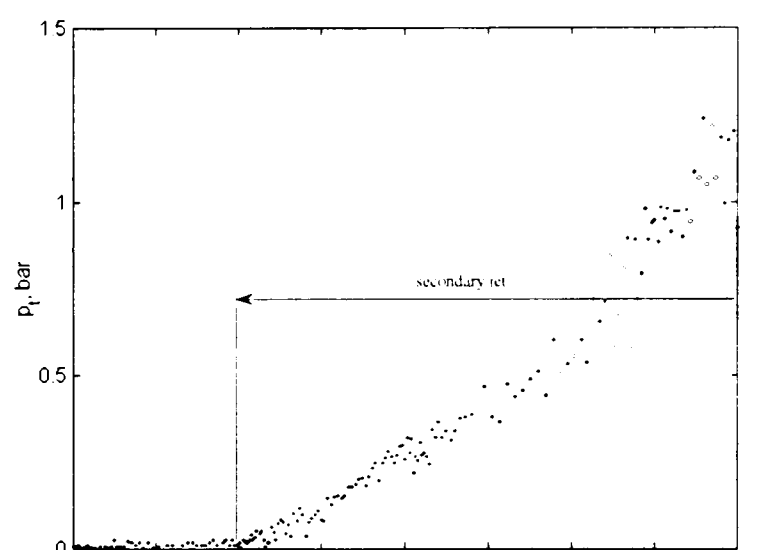


Figure 5-25 Pitot pressure for Mach 5 (TM5) twinjet on *y*-*z* plane with N_2 injection in quiescent at 40 mm downstream *(LT183, lower half)*

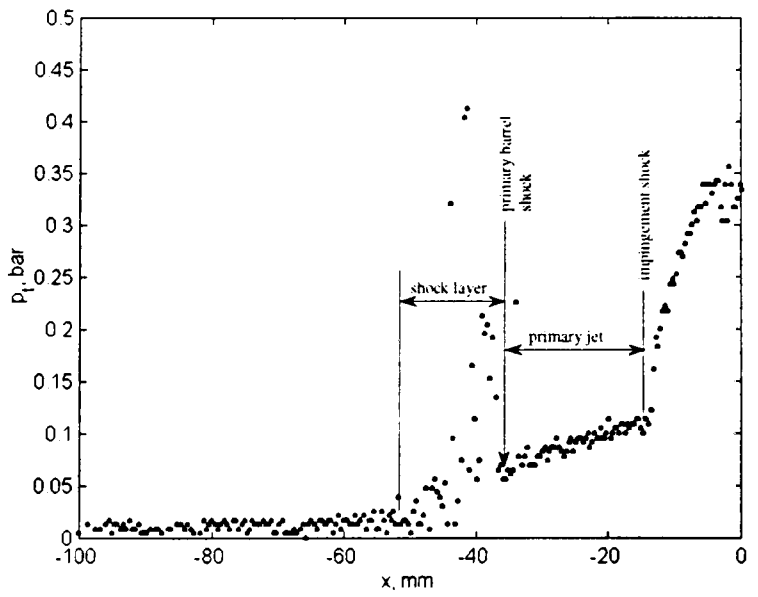


Figure 5-26 Pitot pressure for Mach 5 (TM5) twinjet on *x*-*z* plane with N_2 injection in quiescent at 100 mm downstream *(LT145, lower half)*

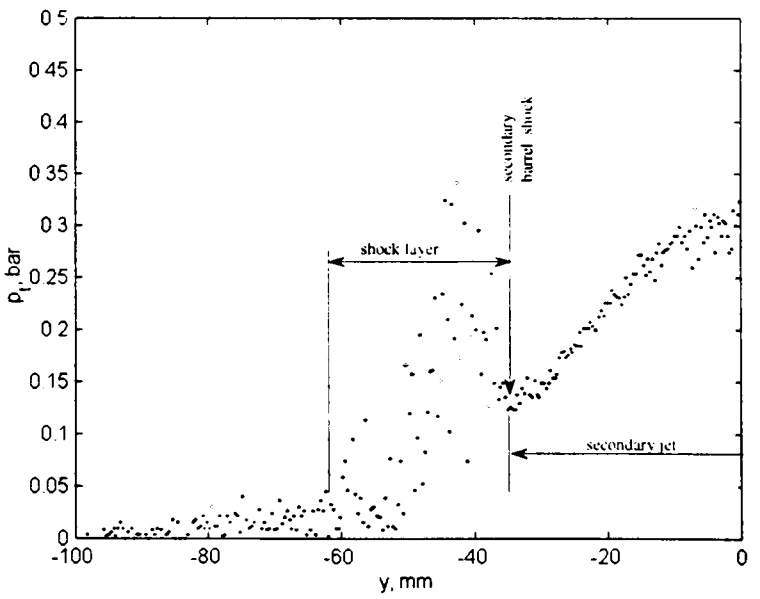


Figure 5-27 Pitot pressure for Mach 5 (TM5) twinjet on *y*-*z* plane with N_2 injection in quiescent at 100 mm downstream *(LT195, lower half)*

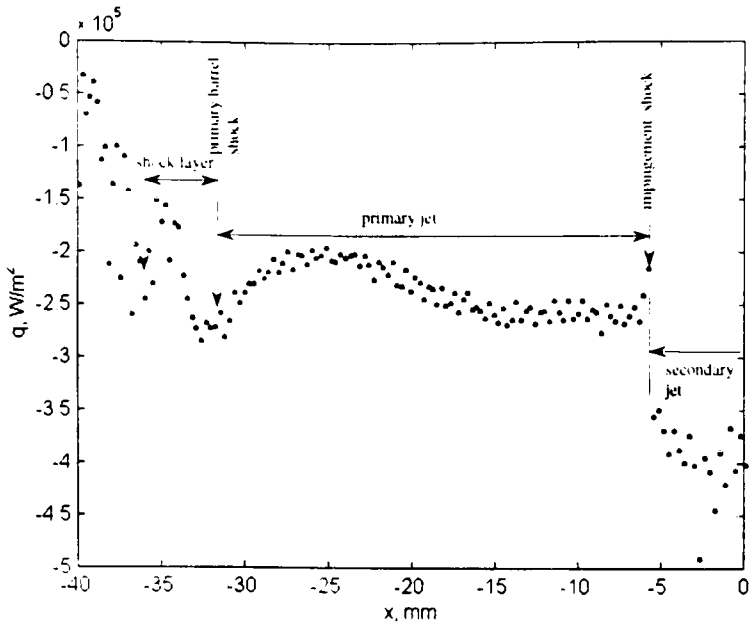


Figure 5-28 Heat flux for Mach 5 (TM5) twinjet on x-z plane with N_2 injection in quiescent at 40 mm downstream *(LT156, below plane of symmetry)*

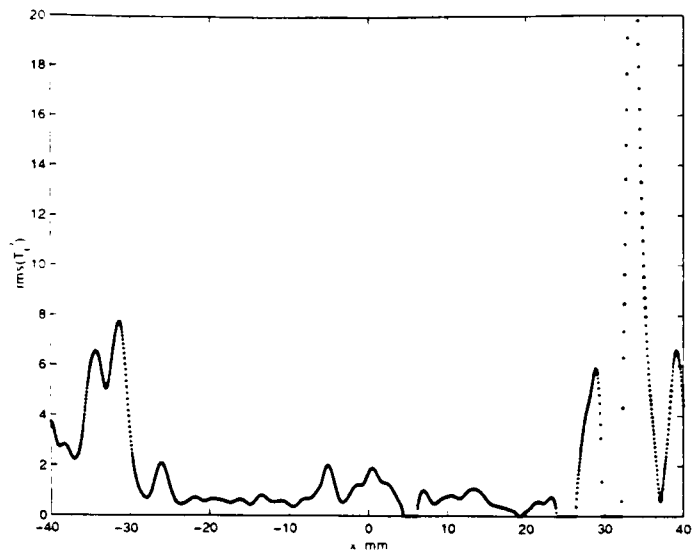


Figure 5-29 $\sqrt{\overline{T_t'^2}}$ variation along x-axis at 40 mm downstream

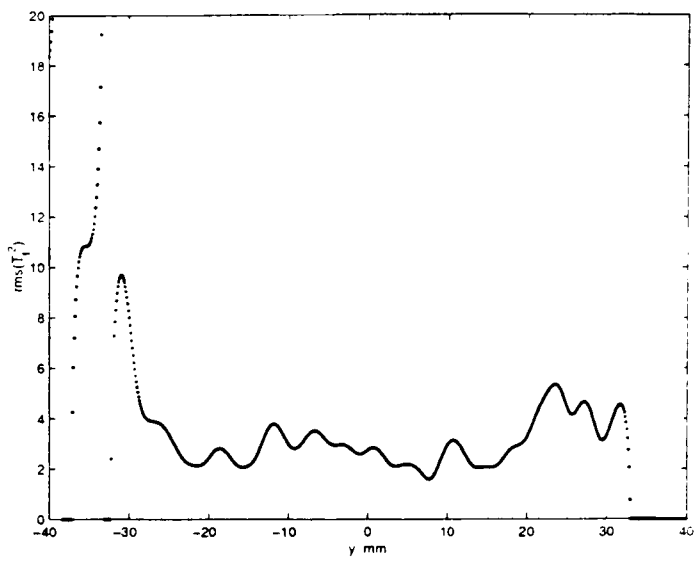


Figure 5-30 $\sqrt{\overline{T_t'^2}}$ variation along y-axis at 40 mm downstream

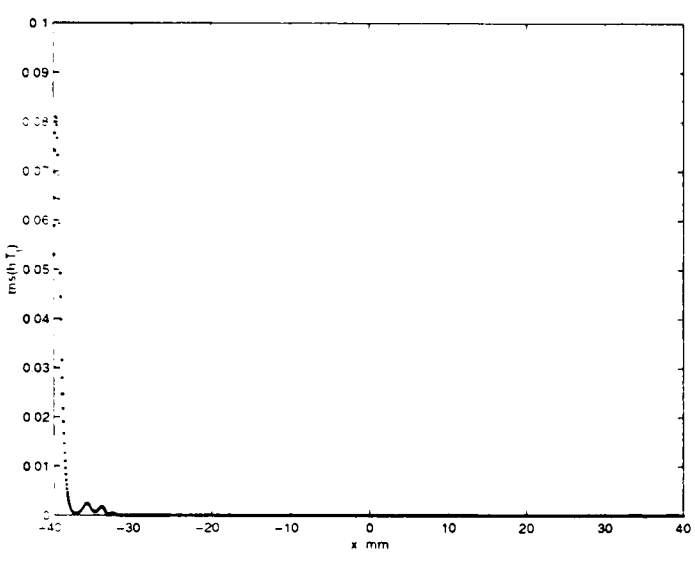


Figure 5-31 $\overline{h'T_t'^2}$ variation along x-axis at 40 mm downstream

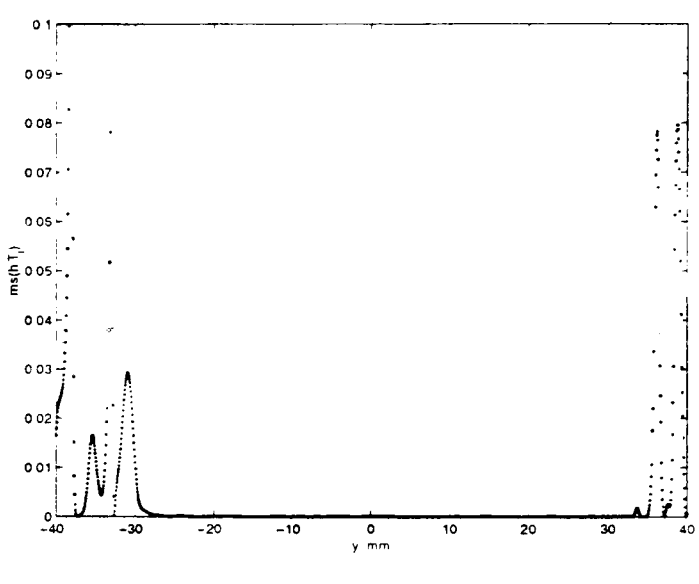


Figure 5-32 $\overline{h'T_t'^2}$ variation along y-axis at 40 mm downstream

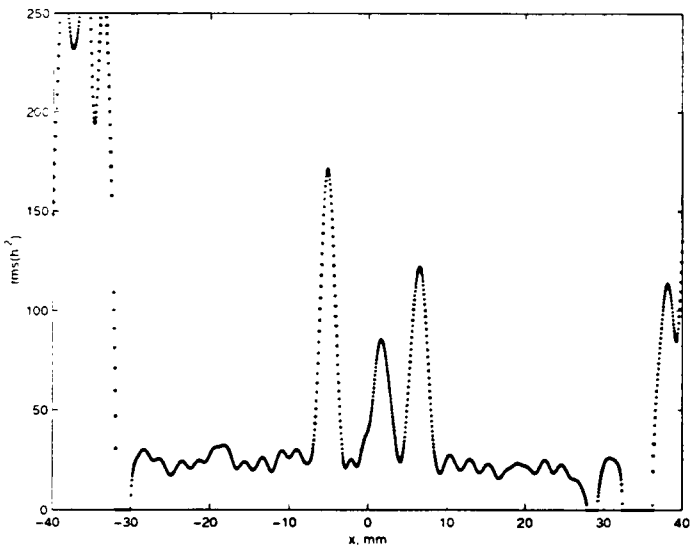


Figure 5-33 $\sqrt{\overline{h'^2}}$ variation along x-axis at 40 mm downstream

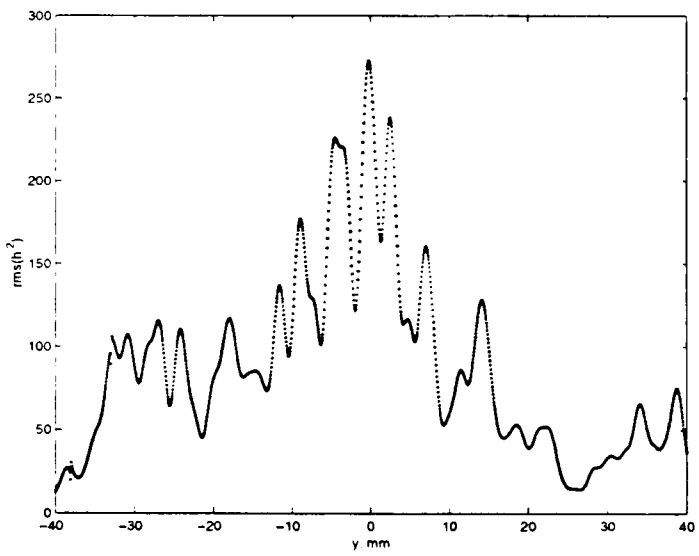


Figure 5-34 $\sqrt{\overline{h'^2}}$ variation along y-axis at 40 mm downstream

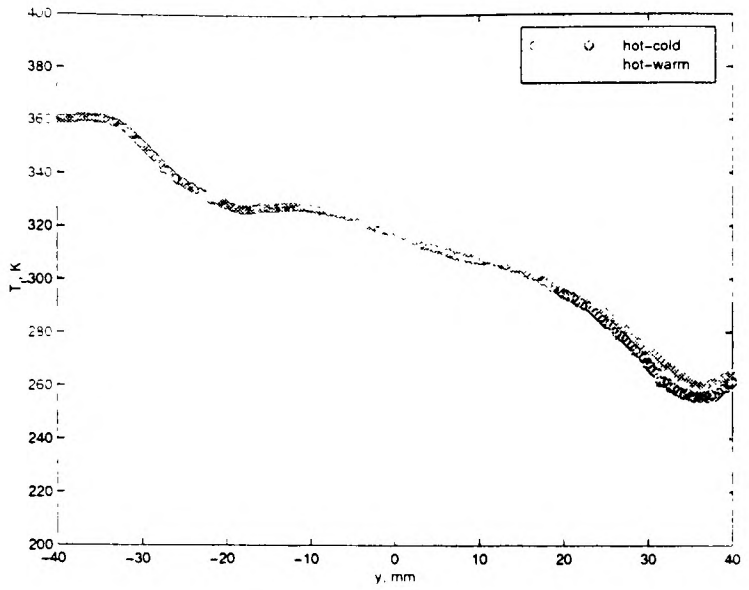


Figure 5-35 Total temperature for Mach 5 (TM5) twinjet in quiescent on *y-z* plane at 100 mm downstream *(LT195)*

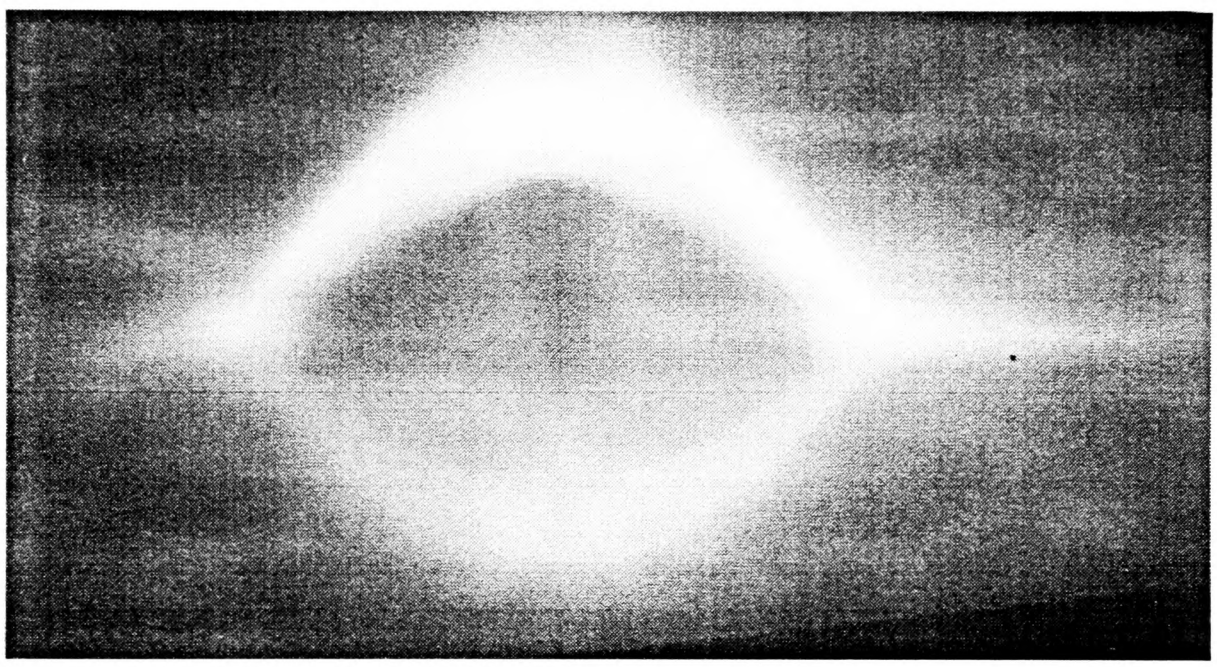


Figure 5-36 Crossflow view of a Mach 4.43 twinjet on *x-y* plane with N_2 injection in quiescent at approximately one nozzle diameter downstream *(Welsh, 1997)*

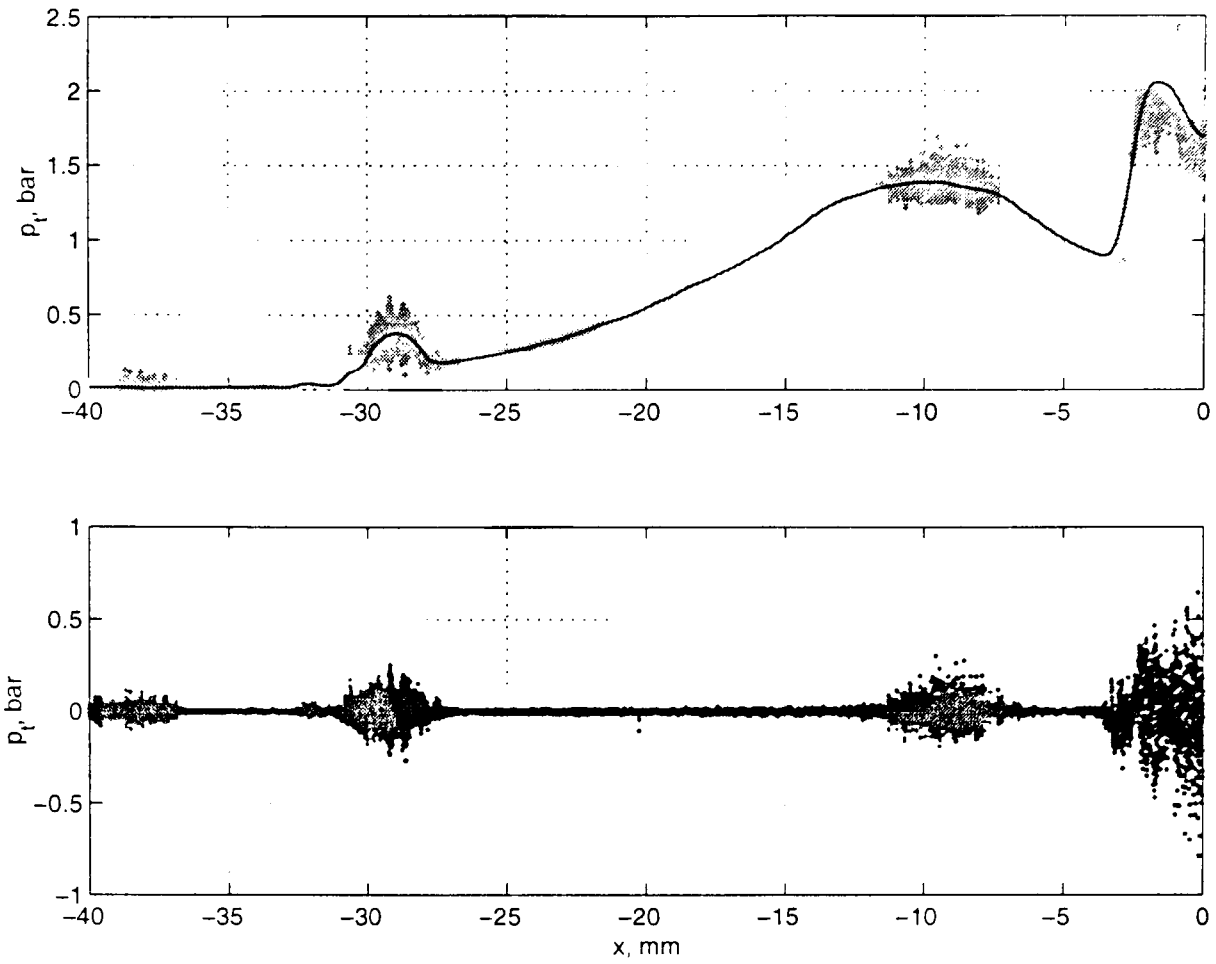


Figure 5-37 Fluctuating RPT Pitot pressure for Mach 5 (TM5) twinjet in quiescent on *x*-*z* plane at 40 mm downstream *(LT150)*

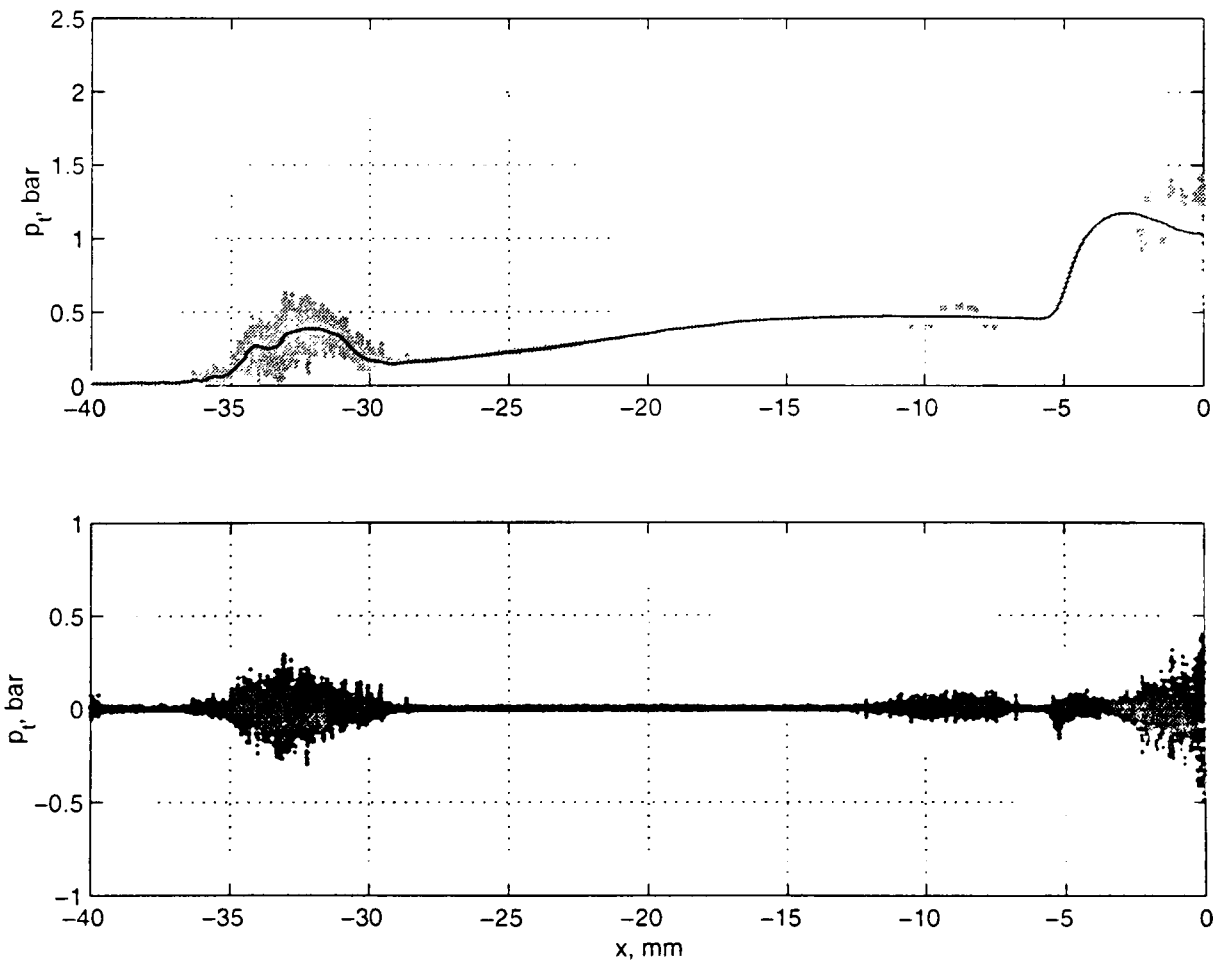


Figure 5-38 Fluctuating RPT Pitot pressure for Mach 5 (TM5) twinjet in quiescent on *x*-*z* plane at 60 mm downstream *(LT148)*

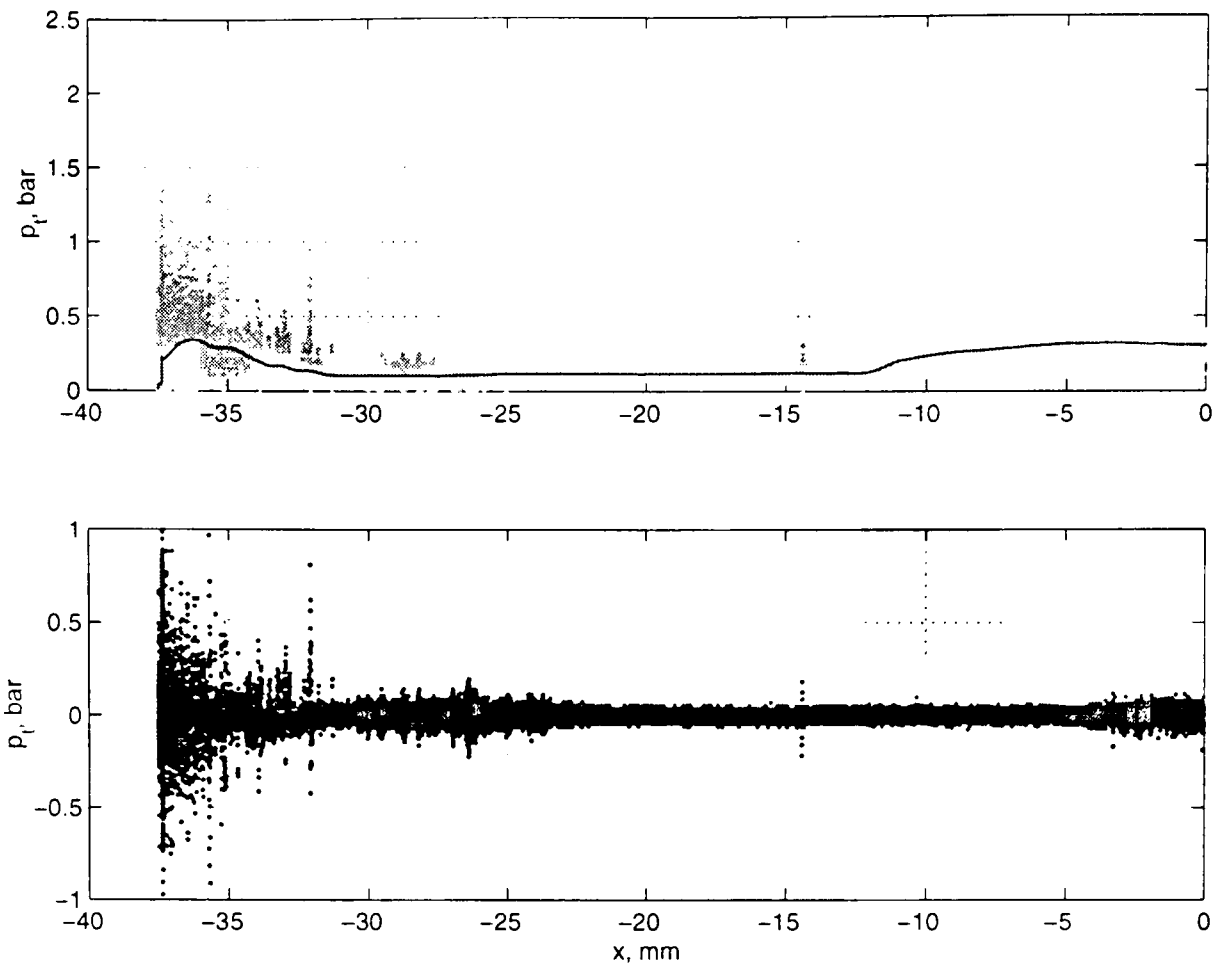


Figure 5-39 Fluctuating RPT Pitot pressure for Mach 5 (TM5) twinjet in quiescent on x-z plane at 100 mm downstream *(LT145)*

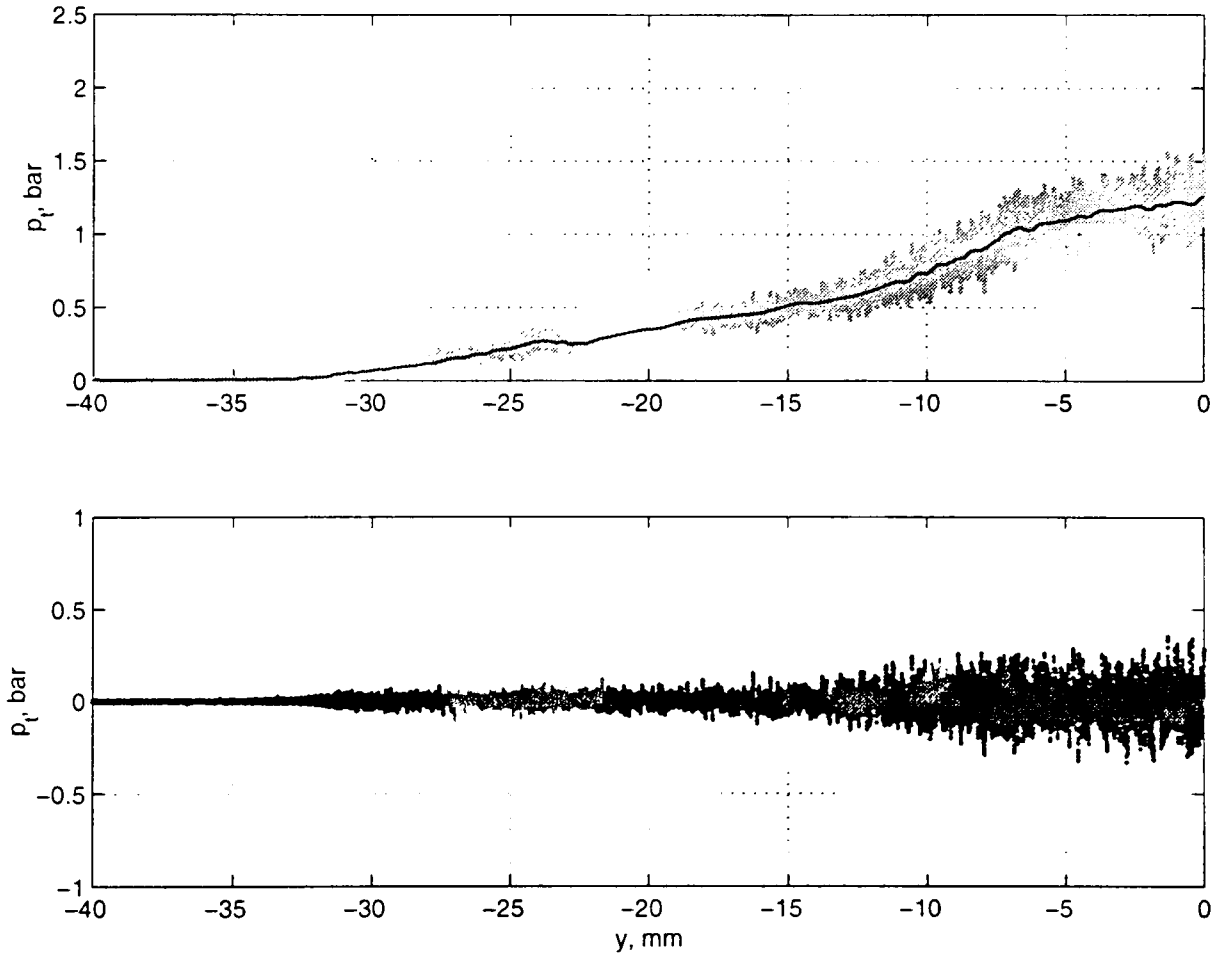


Figure 5-40 Fluctuating RPT Pitot pressure for Mach 5 (TM5) twinjet in quiescent on y-z plane at 40 mm downstream *(LT183)*

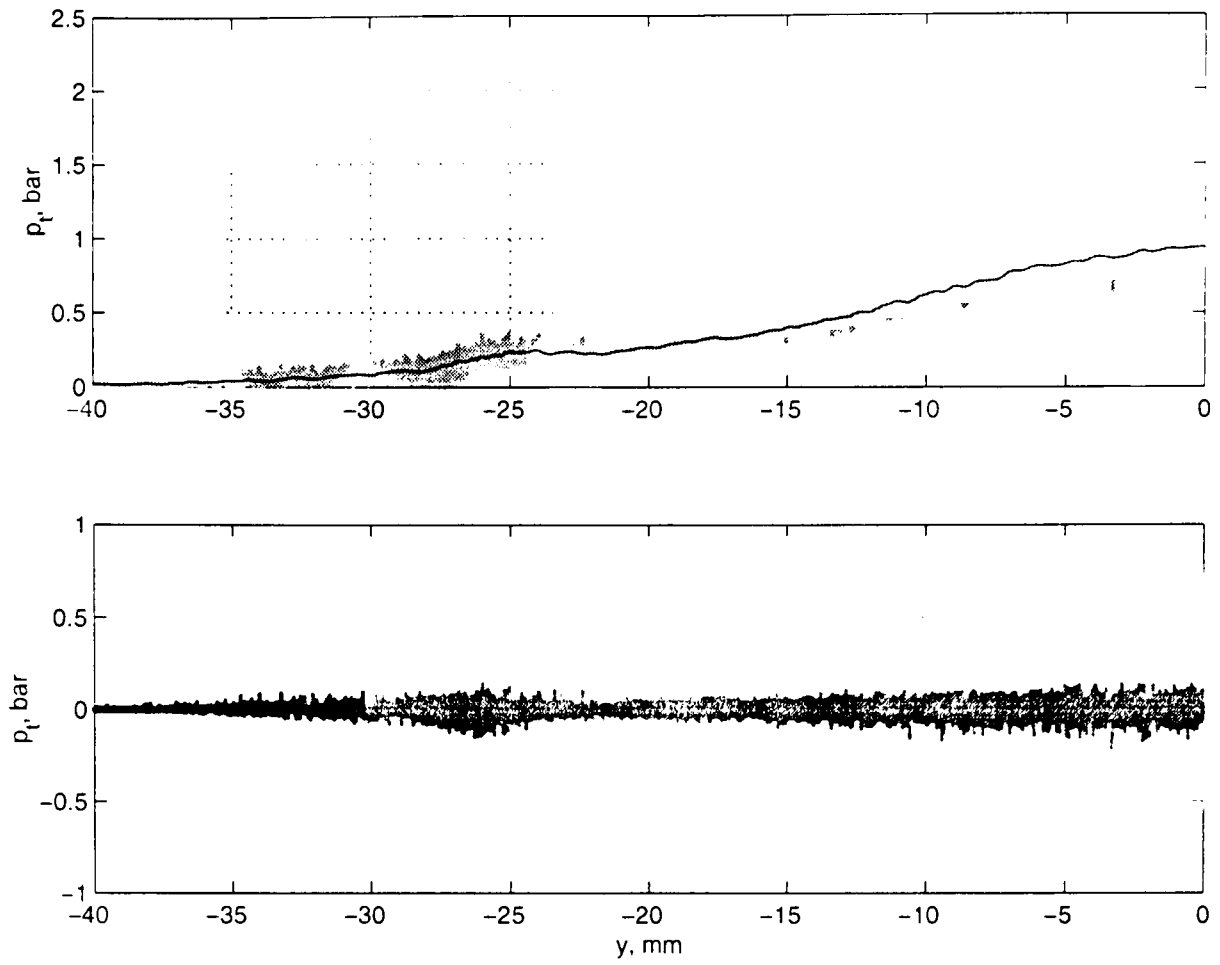


Figure 5-41 Fluctuating RPT Pitot pressure for Mach 5 (TM5) twinjet in quiescent on y-z plane at 60 mm downstream *(LT179)*

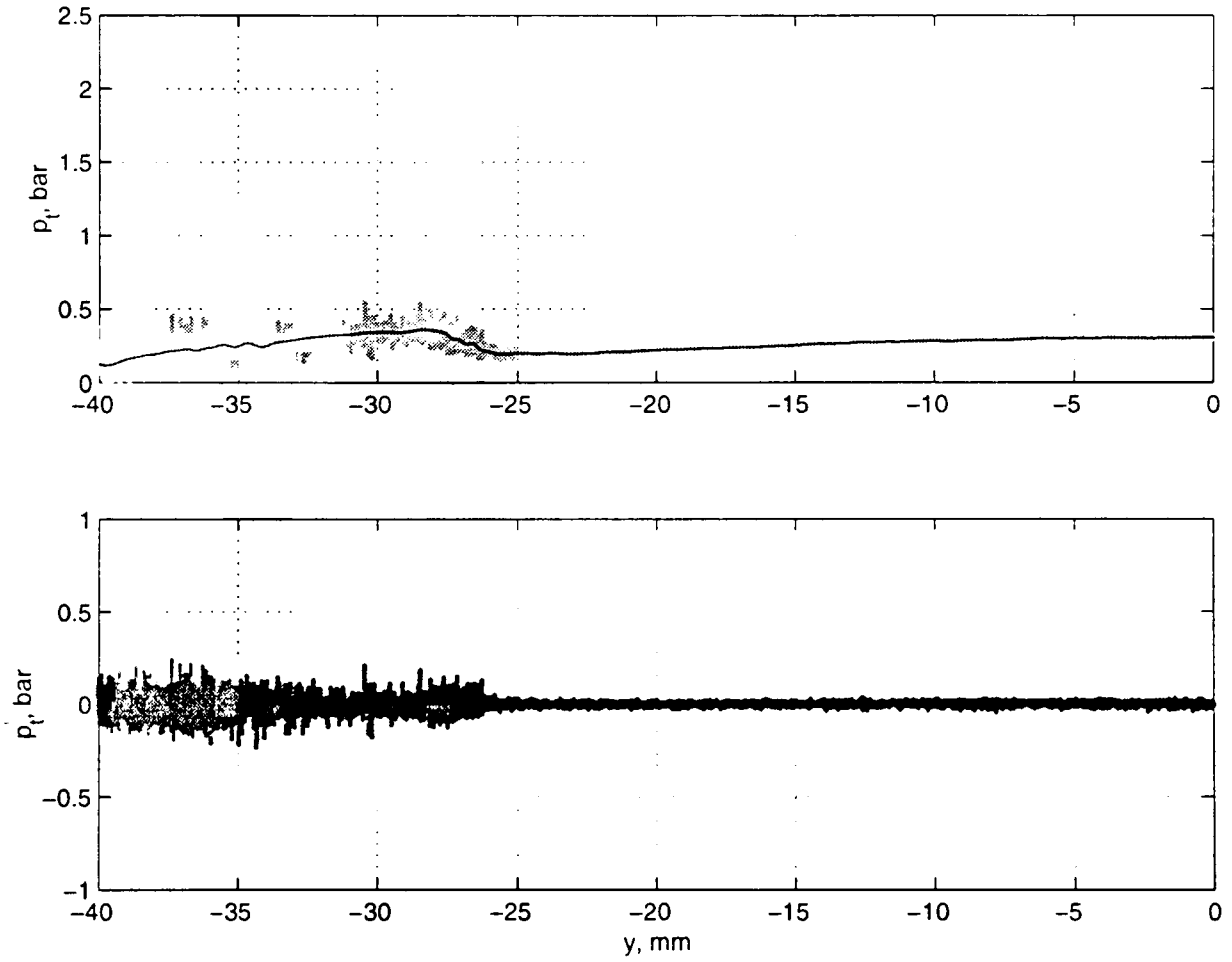


Figure 5-42 Fluctuating RPT Pitot pressure for Mach 5 (TM5) twinjet in quiescent on y-z plane at 100 mm downstream *(LT195)*

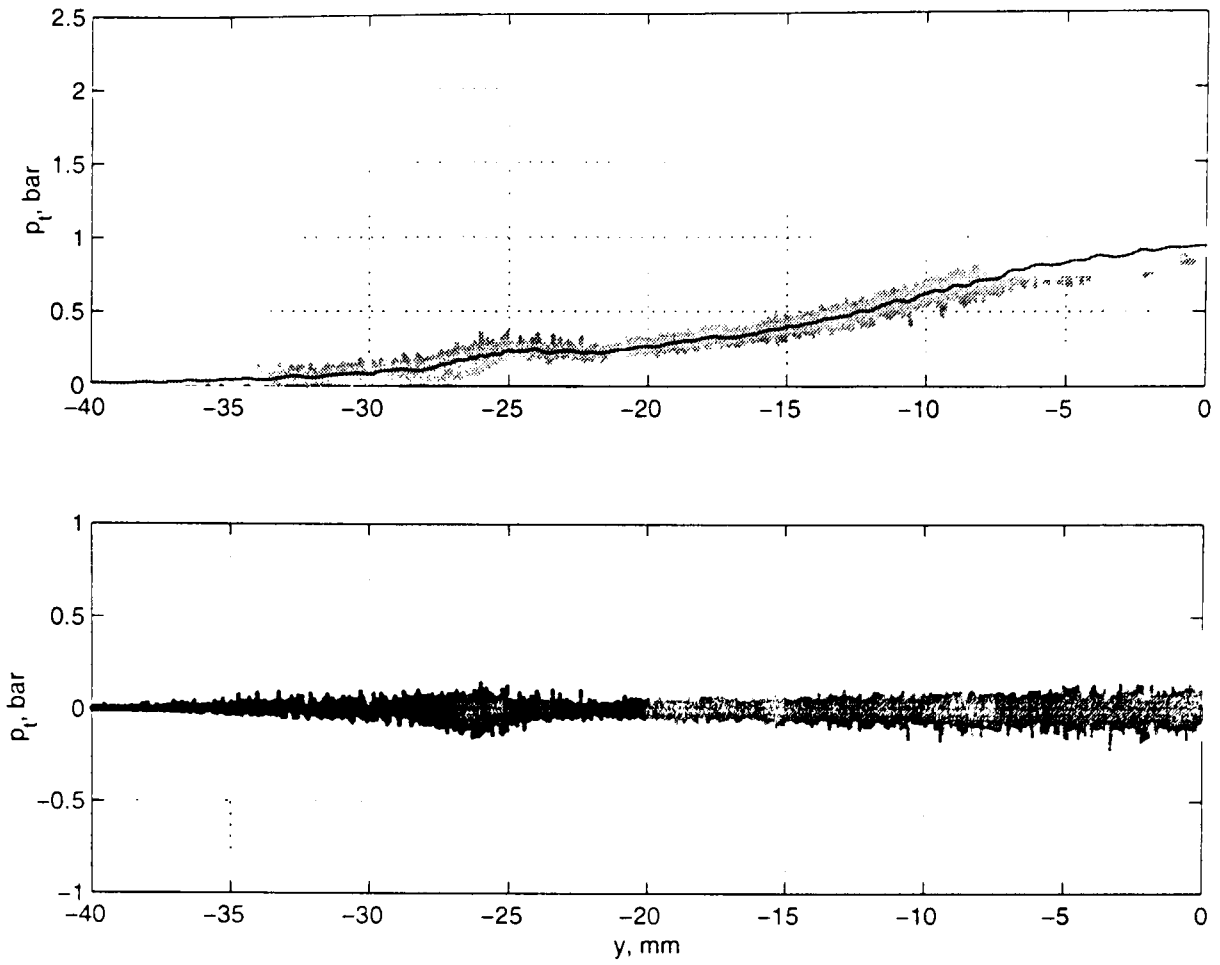


Figure 5-41 Fluctuating RPT Pitot pressure for Mach 5 (TM5) twinjet in quiescent on y-z plane at 60 mm downstream *(LT179)*

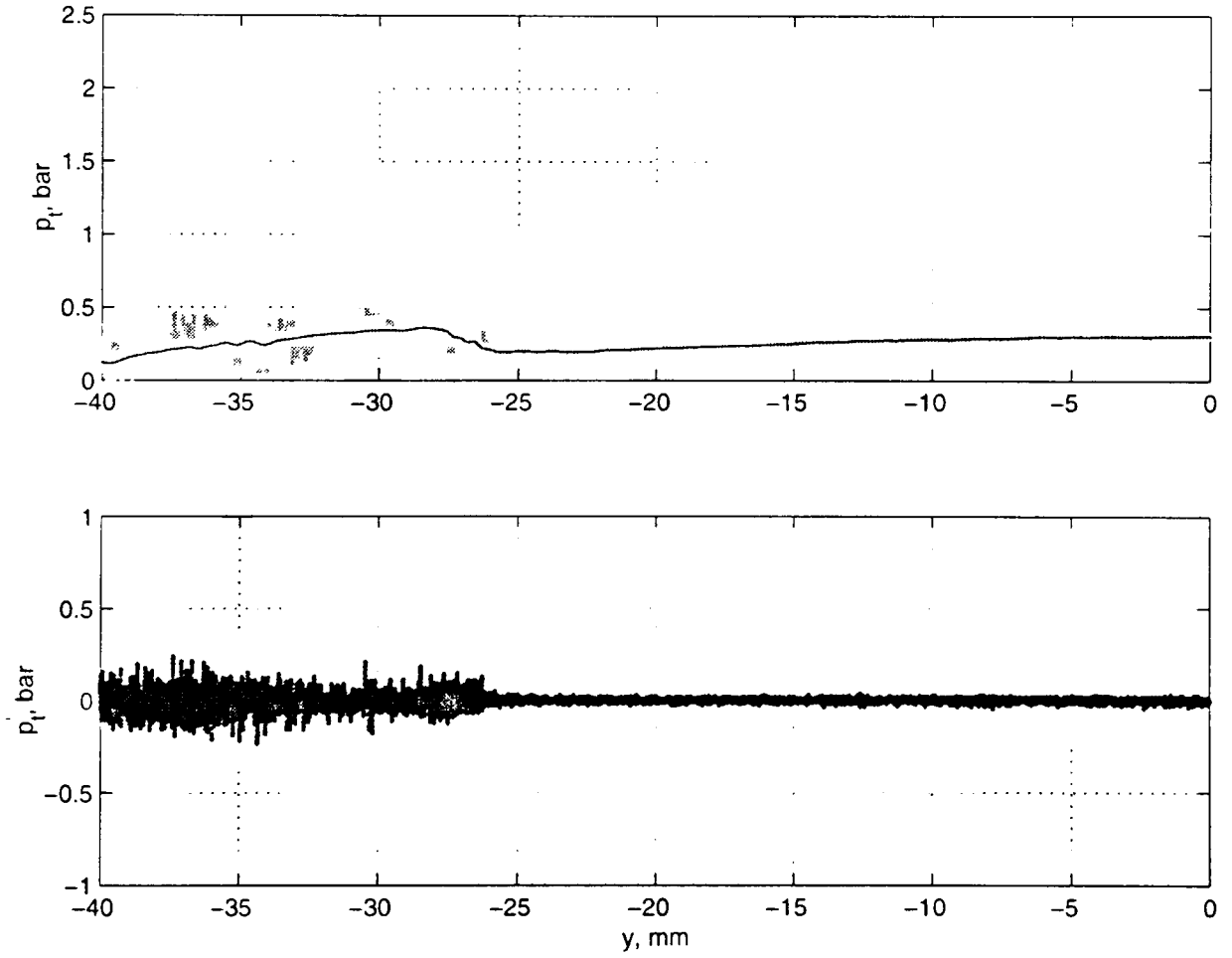


Figure 5-42 Fluctuating RPT Pitot pressure for Mach 5 (TM5) twinjet in quiescent on y-z plane at 100 mm downstream *(LT195)*

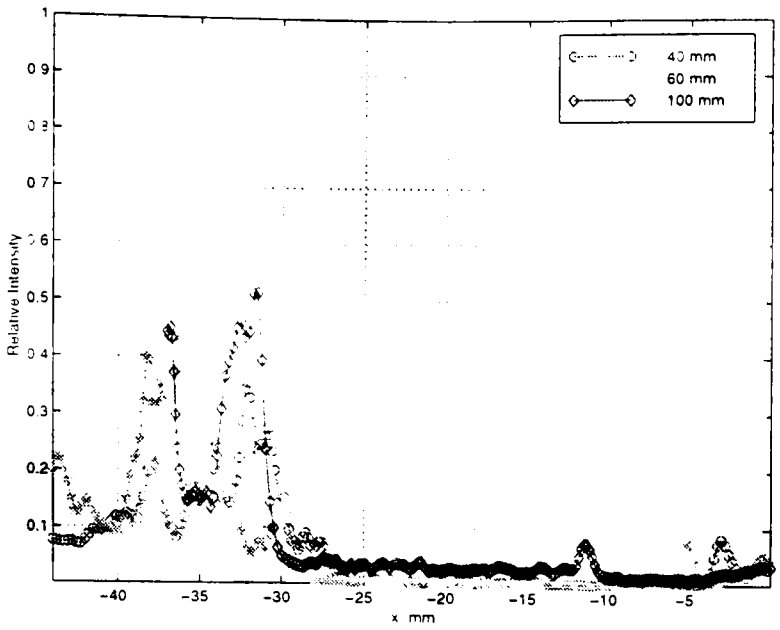


Figure 5-43 Relative Pitot pressure turbulence intensities for Mach 5 (TM5) twinjet on *x*-*z* plane *(40 mm: LT150; 60 mm: LT148; 100 mm: LT145)*

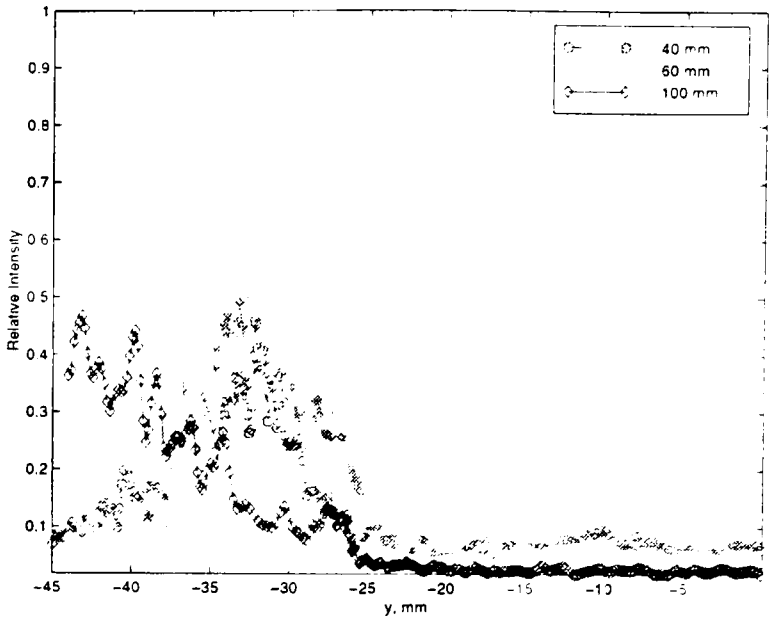


Figure 5-44 Relative Pitot pressure turbulence intensities for Mach 5 (TM5) twinjet on *y*-*z* plane *(40 mm: LT183; 60 mm: LT179; 100 mm: LT195)*

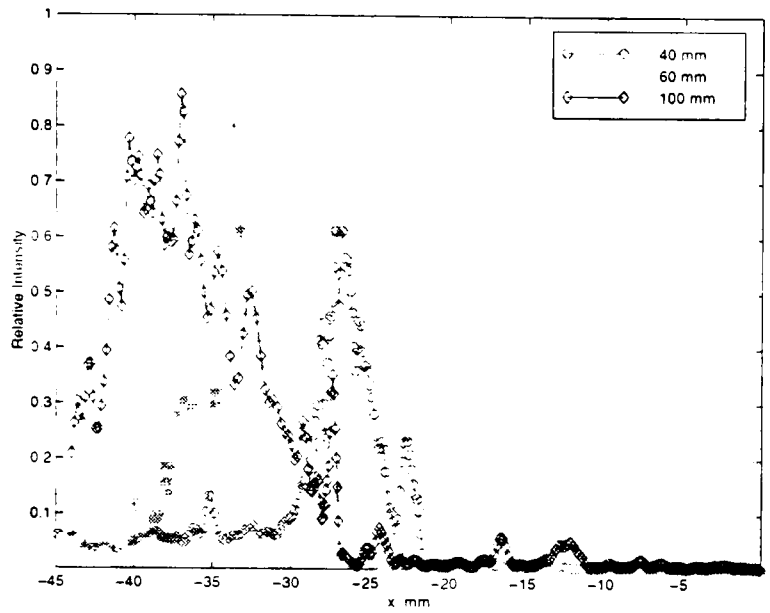
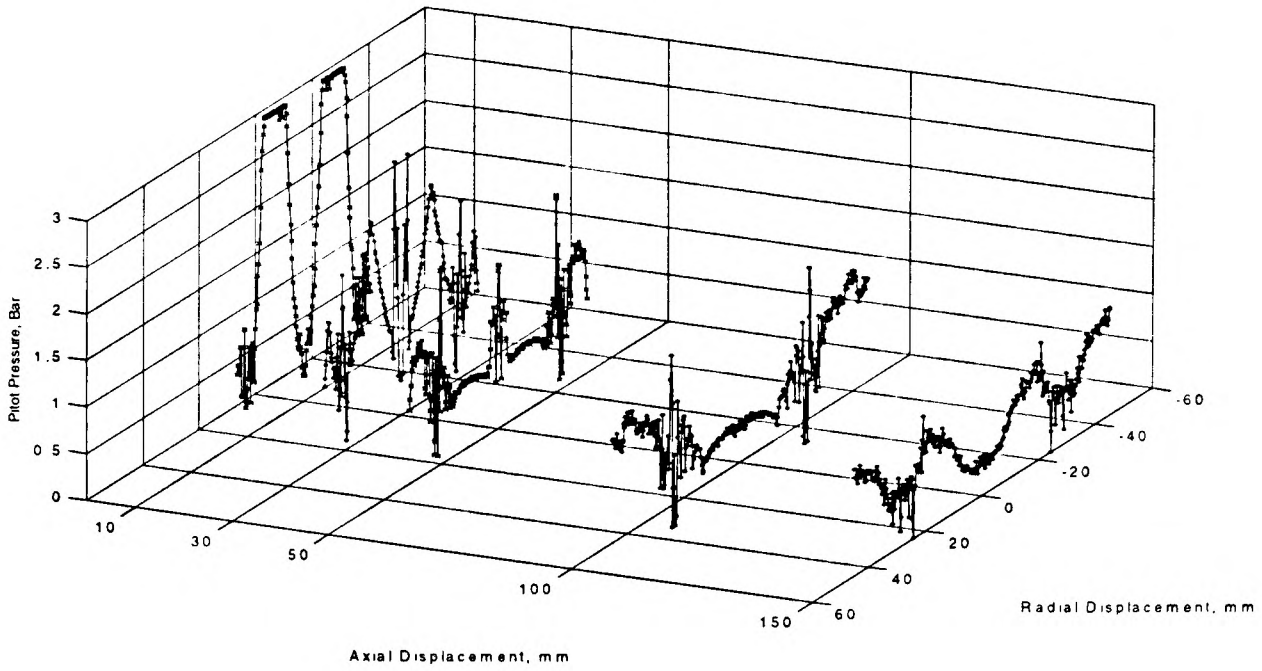


Figure 5-45 Relative Pitot pressure turbulence intensitis for Mach 5 (SM5M) single jet *(40 mm: LT182; 60 mm: LT181; 100 mm: LT196)*



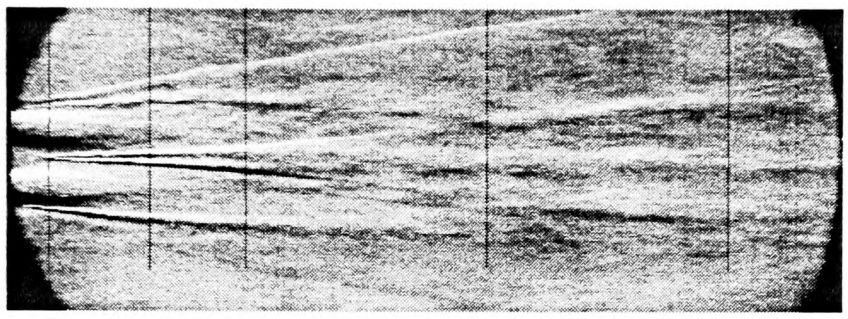
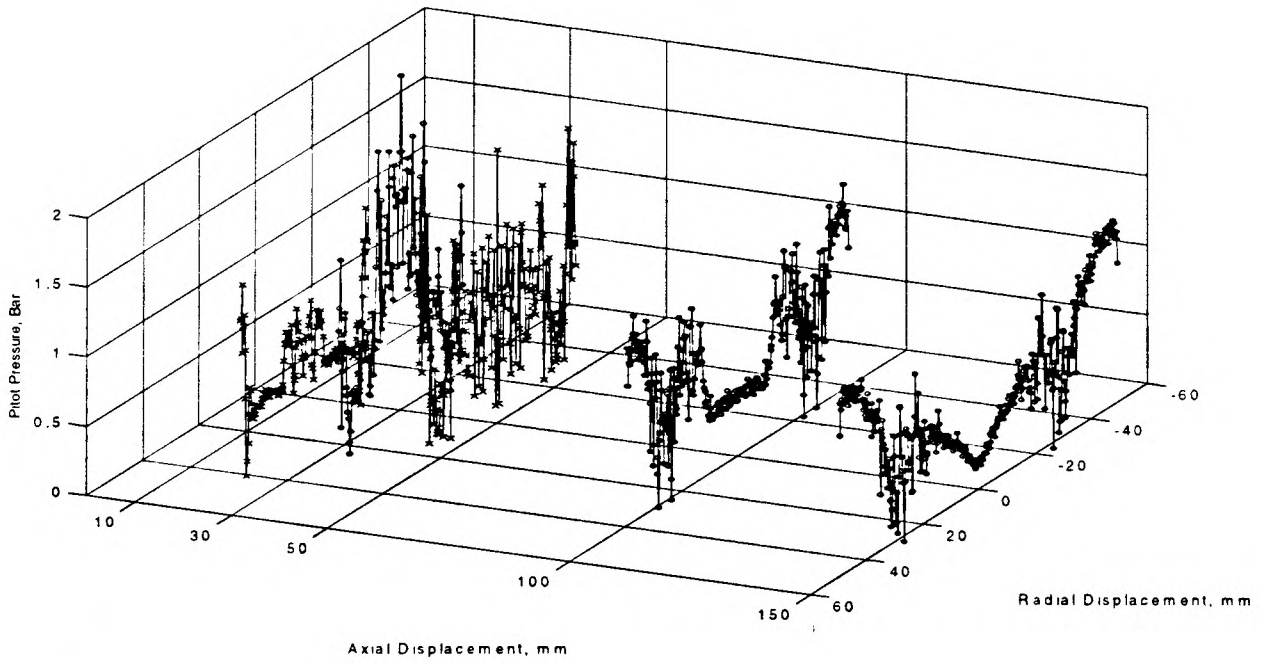


Figure 5-46 Pitot pressure profiles for co-flow Mach 5 (TM5) twinjet on x-z plane with corresponding location shown on Schlieren photograph



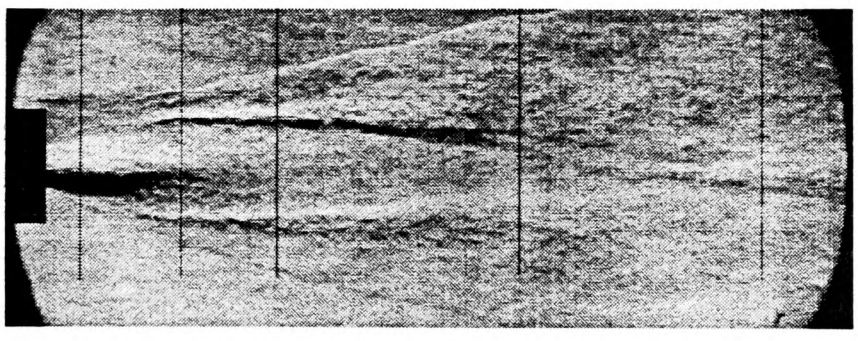


Figure 5-47 Pitot pressure profiles for co-flow Mach 5 (TM5) twinjet on y-z plane with corresponding location shown on Schlieren photograph

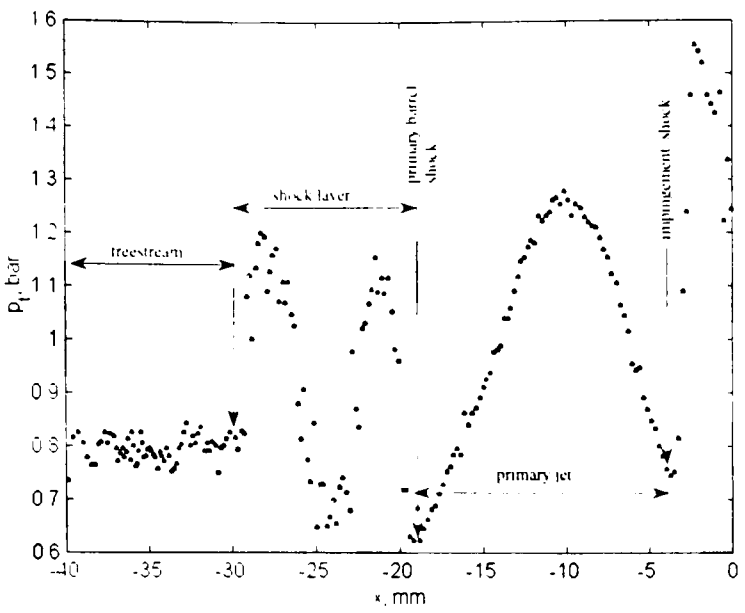


Figure 5-48 Pitot pressure for Mach 5 (TM5) twinjet injection in Mach 7 freestream at 40 mm downstream on *x*-*z* plane *(GT737)*

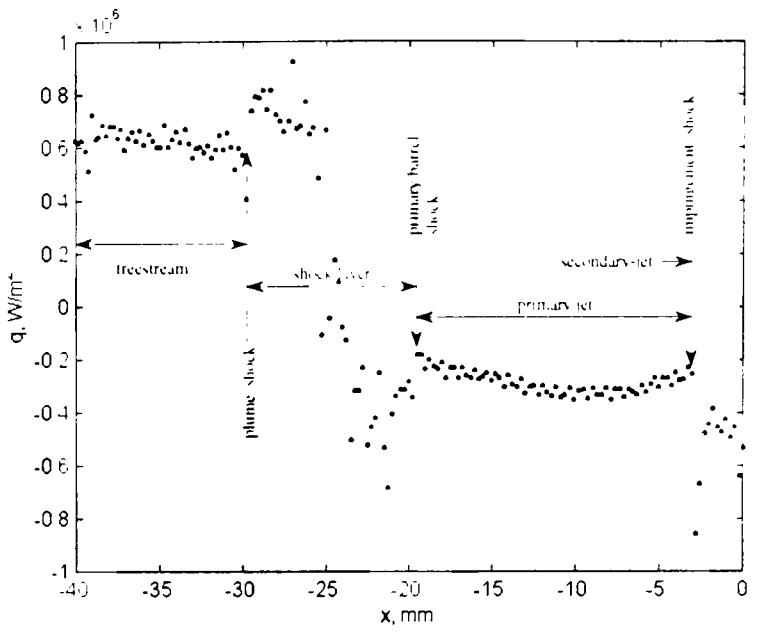


Figure 5-49 Heat flux for Mach 5 (TM5) twinjet injection in Mach 7 freestream at 40 mm downstream on *x*-*z* plane *(GT737)*

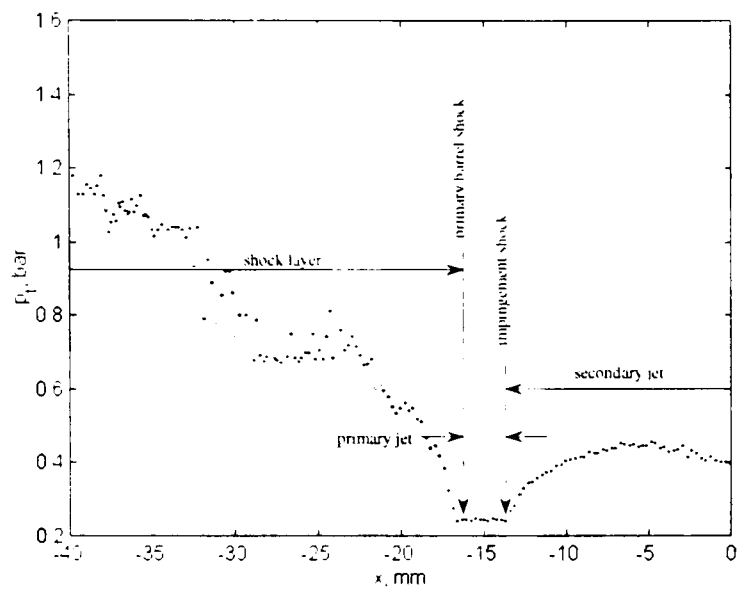


Figure 5-50 Pitot pressure for Mach 5 (TM5) twinjet injection in Mach 7 freestream at 100 mm downstream on *x*-*z* plane *(GT744)*

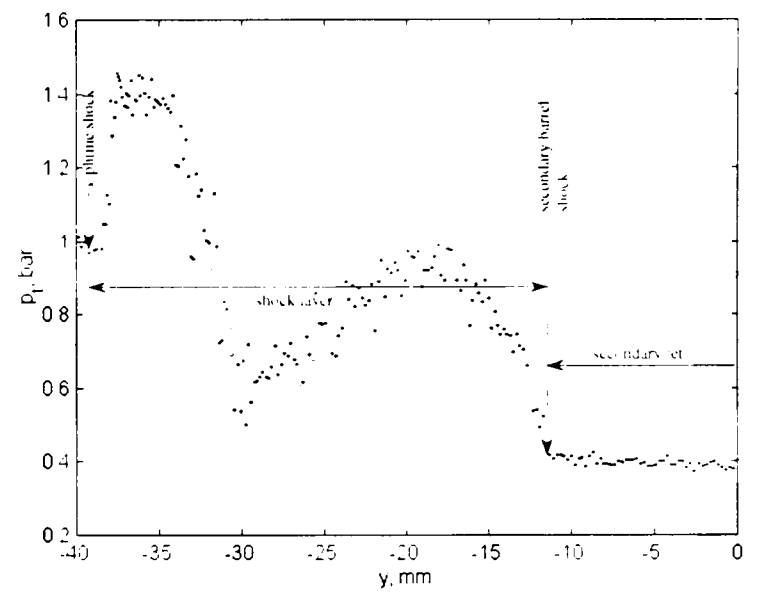


Figure 5-51 Pitot pressure for Mach 5 (TM5) twinjet injection in Mach 7 freestream at 100 mm downstream on *y*-*z* plane *(GT741)*

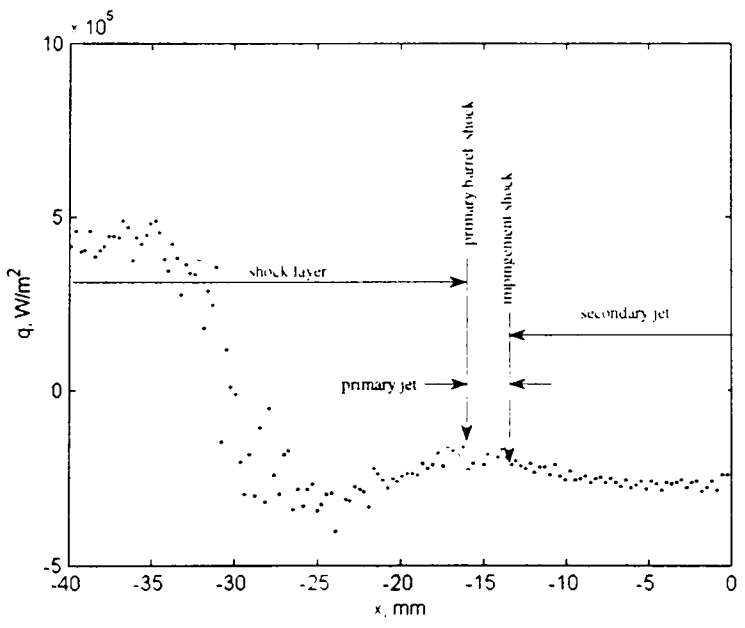


Figure 5-52 Heat flux for Mach 5 (TM5) twinjet injection in Mach 7 freestream at 100 mm downstream on *x*-*z* plane *(GT744)*

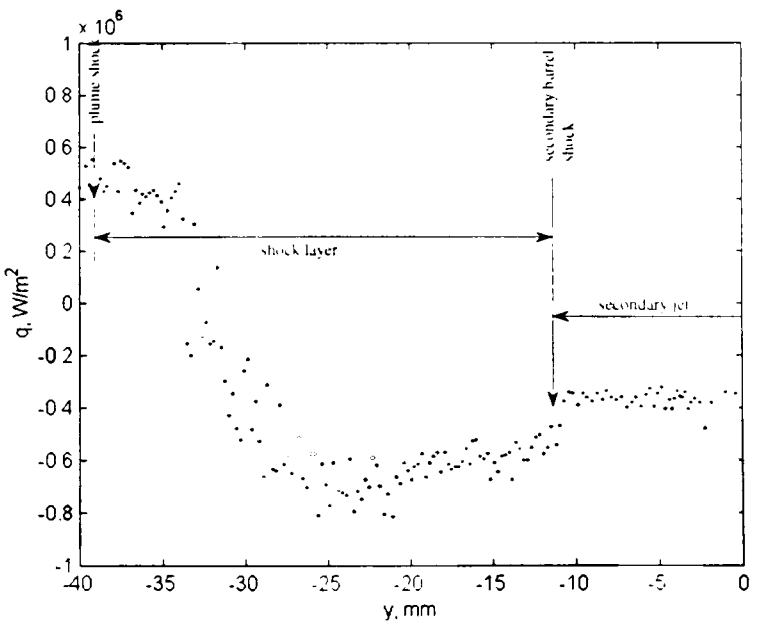


Figure 5-53 Heat flux for Mach 5 (TM5) twinjet injection in Mach 7 freestream at 100 mm downstream on *y*-*z* plane *(GT741)*

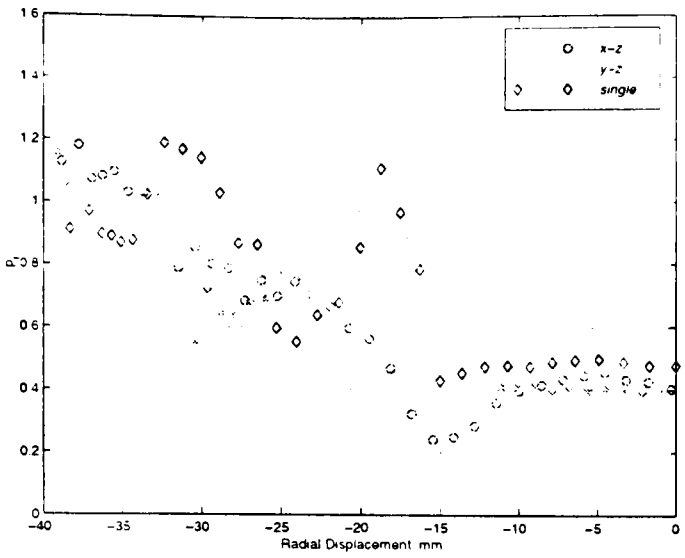


Figure 5-54 Pitot pressure for Mach 5 (TM5) twinjet with N_2 injection in Mach 7 freestream at 100 mm downstream

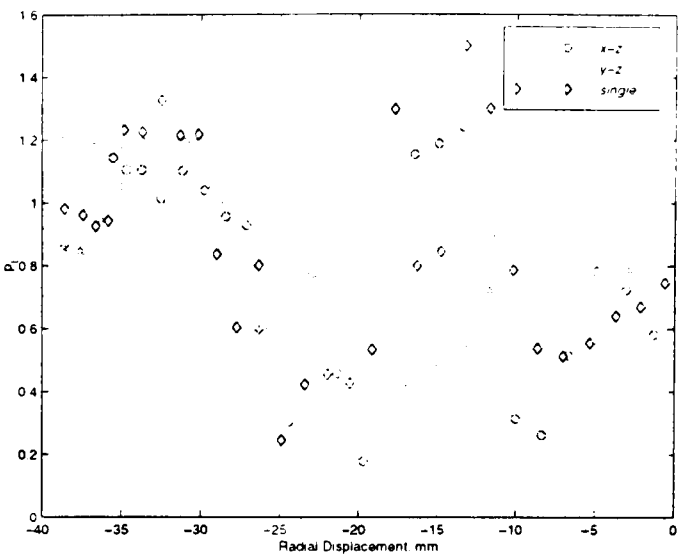


Figure 5-55 Pitot pressure for Mach 5 (TM5) twinjet with H_2 injection in Mach 7 freestream at 100 mm downstream

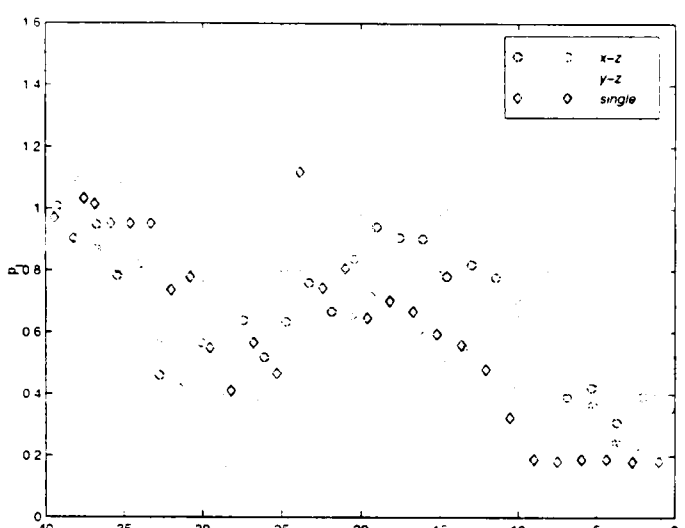


Figure 5-56 Pitot pressure for Mach 5 (TM5) twinjet with N_2 injection in Mach 7 freestream at 150 mm downstream

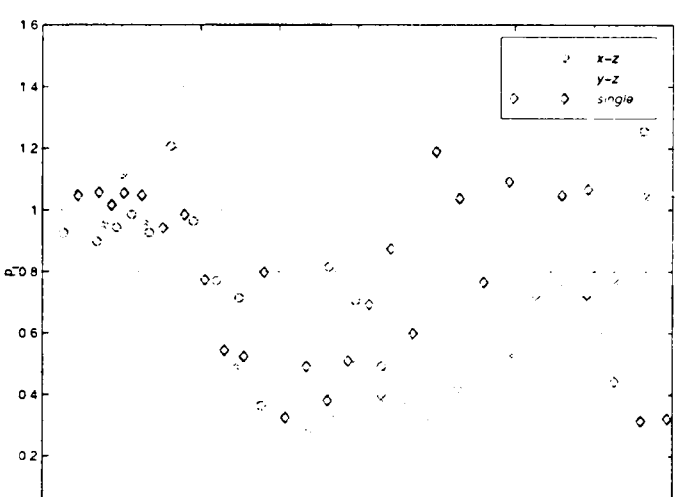


Figure 5-57 Pitot pressure for Mach 5 (TM5) twinjet with H_2 injection in Mach 7 freestream at 150 mm downstream

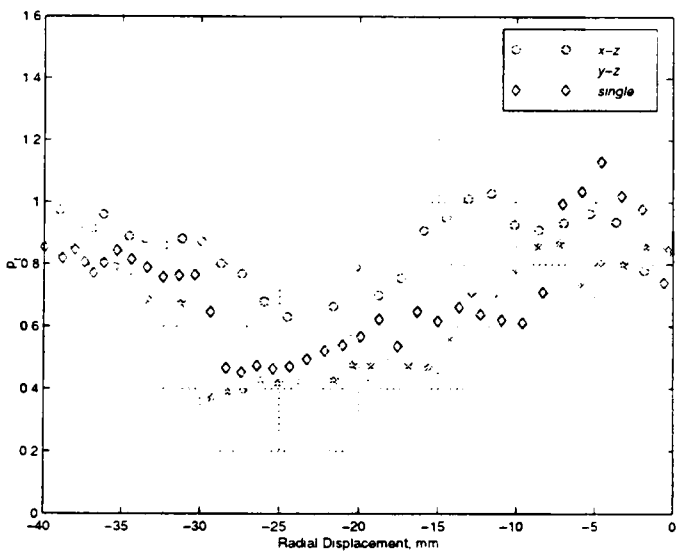


Figure 5-58 Pitot pressure for Mach 5 (TM5) twinjet with N_2 injection in Mach 7 freestream at 250 mm downstream

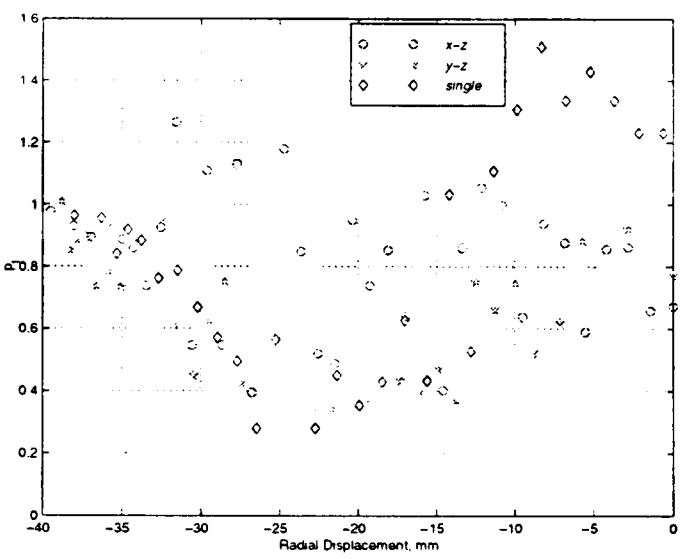


Figure 5-59 Pitot pressure for Mach 5 (TM5) twinjet with H_2 injection in Mach 7 freestream at 250 mm downstream

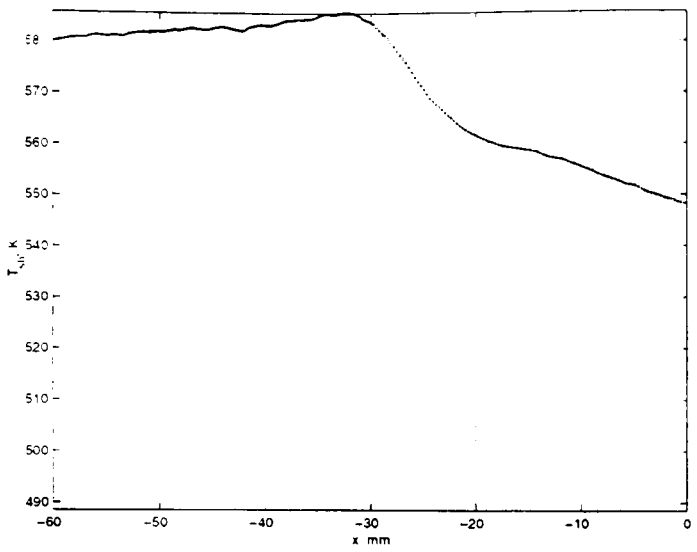


Figure 5-60 Substrate temperature signal for co-flow Mach 5 (TM5) twinjet on *x*-*z* plane *(hot probe, GT744)*

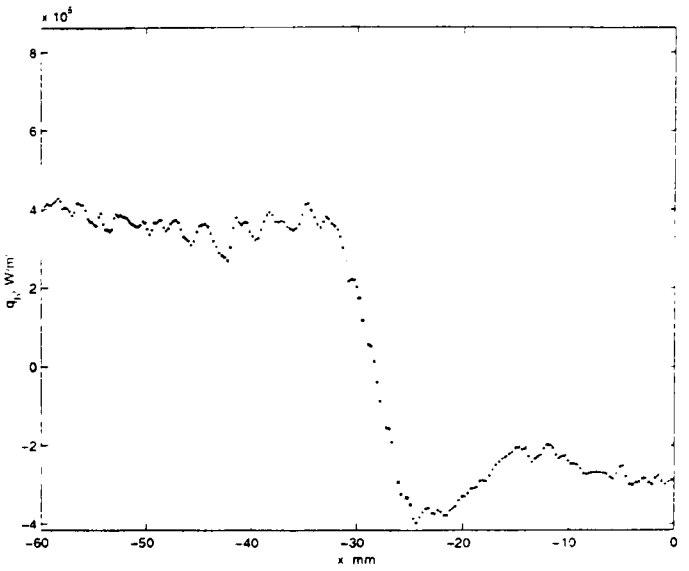


Figure 5-61 Heat flux signal for co-flow Mach 5 (TM5) twinjet on *x*-*z* plane *(hot probe, GT744)*

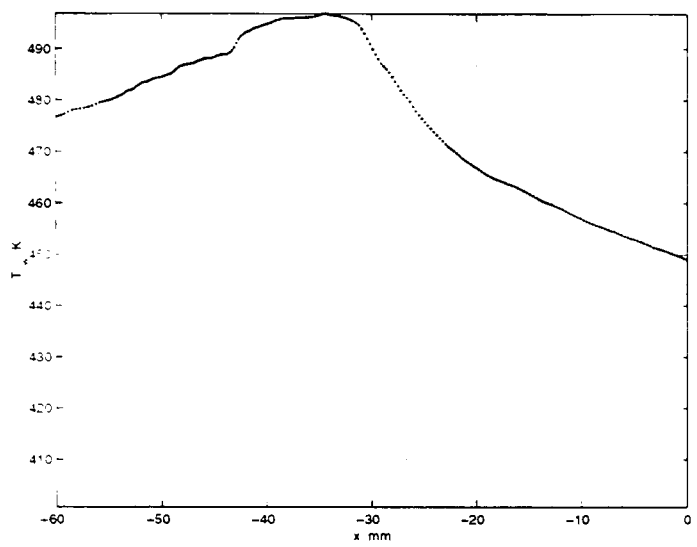


Figure 5-62 Substrate temperature signal for co-flow Mach 5 (TM5) twinjet on *x*-*z* plane *(warm probe, GT744)*

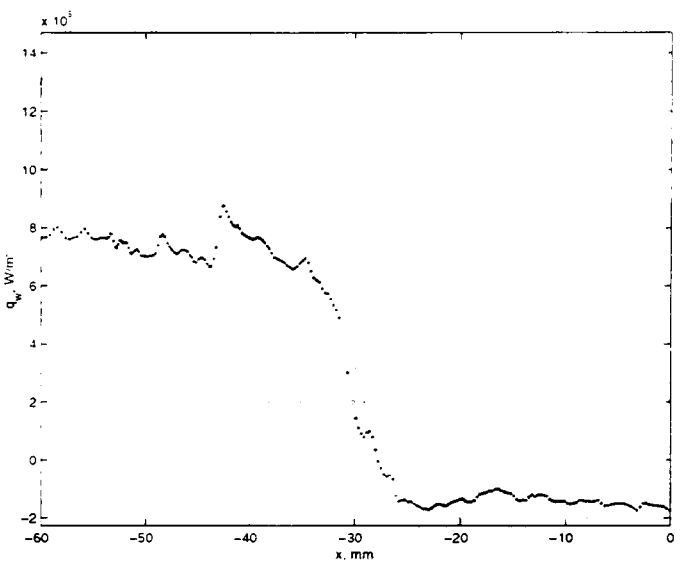


Figure 5-63 Heat flux signal for co-flow Mach 5 (TM5) twinjet on *x*-*z* plane *(warm probe, GT744)*

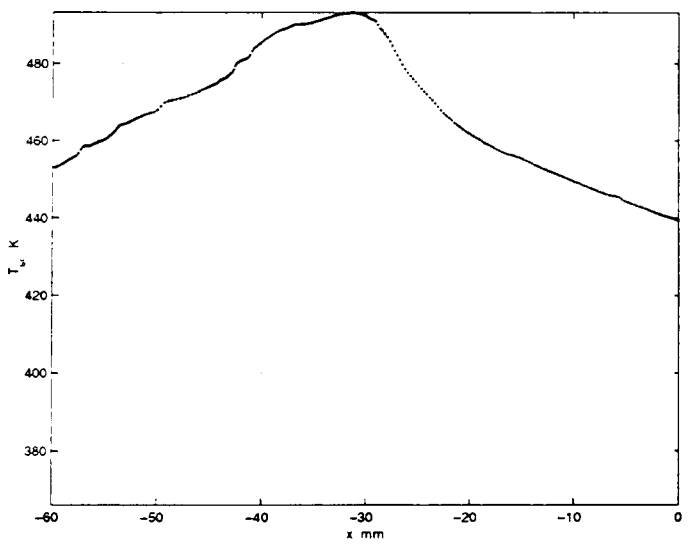


Figure 5-64 Substrate temperature signal for co-flow Mach 5 (TM5) twinjet on *x*-*z* plane *(cold probe, GT744)*

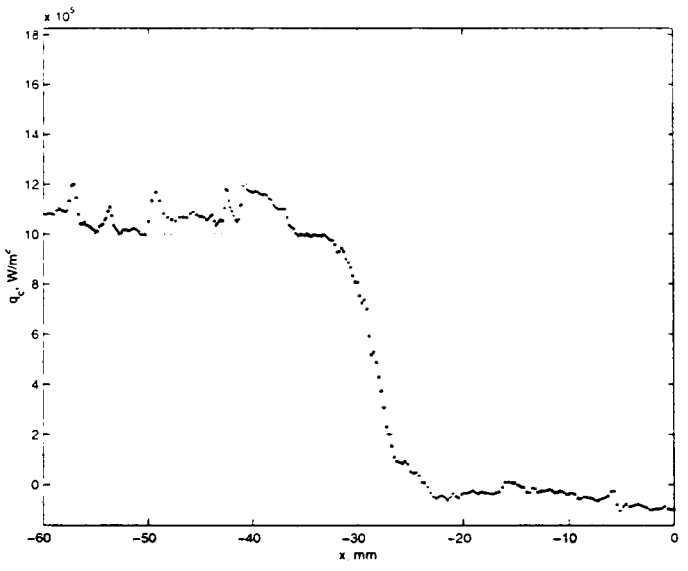


Figure 5-65 Heat flux signal for co-flow Mach 5 (TM5) twinjet on *x*-*z* plane *(cold probe, GT744)*

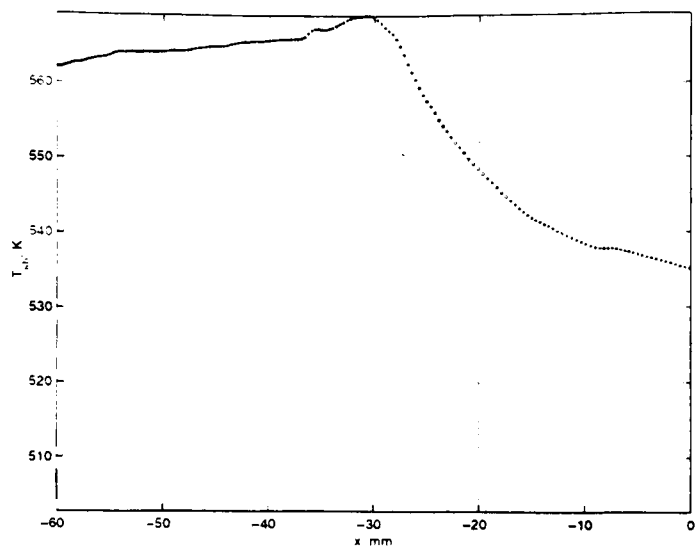


Figure 5-66 Substrate temperature signal for co-flow Mach 5 (TM5) twinjet on y-z plane *(hot probe, GT746)*

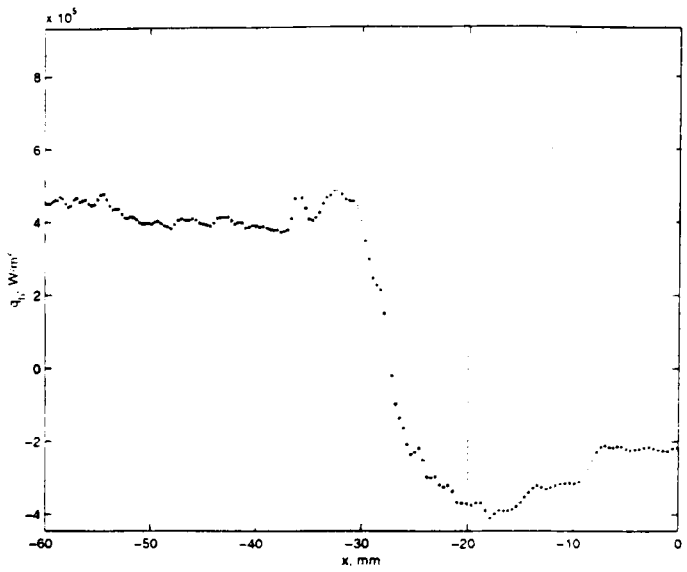


Figure 5-67 Heat flux signal for co-flow Mach 5 (TM5) twinjet on y-z plane *(hot probe, GT746)*

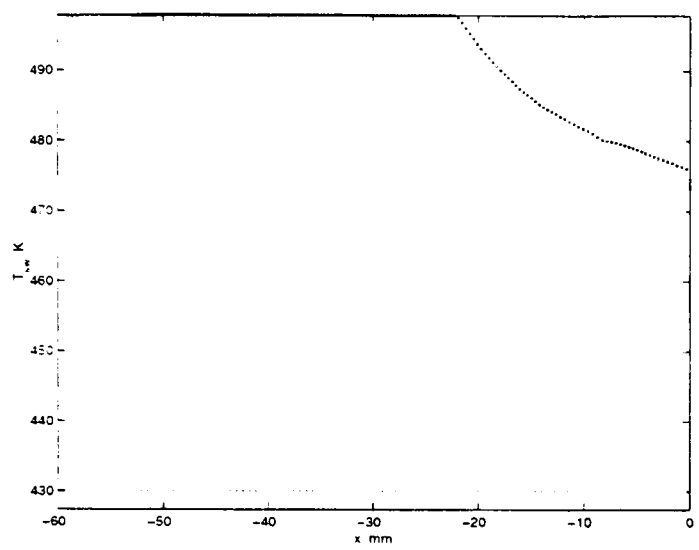


Figure 5-68 Substrate temperature signal for co-flow Mach 5 (TM5) twinjet on y-z plane *(warm probe, GT746)*

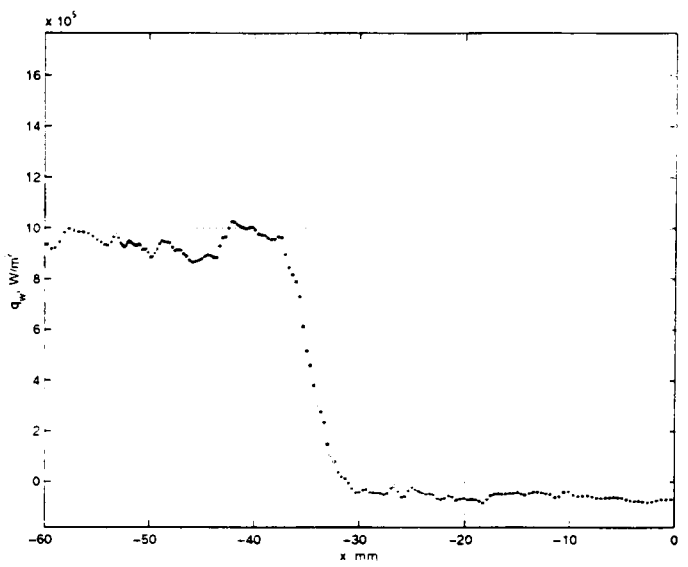


Figure 5-69 Heat flux signal for co-flow Mach 5 (TM5) twinjet on y-z plane *(warm probe, GT746)*

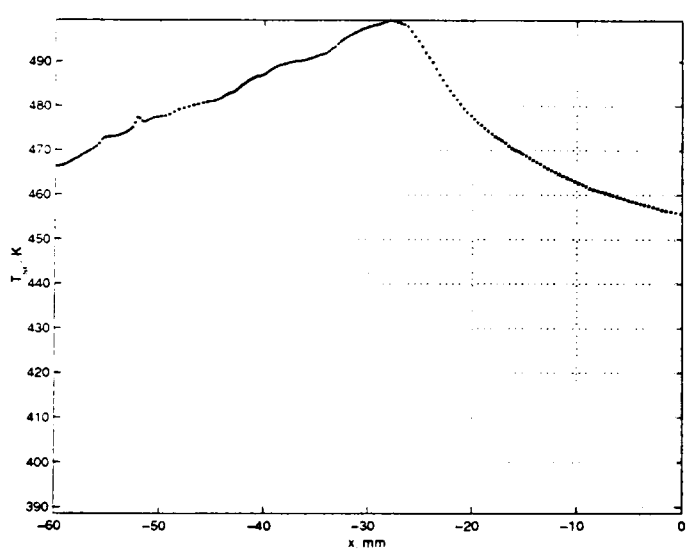


Figure 5-70 Substrate temperature signal for co-flow Mach 5 (TM5) twinjet on y-z plane *(cold probe, GT746)*

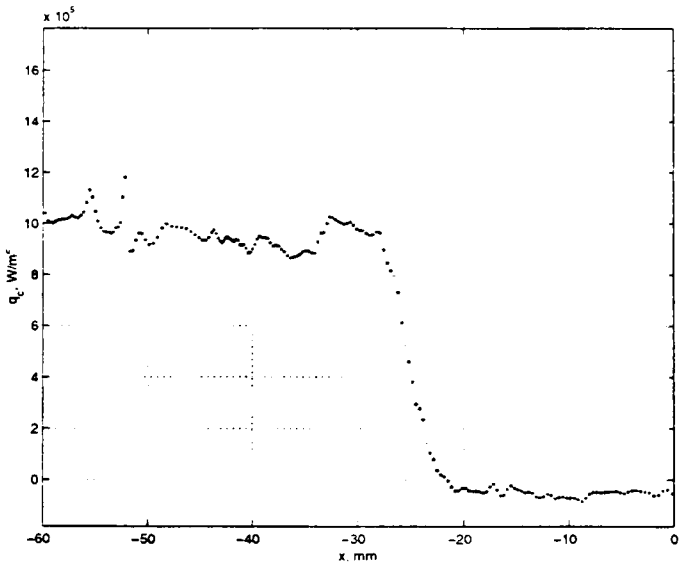


Figure 5-71 Heat flux signal for co-flow Mach 5 (TM5) twinjet on y-z plane *(cold probe, GT746)*

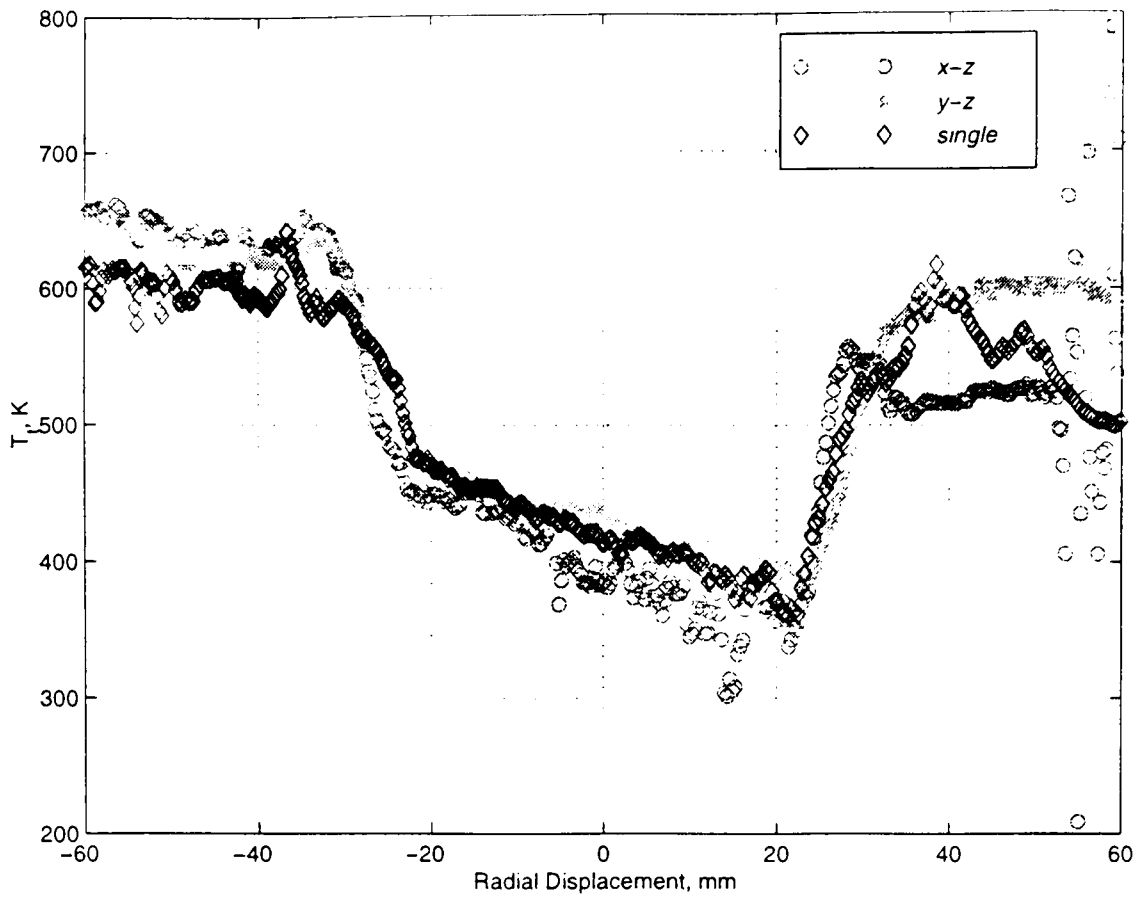


Figure 5-72 Total temperature for Mach 5 hypersonic co-flow flowfield at 100 mm downstream *(x-z plane: GT744, y-z plane: GT746, single: GT747)*

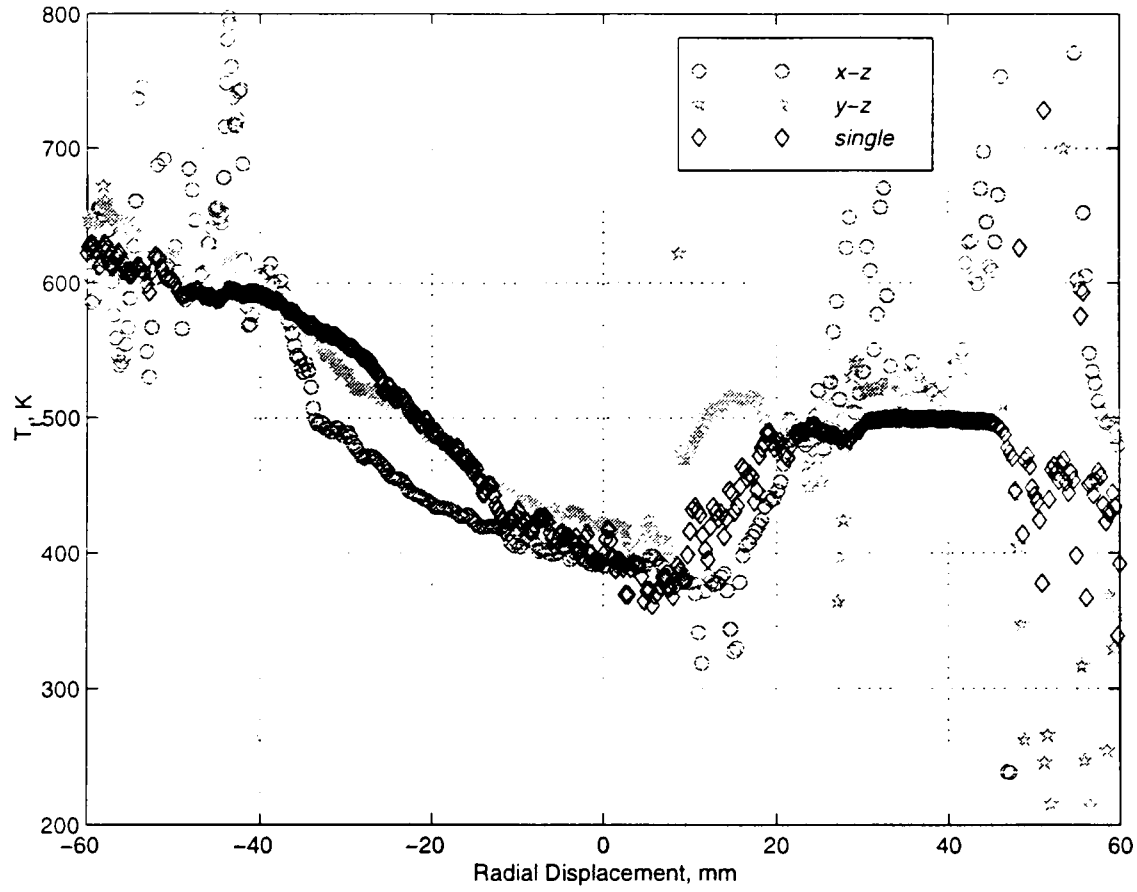


Figure 5-73 Total temperature for Mach 5 hypersonic co-flow flowfield at 250 mm downstream *(x-z plane: GT745, y-z plane: GT749, single: GT748)*

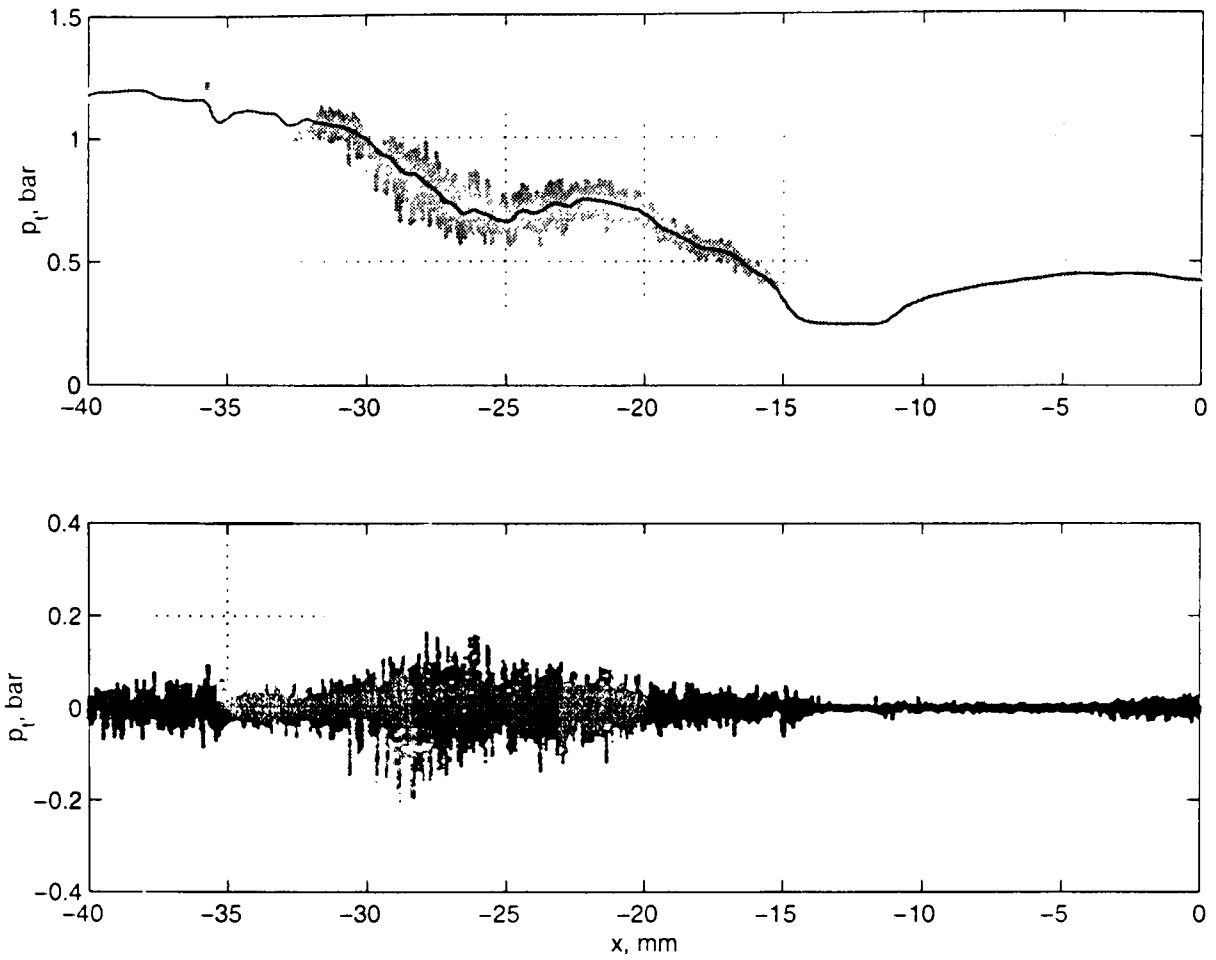


Figure 5-74 Fluctuating BPT Pitot pressure for Mach 5 (TM5) twinjet with N_2 injection in Mach 7 freestream on x-z plane at 100 mm downstream *(GT744)*

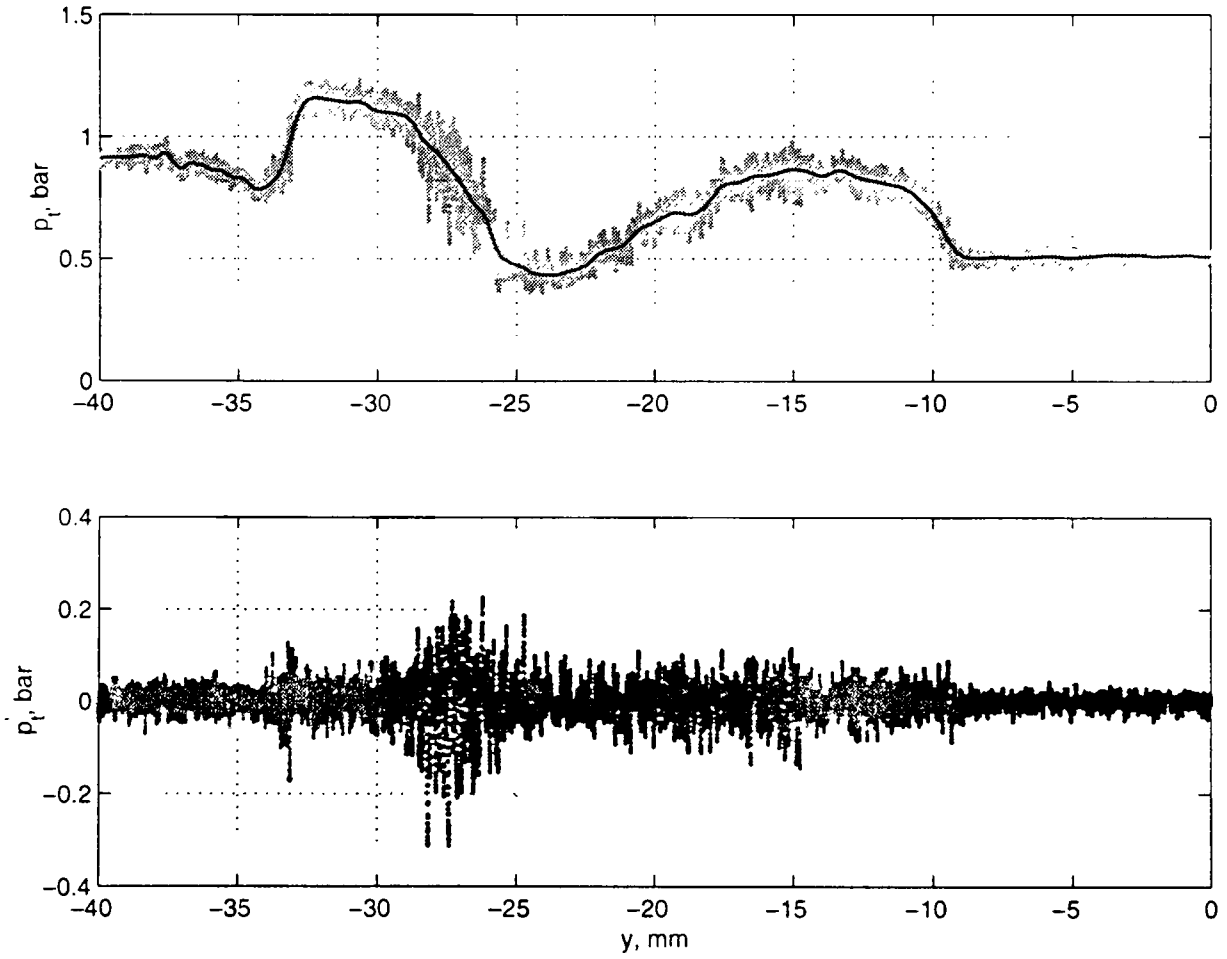


Figure 5-75 Fluctuating BPT Pitot pressure for Mach 5 (TM5) twinjet with N_2 injection in Mach 7 freestream on y-z plane at 100 mm downstream *(GT746)*

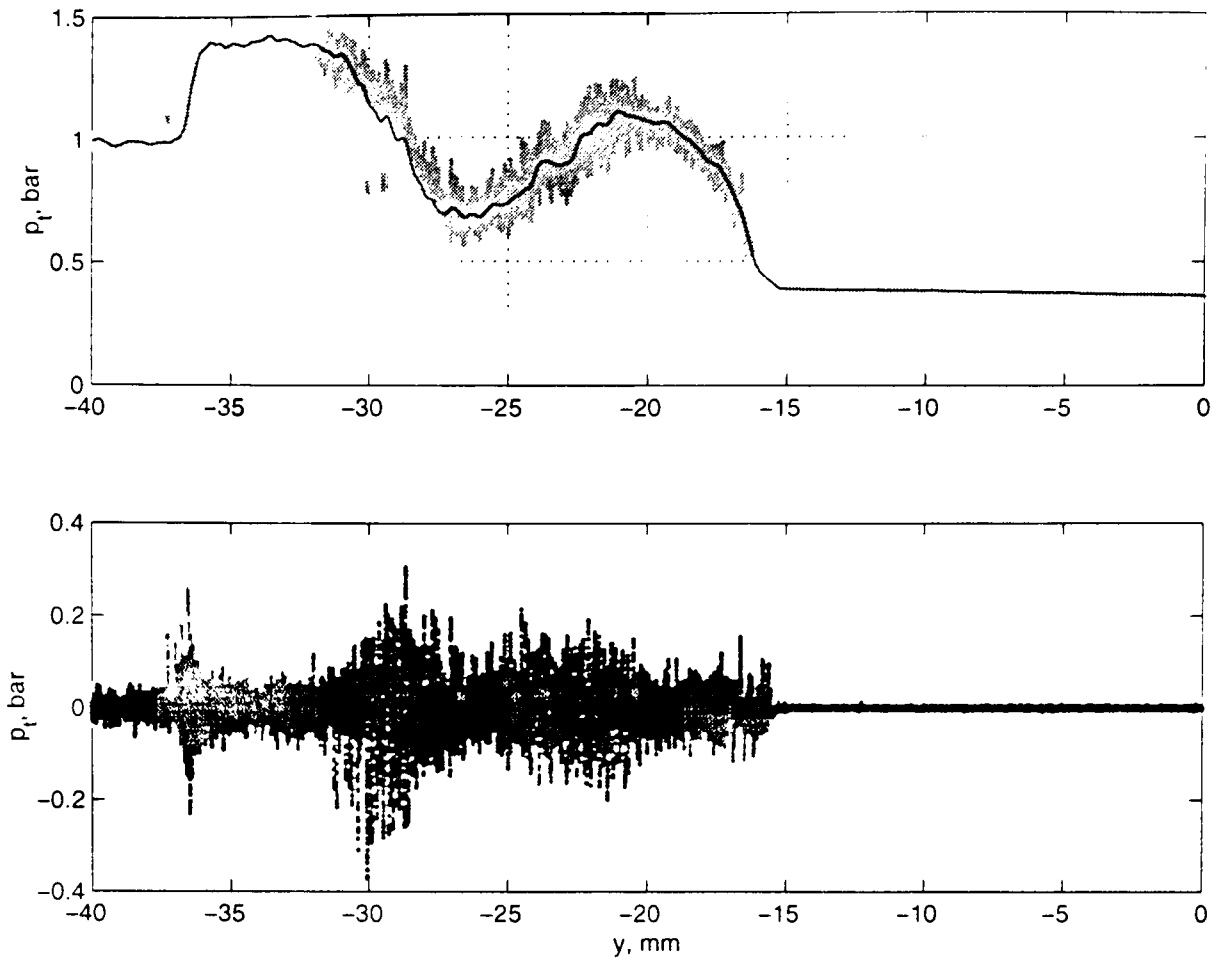


Figure 5-76 Fluctuating BPT Pitot pressure for Mach 5 (SM5M) single jet with N_2 injection in Mach 7 freestream at 100 mm downstream *(GT740)*

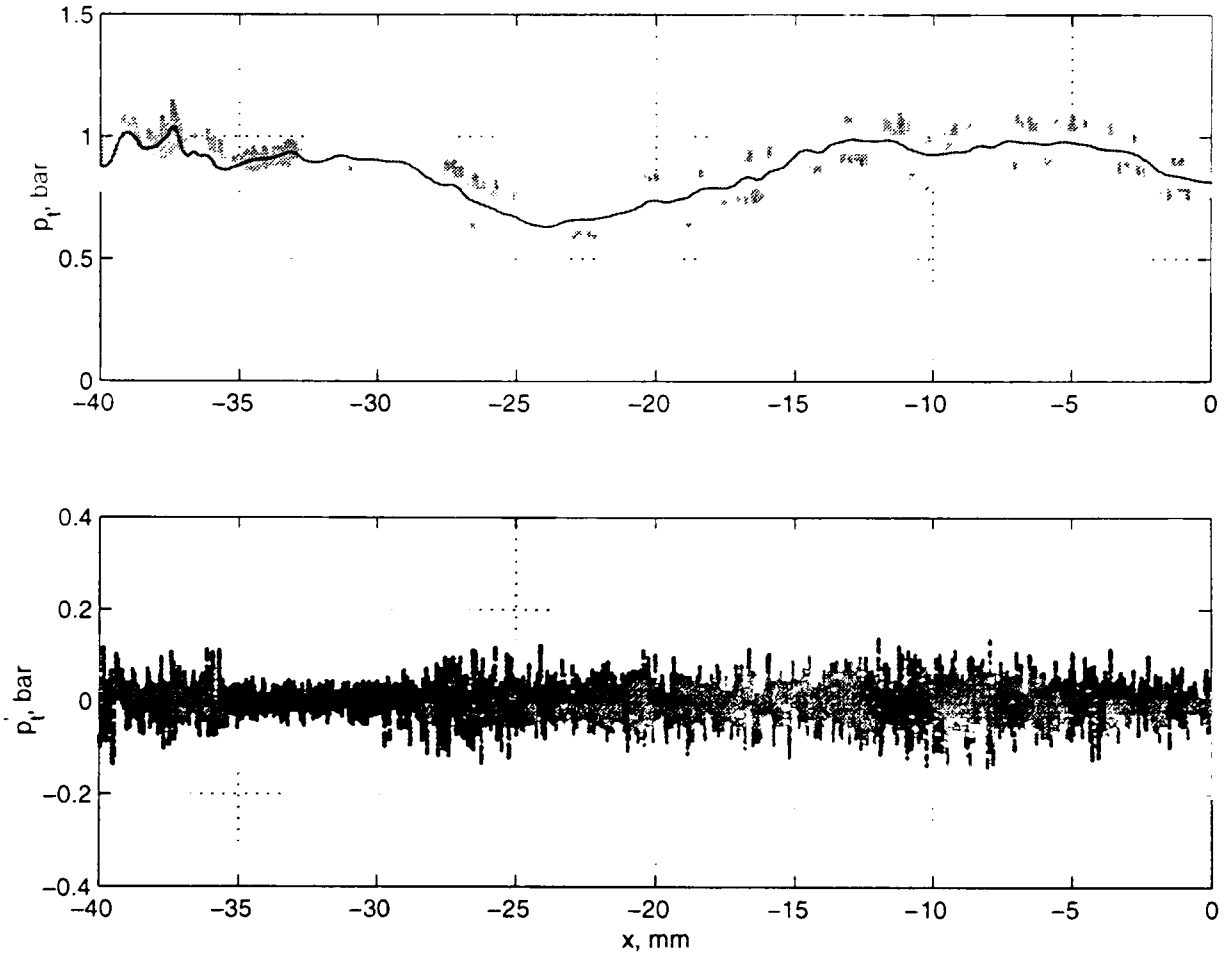


Figure 5-77 Fluctuating BPT Pitot pressure for Mach 5 (TM5) twinjet with N_2 injection in Mach 7 freestream on x-z plane at 250 mm downstream *(GT745)*

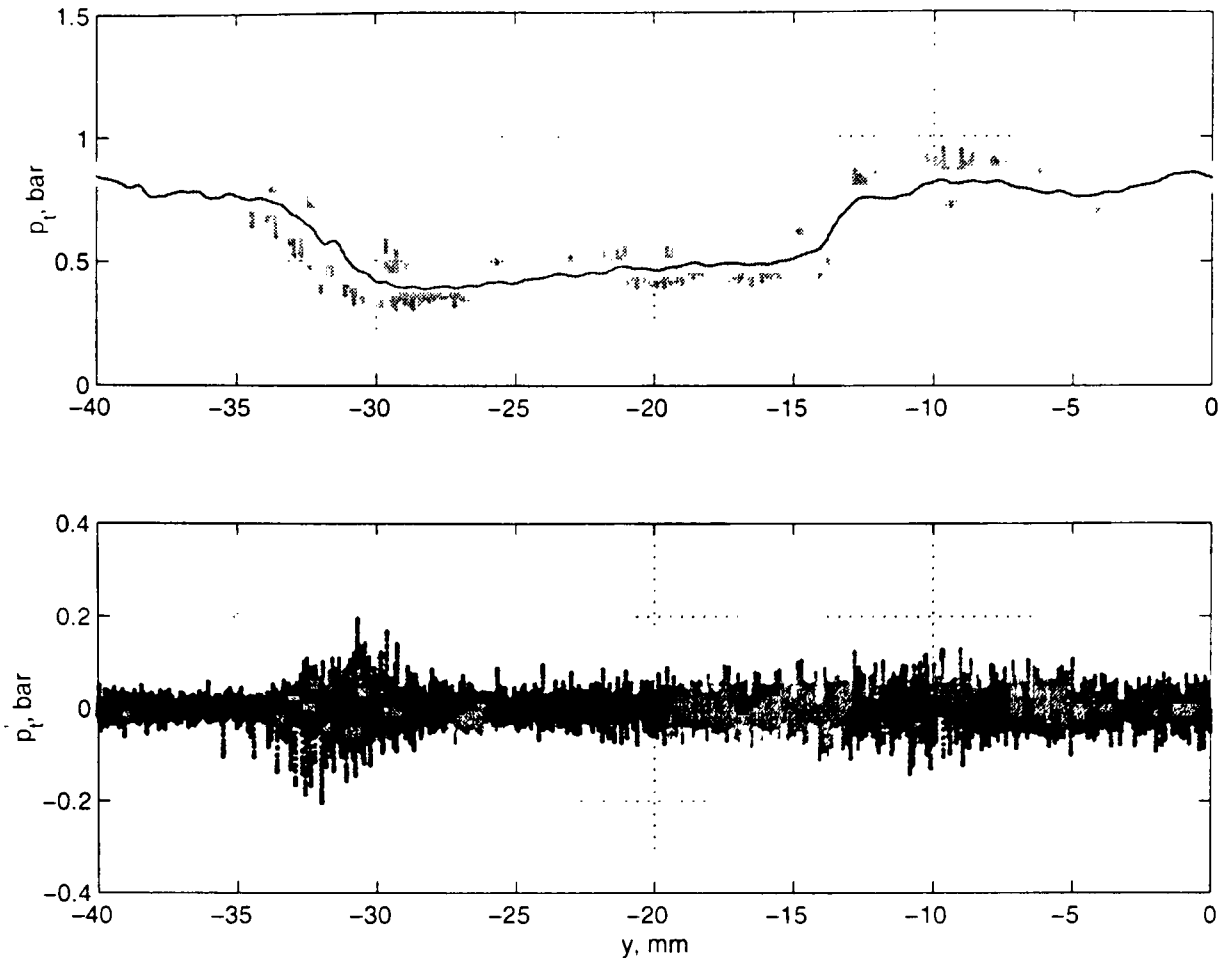


Figure 5-78 Fluctuating BPT Pitot pressure for Mach 5 (TM5) twinjet with N_2 injection in Mach 7 freestream on y-z plane at 250 mm downstream *(GT749)*

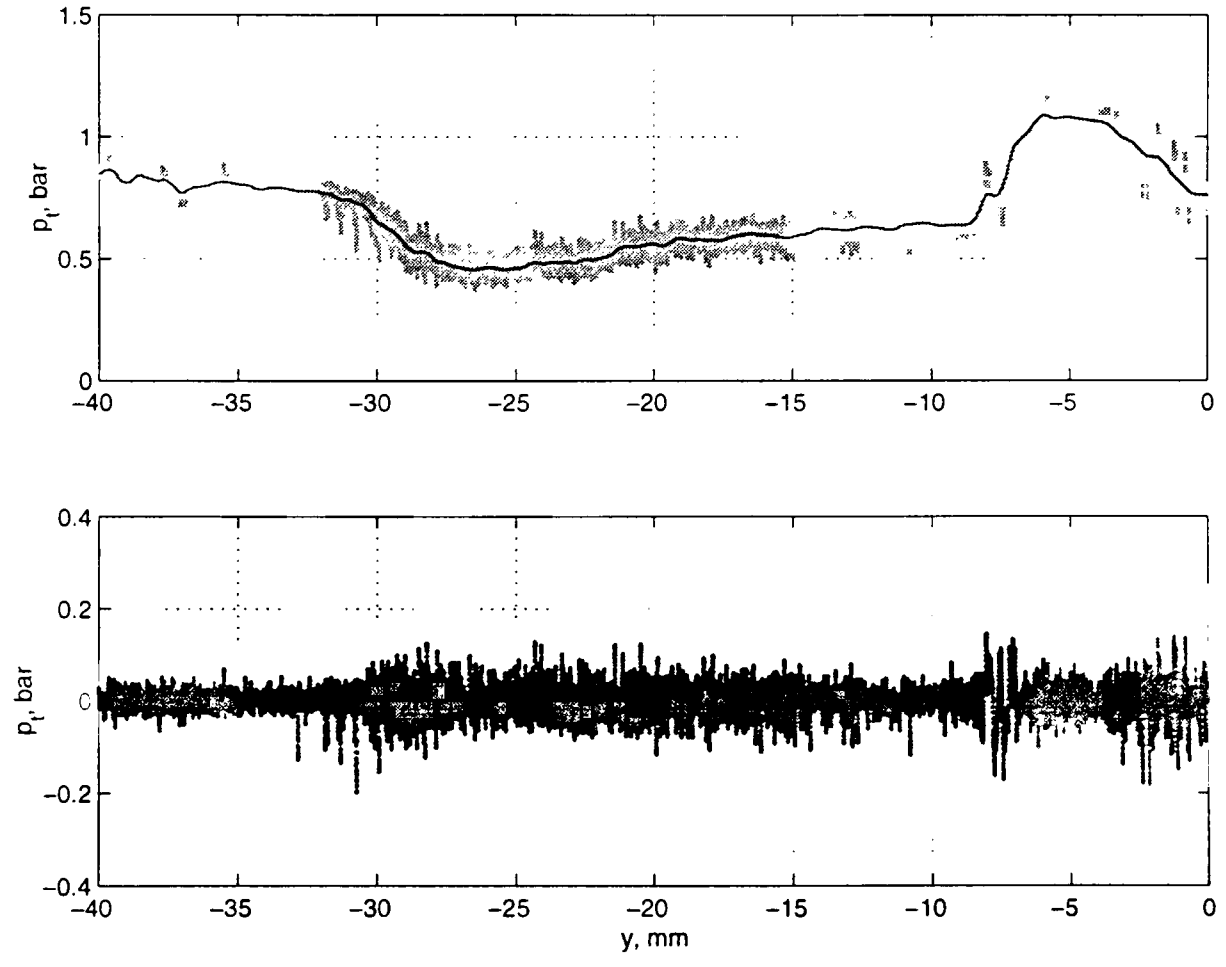


Figure 5-79 Fluctuating BPT Pitot pressure for Mach 5 (SM5M) single jet with N_2 injection in Mach 7 freestream at 250 mm downstream *(GT748)*

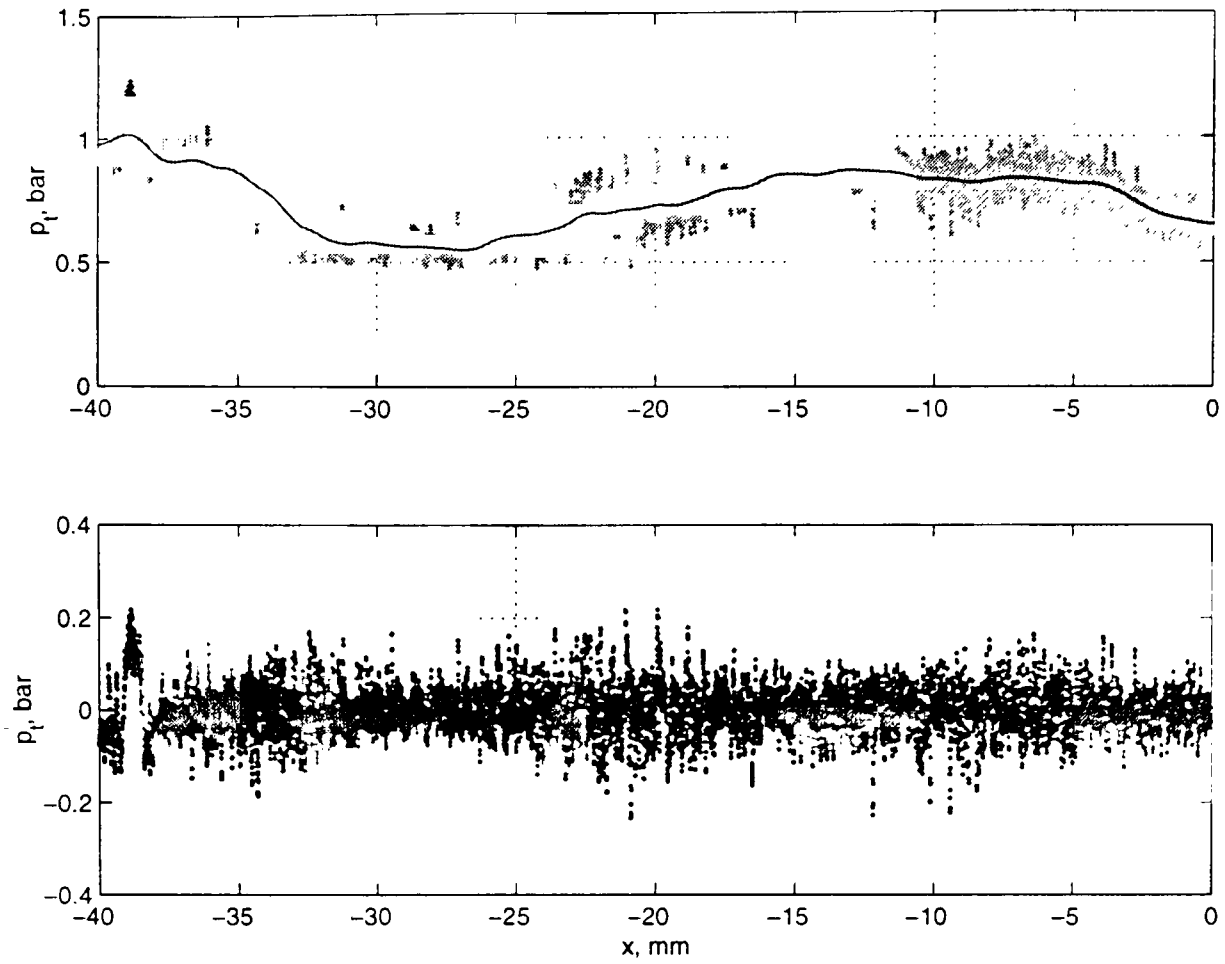


Figure 5-80 Fluctuating BPT Pitot pressure for Mach 5 (TM5) twinjet with H_2 injection in Mach 7 freestream on *x*-*z* plane at 250 mm downstream *(GT727)*

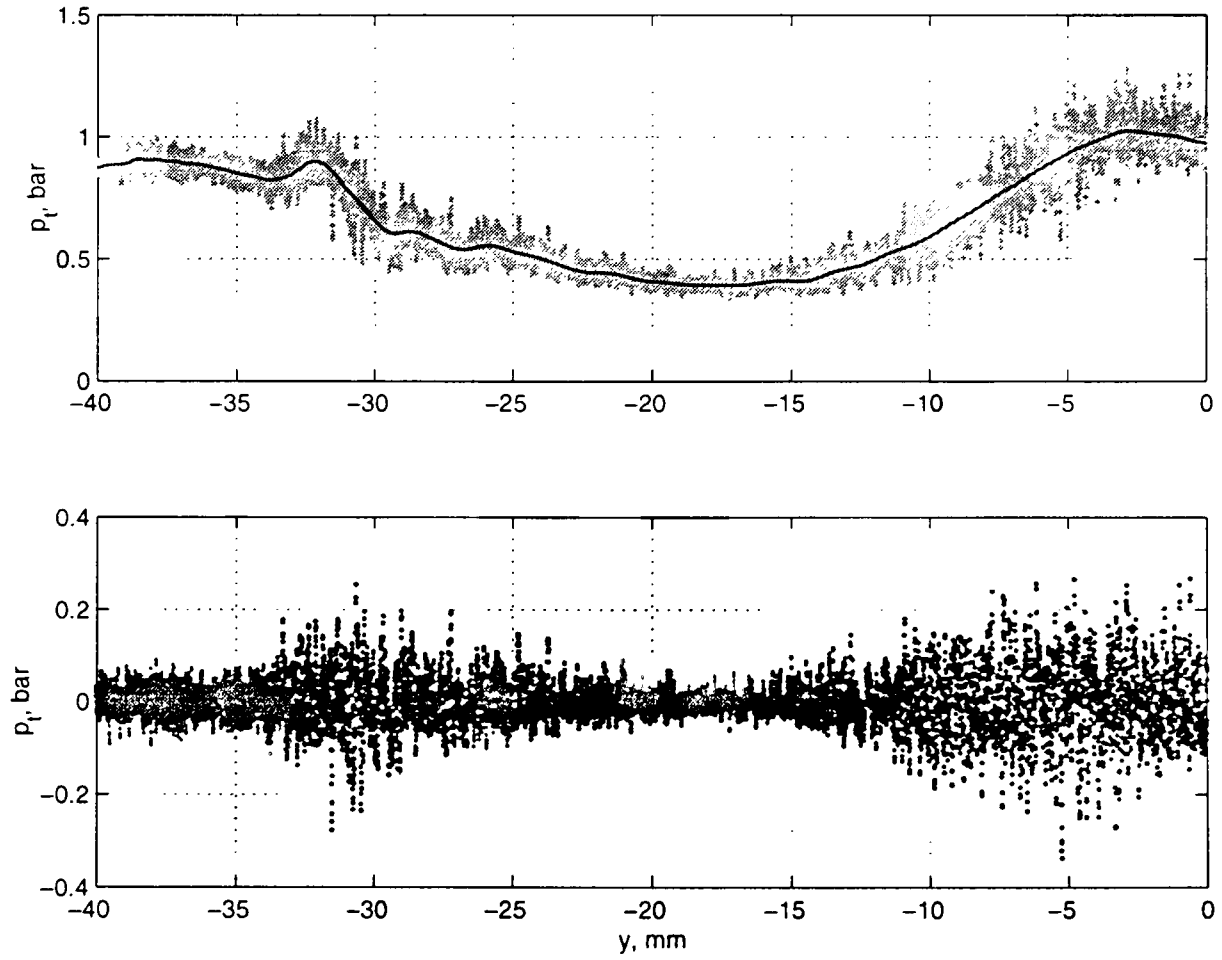


Figure 5-81 Fluctuating BPT Pitot pressure for Mach 5 (TM5) twinjet with H_2 injection in Mach 7 freestream on *y*-*z* plane at 250 mm downstream *(GT726)*

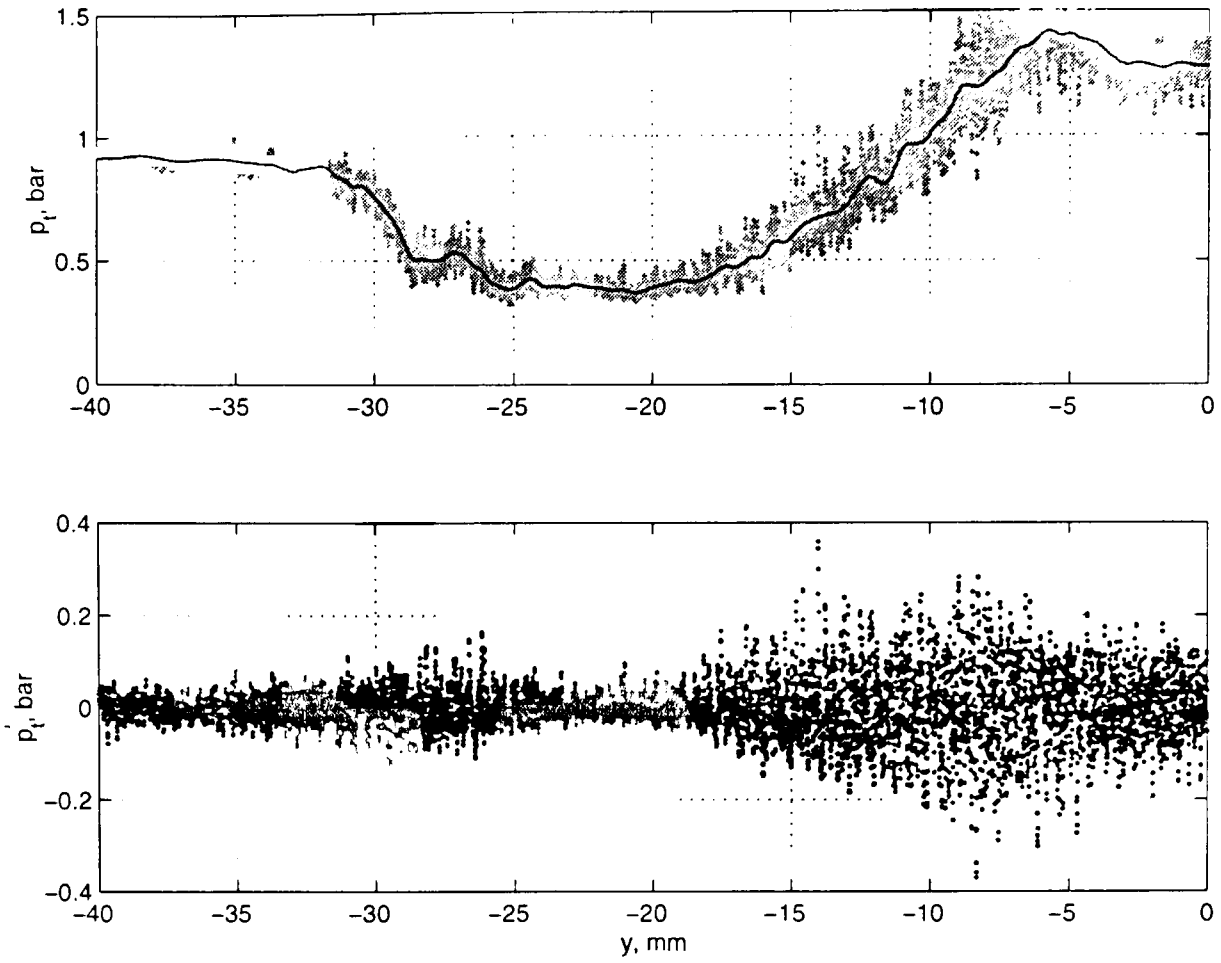


Figure 5-82 Fluctuating BPT Pitot pressure for Mach 5 (SM5) single jet with H_2 injection in Mach 7 freestream at 250 mm downstream *(GT725)*

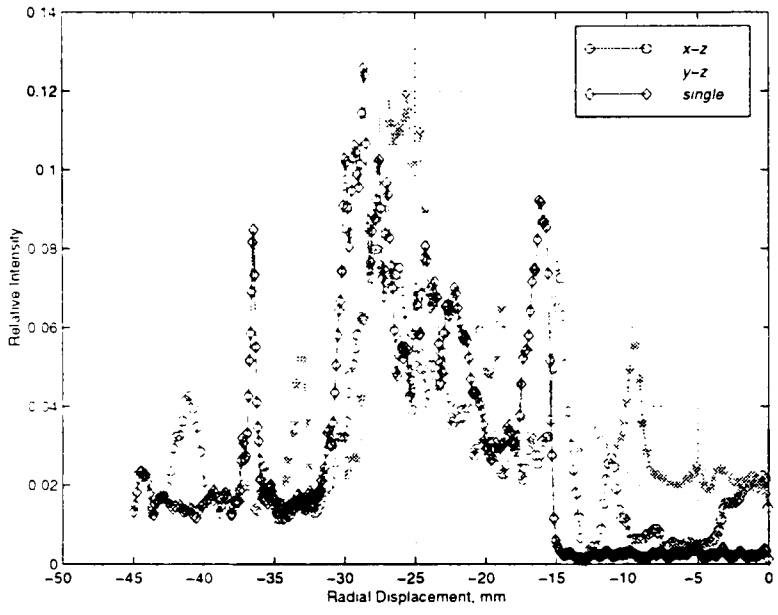


Figure 5-83 Relative Pitot pressure turbulence intensities at 100 mm downstream *(x-z plane: GT744, y-z plane: GT746, single: GT740)*

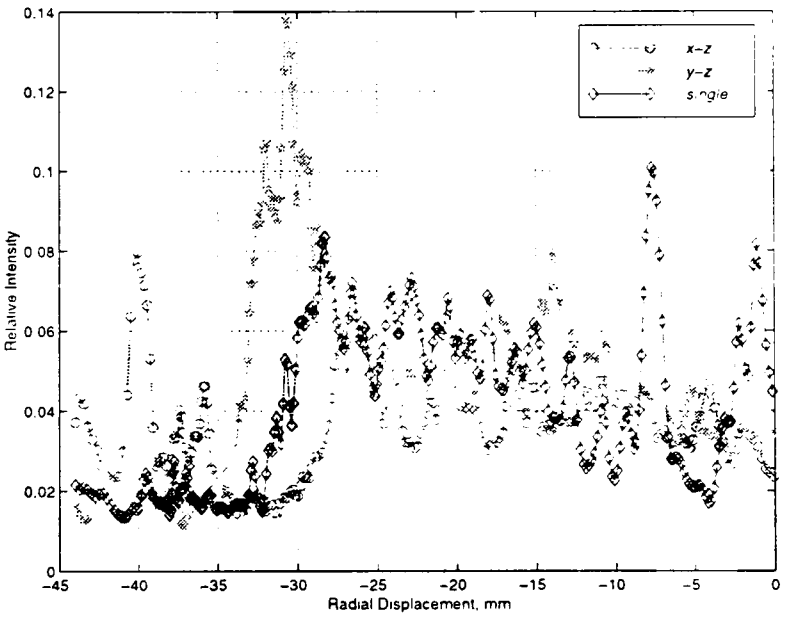


Figure 5-84 Relative Pitot pressure turbulence intensities at 250 mm downstream *(x-z plane: GT745, y-z plane: GT749, single: GT748)*

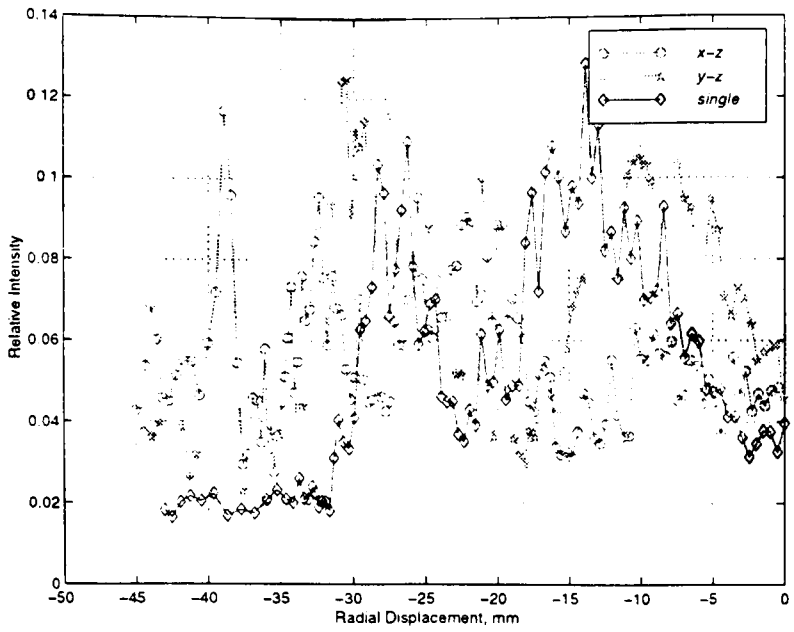


Figure 5-85 Relative Pitot pressure turbulence intensities with H_2 injection at 250 mm downstream *(x-z plane: GT727, y-z plane: GT726, single: GT725)*

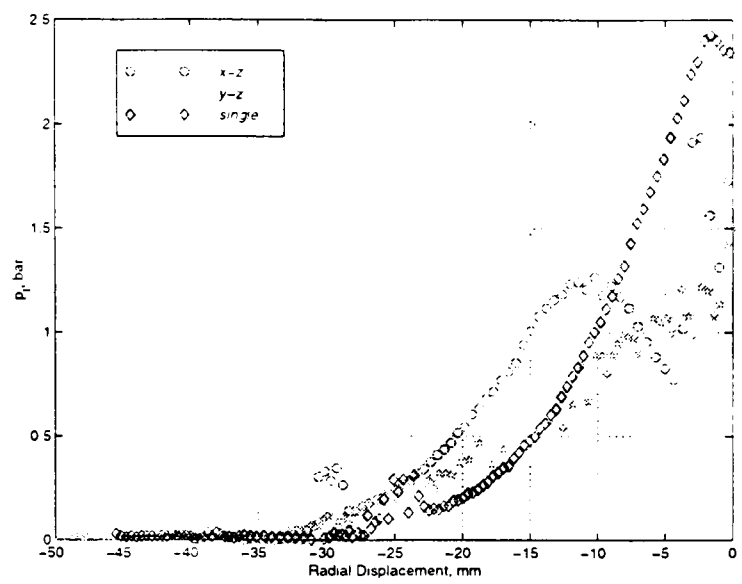


Figure 5-86 Mach 5 (TM5) twinjet Pitot pressure at 40 mm downstream with N_2 injection in quiescent *(below plane of symmetry)*

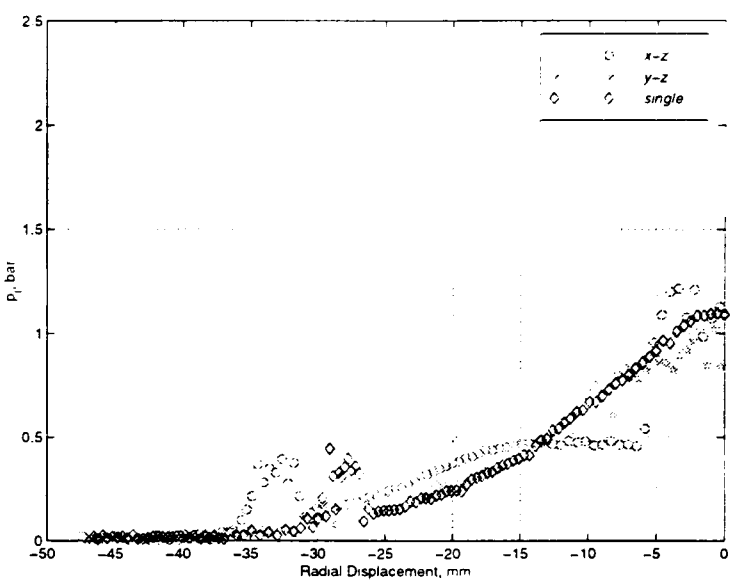


Figure 5-87 Mach 5 (TM5) twinjet Pitot pressure at 60 mm downstream with N_2 injection in quiescent *(below plane of symmetry)*

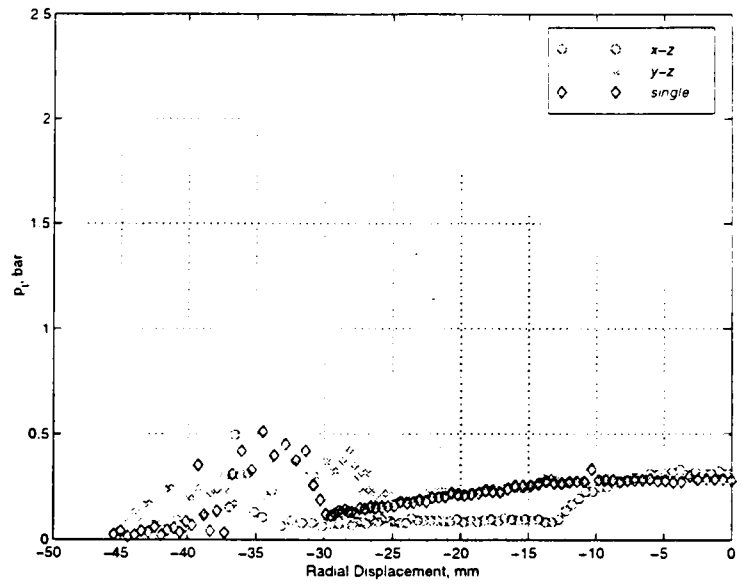


Figure 5-88 Mach 5 (TM5) twinjet Pitot pressure at 100 mm downstream with N_2 injection in quiescent *(below plane of symmetry)*

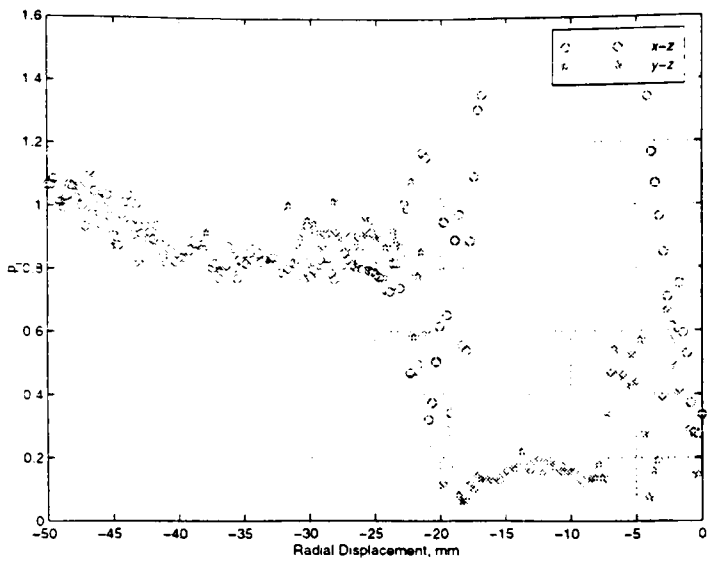


Figure 5-89 Pitot pressure for Mach 5 (TM5) twinjet injection in Mach 7 freestream at 10 mm downstream *(x-z plane: GT700, y-z plane: GT709)*

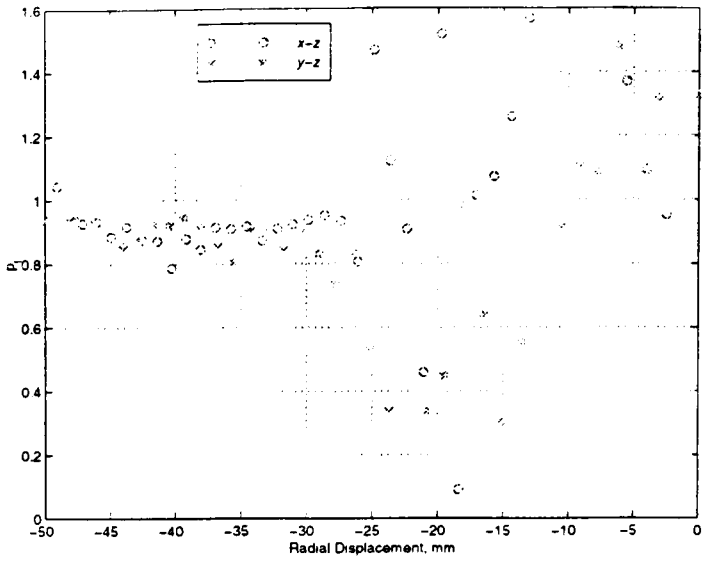


Figure 5-90 Pitot pressure for Mach 5 (TM5) twinjet injection in Mach 7 freestream at 30 mm downstream *(x-z plane: GT699, y-z plane: GT708)*

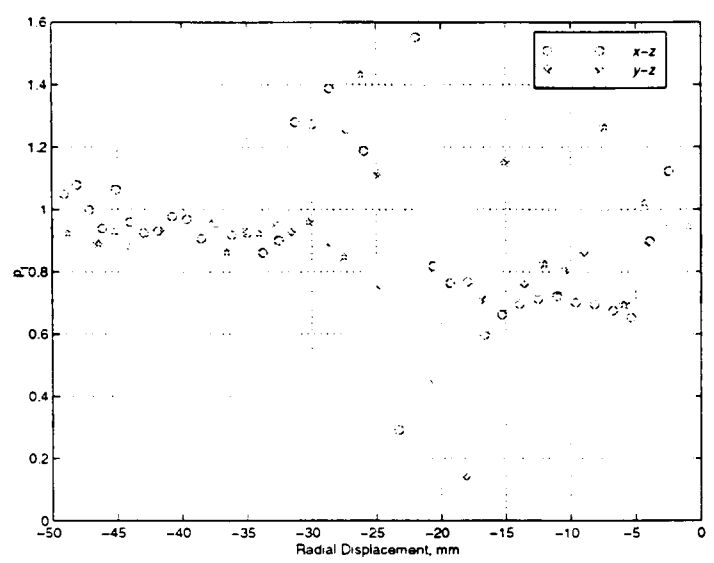


Figure 5-91 Pitot pressure for Mach 5 (TM5) twinjet injection in Mach 7 freestream at 50 mm downstream *(x-z plane: GT698, y-z plane: GT707)*

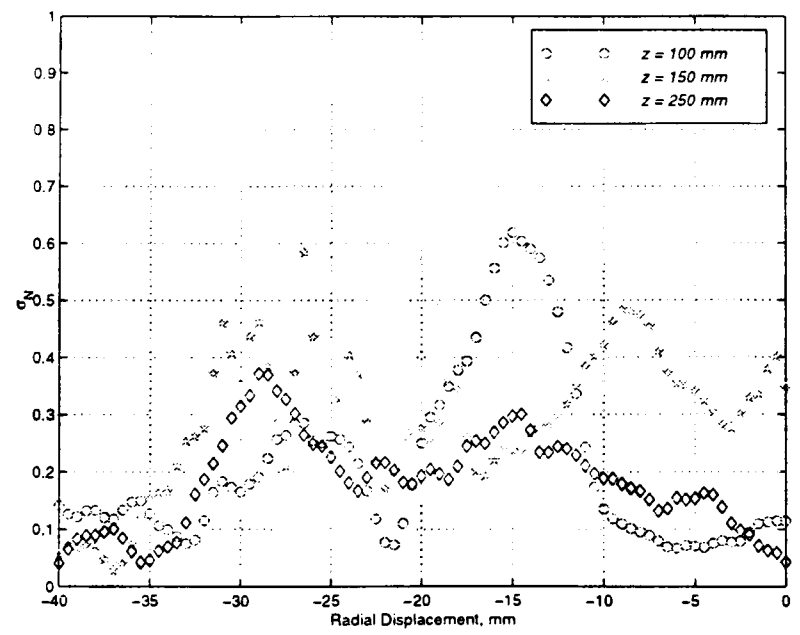


Figure 5-92 Normalised standard deviations for Mach 5 N_2 injection in Mach 7 N_2 freestream

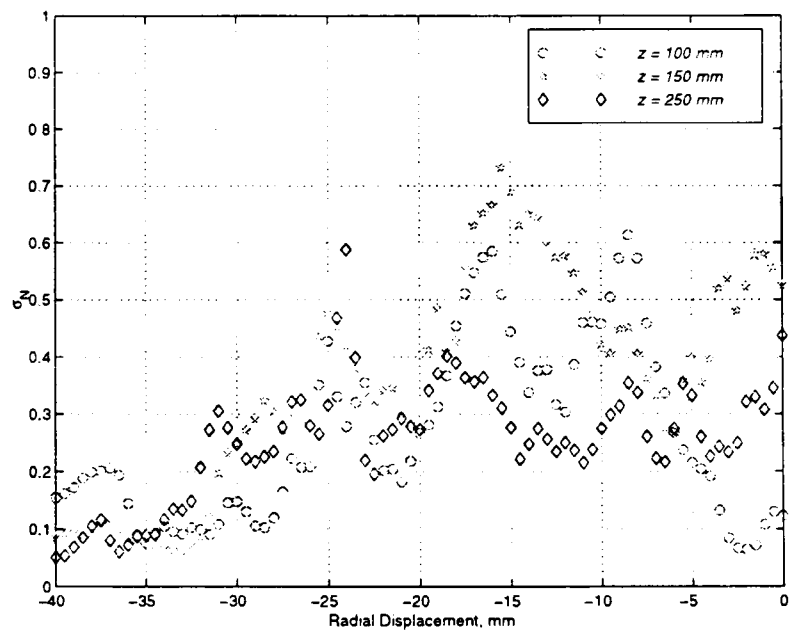


Figure 5-93 Normalised standard deviations for Mach 5 H_2 injection in Mach 7 N_2 freestream

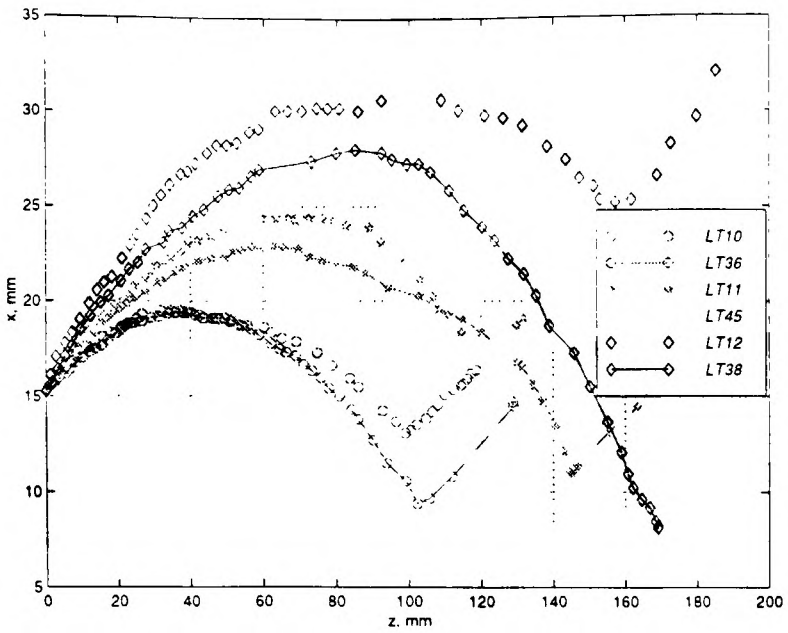


Figure 5-94 Comparison of barrel shock positions of blocked (symbols with lines) and unblocked (symbols) twinjet nozzles in quiescent *(gauge injection pressures: 30 bar LT10 & LT36, 50 bar LT11 & LT45, 70 bar LT12 & LT38)*

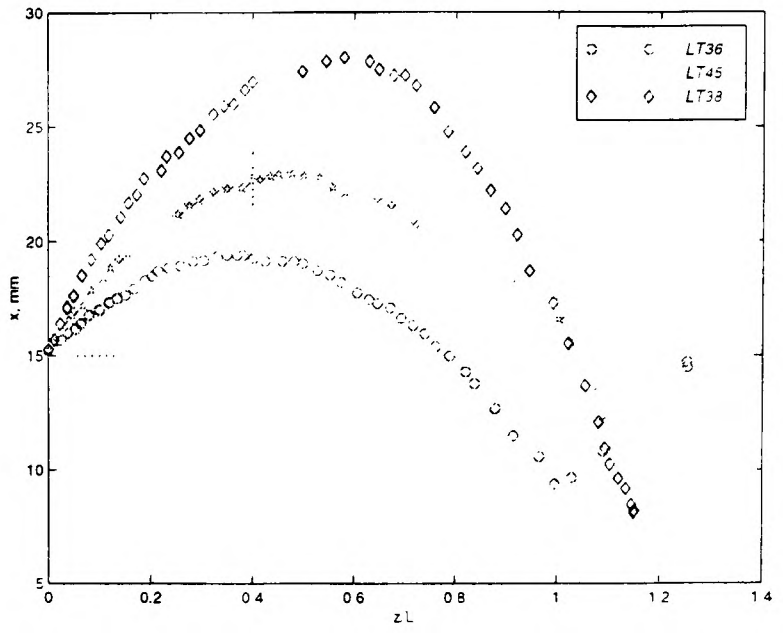


Figure 5-95 Scaled barrel shock positions for blocked Mach 5 (TM5) twinjet nozzle in quiescent *(gauge injection pressures: 30 bar LT36, 50 bar LT45, 70 bar LT38)*

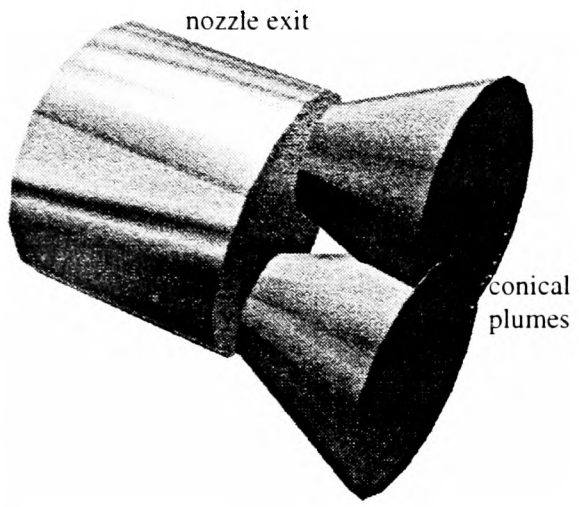


Figure 5-96 Twin-cone simplified model for impingement locus analysis

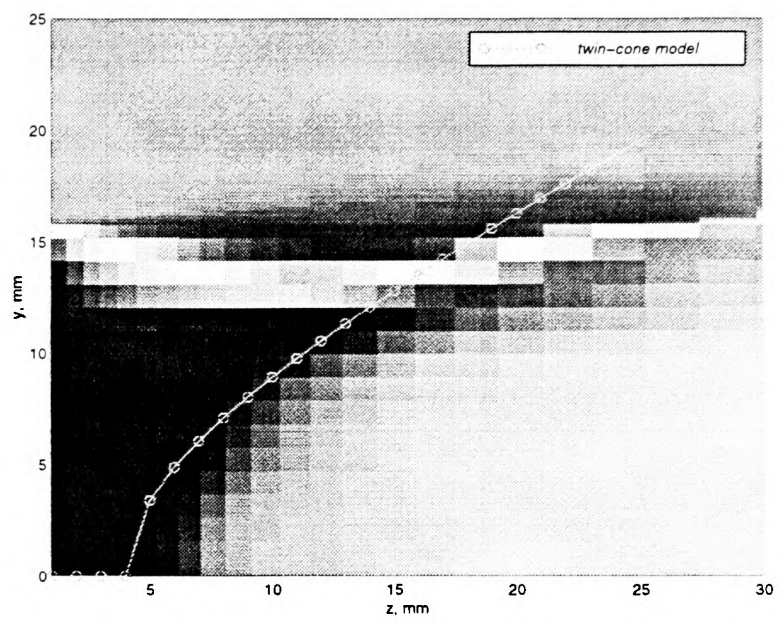


Figure 5-97 Twin-cone model predicted impingement locus superimposed on CFD Mach number contours

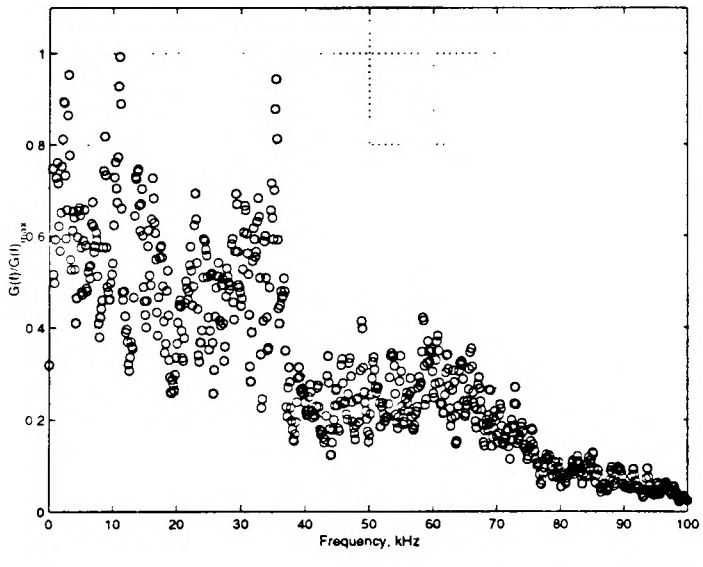


Figure 5-98 Power spectrum for Mach 5 (TM5) twinjet with N_2 injection in Mach 7 freestream at 40 mm downstream *(LT184)*

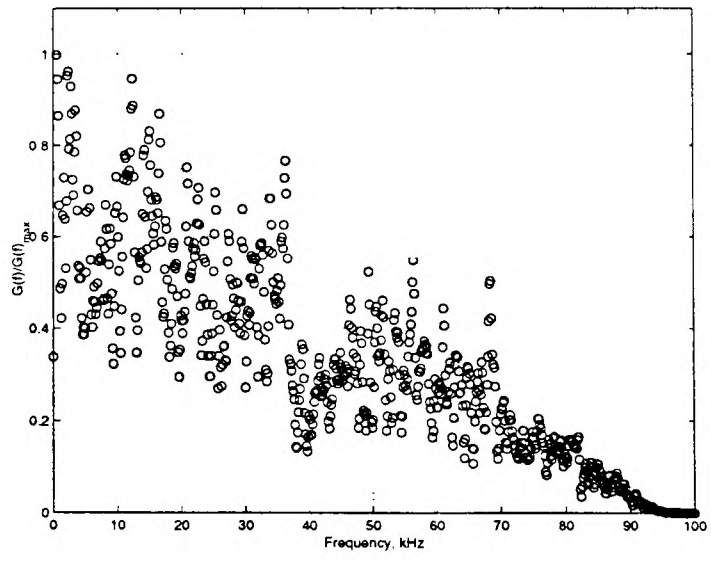


Figure 5-99 Power spectrum for Mach 5 (TM5) twinjet with N_2 injection in Mach 7 freestream at 60 mm downstream *(LT185)*

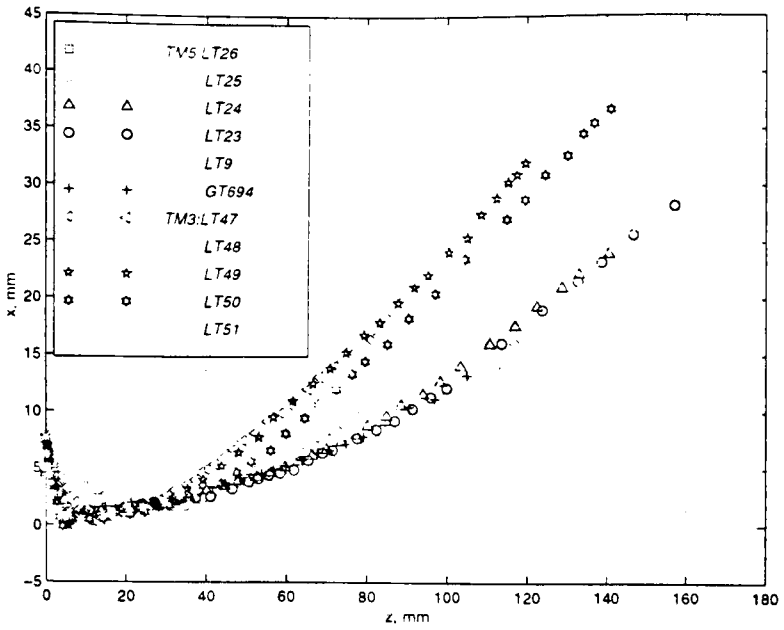


Figure 5-100 Impingement shock locations for quiescent and co-flow Mach 5 (TM5) and Mach 3 (TM3) twinjets

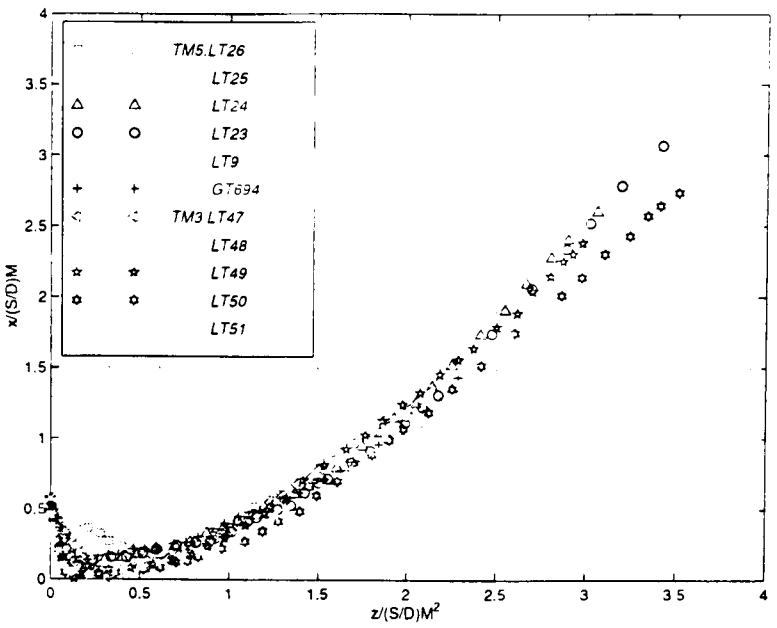


Figure 5-101 Scaled impingement shock locations for quiescent and co-flow Mach 5 (TM5) and Mach 3 (TM3) twinjets

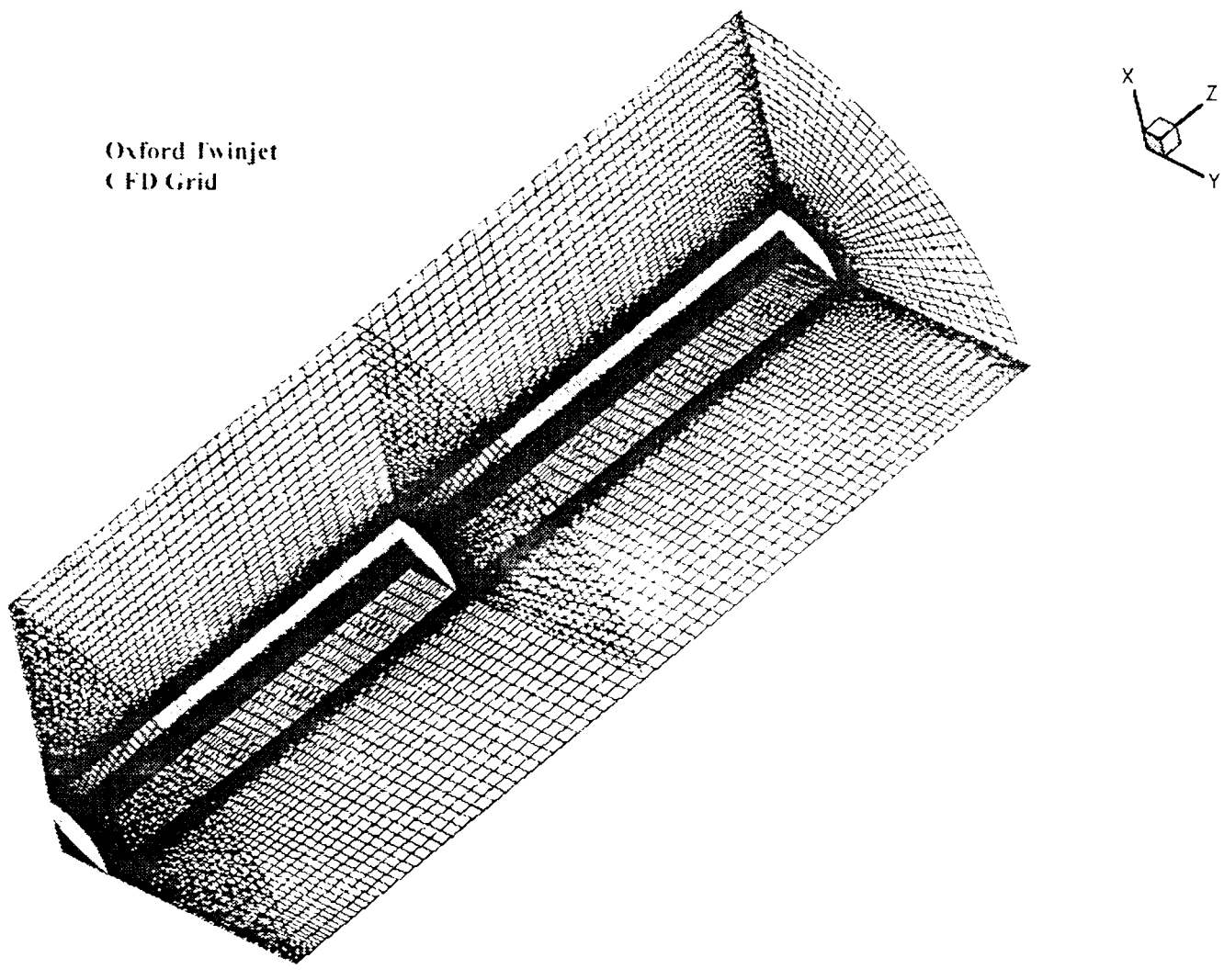


Figure 5-102 DRA CFD three-dimensional computation field mesh grids for Mach 5 twinjet in Mach 7 freestream simulation

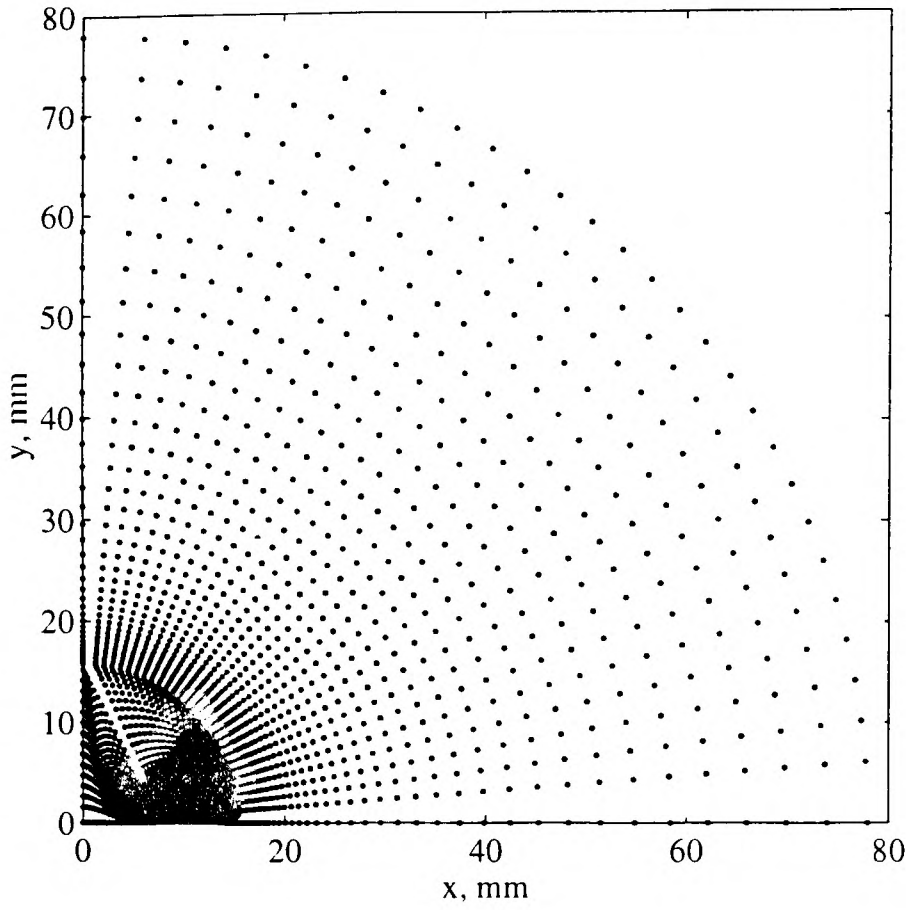


Figure 5-103 DRA CFD computation crossflow mesh grids for Mach 5 twinjet in Mach 7 freestream simulation

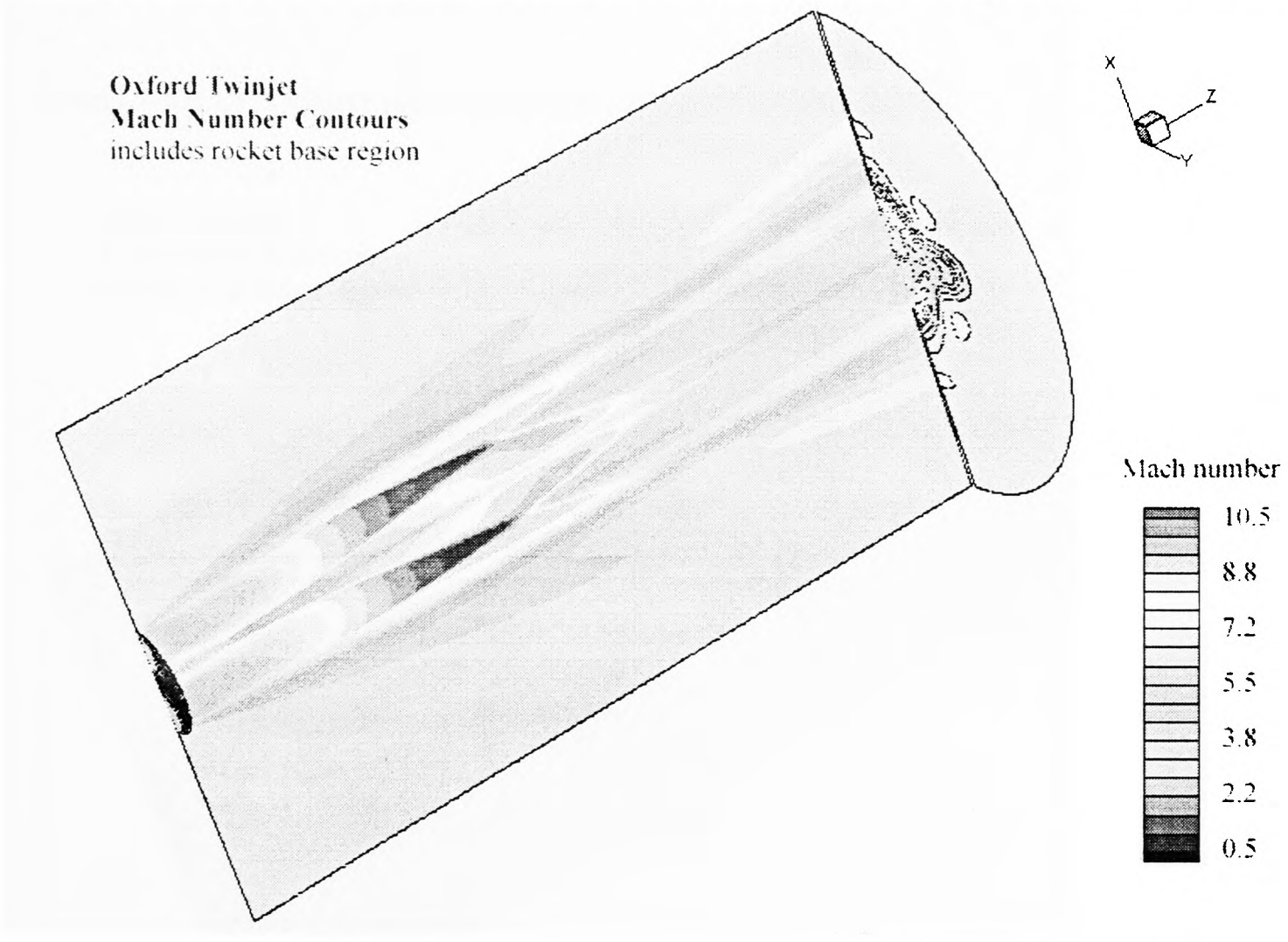


Figure 5-104 CFD Mach number contours for Mach 5 twinjet

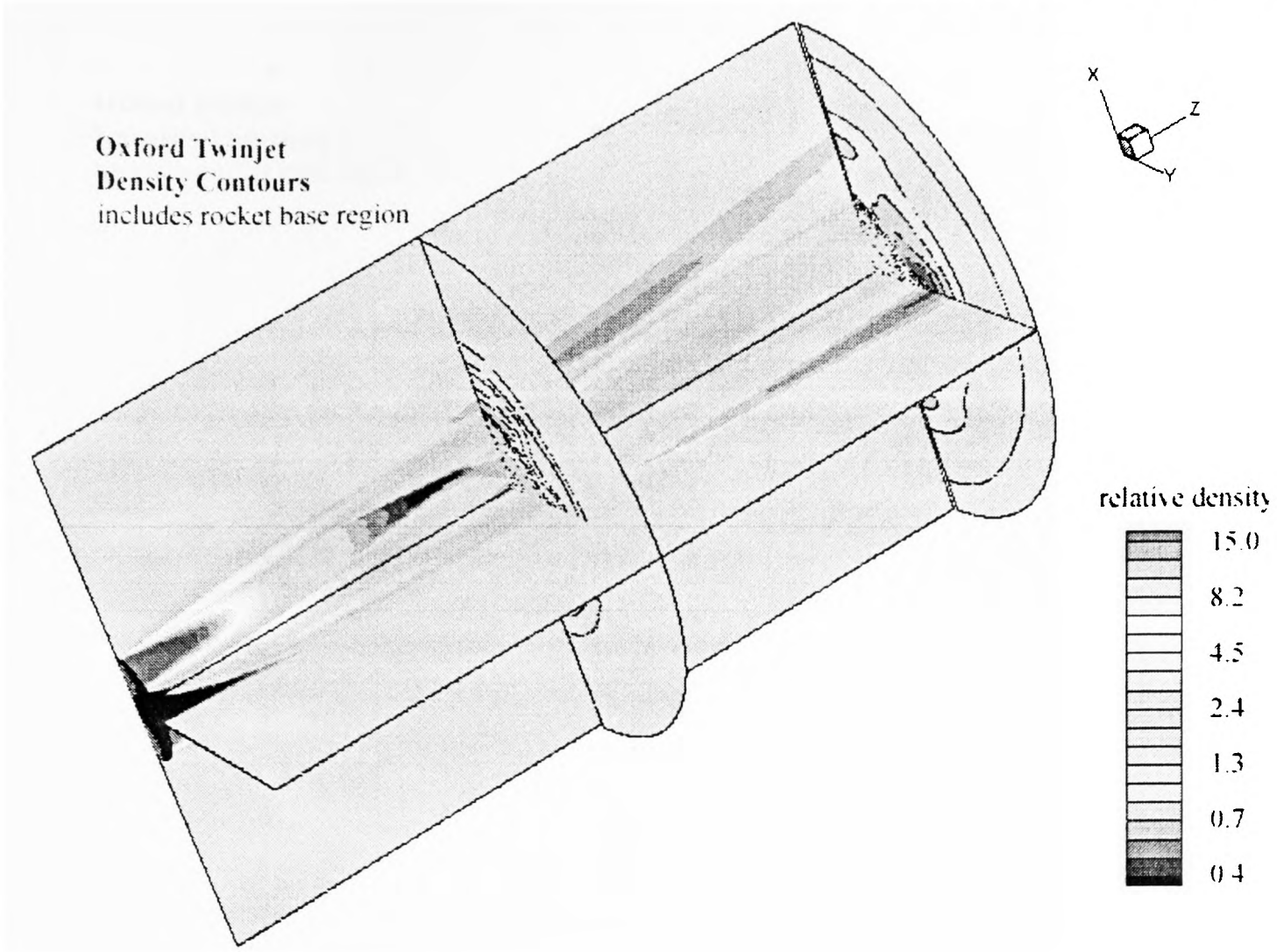


Figure 5-105 CFD relative static density ρ/ρ_∞ contours for Mach 5 twinjet

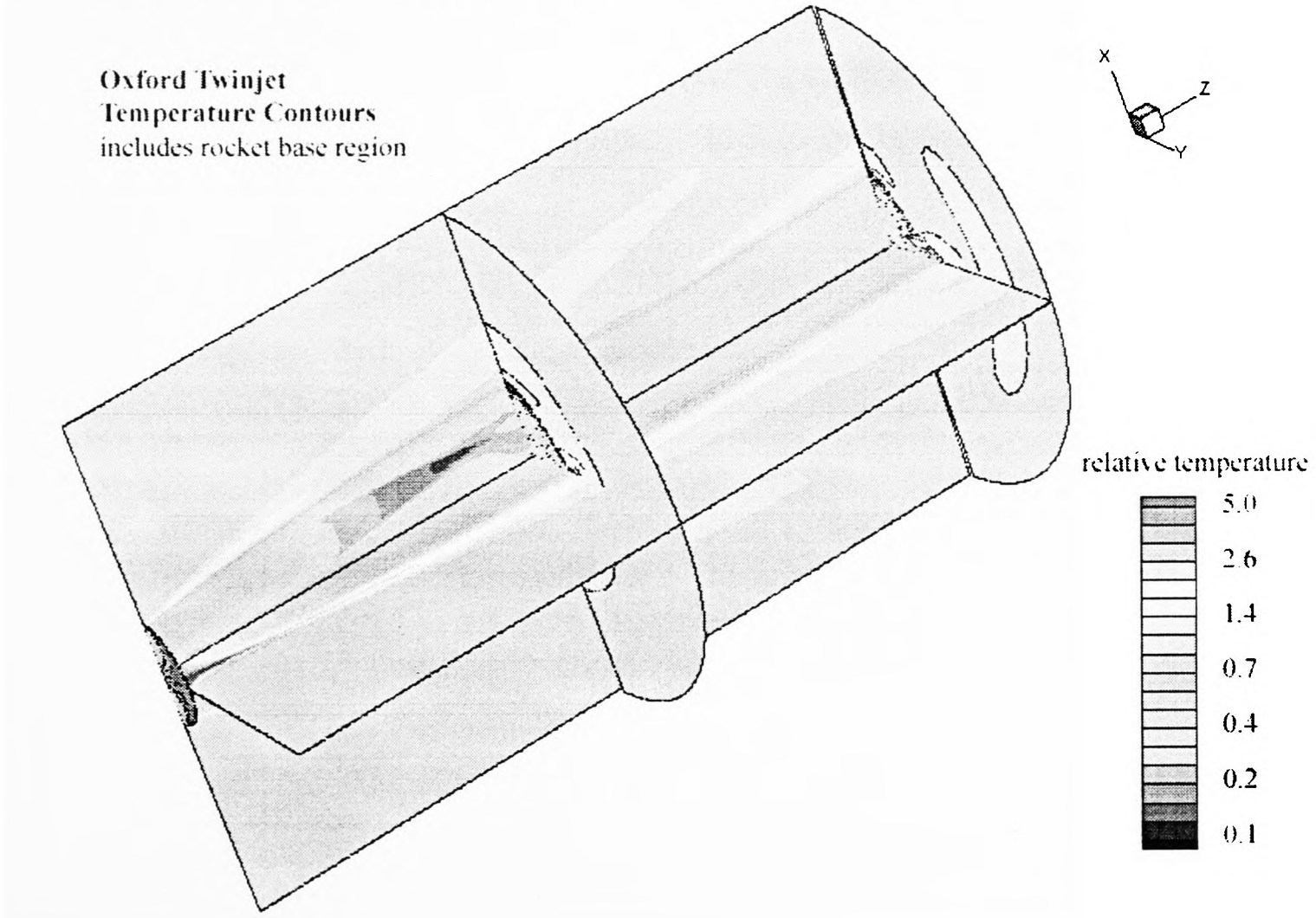


Figure 5-106 CFD relative static temperature T/T_∞ contours for Mach 5 twinjet

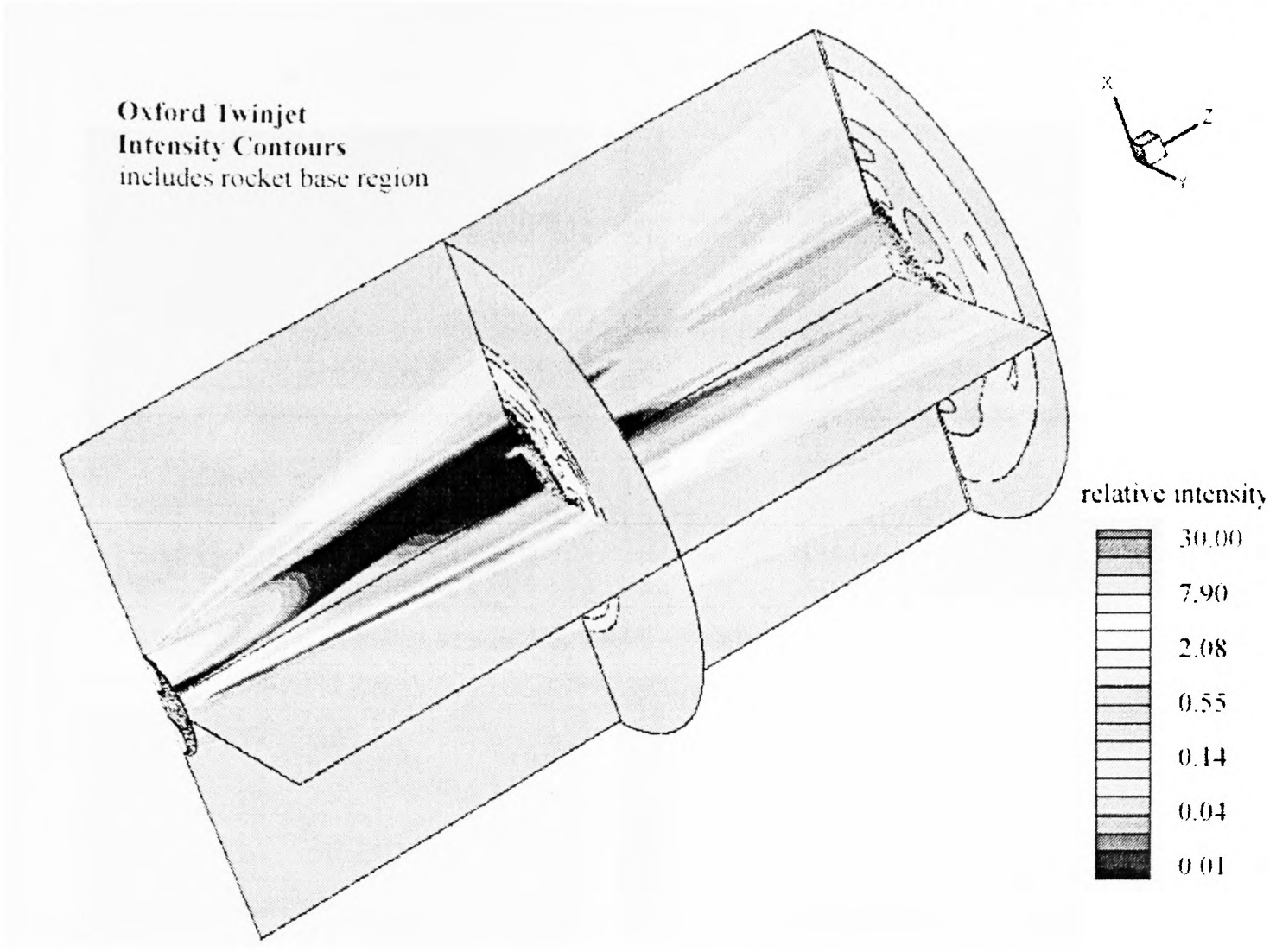
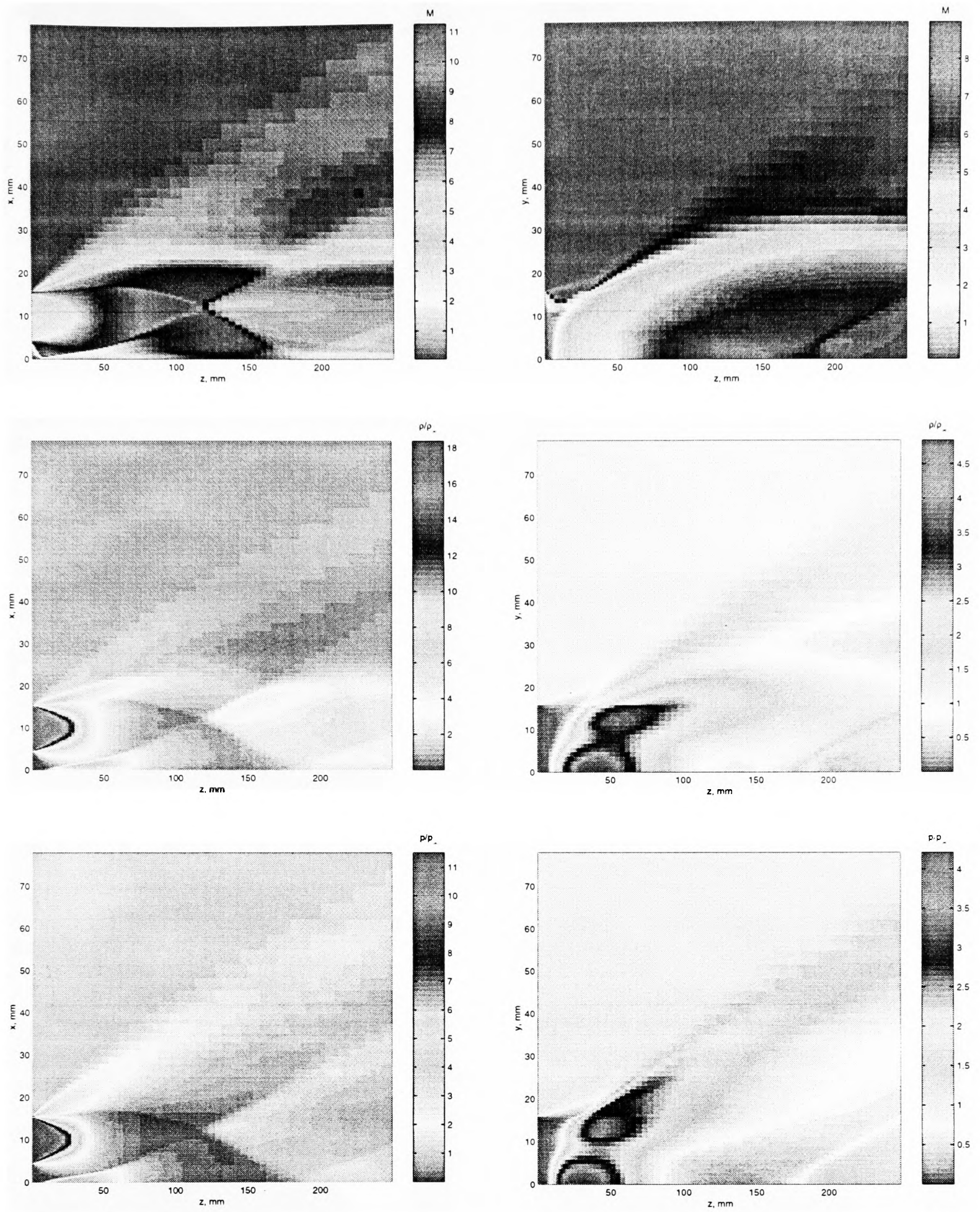


Figure 5-107 CFD relative intensity $\rho T^4/\rho_\infty T_\infty^4$ contours for Mach 5 twinjet



x-z plane *y-z plane*

Figure 5-108 CFD predicted contours on *x-z* and *y-z planes* plane for Mach 5 twinjet in Mach 7 freestream

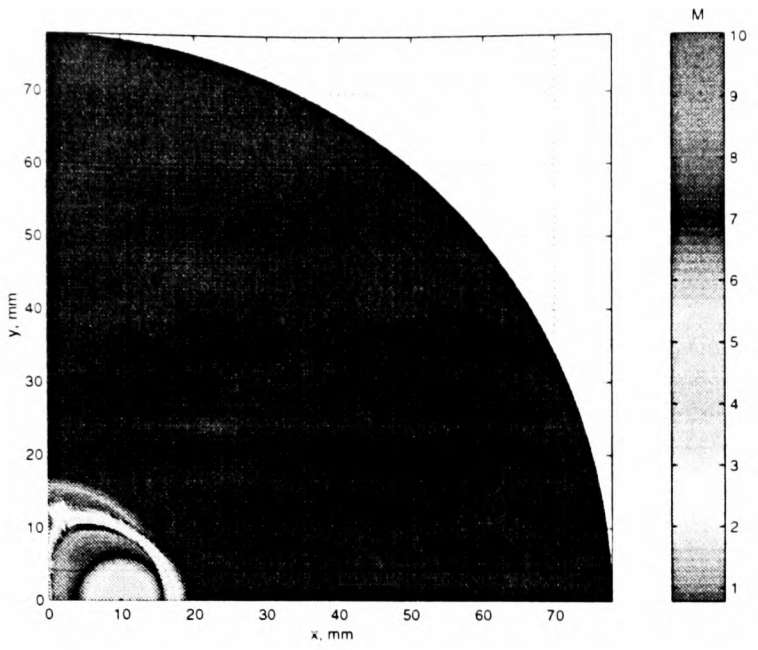


Figure 5-109 CFD Mach number distribution on *x*-*y* plane at *z*=10.3 mm

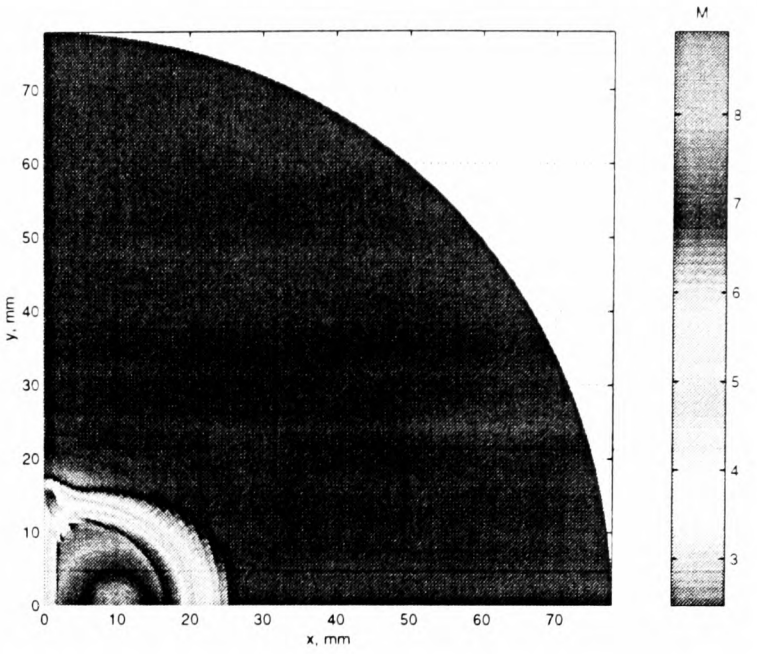


Figure 5-110 CFD Mach number distribution on *x*-*y* plane at *z*=34.9 mm

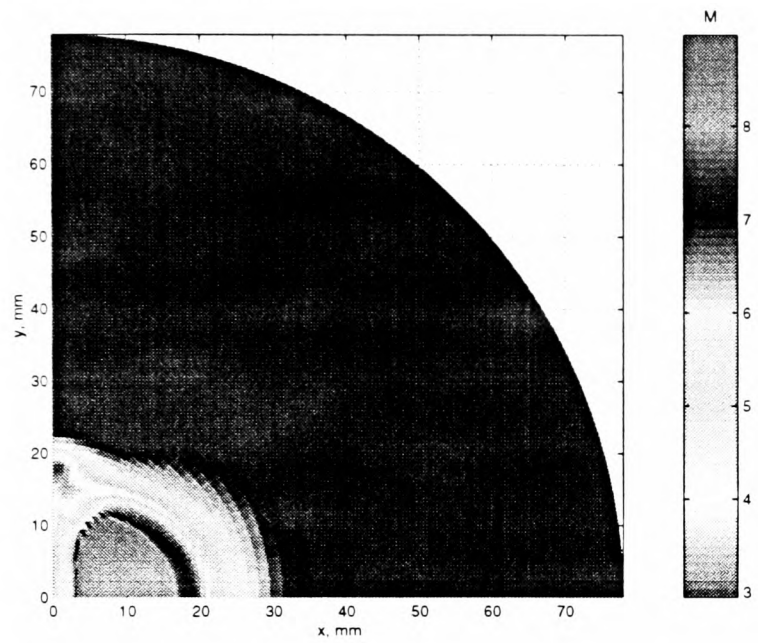


Figure 5-111 CFD Mach number distribution on *x*-*y* plane at *z*=53.1 mm

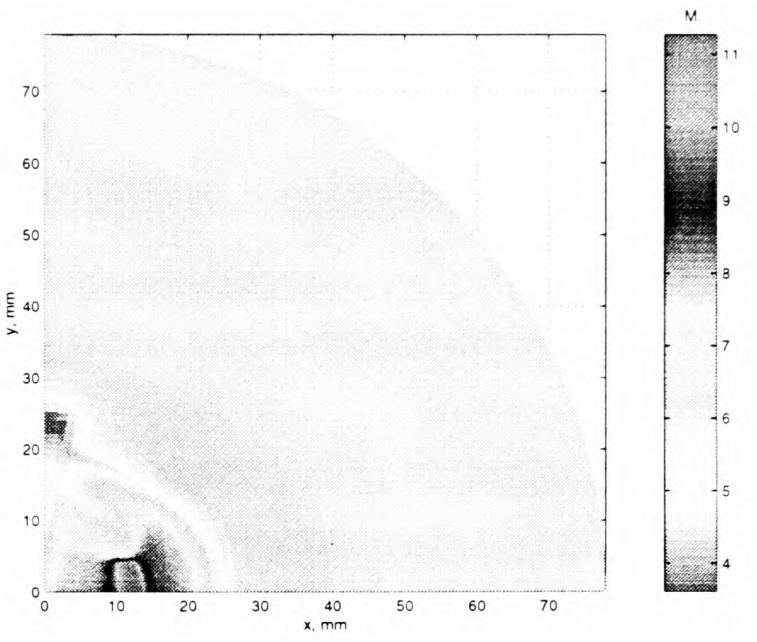


Figure 5-112 CFD Mach number distribution on *x*-*y* plane at *z*=100.5 mm

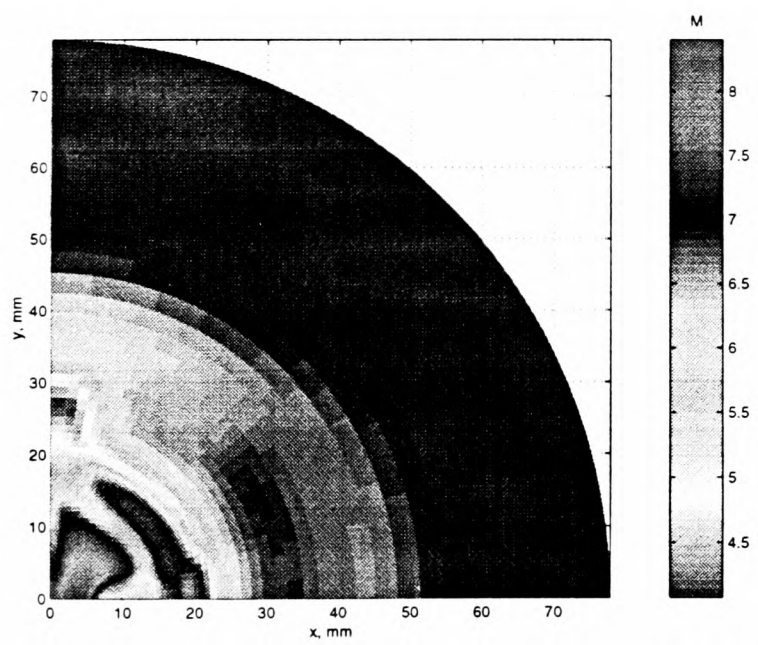


Figure 5-113 CFD Mach number distribution on *x*-*y* plane at *z*=149.5 mm

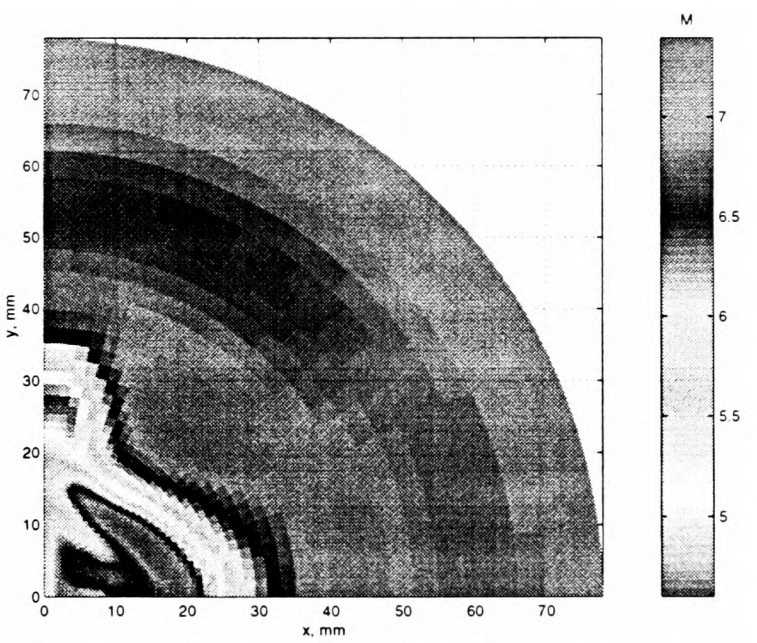


Figure 5-114 CFD Mach number distribution on *x*-*y* plane at *z*=249.7 mm

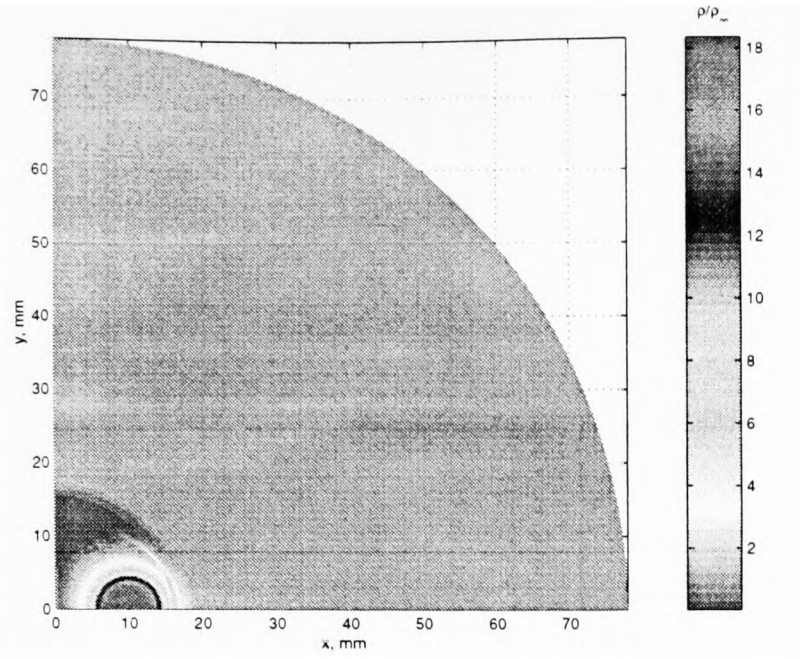


Figure 5-115 CFD relative density distribution on *x*-*y* plane at *z*=10.3 mm

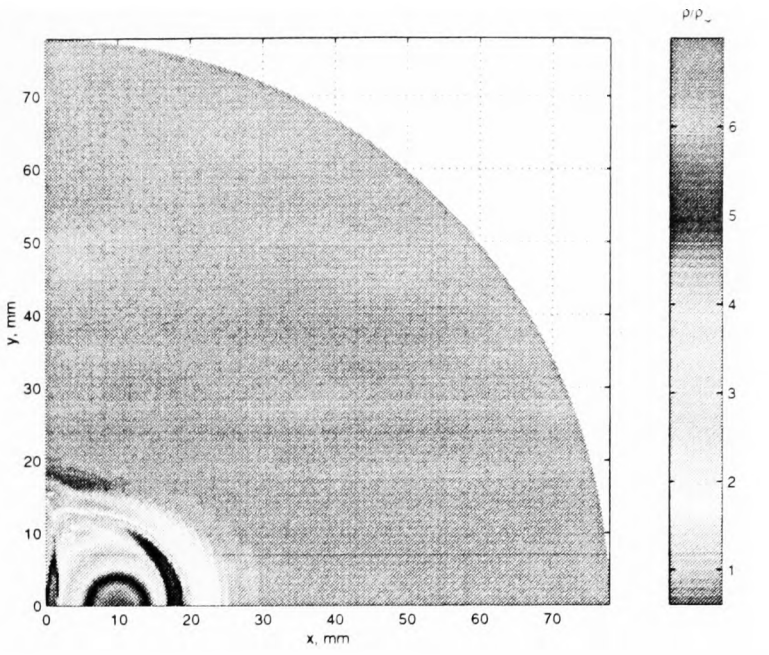


Figure 5-116 CFD relative density distribution on *x*-*y* plane at *z*=34.9 mm

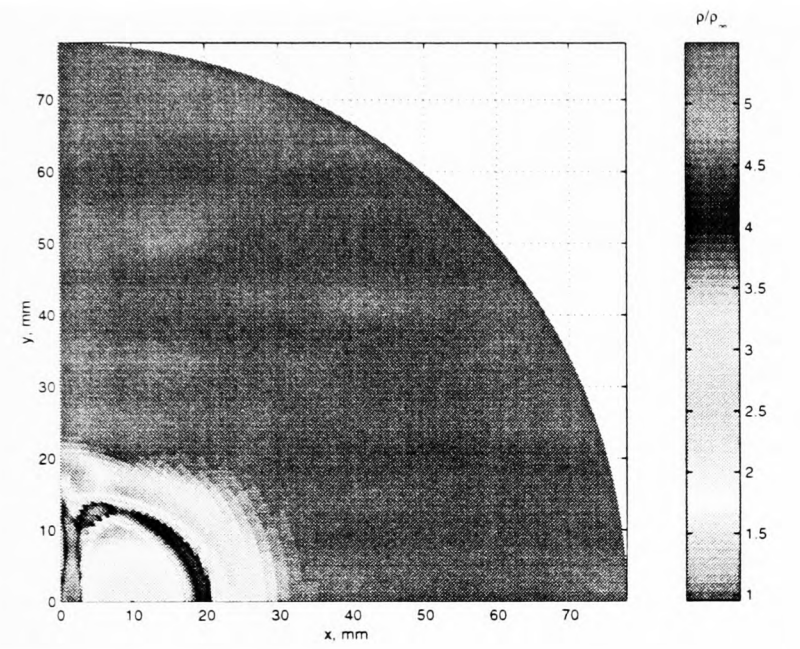


Figure 5-117 CFD relative density distribution on *x*-*y* plane at *z*=53.1 mm

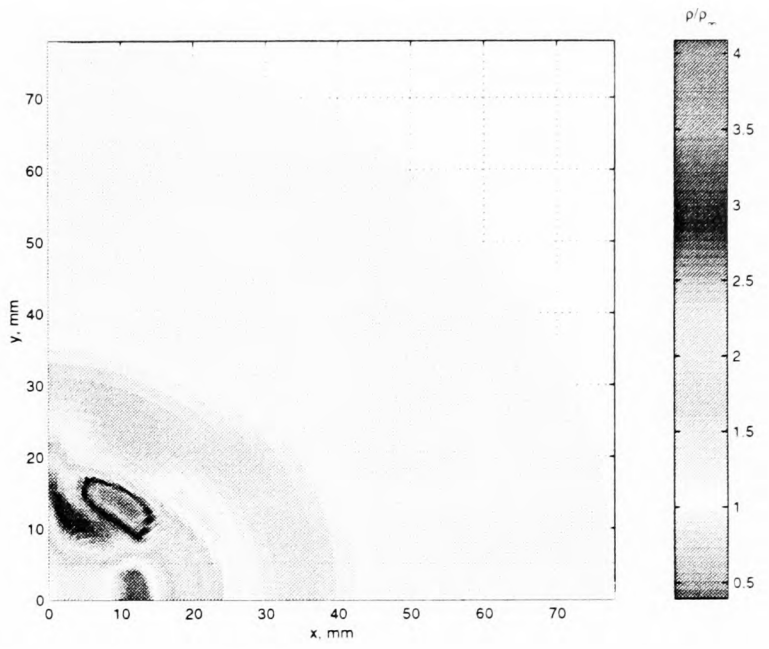


Figure 5-118 CFD relative density distribution on *x*-*y* plane at *z*=100.5 mm

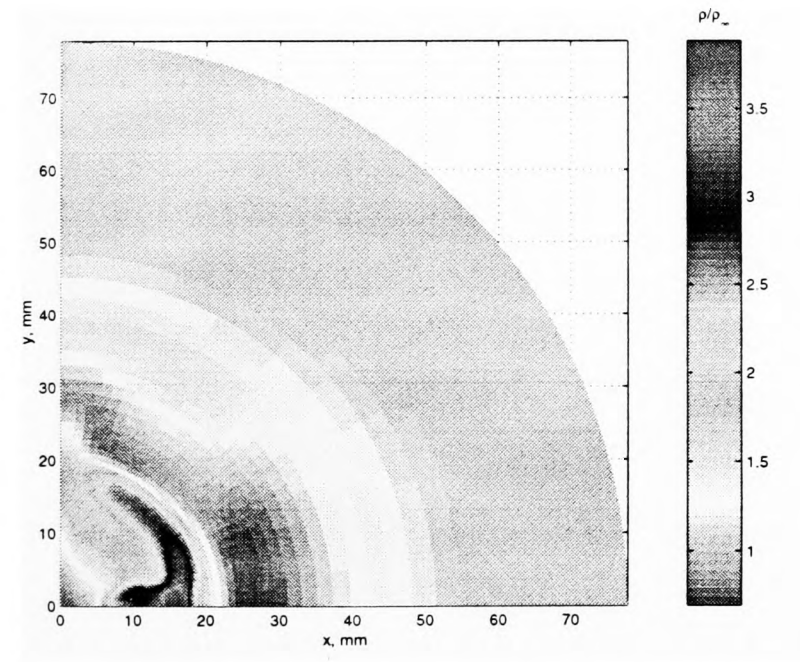


Figure 5-119 CFD relative density distribution on *x*-*y* plane at *z*=149.5 mm

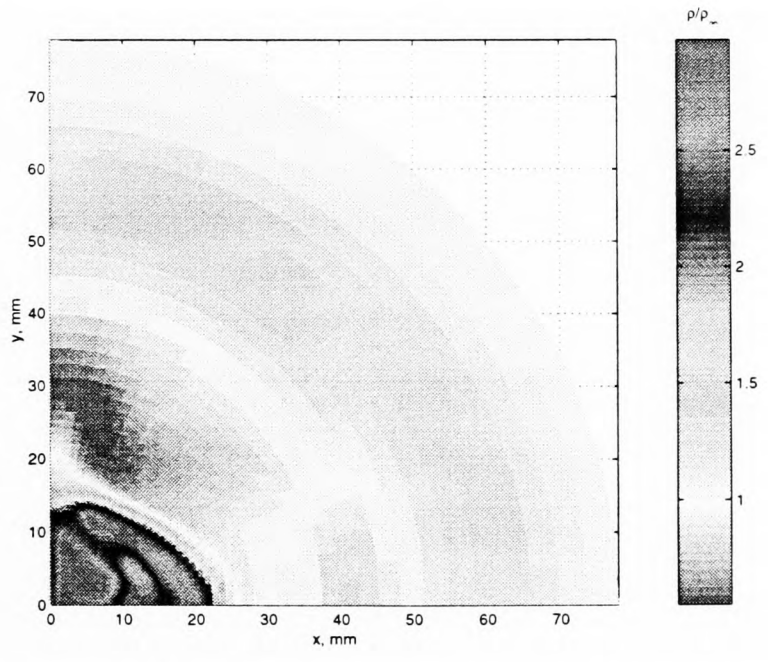


Figure 5-120 CFD relative density distribution on *x*-*y* plane at *z*=249.7 mm

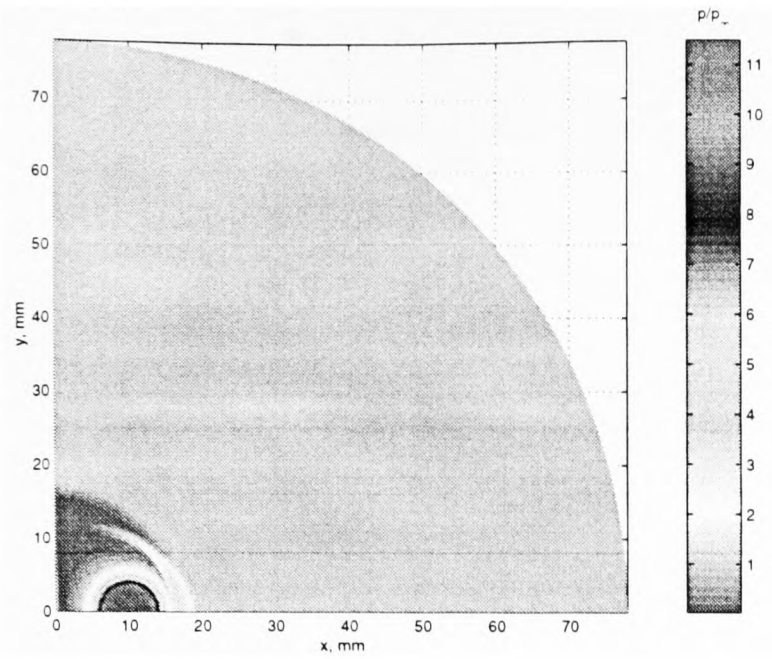


Figure 5-121 CFD relative static pressure distribution on x-y plane at z=10.3 mm

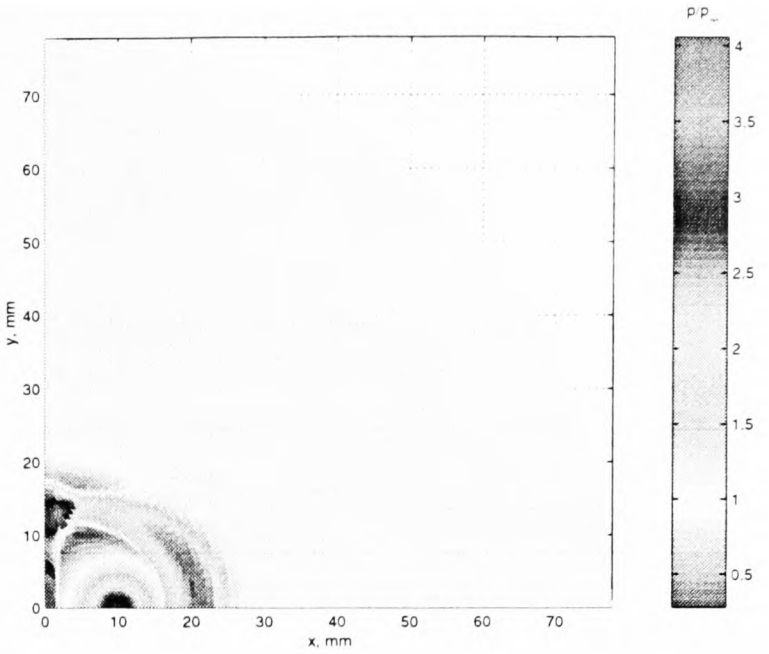


Figure 5-122 CFD relative static pressure distribution on x-y plane at z=34.9 mm

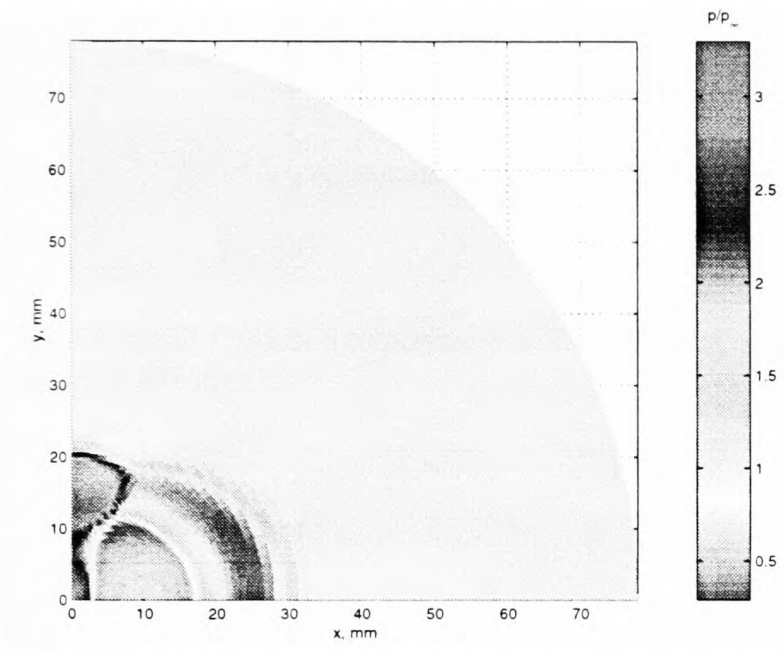


Figure 5-123 CFD relative static pressure distribution on x-y plane at z=53.1 mm

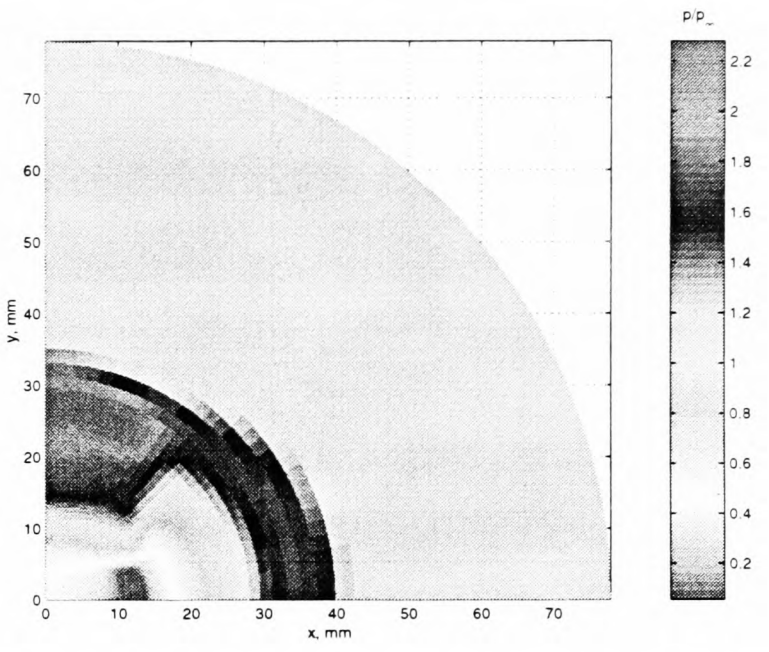


Figure 5-124 CFD relative static pressure distribution on x-y plane at z=100.5 mm

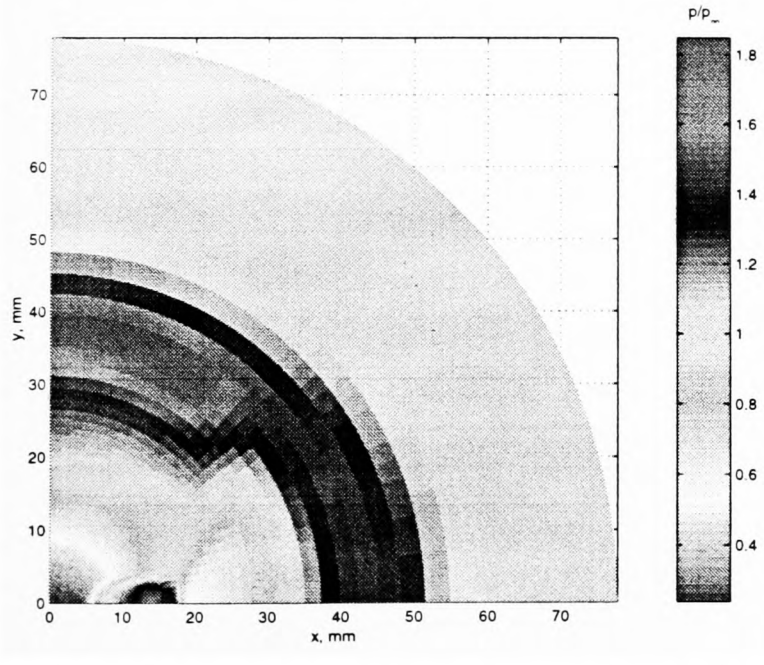


Figure 5-125 CFD relative static pressure distribution on x-y plane at z=149.5 mm

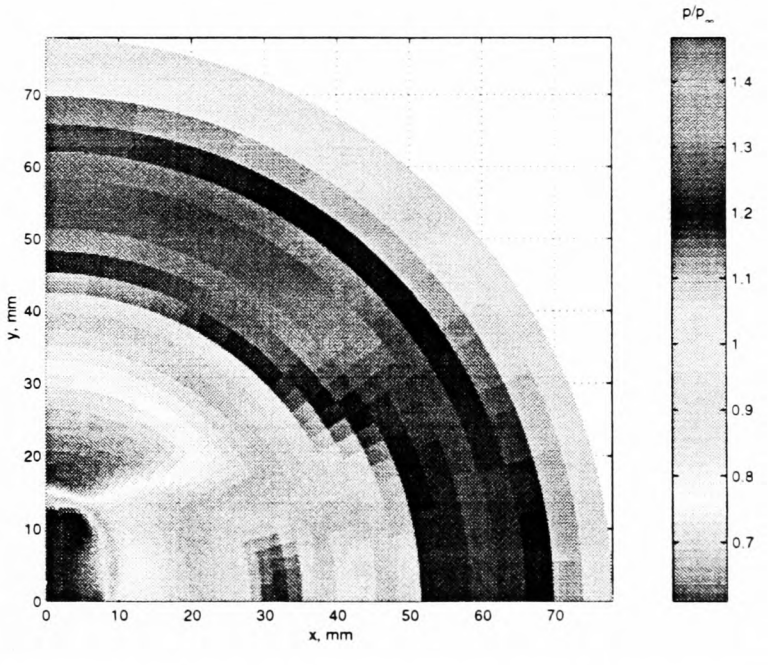


Figure 5-126 CFD relative static pressure distribution on x-y plane at z=249.7 mm

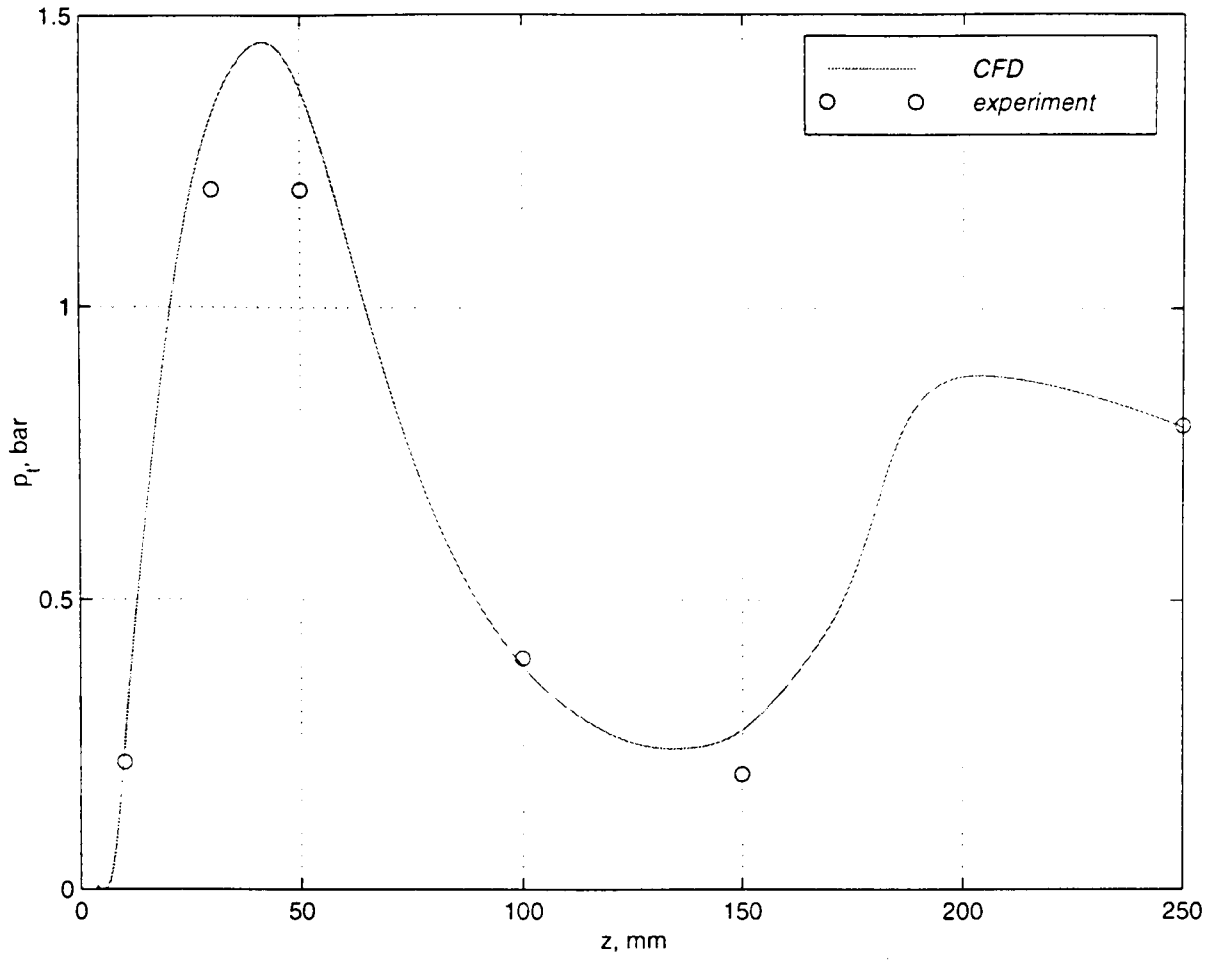


Figure 5-127 CFD and experimental Pitot pressure variations along z-axis for Mach 5 (TM5) twinjet injection in Mach 7 freestream

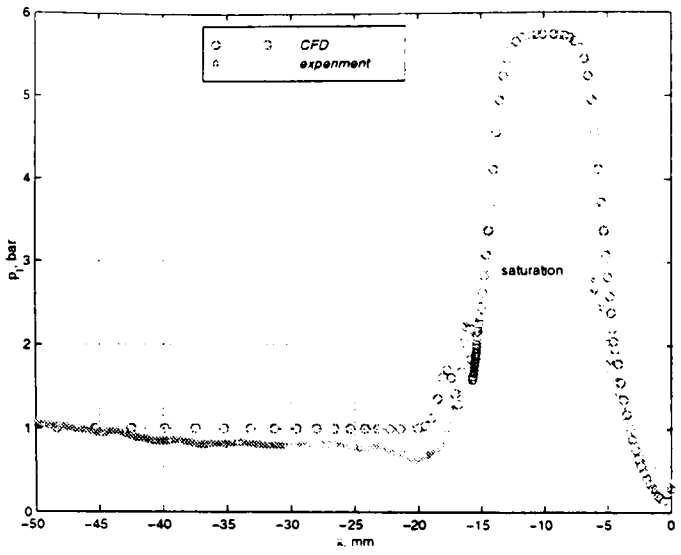


Figure 5-128 CFD and experimental Pitot pressure on x-z plane at 10 mm downstream

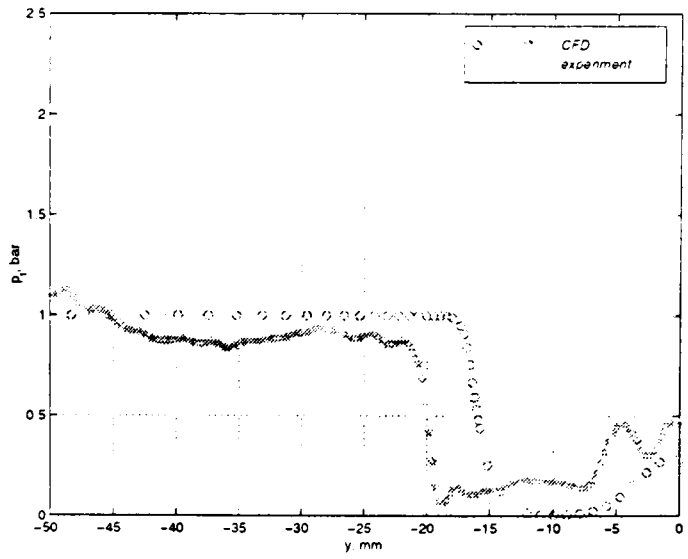


Figure 5-129 CFD and experimental Pitot pressure on y-z plane at 10 mm downstream

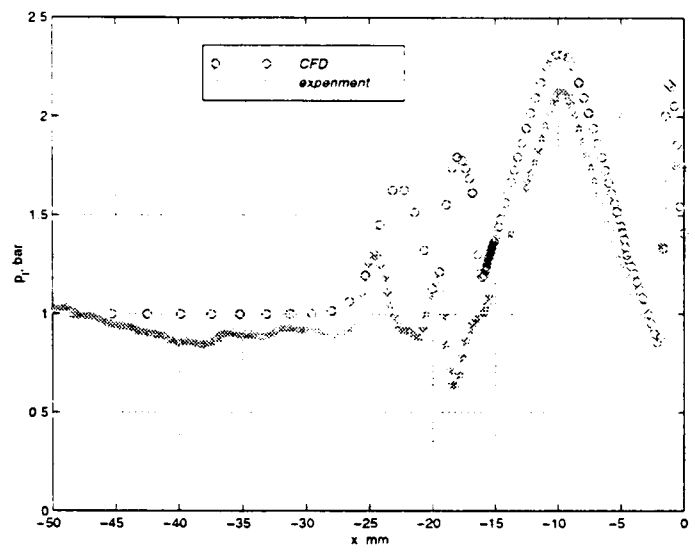


Figure 5-130 CFD and experimental Pitot pressure on x-z plane at 30 mm downstream

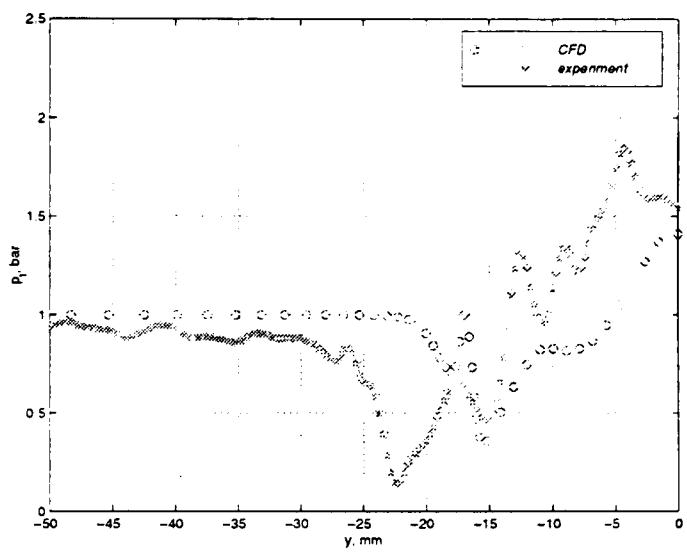


Figure 5-131 CFD and experimental Pitot pressure on y-z plane at 30 mm downstream

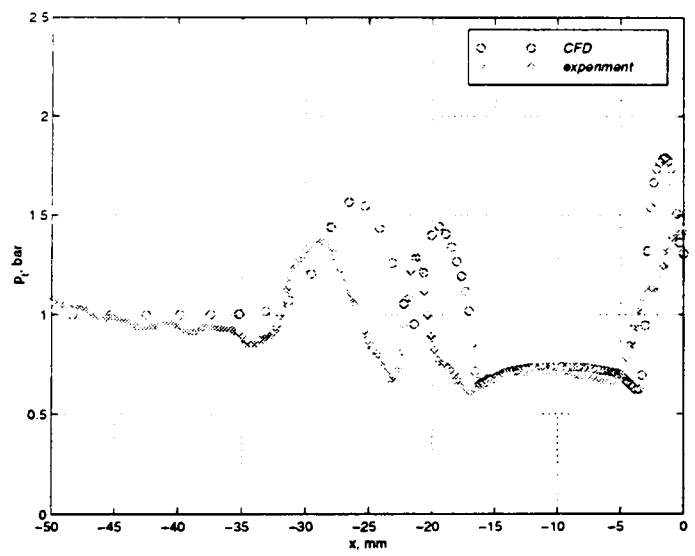


Figure 5-132 CFD and experimental Pitot pressure on x-z plane at 50 mm downstream

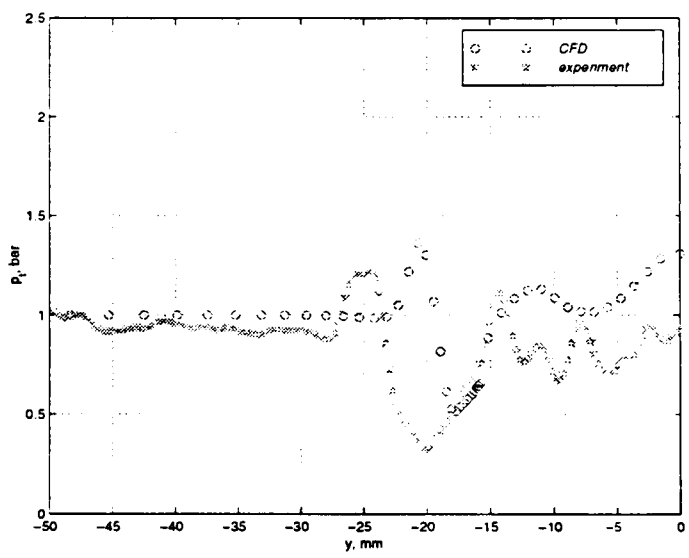


Figure 5-133 CFD and experimental Pitot pressure on y-z plane at 50 mm downstream

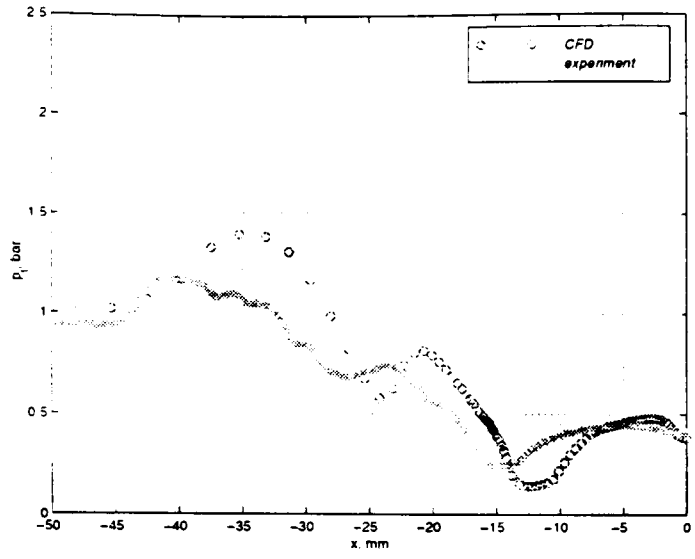


Figure 5-134 CFD and experimental Pitot pressure on x-z plane at 100 mm downstream

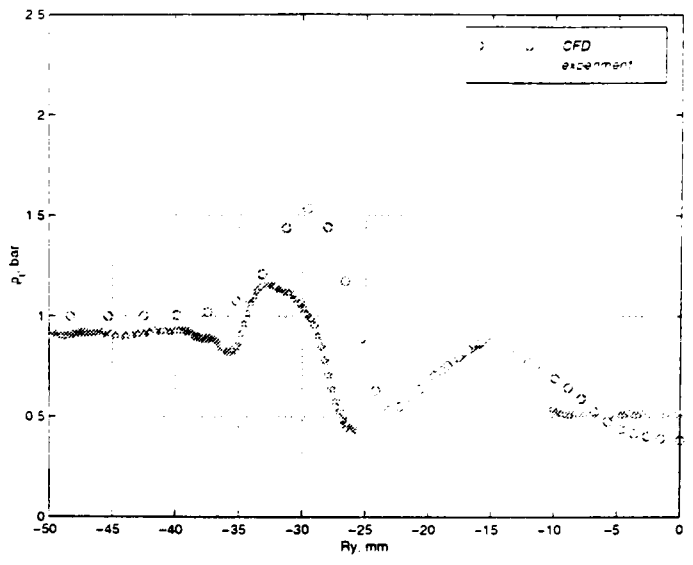


Figure 5-135 CFD and experimental Pitot pressure on y-z plane at 100 mm downstream

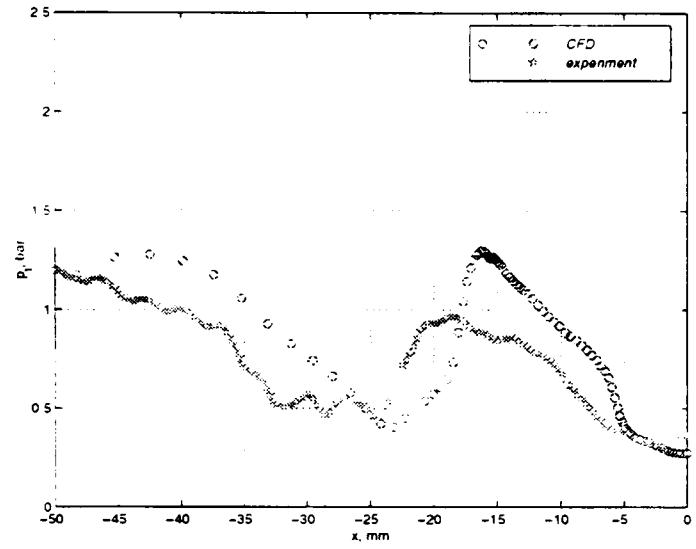


Figure 5-136 CFD and experimental Pitot pressure on x-z plane at 150 mm downstream

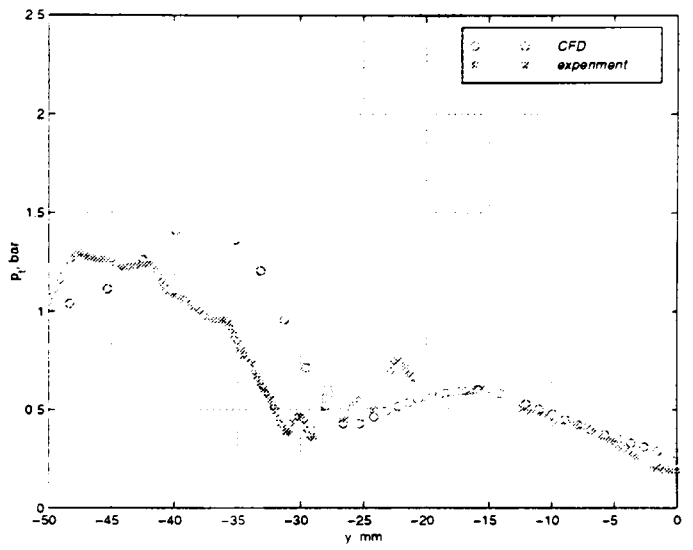


Figure 5-137 CFD and experimental Pitot pressure on y-z plane at 150 mm downstream

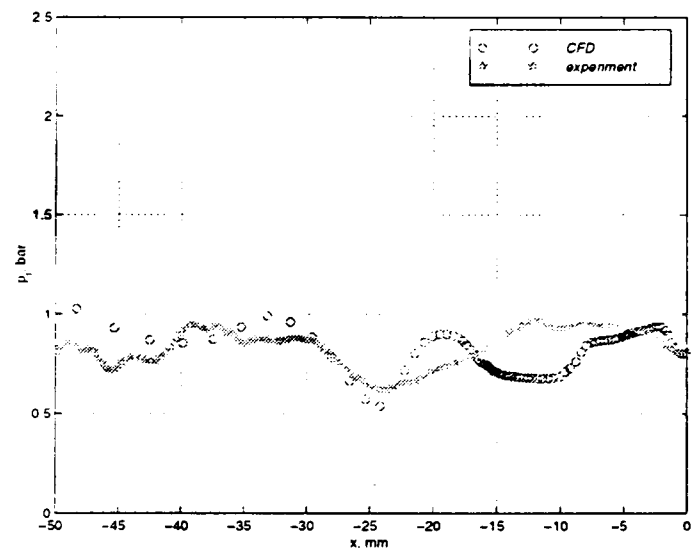


Figure 5-138 CFD and experimental Pitot pressure on x-z plane at 250 mm downstream

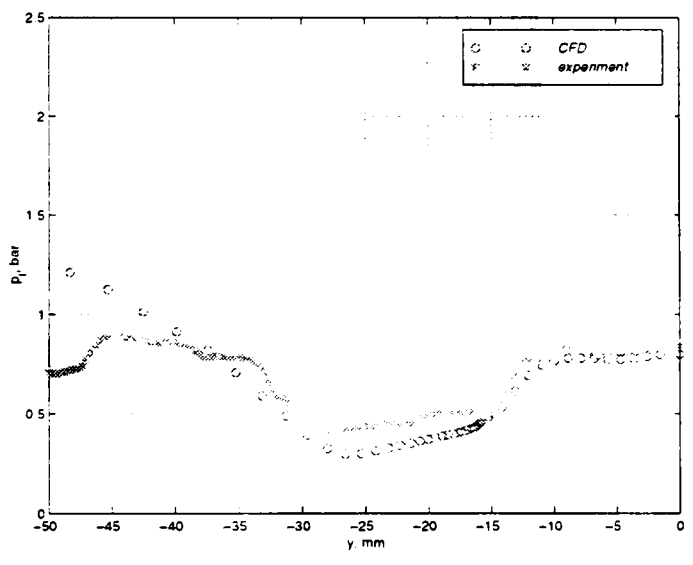


Figure 5-139 CFD and experimental Pitot pressure on y-z plane at 250 mm downstream

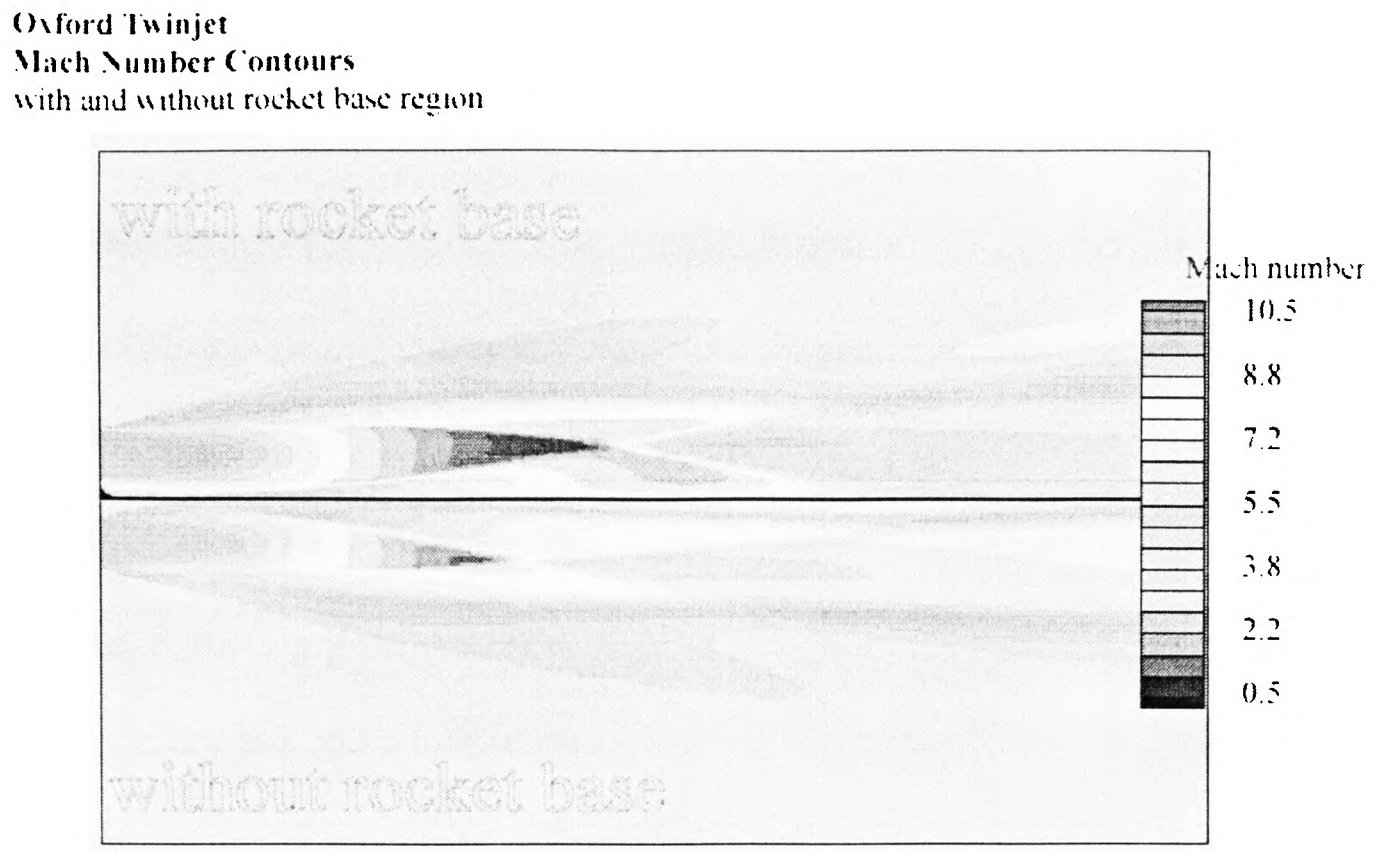


Figure 5-140 CFD Mach number contours on x-z plane with and without inclusion of rocket base region in calculation

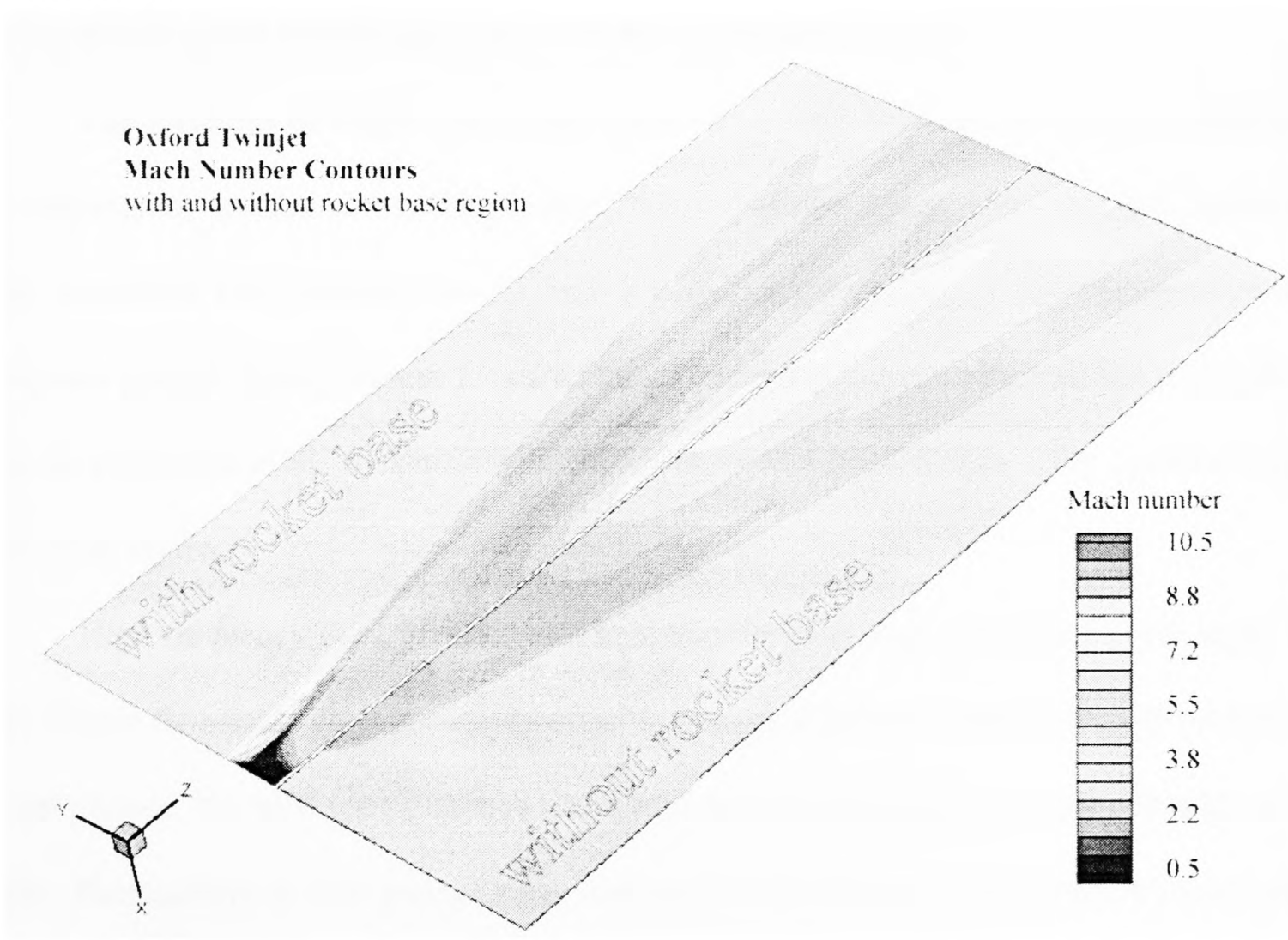


Figure 5-141 CFD Mach number contours on y-z plane with and without inclusion of rocket base region in calculation

6. Summary and Conclusions

6.1 CONCLUSIONS

This thesis constitutes the first major study on hypersonic co-flowing twinjets. Detailed measurements of Pitot pressure, total temperature and thin-film heat transfer were obtained and Schlieren photographs were taken. High and low frequency data were acquired for the mean and fluctuating Pitot pressure, heat transfer and total temperature profiles throughout the flowfield. A scaling parameter was suggested for the impingement shock surface between the two primary jets and a twin-cone model was suggested for the impingement locus. It was found that the secondary jet, as defined in the text, was not significantly contaminated by the freestream, at least up to the first shock cell if both the injection and the freestream gas have similar properties. CFD code for this complex flowfield was successfully validated and shown to be in good overall agreement with the experimental results.

The locations of single and twinjet shear layers were obtained using the measured total temperature profiles across the plumes. This well-defined region was in good agreement with measured Pitot pressure levels and density variations across the region shown on Schlieren images. Pitot pressure losses in the shear layer were investigated and it was found that the effect due to the rocket body boundary layer was small compared to viscous dissipation in the region.

High frequency Pitot pressure and heat transfer data were obtained for the single and twin nozzle flowfield. They provided crucial information on the turbulence characteristics of rocket plumes. No published data was found to rival the sampled frequency bandwidth in this thesis. Fluctuations in total temperature, convective heat transfer coefficient and their correlation were successfully deduced using three heat transfer probes.

A unique Pitot pressure probe was developed and shown to have superior frequency response and improved robustness over conventional designs.

Over 500 tests were carried out for this thesis over the period of three years. Of the 139 successful tests used in this thesis, 90 were quiescent injection runs and the remaining 49 were co-flow runs with a Mach 7 hypersonic freestream. This database is available with the thesis and constitutes permanent record for CFD validation and other theoretical analysis.

6.2 SUMMARY

A detailed summary is given below, which lists the purpose and key findings of the five main chapters in the thesis.

6.2.1 Summary of Chapter 1

- Hypersonic aerodynamics and rocket exhaust flowfield were introduced.
- The difference between an over-expanded and an under-expanded plume was given.

6.2.2 Summary of Chapter 2

- The initial unsteady process of the injection system was investigated. It was found that although the injection pressure could appear to be steady as measured by the pressure transducer in the plenum chamber, the total temperature of the injected gas was not. This process seemed to depend on nozzle flow rate and the characteristics of the injection gas used.
- A significant change in background pressure for quiescent runs was measured. This was believed to be mainly due to the ejector action of the rocket plume. The implications of this on measurements were analysed using Pitot pressure and thin-film heat transfer probes.
- The effects of model stings on the downstream flowfield were investigated using multiple Pitot pressure traverses and Schlieren photography. It was found that its influence could be significant on measurements taken on the sting side. However, influence on the undisturbed side could be safely neglected.

- A detailed operation procedure for the Oxford Gun Tunnel was documented for reference.
- Data conversion process was automated using a GUI programme incorporating correction for the thin-film heat transfer probes.

6.2.3 Summary of Chapter 3

- Total temperatures of the injection gas downstream of the nozzle exit were obtained by means of the total temperature probe. The dependence of these values on the injection pressure was shown and found to be mainly due to the non-ideal behaviour of the highly expanded nitrogen.
- A new Pitot probe design was developed and analysed using a combination of experimental testing and analytical models. It showed a good spatial and frequency response and its robustness in a debris-laden flow was unquestionable.
- Frequency response of the Pitot probes were obtained by shock tube tests. Results were compared to three types of models. Attempts were also made to correct for probe resonance characteristics.
- Fluctuations in convective heat transfer coefficient, flow total temperature and their correlation terms were solved by means of a set of three thin-film heat transfer probes. It was found that the fluctuations in Pitot pressure and total temperature were closely correlated.
- A modular probe holder was designed to facilitate probe calibration and interchange.

6.2.4 Summary of Chapter 4

- Detailed descriptions of a typical rocket plume flowfield in quiescent and in a hypersonic freestream were given with support of experimental results.

- Influence of the nozzle exit angle on the downstream flowfield in the co-flow case was investigated and it was found that this angle could have a small effect on shock structures.
- Quiescent plume scale was investigated and validated with experimental results.
- An expression for the Pitot pressure variation along the axis of symmetry was obtained based on a conical expansion model. The agreement with experiments was shown to be good for a range of injection pressures and exit Mach numbers.
- Total temperature was obtained bases on a regression process using two heat transfer probes made to traverse across the plume at high speed.
- A detailed analysis on Pitot pressure and heat flux signals across the plume was presented. Typical shock structure of single jets were identified and explained.
- Total pressure losses in the shear layer was investigated theoretically and experimentally. It was found that large losses could result due to turbulent dissipation, which contributed to the Pitot pressure losses in this region. This was previously believed to be mainly caused by the rocket body boundary layer.
- Turbulence fluctuation intensity was investigated by means of the normalised standard deviation parameter for the Pitot pressure signals. It was found that the exit Mach number could have a significant influence on the level of turbulence in the shear layer.
- Frequency contents in the shear layer of quiescent and co-flow single nozzle rocket plumes were deduced by means of power spectrum analyses.

6.2.5 Summary of Chapter 5

- The behaviour of twinjet in quiescent and hypersonic freestream was investigated using a combination of Schlieren photography, Pitot pressure and thin-film heat transfer measurements.

- Shock structure for a typical twinjet was proposed and validated with experiments and CFD simulations.
- Detailed analysis of Pitot pressure and heat flux signals across a twinjet was presented.
- Approximate single nozzle representation of a twinjet flowfield was investigated using N_2 and H_2 injections in quiescent and in the N_2 Mach 7 freestream. It was found that the agreement for the N_2 injection was good after the first primary reflection on the x-z plane. A normalised standard derivation factor based on Pitot pressure signals was introduced to facilitate comparison.
- Total temperatures across the twinjet flowfield were deduced from the measured heat flux signals. It suggested that the secondary jet was not affected by the freestream, which meant that the freestream gas was not entrained into this region.
- The impingement shock surface was found to be insensitive to the pressure ratio N. A scaling parameter based on exit diameter and Mach number, and nozzle spacing was proposed and shown to be reasonably effective.
- The impingement locus was modelled by a twin-cone model and shown to be effective up to the point where the locus met the freestream.
- Turbulence intensity of the secondary jet was investigated. Spectrum analysis showed the possible existence of large structures in this region.
- Experimental results were shown to be in reasonable agreement with CFD simulations based on a full three-dimensional Navier-Stokes code.
- Base region of the rocket nozzle was shown to have a significant influence on the downstream flowfield.

6.3 RECOMMENDATIONS

6.3.1 Thin-film heat transfer probes

- Spatial and frequency resolution can be further improved by adopting new manufacturing technologies to give thinner film deposit and smaller probe radius.
- Spacing between the probes should be minimised if they are to be used in a traverse.
- Alternative method of heating could be adopted; e.g. high-power laser could be used in the future so the probes could be place closer together without having to accommodate the external heater.
- Since heat flux at the stagnation point is inversely proportional to the nose radius, this means that a reasonable difference in heat flux can be obtained if probes of different nose radii are used. This will eliminate the need for pre-heating entirely.
- Despite its robustness compares to thin-wires, particle impact at hypersonic speeds can still have an effect on the measured signal. Thin deposit of an appropriate material over the stagnation region is recommended in the future.
- Length of the exposed probe shaft could be reduced to minimised vibration and the impulsive shear loading when the probes are stopped at the end of the traverse.

6.3.2 Pitot pressure probes

- Miniaturisation can further improve the frequency and spatial response of the FPT Pitot probe.

6.3.3 Nozzle Design

- A new rocket body could be used in the future to allow nozzles with larger throat diameters. This will minimise the effect of the unsteady compression process in the injection gas.

- Model sting could be mounted from the top of the test section where the traverse starts, so it could protect the probes during the start-up process of the gun tunnel where most of the debris is present.
- Spark erosion method is recommended for new nozzles. This will give a smoother finish and hence eliminate the formation of shock waves on the nozzle wall.

Appendix A References

Adamson, T. C., "The Structure of the Rocket Exhaust Plume without Reaction at Various Altitudes," University of Michigan Report No. 4613-45-T, June 1963.

Adamson, T. C., Nicholls, J. A., "On the Structure of Jets From Highly Underexpanded Nozzles into Still Air," Journal of Aerospace Science, Vol. 26, No. 16, 1959.

Ainsworth, R. W., Allen, J. L., "Investigating the Performance of Miniature Semiconductor Pressure Transducers for Use in Fast Response Aerodynamic Probes," Measuring Techniques for Transonic and Supersonic Flows in Cascades and Turbomachines, Proceeding of 10th Symposium, VKI, September 17-18, 1990

Albini, F. A., "Approximate Computation of Underexpanded Jet Structure," AIAA Journal, No. 3, 1965, pp. 1535-1537.

Alden, R. L., Habert, R. H., "Gas Dynamics of High Altitude Rocket Plumes," MITHRAS Report MC-63-80-R1, July 1964

Anderson, J. D., "Hypersonic and High Temperature Gas Dynamics," McGraw-Hill International Editions

Antonia, R. A., Browne, L. W. B., Chamber, A. J., "Determination of Time Constants of Cold-Wires," Preview of Scientific Instrumentation, Vol. 52, pp. 1382-5, 1981

Bailey, A. B. et al., "Effect of Ambient Pressure on Nozzle Centreline Flow Properties," AIAA Journal, VOL. 23, No. 6, June 1985, pp. 953-954.

Bailey, A. B., "Flow Angle Measurement in a Rarefied Nozzle Plume," AIAA Journal, Vol. 25, No. 10, 1987, pp. 1301-1304.

Bergh, H., Tijdeman, H., "Theoretical and Experimental Results for the Dynamic Response of Pressure Measuring Systems," NLR-TR F.238, January 1965.

Bertin, J. J., "General Characterisation of Hypersonic Flows," 1st Joint Europe-US Short Course on Hypersonics, Paris, December, 1987

Bird, G A "The Nozzle Lip Problem," Proceedings of the Ninth International Symposium on Rarefied Gas Dynamics, DFVLR Press, Pro-Wahn, FRG, 1974, Vol. 1, pp. A22-1-A22-8.

Bocher, J. M., " Noise and Flow Characteristics of Linear Array of Jets and Ejector Flow Systems," PhD Thesis, University of Tennessee, 1976

Boerrigter, H. L., "A Simulation Programme to Determine the Frequency and Time Response of a Pressure Measurement System," Private Communication, 1995.

Boynton, F. P., "Highly Underexpanded Jet Structure: Exact and Approximate Calculations," AIAA Journal, Vol. 5, No. 9, 1967, pp. 1703-1704

Brescianini, C. P., "A Modified k-e Model for Compressible Shear Flows," AIAA Journal, Vol. 30, No. 8, 1992, pp. 2161-2163.

Brown, G. L., Roshko, A., "On Density Effects and Large-Scale Structure in Turbulent Mixing Layers," Journal of Fluid Mechanics, Vol. 64, No. 4, 1974, pp. 775-816

Buttsworth, D. R., "A Fast-Response Total Temperature Probe for Unsteady Compressible Flows," ASME, International Gas Turbine and Aeroengine Congress, June 10-13, Birmingham, United Kingdom.

Buttsworth, D. R., and Jones, T. V., "A Fast-Response High Spatial Resolution Total Temperature Probe Using a Pulsed Heating Technique," 42nd ASME International Gas Turbine and Aeroengine Congress, 1997.

Buttsworth, D. R., Jones, T. V., "Radial Conduction Effects in Transient Heat Transfer Experiments," Internal Report, University of Oxford, 1997.

Cain, T. M., "An Experimental Study of Under-Expanded Jets," Report No. OUEL 1959/92, University of Oxford, 1992.

Cain, T. M., Jones, T. V., "Pitot Measurements in the Exhaust of a Cluster of Four Small Scale Supersonic Nozzles," OUEL Report 1862/90, University of Oxford, Department of Engineering Science, 1990.

Cain, T. M., Jones, T. V., "Pitot Surveys of Two Moderately Underexpanded Jets," AGARD, Conference Proceedings No. 479.

Cherrett, M. A., "Temperature Error Compensation Applied to Pressure Measurements Taken with Miniature Semiconductor Pressure Transducer in a High Speed Research Compressor," Measuring Techniques for Transonic and Supersonic Flows in Cascades and Turbomachines, Proceeding of 10th Symposium, VKI, September 17-18, 1990

Chu, S. H., "Pressure Probes for Fluid Measurements," Progr. Aerospace Science, Vol. 16, No. 2, 1975, pp. 147-223

Cox, R. N., "General Characteristics of Hypersonic Flow Fields," Journal of the Royal Aeronautical Society, Vol. 63, September 1959

Cox, R. N., Winter, D. F. T., "The Light Gas Hypersonic Gun Tunnel at ARDE, For Halstead, Kent," AGARD Report No. 139, July 1957

Crist, S., Sherman, P. M., and Glass, D. R., "Study of the Highly Underexpanded Sonic jet," AIAA Journal, Vol. 4, January 1966.

Dankert C. and Koppenwallner G., "An Experimental Study of Nitrogen Condensation in a Free Jet Expansion," RGD 11, Cannes, pp 1107-1118, 1978

Dankert, C., Koppenwallner, G., "Experimental Study of the Interaction Between Two Rarefied Jets," DFVLR Institute for Experimental Fluid Mechanics, Bunsenstrasse 10, D-3400 Gottingen, Federal Republic of Germany.

Dash, S. M., "Rocket Motor Plume Flowfield: Phenomenology and Simulation," AGARD Lecture Series 188, June 1993.

Dash, S. M., Pearce, B. E., Pergament, H. S., Fishburne, E. S., "Prediction of Rocket Plume Flowfields for Infrared Signature Studies," Journal of Spacecraft and Rockets, Vol. 17, No. 3, May 1980

Davies, W. R., Bernstein, L., "Heat Transfer and Transition to Turbulence in the Shock-Induced Boundary Layer on a Semi-Infinite Flat Plate," Journal of Fluid Mechanics, Vol. 36, Par 1, pp. 87-112, 1969

Davis, R. T., "Numerical Solution of the Hypersonic Viscous Shock-Layer Equations," AIAA Journal, Vol. 8, No. 5, May 1970, pp. 843-851

Ducoffe, A. L., "Pressure Response in Supersonic Wind-Tunnel Pressure Instrumentation," Journal of Applied Physics, Vol. 24 No. 11, November 1953. pp1144-pp1155

Eckert, E R G., "Engineering Relations for Heat Transfer and Friction in High-Velocity Laminar and Turbulent Boundary-Layer Flow Over Surfaces with Constant Pressure and Temperature," Trans. of the ASME, vol. 78, no. 6, August 1956, pp. 1273.

Edney, B. E., "Temperature Measurements in a Hypersonic Gun Tunnel using Heat Transfer Methods," Journal of Fluid Mechanics, Vol. 27, pp.503-512.

Elbanna, H, Gahin, S., Rashed, M. I. I., "Investigation of Two Plane Parallel Jets," AIAA Journal, Vol. July 1983.

Emden, R., "Ueber die Ausstroemungserscheinungen permanenter Gase," Annalen der Physik und Chemie 69, 1899, pp. 264-269, 426-455

Gamal, H. M., "Interaction of Axisymmetric Supersonic Twin Jets," AIAA Jounal, Vol. 3, No. 5, May 1995.

Gamal, H. M., "Experimental and Numerical Investigation of Subsonic, Sonic and Supersonic Multiple Free Jets." PhD Thesis, Indian Institute of Technology, Kanpur, India, August 1992.

Gilmore, M., DRA Farnborough, Defence Research Agency, MoD, Private Communication.

Gnoffo, P. A., "An Up-wind Biased, Point Implicit Relaxation Algorithm for Viscous, Compressible Perfect Gas Flows," NASA TP 2953, 1990.

Goebel, S. G., Dutton, J. C., "Velocity Measurement of Compressible Turbulent Shear Layer," AIAA Paper 90-0709, Jan. 1990.

Grande, E. and Oates, G. C., "Response of Miniature Pressure Transducers to Fluctuations in Supersonic Flow," Progress in Astronautics and Aeronautics, Instrumentation for Airbreathing Propulsion, edited by A. E. Fuhs and M. Kingery, MIT Press, Vol. 34, 1974

Hartunian, R. A., Russo, A. L., Marrone, P. V., "Boundary Layer Transition and Heat Transfer in Shock Tubes," Journal of Aerospace Science, Vol. 27, pp. 587-594.

Hill, J. A. F., Habert, R. H., "Gas Dynamics of High Altitude Rocket Plumes," MITHRAS Report No. MC-61-18-R1, January 1963.

Holder, D. W., "Experimental Facilities and Measuring Techniques," Jounal of The Royal Aeronautical Society, Vol. 63, September 1959.

Hsu, A. T., Liou, M. S., "A Computational Analysis of Underexpanded Jets in the Hypersonic Regime," AIAA Journal of Propulsion, Vol. 7, No. 2, 1991, pp. 297-299

Hubbard, E. W., "Approximate Calculation of Highly Underexpanded Jets," AIAA Journal, No. 4, 1966, pp. 1877-1879.

Hurdle, C. V., "Some Properties of Quadruple Free Jet Plumes," Memorandum 61/68, Royal Armament Research and Development Establishment, February 1984.

Jarvinen, P. O., Hill, J. A. F., Drapper, J. S., Earl, R., "High Altitude Rocket Plumes," AFCRL 66-656, June 1966.

Jenkins, R. C., "Effects of Pitot Probe Shape on Measurement of Flow Turbulence," AIAA Journal, Vol. 25, No. 6, 1987, pp. 889-892.

Kendall, J. M., "Optimized Design of Systems for Measuring Low Pressure in Supersonic Wind Tunnels," AGARD Report 174, March 1958.

Kim, S. C., "New Mixing Length Model for Supersonic Shear Layers," AIAA Journal, Vol. 28, 1990, pp. 1999-2000.

Koppenwallner, G., Boettcher, R. D., Dettleff, G., Legge, H., "Rocket Exhaust Plume Flow into Space," Proceedings of symposium: "Fluid Dynamics and Space," VKI, Rhode-Saint-Genese, 25 & 26 June 1986.

Koppenwallner, G., "Scaling Laws for Rarefied Plume Interference with Application to Satellite Thrusters," 14th International Symposium on Space Technology and Science, Tokyo, Japan, May 28 – June 2, 1984.

Krasnov, N. F., "Aerodynamics of Bodies of Revolution," Edited and Annotated by Morris, N., American Elsevier Publishing Company, Inc., New York, 1970.

Krothapalli, A., "An Experimental Study of Multiple Jet Mixing," PhD Thesis, Stanford University, Stanford, California, 1979

Lengrand, J-C., "Underexpanded Free Jets and their Interaction with Adjacent Surfaces," AIAA Journal, Vol. 20, No. 1, January 1982.

Lepicovsky, J., Ahija, K. K., Brown, W. H., Rurrin, R. H., "Coherent Large-scale Structures in High Reynolds Number Supersonic Jets," AIAA J. 25, 1987, 1419-1425

Lewis, C., Carlson, J., "Normal Shock Location in Underexpanded Gas and Gas-Particle Jets," AIAA Journal, Vol2, No. 4, pp. 776-777

Ljung, Lennart., "System Identification Toolbox for Use with Matlab," Manual for the Matlab Toolbox Series, 1995.

Lukasiewicz, J., "Experimental Methods of Hypersonics," Marcel Dekker, Inc, New York, 1973, pp. 78-84

Mach, E., Salcher, P., "Optische Untersuchungen der Luftstrahlen," Sitzungsberichte Wien 98, Iia, 1889, pp. 1303-1309

Marsters, G. F., "Interaction of Two Plane, Parallel Jets," AIAA Journal, Vol. 15, No. 12, December 1977

Matin, J. J., "Atmospheric Re-entry, An Introduction to its Science and Engineering," Prentice-Hall, Inc., Englewood Cliffs, N. J., 1966

Miller, D. R., Comings, E. W., "Force Momentum Fields in a Dual Jet Flow," Journal of Fluid Mechanics, Vol. 18, No. 7, 1959, pp. 237-256.

Mirels, H., Mullen, J. F., "Expansions of Gas Clouds and Hypersonic Jets Bounded by a Vacuum," Aerospace Corp, Rept. TDR-169 (3230-12) TR-1, September 1962.

Monaghan, N. A., "Problems of Hypersonic Aerodynamics – A Survey," Journal of the Royal Aeronautical Society, Vol. 63, No. 585, September 1959

Moretti, G., "Floating Shock Fitting Technique for Imbedded Shocks in Unsteady Multidimensional Flow," Proceedings of the 1974 Heat Transfer and Fluid Mechanics Institiute, Stamford University Press, 1974.

Morris, N. A., "An Experimental and Computational Study of Moderately Under-Expanded Rocket Exhaust Plumes in a Co-Flowing Hypersonic Free Stream," D.Phil. Thesis, CB/FRN/9/4/2057/122, University of Oxford, 1995

Morris, N. A., Buttsworth, D. R., Brescianini, C. P., Jones, T. V., "An Experimental and Computational Study of Moderately Underexpanded Rocket Exhaust Plumes in a Co-Flowing Hypersonic Freestream," AIAA Paper, 1995.

Moss, R. W. and Oldfield, M. L. G., "Comparisons Between Turbulence Spectra Measured with Fast Response Pressure Transducers and Hot Wires," Symposium on Aerodynamic Measuring Techniques for Tansonic and Supersonic Flow in Cascades and Turbomachines, Brussels, September 17-19, 1990

Moss, R. W. and Oldfield, M. L. G., "Measurements of Hot Combustor Turbulence Spectra," ASME, International Gas Turbine and Aeroengine Congress and Exposition, Orlando, FL June 3-6, 1991

Ng, W. F., Epstein, A. H., "High-Fequency Temperature and Pressure Probe for Unsteady Compressible Flows," Revision of Scientific Instrumentation, Vol. 52, pp. 1678-1683, 1983.

Norman, L., Kinslow, M., Lewis, J. W. L., "Experimental Study of Simulated High Altitude Rocket Exhaust Plumes," AEDC-TR-71-25, 1970

Novopashin, S. A., Perepelkin, A. L., "Axial Symmetry Loss of a Supersonic Preturbulent Jet," Physics Letters A, Vol. 135, No. 4, 1989, pp. 290-293.

Oldfield, M. L. G., "Experimental Techniques in Unsteady Flows," Report No. OUEL 1843/90, University of Oxford.

Oldfield, M. L. G., Burd, H. J., and Doe, N. G., "Design of Wide-Bandwidth Analogue Circuits for Hear Transfer Instrumentation in Transient Tunnels," 16th Symposium of ICHMT, Dubrovnik, Hemisphere Publishing, 1982.

Papamoschou, D., "Thrust Loss Due to Supersonic Mixing," Journal of Propulsion and Power, Vol. 10, No. 6, 1994

Potter, J. L., "Transitional, Hypersonic Aerodynamics Simulation and Scaling," Progress of Astronautics and Aeronautics, Vol. 103, 1985, pp. 79-96

Potter, J. L., Carden, W. H., "Design of Axisymmetric Contoured Nozzles for Laminar, Hypersonic Flow," Journal of Spacecraft & Rockets, 5(9), 1968, pp. 1095-1100

Prandtl, L., "Neue Untersuchungen ueber die stroemende Bewegung der Gases und Daempfe," Physik, Z. 8, 1907, pp. 23-32.

Prandtl, L., "Ueber die stationaeren Wellen in einem Gasstrahle," Physik. Z. 5, 1904, pp. 559-601

Raghunathan, S., Reid, I. M., "A Study of Multiple Jets," AIAA Journal, Vol. 19, January 1981.

Rayleigh, "On the Discharge of Gases under High Pressure," Phil. Mag. 6, 1916, pp. 177-187

Roe, P. L., "Approximation Riemann Solvers, Parameter Vectors, and Difference Schemes," Journal of Comp. Phy., Vol 43, pp 357-373, 1981.

Ruck, G., Stetter, H., "Unsteady Velocity and Turbulence Measurement with a Fast Response Pressure Probe," Gas Turbine and Aeroengine Congress and Exposition, Brussels, Belgium, 1990

Rudman, S., "Multinozzle Plume Flow Fields – Structure and Numerical Calculation," Grumman Aerospace Corporation, Research Department, Contract No. F44620-76-C-0021.

Sauer, R., "Theoretical Gas Dynamics," Edwards, Ann Arbor, 1947

Schaefer, M., "Outflow of a Jet of Compressed Air into Moving Air," Air Material Command Technical Report No. F-TS-1213-1A, May 1949.

Schultz, D. L., and Jones, T. V., 1973, "Heat Transfer Measurements in Short-Duration Hypersonic Facilities," Agardograph No. 165.

Seiner, J. M., Manning, J. C., Ponton, M. K., "Dynamic Pressure Loads Associated with Twin Supersonic Plume Resonance," AIAA Journal, Vol. 26, No.8, August 1988.

Shau, Y. R. and Dolling, D. S., "Exploratory Study of Turbulent Structure of a Compressible Shear Layer Using Fluctuating Pitot Pressure Measurements," Experiments in Fluids 12, 293-306 (1992)

Shek, H. H. W., "An Experimental Study of Under-Expanded Rocket Exhaust Plumes in a Co-Flowing Hypersonic Free Stream," First Year Report, University of Oxford, 1995.

Steenken, W. G., "Effect fo Transducer Diameter on Resolution of Total Pressure Fluctuations I a Turbulent Flow," Progress in Astronautics and Aeronautics, Instrumentation for Airbreathing Propulsion, edited by A. E. Fuhs and M. Kingery, MIT Press, Vol. 34, 1974

Stollery, J. L., "Supersonic Turbulent Boundary Layers: Some Comparison Between Experiment and a Simple Theory," Aero. Quart., 1977, pp. 87-98

Thole, K. A., Bogard, D. G., "Simultaneous Temperature and Velocity Measurements," Measurement Science Technology, Vol. 5, pp. 435-439, 1994.
Toulokian, Y. S., "Thermophysical Properties of Matter," The TPRC Data Series, Vol. 2 and Vol. 5, 1970

Traugott, S. C., "Some Features of Supersonic and Hypersonic Flow about Blunted Cones," Journal of the Aerospace Science, Vol. 29, No. 4. April 1962, pp. 389-399.

Vick, A. R., Andrews , E. H., "An Experimental Investigation of Highly Underexpanded Free Jets Impinging Upon a Parallel Flat Surface," NASA TN D-2326, NASA, Langley Station, Hampton, Va., February 18, 1964

Von Karman, Th., "Uber stationaeren Wellen in Gasstrahlen," Physik, Z. 8, 1907, pp. 209-211

Welsh, P. F., Private Communication 1997.

White, F. M., "Viscous Fluid Flow," 1st Edition, McGraw Hill, 1974.

Whitefield, D. L., Lewis, C. H., "Boundary Layer Analysis of Low-Density Nozzles Including Displacement, Slip and Traverse Curvature," Journal of Spacecraft & Rockets, 7(4), pp. 462-468, 1970

Wilhite, A. W., "Optimum Wing Sizing of Single-Stage-to-Orbit Vehicle," Journal of Spacecraft and Rockets, Vol. 20, No. 2, 1983, pp. 115-121

Wlezien, R. W., "Nozzle Geometry Effects on Supersonic Jet Interaction," AIAA Journal, Vol. 27, No. 10, October 1989

Yee, H. C., "Construction of Explicit and Implicit Symmetric TVD Schemes and their Applications," Journal of Comp. Phys., Vol 68, pp 151-179, 1987.

Appendix B Gun Tunnel Operation and Troubleshooting

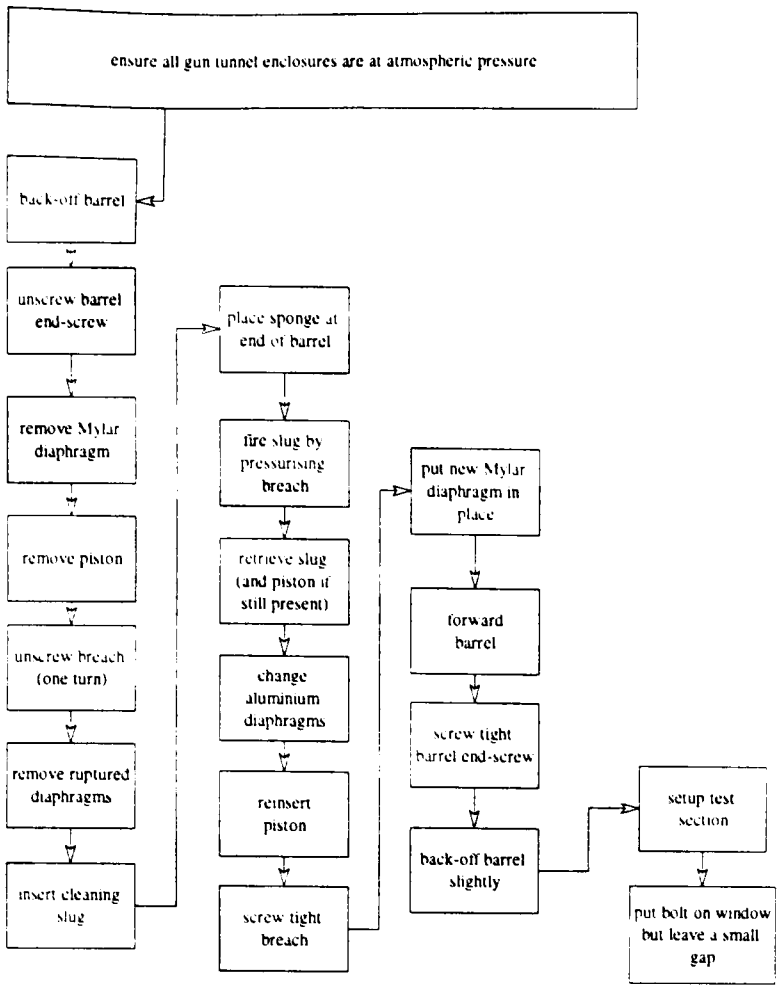


Figure B-1 Preparing the Gun Tunnel for co-flow experiments

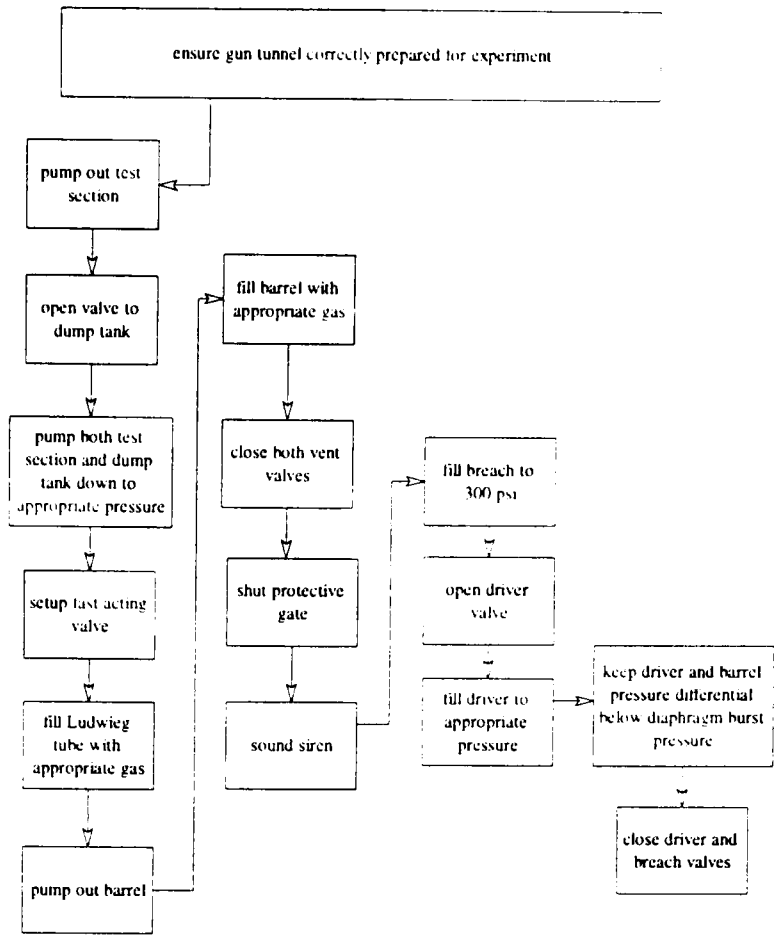


Figure B-2 Pre-run procedures for the Gun Tunnel

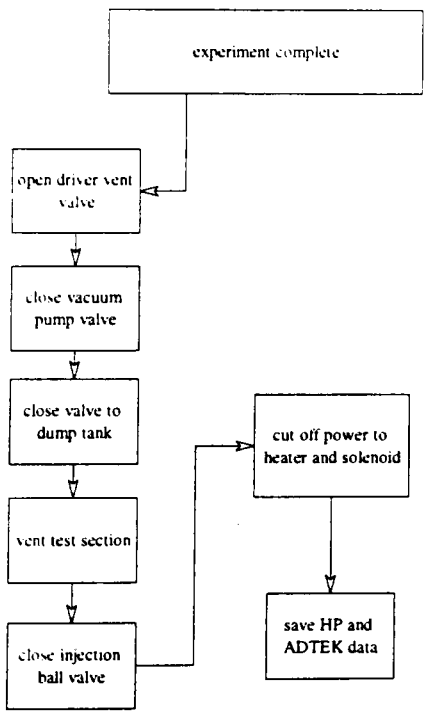


Figure B-3 Post-run procedures for the Gun Tunnel

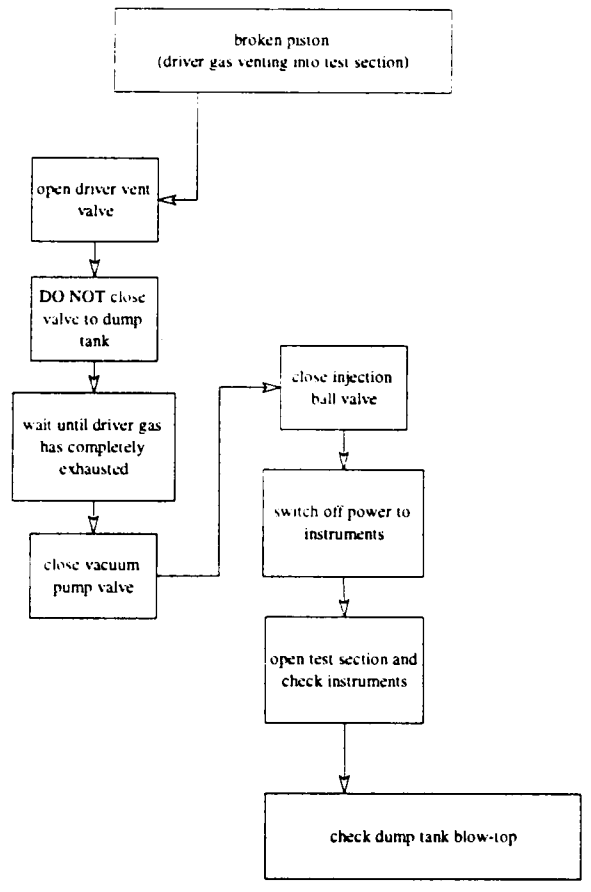


Figure B-4 Troubleshooting: broken piston

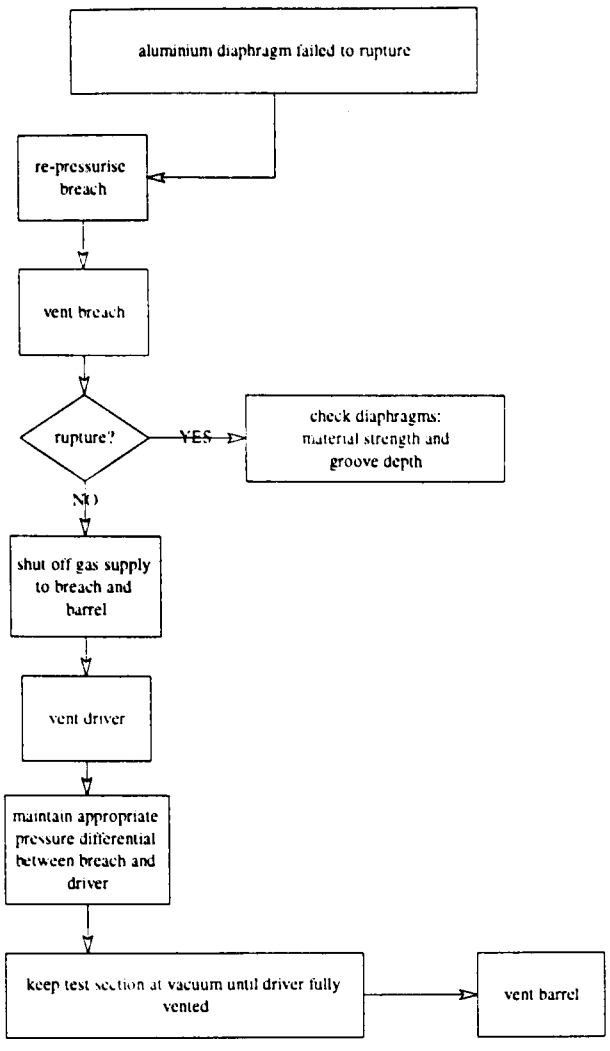


Figure B-5 Troubleshooting: aluminium diaphragms failed to rupture

Appendix C Run Conditions

Injection Gas	Run Number	z mm	P_{0c} bar	T_{0c} K	$P_{0\infty}$ bar	Probes	Fast Data	Sampling Frequency kHz	N
N_2	GT692	-	-	286.0	-	S	-	-	-
N_2	GT694	-	92	290.0	69	S	-	-	5520
N_2	GT695	-	-	286.0	-	S	-	-	-
N_2	GT697	100	91	287.0	69	P, S	-	-	5460
N_2	GT698	50	92	287.0	69	P, S	-	-	5520
N_2	GT699	30	92	285.0	69	P, S	-	-	5520
N_2	GT700	10	93	286.0	69	P, S	-	-	5580
N_2	GT701	150	91	286.0	70	P, S	-	-	5382
H_2	GT721	100	85	286.0	71	P, S, H	F121354	472.30	4956
H_2	GT722	150	86	288.0	70	P, S, H	F163649	472.30	5086
H_2	GT727	250	87	286.0	64	P, S, H	F120459	472.30	5628
N_2	GT728	250	92	287.0	71	P, S, H	-	-	5364
N_2	GT730	300	91	291.0	70	P, S, H	-	-	5382
N_2	GT732	40	92	289.9	65	P, H	FGT732	1132.8	5850
N_2	GT733	40	93	291.8	69	P, H	FGT733	1132.8	5580
N_2	GT734	40	89	292.3	62	P, H	FGT734	1132.8	5943
N_2	GT736	40	90	288.7	68	P, H	FGT736	1132.8	5479
N_2	GT737	40	92	288.7	58	P, H	FGT737	1132.8	6567
N_2	GT744	100	92	289.9	70	P, H	FGT744	1132.8	5441
N_2	GT745	250	93	289.9	69	P, H	FGT745	1132.8	5580

Table 1 Mach 5 twinjet (TM5) in Mach 7 freestream on *x-z* plane

Injection Gas	Run Number	z mm	P_{0c} bar	T_{0c} K	$P_{0\infty}$ bar	Probes	Fast Data	Sampling Frequency kHz	N
N_2	GT703	250	93	287.0	71	P, S	-	-	5423
N_2	GT704	100	92	288.0	70	S	-	-	5441
N_2	GT705	100	92	287.0	70	P, S	-	-	5441
N_2	GT706	50	91	286.0	70	S	-	-	5382
N_2	GT707	50	91	287.0	70	P, S	-	-	5382
N_2	GT708	30	91	285.0	71	P, S	-	-	5306
N_2	GT709	10	92	286.0	70	P, S	-	-	5441
N_2	GT710	150	92	287.0	70	P, S	-	-	5441
H_2	GT712	250	-	-	-	P, S	-	-	-
H_2	GT720	100	85	288.0	69	P, S, H	F173947	472.00	5100
H_2	GT723	150	85	289.0	71	P, S, H	F181251	472.00	4956
H_2	GT726	250	85	290.0	70	P, S, H	F165047	472.00	5027
N_2	GT729	250	-	289.3	-	P, S, H	F154652	1416.0	-
N_2	GT741	100	91	290.2	70	P, H	FGT741	1132.8	5382
N_2	GT746	100	93	289.9	70	P, H	FGT746	1132.8	5500
N_2	GT749	250	92	290.9	70	P, H	FGT749	1132.8	5441

Table 2 Mach 5 twinjet (TM5) in Mach 7 freestream on *y-z* plane

Injection Gas	Run Number	z mm	P_{0c} bar	T_{0c} K	$P_{0\infty}$ bar	Probes	Fast Data	Sampling Frequency kHz	N
H_2	GT712	250	-	285.8	-	P, S, T	-	-	-
N_2	GT713	250	-	287.6	-	P, S, H	F155712	1416.0	-
N_2	GT714	250	91	290.0	70	P, S, H	F200843	1416.0	5382
N_2	GT715	250	90	290.0	70	P, S, H	F153547	1416.0	5323
N_2	GT716	150	91	291.0	70	P, S, H	-	-	5382
N_2	GT717	100	91	292.0	70	P, S	F164309	1416.0	5382
H_2	GT719	100	85	290.0	71	P, S, T	F160305	472.00	4956
H_2	GT724	150	85	286.0	71	P, S, T	F110241	472.00	4956
H_2	GT725	250	85	287.0	70	P, S, T	F123818	472.00	5027
N_2	GT738	100	90	290.8	72	P, H	FGT738	1132.8	5175
N_2	GT739	100	91	290.8	70	P, H	FGT739	1132.8	5382

Table 3 Mach 5 single jet (SM5) in Mach 7 freestream

Injection Gas	Run Number	z mm	P_{0c} bar	T_{0c} K	$P_{0\infty}$ bar	Probes	Fast Data	Sampling Frequency kHz	N
N_2	GT740	100	91	290.2	70	P, H	FGT740	1132.8	5382
N_2	GT747	100	92	289.9	71	P, H	FGT747	1132.8	5364
N_2	GT748	250	91	290.9	71	P, H	FGT748	1132.8	5306

Table 4 Mach 5 single jet (SM5M) in Mach 7 freestream

Injection Gas	Run Number	z (y) mm	P_{0c} bar	T_{0c} K	$P_{0\infty}$ bar	Probes	Fast Data	Sampling Frequency kHz	N
N_2	GT623	100 (0)	83	289.0	66	P	-	-	5206
N_2	GT624	100 (10)	82	289.0	65	P	-	-	5223
N_2	GT626	100 (30)	81	291.0	65	P	-	-	5159
N_2	GT646	100 (15)	82	291.0	65	P	-	-	5223

Table 5 Mach 5 single jet (M5) in Mach 7 freestream on crossflow plane at 100 mm downstream

Injection Gas	Run Number	z (y) mm	P_{0c} bar	T_{0c} K	$P_{0\infty}$ bar	Probes	Fast Data	Sampling Frequency kHz	N
N_2	GT634	70 (0)	64	289.0	65	P	-	-	4076
N_2	GT637	70 (5)	64	289.0	66	P	-	-	4014
N_2	GT638	70 (10)	64	289.0	65	P	-	-	4076
N_2	GT647	70 (17)	64	291.0	64	P	-	-	4140
N_2	GT648	70 (14)	64	291.0	66	P	-	-	4014

Table 6 Mach 3 single jet (M3) in Mach 7 freestream on crossflow plane at 70 mm downstream

Injection Gas	Run Number	z mm	P_{0c} bar	T_{0c} K	Probes	Fast Data	Sampling Frequency kHz	N
N_2	LT 9	-	91	286.0	S	-		7165
N_2	LT 10	-	29	286.5	S	-	-	2283
N_2	LT 11	-	46	286.5	S	-	-	3622
N_2	LT 12	-	62	286.6	S	-	-	4882
N_2	LT 22	-	81	285.5	S	-	-	6378
N_2	LT 23	-	69	285.5	S	-	-	5433
N_2	LT 24	-	53	285.5	S	-	-	4173
N_2	LT 25	-	38	285.5	S	-	-	2992
N_2	LT 26	-	19	285.5	S	-	-	1496
N_2	LT 27	-	10	285.5	S	-	-	787
N_2	LT144	150	92	289.4	P, H	FLT144	1132.8	7244
N_2	LT145	100	87	289.4	P, H	FLT145	1132.8	6850
N_2	LT148	60	92	291.0	P, H	FLT148	1132.8	7244
N_2	LT149	120	87	291.0	P, H	FLT149	1132.8	6850
N_2	LT150	40	83	290.3	P, H	FLT150	1132.8	6535
N_2	LT156	40	92	292.2	P, H	FLT156	1132.8	7244
He	LT192	100	91	290.0	P, H	FLT192	1132.8	7165

Table 7 Mach 5 twinjet (TM5) in quiescent on *x*-*z* plane

Injection Gas	Run Number	z mm	P_{0c} bar	T_{0c} K	Probes	Fast Data	Sampling Frequency kHz	N
N_2	LT36		29	287.3	S	-	-	2283
N_2	LT37	-	28	287.6	S	-	-	2205
N_2	LT38	-	59	287.8	S	-	-	4646
N_2	LT39	-	84	289.7	S	-	-	6614
N_2	LT44	-	9.5	289.3	S	-	-	748
N_2	LT45	-	47	289.7	S	-	-	3701
N_2	LT46	-	91	289.7	S	-	-	7365

Table 8 Mach 5 twinjet (TM5) in quiescent on *x*-*z* plane with upper nozzle only

Injection Gas	Run Number	z mm	P_{0c} bar	T_{0c} K	Probes	Fast Data	Sampling Frequency kHz	N
N_2	LT 13	-	65	287.2	S	-	-	5118
N_2	LT 14	-	47	287.3	S	-	-	3701
N_2	LT 15	-	29	287.3	S	-	-	2283
N_2	LT 16	-	92	286.4	S	-	-	7244
N_2	LT 17	-	92	286.5	S	-	-	7244
N_2	LT 18	-	10	285.0	S	-	-	787
N_2	LT 19	-	19	285.0	S	-	-	1796
N_2	LT 20	-	38	285.0	S	-	-	2992
N_2	LT 21	-	56	285.0	S	-	-	4409
N_2	LT 28	-	74	286.6	S	-	-	5827
N_2	LT 29	-	-	286.6	S	-	-	-
N_2	LT179	60	92	290.8	P, H	FLT179	1132.8	7244
N_2	LT183	40	92	292.3	P, H	FLT183	1132.8	7244
N_2	LT184	40	92	282.3	P, H	FLT184	1132.8	7244
N_2	LT185	60	92	292.3	P, H	FLT185	1132.8	7244
He	LT193	100	92	290.0	P, H, T	FLT193	1132.8	7244
N_2	LT195	100	91	290.0	P, H	FLT195	1132.8	7165

Table 9 Mach 5 twinjet (TM5) in quiescent on *y*-*z* plane

Injection Gas	Run Number	z mm	P_{0c} bar	T_{0c} K	Probes	Fast Data	Sampling Frequency kHz	N
N_2	LT40	-	29	288.5	S	-	-	2283
N_2	LT41	-	47	288.5	S	-	-	3701
N_2	LT42	-	59	288.5	S	-	-	4646
N_2	LT43	-	84	288.5	S	-	-	6614

Table 10 Mach 5 twinjet (TM5) in quiescent on *y*-*z* plane with upper nozzle only

Injection Gas	Run Number	z mm	P_{0c} bar	T_{0c} K	Probes	Fast Data	Sampling Frequency kHz	N
N_2	LT47	-	11	292.2	S	-	-	866
N_2	LT48	-	38	292.2	S	-	-	2992
N_2	LT49	-	56	292.2	S	-	-	4409
N_2	LT50	-	66	292.2	S	-	-	5197
N_2	LT51	-	82	292.2	S	-	-	6457

Table 11 Mach 3 twinjet (TM5) in quiescent on *x*-*z* plane

Injection Gas	Run Number	z mm	P_{0c} bar	T_{0c} K	Probes	Fast Data	Sampling Frequency kHz	N
N_2	LT5	-	46	287.5	S	-	-	3622
N_2	LT6	-	28	287.4	S	-	-	2205
N_2	LT7	-	60	287.5	S	-	-	4724
N_2	LT8	-	90	287.4	S	-	-	7087
N_2	LT30	-	80	286.6	S	-	-	6299
N_2	LT31	-	61	286.7	S	-	-	4803
N_2	LT32	-	53	286.7	S	-	-	4173
N_2	LT33	-	38	286.8	S	-	-	2992
N_2	LT34	-	20	286.8	S	-	-	1575
N_2	LT35	-	10	286.9	S	-	-	787
N_2	LT157	-	40	290.2	P, H	FLT157	1132.8	3150

Table 12 Mach 5 single jet (SM5) in quiescent

Injection Gas	Run Number	z mm	P_{0c} bar	T_{0c} K	Probes	Fast Data	Sampling Frequency kHz	N
N_2	LT110	-	21	295.0	S	-	-	1654
N_2	LT111		-	295.0	S	-	-	-
N_2	LT112	-	56	295.8	S	-	-	4409
N_2	LT113	-	74	294.9	S	-	-	5827
N_2	LT114	-	74	294.9	S	-	-	5827
N_2	LT115	-	73	294.9	S	-	-	5748
N_2	LT116	-	92	295.2	S	-	-	7244
N_2	LT117	65	31	292.7	P	FLT117	472.00	2441
N_2	LT118	114	31	293.6	P	FLT118	472.00	2441
N_2	LT129	100	-	293.0	P, H	FLT129	1132.8	-
N_2	LT130	60	64	293.0	P	FLT130	1132.8	5039
N_2	LT132	40	70	291.5	P, H	FLT132	1132.8	5512
N_2	LT139	120	69	293.0	P, H	FLT139	1132.8	5433
N_2	LT140	-	-	293.0	CBC	FLT140	1132.8	-
N_2	LT181	60	91	292.3	P, H	FLT181	1132.8	7165
N_2	LT182	40	91	292.3	P, H	FLT182	1132.8	7165
He	LT186	60	61	291.8	P, H	FLT140	1132.8	4803
He	LT191	100	92	290.0	P, H	FLT140	1132.8	7244

Table 13 Mach 5 single jet (SM5M) in quiescent

Injection Gas	Run Number	z mm	P_{0c} bar	T_{0c} K	Probes	Fast Data	Sampling Frequency kHz	N
N_2	LT187	11	73	293.9	P, H, T	-	-	5748
N_2	LT188	11	38	293.9	P, H, T	-	-	2992
N_2	LT189	11	94	293.9	P, H, T	-	-	7402
He	LT190	11	69	293.9	P, H, T	-	-	5433

Table 14 Mach 5 single jet (M5) in quiescent

Injection Gas	Run Number	z mm	P_{0c} bar	T_{0c} K	Probes	Fast Data	Sampling Frequency kHz	N
N_2	LT121	168	-	291.0	P	FLT121	472	-
N_2	LT122	168	40	291.0	P	FLT122	472	3150
N_2	LT123	139	41	291.0	P	FLT123	472	3228
N_2	LT124	53	41	291.0	P	FLT124	472	3228
N_2	LT125	80	41	293.8	P	FLT125	472	3228
N_2	LT126	103	40	293.8	P	FLT126	472	3150
N_2	LT127	117	40	292.9	P	FLT127	472	3150

Table 15 Mach 3 single jet (SM3) in quiescent

Station	Nozzle	Run	Schlieren	Total Temperature	Pitot pressure fluctuation	Heat Flux Fluctuation
40	TM5, x-z	LT150	LT9	Y	Y	Y
40	TM5, y-z	LT183	LT17	Y	Y	Y
40	SM5M	LT182	LT116	Y	Y	Y
60	TM5, x-z	LT148	LT9	Y	Y	Y
60	TM5, y-z	LT179	LT17	Y	Y	Y
60	SM5M	LT181	LT116	Y	Y	Y
100	TM5, x-z	LT145	LT9	Y	Y	Y
100	TM5, y-z	LT195	LT17	Y	Y	Y
100	SM5M	LT196	LT116	Y	Y	Y

Table 16 Quiescent twinjet and single equivalent nozzle downstream flowfield comparison

Station	Nozzle	Run	Schlieren	Total Temperature	Pitot pressure fluctuation	Heat Flux Fluctuation
10	TM5, x-z	GT700	Y	-	-	-
10	TM5, y-z	GT709	Y	-	-	-
30	TM5, x-z	GT699	Y	-	-	-
30	TM5, y-z	GT708	Y	-	-	-
50	TM5, x-z	GT698	Y	-	-	-
50	TM5, y-z	GT707	Y	-	-	-
100	TM5, x-z	GT744	Y	Y	Y	Y
100	TM5, y-z	GT746	Y	Y	Y	Y
100	SM5M	GT747	Y	Y	Y	Y
150	TM5, x-z	GT701	Y	-	-	-
150	TM5, y-z	GT710	Y	-	-	-
150	SM5M	GT716	Y	-	-	-
250	TM5, x-z	GT745	Y	Y	Y	Y
250	TM5, y-z	GT749	Y	Y	Y	Y
250	SM5M	GT748	Y	Y	Y	Y

Table 17 Gun tunnel co-flowing twinjet and single equivalent nozzle downstream flowfield comparison, N_2 injection

Station	Nozzle	Run	Schlieren	Total Temperature	Pitot pressure fluctuation	Heat Flux Fluctuation
100	TM5, x-z	GT721	Y	-	Y	Y
	TM5, y-z	GT720	Y	-	Y	Y
	SM5	GT719	Y	-	Y	Y
150	TM5, x-z	GT722	Y	-	Y	Y
	TM5, y-z	GT723	Y	-	Y	Y
	SM5	GT724	Y	-	Y	Y
250	TM5, x-z	GT727	Y	-	Y	Y
	TM5, y-z	GT726	Y	-	Y	Y
	SM5	GT725	Y	-	Y	Y

Table 18 Gun tunnel co-flowing twinjet and single equivalent nozzle downstream flowfield comparison, H_2 injection

Station	Nozzle	Run	Schlieren	Total Temperature	Pitot pressure fluctuation	Heat Flux Fluctuation
40	TM5, y-z	LT184	Y	-	Y	Y
60	TM5, y-z	LT185	Y	-	Y	Y

Table 19 Quiescent twinjet secondary jet stationary RPT probe signal